

# Spey MK202 Engine Design and Test Data Compilation

## Volume 2 - Translated from Chinese

### Selected Compilation of Spey MK202 Aircraft Engine Design and Test Documentation - Volume 2

This document is an extracted compilation of technical materials related to the design and testing of the Spey MK202 aircraft engine. The content includes detailed engineering data, experimental results, and analytical methodologies.

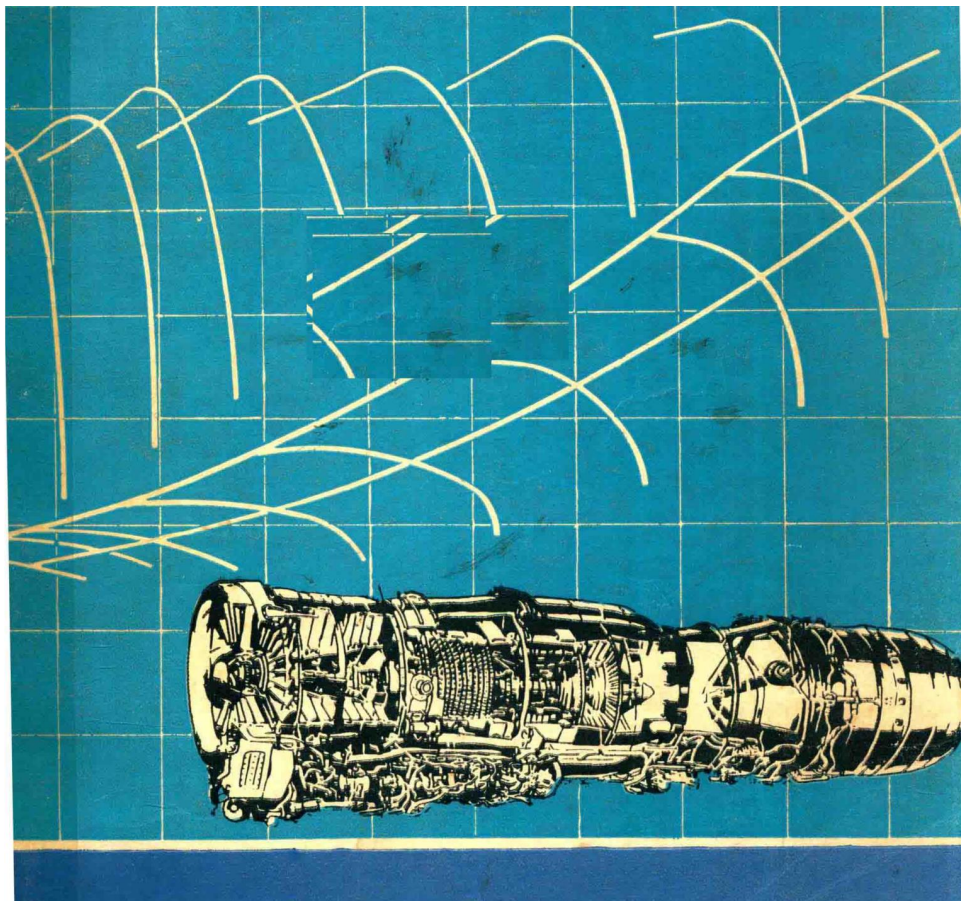
#### Processing Information

- Source document: 斯贝MK202发动机设计、试验资料选编 第2分册,4364872.pdf
- Processing date: December 14, 2025
- Processing time: 15:55:13.766372

# Spey MK202 Engine

## Selected Design and Test Documents

### Volume II



Spey MK202 Engine

Technical diagram of the Spey MK202 turbofan engine.

# Spey MK202 Engine

## Selected Design and Test Reports

### Volume II

(Internal Distribution)

Jiangsu Institute of Technology Library Collection Seal

State-Owned Hongqi Machinery Factory

### Publisher's Note

According to the provisions of the Spey MK202 engine (i.e., WS9 turbofan engine) technology import patent contract, Rolls-Royce provided 132 original design calculation reports and development test reports for the Spey MK202 engine. The content covers aerodynamic and thermodynamic design and development testing of the engine's compressor, combustion chamber, turbine, mixer, and afterburner; cooling design and testing of turbine blades; technical design of the fuel regulation system, anti-icing system, cooling system, air supply system, lubrication system, and anti-surge mechanism; stress analysis of casings, shafts, disks, blades, and mounting nodes; design concepts for gears and bearings; as well as engine starting performance and endurance testing processes. This systematically introduces the design concepts, methods, and improvement processes of the Spey MK202 engine.

This is the first time China has imported a relatively complete set of turbofan engine design materials. When these materials arrived at the factory in 1976, the Sixth Academy of the Ministry of Aviation Industry organized relevant factories, design research institutes, and universities under its jurisdiction to study and digest them in the form of reverse engineering, learning many useful design methods in the process. Some of these materials indeed have reference value for the development of new engines in China.

To facilitate the promotion of Spey design technology, in early 1981, the ministry leadership assigned Comrade Wu Da Guan to be specifically responsible for the evaluation and publication of these materials. In February of the same year, a publication review meeting for Spey engine design and test materials was held with the participation of relevant factories, design research institutes, and universities under the Sixth Academy of the Ministry of Aviation Industry. At this meeting, all 132 reports were evaluated one by one and classified into the following four categories:

1. Those with reference value for the development of new aero-engines in China;
2. Those with reference value for the modification and development of the Spey MK202 engine itself;
3. Those with reference value for the design and development of industrial gas turbines and marine gas turbines in China;
4. Those with generally outdated content and limited reference value.

Based on this classification, all 26 reports from the first category and 20 reports from the second and third categories were selected for publication, totaling 46 reports. The review meeting also recommended publishing the lecture notes "Spey MK202 Engine Technical Design (EGD-6)" and "Spey MK202 Engine Stress Analysis (EGD-7)" compiled by Rolls-Royce during the training of Chinese technical personnel in the UK.

Although only 46 reports are selected for this compilation, the content remains relatively comprehensive, essentially retaining the essence of each type of report. We hope that this compilation, along with the already published "EGD-3," "EGD-6," and "EGD-7," will be helpful to those engaged in gas turbine research, design, manufacturing, and teaching, enabling Spey technology to play its due role in promoting the development of China's gas turbine industry.

This compilation is published in three volumes: Volume I covers the design and development of compressor and turbine components; Volume II covers the design and development of the main combustion chamber, afterburner, fuel regulation system, nozzle control system, and anti-surge mechanism; Volume III covers stress analysis of disks, shafts, casings, mounting nodes, gears, and bearings, as well as technical design of the lubrication system and starting system.

## Translation and Review Team for Volume II

- Li Jianmin, Tang Ruixin, Dong Zhenglin, Zhao Qingjie, Zhang Maoxi, Jiang Yijun, Zhang Dunyu, Zhao Chengsheng, Chen Zhijie, Liu Dawei, Rong Weijun, Xuan Baohua, Xu Juzhen, Xu Zhenyong, Fan Zuomin, Liang Junxiang (624 Institute)
- Yang Maolin, Liu Gaoen, Li Xiangyi, Gu Shanjian, Chen Nengkun, Zhao Qishou, Wang Huafang, Wu Shousheng, Cao Minghua (Beijing University of Aeronautics and Astronautics)
- Cao Lidan, Deng Guoming, Fu Sen, Xu Xingyan, Zhang Xiuying, Zhou Qingtai (Factory 113)

After the Volume II translation was collected at Hongqi Machinery Factory, Comrade Wang Zhizhong from the publishing team conducted a comprehensive review, and it was finally reviewed and finalized by Comrade Wu

Da Guan.

Readers are welcome to criticize and correct any inappropriate translations in this book.

Spey Design and Test Materials Publishing Group

## Volume 2 Table of Contents

1. CRR12086 Aerothermodynamic Design of the Spey MK202 Combustion Chamber (1)
2. CRR12087 Design of the Spey MK202 Fuel Nozzles (9)
3. CRR12091 Performance of the Spey MK202 Finalized Combustion System (58)
4. CRR12078 Development of the Spey MK202 Afterburning System (64)
5. CRR12019 Research on the Stability of Spey MK202 Afterburning Combustion (77)
6. CRR86020 Afterburning Ignition Tests of the Spey MK202 Afterburning System Conducted on the Altitude Test Facility (Catalytic Igniter Installed in the Afterburner Center) (85)
7. DTR86052 Results of Afterburning Ignition and Extinction Tests Conducted on Engine No. 41/15, Recommendations for Future Tests (96)
8. DTR86055 Summary of Afterburning Ignition and Extinction Tests of Engine No. 20003 with H366T Afterburner Conducted on the Altitude Test Facility (97)
9. PTR12257 Test Results and Discussion of the H346 Afterburner Installed on the Spey MK202 Engine Simulator at the Altitude Test Facility (107)
10. PTR12169 Results and Discussion of High and Low Operating Line Calibration Tests in Non-Afterburning Mode Using the Spey MK202 Simulator on the Altitude Test Facility (114)
11. PTR12571 Altitude Test Facility Tests of Spey MK202 Engine No. 20003/7 – Establishing Standards for the Current Production Afterburning System (128)
12. CRR12043 Ignition Tests of the Catalytic Igniter Installed at the Center of the Spey MK202 Afterburner (152)
13. CRR12079 Review of Spey MK202 Afterburner Design Methods (166)
14. CRR12080 Derivation of the King's Combustion Efficiency Relationship for the Spey MK202 (204)
15. CRR12081 Design of the Spey MK202 Afterburner Catalytic Ignition System (207)
16. CRR12082 Design of the Spey MK202 Afterburner Heat Shield (216)
17. CRR12083 Design of the Spey MK202 Afterburner Fuel Manifold (233)
18. CRR12084 Development of the Spey MK202 Afterburner Vaporizing Stabilizer (246)
19. CRR12051 Development of the Spey MK202 Mixer (255)
20. TDR7787A Spey MK202 Fuel Control System – High-Pressure Fuel Pump Design Data (261)
21. TDR784 Estimation of Maximum Fuel Flow for the Spey MK202 (275)
22. TDR3934 Determination of High-Pressure Fuel Pump Output Pressure for the Spey MK202 (278)
23. TDR3954 Flow Requirements for the Spey MK202 High-Speed Flushing Filter and High-Pressure Fuel Pump (279)
24. TDR4167 Explanation of the Use of Engine Main Pump Flow in the Spey MK202 Afterburner Acceleration Control System (282)
25. TDR7357 Estimation of Servo Pressure Drop for the Spey MK202 – Recommendations for Redesigning the High-Pressure Pump Servo Piston to Improve AVCAT Fuel Relight Capability (283)
26. TDR7787B Spey MK202 Fuel Control System – CASC Design Data (285)
27. TDR796 Estimation of Flight Idle Speed for the Spey MK202 (302)
28. TDR797 Proposed N<sub>2</sub> - T<sub>1</sub> and T<sub>6</sub> - T<sub>1</sub> Control for the Spey MK202 (311)
29. TDR3918 Relationship Between Net Thrust and Engine Control Input Angle for the Spey MK202 (313)
30. TDR4121 Method for Estimating Engine Idle Speed for the Spey MK202 (315)
31. TDR4181 Drift of the High-Pressure Rotor Speed Regulator for the Spey MK202 Under Various Flight Conditions (321)
32. TDR4184 Estimation of Idle Conditions for the First Flight Engine of the Spey MK202 (321)
33. TDR7799 Estimation of Maximum High-Pressure Compressor Outlet Pressure Due to Failure of the P<sub>3</sub> Limiter for the Spey MK202 (327)

34. TDR7787C Spey MK202 Fuel Control System – Maximum Temperature Limiter, Low-Pressure Shaft Speed Limiter, and Other Items (3)
35. TDR7754 Characteristics of Secondary Nozzle Fuel Flow Relative to Main Nozzle Fuel Flow for the Spey MK202 (3)
36. TDR7778 Adoption of the Overflow Valve in the Spey MK202 Acceleration Control Device (351)
37. TDR7782 Spey MK202 Pressure Ratio Regulator's Two- and Three-Taper Needle Valves (353)
38. FDR10311 Role of the Dual-Function  $P_3$  /  $P_6$  Needle Valve Under Rapid Afterburner Acceleration Conditions (355)
39. TDR7788 Spey MK202 Afterburner Fuel Control System (359)
40. TDR770 Design Requirements for the Spey MK202 Afterburner Fuel Control System (366)
41. TDR7789 Spey MK202 Pressure Ratio Regulator and Nozzle Control System (37)
42. TDR779 Determination of Servo Needle Valve Profile and Estimation of Afterburner Response Characteristics for the Spey MK202 Afterburner Nozzle Control System (381)
43. TDR4159 Reduction of Air from the 7th Stage for Pressurizing the Nozzle Control System Oil Tank in the Spey MK202 (393)
44. TDR7107 Compensation for Engine Performance During Forward Acceleration for the Spey MK202 (395)
45. TDR7791 Spey MK202 Inlet Guide Vane and Bleed Valve Control System (41)
46. TDR2633 Principles of the Inlet Guide Vane and Bleed Valve Control System for a Twin-Spool Engine Using the Spey MK202 (403)
47. TDR2638 Principles of Programmed Control for the Inlet Guide Vanes of a Twin-Spool Engine Using the Spey MK202 (407)
48. TDR2664 Requirements for the  $T_1$  Thermocouple and Ejector Design Principles for a Twin-Spool Engine Using the Spey MK202 (413)
49. TDR3990 Interim Description of the  $T_1$  Thermocouple and Ejector System Performance for the Spey MK202 (418)
50. TDR4115 Errors in the  $T_1$  Thermocouple and Inlet Guide Vane System for the Spey MK202 (420)
51. TDR4147 Estimation of Allowable Rate of Change of Inlet Temperature ( $T_1$ ) for the Spey MK202 (421)
52. TDR4164 Estimation of the Limit for Inlet Temperature Rate of Change to Prevent High-Pressure Compressor Surge in the Spey MK202 (425)

## Appendices

- Appendix I: CASC System Theory (331)
- Appendix II: Examples of Initial CASC Calculations (333)

Combustion Research Report

Report Type	Report Number
	CRR 12086
Spey MK202 Engine Combustion Chamber Aerothermodynamic Design	

## 1. Introduction

Reference [1] outlines the performance requirements for the MK202 combustion chamber. This report describes the methods used in the design of the tubo-annular combustion chamber to meet these requirements.

The design of the MK202 is fundamentally based on the civil Spey design, which was initially derived from existing engine designs at the time. After the initial design phase, experience was accumulated, and design methods were revised where necessary. This report presents these methods, which can now be used at the start

of a new design, rather than the methods originally employed for the Spey.

## 2. Combustion Chamber Overview

The combustion chamber consists of a number of circular flame tubes. Each flame tube is equipped with an air intake (commonly referred to as a 'snout') and a fuel nozzle at the front (upstream) end, and a gas duct at the rear to guide high-temperature gases into the turbine. The flame tubes are secured within an annular cavity formed by the inner and outer casings. For ignition, interconnector tubes are installed between the flame tubes to allow flame propagation from the two flame tubes equipped with ignition plugs.

Before the airflow enters the intake holes of the flame tube, the velocity of the airflow from the compressor must be significantly reduced. Control of this diffusion process is critical to the successful operation of the combustion chamber.

The combustion chamber space (the volume enclosed by the flame tube and gas duct) can be divided into three zones (see Figure 1):

- (i) Primary Zone or Recirculation Zone: In this zone, fuel is injected as a well-atomized spray cone, and the flame is stabilized by continuous recirculation of a portion of the high-temperature combustion gases. The high-temperature gases flow back from the rear of the flame tube into the fuel spray. This zone extends from the front of the flame tube to the rear of the secondary air holes.
- (ii) Intermediate Zone or Secondary Zone: In most cases, combustion reactions are completed in this zone. The amount of air entering this zone depends on the average fuel-air ratio required to be below a certain limit, as explained in Section 4.1.
- For the Spey, apart from the air entering from the primary zone, the air entering this zone comes through the wall cooling holes.
- (iii) Dilution Zone or Tertiary Zone: The remaining air is supplied to this zone to meet the temperature distribution requirements at the gas duct outlet, as specified in Section 4.6 of Reference [1].

At the secondary air hole section, 5.5% of the compressor discharge air is extracted through the inner casing to cool the turbine. Additionally, 3.8% of the air is extracted from the rear of the gas duct to cool the turbine guide vanes.

## 3. Combustion Chamber Flame Tube Dimensions

The design of the tubo-annular combustion chamber must meet the following requirements:

1. The volume of the primary zone must be sufficiently large to ensure an adequate in-flight relight envelope (Section 4.1 of Reference [1]).
2. The length-to-depth ratio of the flame tube must be sufficiently large to ensure adequate mixing of the fuel-air mixture before the gas duct outlet plane.
3. The total volume enclosed by the flame tube and gas duct must be sufficiently large to avoid limiting the temperature rise required by the engine when accelerating to idle after an in-flight relight.
4. To minimize flow disturbances, the flame tube should be positioned as close as possible to the average radius of the compressor outlet.
5. When installed in the engine, there must be adequate spacing between flame tubes. The following factors must also be considered:
  6. The flow area for flame tube cooling air.
  7. The length of the interconnector tubes must be minimized.
- The combustion chamber should be as short as possible to reduce weight and minimize the amount of cooling air required for the flame tube (this is critical for controlling the temperature distribution at the flame tube outlet section).

To meet the above requirements, the number and size of the flame tubes are matched as follows:

- 3.7.1 The structure of the primary zone is determined based on earlier designs with good relight performance. The latter had an ignition range similar to or slightly better than the new design requirements.

The scaling method is based on the following:

- (a) Under similar fuel atomization characteristics and constant inlet pressure and temperature, the ignition performance of the combustion chamber is proportional to the volume ( $V$ ) of the primary zone and inversely proportional to the airflow ( $M_p$ ) entering the primary zone.
- (b) At any flight speed and altitude, when the engine flames out (windmilling condition), the pressure and temperature at the combustion chamber inlet remain essentially constant, regardless of the engine type. Thus, the total airflow ( $M$ ) through the flame tube is proportional to the 'effective throat area of the high-pressure turbine guide vanes ( $A_\square$ ).'
- $A_\square$  is defined as 'the area at which choking occurs (Mach number = 1.0) at the gas duct outlet under design or takeoff conditions.'
- (c) For a single flame tube, the volume of the primary zone is proportional to the cube of the flame tube diameter ( $D$ ). Therefore, the total volume of the primary zone is proportional to  $N D^3$ , where  $N$  is the number of flame tubes.
- (d) The proportion of airflow entering the primary zone  $M_\square / M$  is derived from the richest stable combustion condition (see Section 4.1).
- As described above, when ignition performance remains constant,  $V \propto N D^3 \propto M_\square \propto (\text{rac}M_\square M \text{imes} M \text{ight}) \propto \text{rac}M_\square M \cdot A_\square$ . For the MK202,  $A_\square = 41.8 \text{ in}^2$ , and  $\text{rac}M_\square M = 37.5\%$ .
- Based on this scaling of earlier designs, the required  $N D^3$  value to meet relight requirements at 33,500 feet altitude is  $1,400 \text{ in}^3$ .

$$N = (9.67 \times 2 \pi) / (D + 0.57)$$

Formula for calculating the number of flame tubes based on the pitch radius and flame tube diameter.

### 3.7.2 Number of Flame Tubes

To meet the requirements in Sections 3.5.1 and 3.5.2, the minimum spacing between flame tubes when installed in the engine is set at 0.27 inches. Thus, the distance between the inner diameters ( $D$ ) of the flame tubes is 0.57 inches. When arranging the flame tubes along the average radius of 9.67 inches at the compressor outlet, the number of flame tubes can be approximated by the following formula:

$$N = (9.67 \times 2 \pi) / (D + 0.57)$$

Approximate formula for calculating the number of flame tubes.

Considering the requirement for  $N D^3$  ( $= 1,400 \text{ in}^3$ ), the number of flame tubes is calculated to be 10.8, which is rounded to 10. To maintain the same spacing between flame tubes, the radius of the flame tube centerline is reduced to 9.35 inches.

### 3.7.3 Combustion Length

Once the diameter of the primary zone flame tube is determined, the combustion length (from the fuel injection plane to the gas duct outlet) can be derived based on the length-to-diameter ratio applicable to various combustion chambers. The length-to-diameter ratio for the Spey is 2.66, which is relatively short compared to many other designs but has proven to be highly satisfactory.

### 3.7.4 Total Combustion Volume

Although the combustion volume (the volume enclosed by the flame tube and gas duct) is effectively determined by the primary zone dimensions and combustion length, the ability of the combustion chamber to handle high-altitude relight requirements should also be considered.

This volume is only critical during relight at high altitude and low speed (Mach number below 0.6). Under these conditions, it is possible for the combustion chamber to ignite but the engine fails to accelerate to idle speed. This occurs due to low combustion efficiency, a phenomenon common to all combustion chambers when inlet pressure and temperature are very low. As altitude increases, pressure and temperature become extremely low, and combustion efficiency drops significantly (typical value of 10%), resulting in insufficient temperature rise in the combustion chamber to accelerate the engine, regardless of the amount of fuel injected.

One method to improve combustion efficiency is to increase the combustion volume. This raises the altitude at which 'acceleration failure' occurs. This issue has not been encountered in the Spey engine. However, to ensure cold relight capability at 28,500 feet, it is undesirable to reduce the scaled combustion volume determined for the Spey. The scaled volume for the Spey was determined by considering both ignition performance and length-to-depth ratio, with the minimum ratio given by:

$$((354)/(40) + (3)/(4) \times 11)/(A\Box) = (2540 \times 11.5 \times 7)/(41.8 \times 11.5 \times 7) = 60.7$$

Minimum scaled combustion volume ratio for the Spey MK202.

### 3.7.5 Casing Dimensions

After determining the flame tube dimensions and arrangement radius (pitch radius), the diameters of the inner and outer casings are set as follows:

- (a) The inner diameter of the outer casing is set at 24.56 inches, with a minimum practical clearance of 0.2 inches between the casing and the flame tube.
- (b) The inner casing was initially arranged such that the airflow area on the inner half of the flame tube (supply area) to the open hole area ratio was equal to that of the outer half. During development, the size of the flame tube openings was changed, and this ratio is no longer equal. However, this is not considered critical.

The inner casing diameter is 12.02 inches, with a clearance of 0.6 inches between the casing and the flame tube.

## 4. Flow Distribution

The airflow distribution entering the combustion chamber is shown in Figure 2. The rationale for this distribution is as follows:

### 4.1 Primary Zone

This zone extends to the rear of the secondary air holes (see Figure 1). The total airflow is set such that under the richest stable combustion conditions, the average fuel-air ratio at the zone outlet is 0.057. This mixture concentration ensures sufficient oxygen is supplied to complete combustion in the intermediate zone while preventing excessive heat flux radiated to the flame tube walls. Under these conditions, the total airflow entering the primary zone accounts for 37.5% of the combustion chamber airflow.

The distribution of airflow between the swirler, secondary air, and cooling air is primarily based on earlier experience. While it is desirable to use most of the air for cooling the flame tube head, this proportion must balance wall temperature and combustion efficiency, as excessive cooling air can severely impact combustion efficiency.

$$\frac{\text{燃烧容积}}{A_T} = \frac{2540 \text{ 英寸}^3}{41.8 \text{ 英寸}^2} = 60.7$$

Figure 1: Schematic of the Spey MK202 Combustion Chamber Zones

Diagram showing the three zones of the Spey MK202 combustion chamber: primary (recirculation), intermediate (secondary), and dilution (tertiary) zones.

$$N = \frac{9.67 \times 2\pi}{D + 0.57}$$

Figure 2: Airflow Distribution in the Spey MK202 Combustion Chamber

Diagram illustrating the airflow distribution into the primary, secondary, and dilution zones of the Spey MK202 combustion chamber.

## 4.2 Intermediate Zone

As mentioned in Section 2, the amount of air required for the zone where only cooling air enters the flame tube is still determined based on early experience and subsequent tuning on combustion test rigs. The mechanism of heat transfer to the wall is too complex to allow reliable analysis at the design stage, although wall temperatures can be calculated analytically under conditions of mild extrapolation. The description of this method is provided in Appendix 1.

## 4.3 Mixing Zone

The primary consideration for the mixing zone is effective wall cooling. The remaining air can then be introduced through mixing holes. The size and arrangement of the mixing holes are discussed in Section 7.3.

# 5. Pressure Drop Selection

Although the pressure drop across the combustion chamber does not significantly affect engine performance, it is clearly desirable to minimize it. A key requirement for the combustion chamber is to accommodate the basic total pressure distribution at the compressor outlet and to minimize changes in combustion chamber performance caused by variations in this total pressure distribution during engine operation. For this reason, pressure loss is typically related to the dynamic head at the compressor outlet (the difference between average total pressure and static pressure). In this case, the total loss through the combustion chamber equals one dynamic head calculated based on a compressor outlet area of 74.7 square inches.

This loss can be divided into four parts:

1. Loss between the compressor outlet and the inlet front end.
2. Loss from the inlet front end to the flame tube.
3. Pressure drop along the flame tube.
4. Basic loss due to heating (a function of the temperature ratio  $T_{outlet}/T_{inlet}$  across the combustion chamber).

The approximate values for the four pressure drops are: (a) 0.13 velocity heads, (b) 0.13 velocity heads, (c) 0.67 velocity heads, (d) 0.07 velocity heads when  $T_{outlet}/T_{inlet} = 2.0$ .

# 6. Diffuser Design

The air from the compressor outlet must be decelerated before entering the flame tube for the following reasons:

- The higher the airflow velocity near the holes, the lower the flow coefficient. This requires an increase in hole area.
- High airflow velocity between the flame tube and casing demands a very small air gap, which is impractical.
- Changes in channel shape or obstacles (fuel pipes, igniters, interconnector tubes) will cause large pressure drops and severe flow disturbances.

In the cannular combustion chamber design, controlling this diffusion process is challenging. The inlet channel is annular, but downstream, a significant amount of air flows into the space between the circular flame tubes and the annular casing. The problems caused by this change in channel shape are exacerbated by large struts and non-uniform total pressure distribution at the compressor outlet section.

For the section before the channel shape changes, the Spey engine employs a large-angle diffuser (included angle of 14°), increasing the annular cross-sectional area by 0.5 times. The channel shape is then altered through the air inlet at the front of the flame tube. The diffuser profile is designed to ensure that the flow area

remains virtually unchanged during the channel shape transition.

The front end of the inlet is positioned at the location of the highest pressure at the diffuser outlet. This is not only to direct air into the first zone of the flame tube but also to divert air backward into the gaps between the flame tube and the inner and outer casings. Without this device, the airflow entering the gaps between the flame tube and the inner and outer casings would consist of low-pressure air from the compressor blade roots, tips, and along the diffuser walls. The resulting poor annular channel velocity distribution would seriously affect the flame tube wall temperature (see Section 2 and Figure 5 in Reference 2).

Baffles and deflectors installed at and behind the mixing holes are also used to mitigate the effects of poor total pressure distribution. For a simple open channel with side-wall exhaust, variations in supply pressure will create strong disturbances downstream. These disturbances generate local vortices, which, if their centers are at the intake holes, will reduce the flow through the holes. In extreme cases, this can cause hot gas to flow from the flame tube into the annular cavity. The presence of deflectors can significantly reduce such disturbances, while any smaller vortices are controlled and minimized by baffles (see Section 2 and Figure 4 in Reference 2).

## 7. Flame Tube Design

### 7.1 Primary Zone

In the primary zone (see Figure 1), a swirler is installed around the fuel nozzle to create a recirculation of hot gases. The swirler channels 11% of the total flame tube airflow, with ten straight blades set at a  $45^\circ$  angle to induce rotation. This swirling air then flows into a hemispherical head, providing a sufficiently large contact area to carry away the hot gases from the recirculation zone.

Secondary air jets injected from ten secondary air holes (matching the number of swirler blades) enhance the recirculation. The arrangement of these secondary air holes is one of the most critical aspects of combustion chamber design. This is because the secondary air serves two purposes: controlling the flow pattern in the recirculation zone and providing a satisfactory mixture distribution for the intermediate zone. Extensive research was conducted on the secondary air intake scoops in this design to achieve satisfactory mechanical and thermal performance (see Section 7 in Reference 2).

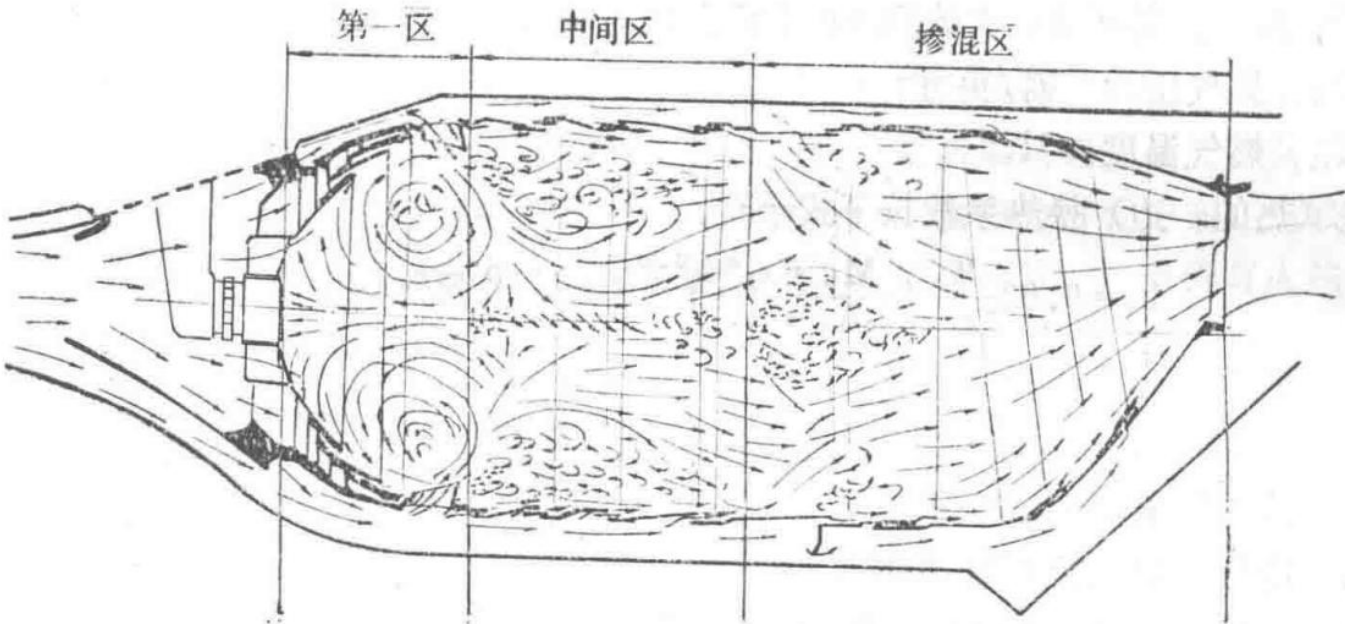


Figure 1 Flow Pattern in the Spey MK202 Combustion Chamber

Diagram illustrating the airflow patterns within the primary, intermediate, and mixing zones of the Spey MK202 combustion chamber.

## 7.2 Intermediate Zone

The intermediate zone accounts for 32% of the total combustion volume. Its functions are to complete the reaction processes initiated in the primary zone and to provide a mixing length before the introduction of dilution air. Under high-pressure conditions, it also serves to burn off a significant amount of carbon (or soot) produced in the primary zone.

The flame tube walls are cooled by a series of slots controlled by corrugated strips. Ideally, cooling air film would be introduced into the flame tube through a continuous annular passage, but this is impractical. Extensive research was conducted on the design of the cooling strips, and it has been demonstrated that corrugated strips offer the best compromise among cooling efficiency, mechanical reliability, and cost (including manufacturing and maintenance).

## 7.3 Mixing Zone

The primary mixing holes must serve two functions:

- Evenly distribute cold air into the combustion gases.
- Generate high mixing velocities.

Although small-hole jets mix faster than large-hole jets, they cannot penetrate to the center of the flame tube. Therefore, most of the dilution air is injected through four large holes from the deepest part of the annular cavity between the flame tube and the inner and outer casings into the hot gases from the intermediate zone.

Achieving the required outlet temperature distribution (as specified in Section 4.6 of Reference 1) relies almost entirely on tuning conducted on combustion test rigs or engines. It was during this tuning process that three smaller holes were added. Based on mechanical and aerodynamic considerations, all mixing holes are equipped with radial flanges. These flanges reduce crack propagation from the edges, and the flange radius helps maintain a nearly constant jet penetration angle.

All cooling air for the gas duct section in this zone is introduced through splash cooling rings. This air cools the liner strips by splashing or impingement before forming a film as it enters the combustion space. This type of ring is less effective than corrugated strips but is the only mechanically adaptable form for the complex profile of the gas duct, especially where it intersects with the ten turbine bearing struts and transitions from circular to annular shape.

## 7.4 Interconnector Tube Design

The primary zones of the ten flame tubes are interconnected by interconnector tubes. During engine start-up, these tubes allow the flame to propagate from the two flame tubes equipped with igniters to the remaining flame tubes. To effectively propagate the flame (especially during high-altitude relight), the interconnector tubes should be positioned as close as possible to the flame tube head, their cross-sectional area should be maximized, and their length should be minimized. Cold air entering the interconnector tubes (whether for cooling or due to leakage) will cool the propagating flame and impair ignition propagation characteristics. However, without cooling air, the interconnector tubes may overheat, and if the tubes are too large, the downstream flow may be affected, leading to localized overheating of the flame tube. Therefore, extensive tuning was required to determine a satisfactory compromise for the interconnector tube area (see Sections 8 and 9 in Reference 2). Once all flame tubes are ignited, there is no longer a need for hot gas to flow through the interconnector tubes.

## References

- [1] CRR12085 - Performance Requirements for the Spey MK202 Combustion System
- [2] CRR12090 - Development of the Spey MK202 Combustion System

# Appendix 1

## Heat Transfer Processes in the Combustion Chamber

Under steady-state conditions, the wall temperature at any point on the combustion chamber flame tube is the result of a balance among four heat flows:

$$R_1 + C_1 = R_2 + C_2$$

Heat balance equation for the flame tube wall, where  $R_1$  is radiative heat transfer from gas to wall,  $C_1$  is convective heat transfer from gas flow to wall,  $R_2$  is radiative heat transfer from wall to casing, and  $C_2$  is convective heat transfer from wall to external air.

Where: -  $R_1$ : Radiative heat transfer from gas to wall -  $C_1$ : Convective heat transfer from gas flow inside the flame tube to the wall (sometimes negative) -  $R_2$ : Radiative heat transfer from wall to casing -  $C_2$ : Convective heat transfer from flame tube to external air

Note: Heat conduction through the flame tube wall is typically negligible and is not considered here. The above quantities are all functions of wall temperature:

$$R_2 = 1.01 \times 10^{-8} E\Box FF (TW^4 - TC^4)$$

Radiative heat transfer from wall to casing, where  $E\Box FF$  is the effective emissivity,  $TW$  is wall temperature, and  $TC$  is casing temperature.

Where: -  $EW$ : Wall emissivity (taken as 0.7) -  $EG$ : Gas emissivity (see below) -  $TG$ : Gas temperature ( $^{\circ}K$ ) -  $TW$ : Wall temperature ( $^{\circ}K$ ) -  $TC$ : Casing temperature (based on compressor discharge temperature) ( $^{\circ}K$ ) -  $E\Box FF$ : Effective emissivity for specific geometry (taken as 0.396  $CHU/ft^2 \cdot hr \cdot K^4$ )

$$C_1 = h_1 (TF - TW)$$

Convective heat transfer from gas to wall, where  $h_1$  is the heat transfer coefficient and  $TF$  is the film temperature.

$$C_2 = h_2 (TW - TC)$$

Convective heat transfer from wall to external air, where  $h_2$  is the heat transfer coefficient.

Where: -  $h_1$ : Heat transfer coefficient ( $CHU/ft^2 \cdot hr \cdot K$ ) (see below) -  $TF$ : Film temperature (function of the amount of hot gas entrained in the film, determined by the dimensionless film temperature  $\eta F$ ) -  $h_2$ : Heat transfer coefficient for airflow over the flame tube outer wall (see below) -  $TC$ : Air temperature outside the flame tube (based on compressor discharge temperature) ( $^{\circ}K$ )

The gas emissivity (EG) is calculated as follows:

$$EG = 1 - [ -1.09 \times 10^3 PG L (r \cdot I)^{0.5} TG^{-1.5} ]$$

Gas emissivity equation, where  $PG$  is gas pressure,  $L$  is luminosity factor,  $r$  is fuel-air ratio,  $I$  is radiation length, and  $TG$  is gas temperature.

Where: -  $L$ : Luminosity factor (1.72 for kerosene) -  $r$ : Fuel-air ratio (local value) -  $I$ : Radiation length (0.6 times diameter for circular flame tube) (ft) -  $PG$ : Gas pressure ( $lb/in^2$ ) -  $TG$ : Gas temperature ( $^{\circ}K$ )

The heat transfer coefficient on the inner wall (hot side) is given by:

$$h_1 = (K_1)/(x_1) ( (MF x_1)/(AF \mu) )^{0.8}$$

Heat transfer coefficient for the inner wall, where  $K_1$  is thermal conductivity of the cooling air film,  $x_1$  is hydraulic diameter,  $MF$  is film flow rate,  $AF$  is initial film area, and  $\mu$  is dynamic viscosity.

Where: -  $K_1$ : Thermal conductivity of the cooling air film (CHU/ft·hr·°K) -  $x_1$ : Hydraulic diameter of the film =  $2 \times$  film slot height - MF: Cooling film flow rate (lb/hr) - AF: Initial film area ( $\text{ft}^2$ ) -  $\mu$ : Dynamic viscosity of the cooling film flow (lb/ft·hr)

The film temperature TF is a function of the amount of hot gas entrained in the film and is determined by the dimensionless film temperature  $\eta F$ , commonly referred to as film efficiency:

$$\eta F = (TG - TF)/(TG - TC)$$

Film efficiency, where TG is gas temperature, TF is film temperature, and TC is cooling air temperature.

Thus:

$$TF = TG - \eta F (TG - TC)$$

Film temperature as a function of gas temperature, cooling air temperature, and film efficiency.

The empirical relationship for  $\eta F$  is:

$$\eta F = 1 - ( -44.1 / X )$$

Empirical relationship for film efficiency, where X is a dimensionless parameter.

Where:

$$X = \alpha ( (VG)/(VC) )^{0.8} ( (TG)/(TC) )^{0.2} (x^{0.8})/(s) \quad (\text{when } (VG)/(VC) \geq 0.8)$$

Dimensionless parameter X for film efficiency when  $VG/VC \geq 0.8$ .

$$X = \alpha ( (VG)/(VC) )^{0.6} ( (TG)/(TC) )^{0.2} (x^{0.8})/(s) ( (VG)/(VC) + 0.2 )^{-1.25} \quad (\text{when } (VG)/(VC) < 0.8)$$

Dimensionless parameter X for film efficiency when  $VG/VC < 0.8$ .

Where: -  $\alpha$ : Empirical coefficient dependent on film slot geometry (for Spey corrugated strips,  $\alpha = 3.0$ ) -  $x$ : Distance along the flow direction from the film inlet plane (inches) -  $s$ : Film slot height (inches) - VG, VC: Velocities of hot gas and film at the inlet, respectively

The heat transfer coefficient on the outer wall (cold side) of the flame tube ( $h_2$ ) is given by:

$$h_2 = 0.02 (K_2)/(x_2) ( (M \square x_2)/(A \square \mu) )^{0.8}$$

Heat transfer coefficient for the outer wall, where  $K_2$  is thermal conductivity of cooling air,  $x_2$  is hydraulic diameter,  $M \square$  is airflow rate,  $A \square$  is flow area, and  $\mu$  is dynamic viscosity.

Where: -  $K_2$ : Thermal conductivity of cooling air (CHU/ft·hr·°K) -  $x_2$ : Hydraulic diameter of the supply annulus =  $4 \times$  flow area / wetted perimeter -  $M \square$ : Airflow rate outside the flame tube (lb/hr) -  $A \square$ : Flow area of the annulus ( $\text{ft}^2$ ) -  $\mu$ : Dynamic viscosity of the annulus airflow (lb/ft·hr)

Since the metal wall temperature  $TW$  is unknown, the heat balance equation is solved using an iterative approximation method. Given the large computational load, the solution process is typically performed on a digital computer.

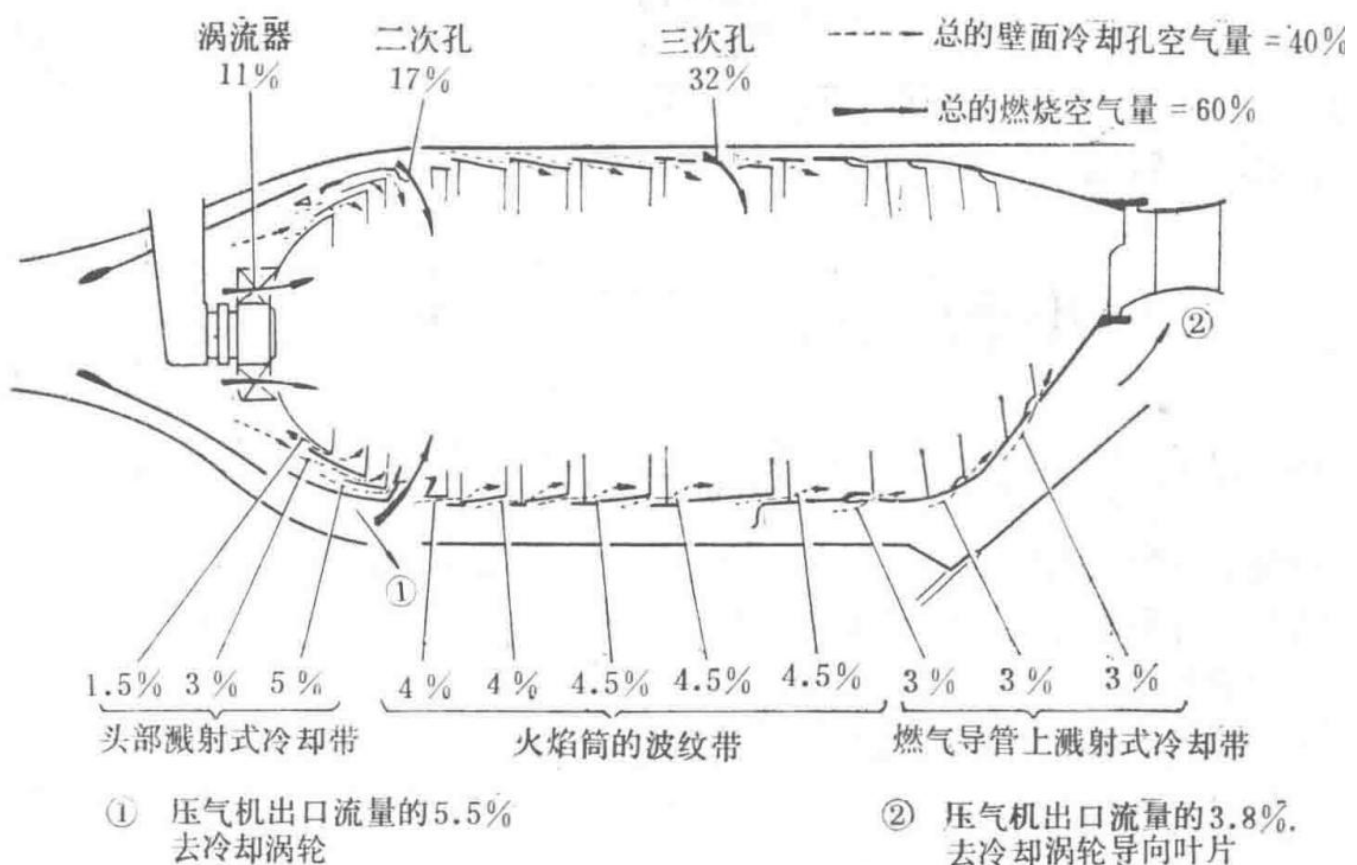


Figure 2 Airflow Distribution in the Spey MK202 Combustion Chamber

Diagram showing the distribution of airflow within the Spey MK202 combustion chamber, including primary, intermediate, and dilution zones.

— Section 4 —  
Content from Original Document (Pages 16-20)

Document Header

Report Title	Report Number
Combustion Research Report	CRR12087
	Spey MK202 Engine Fuel Nozzle Design

## Introduction

A centrifugal nozzle consists of a swirl chamber and a nozzle orifice. Fuel enters the swirl chamber through tangential slots (machined tangentially to the swirl chamber wall), then exits the nozzle orifice in the form of a well-atomized spray cone.

The tangential velocity of the fuel, generated by the pressure drop across the inlet slots, is converted into three velocity components (tangential, radial, and axial), forming a free vortex with superimposed axial velocity. As the fuel exits the nozzle orifice, it possesses both tangential and axial velocity components, creating a hollow spray cone.

The theory describing this mechanism, considering friction, boundary layers, and viscous effects, is highly complex. Rolls-Royce's approach involves designing nozzles using empirical methods. These methods are based on the theory of single-circuit centrifugal nozzles (ignoring losses) and are established through data accumulated from numerous practical designs.

## Abstract

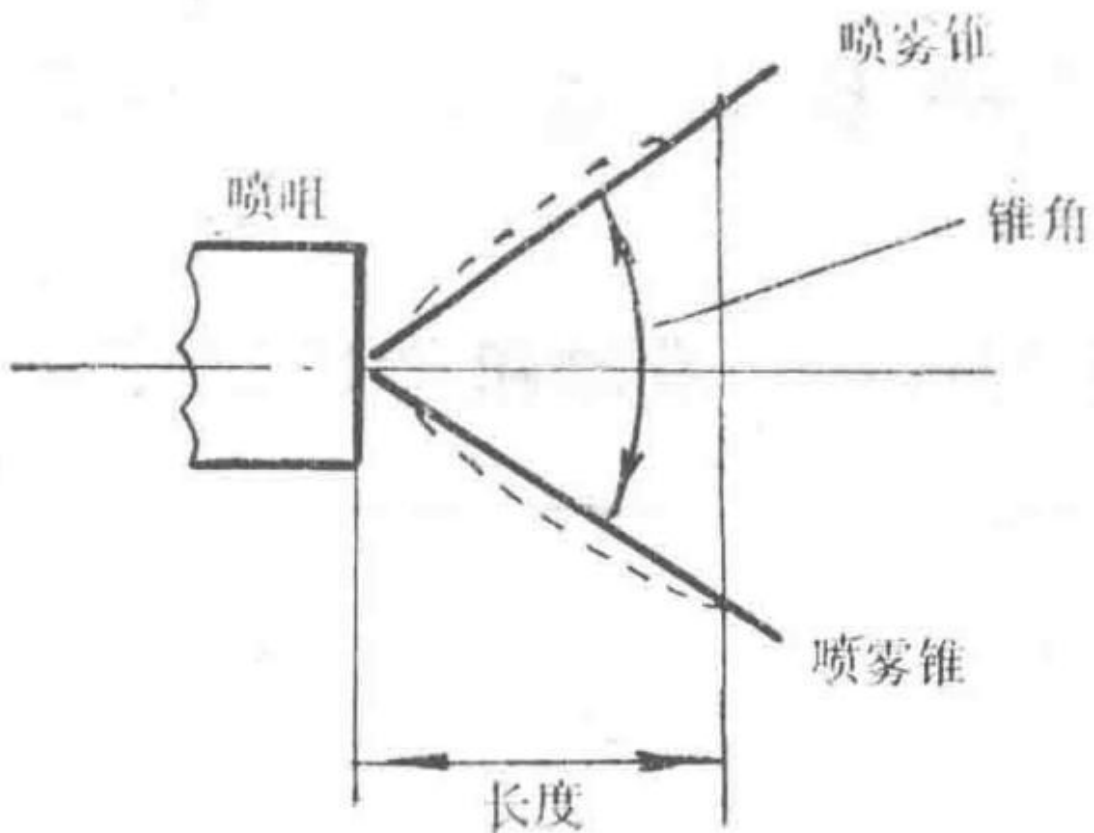
Centrifugal nozzles can now be designed to meet the following conditions: flow number range of 0.2-0.9 with an error of  $\pm 5\%$ , and spray cone angle of  $70^{\circ}15'$  with an error of  $\pm 5'$ . Most fuel nozzles used by Rolls-Royce are dual-circuit, consisting of two single-circuit nozzles in parallel. One is nested inside the other, and the additional design features required for such nozzles are provided in Appendix 2.

## Basic Definitions

$$\text{Flow Number (FN)} = (Q)/(\sqrt{P})$$

Flow number definition, where Q is the flow rate and P is the pressure drop across the nozzle.

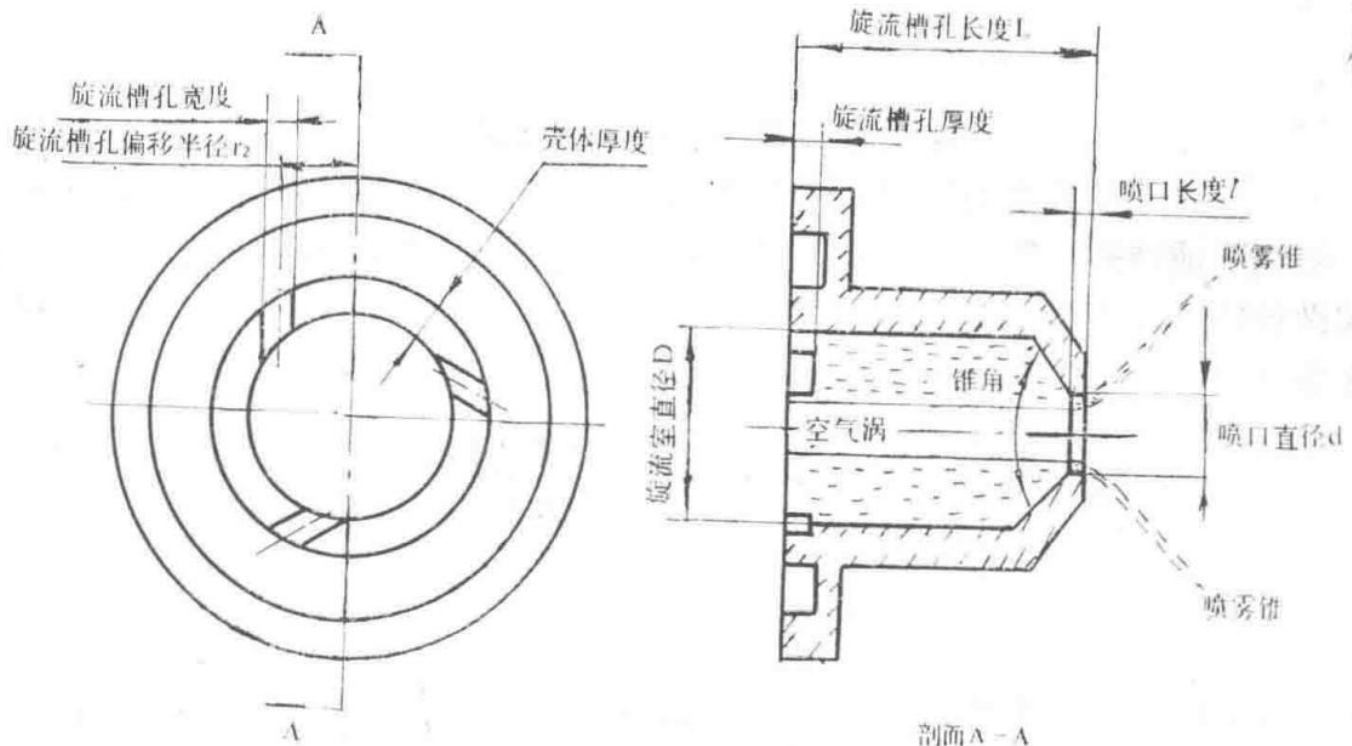
Spray Cone Angle = The angle formed by the fuel spray cone, determined as shown in the following diagram:



Spray Cone Angle Diagram

Diagram illustrating the spray cone angle formed by the fuel spray.

Where: - P = Pressure drop across the nozzle (psi) - K = Flow coefficient -  $A\Box$  = Swirl slot area ( $\text{in}^2$ ) - D = Swirl chamber diameter (in) - d = Nozzle orifice diameter (in) - L = Swirl chamber length (in) -  $r_1$  = Nozzle orifice radius ( $d/2$ ) (in) - l = Nozzle orifice length (in) -  $r_2$  = Offset radius of swirl slots (in) - Reynolds number  $Re = (V d \rho)/(\mu)$ , where: - V = Velocity -  $\rho$  = Density -  $\mu$  = Dynamic viscosity - d = Characteristic dimension



## Swirl Chamber and Nozzle Cross-Section

Cross-sectional diagram of the swirl chamber and nozzle, showing key dimensions and features.

## Derivation of Design Rules

Since the development of gas turbine engines, the theoretical description of fuel flow characteristics within centrifugal nozzles has been a research topic. The primary difficulty lies in viscous and frictional losses, but relationships between nozzle dimensions and spray characteristics can still be derived.

For example, Giffen and Muraszew used the theory of single-circuit inviscid flow nozzles to derive the relationship between the flow coefficient, spray cone angle, and nozzle dimensions  $((A\square)/(D_2 D_1))$  (see appendix of this report).

Radcliffe studied the performance of centrifugal nozzles with different geometries, providing relationships between the spray cone angle, nozzle orifice diameter, and swirl slot area  $(A\square)$ .

It is known that the flow coefficient  $K$  varies with the Reynolds number  $Re$  (with the characteristic dimension taken as the orifice diameter). Carlisle derived an improved functional relationship by correlating flow coefficients at the same Reynolds number  $Re$ . The  $(d \sqrt{P})/(21000)$  relationship in the design method accounts for Reynolds number effects.

A comparison of Radcliffe's research with Rolls-Royce's experimental data by Carlisle showed good agreement in spray cone angles and flow coefficients. This agreement was achieved by accounting for deviations in the theoretical spray cone angle due to Reynolds number effects within the nozzle orifice.

This "consideration" is also reflected in the design method (relationship between  $(Kd)/(21000)$  and spray cone angle deviation).

Based on these relationships, a design method was developed, and all pressure-atomizing nozzles subsequently used by Rolls-Royce were designed using this approach.

Note: The following documents are attached at the end of this report: - "Theory of Centrifugal Nozzles" by Giffen and Muraszew - "Performance of Centrifugal Nozzles" by Radcliffe (including Carlisle's comments)

## Nozzle Design for Given Flow Number and Spray Angle Using Kerosene with Specific Gravity of 0.8

1. From Figure 1 (relationship between spray cone angle and flow coefficient  $K$ ), determine the approximate flow coefficient  $K$  corresponding to the selected spray cone angle.
2. Substitute this  $K$  value into the following equation to calculate the nozzle orifice diameter:  $d = 0.0245 \sqrt{((FN)/(K))}$  (see Appendix 1(a)).
3. Use Figure 2 (relationship between  $(Kd)/(21000)$  and spray cone angle deviation) for Reynolds number correction. If a positive deviation is indicated, subtract this value from the selected spray cone angle design value and determine a new  $K$  from Figure 1. Similarly, if a negative deviation is indicated, add this value to the selected spray cone angle design value to obtain a new  $K$ .
4. Recalculate the nozzle orifice diameter using the new  $K$  value with the following equation:  $d = 0.0245 \sqrt{((FN)/(K))}$
5. Carlisle's Reynolds number correction is relative to  $d \sqrt{P} = 0.707$ . Using the nozzle's operating pressure (typically selected at maximum fuel flow conditions) and the orifice diameter obtained in step (4), apply the correction using Figure 3. If  $d \sqrt{P} \neq 0.707$ , use the reference flow number in the following formula and apply the  $K$  value obtained in step (3):  
$$K' = K \left( \frac{0.707}{d \sqrt{P}} \right)^{1/2}$$
6. The ideal swirl chamber dimension ratio is:  $(L)/(D) = 1.0$ ,  $(D)/(d) = 2.5$ . If this ratio cannot be applied, correct the  $K$  value using Figure 4 (relationship between base value and  $(L)/(D) \times (D)/(d)$ ).
7. Use the ideal  $K$  value obtained from Figure 4 to determine the value of  $(A\square)/(\pi r_1 r_2)$  (from Figure 5).
8. If the offset radius ( $r_2$ ) of the swirl chamber is known, the swirl slot area can be calculated. However,  $r_2$  cannot be precisely determined before the swirl slot dimensions are finalized. Therefore, an approximate

value for  $r_2$  (e.g., using the swirl chamber diameter) is used to calculate the swirl slot area and dimensions, followed by recalculation with the precise  $r_2$  value. General guidelines for the number of swirl slots: use 2 or 3 slots for flow numbers less than 1.0, and 6 slots for flow numbers greater than 3.0. Swirl slots are typically milled and should be as close to square as possible (i.e., depth = width). Note: More swirl slots result in better fuel distribution, but each slot should not be smaller than 0.010 inches to prevent clogging by debris. These guidelines apply to most nozzles.

## Spey Main Fuel Nozzle Demonstration Calculation

Flow Number (FN) = 5.5, Spray Cone Angle =  $100^\circ$  (Nominal) Operating Pressure (Pressure Drop) = 500 psi

From Figure 3,  $K = 0.184$ ;  $d = 0.0245 \sqrt{((5.5)/(0.184))} = 0.134$

$K(d)/(21000) = 12.3$ ; From Figure 2, Deviation =  $+8.8^\circ$

From Figure 1, Spray Cone Angle =  $91.2^\circ$ ;  $K = 0.233$ ;  $d = 0.120$

$d \sqrt{P} = 2.68$ ; From Figure 3, Required FN =  $0.955 \times$  Reference FN; Reference FN = 5.76

$$d = 0.0245 \sqrt{((5.76)/(0.233))} = 0.122$$

$$(L)/(D) = (0.295)/(0.222) = 1.33; (D)/(d) = (0.222)/(0.122) = 1.82$$

$$\text{Base } (K)/(K) = 0.83; \text{ Ideal } K = (0.233)/(0.83) = 0.28$$

$$(A\Box)/(\pi r_1 r_2) = 0.475; \text{ Assume } r_2 = (D)/(2)$$

$$A\Box = 0.475 \times \pi \times 0.061 \times 0.111 = 0.0101$$

Using 6 slots: Width of each slot =  $\sqrt{((0.0101)/(6))} = 0.041$ ; Area of each slot =  $0.041 \times 0.041$

$$\text{True value of } r_2 = (0.222 - 0.041)/(2) = 0.0905$$

$$A\Box = 0.475 \times \pi \times 0.061 \times 0.0905 = 0.00824$$

Using 6 slots: Each slot =  $0.037 \times 0.037$  or  $0.040 \times 0.034$  Actual dimensions (EU44239): -  $d = 0.122$  - Swirl slots:  $6 \times 0.040 \times 0.034$

## Design Considerations

- **Nozzle Orifice Length**: Within the limits of mechanical reliability, the nozzle orifice length should be as short as possible. For small nozzles, a length-to-diameter ratio of 1:7 is satisfactory. For larger flow numbers and wider spray cone angles, a ratio of 1:10 should be used. For example, for a nozzle orifice diameter of 0.140 inches, the length should be 0.014 inches.
- **Swirl Chamber Cone Angle** (see diagram on page 10): As the cone angle decreases, viscous losses within the swirl chamber increase, resulting in a reduced spray cone angle and increased flow number. Therefore, the maximum swirl chamber cone angle should be used, consistent with structural practicality.
- **Number of Swirl Slots**: Increasing the number of swirl slots improves the spray cone angle. Typically, 2–3 slots are used for flow numbers less than 1.0, and 6 slots for flow numbers greater than 3.0. Note: Swirl slot dimensions should not be too small to avoid clogging by solid particles in the fuel. Thus, nozzles with small flow numbers (<1.0) use only 2 or 3 slots to maintain dimensions no smaller than 0.01 inches.
- **Swirl Slot Housing Thickness** (see diagram on page 10): If the ratio of swirl slot width to housing thickness is greater than 1.0, radial velocity components may appear, reducing nozzle efficiency. Therefore, the housing thickness should be greater than the swirl slot width.
- **Materials**: Use hardened stainless steel to prevent corrosion and reduce erosion. Hardened steel also facilitates the removal of machining burrs from swirl slots and nozzle orifices.
- **Surface Finish**: All fuel-wetted surfaces must be polished and deburred. All sealing surfaces must be carefully lapped.

- **\*\*Tolerances\*\*:** In addition to normal machining tolerances, grinding tolerances are required for the nozzle orifice and surfaces affecting fuel flow and spray cone angle to allow adjustment and matching of nozzle sets installed in the engine. Grinding tolerances are typically 0.001 0.002 inches.

## 8. Clearance

To ensure a smooth fuel inlet for the swirl chamber, a clearance of 0.002 0.003 inches must be maintained between the swirl chamber diameter and the edge of the tangential slot.

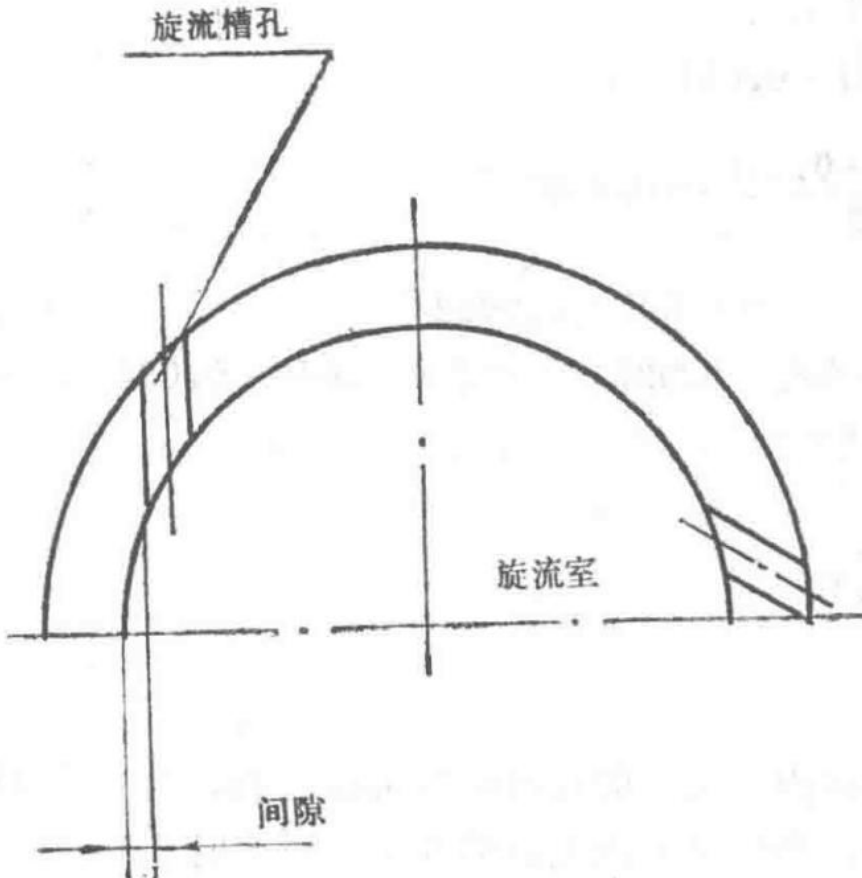


Diagram illustrating the clearance between the swirl chamber diameter and the tangential slot edge.

## 9. Concentricity

All nozzle diameters must be concentric, particularly ensuring that the orifice and swirl chamber diameters remain concentric.

The latest dual-circuit nozzle design of the Spey engine is shown in the figure. The rationale for selecting a dual-circuit design and additional design information are provided in Appendix 2.

## Appendix 1(a) Derivation of the Formula for Determining Orifice Diameter

When an incompressible fluid flows through an orifice:

$$\Delta P_1 = D_1 = \rho (V^2)/(2 g)$$

Pressure drop across the orifice related to dynamic pressure head.

$$V = \sqrt{(\Delta P \cdot 2g)/(\rho)}$$

Velocity of the fluid at the minimum cross-section of the jet.

Where:

- $\Delta P$  = Pressure differential across the orifice ( $\text{lb}/\text{ft}^2$ )
- $D_1$  = Dynamic pressure head at the minimum cross-section of the jet ( $\text{lb}/\text{ft}^2$ )
- $V$  = Velocity at the minimum cross-section of the jet ( $\text{ft}/\text{s}$ )
- $g$  = Gravitational acceleration =  $32.2 \text{ ft}/\text{s}^2$
- $\rho$  = Density of the fluid (kerosene density =  $50.0 \text{ lb}/\text{ft}^3$ )

Substituting the known values into equation (1):

$$V = \sqrt{(\Delta P_1 \times 2 \times 32.2)/(50)} = \sqrt{\Delta P_1 \times 1.288}$$

Velocity derived from pressure drop and fluid properties.

The volumetric flow rate through the orifice  $Q_1$  is given by:

$$Q_1 = K \times A \times V$$

Volumetric flow rate equation.

$$Q_1 = K \times (\pi d_1^2)/(4) \times V$$

Volumetric flow rate expressed in terms of orifice diameter.

Where:

- $K$  = Flow coefficient
- $A$  = Orifice area:  $K \times A$  = Area at the minimum cross-section of the jet
- $d_1$  = Orifice diameter (ft)

Substituting equation (2) into equation (3):

$$Q_1 = K \times (\pi d_1^2)/(4) \times \sqrt{\Delta P_1 \times 1.288} = K \times d_1^2 \times \sqrt{\Delta P_1} \times 0.891$$

Volumetric flow rate after substitution.

When converting variables to commonly used units:

- $d_1 = d$  (inches) / 12
- $\Delta P_1 = \Delta P$  ( $\text{lb}/\text{in}^2$ ) × 144
- $Q_1 = Q$  (gallons/hour) / ( $6.24 \times 3600$ ) ( $1 \text{ ft}^3 = 6.24 \text{ gallons}$ )

Substituting into equation (4):

$$(Q)/(6.24 \times 3600) = K \times ((d)/(12))^2 \times \sqrt{(\Delta P \times 144)} \times 0.891$$

Conversion of flow rate to common units.

$$Q = K d^2 \sqrt{(\Delta P)} \times 1670$$

Simplified flow rate equation.

Orifice diameter  $d$  is given by:

$$d = \sqrt{((FN)/(K)) \times 0.0245} \text{ (inches)}$$

Formula for determining orifice diameter.

Effective orifice area =  $KA = K \pi d^2 = K (\pi d^2)/(4) = FN \times 4.71 \times 10^{-4} \text{ (inches}^2)$

## Appendix 1(b) Changes in the Formula for Determining Orifice Diameter When Using Fuels Other Than Kerosene

Kerosene specific gravity = 0.8 (nominal value).

Let subscript R denote the liquid fuel used.

$$FN = FN \sqrt{(\rho)} / (\sqrt{0.8})$$

Flow number adjustment for different fuel densities.

$$d = 0.0259 \sqrt{(FN)} / (K) \sqrt{(\rho) / (0.8)}$$

Orifice diameter adjustment for different fuel densities.

## Appendix 2

### (a) Rationale for Adopting Dual-Circuit Nozzles

The fuel flow rate of a nozzle is proportional to the square root of the pressure drop across the nozzle, i.e., Fuel Flow Rate ( $Q$ ) = Flow Number ( $FN$ )  $\times \sqrt{(\text{Pressure } (P))}$  (since  $FN = (Q) / (\sqrt{P})$ ).

Engines requiring high fuel flow rates also demand high fuel pressures; otherwise, a high flow number must be adopted. The disadvantage of a high flow number is that at low fuel flow rates (such as during ignition), the fuel pressure is too low to achieve proper atomization.

For example:

- Assume the required maximum fuel flow rate = 100 gallons/hour
- Maximum fuel pressure = 500 lb/in<sup>2</sup>
- Then, since  $FN = (Q) / (\sqrt{P})$ ,  $FN = 4.47$
- Assume ignition fuel flow rate = 10 gallons/hour, then  $FN = (10) / (\sqrt{30}) = 1.8$
- The required fuel pressure at maximum fuel flow rate =  $((100) / (1.8))^2 = 3086 \text{ lb/in}^2$

In practice, the maximum achievable fuel pressure is typically less than 1000 lb/in<sup>2</sup> (approximately 700 lb/in<sup>2</sup>).

In summary, a nozzle with a low flow number can achieve the required good atomization during ignition but demands extremely high fuel pressure at maximum fuel flow rates. Conversely, a nozzle with a high flow number requires acceptable fuel pressure at maximum fuel flow rates but provides poor atomization during ignition.

Therefore, dual-circuit nozzles must be adopted to:

1. Reduce pump pressure.
2. Improve lean blowout limits.
3. Enhance relight capability.
4. Expand the engine's operating range.

### (b) Supplementary Design Rules for Dual-Circuit Nozzles

A dual-circuit nozzle consists of two single-circuit nozzles arranged in parallel, one nested inside the other. The outer nozzle supplies most of the fuel, while the inner nozzle ensures good fuel atomization at low flow rates. Both circuits of the nozzle are designed according to the aforementioned design methods, but the following additional rules must be observed:

1. The clearance between the main swirl chamber and the secondary orifice outer diameter should be greater than the maximum dimension (including width and depth) of the main nozzle swirl slot holes.
2. The secondary spray cone angle should not impinge on the main orifice, as this would adversely affect combustion chamber performance.

- The main orifice and secondary orifice should be concentric with each other and maintained within precision limits, for example, between 0.001 and 0.002 inches.
- The design of the secondary orifice tip profile should not affect the spray performance of the main orifice.
- The Spey MK202 secondary orifice features six spray slots extending from the downstream surface of the secondary orifice to the end of the main orifice (see Figure 6). This structure (known as the micro-cage type) stratifies the secondary spray to improve high-altitude relight performance. The presence of this feature does not affect the design rules for the secondary orifice flow number or spray cone angle (the spray jet can clean the spray slots).

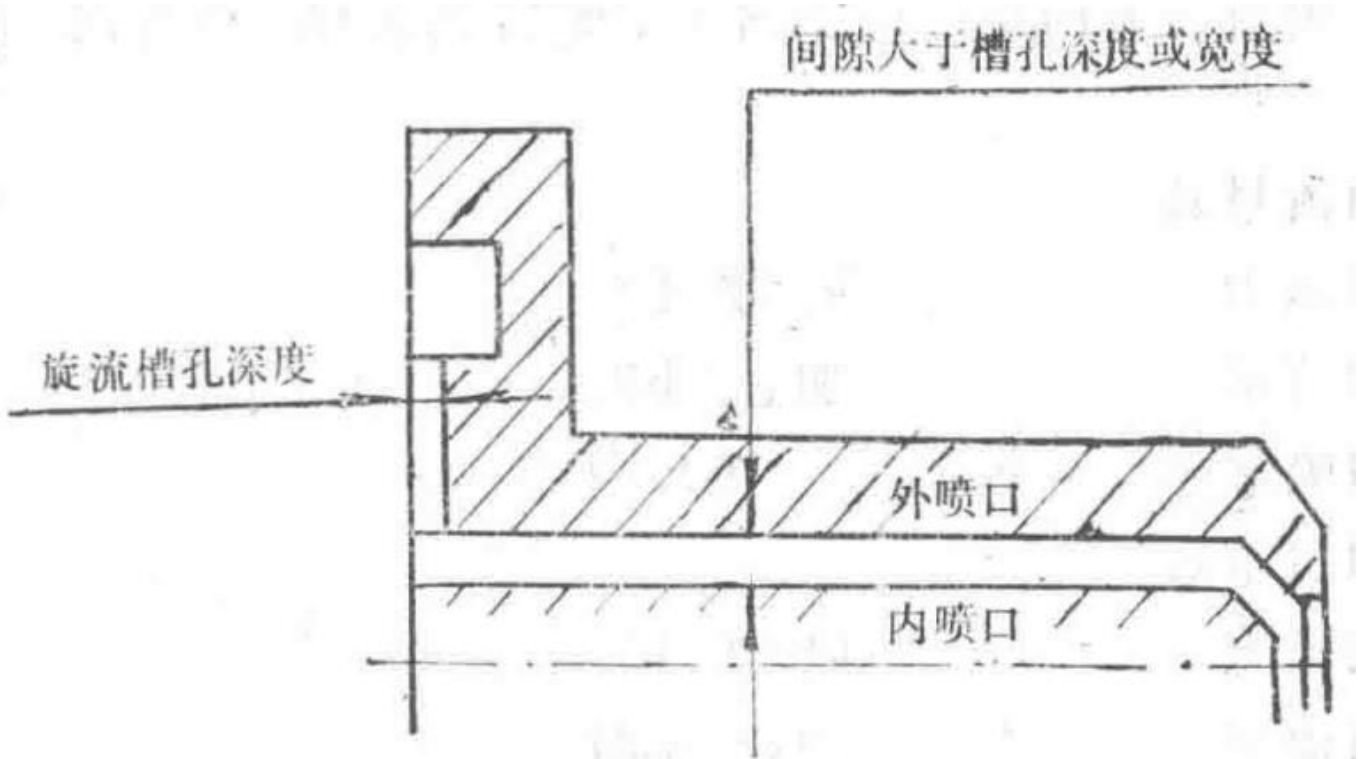


Diagram showing the clearance between the main swirl chamber and secondary orifice.

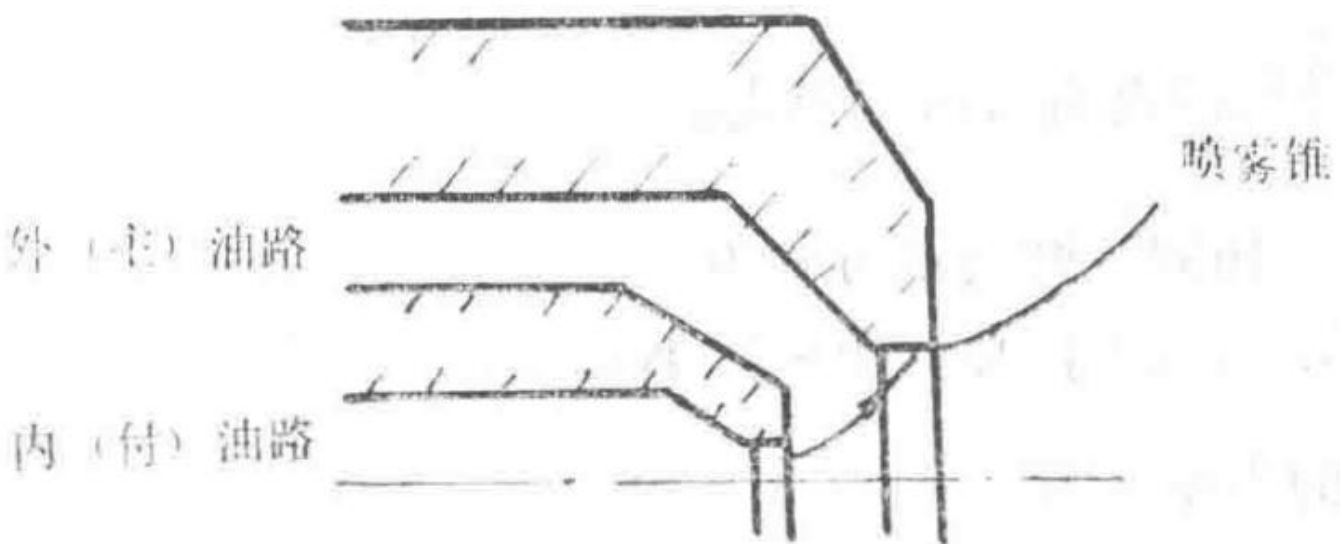


Diagram illustrating the secondary spray cone angle relative to the main orifice.

### (c) Pressure-Limiting Valve Characteristics and Atomization

A dual-circuit nozzle essentially consists of two single-circuit nozzles. The inner nozzle, or secondary orifice, has a low flow number, while the outer nozzle, or main orifice, has a high flow number. The secondary orifice holes are positioned relative to the main orifice holes to ensure that the secondary spray does not interfere with the

main orifice or its spray pattern. When the secondary flow reaches a predetermined value, the fuel system's pressure-limiting valve opens, allowing low-pressure fuel to flow to the main orifice.

Although atomization is poor in this scenario, it does not severely impact combustion efficiency because the secondary spray energy is sufficiently high to compensate for the low spray energy of the main orifice.

Factors contributing to good spray formation include:

- Rapid expansion into a conical fuel film.
- Turbulence generated by the relative velocity between air and the spray, which tears the fuel film.
- Initial disturbances in the fuel film.

The most significant influences on these factors are spray velocity and initial film thickness. The initial film thickness is determined by the flow number and spray angle, with wider spray angles producing thinner films.

Given a fixed flow number, the most important control factor is spray velocity or nozzle pressure.

Assuming the direction of fuel flow from the secondary orifice is similar to that from the main orifice, the two spray streams will combine their momenta.

- $\varphi$  = Secondary orifice flow number
- $p$  = Secondary orifice pressure ( $\text{lb/in}^2$ )
- $q$  = Secondary orifice flow rate (gallons/hour)
- $V$  = Secondary orifice spray velocity =  $K \sqrt{(p)}$  (ft/s)
- $\Phi$  = Main orifice flow number
- $P$  = Main orifice pressure ( $\text{lb/in}^2$ )
- $\Delta Q$  = Main orifice flow rate (gallons/hour)
- $V$  = Main orifice spray velocity =  $K \sqrt{(P)}$  (ft/s)

Where:  $K = \sqrt{((2g)/(p))}$ , assuming no losses within the orifice.

Assuming the same  $K$  for each orifice, the momentum equation is:

$$K \sqrt{(p)} \cdot q + K \sqrt{(P)} \cdot Q = (q + Q) K \sqrt{(P\bar{Q})}$$

Momentum equation for combined spray streams.

Where:  $P\bar{Q}$  = Equivalent pressure for combined velocity

$$\varphi p + \Phi P = \Phi (\varphi \sqrt{(p)} + \Phi \sqrt{(P)}) \sqrt{(P\bar{Q})}$$

Relationship between pressures and flow numbers.

$$(\Phi)/(\varphi) = R$$

Ratio of main to secondary flow numbers.

$$\sqrt{(P\bar{Q})} = p + R P \sqrt{(p + R \sqrt{(P)})}$$

Equivalent pressure for combined spray streams.

The pressure  $P\bar{Q}$  represents the equivalent atomization quality, i.e., the atomization quality equivalent to that of a single-circuit nozzle at this pressure. For a given  $p$ , the minimum value of  $P\bar{Q}$  occurs when  $(d P\bar{Q})/(d P) = 0$ .

$$(\sqrt{(p)} + R \sqrt{(P)}) = (p + R P)/(2 \sqrt{(P)})$$

Condition for minimum equivalent pressure.

$$2 \sqrt{(p)} \cdot \sqrt{(P)} + 2 R P = p + R P$$

Simplification of the condition for minimum equivalent pressure.

$$R P + 2 \sqrt{p} \cdot \sqrt{P} - p = 0$$

Final quadratic equation for minimum equivalent pressure.

Solving the quadratic equation:

$$\sqrt{P} = (-2 \sqrt{p} \pm \sqrt{(4 p + 4 R p)}) / (2 R)$$

Solution for the quadratic equation (corrected from original text).

— Section 6 —  
Content from Original Document (Pages 26-30)

$$P = p R ( 1 + R - 1 )$$

Equation for the value of P that yields minimum atomization quality.

This gives the value of P for minimum atomization quality:

$$P = p ( 1 + R \sim \sim 1 R ) ^ 2$$

By solving equations (1) and (2) simultaneously, the minimum value is obtained:

$$\text{array } r l \& P r = p + R p ( 1 + R - 1 R ) ^ 2 p + p ( 1 + R - 1 ) \backslash \& = 2 p R ( 1 + R - 1 ) \text{ array}$$

The fuel flow rate in this case is:

$$\text{array } l = \phi \sim p \sim + \Phi \sim P \sim = \Phi \sim p \sim + \Phi \sim p \sim \sim R \sim ( 1 + \sim R \sim \sim 1 ) \backslash \& = \Phi \sim p \sim 1 + R \sim \text{ array}$$

Thus, for any combination of main and pilot nozzle flow numbers and for any opening pressure of the pressure-limiting valve, the minimum value of  $P \square$  can be calculated, which serves as the basis for comparing atomization quality. The fuel flow rate at which minimum atomization quality occurs can also be calculated.

This poor atomization condition is related to high-altitude flight. When selecting the flow numbers for the main and pilot nozzles and the opening pressure of the pressure-limiting valve, this poor spray condition must be carefully considered.

## (d) Nozzle Air Shroud Design

Near the nozzle tip, the amount of air entrained by the fuel spray is greater than the amount of air that the nozzle air shroud can supply. Consequently, contaminated air containing carbon and incomplete combustion products is drawn back to the nozzle tip. This process causes carbon deposits on the air shroud and nozzle, which distorts the fuel spray and further affects combustion performance. Increasing the airflow through the nozzle air shroud is possible, but this reduces the spray cone angle, leading to combustion instability. Using a wider spray cone angle can compensate for the reduction in spray cone angle caused by increased air shroud airflow, but this compensation has certain limits.

It can be seen that the effect of air shroud airflow on the spray cone angle is complex. Lean stability, combustion efficiency, and ignition altitude are all influenced by this relationship between air shroud airflow and spray angle.

For these reasons, the airflow through the air shroud must be precisely controlled. Similarly, a new nozzle design should be based on experience gained from other engines, and flow tests should be conducted on the nozzle. Additionally, tests should be performed on combustion chamber test equipment to determine the appropriate nozzle air shroud.

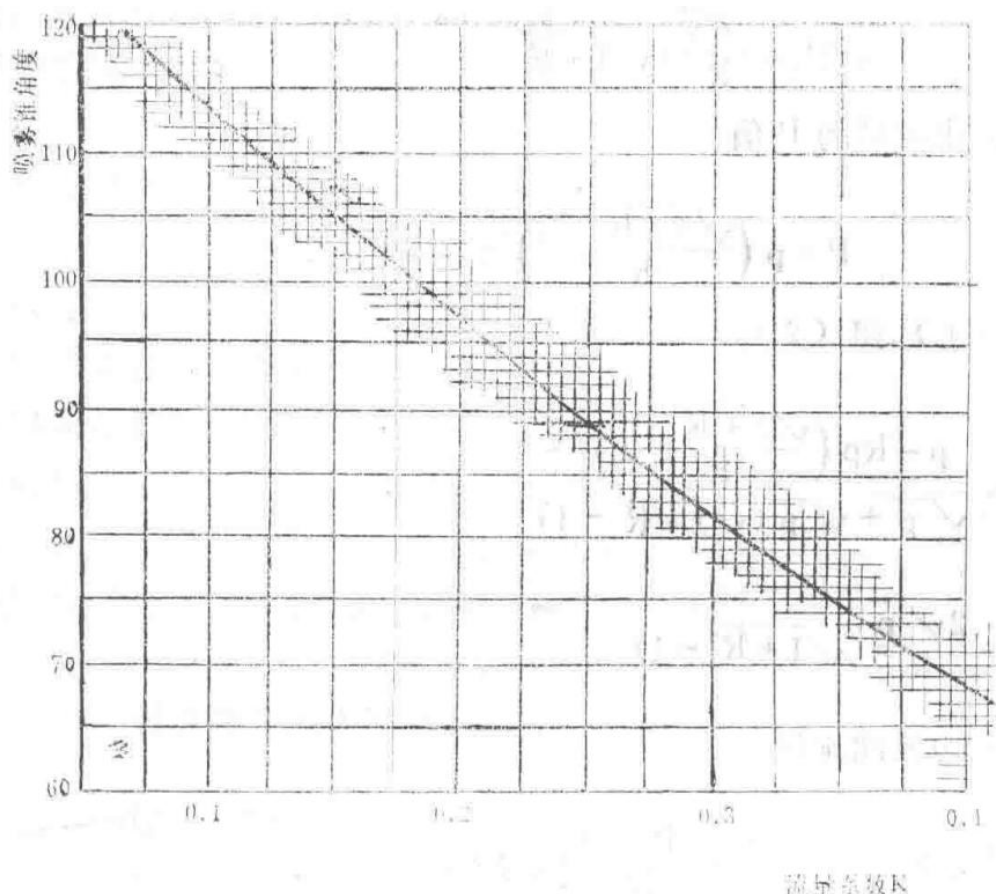


Figure 1 Relationship between spray cone angle and approximate flow coefficient (K)

Graph showing the correlation between the spray cone angle and the flow coefficient (K) for the nozzle.

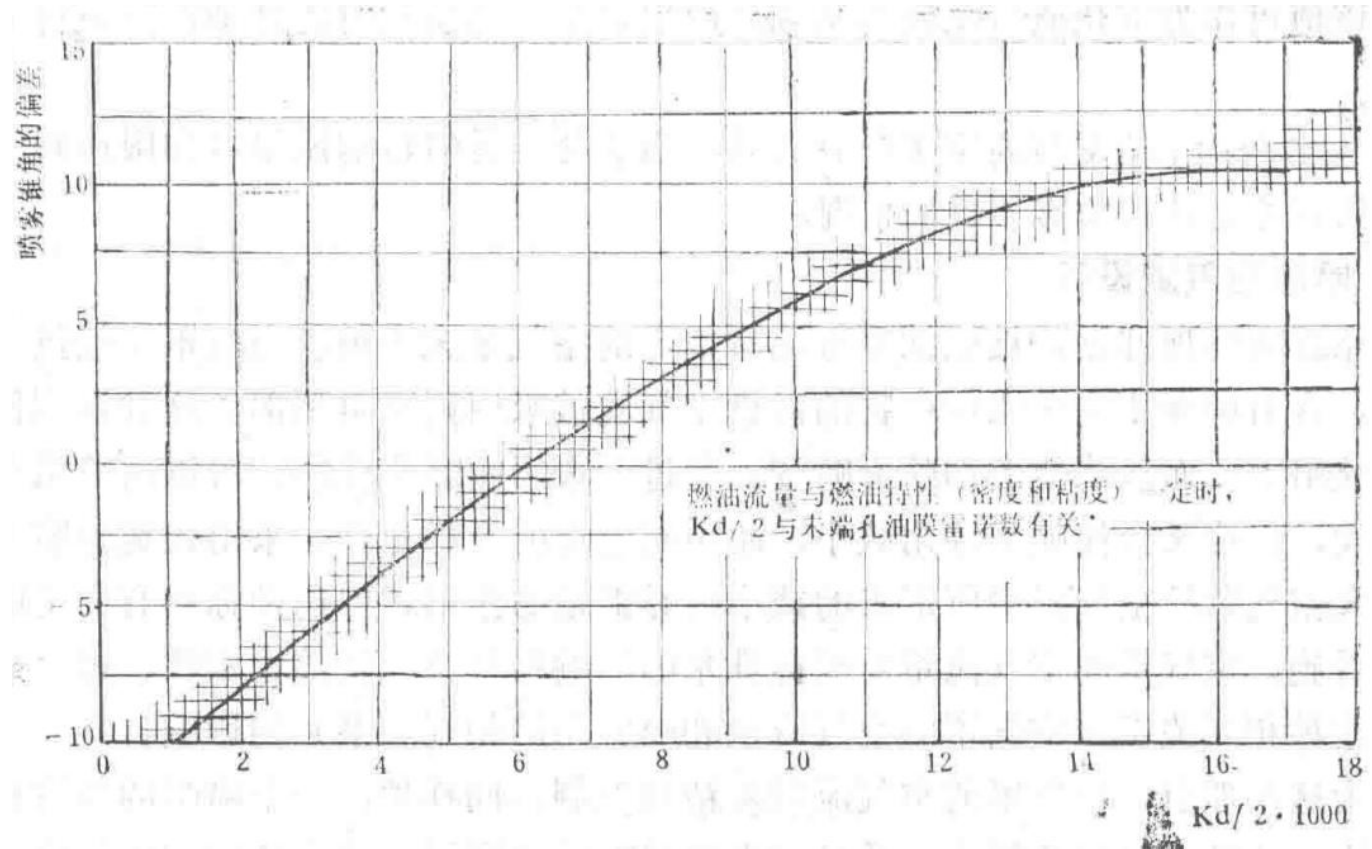


Figure 2 Reynolds number correction for spray cone angle (Re calculated based on nozzle diameter)

Graph depicting the correction factor for spray cone angle based on Reynolds number (Re), calculated using the nozzle diameter.

Refer to Appendix 3 for the required flow number and baseline flow number.

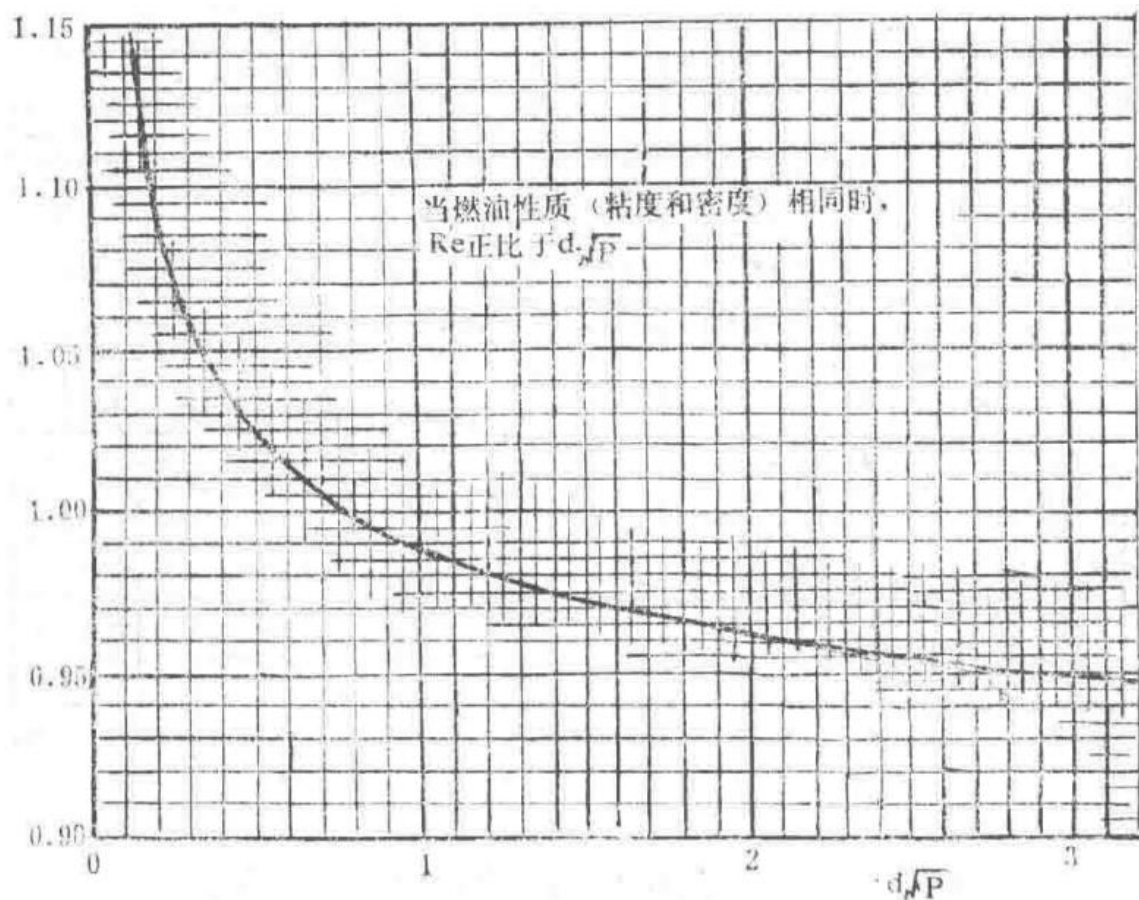


Figure 3 Reynolds number correction for flow number (Re calculated based on nozzle diameter)

Graph showing the correction factor for flow number based on Reynolds number (Re), calculated using the nozzle diameter.

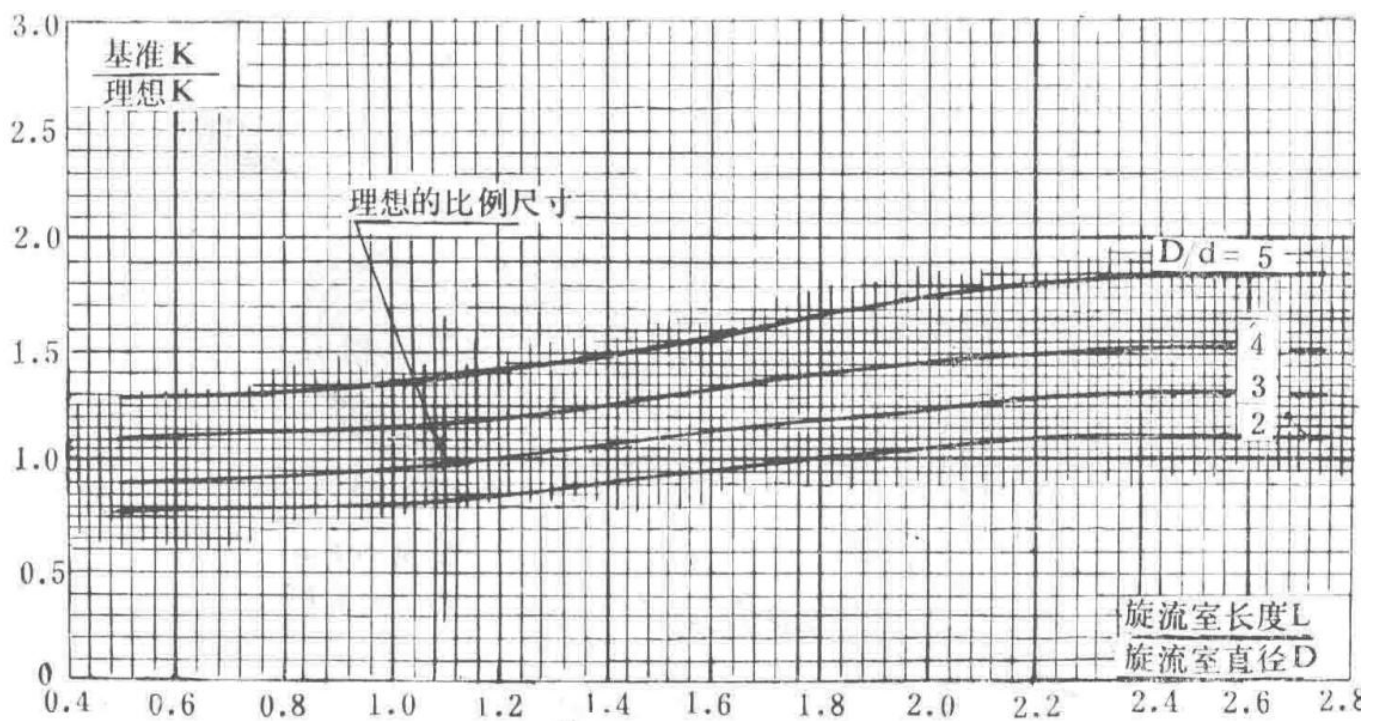


Figure 4 Effect of swirl chamber dimension ratio on flow coefficient K

Graph illustrating how the dimension ratio of the swirl chamber affects the flow coefficient K.

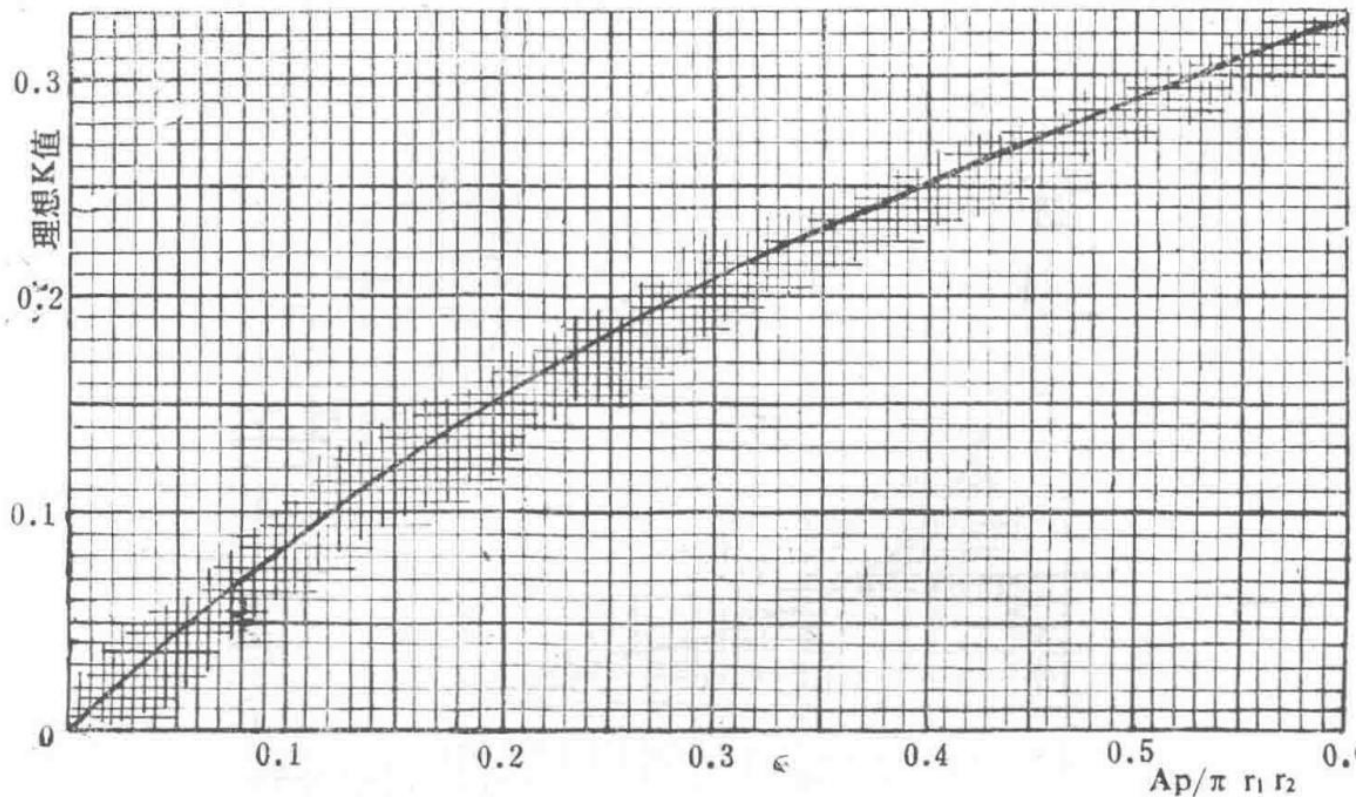


Figure 5 Relationship between swirl slot area parameter and flow coefficient

Graph showing the relationship between the swirl slot area parameter and the flow coefficient.

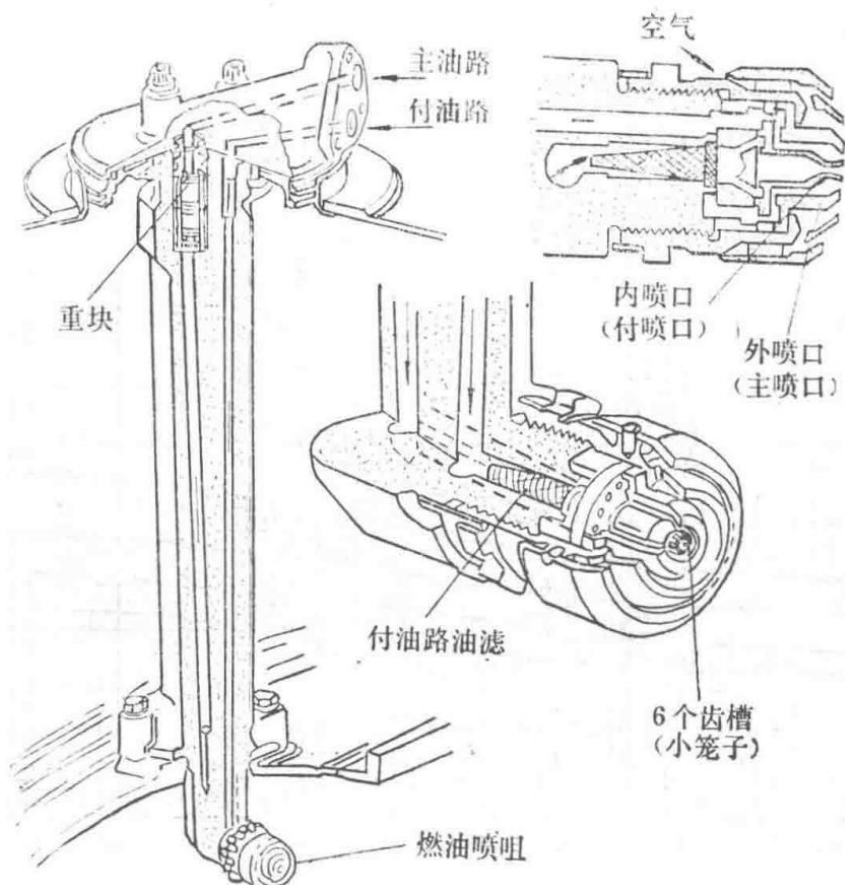


Figure 6 Spey MK202 dual-circuit nozzle

Diagram of the Spey MK202 dual-circuit fuel nozzle.

## Theoretical Calculation of Flow Coefficient and Spray Cone Angle

(Excerpt from \*Atomization of Liquid Fuels\* by E. Giffen and A. Muraszew, 1953 edition)

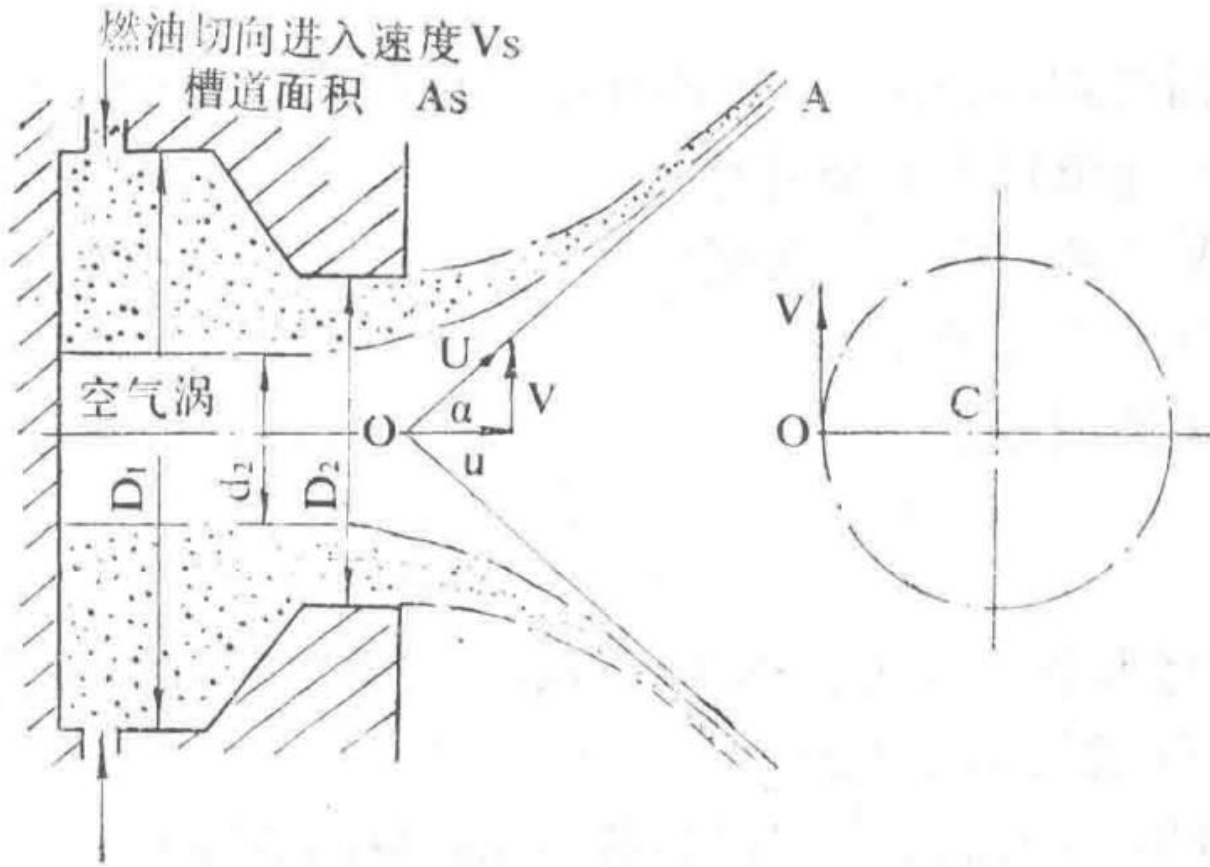


Figure 1

Diagram related to the theoretical analysis of a single-circuit centrifugal nozzle.

This section analyzes a single-circuit centrifugal nozzle. The liquid is introduced into the swirl chamber through tangential passages, resulting in a conical spray flow exiting the nozzle.

These calculations assume the liquid is inviscid and do not consider boundary layer effects. It is also assumed that the flow is a conical spiral free vortex, including both radial and axial motion as a free vortex.

Thus, the tangential velocity  $V$  satisfies the following condition:

$$V \sim r \sim = \text{constant}$$

Where:

- $v_\square$  is the tangential velocity at the inlet passage
- $R_1$  is the inner surface radius of the swirl chamber
- $A_\square$  is the area of the inlet passage
- $Q$  is the fuel flow rate

Then,  $V_\square R_1 = V_\Gamma$ , but  $\Delta V \Delta A_\square = Q / A_\square$ .

Therefore, at radius  $r_2$ , the tangential velocity  $V_2$  can be determined by the following equation:

$$V_2 \Gamma_2 = Q R_1 A_s$$

Within the nozzle (where radial velocity is zero), the Bernoulli equation can be applied. Since the total pressure is constant, the axial velocity  $u_2$  through any cross-section must also be constant.

Where:

- $u_2$  is the axial velocity within the nozzle
- $A_2$  is the cross-sectional area of the nozzle
- $a_2$  is the cross-sectional area of the air vortex

$$u_2 = Q A_2 - a_2$$

The flow coefficient C of the nozzle is defined as follows:

— Section 7 —  
Content from Original Document (Pages 31-35)

$$Q = C A_2 \sqrt{(\rho \Delta P g)}$$

Flow rate equation for the nozzle, where  $P$  is the pressure drop across the nozzle and  $\rho$  is the density.

Where:  $P$  is the pressure drop across the nozzle,  $\rho$  is the density.

Consider the velocity triangle at an arbitrary radius point  $O$  on the nozzle exit cross-section. The radial velocity  $w = \epsilon 0$ , and let:

- $u$  be the axial velocity inside the nozzle
- $V$  be the tangential velocity inside the nozzle
- $U$  be the resultant velocity
- $\alpha$  be the helix angle

$$\alpha = (V)/(U)$$

Relationship between the helix angle  $\alpha$ , tangential velocity  $V$ , and resultant velocity  $U$ .

After the oil droplet leaves the nozzle at point  $O$  with velocity  $U$  in the direction of  $OA$ , it continues to spray linearly toward  $A$ . The intersection line of the resulting spray cone forms a cone with a semi-vertex angle of  $\alpha$  at the vertex  $O$ .

For the liquid flow from the inlet slot to the air vortex surface inside the nozzle, applying Bernoulli's equation yields the following relationship:

$$P = (\rho)/(2 g) (V\Omega^2 + u\Omega^2)$$

Bernoulli's equation applied to the liquid flow inside the nozzle.

Substituting the values of  $\Delta V_2$  and  $U_2$  from equations (1) and (2):

$$P = (\Delta \rho)/(2 g) [ ( (Q R_1)/(A s r_2) )^2 + ( (\Delta Q)/(A_2 - a_2) )^2 ]$$

Pressure equation after substituting flow parameters.

Substituting the value of  $Q$  from equation (3):

$$(1)/(C^2) = (A_2^2 R_1^2)/(A \square^2 r_2^2) + ( (A_2)/(A_2 - a_2) )^2$$

Relationship between the flow coefficient  $C$  and nozzle geometric parameters.

$$A_1 = (\pi)/(4) D_1^2$$

Area of the swirl chamber, where  $D_1$  is the inner diameter of the swirl chamber.

$$A_2 = (\pi)/(4) D_2^2$$

Area of the nozzle orifice, where  $D_2$  is the inner diameter of the nozzle.

$$(1)/(C^2) = (\pi^2 D_1^2 D_2^2)/(16 A \square^2) \cdot (A_2)/(a_2) + (1)/(1 - ( (a_2)/(A_2) )^2)$$

Refined relationship incorporating nozzle dimensions.

$$\text{array} K = (A s)/(D_1 D_2) \text{ } \& X = (a_2)/(A_2) \text{ array .}$$

Definitions of dimensionless parameters  $K$  and  $X$ .

$$(1)/(C^2) = (\pi^2)/(16 K^2 X) + (1)/((1 - X)^2)$$

Final relationship between C and the dimensionless parameters K and X.

Assuming the formation of the air vortex maximizes the fuel flow rate at a given pressure, the value of  $(1)/(C^2)$  will be minimized. Thus, X can be eliminated using the following equation:

$$(d((1)/(C^2)))/(dX) = 0$$

Condition for minimizing  $(1)/(C^2)$ .

This yields the expression for X:

$$32K^2X^2 = \pi^2(1-X)^3$$

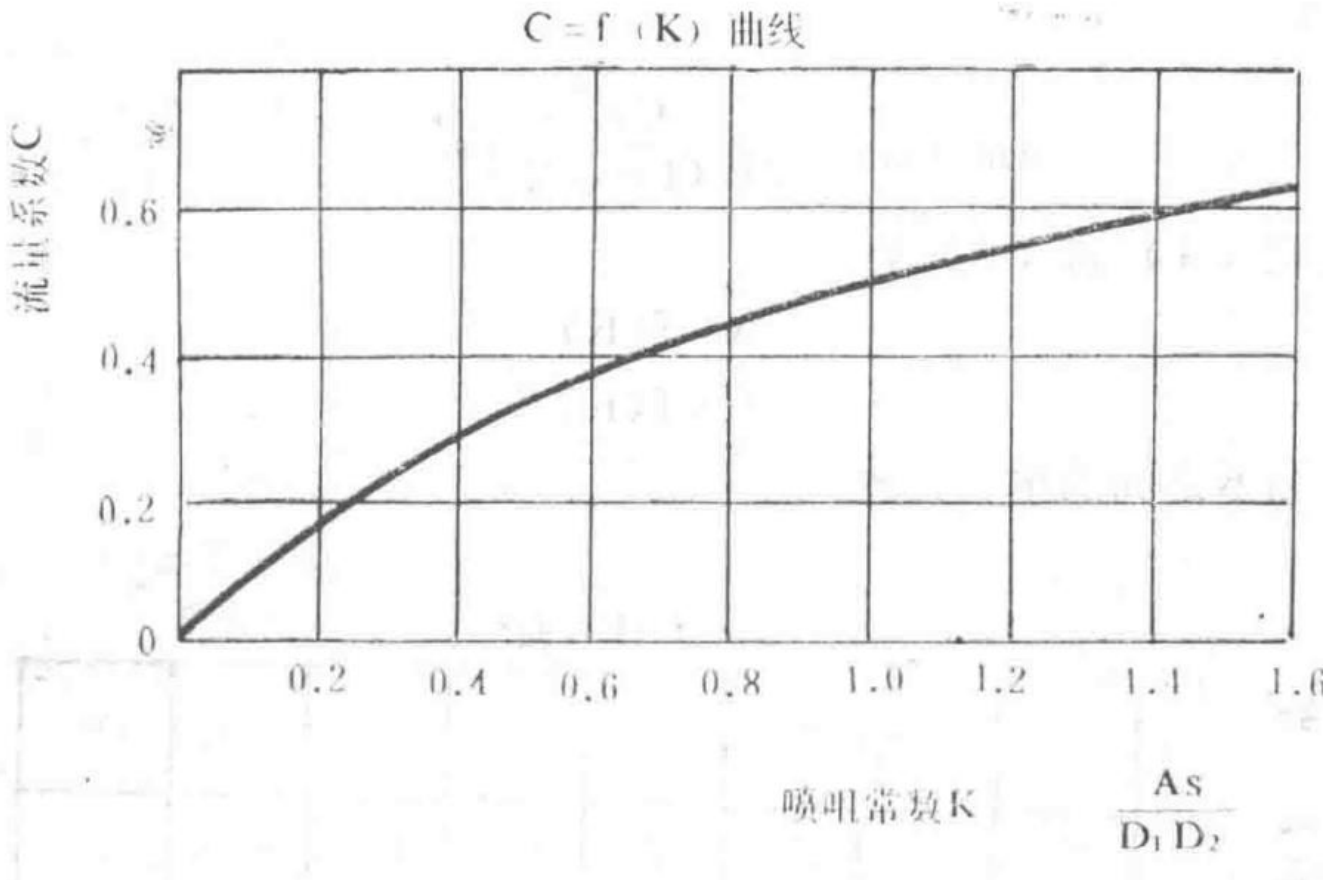
Equation relating K and X.

Substituting K from the above equation into equation (5):

$$C = \sqrt{((1-X)^3)/(1+X)}$$

Expression for the flow coefficient C in terms of X.

From equations (6) and (7), a unique relationship between C and K can be derived.



Relationship between flow coefficient C and nozzle constant K.

Graph showing the dependency of the flow coefficient C on the nozzle constant K.

The spray cone angle can be derived from equation (4), where the kinetic energy represented by the resultant velocity equals the available pressure energy at the inlet.

$$U = \sqrt{(2gP)/(\rho)}$$

Resultant velocity U in terms of pressure drop P and density  $\rho$ .

At the nozzle exit cross-section, the farther from the air vortex, the higher the static pressure of the liquid. Therefore, some pressure energy will be converted into kinetic energy, either axially or tangentially. Assuming all energy is used to increase axial velocity results in the minimum spray angle.

The average spray angle can be defined as:

$$\alpha \square = -1 ( (V \square) / (U) )$$

Definition of the average spray angle  $\alpha_m$ .

Where  $V \Omega \square$  is the average tangential velocity. Considering the momentum of the fuel flowing through an elemental annular ring of radius  $r$  and width  $\delta r$ :

$$2 \pi \rho u_2 \delta r = \mu$$

Momentum equation for the elemental annular ring.

$Q_R =$  Tangential velocity  $V$

Thus, the momentum of the elemental ring is:

$$(2 \pi \rho u_2 Q R_1 \delta r) / (A s)$$

Momentum of the elemental annular ring.

Integrating between  $r_2$  and  $R_2$ , the total annular momentum is:

$$(2 \pi \rho u_2 Q R_1 (R_2 - r_2)) / (A s) = V \square M = V \square \rho Q$$

Total momentum of the annular flow.

$$V \square = (2 \pi u_2 R_1 (R_2 - r_2)) / (A s)$$

Average tangential velocity  $V_m$ .

$$u_2 = (C A_2 U) / (A_2 - a_2)$$

Axial velocity  $u_2$  in terms of flow coefficient  $C$  and nozzle parameters.

$$(V \square) / (U) = (2 \pi C A_2 R_1 (R_2 - r_2)) / (A s (A_2 - a_2)) = ((\pi) / (4) 2 C) / (K (1 + \sqrt{X}))$$

Ratio of average tangential velocity  $V_m$  to resultant velocity  $U$ .

$$\alpha \square = -1 [ (C \pi) / (2 K (1 + \sqrt{X})) ]^*$$

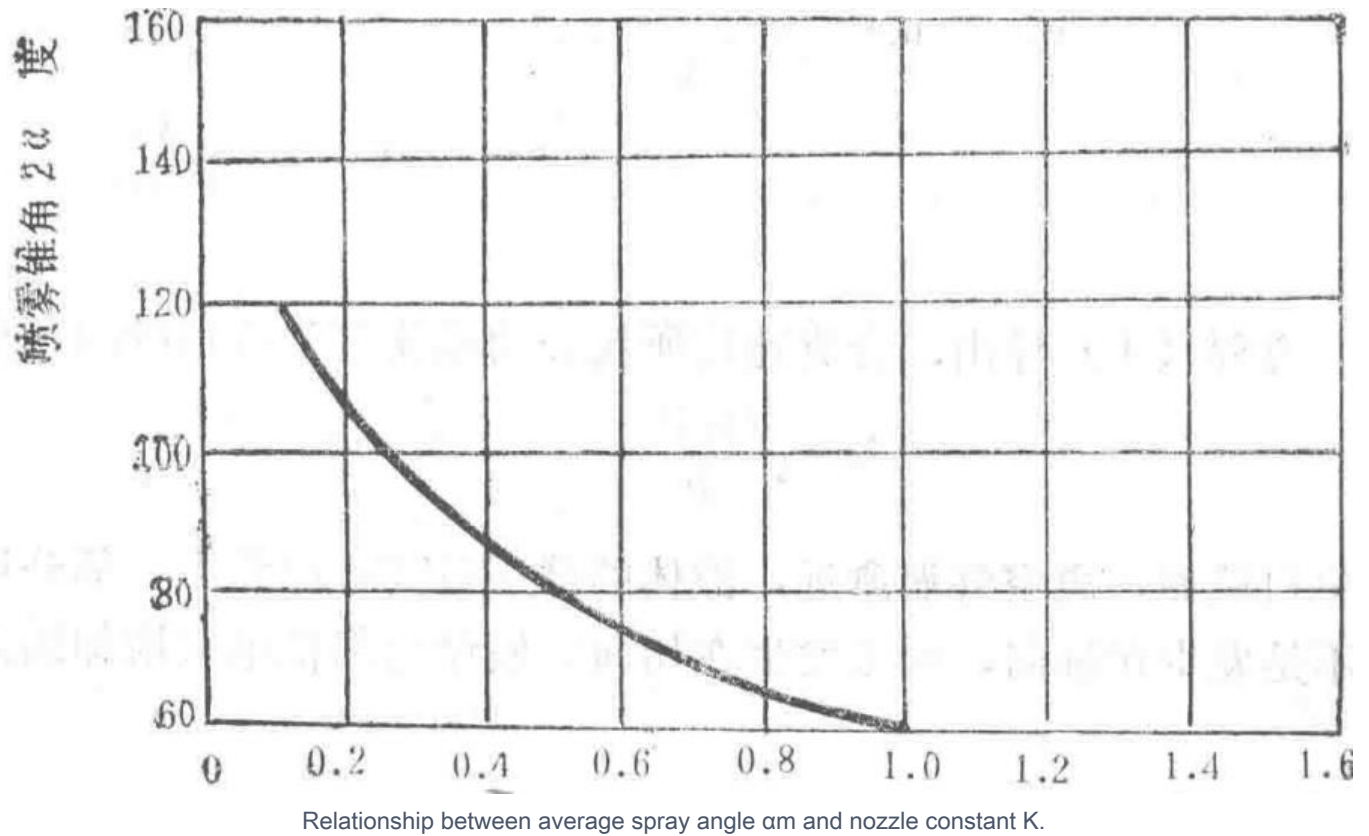
Expression for the average spray angle  $\alpha_m$ .

However, from equations (6) and (7), we have:

$$\text{array} X = f(K) \text{ } \& \text{ } C = f(K) \text{ array}$$

Relationships showing  $X$  and  $C$  as functions of  $K$ .

Thus, a unique relationship between  $\alpha_m$  and  $K$  can be derived.



Graph showing the dependency of the average spray angle  $\alpha_m$  on the nozzle constant K.

## Nozzle Constant KAs

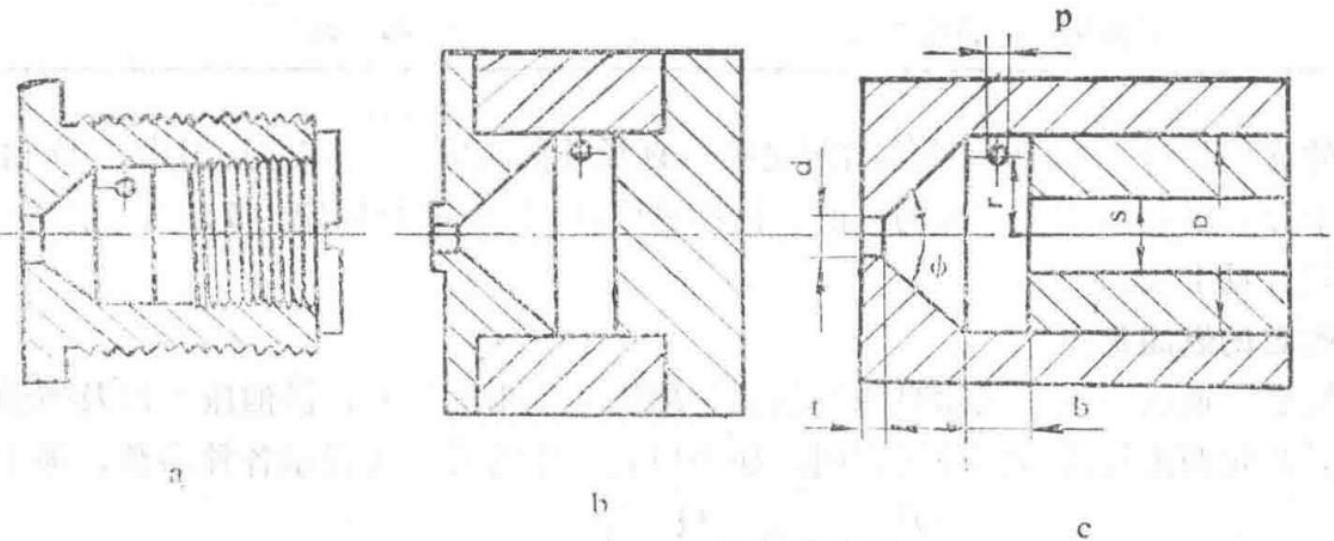
# Appendix 4: Performance of Centrifugal Nozzles

By A.Radcliffe, B.Sc. (Excerpt from the Proceedings of the Institution of Mechanical Engineers, Volume 169, 1955)

## Preface

Fuel is typically injected into gas turbines via a rotating jet. While all rotating jets operate on the same principle, performance variations among different nozzle designs can be difficult to estimate for those who have not been involved in the production of a specific nozzle model.

Figure 1a shows a structural diagram of one type of nozzle.



Structural diagram of the nozzle.

Diagram illustrating the structural form of the nozzle, including key dimensions and components.

## Figure 1: Nozzle Structural Forms

- b - Swirl chamber cylinder length
- r - Tangential hole offset radius
- D - Swirl chamber diameter
- S - Return hole diameter
- d - Nozzle orifice diameter
- t - Nozzle orifice length
- p - Tangential hole diameter
- $\Phi$  - Swirl chamber cone angle

It consists of a main body and a plunger, with several flat surfaces on the nozzle side walls to allow unrestricted fuel flow into each tangential hole when the main body is tightened onto the fuel pipe. Figure 1b shows another nozzle structural form, where the orifice plate and plunger are inserted into the swirl sleeve. After assembling the three components, fuel can flow into the two swirl holes. Detailed structural features of this nozzle are shown in Figure 1c. Generally, fuel enters the swirl chamber through two holes of diameter  $p$ . The swirl chamber can be considered a very short cylinder with diameter  $D$  and length  $b$ , leading to a conical surface with a cone angle  $\Phi$ . Inside the swirl chamber, fuel is sprayed out through the nozzle orifice of diameter  $d$  in a vortex form. The mechanism of this flow has been explained (Taylor, 1950).

When the nozzle is in good working condition, there is an air vortex at the center of the swirl, causing the fuel to exit the nozzle as a thin film with both axial and tangential velocities. Upon leaving the nozzle, the fuel disperses into a cone with angle  $\theta$ . The surface gradually forms transverse waves and then breaks into oil filaments and droplets (Squire, 1953). If the fuel pressure drops excessively or the fuel viscosity increases too much, the surface tension acting on the cone can transform the oil cone into a tulip-like shape. In worse cases, the air vortex disappears, and the fuel sprays out from the nozzle orifice as one or several oil filaments, resulting in poor atomization quality.

Simons (1946) noted in an unpublished work that nozzles perform satisfactorily when the relationships between different dimensional parameters are arranged as shown in Table 1.

Dimensions of Standard Nozzles

Parameter	Symbol	Relationship
Nozzle orifice diameter	d	

Tangential hole diameter	$p$	$p = d$
Nozzle orifice length	$t$	$t = 2d/3$
Swirl chamber diameter	$D$	$D = 6d \sim 9d$
Swirl chamber cylinder length	$b$	$b = 2d$
Tangential hole offset radius	$r$	$r = D/2 \sim 3d/4$
Swirl chamber cone angle	$\Phi$	$\Phi = 60^\circ \sim 90^\circ$

Most of the listed dimensions are given in relation to the nozzle orifice diameter  $d$ . In practical applications, the selection ranges for  $D$  and  $\Phi$  are quite useful. For the purposes of this paper, a standard nozzle is defined with  $D$  fixed at  $7.5d$  and a cone angle  $\Phi = 90^\circ$ , with the remaining dimensions as shown in the table above.

## Fuel Flow Rate of Standard Nozzles

It has long been known that the fuel flow rate through a nozzle of a given shape depends on the nozzle dimensions, supply pressure, and the viscosity and density of the fuel. Dimensional analysis of this problem shows that if the parameters are represented by the symbols in Table 2, then:

$$(Q^2)/(d^4 P \rho) = f((Q)/(\mu d))$$

Dimensional analysis relationship for fuel flow rate through the nozzle.

Preliminary tests on specially made nozzles with fuels of the same density but different viscosities (i.e., kerosene, hydraulic oil, and different mixtures of D.T.D 44D) and fuels with the same viscosity but different densities (kerosene and carbon tetrachloride mixtures) showed that equation (1) can represent the flow rate through the nozzle. Subsequently, a series of nozzles with identical shapes but different sizes were manufactured, and the flow rates through these nozzles were measured for seven different fuels. These fuels were: (1) carbon tetrachloride, (2) gasoline, (3) kerosene, (4)-(7) four mixtures of kerosene and hydraulic oil. The density range was 0.75 to 1.6 g/cm<sup>3</sup>, the viscosity range was 0.5 to 25 centipoise, and the pressure range was 5 to 1000 psi. The nozzle orifice diameters were 0.020, 0.030, 0.040, 0.050, 0.060, and 0.070 inches, labeled as (2) to (7). The measured dimensions of these nozzles are listed in Table 3.

Parameters Controlling Flow Rate in Centrifugal Nozzles

Parameter	Symbol	Dimension
Flow rate	$Q$	$M/T$
Pressure	$P$	$M/LT^2$
Nozzle orifice diameter	$d$	$L$
Fuel density	$\rho$	$M/L^3$
Fuel viscosity	$\mu$	$M/LT$

**Table 3 Dimensions of Nozzles with Identical Shapes (Unit: inches)**

Dimensions of Nozzles with Identical Shapes

Nozzle Number	Orifice Diameter d	Orifice Length t	Tangential Hole Diameter p	Swirl Chamber Diameter D	Swirl Chamber Length b	Offset Radius r
(2)	0.0184	0.010	0.0226	0.150	0.040	0.058
(3)	0.0285	0.015	0.0204	0.219	0.058	0.057
(4)	0.0406	0.020	0.0419	0.299	0.090	0.118
(5)	0.0514	0.025	0.0527	0.389	0.103	0.155
(6)	0.0588	0.030	0.0616	0.443	0.117	0.175
(7)	0.0692	0.035	0.0732	0.520	0.141	0.205

During each experiment, the volumetric flow rate, temperature, and fuel supply pressure of the fuel were measured. By measuring the temperature, the viscosity and density of the fuel could be estimated based on pre-determined relationships between fuel viscosity, density, and temperature parameters. Thus, for each test, the following parameters were determined:  $Q$  (lb/hr),  $P$  (lb/in<sup>2</sup>),  $d$  (inches),  $\rho$  (g/cm<sup>3</sup>), and viscosity  $\mu$  (centipoise). Although the units used were not consistent, these are the units commonly used by most people working with fuel nozzles in the UK. The values of  $Q^2 / d^4 P \rho$  and  $Q / \mu d$  for nozzles (2) to (7) were calculated and plotted. The data points for each nozzle closely aligned with a common curve. Figures 2a and 2b show the data for nozzle (3) and nozzle (6).

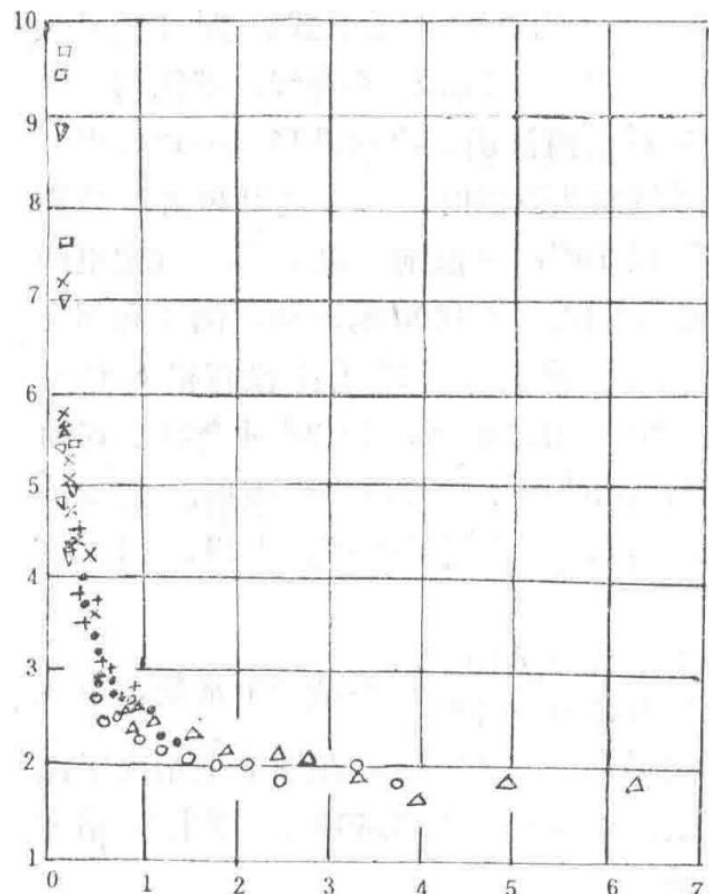
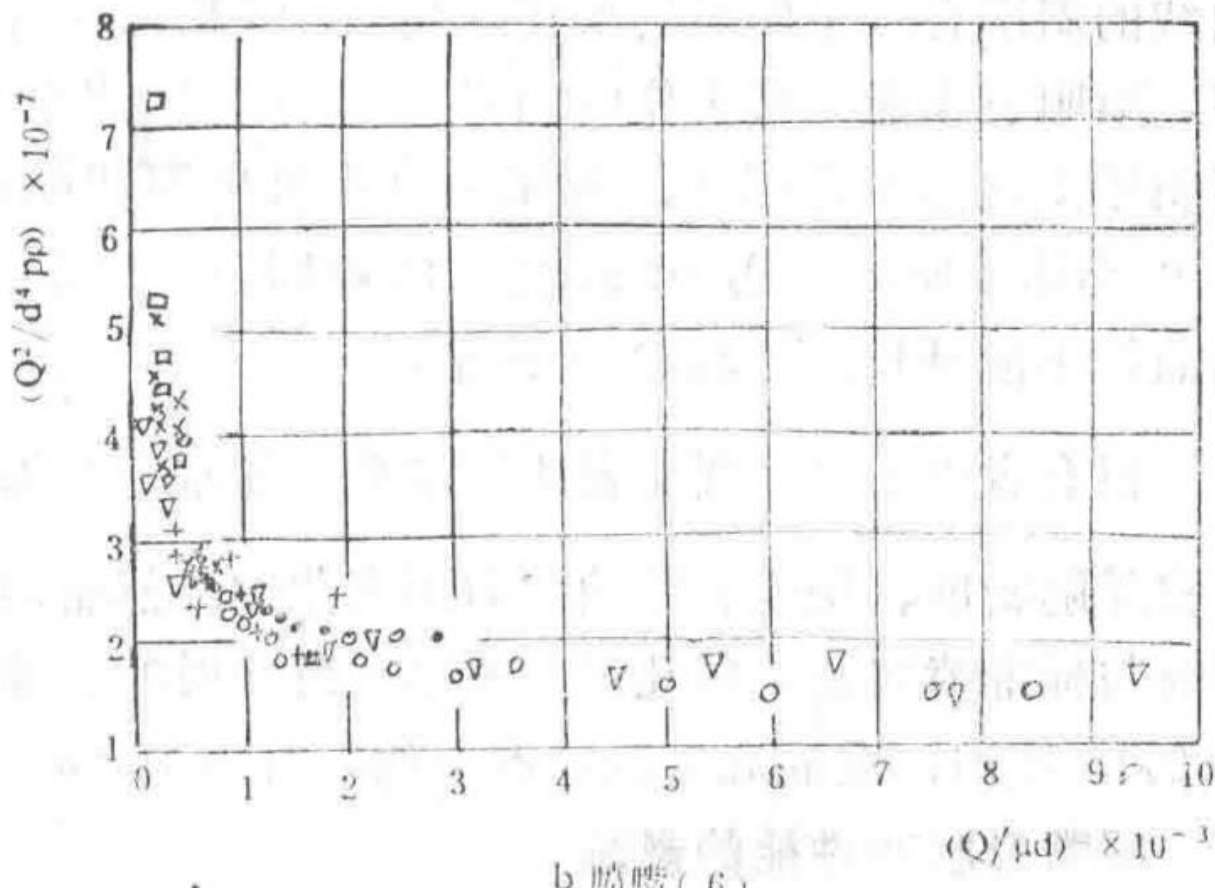


Figure 2a Nozzle (3) Data ( $Q/\mu d$ )  $\times 10^{-3}$

Plot showing the relationship between  $Q^2 / d^4 P \rho$  and  $Q / \mu d$  for nozzle (3) with various fuels.



Legend for Fuel Types

Legend indicating the symbols used for different fuels: Kerosene ( $\Delta$ ), Gasoline ( $\circ$ ), Carbon Tetrachloride (+), 1 part DTD44D fuel and 1 part Kerosene ( $\times$ ), 3 parts DTD44D fuel and 1 part Kerosene ( $\blacktriangle$ ), 7 parts DTD44D fuel and 1 part Kerosene ( $\triangledown$ ), 15 parts DTD44D fuel and 1 part Kerosene ( $\bullet$ ).

Figure 3 shows the best-fit curve for all data points from the six nozzles. The values of  $Q^2 / d^4 P \rho$  and  $Q / \mu d$  have been adjusted to consistent units. The errors in measuring  $Q$ ,  $P$ ,  $\rho$ , and  $\mu$ , as well as the assumption that  $d$  represents the dimensions of each nozzle, vary with experimental conditions. However, except for density  $\rho$ , the standard error of all measurements is approximately 1%. This level of random error easily explains the scatter of the data points.

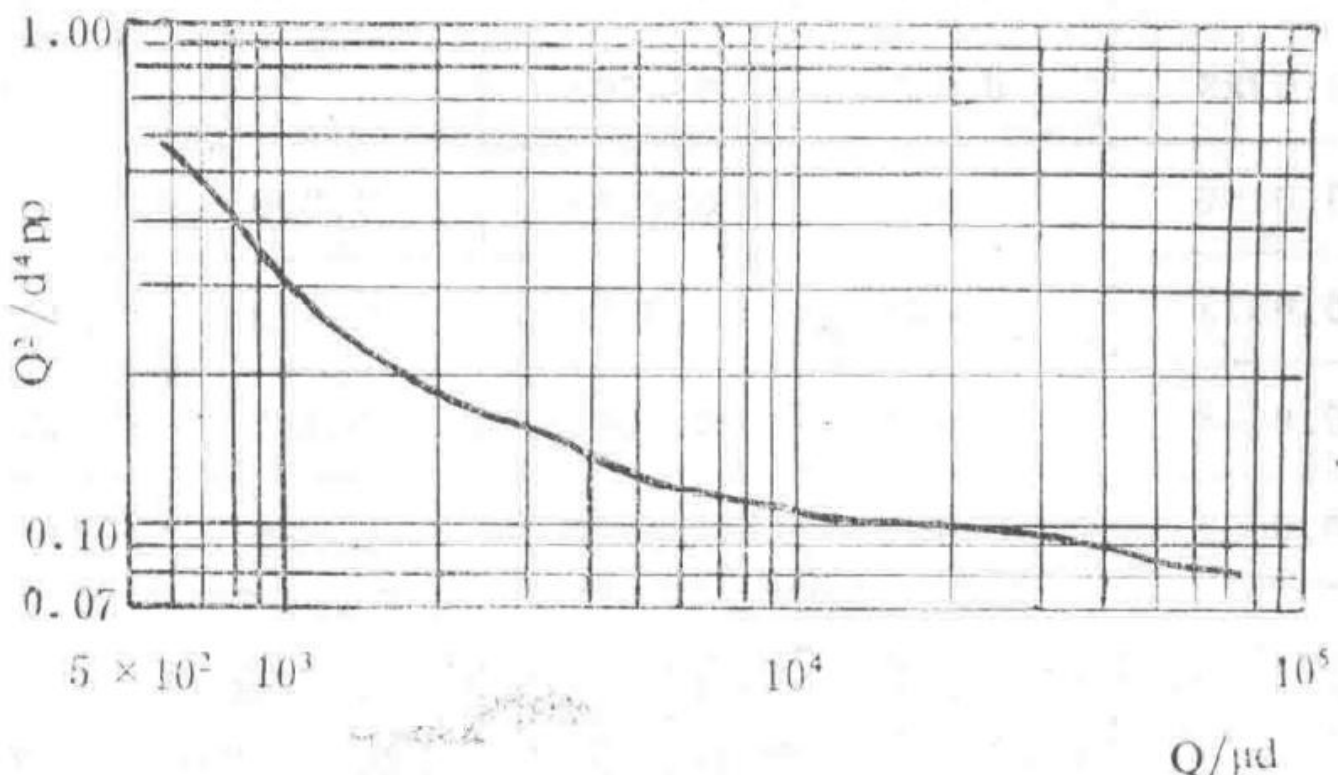


Figure 3 Relationship between  $Q^2 / d^4 P \rho$  and  $Q / \mu d$  (Consistent Units)

Best-fit curve showing the relationship between  $Q^2 / d^4 P \rho$  and  $Q / \mu d$  for all tested nozzles with consistent units.

Using the curve in Figure 3, the relationship between  $Q^2 / d^4 P \rho$  and  $Q / \mu d$  can be derived for any value of  $d$ . Figure 4 shows ten such curves plotted on logarithmic coordinates for  $d$  values ranging from 0.010 to 0.100 inches. These curves allow the determination of the orifice diameter and other dimensions of a standard nozzle for a wide range of pressure, density, and viscosity conditions through interpolation. When the values of  $Q^2 / P \rho$  and  $Q / \mu$  exceed the range of the curves, the curves can be extended for applicability by dividing  $Q / P \rho$  by  $10^m$  and  $Q / \mu$  by  $10^m$ , while multiplying the  $d$  value by  $10^m$  (where  $m$  is a positive number). Notably, for  $Q / \mu d$  values around 1600 (in consistent units), there is a distinct change in the slope of the curves in Figures 3 and 4. As the  $Q / \mu d$  value decreases, the nozzle tends to malfunction due to inadequate spray formation or poor atomization. Only when the  $\mu$  value increases to about 30 centipoise does  $Q / \mu d$  fall into the left region of the slope change. If both  $Q / \mu d$  and  $\mu$  are low, the nozzle fails to form a conical spray. For example, when  $\mu$  is as low as 1 centipoise and  $Q / \mu d$  is below 1600, the nozzle may not operate properly. There is no clear reason why the curves in Figure 4 cannot be extended to higher  $Q / \mu$  values.

Interestingly, Figure 4 shows that the flow number (typically defined as a constant based on pressure in  $\text{lb/in}^2$ ) is not actually constant but varies with density, viscosity, and fuel pressure. However, since it still has some utility, Figure 7 presents the relationship between the flow number and the orifice diameter of standard nozzles. The fuel used was kerosene with a density of  $0.800 \text{ g/cm}^3$ , a viscosity of 2.15 centipoise, and a fuel pressure of  $100 \text{ lb/in}^2$  at the measurement point.

## Effect of Nozzle Shape on Performance

To determine the effect of nozzle shape on fuel flow rate and spray cone angle, a set of nozzles was fabricated according to the design shown in Figure 1b. This set included 31 swirl sleeves, 9 orifice plates, one plunger, and one main body. The swirl sleeves and orifice plates were interchangeable, allowing for 279 different nozzle configurations. The orifice plates had a cone angle of  $90^\circ$  and a maximum diameter  $D = 0.500$  inches, but varied in orifice diameter and length, as shown in Table 4. The 31 swirl sleeves had an inner diameter of 0.500 inches, with varying tangential hole diameters ( $p$ ) and offset radii ( $r$ ), as detailed in Table 5. The dimensions of the swirl sleeves, orifice plates, and plunger ensured that the cylindrical length of the swirl chamber was 0.1125 inches.

The swirl sleeves were numbered (1) to (31), and the orifice plates were numbered (1) to (9). Different combinations were represented by listing the swirl sleeve number followed by the orifice plate number (e.g., 27/8).

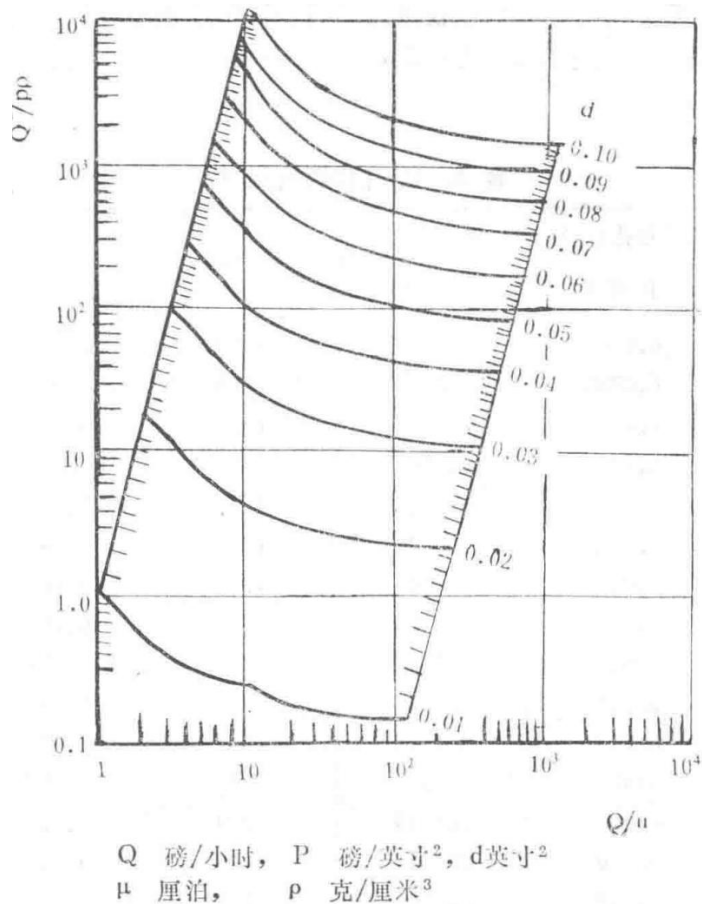


Figure 4 Relationship between  $Q^2 / P \rho$  and  $Q / \mu$  with  $d$  as a Parameter

Curves showing the relationship between  $Q^2 / P \rho$  and  $Q / \mu$  for different orifice diameters ( $d$ ) on logarithmic coordinates.

#### Table 4 Dimensions of Orifice Plates

Dimensions of Orifice Plates

Orifice Plate Number	Orifice Diameter (inches) $d$	Orifice Length (inches) $t$
(1)	0.016	0.015
(2)	0.0195	0.020
(3)	0.033	0.0305
(4)	0.042	0.039
(5)	0.052	0.053
(6)	0.067	0.040
(7)	0.076	0.044
(8)	0.100	0.063
(9)	0.120	0.065

For each nozzle configuration, tests were conducted to measure the fuel flow rate and spray cone angle, with a fuel density of 0.800 g/cm<sup>3</sup> and a viscosity of 2.15 centipoise. A calibrated rotameter using the volumetric

displacement method was used to measure the fuel flow rate. The spray cone angle was determined by projecting the shadow of the spray cone onto a ground glass screen, which accurately measured the cone angle of the nozzle spray envelope.

## Table 5 Dimensions of Swirl Sleeves

Dimensions of Swirl Sleeves

Sleeve Number	Tangential Hole Diameter p (inches)	Offset Radius r (inches)	Sleeve Number	Tangential Hole Diameter p (inches)	Offset Radius r (inches)
(1)(2)	0.016	0.050	(17)	0.020	0.198
(2)(3)	0.020	0.019	(18)	0.031	0.198
(4)	0.040	0.0495	(19)	0.040	0.1985
(5)	0.052	0.0495	(20)	0.052	0.1985
(6)	0.016	0.096	(21)	0.077	0.095
(7)	0.020	0.096	(22)	0.083	0.0935
(8)	0.031	0.0965	(23)	0.105	0.095
(9)(10)(11)(12)(13)	0.010-0.052	0.097	(24)	0.122	0.096
(14)	0.040	0.152	(25)	0.077	0.1505
(15)	0.052	0.151	(26)	0.081	0.151
(11)	0.016	0.152	(27)	0.102	0.148
(12)	0.020	0.152	(28)	0.122	0.150
(13)	0.031	0.1515	(29)	0.076	0.1985
(16)	0.016	0.198	(30)	0.083	0.198
			(31)	0.100	0.197

In each experiment measuring fuel flow rate and spray cone angle, the fuel supply pressure was 100 lb/in<sup>2</sup>. Additionally, flow rate experiments were conducted on nozzles (20/5), (29/7), and (31/8), which closely matched Simon's proposed design, at fuel supply pressures ranging from 10 to 200 lb/in<sup>2</sup>. Table 6 lists the experimental results for fuel flow rate and spray cone angle for all 279 nozzles.

## Nozzle Shape and Its Effect on Fuel Flow Rate

Figures 5, 8, and 9 present some of the experimental results on nozzle flow rates that can be represented graphically. Figure 8 shows the variation of fuel flow rate with orifice diameter when the tangential hole diameter is kept constant. Within the range of  $d = D / 7.5$ , the fuel flow rate is proportional to  $d^{0.94}$ . Similarly, Figure 9 shows the variation of fuel flow rate with tangential hole diameter, with the relationship being  $Q \propto p^{0.70}$ . If both the orifice diameter and tangential hole diameter vary simultaneously, it is expected that the flow rate Q will be proportional to the 1.64th power of d or p. Figure 5 confirms this result within experimental error. For standard nozzles, based on Figure 3, when the fuel supply pressure is 100 lb/in<sup>2</sup> and d, p, and D/7.5 are approximately 0.067 inches,  $\Delta Q \propto d^{1.93}$ . Thus, the effect of changes in linear dimensions (which do not automatically change with orifice and tangential hole diameters) causes the fuel flow rate to vary proportionally to  $L^{0.28}$ . Therefore, the effect of nozzle shape changes on fuel flow rate can be summarized in the following equation:

$$Q = A d^{0.94} p^{0.70} L^{0.28}$$

Equation summarizing the effect of nozzle shape changes on fuel flow rate, where A is a constant.

This relationship is relatively accurate within a limited range but can always provide an approximate estimate of the effects of nozzle shape changes.

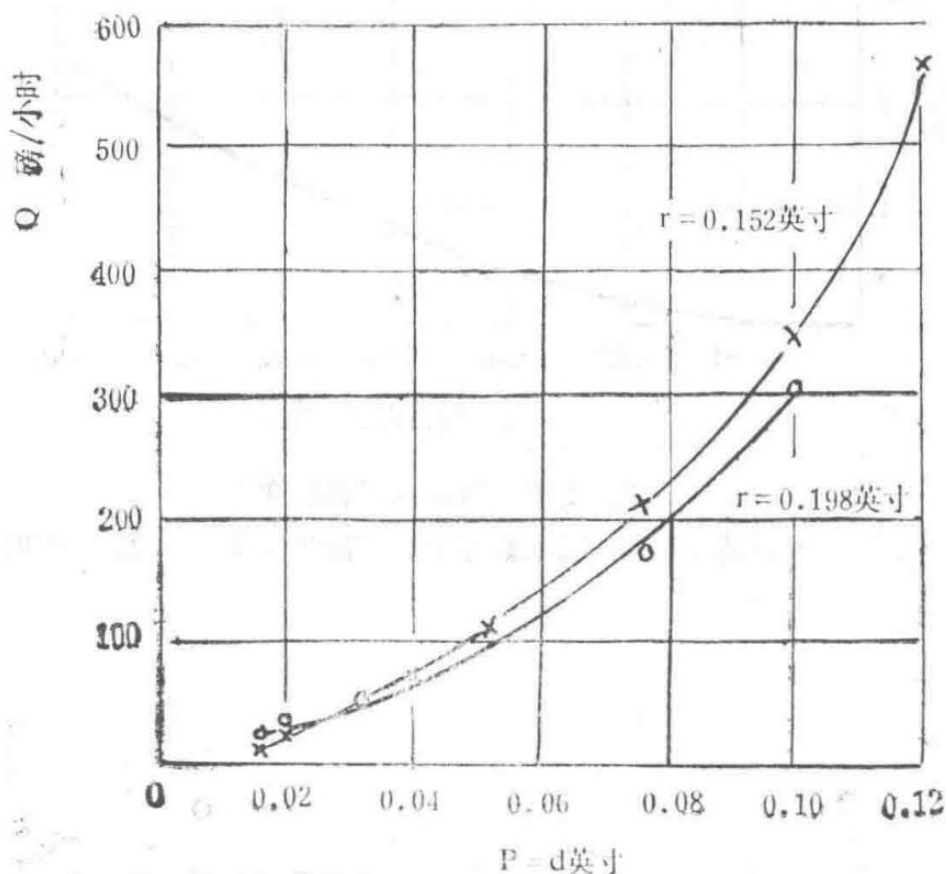


Figure 5 Relationship between Fuel Flow Rate and Nozzle Tangential Hole and Orifice Diameter

Plot showing how fuel flow rate varies with changes in tangential hole diameter and orifice diameter.

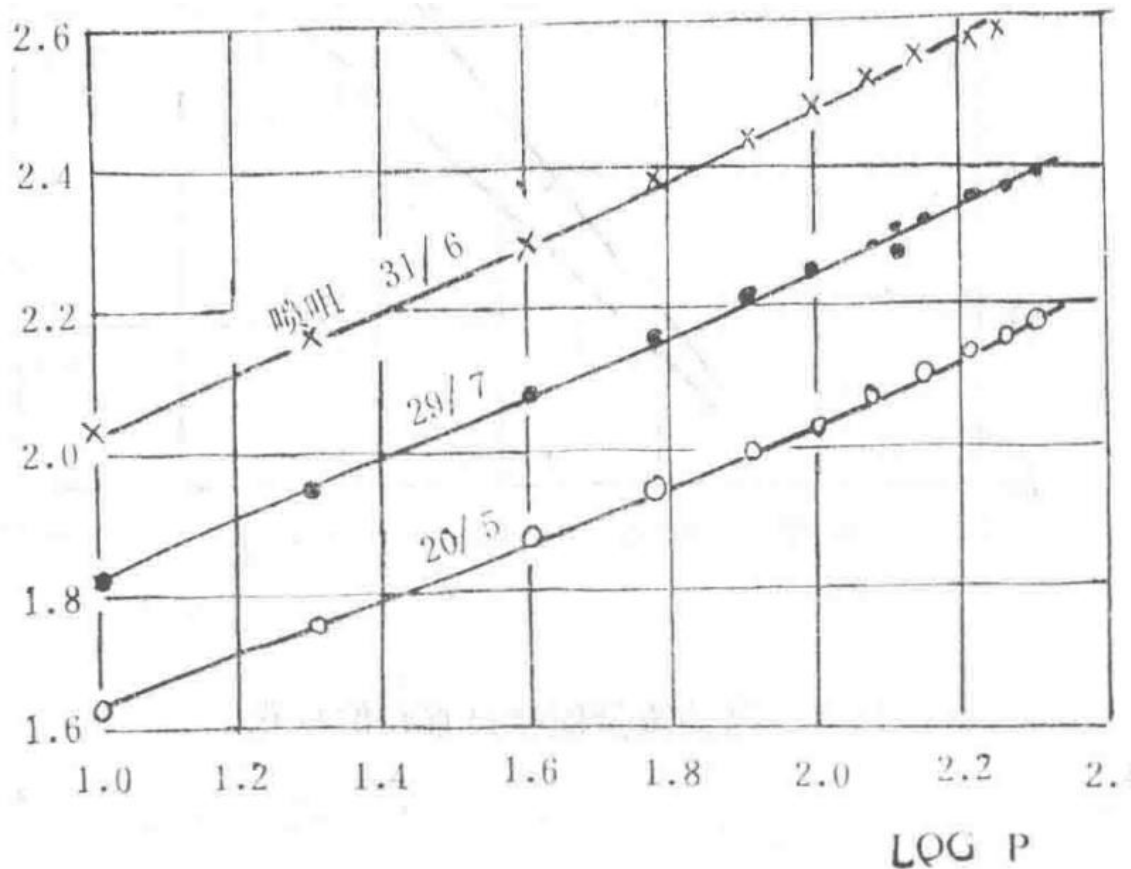


Figure 6 Variation of Kerosene Flow Rate with Pressure for Three Different Nozzles

Plot showing the relationship between kerosene flow rate and pressure for three different nozzle configurations.

— Section 9 —  
Content from Original Document (Pages 41-45)

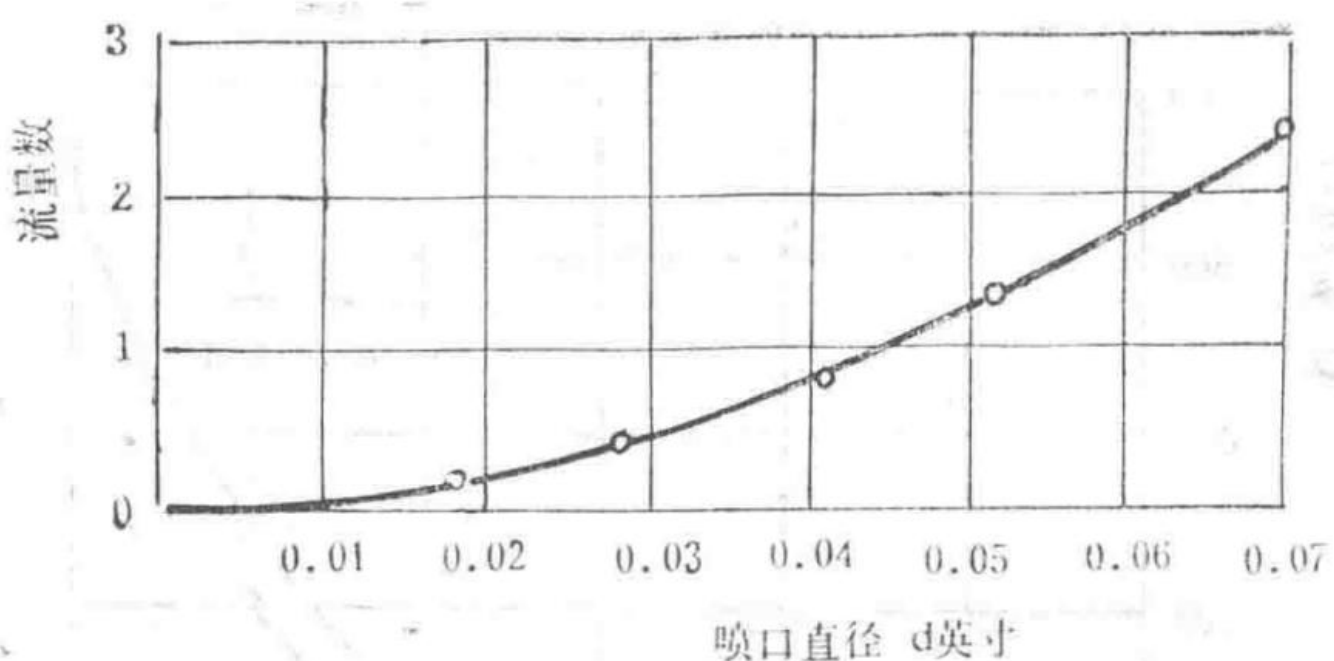


Figure 7 Variation of Kerosene Flow Number with Nozzle Diameter

Graph showing the relationship between kerosene flow number and nozzle diameter at a pressure of 100 psi.

At a pressure of 100 psi, the flow number equals 1/10 of the fuel flow rate (gallons/hour).

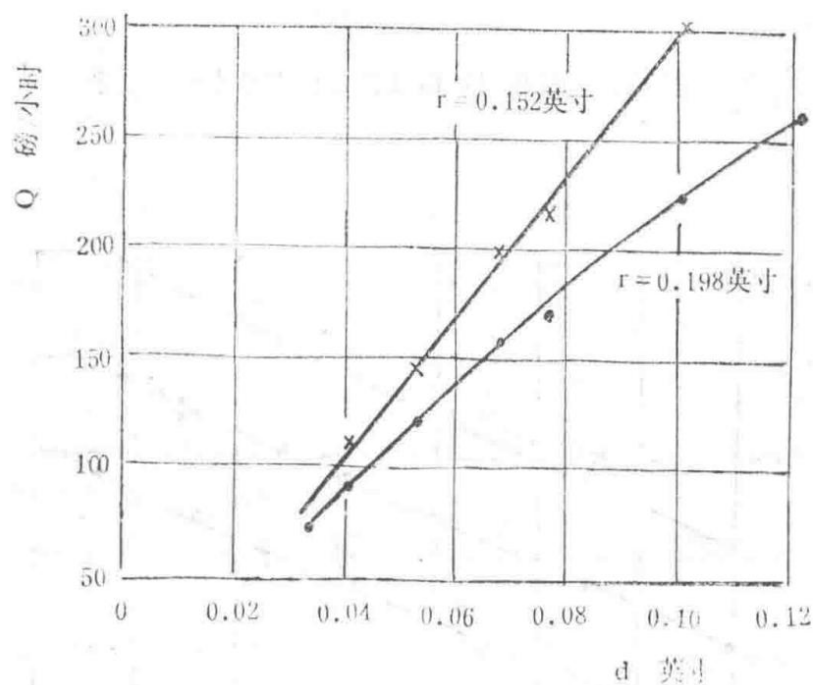


Figure 8 Variation of Fuel Flow Rate with Nozzle Diameter

Graph depicting how fuel flow rate changes with nozzle diameter.

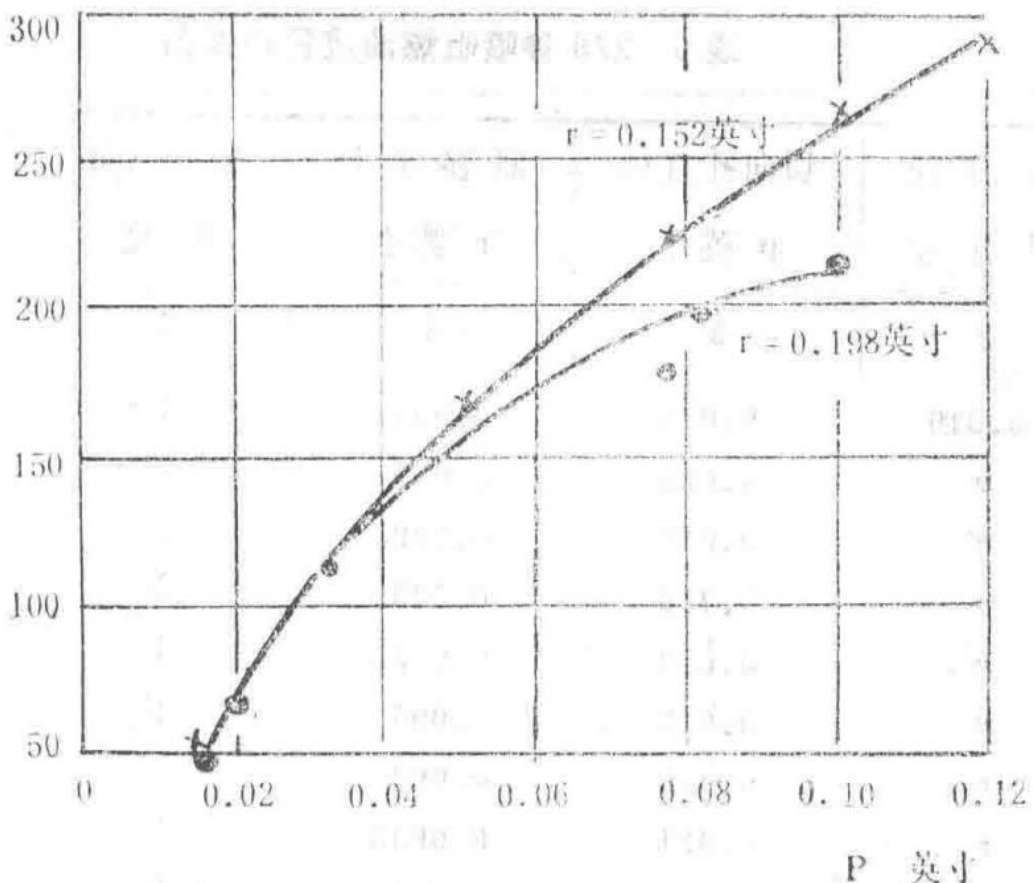


Figure 9 Variation of Fuel Flow Rate with Tangential Hole Diameter

Graph illustrating the relationship between fuel flow rate and tangential hole diameter.

Figure 6 presents the fuel flow rate versus pressure curves for three different nozzles. It is noteworthy that the rate of change of fuel flow with pressure is very small.

Changing the fuel supply pressure can alter the nozzle flow rate, but practical difficulties limit the possible pressure ratio to slightly over 100:1, and the fuel flow rate to no more than about 10:1. Another method of changing the nozzle fuel flow rate depends on the return oil hole in the wall behind the swirl chamber. Figure 10 shows a typical nozzle structure with a return oil hole diameter of  $S$ .

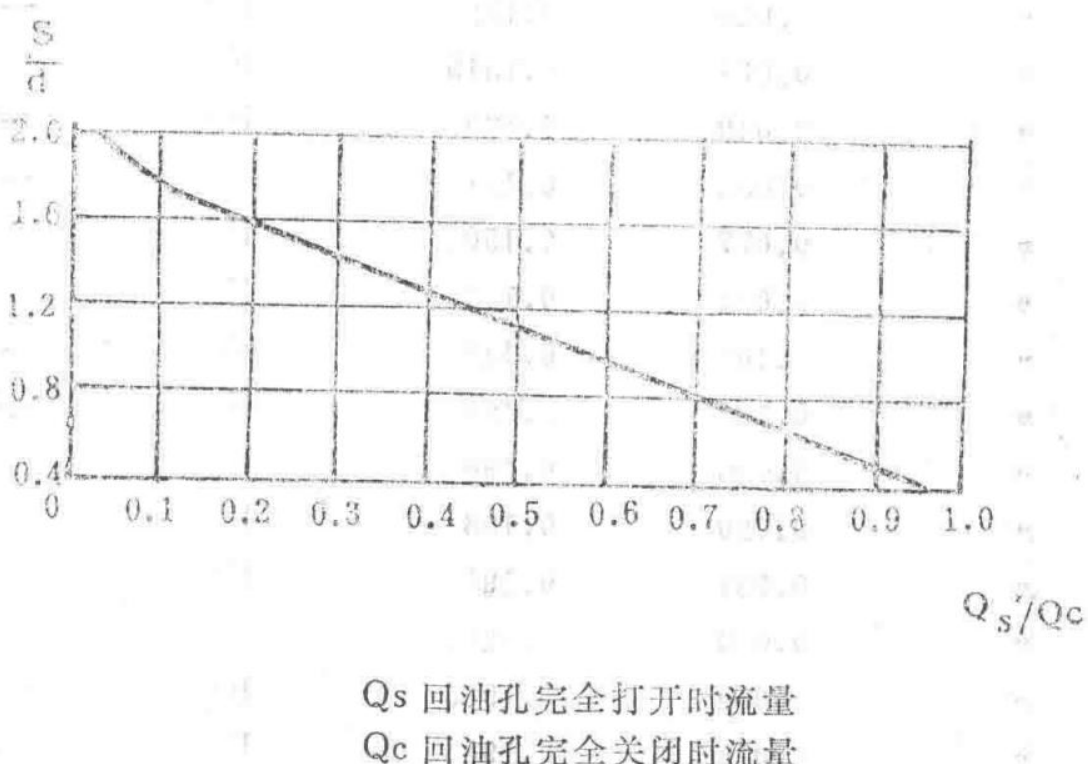


Figure 10 Effect of Return Oil Hole Diameter on Flow Rate

Graph and schematic showing how varying the return oil hole diameter affects the nozzle flow rate and spray cone angle.

By changing the pressure in the return oil pipe, the return oil flow rate can be adjusted, which affects the nozzle output in two ways. When the return oil pipeline is opened to reduce oil pressure, the fuel flow rate through the hole diameter  $d$  decreases, and the spray cone angle increases, even when the supply oil pressure remains constant. Therefore, the fuel flow rate can vary by a ratio related to the diameter ratio of the return oil hole  $S$  to the nozzle diameter  $d$ . According to Simon's method, Figure 10 shows the relationship curves of these ratios. By combining (1) changing the supply oil pressure and (2) changing the oil port pressure, the fuel flow rate can be adjusted by 100 times or more.

## Table 6: Fuel Flow Rate and Cone Angle for 27 Types of Nozzles

Table 6 Fuel Flow Rate and Cone Angle for Various Nozzles

Nozzle No.	Nozzle Orifice Diameter $d$ (inches)	Tangential Hole Diameter $p$ (inches)	Offset Radius $r$ (inches)	Cone Angle $\theta$ (degrees)	$\operatorname{tg}(\theta/2)$	Flow Rate (lb/hour)
(1/1)	0.016	0.016	0.050	F*	—	—
(2/1)	0.016	0.020	0.049	F	—	—
(3/1)	0.016	0.031	0.0495	F	—	—
(4/1)	0.016	0.040	0.0495	F	—	—
(5/1)	0.016	0.052	0.0495	F	—	—
(6/1)	0.016	0.016	0.096	F	—	—
(7/1)	0.016	0.020	0.096	F	—	—
(8/1)	0.016	0.031	0.0965	F	—	—
(9/1)	0.016	0.040	0.097	F	—	—

(10/1)	0.016	0.052	0.052	F	—	—
(21/1)	0.016	0.077	0.095	F	—	—
(22/1)	0.016	0.083	0.093	F	—	—
(23/1)	0.016	0.105	0.095	F	—	—
(24/1)	0.016	0.122	0.096	F	—	—
(11/1)	0.016	0.016	0.152	53	0.499	23.5
(12/1)	0.016	0.020	0.152	F	—	—
(13/1)	0.016	0.031	0.1515	F	—	—
(14/1)	0.016	0.040	0.162	F	—	—
(15/1)	0.016	0.052	0.151	F	—	—
(25/1)	0.016	0.077	0.1505	F	—	—
(26/1)	0.016	0.084	0.151	F	—	—
(27/1)	0.016	0.102	0.148	F	—	—
(28/1)	0.016	0.122	0.150	F	—	—
(16/1)	0.016	0.016	0.198	F	—	—
(17/1)	0.016	0.020	0.198	F	—	—
(18/1)	0.016	0.031	0.198	F	—	—
(19/1)	0.016	0.040	0.1985	F	—	—
(20/1)	0.016	0.052	0.1985	F	—	—
(29/1)	0.016	0.076	0.1985	F	—	—
(30/1)	0.016	0.083	0.198	F	—	—
(31/1)	0.016	0.100	0.197	F	—	—
(1/2)	0.0195	0.016	0.050	64	0.625	28.4
(2/2)	0.0195	0.020	0.049	63	0.613	34.9
(3/2)	0.0195	0.051	0.0495	F	—	—
(4/2)	0.0195	0.040	0.0495	F	—	—
(5/2)	0.0195	0.052	0.0495	F	—	—
(6/2)	0.0195	0.016	0.096	60	0.577	26.5
(7/2)	0.0195	0.020	0.096	63	0.613	29.4
(8/2)	0.0195	0.031	0.0965	57	0.543	41.1
(9/2)	0.0195	0.040	0.097	F	—	—
(10/2)	0.0195	0.052	0.052	58	0.499	45.4
(21/2)	0.0195	0.077	0.095	F	—	—
(22/2)	0.0195	0.083	0.093	F	—	—
(23/2)	0.0195	0.105	0.095	F	—	—
(24/2)	0.0195	0.122	0.096	F	—	—
(11/2)	0.0195	0.016	0.152	55	0.521	25.25
(12/2)	0.0195	0.020	0.152	57	0.543	28.7

(13/2)	0.0195	0.031	0.1515	59	0.566	39.0
(14/2)	0.0195	0.040	0.152	62	0.601	42.9
(15/2)	0.0195	0.052	0.151	F	—	—
(25/2)	0.0195	0.077	0.1505	F	—	—
(26/2)	0.0195	0.084	0.151	F	—	—
(27/2)	0.0195	0.102	0.148	F	—	—
(28/2)	0.0195	0.122	0.150	F	—	—
(16/2)	0.0195	0.016	0.198	53	0.499	25.8
(17/2)	0.0195	0.020	0.198	51	0.477	31.0
(18/2)	0.0195	0.031	0.198	55	0.521	38.3
(19/2)	0.0195	0.040	0.1985	F	—	—
(20/2)	0.0195	0.052	0.1985	F	—	—
(29/2)	0.0195	0.076	0.1985	F	—	—
(30/2)	0.0195	0.083	0.198	F	—	—
(31/2)	0.0195	0.100	0.197	F	—	—
(1/3)	0.033	0.016	0.050	70	0.700	40.35
(2/3)	0.033	0.020	0.049	67	0.637	50.6
(3/3)	0.033	0.031	0.0495	53	0.499	71.2
(4/3)	0.033	0.040	0.0495	43	0.394	88.5
(5/3)	0.033	0.052	0.0495	47	0.435	95.5
(6/3)	0.033	0.016	0.096	75	0.767	38.7
(7/3)	0.033	0.020	0.096	71	0.713	36.8
(8/3)	0.033	0.031	0.0965	65	0.637	62.0
(9/3)	0.033	0.040	0.097	58	0.554	70.0
(10/3)	0.033	0.052	0.052	54	0.510	80.9
(21/3)	0.033	0.077	0.095	F	—	—
(22/3)	0.033	0.083	0.093	F	—	—
(23/3)	0.033	0.105	0.095	F	—	—
(24/3)	0.033	0.122	0.096	F	—	—
(11/3)	0.033	0.016	0.152	63	0.613	36.5
(12/3)	0.033	0.020	0.152	70	0.700	44.8
(13/3)	0.033	0.031	0.1515	63	0.601	58.2
(14/3)	0.033	0.040	0.152	65	0.637	62.7
(15/3)	0.033	0.052	0.151	58	0.554	69.4
(25/3)	0.033	0.077	0.1505	52	0.488	82.5
(26/3)	0.033	0.084	0.151	F	—	—
(27/3)	0.033	0.102	0.148	F	—	—
(28/3)	0.033	0.122	0.150	F	—	—

(16/3)	0.033	0.016	0.198	72	0.740	37.0
(17/3)	0.033	0.020	0.198	65	0.637	46.4
(18/3)	0.033	0.031	0.198	68	0.675	56.9
(19/3)	0.033	0.040	0.1985	63	0.613	59.9
(20/3)	0.033	0.052	0.1985	58	0.554	67.5
(29/3)	0.033	0.076	0.1985	54	0.510	74.0
(30/3)	0.033	0.083	0.198	48	0.445	75.5
(31/3)	0.033	0.100	0.197	48	0.445	83.0
(1/4)	0.042	0.016	0.050	75	0.767	46.4
(2/4)	0.042	0.020	0.049	73	0.734	60.0
(3/4)	0.042	0.031	0.0495	60	0.577	91.5
(4/4)	0.042	0.040	0.0495	67	0.662	113
(5/4)	0.042	0.052	0.0405	58	0.554	128
(6/4)	0.042	0.016	0.096	83	0.885	44.1
(7/4)	0.042	0.020	0.096	79	0.824	55.7
(8/4)	0.042	0.031	0.0965	69	0.687	78.1
(9/4)	0.042	0.040	0.097	65	0.637	90.4
(10/4)	0.042	0.052	0.052	61	0.589	108
(21/4)	0.042	0.077	0.095	48	0.445	136
(22/4)	0.042	0.083	0.093	45	0.414	142
(23/4)	0.042	0.105	0.095	F	—	—
(24/4)	0.042	0.122	0.096	F	—	—
(11/4)	0.042	0.016	0.152	78	0.810	40
(12/4)	0.042	0.020	0.152	77	0.795	53.5
(13/4)	0.042	0.031	0.1515	75	0.767	72.5
(14/4)	0.042	0.040	0.152	72	0.727	79.6

— Section 10 —  
Content from Original Document (Pages 46-50)

F indicates that the fuel film cannot expand.

#### Nozzle Shape and Spray Cone Angle

Table 4 provides the measured data of the spray cone angle. Based on this data, multiple curves can be plotted. Figures 11 to 13 show three of these curves, illustrating the relationship between the tangent of half the cone angle,  $\operatorname{tg}(\theta/2)$ , and (1) nozzle orifice diameter, (2) tangential hole diameter, and (3) nozzle swirl chamber diameter.

Table 6 (Continued) - Measurement Data of Spray Cone Angle

Figure 11: Variation of Cone Angle  $\theta$  with Nozzle Orifice Diameter  $d$  (Swirl Chamber Diameter = 0.5 in, Tangential Hole Diameter = 0.077 in, Offset Radius = 0.198 in)

— Section 11 —  
Content from Original Document (Pages 51-55)

The relationship between the spray cone angle and the variation of both the orifice diameter and the tangential hole diameter is of interest. The spray cone angle increases with the increase of the orifice diameter and decreases with the increase of the tangential hole diameter. When both diameters increase simultaneously, the spray cone angle increases. However, the measured curves of the spray cone angle exhibit certain inconsistencies due to the difficulty in maintaining the required machining precision for each part of the nozzle. In particular, achieving satisfactory holes with diameters of a few thousandths of an inch is challenging.

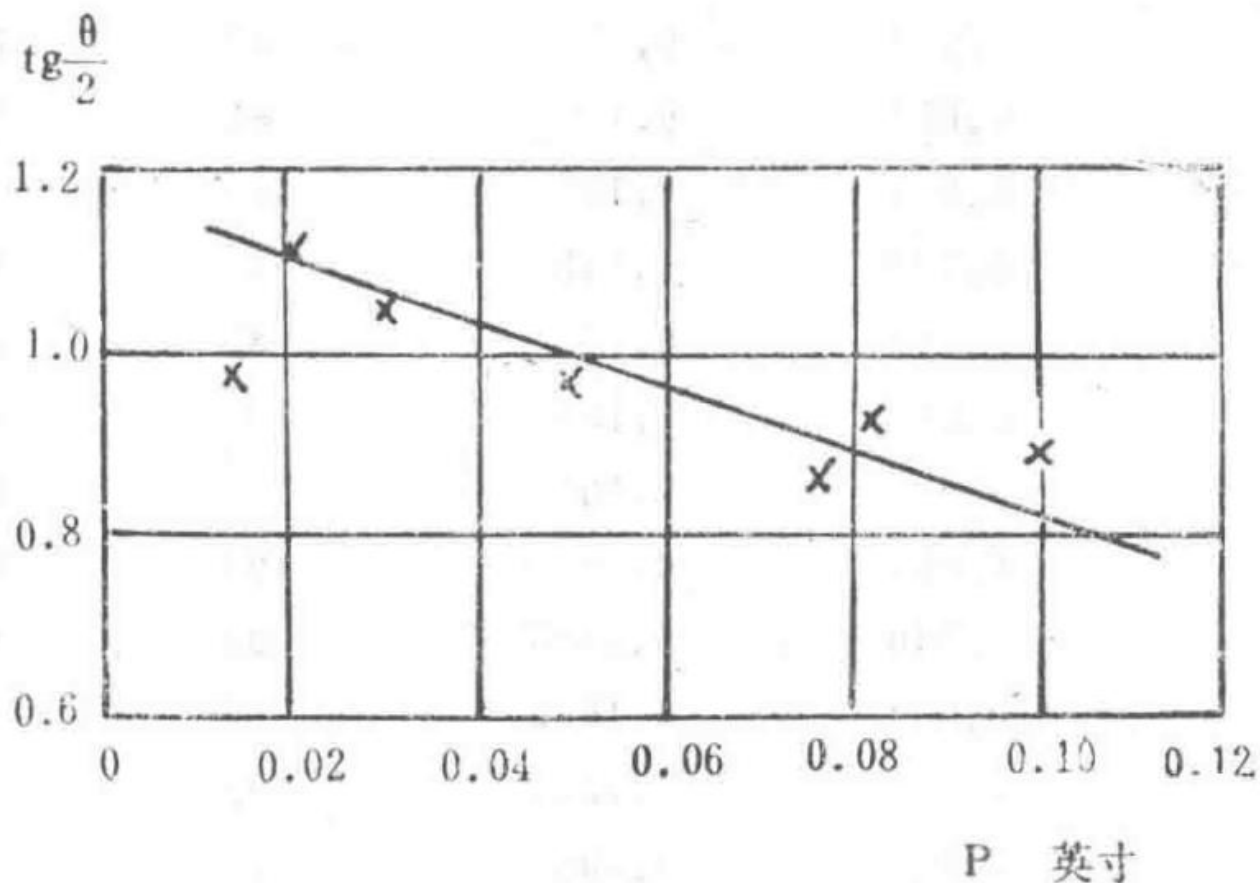


Figure 12 Variation of cone angle  $\theta$  with tangential hole diameter  $P$  for a nozzle with a swirl chamber diameter of 0.5 inches, offset radius of 0.198 inches, and orifice diameter of 0.077 inches

This image shows a graph depicting how the spray cone angle  $\theta$  changes with the tangential hole diameter  $P$  under specified nozzle dimensions.

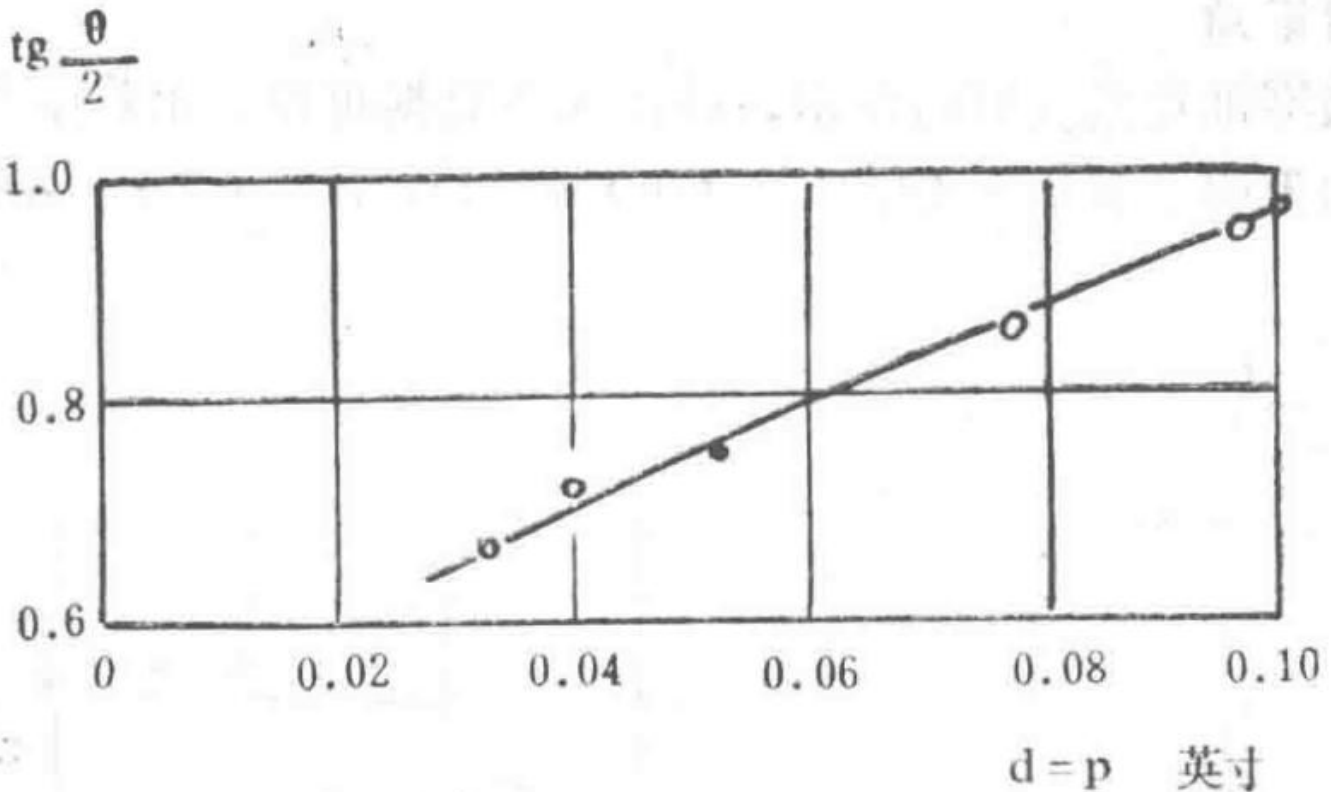


Figure 13 Relationship of cone angle  $\theta$  with simultaneous variation of tangential hole diameter  $p$  and orifice diameter  $d$

This image illustrates the relationship between the spray cone angle  $\theta$  and the combined changes in tangential hole diameter  $p$  and orifice diameter  $d$ .

## Spray Droplet Size

The droplet size distribution produced by centrifugal nozzles generally conforms to Equation (3):

$$R = e^{-(x \sqrt{x})^n}$$

Equation representing the weight fraction  $R$  of spray droplets larger than size  $X$ , where  $\sqrt{X}$  and  $n$  are constants determining droplet size and distribution.

Where  $R$  is the weight fraction of spray droplets with diameters larger than  $X$ ;  $\sqrt{X}$  and  $n$  are two constants that determine the droplet size and its distribution. Needham (1946) studied the relationship between the surface mean diameter of fuel droplets and  $\sqrt{X}$  for nozzles of different sizes and shapes from Lucas Company. He concluded that there is a good correlation between droplet size and  $182 Q^{0.25} / P^{0.4}$ . The experimental results were obtained within a pressure range of 6 to 125 psi and a flow number range of 0.5 to 4.15. The relationship between droplet size, flow rate, and pressure was also studied for a jet engine nozzle with an orifice diameter  $d = 0.040$  inches, tangential hole diameter  $p = 0.028$  inches, return oil hole of 0.060 inches, and swirl chamber diameter of 0.2 inches. When there was no difference between the experimental conditions with the return oil passage open or closed, he found that the droplet diameter, where the surface area to volume ratio matches the corresponding value in the spray (this diameter is sometimes referred to as the Surface Mean Diameter, S.M.D.), conforms to the following relationship:

Upon re-examining these results, it was found that for jet engine nozzles with the return oil passage closed, a more precise relationship between S.M.D.,  $Q$ , and  $P$  (as shown in Figure 14) is given by:

$$S.M.D = 325 Q^{0.318} / P^{0.530}$$

Equation representing the relationship between Surface Mean Diameter (S.M.D.), fuel flow rate  $Q$ , and pressure  $P$ .

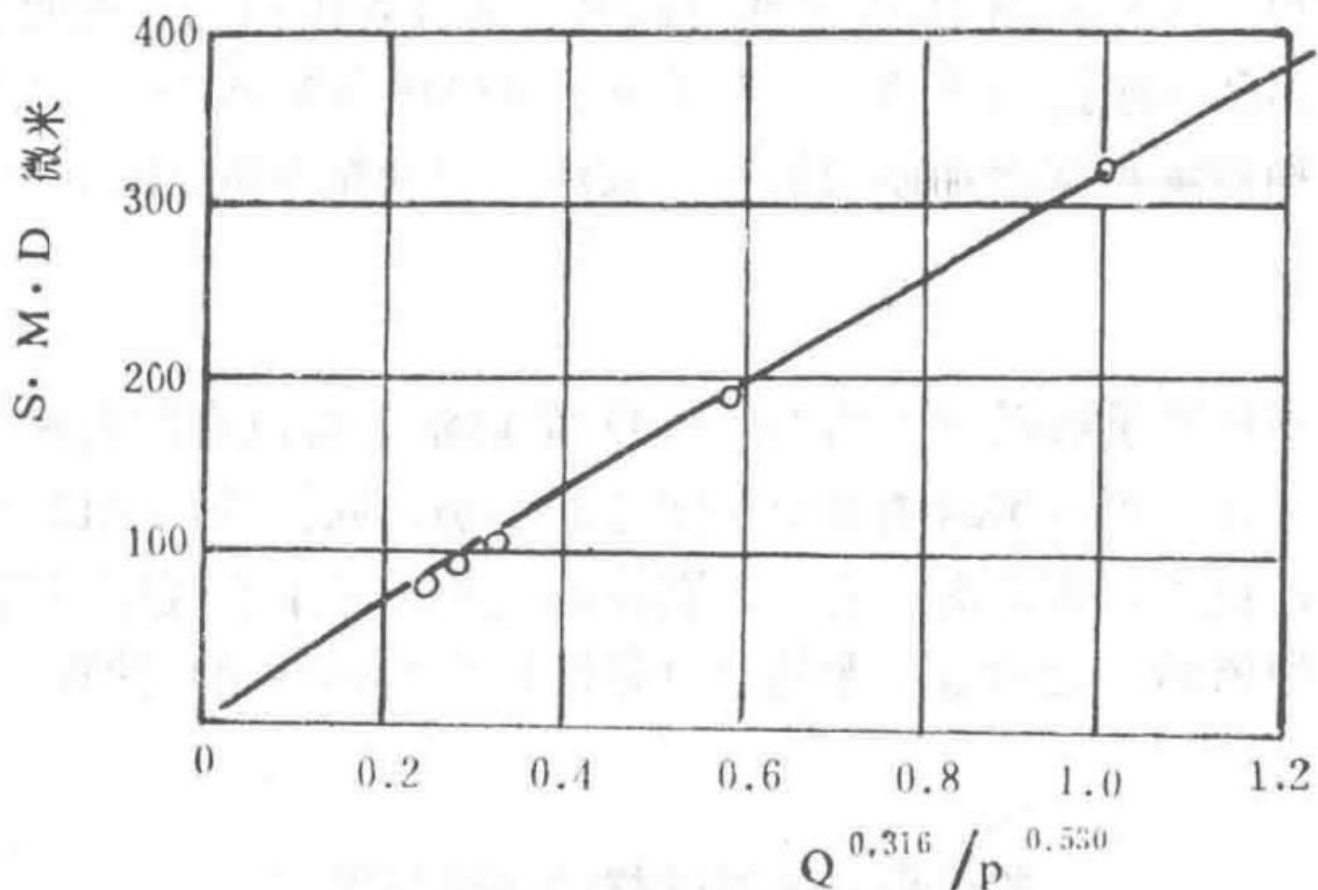


Figure 14 Variation of Surface Mean Diameter with fuel flow rate (lb/hr) and pressure P (psi)

This image shows a graph depicting how the Surface Mean Diameter (S.M.D.) changes with fuel flow rate and pressure.

$\frac{\text{S.M.D. (回油孔开)}}{\text{S.M.D. (回油孔关)}}$

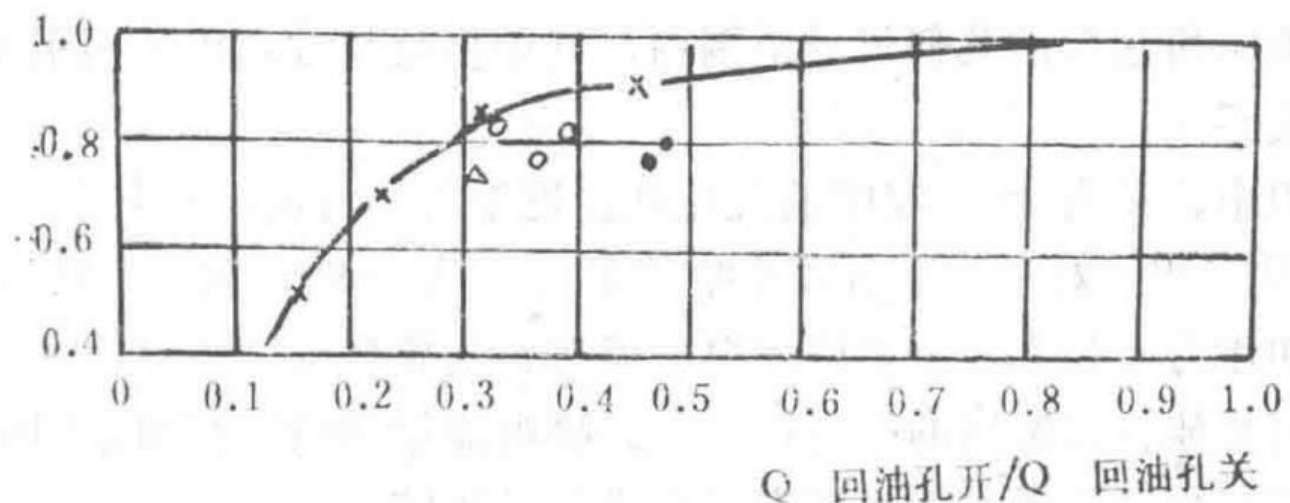


Figure 15 Variation of Surface Mean Diameter with fuel flow rate when changing fuel flow by controlling the return oil hole

Symbols:  $\times$  Nozzle A,  $\circ$  Nozzle B,  $\triangle$  Nozzle C,  $\cdot$  Nozzle D. This image shows the effect of opening the return oil passage on the relationship between the S.M.D. ratio (with return oil passage open to closed) and the corresponding flow rate ratio.

For the same nozzle ( $\Delta$ ), Figure 15 shows the effect of opening the return oil passage on the relationship between: (1) the ratio of S.M.D. of the nozzle spray with the return oil passage open to that with it closed, and (2) the corresponding flow rate ratio. Since Needham demonstrated that different shapes and flow numbers of Lucas nozzles fit Equation (4), it is reasonable to expect that jet engine nozzles with different flow numbers and shapes will fit Equation (5). There is no other data available on the droplet size of jet engine nozzles with the return oil hole closed. However, Joyce referenced three nozzles of nearly standard shape and orifice diameters of 0.036, 0.050, and 0.075 inches (referred to here as Nozzles B, C, and D, respectively) and obtained six measurements. Using Equation (5) to calculate the S.M.D. with the return oil passage closed, the ratio of S.M.D. with the return oil passage open to that with it closed can be determined, and their relationship with the corresponding fuel flow rate ratio (with the return oil passage open to closed) can be plotted. This is shown in Figure 15. The fact that these points closely align with the curve indicates that the S.M.D. of return-flow nozzles can be reliably calculated using Equation (5) and the curve in Figure 15. Nevertheless, further experiments with more nozzles are still desirable. According to curves published by Joyce (1949), the S.M.D. of centrifugal nozzles increases slightly with viscosity, approximately proportional to the 0.2 power of the kinematic viscosity.

## Conclusions

The results indicate that for fuels with sufficiently low viscosity (approximately 20 centipoise), it is possible to design jet engine nozzles to provide appropriate flow rates and predict the effects of nozzle shape changes. Similarly, when the pressure of the air into which the fuel is sprayed is known to be 1 atmosphere, the droplet size of the nozzle spray can also be estimated. Further research on the effect of combustion chamber air pressure on fuel atomization quality and the atomization quality of return-flow nozzles (especially for fuels with relatively high viscosity) would be valuable.

## Correspondence Review on Centrifugal Nozzle Performance

Mr. D.R. Carlisle, B.Sc. (Rolls-Royce), noted that the first section of the authors' paper is valuable as it confirms that geometrically similar nozzles, when using various liquids, exhibit a single-valued functional relationship between the flow coefficient  $\sqrt{(Q^2) / d^4 p \rho}$  and the Reynolds number ( $Q/ud$ ).

However, he did not provide guidance on how to design nozzles to meet required flow rates and spray cone angles, although it is evident that this is the purpose of the work described in the second part of the report.

Within the range of geometric dimensions covered by 279 nozzles, most dimensions exceeded practical requirements, obscuring some useful empirical relationships.

Among these nozzles, only 72 had swirl holes nearly tangential. About half of these nozzles had a  $D/d$  ratio greater than 10. There are indications that for an effective nozzle,  $D$  should not exceed  $5d$ . Additionally, it was found that the orifice length significantly affects the spray cone angle and pressure energy loss. For this reason, the orifice length should be as short as possible, ideally down to  $d/5$ .

Below is a description of the work completed by his company on the relationship between flow rate and spray cone angle for centrifugal nozzles, along with a comparison of their results with the authors' nozzle calibration data.

## Relationship for Centrifugal Nozzles Using Kerosene with a Specific Gravity of 0.8

Taylor's (1948) inviscid nozzle theory indicates that the flow coefficient  $K$  is a single-valued function of the parameter  $(4Ap/\pi Dd)$  (Figures 16 to 26), which is the product of the swirl chamber radius and the orifice radius divided by the inlet area. The spray cone angle is also a single-valued function of  $K$ . In practice, as shown by the authors' work, the use of viscous fluids alters the flow pattern within the swirl chamber, leading to significant deviations from the ideal case.

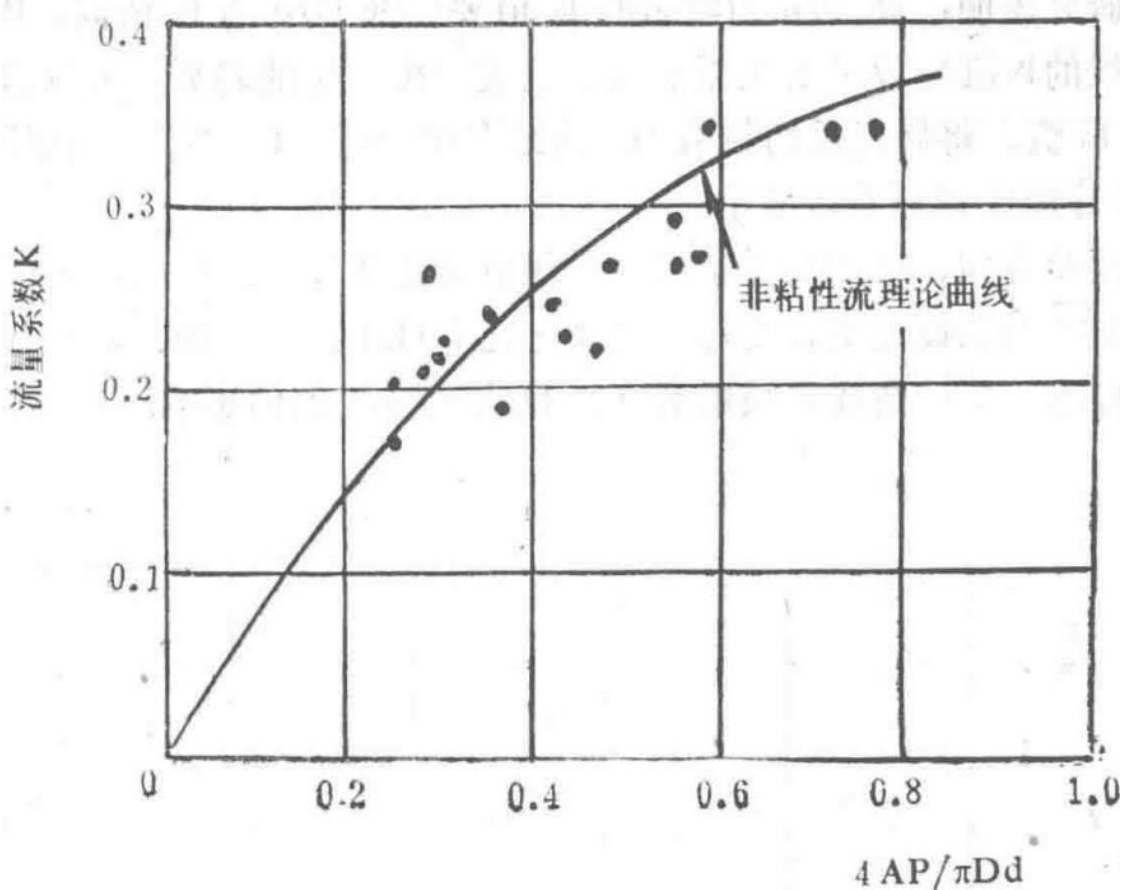


Figure 16 Flow coefficient K for 19 nozzles at a pressure of 700 psi

This image shows the flow coefficient K measured at 700 psi for 19 different nozzles.

Twenty nozzles currently in use were selected for testing, using kerosene as the fuel. Their flow numbers ranged from 0.1 to 0.15, and spray angles from  $70^\circ$  to  $107^\circ$ . Their geometries varied, with some having circular holes and others rectangular slots. Each nozzle was tested for flow rate and spray cone angle within a pressure range of 5 to 700 psi.

### Flow Parameter

Figure 16 shows the flow coefficient K values measured at 700 psi, with the authors presenting the variation of K with Reynolds number Re. The K values in Figure 17 are plotted at pressures where each nozzle yields the same Re, showing some minor scatter in the results.

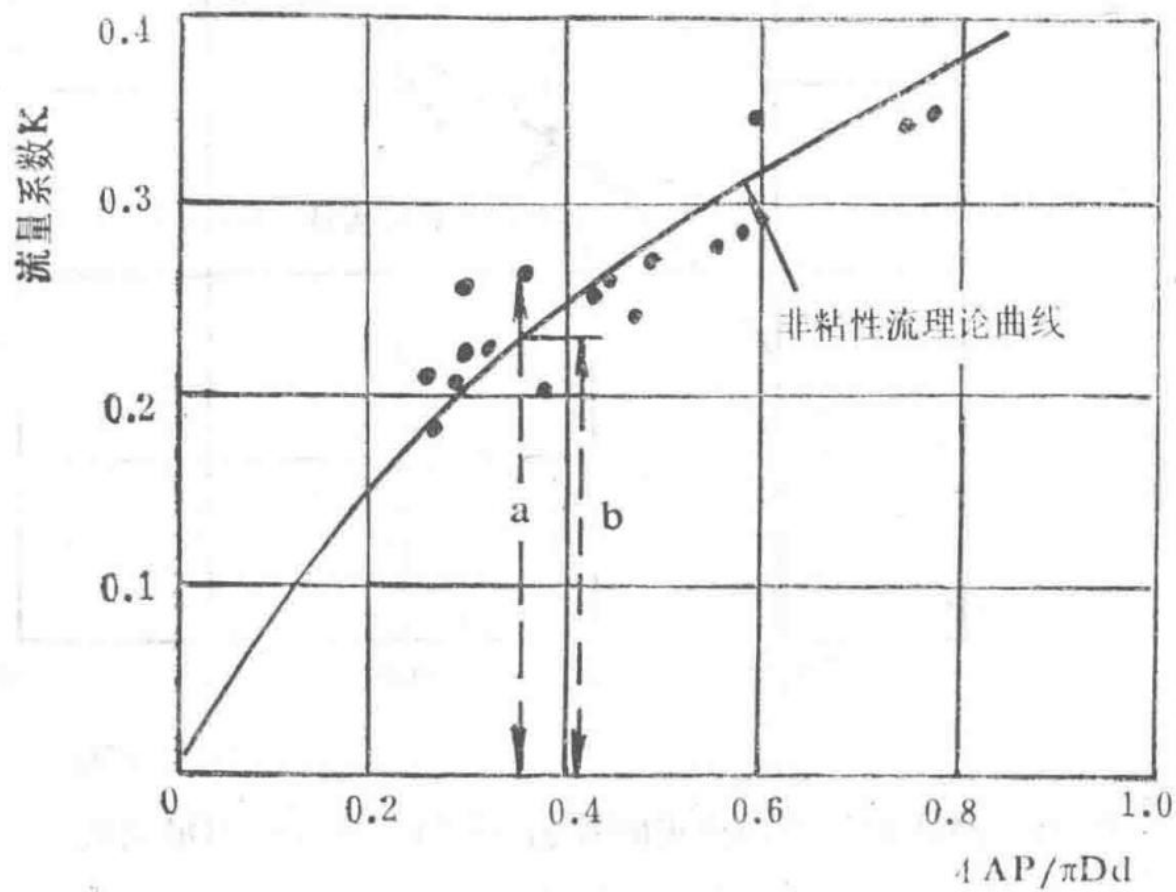


Figure 17 Flow coefficient at the same Reynolds number Re

This image shows the flow coefficient K plotted for nozzles at the same Reynolds number Re.

A study of the scattered points indicates that nozzles with a high D/d ratio have higher K values than those with a low D/d ratio. Therefore, Figure 18 shows the relationship between K values and D/d relative to the theoretical curve, displaying a certain trend. The average curve drawn through these points can be used to correct K values, and the corrected new values K' are plotted in Figure 19 (note: the D/d value on the ideal curve is 3.5). The scatter of points is reduced compared to before.

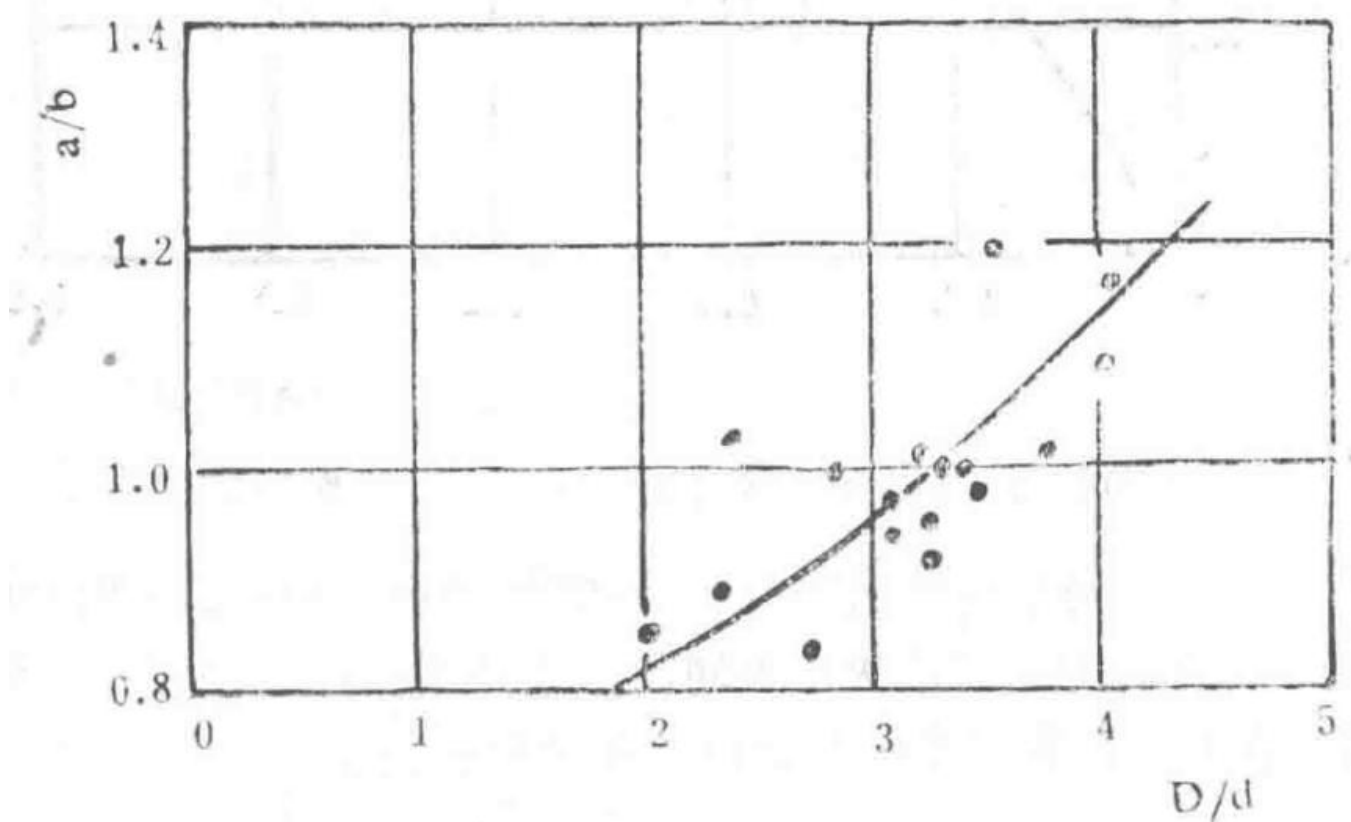


Figure 18 Relationship between the deviation of K values from the ideal curve and the ratio of swirl chamber diameter to orifice diameter D/d ( $a/b$  is the ratio of measured K to ideal K)

This image shows the deviation of K values from the ideal curve as a function of the D/d ratio.

Separate tests showed that increasing the swirl chamber length increases the flow coefficient. Therefore, Figure 20 plots the deviation of K' values from the ideal curve against the ratio of the total swirl chamber length to its diameter (D/L). This curve also shows a certain trend, and similarly, the average curve will be used to correct the effect of D/L on K' values.

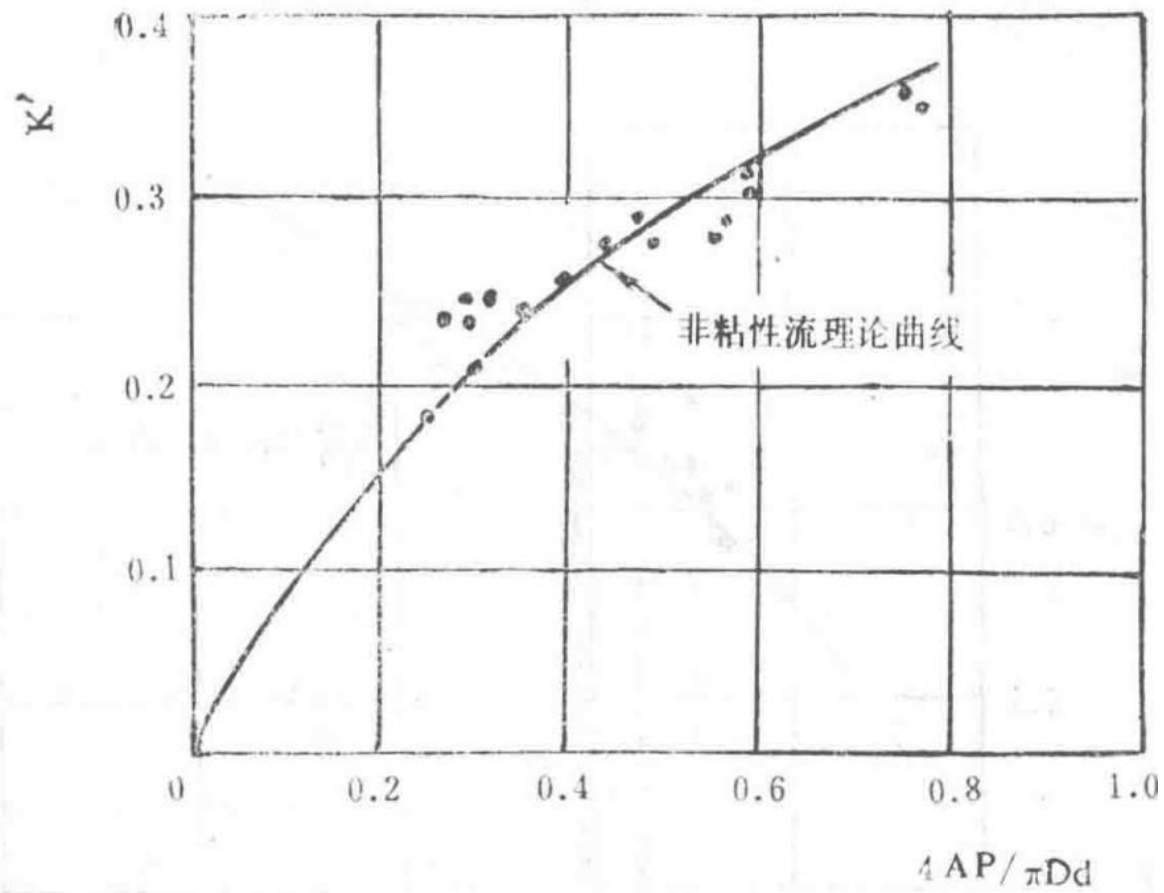


Figure 19 Corrected K values ( $K'$ ) after accounting for  $D/d$  influence, plotted against  $4AP/\pi Dd$

This image shows the corrected K values ( $K'$ ) after adjusting for the influence of the  $D/d$  ratio.

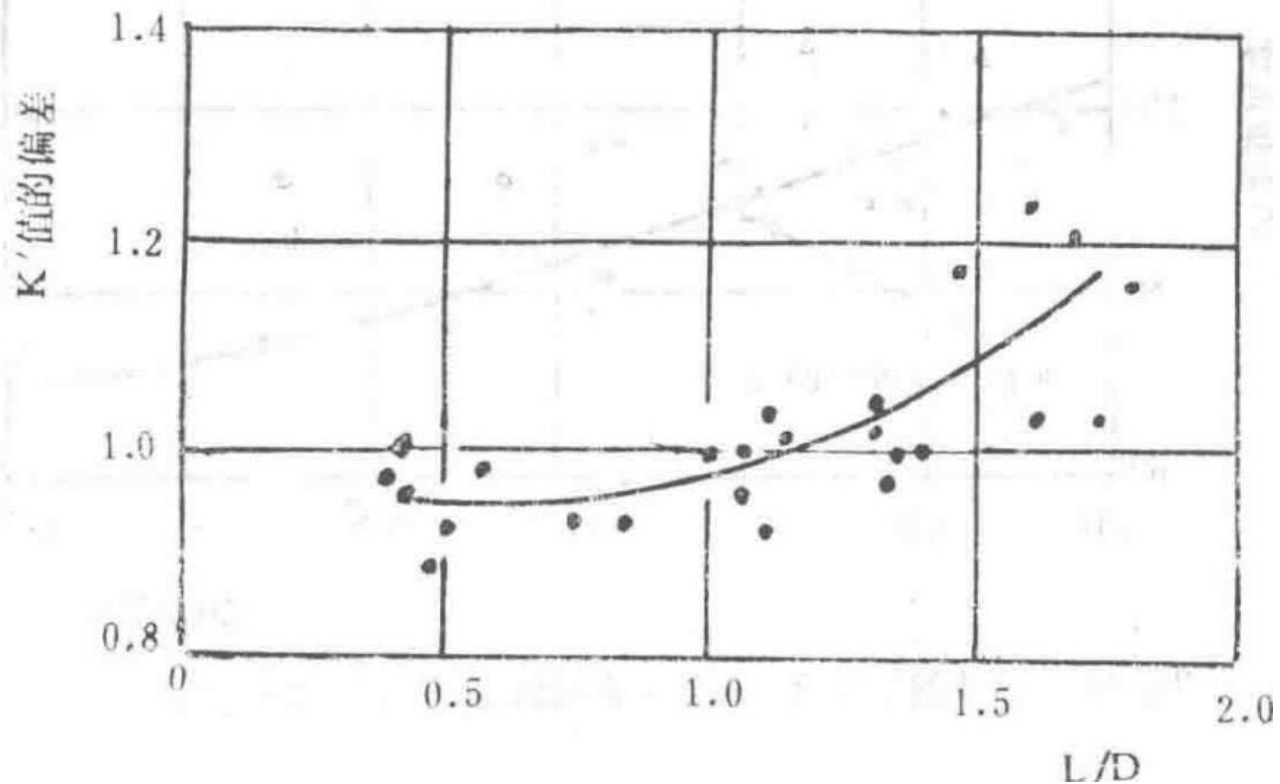


Figure 20: Ratio deviation of  $K'$  value from the ideal curve versus  $L/D$ , where  $I$  is the total length of the swirl chamber

Graph showing the relationship between the proportional deviation of the  $K'$  value from the ideal curve and the length-to-diameter ratio  $L/D$  of the swirl chamber.

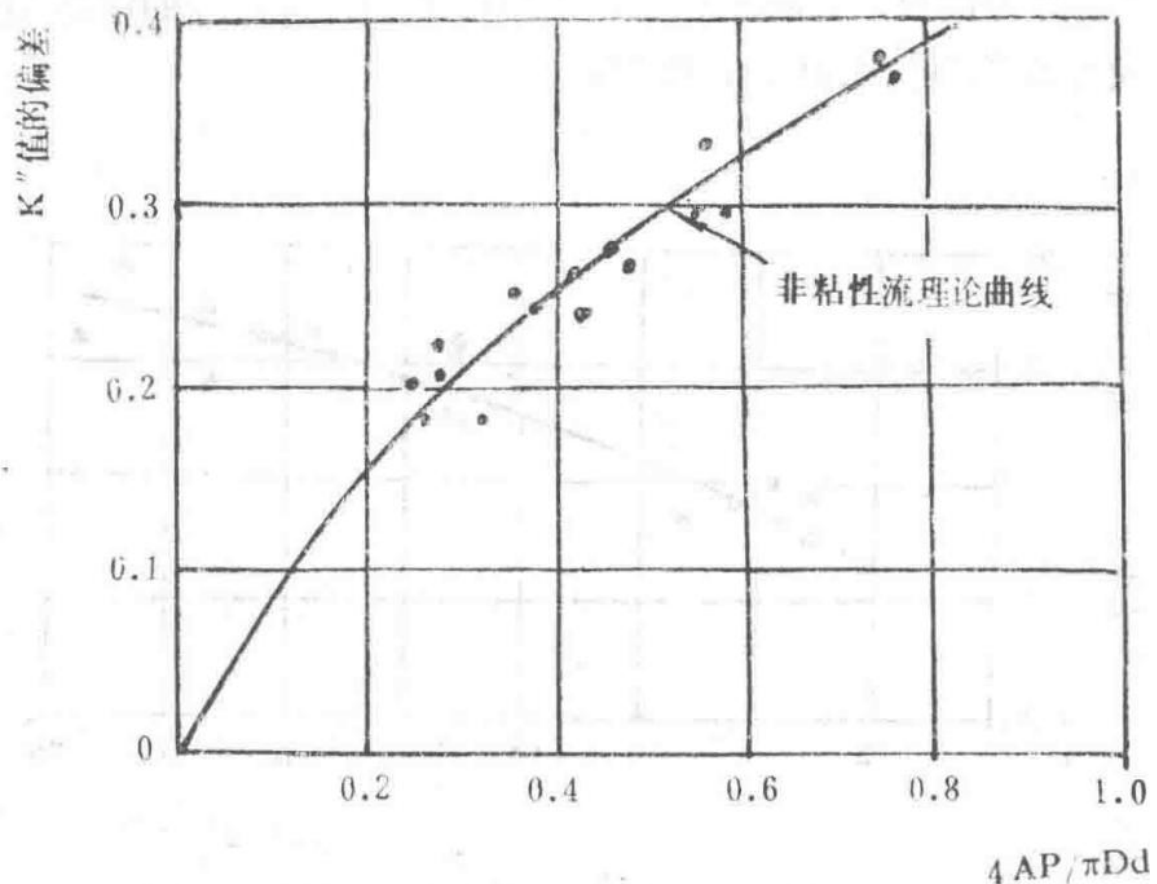


Figure 21: Final corrected  $K''$  versus  $4AP/\pi Dd$ , where  $K''$  is the  $K'$  value after L/D correction

Graph depicting the relationship between the final corrected flow coefficient  $K''$  and the parameter  $4AP/\pi Dd$ .

Figure 21 presents the final corrected flow coefficient  $K''$  curve, where the data points now exhibit a reasonable degree of scatter. The corrections for  $D/d$  and  $L/D$  effects can be conveniently consolidated into a single curve.

## Spray Cone Angle

The spray cone angle is a parameter that is difficult to measure. At low pressures, after the tulip-shaped spray disappears, the spray cone angle gradually increases with pressure until it reaches a maximum value. Subsequently, it decreases due to air entrainment. Different nozzles exhibit their maximum values at different pressures. During the testing process, only the maximum value is considered, regardless of the pressure at which it occurs.

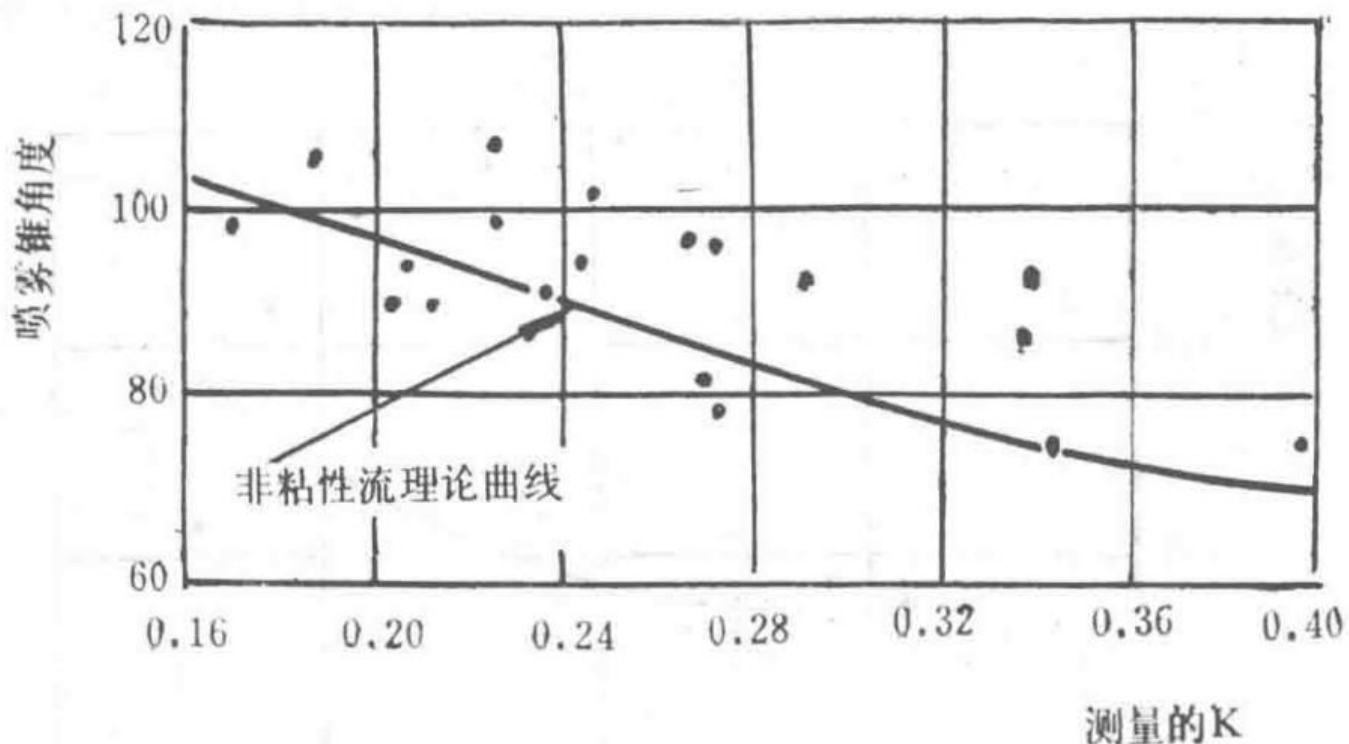


Figure 22: Measured spray cone angle versus measured flow coefficient

Graph showing the relationship between the measured spray cone angle and the measured flow coefficient.

Figure 22 illustrates the relationship between the spray cone angle and the measured flow coefficient. Upon investigation, a trend is observed: nozzles with smaller orifice diameters exhibit smaller spray cone angles compared to those with larger diameters. However, the best correlation is found when plotting the deviation from the ideal curve against the product of the orifice diameter and the flow coefficient ( $K \times d$ ). This latter function approximates the liquid film thickness inside the orifice, which, at constant pressure, is proportional to the Reynolds number  $Re$  based on the liquid film thickness as the characteristic dimension. The aforementioned curve is shown in Figure 23, and the corrected spray cone angle values are presented in Figure 24.

度

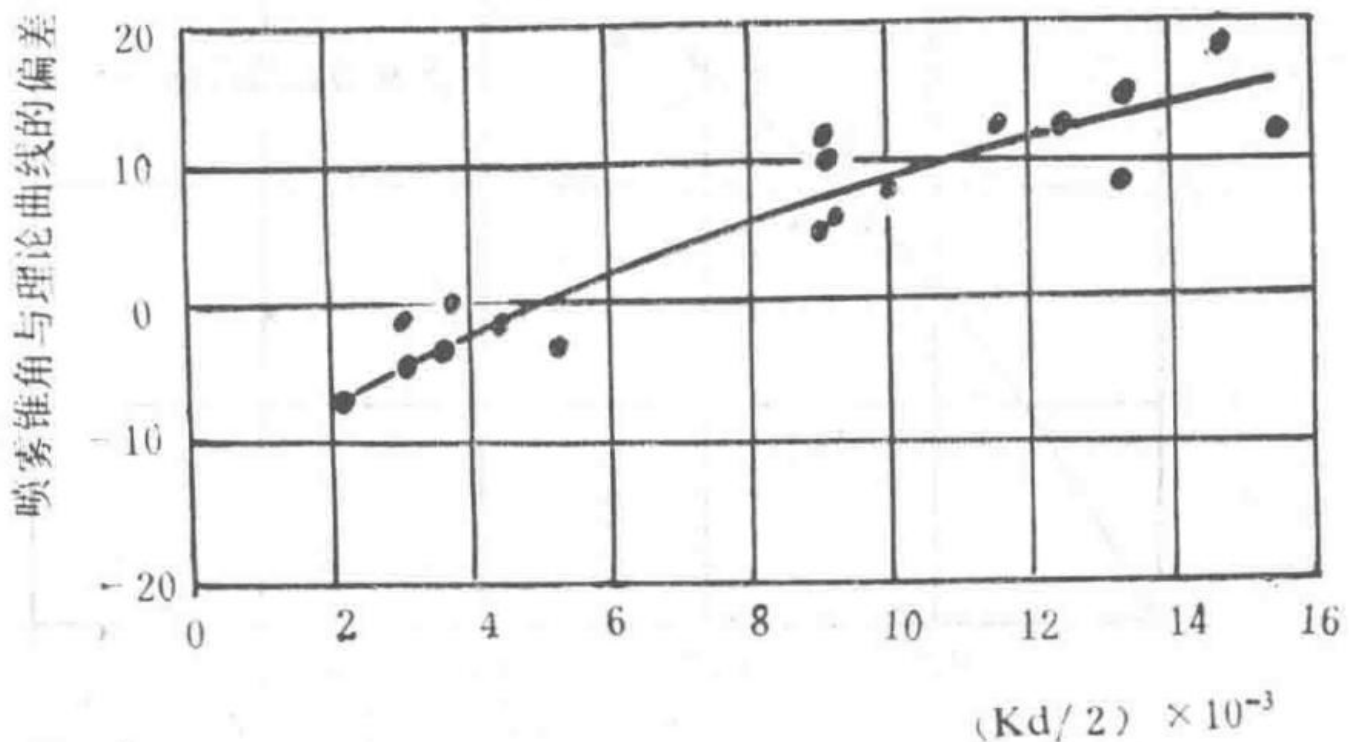


Figure 23: Deviation of spray cone angle from the ideal curve versus  $Kd/2$

Graph depicting the relationship between the deviation of the spray cone angle from the ideal curve and the parameter  $Kd/2$ .

## Design of Kerosene Nozzles for Given Spray Cone Angle and Flow Number

From Figure 24, read the  $K$  value corresponding to the desired spray cone angle, then calculate the orifice diameter using the equation:  $d = 0.0245 \sqrt{(FN / K)}$  (inches).

Next, obtain the spray cone angle deviation from Figure 23. Using the new  $K$  value from Figure 24, recalculate the diameter  $d$ . This  $d$  value should be sufficiently close to the required value (otherwise, iterative approximation is needed).

If possible, the swirl chamber diameter should not exceed 5 times the orifice diameter  $d$ . Use the shortest suitable swirl chamber length and obtain the correction factor for the  $K$  value from Figures 18 and 20. Using the corrected  $K$  (i.e.,  $K''$ ) value, read the  $4AP/\pi Dd$  value from Figure 21 to determine the swirl port area. This process defines the nozzle dimensions for a given flow number and spray cone angle, where the flow number corresponds to the pressure at  $(0.5 / d^2)$  (which relates to the Reynolds number  $Re$  selected for plotting Figure 17).

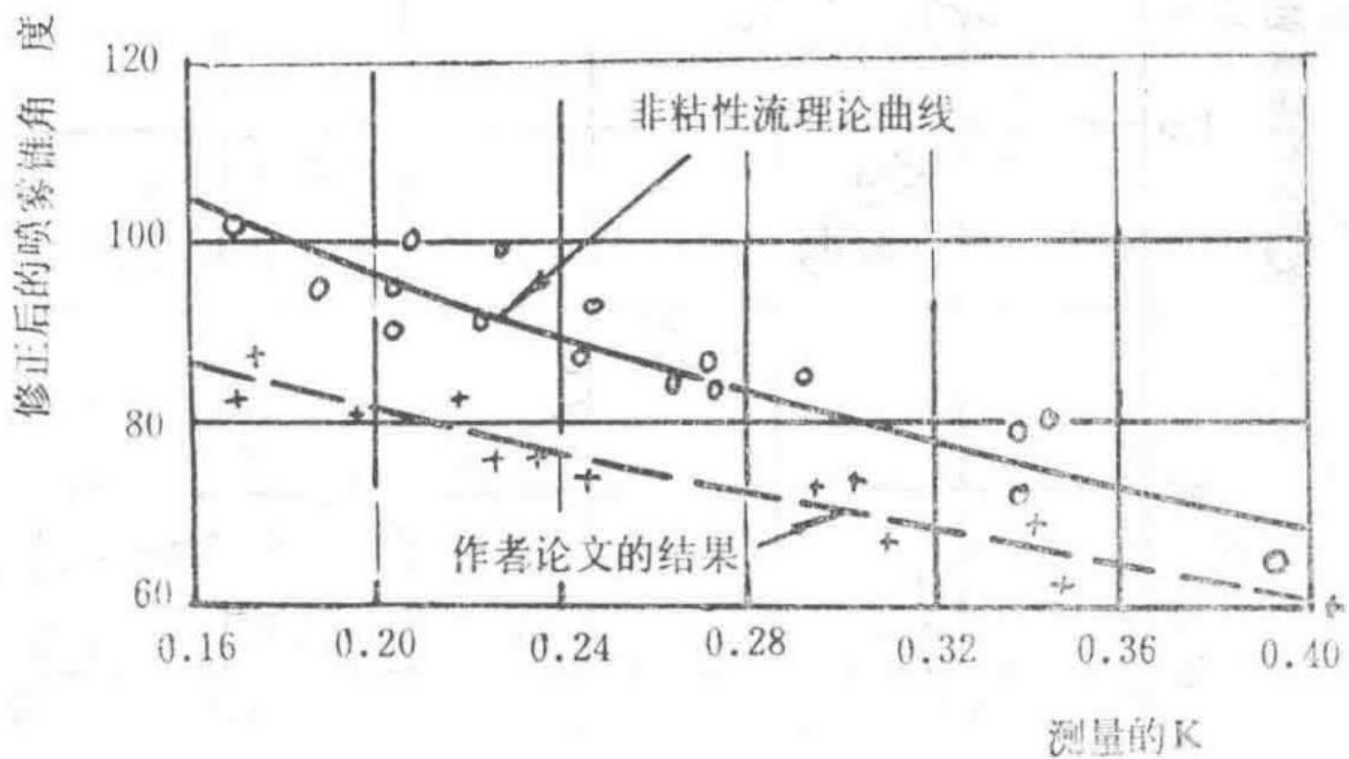


Figure 24: Spray cone angle corrected to the ideal curve using the  $K \cdot d/2$  factor versus measured flow coefficient

Graph showing the relationship between the spray cone angle, corrected using the  $K \cdot d/2$  factor, and the measured flow coefficient.

## Analysis of the Author's Table 6 Results

For the nozzles compiled in Table 6, only those with an offset radius of 0.2 inches and exhibiting spray development at 100 psi were selected. Most nozzles with  $4AP/\pi Dd$  values below 0.1 were excluded, as were nozzles with the N029 sleeve, which were inconsistent with the others.

When these nozzles (36 in total) were corrected for spray cone angle as shown in Figure 25, an excellent relationship between the corrected spray cone angle and the measured flow coefficient was obtained, as depicted in the figure. This curve is also represented in Figure 24. The purpose was to compare it with the results from the author's own company, revealing that the author's spray cone angle curve is  $7^\circ$  to  $17^\circ$  lower. This discrepancy arises from two factors: (1) differences in orifice length, and (2) measurement methods.

Although the spray cone angle relationship is satisfactory, the flow parameter relationship is less clear. The flow parameter results are shown in Figure 26. It can be observed that each orifice size (or  $D/d$  value) has its own  $K$  versus  $4AP/\pi Dd$  relationship curve, which qualitatively confirms the  $D/d$  correction shown in Figure 18. It should also be noted that all data points were obtained at 100 psi, so they could not be plotted at the same Reynolds number  $Re$ . These families of curves are still considered valid, but further testing with more swirl chamber diameters and Reynolds number  $Re$  values would be valuable to confirm them. If the Reynolds number  $Re$  is calculated using the liquid film thickness inside the orifice as the characteristic dimension, these curves might be consolidated into a single-valued curve.

## Summary

It can be seen that for most practical centrifugal nozzles, using inviscid theory and applying corrections for  $D/d$ ,  $L/D$ , and  $Re$  effects allows the design of nozzles with reasonable accuracy to meet specified flow number and spray cone angle requirements.

The relationship between the spray cone angle and K value, corrected for the  $K_d/2$  effect, is particularly valuable. Furthermore, the author's results and those cited from other sources are likely consistent. If more tests with different swirl chamber diameters were conducted to expand these results, the author's K versus  $4AP/\pi D_d$  relationship curve would be less restrictive for design purposes compared to the curves in Figures 16 to 26, enabling application over a broader pressure range.

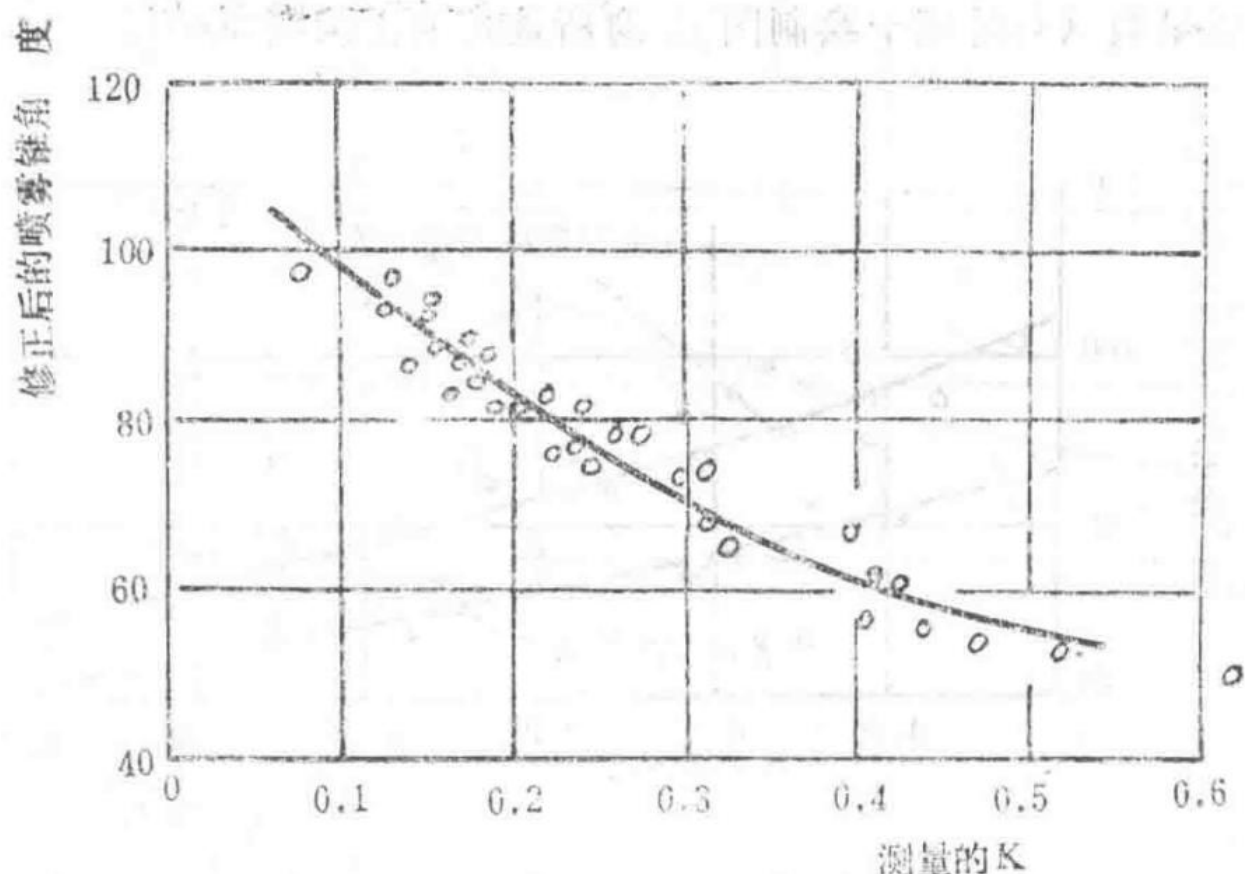


Figure 25: Corrected spray cone angle versus measured flow coefficient for 36 nozzles from the author's paper

Graph showing the relationship between the corrected spray cone angle and the measured flow coefficient for 36 nozzles analyzed in the author's study.

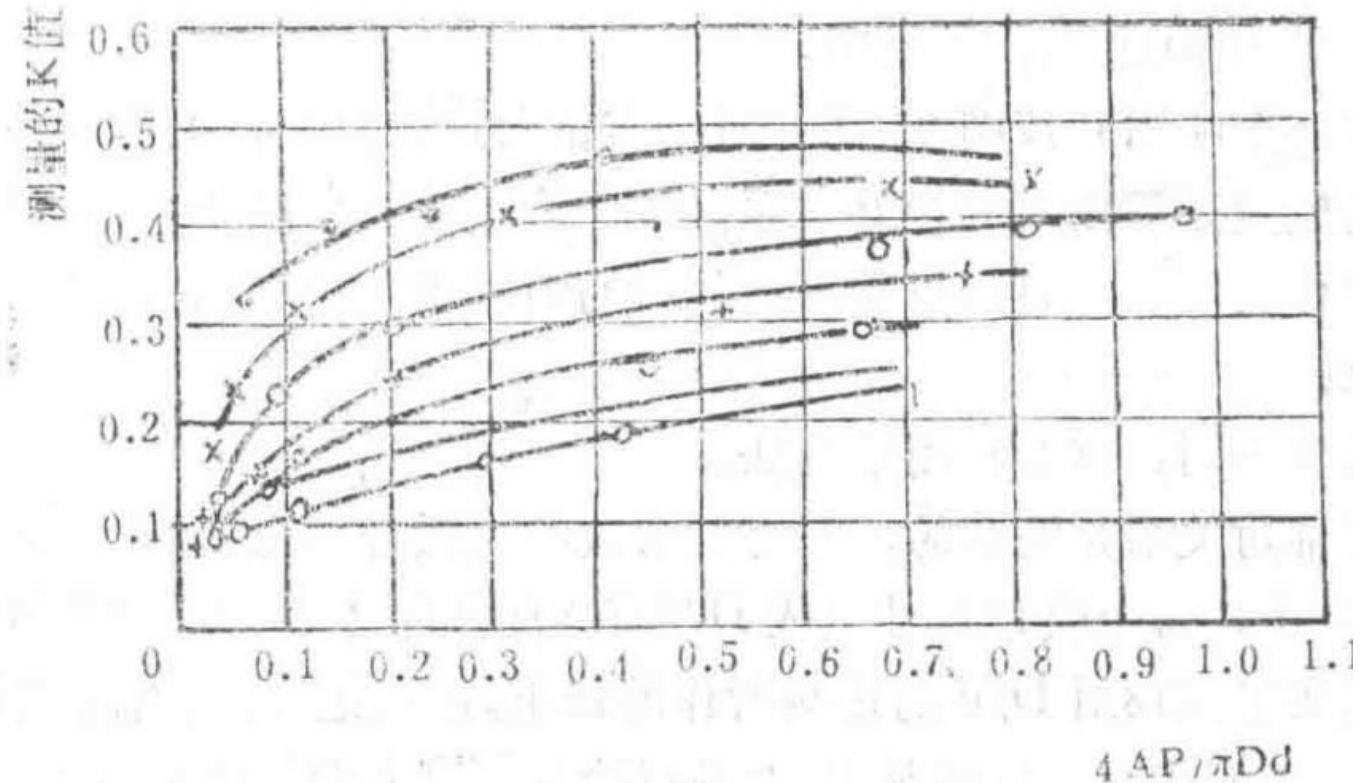


Figure 26: Flow parameter: Author's measured K values versus  $4AP/\pi Dd$

Graph depicting the relationship between the flow parameter K and  $4AP/\pi Dd$  based on the author's measurements.

## Further Comments

As the author pointed out, the flow coefficient varies with pressure, but at higher Reynolds numbers Re, the flow coefficient remains essentially constant, which is very useful.

It should be emphasized that the corrected K value and the spray cone angle correction factor  $Kd/2$  are applicable only to kerosene. However, if the correction factor  $Kd/2$  is processed based on the true Reynolds number using the liquid film thickness inside the orifice as the characteristic dimension, it could be applied to other liquids. Further work in this area would be beneficial.

Exploring pressure losses within the swirl chamber of centrifugal nozzles is a meaningful direction for future research, as the total magnitude of this loss can exceed 50% of the inlet total pressure.

## Remarks by Mr. R·H·Forsrer, B.Sc., B.Eng.

In many centrifugal nozzles, it is noted that the outer edge of the nozzle inlet should be precisely tangent to the swirl chamber to minimize disturbances at the inlet. In fact, the detailed data for the standard-shaped nozzles cited by the author were determined based on this consideration.

It is surprising that the designs selected by the author for testing largely deviate from this rule. Out of 279 tests, only 9 adhered to this principle. The author is curious about the potential impact of this deviation. Conclusions drawn from small nozzle tests appear to contradict this rule.

If the rotation radius increases, the tangential velocity U at the orifice increases according to the relationship  $U \cdot r^{2*}$  being constant. From Table 6, it is clear that as the cone angle widens, the flow rate slightly decreases. Without impact and frictional losses, increasing the offset radius would improve atomization. For the smaller nozzles tested, increasing the offset radius to a certain point causes the oil cone to expand, but further increases in the offset radius prevent the oil cone from expanding, likely due to greater energy loss as the liquid travels a longer path at high speed within the orifice.

It is somewhat unfortunate that the author found it necessary to use different units. The author clearly believes that centrifugal nozzle users in the UK predominantly use these units. However, these nozzles are used for many other fuels, which may require different units. Moreover, outside the UK, using these units is challenging.

In such cases, the use of many dimensionless parameters needs to be discussed. In the author's units, the dimension of the quantity  $Q^2 / d^2 P$  is (pounds or grams)  $\times$  (seconds<sup>2</sup> or hours<sup>2</sup>)  $\times$  (centimeters or inches<sup>2</sup>  $\times$  feet). Converting these units into a consistent system is not straightforward.

## Remarks by Mr. R·P·Fraser, Dr. P·Eisenklam, Dr. H·Dombrowski, and Mr. D·Hasson (London)

The paper provides some very useful data on the influence of two different factors on the flow characteristics of pressure nozzles. First, the author considered the effect of liquid properties on a set of "standard" nozzle similar models (Table 1); second, the influence of various dimensions of non-standard nozzles (Tables 4 and 5). The use of the term "standard" may be inappropriate, as the centrifugal nozzle design used has not been widely adopted by researchers or industry, and no "standard" currently exists.

For non-standard-sized nozzles, the relationship between fluid properties and flow coefficient has not been established, and the application of the design parameter relationship given in equation (2) is limited because their interrelationships were not considered.

The spray cones of the standard nozzles were not provided for various flow rates through the nozzles, making it difficult to determine the overall influence of both flow properties and nozzle size. The spray cone angle determined by flow theory is the maximum spray cone angle obtained from the tangent to the conical liquid film surface (Figure 27).

The author and many other researchers measure the visual cone angle, which is influenced by spray curtain properties such as diffusion boundaries and droplet spatial distribution, rather than the theoretical spray cone angle. This measurement depends on ambient atmospheric pressure and can only be compared under similar conditions. When compared with ideal theory, it can lead to anomalous results. According to ideal theory, the spray cone angle decreases with increasing  $p^2 / 2 r d$ , which aligns with Figures 11 and 12 but contradicts Figure 13. This discrepancy may be attributed to the higher flow number nozzles.

## Reduction of Air Resistance Effects and Spray Cone Angle

The reduction in air resistance effects is explained by the increase in droplet momentum, which more than offsets the reduction in spray curtain cone angle, resulting in an apparent increase in the visually observed spray cone angle.

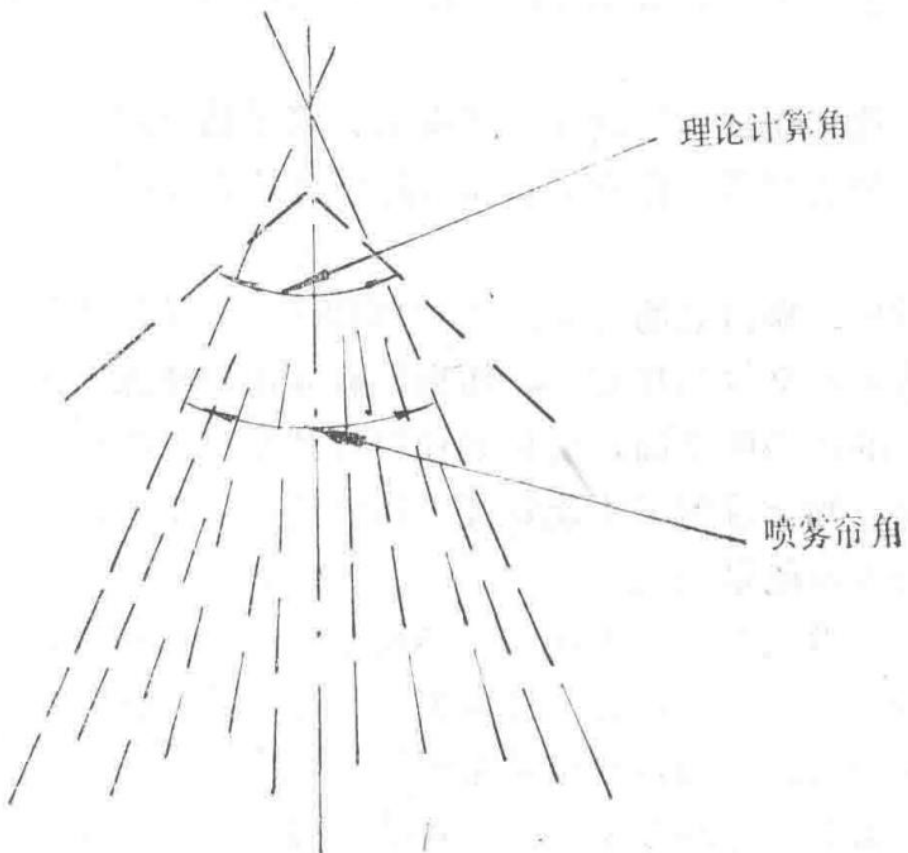


Figure 27: Theoretically Calculated Spray Cone Angle

Theoretical calculation results of the spray cone angle for the Spey MK202 engine fuel nozzle.

According to the author's statement: The equation (5) for droplet size derived from Needham's results (1946) is valid for different flow numbers and various shapes of fuel injection, thus it should also apply to the nozzles under study. However, Needham analyzed sprays with cone angles nearly constant. Since the cone angle affects droplet size, and the author's results show significant variation in cone angle, the use of equation (5) can only be approximate, especially at low pressures.

$$K \square \square c = (\sigma \sigma \sigma \sigma \sigma \sigma) / (\sigma \sigma \sigma \sigma \sigma \sigma) \text{ is fundamentally a function of the parameter } (P^2)/(2 r d).$$

Theoretical flow coefficient as a function of the parameter  $(P^2)/(2 r d)$ .

For standard nozzles, the parameter  $(P^2)/(2 r d)$  is a constant value of 0.167. From the author's relationship  $(Q^2)/(d^4 P \rho) = f((Q)/(\mu d))$ , it follows that  $KQ^2 = \Phi(KQ \times Re)$ , where  $Re$  is the Reynolds number based on the nozzle orifice diameter. Thus, Figure 3 can be redrawn to show the flow coefficient  $KQ$  as a function of  $Re$  (Figure 28).

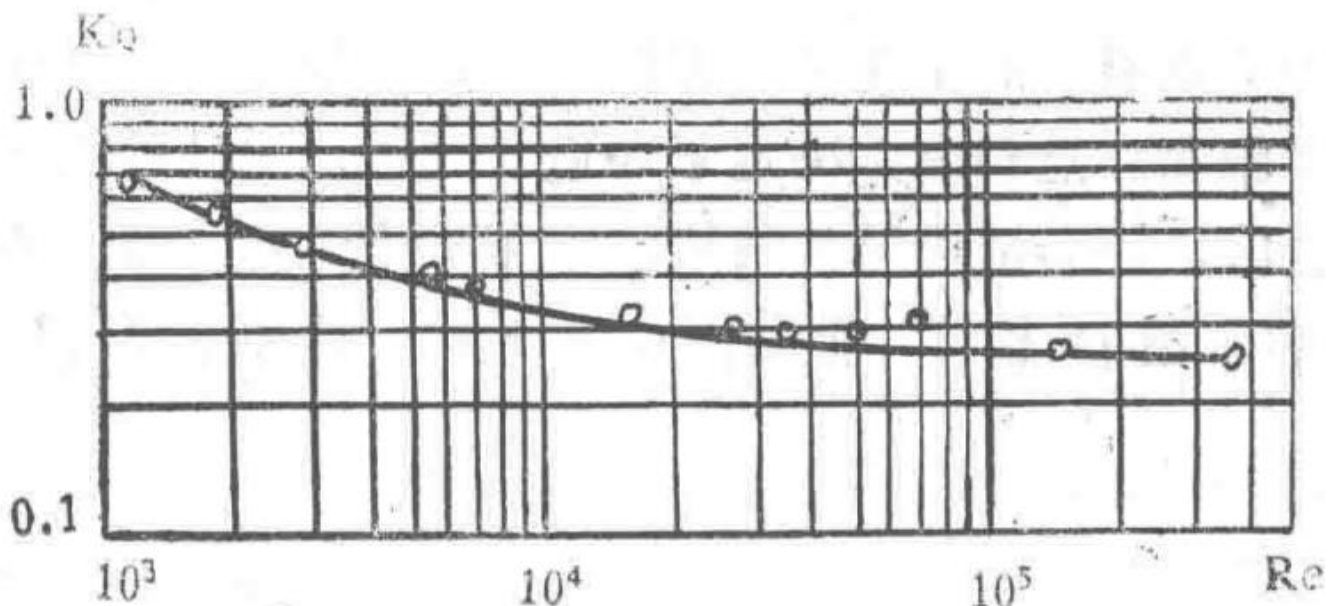


Figure 28: Redrawn Figure 3 Showing Flow Coefficient  $K_Q$  as a Function of  $Re$

Flow coefficient  $K_Q$  plotted against Reynolds number ( $Re$ ) for the studied nozzle.

At the lowest flow rate,  $K_Q = 0.66$ ; within the satisfactory operating pressure range of the nozzle,  $K_Q$  varies between 0.4 and 0.25. This demonstrates that theoretical values are never achieved.

The observation from Figure 4, that the flow number varies with pressure, density, and viscosity, is also a result of friction effects, as given by the relationship:

$$FN = (Q)/(\rho \sqrt{P}) = K \square \square c (\pi)/(4) d^2 \sqrt{(2g)/(\rho)}$$

Flow number (FN) as a function of flow coefficient  $K \square \square c$ .

Thus, it varies with the Reynolds number, as shown in Figure 28 for the studied nozzle.

It is hoped that research results on the impact of friction on the flow coefficients of centrifugal nozzles of different designs will be published. This research was conducted at the High-Speed Fluid Dynamics Laboratory of the Department of Chemical Engineering and Applied Chemistry at the Royal College of Science and Technology.

### Comments from B·E·Knight (London)

Mr. B·E·Knight analyzed the supplementary data referenced in the paper for Needham (1946) and derived an empirical relationship for droplet size (Sauter Mean Diameter, SMD) incorporating the influence of fuel viscosity. He also attempted to obtain the effects of surface tension and gas viscosity in dimensionless form.

$$d = 220 P^{-0.468} Q^{0.209} v \square^{0.215} Sc R \square^{-0.215} W^{-0.115} Re^{-0.251}$$

Empirical relationship for droplet size (SMD) incorporating fuel viscosity, surface tension, and gas viscosity effects.

Where:  $d$  = Sauter Mean Diameter (SMD), micrometers;  $P$  = pressure drop, psi;  $Q$  = mass flow rate, lb/hr;  $v \square$  = fuel kinematic viscosity, centistokes;  $vG$  = gas kinematic viscosity, centistokes;  $\rho G$  = gas density, g/cm<sup>3</sup>;  $\gamma \square$  = surface tension, dyne/cm;  $F$  = fuel flow number, gal/(hr·lb·in<sup>2</sup>);  $S \propto (d)/(F^{1/2})$  = dimensionless droplet size;  $R \square \propto (P^{1/2} F^{1/2})/(v \square)$  = fuel Reynolds number;  $RG \propto (P^{1/2} F^{1/2})/(vG)$  = gas Reynolds number;  $W \propto (\rho G P F^{1/2})/(\gamma \square)$  = Weber number based on gas density.

These results were obtained using weighted average data from Lubbon and Bower (1948), which align with test results from Lucas Company's combustion chambers. Table 7 shows that the data from Needham's equation (Column A) and Equation 6 (Column B) are consistent when  $v \square = 2.3$  centistokes.

Table 7: Sauter Mean Diameter (SMD) in Micrometers

P (psi)	Q (lb/hr)	2		200	
	A	B	A	B	
50	45	52	143	135	
1000	14	13	48	35	

In the dimensionless analysis, replacing  $F^{1/2}$  with nozzle diameter and  $P^{1/2}$  with velocity yields the well-known forms of  $S$ ,  $R\Box$ ,  $RG$ , and  $W$ . The practical selection of these variables is convenient both theoretically and practically, as it avoids introducing fractional powers of fuel density into the scaling factor. This scaling factor was omitted for ease of comparison with standard forms, and because a complete discussion could not be provided.

The attempt to estimate the effects of surface tension and gas viscosity was partially frustrated because the precise relationship between  $W$  and  $RG$  was derived from a small flow range. The corresponding exponents in Equation (7) are insignificant and can vary widely without affecting the data. Reducing the exponent of  $W$  to zero results in an implausibly large exponent for  $RG$ . When the exponent of  $RG$  is reduced to zero, the expression becomes:

$$S \propto R\Box^{-0.211} W^{-0.257}$$

Simplified dimensionless expression for droplet size.

Later private communications indicated that expressions (7) and (8) provide the influence of surface tension between limits.

The following example shows that Equation (6) provides a good representation of sprays from ordinary orifices used in diesel engines:

$P = 3520$  psi,  $v = 5$  centistokes (paraffin spray measurements): - Orifice length 0.4 mm, SMD = 21.3 micrometers - Orifice length 0.9 mm, SMD = 17.9 micrometers

## Comments from H·P·Squire (London)

Professor H·P·Squire noted that measurements of fluid velocity or oil film thickness could provide further insights into the operation of centrifugal nozzles. Such experiments could be conducted using scaled-up models.

He advocated for the use of consistent units in future work in this field.

## Comments from R·Wood (BSc)

Mr. R·Wood noted that the paper provides extensive data on the characteristics of nozzles of different shapes and sizes. Specifically, Figures 3 and 4, along with Equation (5), are useful for calculating the performance of centrifugal nozzles. Unfortunately, many of the nozzles listed in Table 6 are not typically used in practice. In some cases, the offset radius of the tangential holes is smaller than the nozzle outlet radius, while in other extreme cases, the offset radius is often 10 times larger than the outlet radius. Even standard-shaped nozzles have relatively large swirl chamber diameters, resulting in unnecessarily large wetted surfaces. The last column of Table 3, which shows the main dimensions of these nozzles, lists some impossible offset radii for the swirl holes.

Regarding Equation (2), he was interested in the author's explanation of the nozzle parameter (619). Its significance is quite ambiguous, as if the purpose of introducing this parameter was merely to show consistency between Equation (2) and Figure 3. Surprisingly, in the analysis of shape effects, one linear dimension of the nozzle—the offset radius of the tangential holes—was ignored.

An examination of the values in Table 6 reveals that for standard-shaped nozzles,  $Q \propto r^{-0.84}$ . The effect of shape on flow rate is given by:

$$Q = A d^{0.4} p^{0.70} r^{-0.84}$$

Flow rate as a function of nozzle dimensions for standard-shaped nozzles.

Thus, there is no clear relationship between d and r.

In this case, if the swirl angle is constant, then apart from the nozzle length, the dimensions d, p, and r can fully describe the nozzle shape. The significance of another linear dimension is unclear. He valued the author's perspective on this issue.

Equations (2) or (9) strictly apply only to the author's standard-shaped nozzles. If the shape differs significantly, these equations cannot provide even an approximate concept of the effect of shape changes. For more practical nozzle shapes (d = 0.42 inches, p = 0.52 inches, r = 0.96 inches), the shape effect expression becomes:

$$Q = A d^{1.2} p^{0.61} r^{0.24}$$

Flow rate as a function of nozzle dimensions for practical nozzle shapes.

In this case, the influence of the tangential hole offset radius is significantly reduced.

## Author's Response

Mr. A·Radcliffe responded by thanking all correspondents. He had not realized that data capable of determining the influence of swirl chamber shape had been overlooked, as insightfully pointed out by Mr. D·R·Carlisle. He considered Mr. Carlisle's method of using data to be a good approach.

He assured Mr. Foster that he recognized many of the 279 nozzles as unrealistic. They were used to demonstrate what happens when extreme designs are adopted. He agreed with Mr. Foster and Professor Squire that the use of consistent units is desirable and could be satisfactorily applied in Figure 3. Unfortunately, using consistent units elsewhere would make the paper difficult to read.

The author expressed gratitude to Mr. Frazer, Dr. Hisanklam, Dr. Dombrowski, and Mr. Hasson for their precise insights: Nozzle flow is to some extent governed by viscosity or friction. Undoubtedly, they and Mr. Hasson would agree that the inviscid theory (Taylor, 1948) provides unexpectedly good predictions of flow coefficients and spray cone angles as a function of  $(p^2)/(d r)$ , even though the internal flow in the nozzle can be well described by viscous flow (Taylor, 1950).

The author believes that, except near 0° or 180°, the cone angle is not important for controlling droplet size parameters and is best ignored. As Mr. Knight pointed out, many factors may influence particle size. Mr. Wood raised the issue of the parameter " ". It has the dimension of length and accounts for the influence of all other dimensions that do not vary with d or p, including surface finish effects.

# Combustion Research Report CRR 12091

## Performance of the Spey MK202 Engine Finalized Combustion System

First Edition, September 15, 1976

### 1.0 Introduction

This report presents the following basic performance characteristics of the Spey MK202 combustion chamber:

- Ground and altitude starting characteristics.
- Stability characteristics.
- Combustion efficiency characteristics within the engine operating range.
- Exit gas temperature distribution.
- Flame tube and gas duct wall temperatures.

## 2.0 Definitions and Symbols

- $M_3$ : Air mass flow rate at the high-pressure compressor outlet guide vane (OGV) section, lb/sec
- $Mc$ : Combustor air mass flow rate =  $M_3$  – turbine cooling air bleed
- $T_3$ : Air temperature at the high-pressure compressor outlet guide vane section, °K
- $P_3$ : Total air pressure at the high-pressure compressor outlet guide vane section, psi (absolute)
- $A$ : Maximum cross-sectional area of the combustion chamber casing, in<sup>2</sup>
- $d$ : Radial depth between combustion chamber casings, inches
- $e$ : Base of the natural logarithm
- $Q300$ : Combustion loading parameter =  $(P_3^{1.75} \times e^{-(\Delta_3)/(300)} \times A d) / (Mc) \times 10^{-8}$
- $T$ : Maximum temperature at the combustion chamber outlet, °K
- $T_4$ : Average temperature at the combustion chamber outlet, °K
- OTDF: Outlet Temperature Distribution Factor =  $(T - T_4) / (T_4 - T_3) \times 1\%$
- AFR: Air-fuel ratio by weight

## 3.0 Performance Characteristics

### 3.1 Ground and Altitude Starting Characteristics

Figure 1 presents the ignition envelope obtained on a test rig for combustor inlet total pressures  $P_3$  of 3.5, 4.0, and 5.0 psi (absolute). To relate these envelopes to engine operating conditions, Figure 2 shows the windmilling characteristics of the MK202, correlating  $P_3$  with aircraft Mach number and flight altitude.

The air mass flow rates at the peak points of the ignition envelopes for the respective  $P_3$  contours are transferred to the windmilling characteristics to determine the corresponding flight conditions.

On the state coordinate diagram, the ignition boundary line obtained from the test rig can be plotted. This boundary line is then compared with the relight envelope required by the engine, which is overlaid on the same coordinate diagram.

In ignition test rigs, ignition tests are typically limited to the high-altitude, high-Mach number regions within the engine's reliable operating envelope. Experience has shown that it is precisely in this range where starting performance is most sensitive to various local improvements in the combustion chamber.

Ignition and starting at the  $P_3 = 14.7$  psi (absolute) envelope line (Figure 3) simulate ground start conditions. These envelopes were obtained from a test article consisting of three flame tubes, with the central one equipped with an igniter.

## 3.2 Stability Characteristics (Figure 4)

To the left of the  $P_3$  pressure envelope line is the stable combustion region. If the operating point moves outside the envelope due to any of the following reasons, flameout will occur:

1. When pressure  $P_3$  and air mass flow remain constant, the fuel-air ratio changes significantly.
2. When pressure  $P_3$  and fuel-air ratio remain constant, the air flow rate increases.

Stable operation at a flight Mach number of 0.86 and flight boundary (altitude 70,000 feet) corresponds to a point on the curve where  $P_3 = 15.1$  psi (absolute). The most severe possible flameout scenario assumes an instantaneous throttle closure, reducing fuel flow from maximum speed to idle without changing  $M_3$ ,  $T_3$ , and  $P_3$ , and without the influence of a deceleration regulator. Under these assumptions, a sudden deceleration from 70,000 feet altitude and Mach 0.86 would cause the fuel-air ratio to drop from 0.0225 to 0.0168, with the combustion chamber air mass flow rate at 0.59 lb/s per flame tube.

Although the stability envelope for  $P_3 = 15.1$  psi (absolute) is not included in the diagram, it is clear that the lean stability margin is sufficient.

## 3.3 Combustion Efficiency Characteristics within the Engine Operating Range

Figure 5 illustrates the relationship between combustion efficiency and the air/fuel ratio and combustion loading parameter  $\eta_{300}$ .

To determine the combustion efficiency at any operating condition, first calculate the value of  $\eta_{300}$ , then read the combustion efficiency at the corresponding air/fuel ratio from the 'carpet' plot.

For example, under typical ground idle conditions,  $\eta_{300} = 2.0 \times 10^5$ , air/fuel ratio = 70, and efficiency = 86.0%.

## 3.4 Exit Gas Temperature Distribution

Figure 6 shows the temperature distribution measured at the gas duct outlet, obtained from a single-sector combustion chamber test article simulating the engine's maximum speed condition.

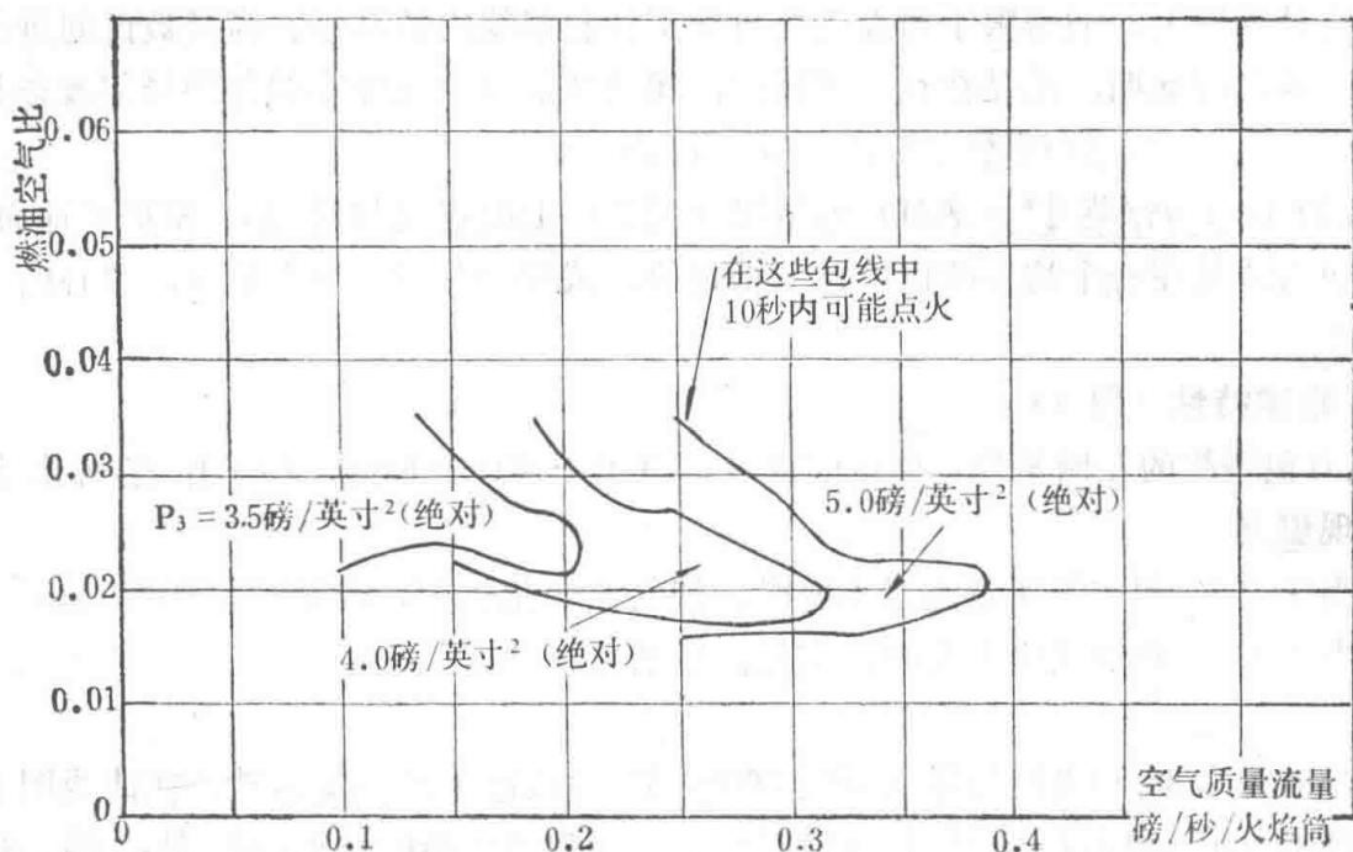
Test No.: 1133 Mass flow = 12.06 lb/s Inlet temperature = 787.5 K Inlet pressure = 314.7 psi (absolute) Air/fuel ratio = 51.9 Outlet temperature = 1477 K Outlet temperature distribution factor = 22.8% Radial temperature distribution factor = 8% (at 40%-60% blade height)

## 3.5 Flame Tube and Gas Duct Wall Temperatures

RLP3278 presents the flame tube wall temperatures obtained from sea-level engine tests, measured using temperature-indicating paint.

The gas duct installed on the flame tube in this test was of an early standard.

Another diagram, RLP4740, shows the temperature of the current MK202 gas duct under the same test conditions. This duct features two splash-cooling rings and five transpiration cooling air holes.



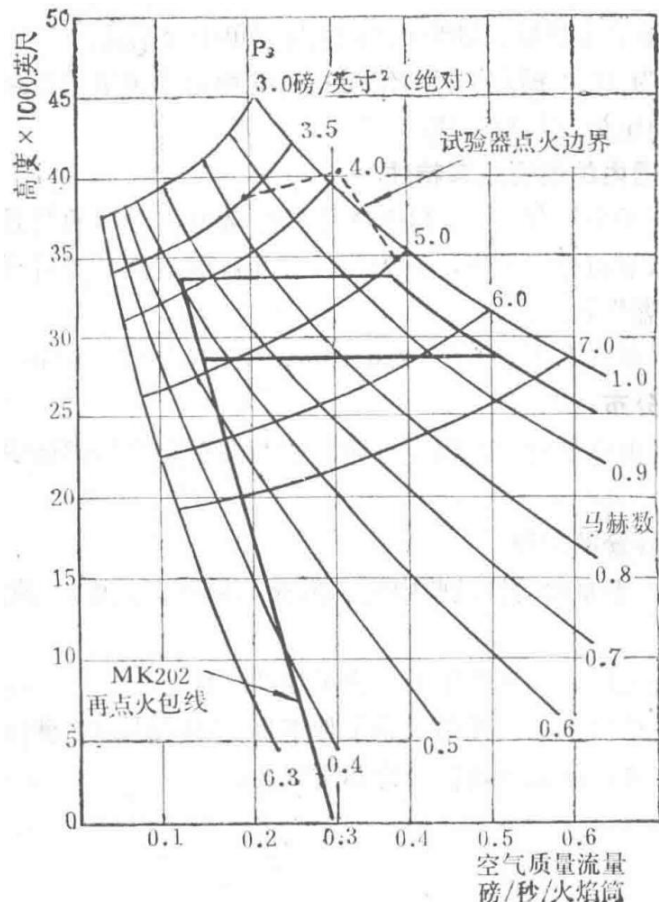


Figure 2 Windmilling Characteristics Plotted on the Ignition Boundary Diagram for Spey MK202

Diagram illustrating windmilling characteristics overlaid on the ignition boundary for the Spey MK202 engine.

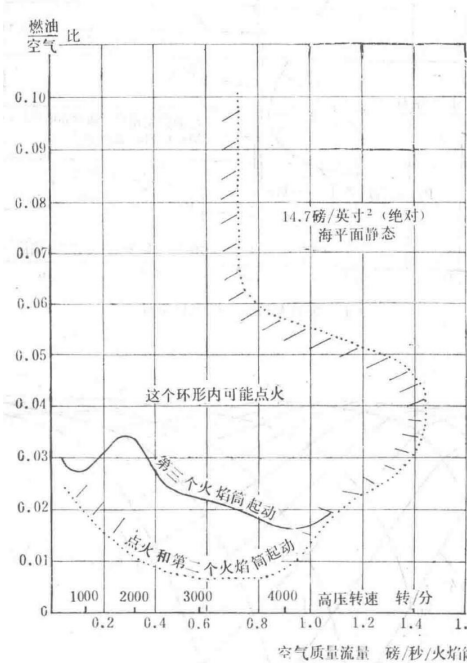


Figure 3 Ignition and Starting Envelope Obtained from a Three-Flame Tube Sector Test Article for Spey MK202

Graph depicting ignition and starting envelopes derived from a three-flame tube sector test article of the Spey MK202 engine.

Figure 3 Data Interpretation

Pressure $P_3$ (psi, absolute)	Condition	Description
14.7	Sea-level static	Simulated ground start conditions
Various	High-altitude, high-Mach	Regions where ignition tests are typically conducted

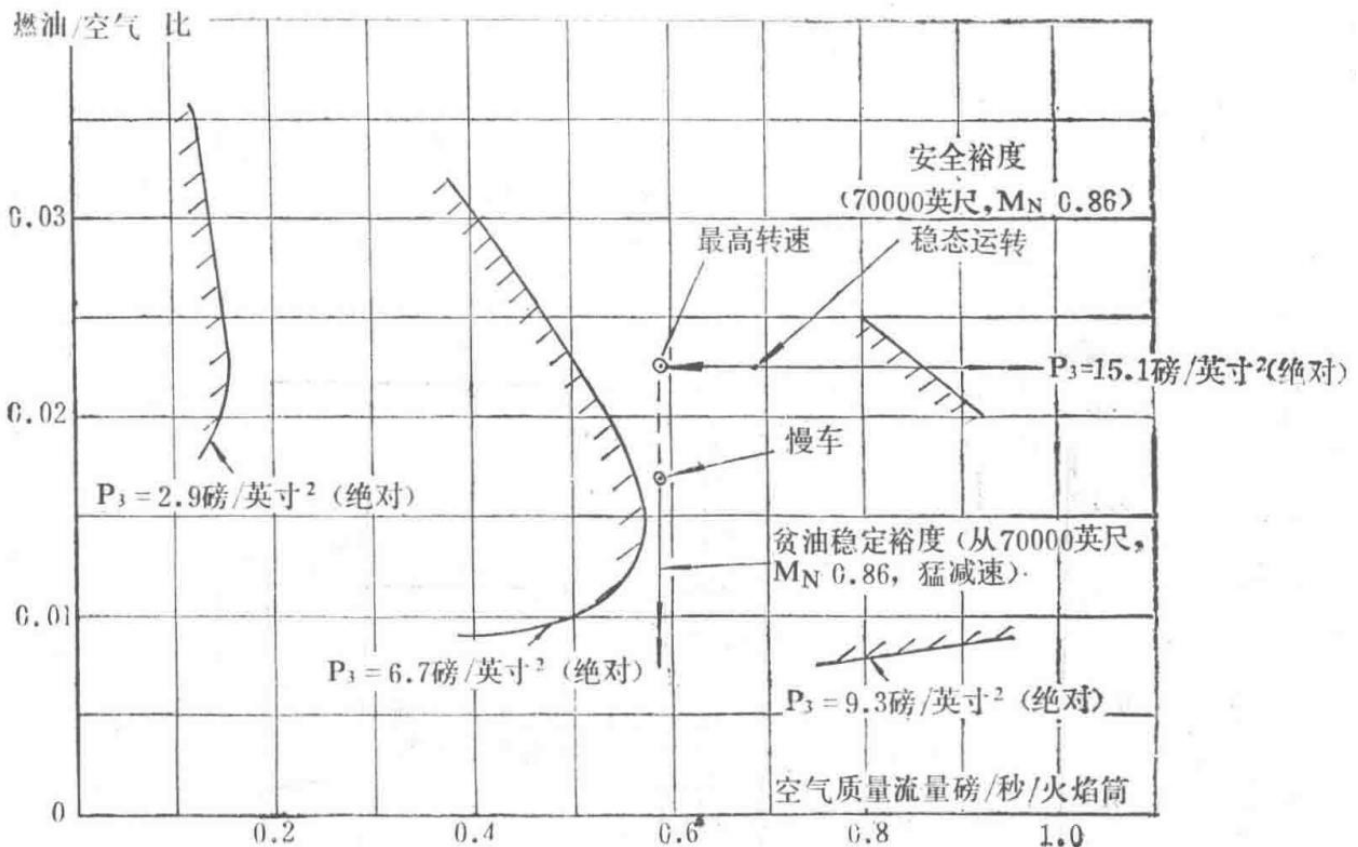


Figure 4 Spey MK202 Combustion Stability

Graph showing the combustion stability characteristics of the Spey MK202 engine, including stable and flameout regions.

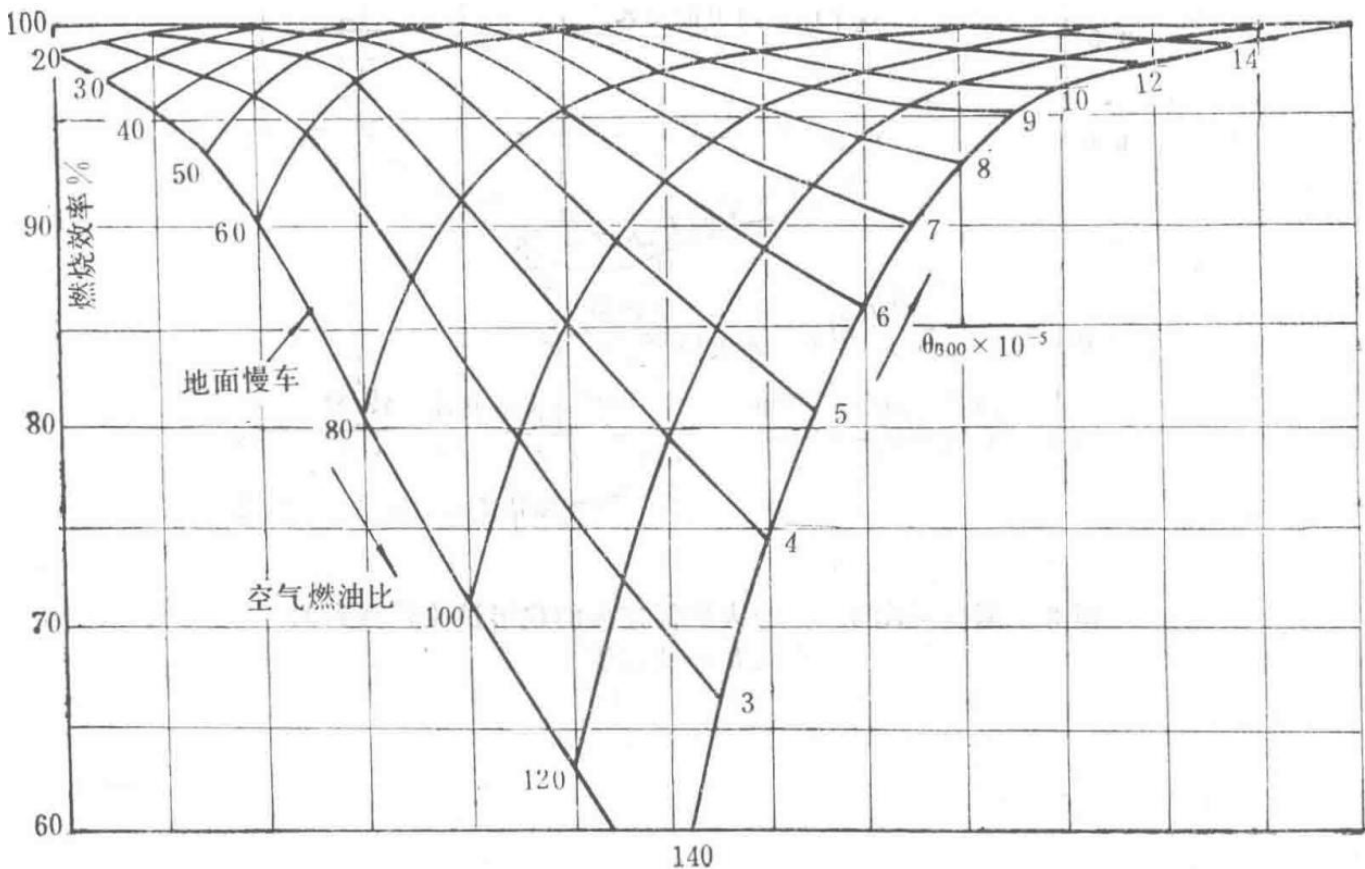
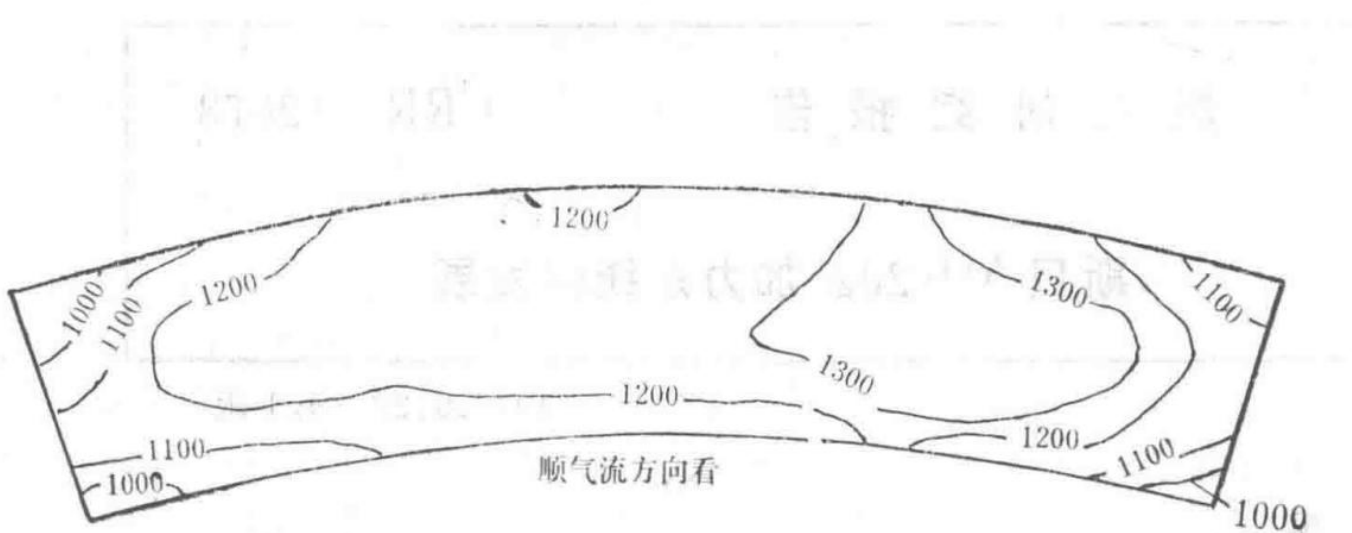


Figure 5 Spey MK202 Combustion Efficiency Characteristics

Carpet plot illustrating the combustion efficiency as a function of air/fuel ratio and combustion loading parameter  $\text{heta}_{300}$ .



Unlabeled diagram, potentially related to flame tube or gas duct wall temperature measurements.

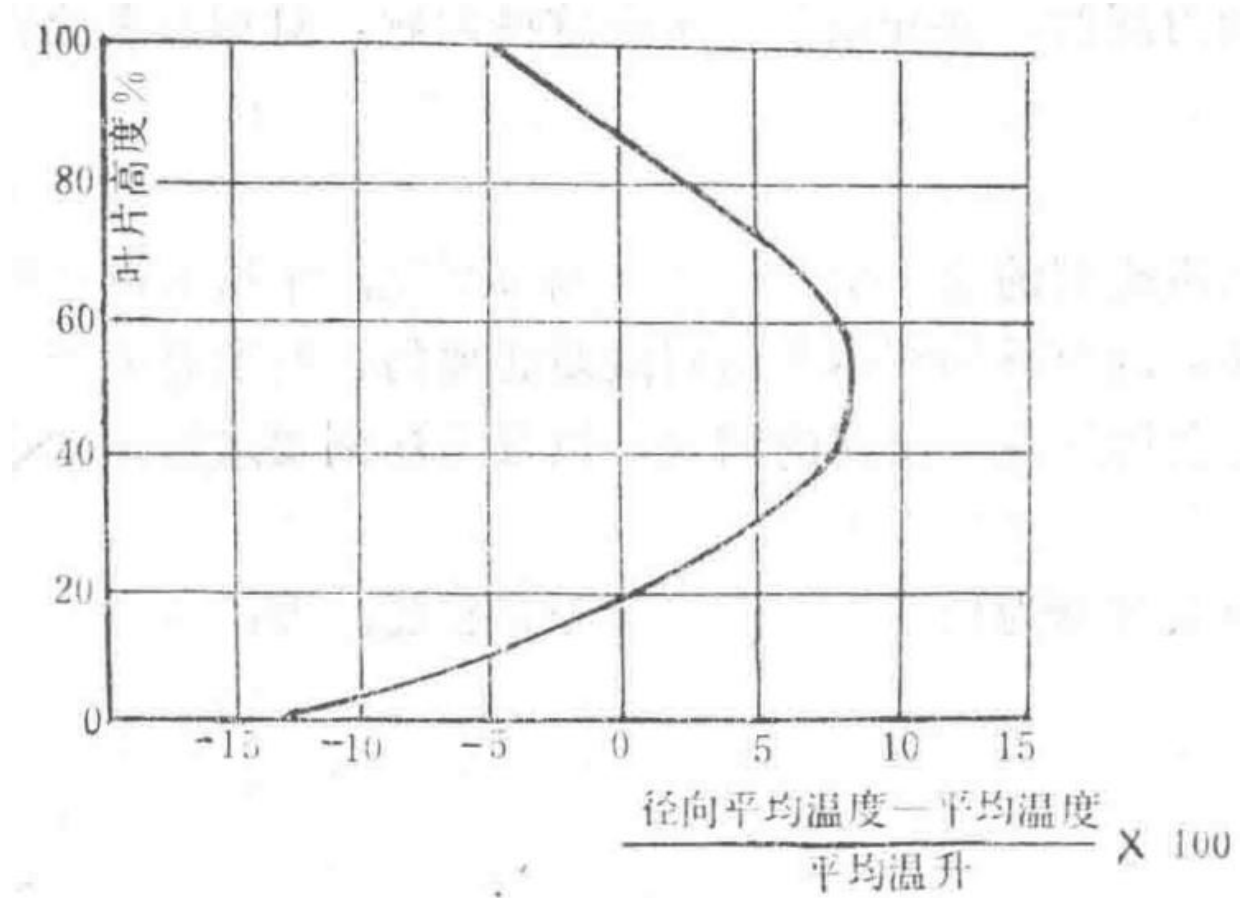


Figure 6 Spey MK202 Combustion Chamber Exit Temperature Distribution

Temperature distribution at the exit of the combustion chamber for the Spey MK202 engine, measured under maximum speed conditions.

Combustion Research Report

Report Title	Report Number
Combustion Research Report	CRR12078
Development of the Spey MK202 Afterburner System	

First Edition, September 22, 1976

## 1.0 Abstract

This report describes the development process of the Spey MK202 afterburner system from its first test in 1956 to the present. It analyzes the mechanical, thermodynamic, and aerodynamic issues encountered during this process and introduces the improvements made to the afterburner system to resolve these problems.

## 2.0 Introduction

The Spey afterburner system was the first fully modulated afterburner system developed for British turbofan engines. The design principles were extrapolated from the experience with turbojet engines, necessitating some technical risks, particularly concerning predicted combustion performance. This report describes the problems encountered during the development phase and the tests conducted to achieve the required afterburner performance.

For the purposes of this report, the afterburner system is divided into three main sections:

1. Combustion chamber
2. Mixer
3. Ignition device

The report also includes sections on combustion instability, specifically the well-known 'buzz' that first appeared during the development of this afterburner system. It presents the relationship between this instability and the fuel-air ratio used, and highlights the impact of 'buzz' on combustion efficiency.

## 3.0 Development of the Combustion Chamber

The afterburner combustion chamber includes flame stabilizers that anchor the pilot flame and fuel manifolds installed upstream of these stabilizers to supply the main fuel. The pilot fuel burned in the wake of the stabilizers is typically referred to as 'wake' fuel, while the fuel supplied by the upstream manifolds is called 'main afterburner fuel.' The flame stabilizers were designed based on test rig results (see Reference [1]), and thus there was no prior engine operational experience to verify the performance characteristics or mechanical reliability of the stabilizers. Therefore, a key development objective was to ensure structural integrity while determining the stability of the designed system to meet specified altitude requirements and operational range.

Issues arising from the use of main afterburner fuel included problems caused by poor fuel distribution or preparation. During development, poor fuel distribution led to various issues such as 'howl' combustion instability, low efficiency, and reduced achievable maximum afterburner thrust. Poor fuel preparation reduced combustion efficiency, thereby lowering the maximum afterburner thrust.

Thus, the afterburner combustion chamber had to be developed to meet three different functional requirements:

- Stability
- Fuel distribution
- Fuel preparation

### 3.1 Stability

The flame stabilizers of the Spey afterburner system were designed based on test rig results (see Reference [1]). The spacing and size of the stabilizers depend on the stability parameter (S), defined as:

$$S = (PWT)/(V)$$

Stability parameter equation where P is pressure, W is a characteristic dimension, T is temperature, and V is velocity.

As shown in Reference [2], while the stability for combustion with only wake fuel was well established through test rig experiments, there was no prior experience regarding the impact of main afterburner fuel on the fundamental flame stabilization characteristics. Therefore, it was assumed that the stability boundary of the vaporizing flame stabilizer (where pilot fuel is introduced inside the stabilizer) extended to the rich-side boundary of the stability limit of the V-gutter flame stabilizer (where no fuel is introduced inside the stabilizer), which had been confirmed through both test rig and engine tests (see Figure 1).

However, during early tests, combustion instability occurred at both sea-level and high-altitude conditions when the fuel load was high, limiting achievable performance. This instability, later termed 'buzz,' manifested as large pressure fluctuations, with amplitude increasing with fuel flow. These pressure fluctuations could cause mechanical damage to the turbine exhaust cone and afterburner combustion chamber. Consequently, much of the development work focused on finding methods to avoid the 'buzz' condition and achieve satisfactory performance.

Early tests indicated that the designed vaporizing flame stabilizer appeared fuel-rich at the inlet. Rig tests with segmented flame stabilizer components showed that fuel overflowed forward from the inlet and immediately created a fuel-rich zone behind the stabilizer at the inlet (see Figure 2). It was believed that the resulting intense flame could induce instability and potential local rich blowout, acting as a source of pressure fluctuations. This issue was resolved by increasing the outlet hole diameter of the distribution tubes to prevent forward overflow (see Reference [3]). The resulting flame was significantly improved, but engine tests showed no noticeable improvement in the 'buzz' limit.

Further studies examined the effects of various geometric parameter changes in the flame stabilizers, with particular attention to avoiding 'buzz.' These included stabilizers with notches to improve mixing at the pilot flame location and elongated inlets. The latter test was conducted to verify the hypothesis that the inlet and distribution tubes acted as Helmholtz resonators, potentially tuning to standing waves in the afterburner. These modifications had no effect on the 'buzz' limit or instability frequency.

Other tests to improve basic stability included redistributing the pilot fuel ratio among the vaporizing stabilizers to ensure consistent 'blowout' across stabilizers.

The variation in pilot fuel pre-metering was studied from two perspectives. First, tests were conducted at high-altitude conditions to determine the optimal fuel-air ratio for the best 'blowout' limit in the combustion chamber. Simultaneously, the required pilot fuel flow for optimal ignition characteristics was determined. To address the filling time and flame propagation issues in vaporizing stabilizers, it was found that the required pre-metered flow was higher than what was needed for basic stability requirements (see References [4], [5], [6]). Thus, a compromise was necessary to determine the pre-metered wake fuel flow value that provided both good ignition performance and high-altitude stability.

### 3.2 Fuel Distribution

Similar to stability, the primary goal of studying fuel distribution was to overcome or reduce the range of combustion instability. It was believed that the simple straight-shot nozzles of the main afterburner fuel manifold incorrectly introduced fuel between stabilizers, contaminating the pilot fuel and causing premature local rich blowout in the wake of the flame stabilizers. Initially, the outer fuel manifold was positioned far upstream of the outer flame stabilizer. To prevent fuel from entering the heat shield annular cavity, a long fuel shield extending upstream of the manifold was installed. One of the initial improvements involved removing the spray bars from

the No. 4 manifold and moving the manifold closer to the outer flame stabilizer (see Figure 3). This arrangement reduced the need for the fuel shield, which was subsequently removed, resulting in reduced cold pressure loss and system weight. Combustion stability also improved, equivalent to allowing a 2 psi reduction in afterburner pressure (see Reference [7]).

Engine tests also confirmed that adjusting the spray positions on the outermost intermediate spray bars improved performance at maximum afterburner conditions (see Reference [7]).

Experience from these tests demonstrated the need for precise drilling of nozzles and careful control of the fuel injection direction in the manifolds. To achieve this, 'target' plates made of annular flat panels were placed at specified distances downstream of the manifolds, requiring fuel to hit them. All manifolds underwent this test during flow calibration before installation in the afterburner. Further improvements included moving all manifolds 4 inches downstream, moving the intermediate (No. 2) flame stabilizer 9 inches downstream, removing the spray bars from the innermost intermediate (No. 2) manifold, and changing the spray angle and pitch circle diameter of the outer (No. 4) manifold. These modifications did not improve performance, and moving the intermediate flame stabilizer and manifold downstream actually worsened the stability limit.

During the development phase, redistribution of the main afterburner fuel improved the maximum afterburner performance achievable before 'buzz' occurred. It became evident from these tests that the No. 1 and No. 4 manifolds contributed most to generating 'buzz.'

The innermost No. 1 manifold underwent extensive optimization tests after installing a catalytic igniter in the combustion chamber (see Section 5). This was necessary because 'buzz' was encountered even at relatively low afterburner ratios. It was hypothesized that the blockage effect of the catalytic igniter caused a redistribution of airflow in the center of the combustion chamber, leading to locally over-rich fuel zones. Shutting off the inner manifold increased the afterburner ratio limited by 'buzz,' but this also caused high-frequency (2 kHz) oscillations known as 'screech,' resulting in mechanical damage. Tests were conducted with a reduced inner manifold flow rate (flow number = 8) as a temporary standard for the afterburner, achieving the desired 'buzz'-free performance while minimizing the tendency to produce 'screech' across most of the flight envelope. However, performance was still insufficient at the guarantee point of 36,000 feet altitude and Mach 2.0, requiring the inner manifold to be completely shut off. To address the 'screech' issue, holes were drilled in the first three segments of the heat shield (see Reference [8]).

The downstream outer main afterburner manifold was located inside the diffuser. To ensure fuel was injected parallel to the airflow and did not impinge on the flame stabilizer walls, the manifold nozzles were angled. Tests showed that varying the angle between 6° and 26° relative to the horizontal axis had virtually no effect on performance. The current afterburner uses a nozzle angle of 13°.

### 3.3 Fuel Preparation

The goal of improving main afterburner fuel preparation was to increase the maximum afterburner limit. It was hypothesized that a circumferentially uniform fuel distribution could reduce local rich zones downstream of circumferentially discontinuous nozzles, achieving a fuel-air ratio distribution closer to that produced by an annular pump. This could serve two purposes:

- If 'buzz' was indeed caused by local fuel over-richness, then more main afterburner fuel could be supplied before 'buzz' occurred.
- Reducing nozzle size and thus improving fuel preparation could lead to higher combustion efficiency.

Such improvements were tested on both engines and simulation rigs. Engine tests included increasing the number of nozzles on all manifolds while maintaining the original total flow number.

These engine tests showed that while some performance improvements were achieved with the 185 in<sup>2</sup> funnel mixer, no benefits were observed when tested behind the ultimately selected slotted mixer. Simulation rig tests, which doubled the number of nozzles on the outer manifold (while keeping the flow number constant), showed no performance improvement. This comparative test was conducted behind a 210 in<sup>2</sup> funnel mixer.

Initially, it was intended to introduce main afterburner fuel in separate circuits for the Spey afterburner regulation, a decision based on early design calculations indicating fuel boiling within the manifolds.

Approximately one year after testing began, engine tests at sea level demonstrated that separate circuit fueling was unnecessary for this scenario. Subsequent engine and simulation rig tests confirmed that separate circuit fueling was also unnecessary under high-altitude conditions. As a result, the separate circuit fueling method was abandoned, and the separate circuit fuel valve was fixed in the open position. In early and current production models, the only function of the separate circuit fuel valve is to open and close during afterburner activation and deactivation, respectively, to prevent fuel leakage.

## 4.0 Mixer

The initial Spey engines for the Phantom aircraft were designed with various funnel mixers, ranging in size from 165 in<sup>2</sup> to 230 in<sup>2</sup>. Early engine and afterburner development demonstrated that a 210 in<sup>2</sup> mixer was necessary to meet specified afterburner performance requirements at sea level with and without bleed air. However, non-afterburning engine performance tests showed that a 185 in<sup>2</sup> mixer provided better specific fuel consumption and higher non-afterburning thrust. Various tests were conducted to achieve velocity and temperature fields in the afterburner combustion chamber similar to those produced by the 210 in<sup>2</sup> mixer while maintaining compatibility with the 185 in<sup>2</sup> mixer. These tests were insufficient to conclude whether changing the mixer was appropriate. All such work was conducted on sea-level test stands, with high-altitude performance derived only from tests with bleed air from the 12th stage. The 185 in<sup>2</sup> mixer never underwent comprehensive comparative high-altitude engine tests.

Measurements of mixer cross-sectional parameters indicated that the more uniform the circumferential distribution of mass flow rate per unit area and temperature in the afterburner combustion chamber, the better the afterburner performance. This was the result obtained with the 210 in<sup>2</sup> funnel mixer. The rationale was that matching fuel distribution with airflow was simpler using annular fuel manifolds. Additionally, circumferential variations in distribution could rotate to different positions under various flight conditions. Thus, even if the match was good in one condition, it could be completely mismatched in another. The 185 in<sup>2</sup> mixer indeed produced more pronounced undesirable distributions compared to the 210 in<sup>2</sup> mixer.

Simulation rig tests with a Spey mixer consisting of 20 slots showed significant improvements in maximum afterburner performance, with virtually no 'buzz' encountered. Further increases in fuel flow led to a drop in combustion efficiency, thereby defining the maximum afterburner limit. A more practical improvement involved removing the funnels from 10 of the Spey funnel mixers. Despite encountering 'buzz' limitations, performance improved significantly due to a more uniform circumferential distribution compared to the 210 in<sup>2</sup> funnel mixer. However, unlike the annular mixer, the temperature and mass flow rate per unit area radial distributions were relatively smooth with this mixer. Both the slotted and annular mixers exhibited differences from the ideal distribution due to sensitivity to bypass ratio.

Engine tests with the 10-slot mixer confirmed the simulation rig results, showing improved afterburner performance based on afterburner temperature at the 'buzz' limit. This was particularly evident at Mach 2. An additional benefit of this slotted mixer was that removing the funnels from the 210 in<sup>2</sup> mixer tended to restore the engine matching closer to that of the 185 in<sup>2</sup> funnel mixer. Thus, in addition to improved afterburner performance, non-afterburning engine performance, specific fuel consumption, and thrust also benefited. However, the non-afterburning engine performance was still not as good as that with the 185 in<sup>2</sup> funnel mixer.

After removing the funnels, connecting pieces or 'tabs' were left on the mixer. A test removing these tabs to clean up the mixer showed that their absence worsened the 'buzz' limit on the test stand engine. Therefore, these structural features are still retained in current engines.

## 5.0 Ignition

The early design of the afterburner igniter consisted of a catalytic igniter assembly with a cone mounted outside the exhaust cone. Fuel was introduced upstream of the gas generator airflow. Ignition relied on the correct

fuel-air ratio mixture flowing into the catalytic assembly, with the resulting cone-stabilized flame propagating downstream. The catalytic igniter was located approximately 3 feet upstream of the afterburner combustion chamber (see Figure 4).

This design had two serious flaws:

- Mechanical failure
- Unreliability

Although the catalytic assembly had a short lifespan when mounted on the exhaust cone, ignition unreliability was the primary factor leading to redesign.

The arrangement of the catalytic igniter fuel supply system made it sensitive to swirl angle. Even small changes in the turbine exit swirl angle could cause significant variations along the exhaust cone surface within the diffuser. Various fuel nozzles were tested over an extended period to overcome this sensitivity to swirl.

Test results led to relocating the catalytic igniter to the center of the combustion chamber, an arrangement that underwent engine testing in January 1966. The centrally mounted catalytic igniter was further modified to include a venturi and dual fuel supply lines: one supplying fuel to the catalytic assembly and another supplying fuel to a manifold that fed the downstream catalytic igniter cone. An early version of the venturi catalytic igniter is shown in Figure 5. Later, it was demonstrated that this centrally mounted catalytic igniter or the one installed in the center of the combustion chamber proved to be mechanically reliable.

Early tests of the centrally mounted catalytic igniter supplied fuel from the inner main afterburner fuel manifold. This arrangement had a narrow operating range and was highly sensitive to throttle angle. At this stage, both the cone and catalytic assembly were supplied by a single fuel line.

Subsequently, a venturi and cone fuel manifold were installed, with separate fuel supplies, and optimization tests were conducted. However, at that time, the catalytic igniter was supplied from the vaporizing stabilizer. This meant the catalytic igniter operated continuously during afterburner operation. Therefore, it was decided to supply fuel via a timer for the catalytic igniter, originally used for the exhaust cone-mounted catalytic igniter. This approach avoided mechanical damage and maximized the lifespan of the catalytic igniter without compromising performance.

After initial development tests, a more practical design with a broader range of variations was prepared, and tests were conducted on this standard catalytic igniter. The tests showed that its performance was far inferior to the development standard, with a significantly reduced operating range and longer ignition times. A series of tests was then initiated to evaluate the impact of various structural changes on performance, using engine components in an 8-inch model test rig.

Test results indicated that the length of the fuel supply pipe was a major factor affecting catalytic igniter performance due to the influence of fuel boiling. Consequently, the focus of rig testing shifted to studying improved catalytic ignition systems (see Reference [9]).

A significant finding from these tests was the need to control the very small fuel flow through the venturi and ensure this small flow was vaporized within the venturi.

The catalytic ignition system in the early stages lacked cleaning. Since the venturi fuel supply was regulated by a 0.025 restrictor, the reliability of the ignition system depended on the reliable operation of this restrictor and the very small venturi nozzle. Thus, it was absolutely essential to prevent blockage of the restrictor and venturi. Experience showed that without cleaning, fuel boiling and cracking occurred in the system when the catalytic igniter was not operating, resulting in gum formation that blocked these nozzles. Consequently, the early-stage catalytic system was highly unreliable.

$$S = \frac{PWT}{V}$$

Figure 1: Stability boundaries of vaporizing and V-gutter flame stabilizers

This figure illustrates the stability limits of vaporizing and V-gutter flame stabilizers as determined through test rig and engine tests.

## 燃 烧 研 究 报 告

CRR 12078

### 斯贝 MK202 加力系统的发展

Figure 2: Fuel overflow in the vaporizing flame stabilizer

This figure shows the fuel overflow issue in the vaporizing flame stabilizer, leading to a fuel-rich zone behind the stabilizer.

— Section 16 —  
Content from Original Document (Pages 76-80)

A simple flushing device was therefore installed. Downstream of the one-way valve, there are two fuel supply lines. One supplies the catalytic igniter, while the other, with a comparable flow rate, directs fuel to the nozzle fish scales, i.e., to the external atmospheric pressure  $p_0$ . When afterburner operation is engaged, fuel flows through both pipelines. When the afterburner is cut off, due to the pressure difference between the afterburner combustion chamber pressure  $P_a$  and atmospheric pressure, the fuel from the catalytic igniter returns to the flushing pipeline and then vents to  $p_0$ . The performance of this system is highly satisfactory and has been applied to current engines, as shown in Figure 6.

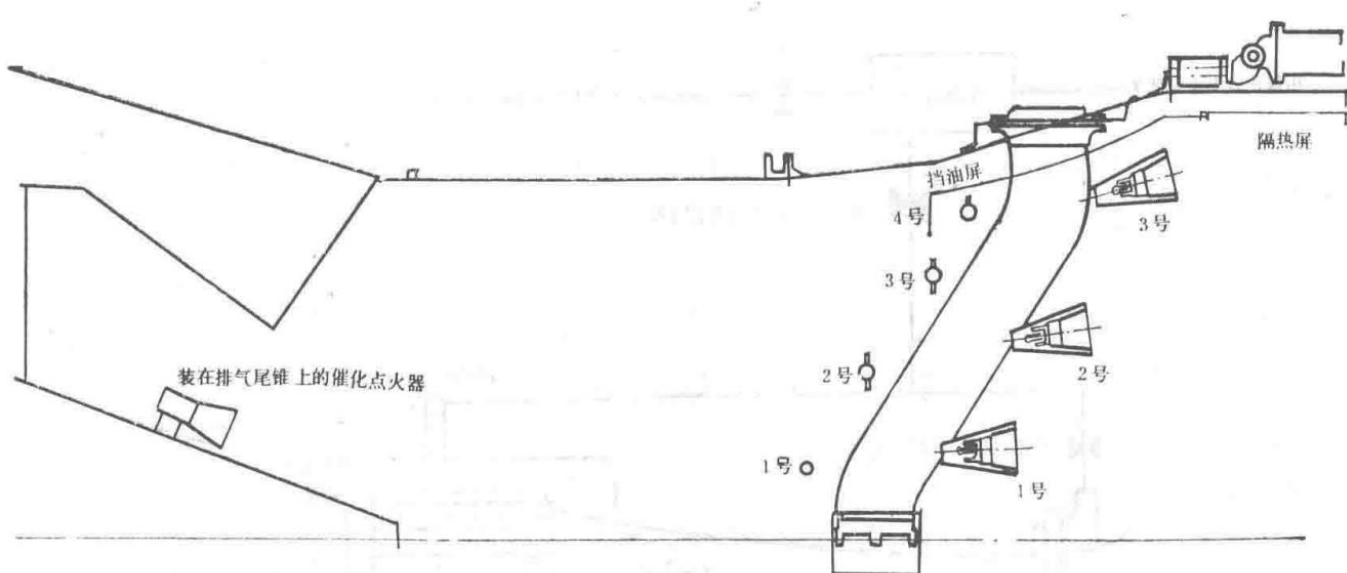


Figure 6: Spey MK202 Afterburner Original Design

Diagram of the original afterburner design for the Spey MK202 engine, illustrating the fuel flow paths and flushing system.

The catalytic ignition system is required to operate within the 3-second timer limit to meet technical specifications. The original technical documents specified an ignition requirement at an afterburner combustion chamber pressure of 6 psi (absolute), equivalent to an altitude of 57,000 feet at Mach 0.9. This limit was not achieved, and the current standard specifies a reduced ignition limit of approximately 12 psi (absolute) for the afterburner combustion chamber pressure, equivalent to 40,000 feet at Mach 0.9. The reduction in the ignition limit is due to various reasons, primarily the predefined fuel supply schedule for the catalytic igniter and flame propagation issues. The aforementioned pressures are steady-state pressures with the nozzle closed. Due to the nozzle being pre-opened, the actual pressure at which the catalytic module ignites is approximately 1 psi lower than these values.

Most of the development work on the Venturi-type catalytic igniter was completed on an 8-inch diameter test rig. The tests demonstrated that the catalytic module could operate at the pressures specified in the original technical documents. However, at such low pressures, the catalytic module was highly sensitive to the predefined fuel supply schedule. Additionally, the ignition time became excessively long. Therefore, if a timer were used, the fuel supply would be cut off before ignition occurred.

Extensive optimization tests were conducted on the afterburner combustion chamber strut restrictor  $R_1$ . The flow rate through the catalytic igniter under flight conditions is determined by the combustion chamber strut restrictor and the one-way valve. Other variables examined included the Venturi restrictor  $R_3$ , the size and number of nozzles in the fuel ring, the inner diameter of the fuel ring, the inner diameter of the Venturi throat, the size of the upstream plate holes, and the type of satellite tube.

1. One-way valve rated pressure: 200 psi

2.  $R_1$ : 0.036
3.  $R_3$ : 0.025
4. Nozzle hole size: 0.03
5. Fuel ring nozzle size: 0.039
6. Number of fuel ring nozzles: 16
7. Fuel ring outer diameter: 0.25
8. Venturi throat inner diameter: 0.25
9. Upstream plate hole size: 0.094
10. Number of upstream plate holes: 12

Bench tests conducted over a wide range of fuel pressures at afterburner combustion chamber pressures demonstrated that the predefined fuel schedule of the early standard was far from optimal. Significant improvements were achieved by reducing the one-way valve rated pressure from 200 psi to 120 psi. This allowed for higher catalytic flow rates and pressures under flight conditions. Additionally, increasing the fuel ring nozzle size to 0.046 and the combustion chamber strut restrictor  $R_1$  to 0.04 reduced the fuel filling time, thereby shortening the ignition time. Apart from later replacing the Venturi restrictor with a 0.035 filtered restrictor, this configuration became the current standard. Combined with changes related to the predefined fuel quantity for the vaporizer stabilizer, the ignition altitude limit at Mach 0.9 was increased by 10,000 feet. This reduced the afterburner ignition pressure by 5 psi, resulting in a  $P_s$  limit pressure of 7 psi (absolute).

The MK202 is required to operate with AVCAT, AVTUR, and AVTAG fuels. Most development work was completed using AVTUR fuel, with occasional checks on the other two fuels. The primary issue with using these three fuels is the required Reid vapor pressure range for operation.

As previously mentioned, the normal operation of the catalytic igniter depends on fuel boiling, particularly within the Venturi fuel circuit. Clearly, a wide range of Reid vapor pressures implies variations in catalytic ignition performance. It can be expected that AVTUR and AVCAT performances are similar. However, with AVTAG, especially at low afterburner combustion chamber pressures, ignition difficulties were indeed observed. The only effective solution to this problem would be to use different control orifices, but this falls outside the scope of the current research. Ultimately, a compromise standard was established to enable operation with all three fuels.

## 6.0 "Buzz" and Combustion Efficiency Correlations

This report devotes considerable space to describing the difficulties encountered in achieving the required performance due to the occurrence of combustion instability known as "buzz." Therefore, during the development process, it was necessary to identify the factors controlling the generation of "buzz" and their correlations. Extensive practical experience has shown that low-frequency oscillations are related to the fuel-air ratio used, and the correlation of combustion efficiency is better represented by the air loading parameter than by the parameters used in the original design.

### 6.1 "Buzz" Correlation

Calculations of conditions with and without "buzz" ensure the maximum allowable hot core flow fuel-air ratio for buzz-free operation, as shown in Figure 7. In Figure 7, it is assumed that 10% of the air entering the afterburner is used for cooling purposes and does not participate in combustion (thus, 0.9  $M_a$  participates in combustion). The  $p_{WT}/V$  parameter is based on the state at the stabilizer lip, assuming all stabilizers are in the same plane.

Therefore:

- $p$ : Static pressure at the stabilizer lip, psi (absolute)
- $\Delta T$ : Total temperature of the airflow at the stabilizer lip, °K
- $V$ : Airflow velocity at the stabilizer lip, ft/s
- $W$ : Stabilizer slot width, inches
- $F\Box$ : Total afterburner fuel flow rate, lb/s

- $M_a$ : Total gas mass flow rate at the afterburner inlet, lb/s

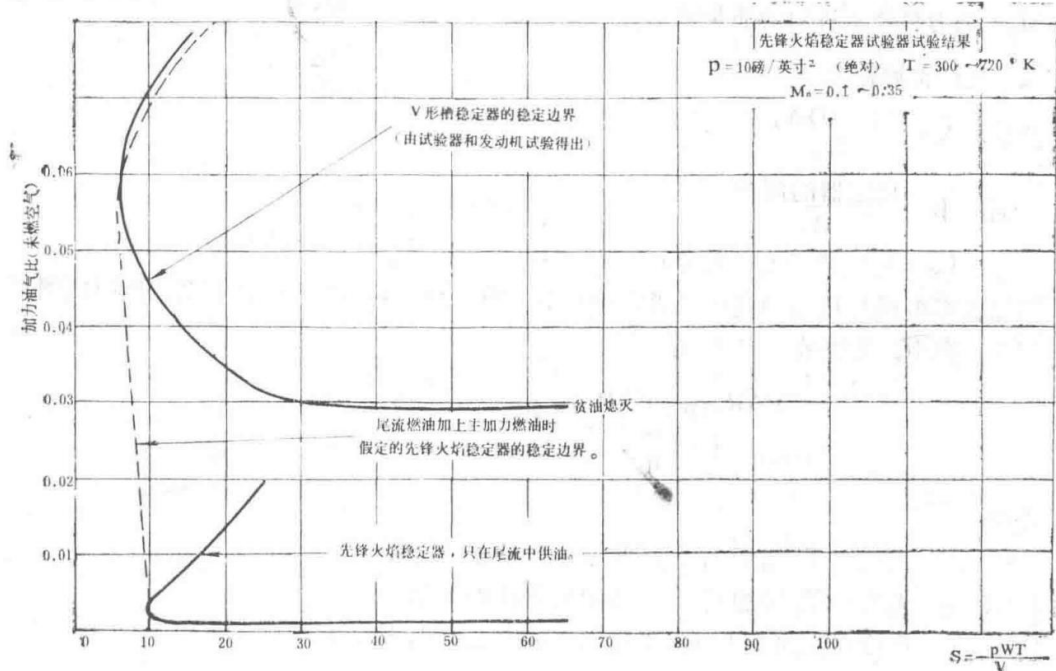


Figure 7: Comparison of Stability Between V-Gutter Stabilizers and Pioneer Flame Stabilizers

Graph showing the correlation between fuel-air ratio and the  $pWT/V$  parameter for conditions with and without "buzz."

## 6.2 Efficiency Correlation

The performance achievable in the initial design was estimated based on the modified King's efficiency correlation , as referenced in [10].

However, analysis of the afterburner performance of the engine under sea-level and high-altitude conditions led to the derivation of a new parameter, called heta. Like the King's parameter, this parameter indicates that combustion efficiency depends on the inlet parameters of the afterburner, the fuel-air ratio used, and the geometric dimensions of the combustion chamber.

$$\theta = ( P_a^{1.4} \times A_a \times L \times e^{\Delta T_a / 1000} ) / ( M_a \times X )$$

Definition of the parameter  $\theta$  used for combustion efficiency correlation.

- $P_a'$ : Total pressure after cold loss, psi (absolute)
- $A_a$ : Total cross-sectional area of the afterburner ( $1075 \text{ in}^2$  for Spey MK202)
- $L$ : Characteristic length (45 inches for Spey MK202)
- $T_a$ : Enthalpy-averaged temperature at the afterburner inlet, K
- $M_a$ : Mass flow rate at the afterburner inlet, lb/s
- $X$ : Flame spread distance, inches, where  $X = (1 - \beta) A LG$
- $\beta = (A_g)/(A)$ : Ratio of stabilizer area to total area
- $LG = \sum (\pi D \square)$ : Stabilizer length, inches

The combustion efficiency  $\eta_c$  varies with the hot core fuel-air ratio (assuming 90% of air is used for combustion) and  $\eta_a$ , as shown in the grid diagram in Figure 8. In this figure, combustion efficiency is defined as:

$$\eta_c = (\text{FAR}_{\text{D}} - \text{FAR}_{\text{C}})/(\text{FAR}_{\text{C}} + ((1 - \eta_a)/(\eta_a)) \text{FAR}_{\text{D}})$$

Definition of combustion efficiency  $\eta_c$ .

- FAR<sub>D</sub>: Theoretical fuel-air ratio required to increase temperature from  $T_1$  to  $T_{\text{C}}$
- FAR<sub>C</sub>: Theoretical fuel-air ratio required to increase temperature from  $T_1$  to  $T_s$
- FAR<sub>C</sub>: Hot core flow fuel-air ratio (calculated based on the air participating in combustion  $\times M_s$ )
- $\eta_a$ : Engine combustion efficiency
- $T_{\text{C}}$ : Temperature of the hot core flow at the tailpipe

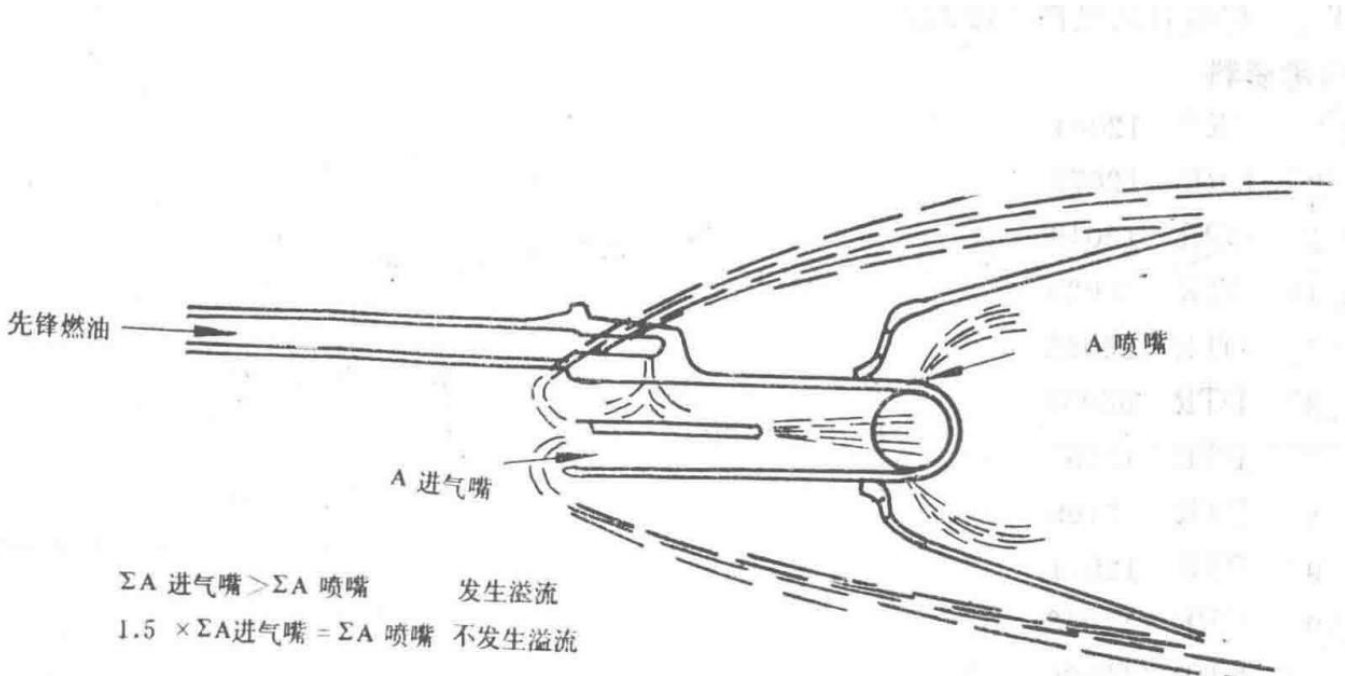


Figure 8: Spey MK202 Vaporizer Afterburner Stabilizer

Diagram of the vaporizer afterburner stabilizer used in the Spey MK202 engine.

## References

- [1] CRR 12084
- [2] CRR 12079
- [3] CRR 12019
- [4] DTR 86020
- [5] DTR 86052
- [6] DTR 86055
- [7] PTR 12257
- [8] PTR 12169
- [9] PTR 12571
- [10] CRR 12043
- [11] CRR 12080

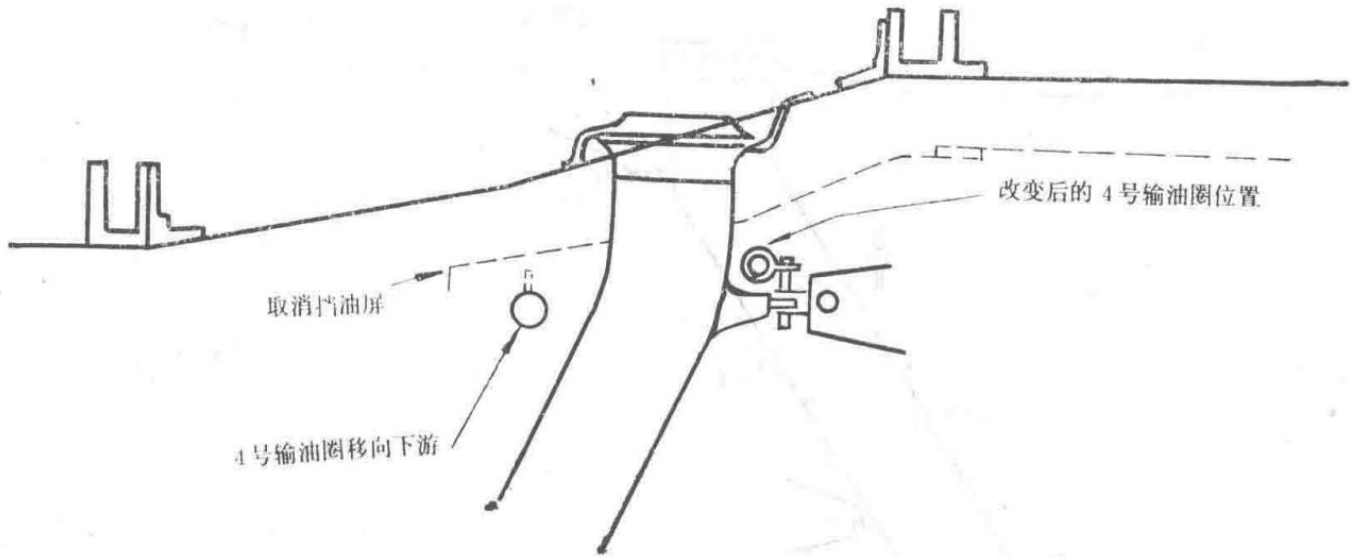


Figure 3: Improvement of the Spey MK202 Afterburner Outer Fuel Ring

Diagram showing the improvements made to the outer fuel ring of the Spey MK202 afterburner.

— Section 17 —  
Content from Original Document (Pages 81-85)

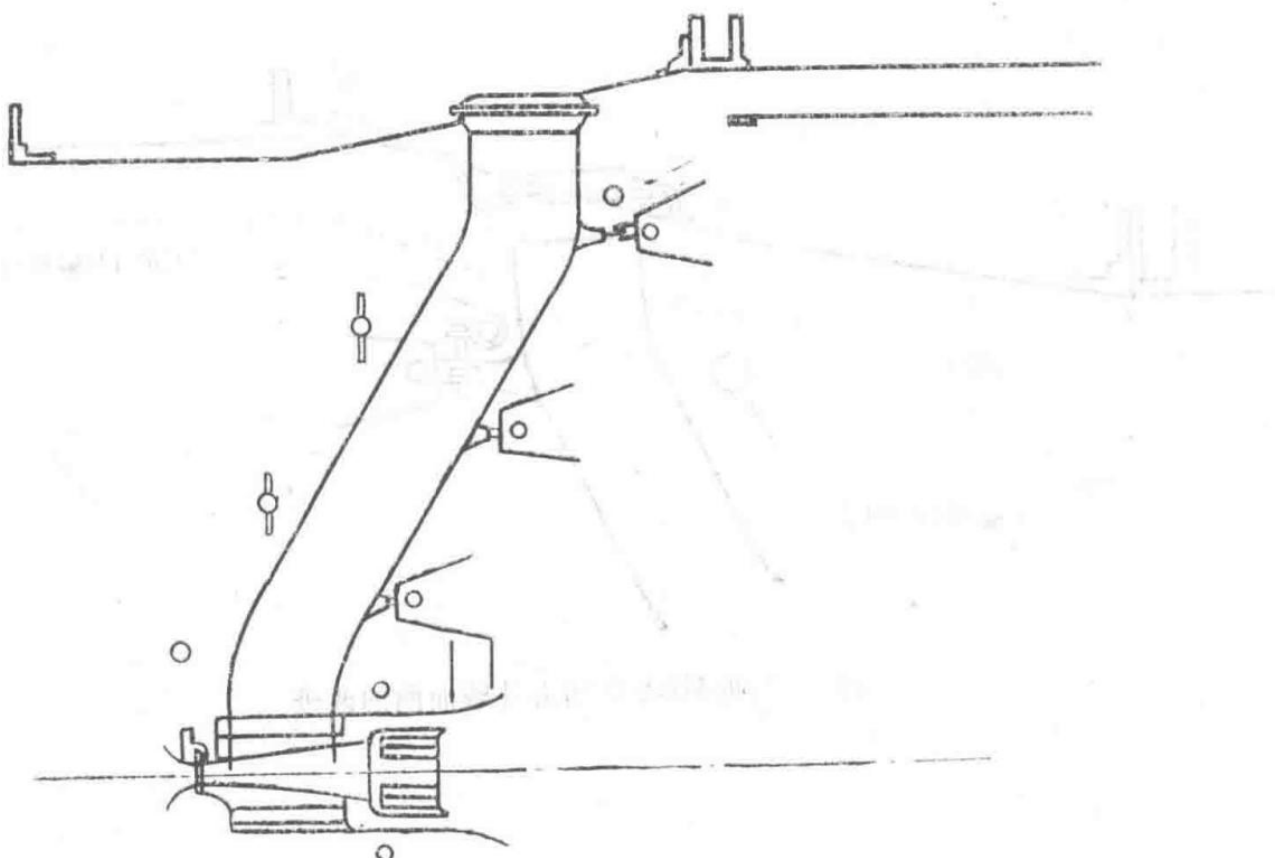


Figure 5 Spey MK202 Afterburner (Catalytic Igniter Installed at the Center of the Afterburner)

Diagram showing the Spey MK202 afterburner with a catalytic igniter positioned at the center of the afterburner chamber.

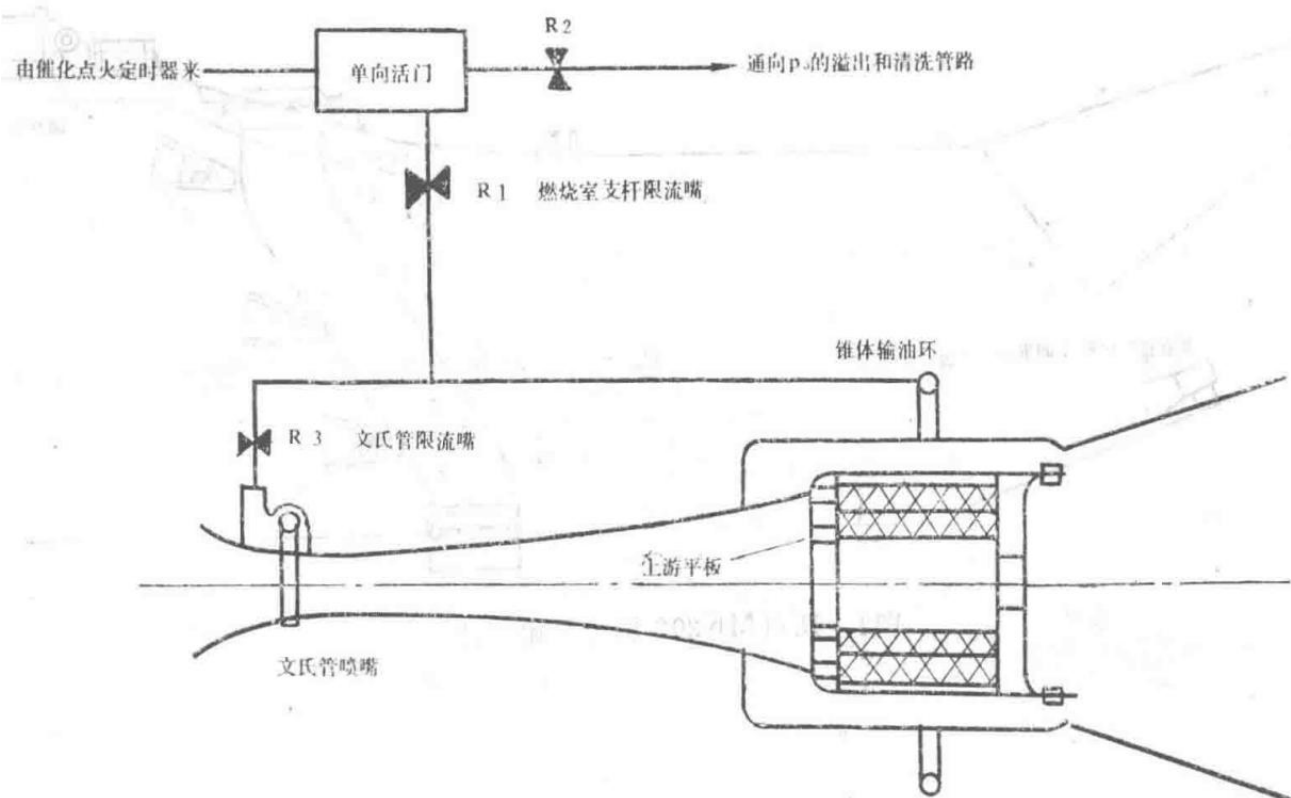


Figure 6 Catalytic Ignition System of the Spey MK202 Afterburner

Diagram illustrating the catalytic ignition system used in the Spey MK202 afterburner.

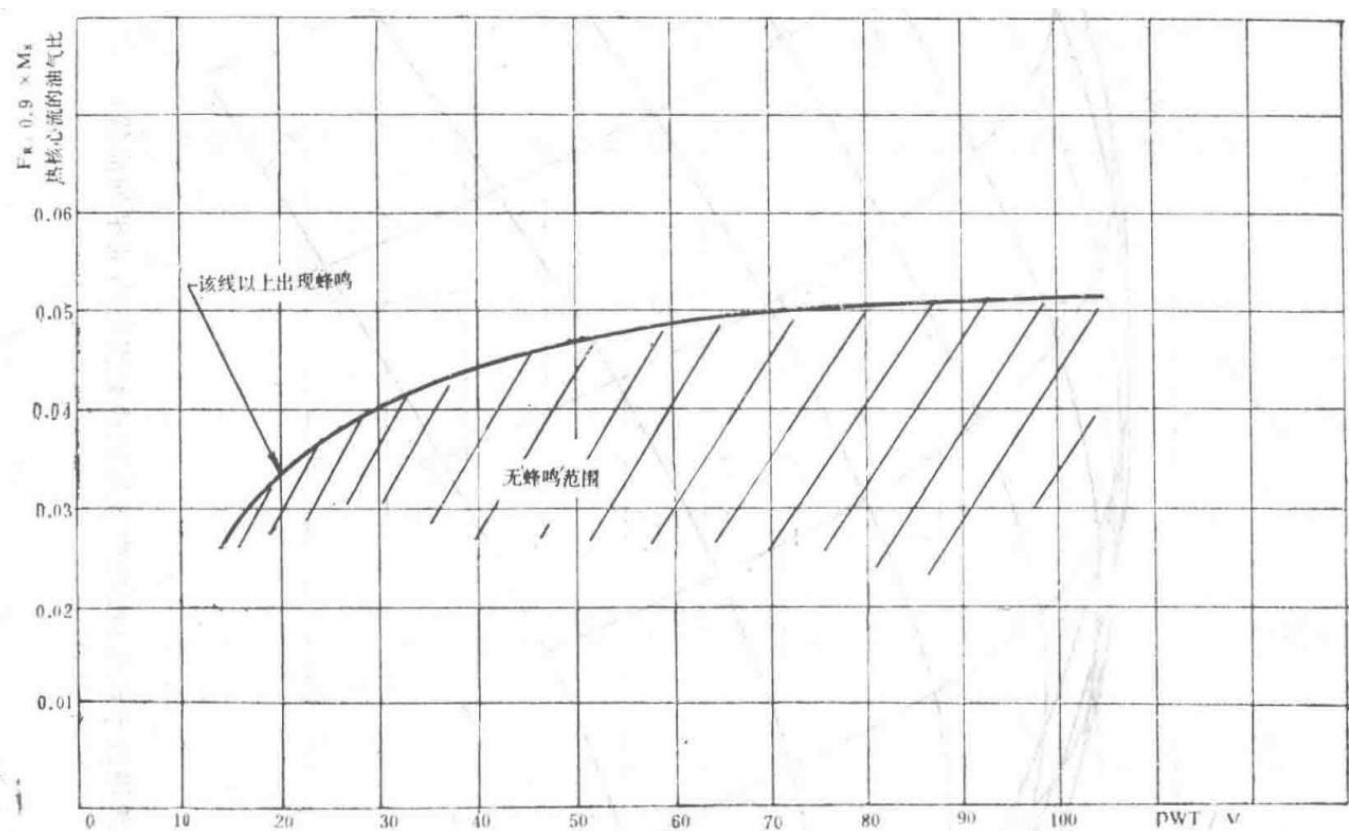
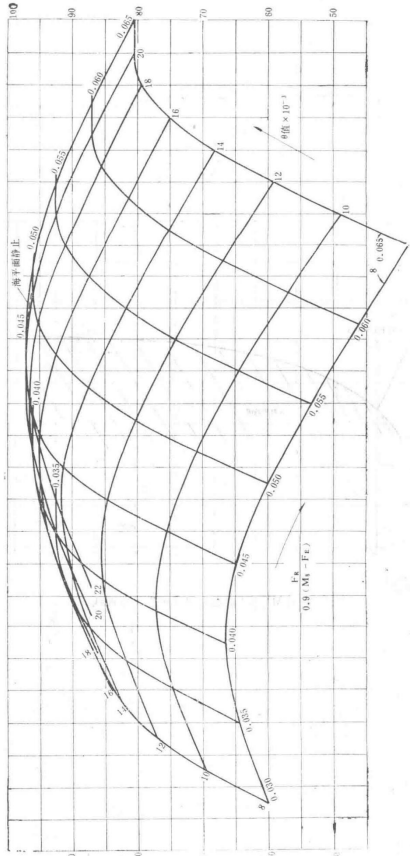


Figure 7 Spey MK202 Afterburner 'Buzz' Relationship Curve

Graph depicting the relationship between combustion instability ('buzz') parameters for the Spey MK202 afterburner.



Technical schematic related to the Spey MK202 afterburner test setup or components.

#### Combustion Research Report

Report Title	Report Number
Combustion Research	CRR12019
Research on Combustion Stability of Spey MK202 Afterburner	

## 1.0 Abstract

This report summarizes the preliminary tests conducted by the combustion department to reduce combustion roughness in the Spey afterburner through various improvement schemes. These improvements included changes to the fuel supply arrangement, fuel distribution, and various types of vaporizer stabilizers.

None of these improvements significantly affected the combustion stability boundary, and no practical enhancements were derived from these tests. This report is merely published as a record of the completed work.

## 2.0 Conclusions

1. The main afterburner fuel distribution in the original design creates a fuel-rich zone near the heat shield, resulting in overheated areas on the afterburner casing.
2. Reducing the fuel flow in the outer fuel ring decreases the tendency for overheating and achieves a wider stable combustion boundary, particularly at altitudes of 45,000 feet and 50,000 feet.
3. The second set of restrictors completely eliminated the occurrence of overheated zones and slightly improved the stable combustion boundary above 50,000 feet.

4. The improved No. 4 fuel ring, with a fuel injection angle of 13°, showed better stability boundaries above 55,000 feet compared to a 26° injection angle.
5. The improved No. 3 fuel ring without fuel rods had minimal impact on the stable combustion boundary, with a measured maximum difference in afterburner nozzle area of 20 inches.
6. The improved vaporizer stabilizer with an outlet-to-inlet area ratio increased to 1.5 had negligible impact on the stable combustion boundary. The maximum difference in area readings was only 10 inches, but this stabilizer appeared to provide much more uniform combustion.
7. Changes to the wake fuel supply and distribution only slightly improved the stable combustion boundary, and such effects are considered secondary for combustion stability.

## 3.0 Test Equipment

The tests were conducted from May 25 to July 19, 1966, in the No. 2 chamber of the "C" area high-altitude test facility using an afterburner with the serial number H347. The afterburner configurations tested are shown in Figure 1, with configuration numbers 12/1, 12/2, 13, 14/1, 14/2, 15/1, and 15/2.

## 4.0 Introduction

In the Spey MK202 engine, combustion instability in the afterburner limits the operation of the afterburning system at fuel flow rates near the maximum afterburning ratio. This instability manifests as an audible 'buzz' with a frequency of 100 to 120 cycles per second. Such unstable combustion occurs across a significant portion of the flight envelope at high altitudes and sea level, particularly when the 12th-stage boundary layer control bleed is active. This document describes a series of initial tests conducted by the combustion department.

## 5.0 Test Objectives

The objective of the tests was to identify the primary factors causing 'buzz' combustion under high-altitude conditions, aiming to completely eliminate 'buzz' at or beyond (if possible) the maximum predetermined fuel flow required for afterburning. Achieving the predetermined fuel flow or a buzz-free fuel flow must also align with obtaining the required afterburning ratio and satisfactory combustion efficiency.

- The influence of fuel distribution ratios among the main fuel rings
- Changes in fuel injection positions
- Types of vaporizer stabilizers
- Changes in the injection angle on the outer fuel ring

## 6.0 Test Rig Description

The test rig is shown in Figure 2 and uses a high-altitude chamber to reduce pressure, simulating high-altitude conditions.

The afterburner is connected to a simulation device consisting of six "Avon" combustion chambers as preheaters and an outer bypass airflow simulating the engine's bypass outlet conditions. Air is supplied to the simulation device by a supply compressor and extracted from the high-altitude chamber by six exhaust compressors. The setup includes the same type of mixer and transition section as on the engine, ensuring that the tested afterburner experiences similar pressure, temperature, and air velocity conditions as in the actual engine. However, the test rig cannot simulate the swirl effects present in the engine.

The ductwork, test chamber, and simulation device are equipped with comprehensive measurement and control systems, allowing precise simulation of flight conditions across a wide range of Mach number/altitude combinations within the afterburner.

## 7.0 Test Procedure

Initially, the test rig was adjusted to achieve specified values of  $p_{\infty}$  and  $p_0$  (Table I) to establish conditions at 45,000 feet with a Mach number ( $M_n$ ) of 1.53. The temperature  $T_e$  was adjusted to its specified value using the maximum temperature controller, while  $T_1$  was allowed to stabilize at 150°C. The afterburner was then ignited using a catalytic igniter installed on the tail cone of the simulation device, with only the vaporizer stabilizer supplied with fuel. Subsequently, the main afterburner fuel flow was increased via the segmented valves to the maximum predetermined fuel flow for the specific altitude. At this point, the automatic data recording system scanned and recorded the primary parameters. If the parameters determining the afterburner Mach number,  $\text{racM } \sqrt{T}/S503$ , and bypass ratio were within the limits specified in Table II, the parameters were recorded, and a set of readings was obtained. If combustion instability occurred before reaching the maximum predetermined main afterburner fuel flow, the fuel flow was reduced to just below the instability threshold, and readings were recorded. If no instability occurred at the maximum predetermined fuel flow, the fuel flow was increased by 15%, and the automatic data recording system scanned and recorded another set of readings. Whenever the nozzle reached its maximum open position (i.e., contacted the stop), the main afterburner fuel flow was no longer increased, and readings were recorded.

During adjustments, attention was paid to ensuring that the inlet Q parameter of the afterburner and the bypass ratio remained within the following limits:

$$169 \leq (M \sqrt{T})/(S503) \leq 171$$

Constraint for the afterburner inlet Q parameter.

$$0.835 \leq \mu \leq 0.865$$

Constraint for the bypass ratio.

The tests were repeated at different altitudes as shown in Table I. Combustion instability was detected using the following methods:

1. Ultraviolet recorder oscillograms showing fluctuations in S503 and vaporizer stabilizer fuel pressure.
2. Monitoring 'buzz' through observation ports.
3. Detection using a vibration meter on the control console, connected to sensors mounted on the afterburner.

## Table I

Parameter	Unit	Value
Altitude	feet	45,000
Mach number		1.53
P <sub>0</sub>	psi (absolute)	2.136
T <sub>0</sub>	K	423
P <sub>0</sub>	psi <sup>2</sup> (absolute)	36.9
M <sub>6</sub>	lb/s	54.0
MB	lb/s	45.9
Fuel flow to vaporizer stabilizer	gallons/hour	216
S503	psi <sup>2</sup> (absolute)	15.7
Orifice area	inches <sup>2</sup>	136
Total fuel flow*	gallons/hour	2200

This includes the fuel flow to the vaporizer stabilizer.

## Table II

Parameter	Unit	50,000 ft	55,000 ft	60,000 ft	65,000 ft	
Altitude	feet	50,000	55,000	60,000	65,000	
P <sub>0</sub>	psi (absolute)	1.679		1.320	1.038	0.816
T <sub>0</sub>	K	423		423	423	423
P <sub>0</sub>	psi <sup>2</sup> (absolute)	29.0	22.8	17.95	14.1	
M <sub>6</sub>	lb/s	42.4	33.35	26.25	20.6	
M <sub>8</sub>	lb/s	36.1	28.4	22.35	17.55	
Fuel flow to vaporizer stabilizer	gallons/hour	170	133	105	82	
S503	psi <sup>2</sup> (absolute)	12.34	9.71	7.63	6.00	
Total fuel flow	gallons/hour	1730	1360	1070	840	

However, during testing, an ultraviolet recorder was used as the sole method to indicate the occurrence of unstable combustion, and the onset of unstable combustion was detected by a sudden increase in the amplitude of S503 pressure fluctuations.

## 8.0 Operating Conditions

The test rig was adjusted to simulate the Spey MK202 operating at a Mach number of 1.53 with a bypass ratio of 0.85 on the low-working line. Strictly speaking, this is not a real operating condition but was used as a slightly more severe condition than those encountered by the engine.

## 9.0 Results Discussion

The test results are presented as curves showing the relationship between nozzle area and altitude at the onset of unstable combustion or at maximum predetermined fuel flow (Figures 3 to 7). Recent tests used the ratio of afterburner to non-afterburner nozzle area or the calculated average nozzle temperature to represent the results. In earlier tests, the automatic data recording equipment did not have the capability to calculate the non-afterburner nozzle area.

### 9.2 Effect of Fuel Distribution Ratio

The first phase of testing aimed to determine the effect of changing the fuel distribution ratio among the fuel manifolds. The distribution ratio was altered by installing restrictors in the main afterburner fuel supply lines. The restrictors were grouped into three sets, and the table below shows the corresponding fuel distribution ratios for each group:

Fuel Distribution Ratios for Different Restrictor Groups

Fuel Zone	1 (Innermost)	2	3	4 (Outermost)
Group 1	6.6%	26.4%	39.8%	27.2%
Group 2	6.3%	28.4%	41.0%	24.3%
Group 3	7.0%	32.2%	48.6%	12.2%
Design Distribution	6.7%	24.7%	38.3%	30.3%

Configuration 12/1 supplied fuel according to the design distribution ratio, resulting in hot zones on the afterburner combustion chamber casing due to a higher percentage of fuel supplied by the No. 4 manifold, causing combustion near the heat shield. The nozzle area achieved with this configuration is shown in Figure 3.

Using the first group of restrictors reduced the fuel supply ratio of the No. 4 manifold from 30.3% to 27.2%, nearly eliminating the hot zones. This improvement also slightly increased the nozzle opening at lower altitudes, as shown in Configuration 12/2 in Figure 3.

Even with this fuel distribution ratio, there was still a tendency to form hot zones. Using the second group of restrictors to further reduce the fuel supply ratio of the No. 4 manifold from 27.2% to 24.3% completely eliminated the hot zones. This arrangement slightly widened the stable combustion boundary at higher altitudes compared to Configuration 12/2, as shown in Configuration 14/2 in Figure 4. Configuration 15/2 demonstrated that the third group of restrictors provided a slightly better stable combustion boundary than the second group, as shown in Figure 5.

### 9.3 Effect of Injection Angle

Configuration 13 in Figure 3 shows that the improved No. 4 manifold with a 13° injection angle for the spray holes slightly improved the stable combustion boundary compared to Configuration 12/2, which had a 26° injection angle.

### 9.4 Effect of Changing Vaporizer Stabilizer Fuel Flow

Configuration 14/2 was used to evaluate the effect of changing the vaporizer stabilizer fuel flow on the "buzz" boundary. At 55,000 feet, the "buzz" boundary was found by controlling the vaporizer stabilizer fuel flow normally and increasing the main manifold fuel flow. The main manifold fuel flow was then reduced until the "buzz" disappeared. The vaporizer stabilizer fuel flow was readjusted to achieve  $\pm 43\%$  ( $\pm 60$  gallons/hour) of the standard fuel flow. The main manifold fuel flow was increased again using the normal method until the "buzz" boundary was reached. The test results shown in Figure 4 indicate that a slightly higher vaporizer stabilizer fuel flow provides better "buzz" margin. Therefore, it can be concluded that for this altitude/Mach number

combination, the original vaporizer stabilizer fuel flow was not optimal. This was not verified at other altitudes.

## 9.5 Effect of Fuel Supply Arrangement

A comparison between Configurations 14/2 and 15/1 in Figure 6 shows that removing the fuel rods from the No. 3 manifold and redrilling holes in the manifold had no significant effect on combustion stability.

## 9.6 Effect of Changing the Vaporizer Stabilizer

A vaporizer stabilizer with an area ratio ( $A_{in}/A_{out}$ ) of 1 (where  $A_{in}$  is the inlet area of the air intake nozzle before the stabilizer, and  $A_{out}$  is the outlet area of the air and fuel holes on the distribution tube) was found to cause fuel overflow around the intake nozzle. Tests on a small-scale rig showed that this created a fuel-rich flame behind the intake nozzle, while the flame toward each end of the distribution tube became weaker. Tests on an open-ended rig also found that for low CD values, increasing the outlet area resulted in a relatively stable blue flame around the stabilizer. This increased the area ratio ( $A_{out}/A_{in}$ ) to 1.5. However, a comparison between Configurations 13 and 14/1 in Figure 7 shows that this relatively stable flame did not significantly improve the stable combustion boundary.

## 9.7 Afterburner Efficiency

To estimate afterburner efficiency, curves were plotted showing the relationship between the nozzle position indicator angle and the total afterburner fuel flow and total airflow (Figure 8). In the absence of non-afterburner nozzle area data, this type of plot was necessary. The plot indicates that for these test configurations, the nozzle area (and thus the afterburner temperature) increases with increasing fuel flow, suggesting that combustion efficiency either increases or at least does not decrease with increasing fuel flow. The curves also show that for each configuration, as the restrictors change from Group 1 to Group 2 to Group 3, the nozzle area (and thus efficiency) tends to decrease. Unfortunately, this trend of decreasing nozzle area coincides with the trend of moving away from "buzz" as shown in previous plots, so it can be concluded that expanding the stable combustion boundary comes at the cost of some afterburner efficiency.

## 9.8 Effect of Manifold Valves

Except for one test in Configuration 15/2 where the manifold valve was fixed in the open position, all other tests were conducted with the manifold valve operating normally. Nozzle position indicator angles were recorded at different fuel-air ratios and plotted in Figure 8. The plot shows that within the test range, efficiency remained clearly constant as the manifold fuel flow increased.

Figure 1: Combustion Stability Test Configurations

Test Date	Configuration	1 Manifold	2 Manifold	3 Manifold	4 Manifold	Vaporizer Stabilizer	Restrictor Group
1966.5.25	12/1	Design	Design	Design	Design (26° spray holes)	Design	Design distribution
1966.5.26							
1966.5.27							
1966.7.1	12/2	"	"	"	"	"	Group 1
1966.7.4							
1966.7.5							
1966.7.8	13	"	"	"	(13° spray holes)	"	Group 1

1966.7.12	14/1	"	"	"	"	A <sub>ut</sub> /A <sub>in</sub> = 1.5	Group 1
1966.7.13	14/2	"	"	"	"	"	Group 2
1966.7.18	15/1	"	"	No spray rods	"	"	Group 2
1966.7.18	15/2	"	"	"	"	"	Group 2

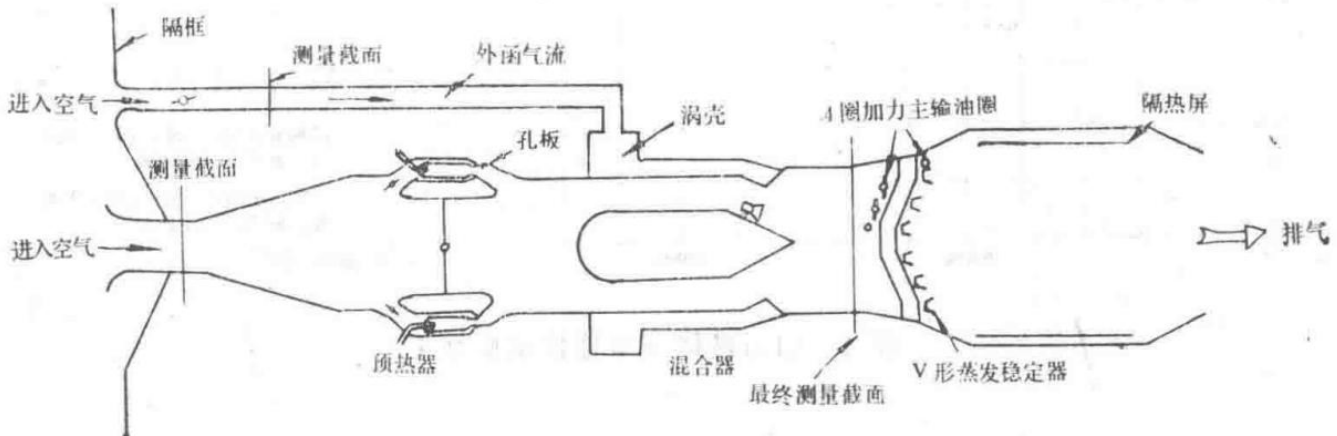


Figure 2: Afterburner Simulation Rig Used in High-Altitude Test Facility

Diagram of the afterburner simulation rig showing the layout of components such as the vaporizer stabilizer, fuel manifolds, and flame stabilizers.

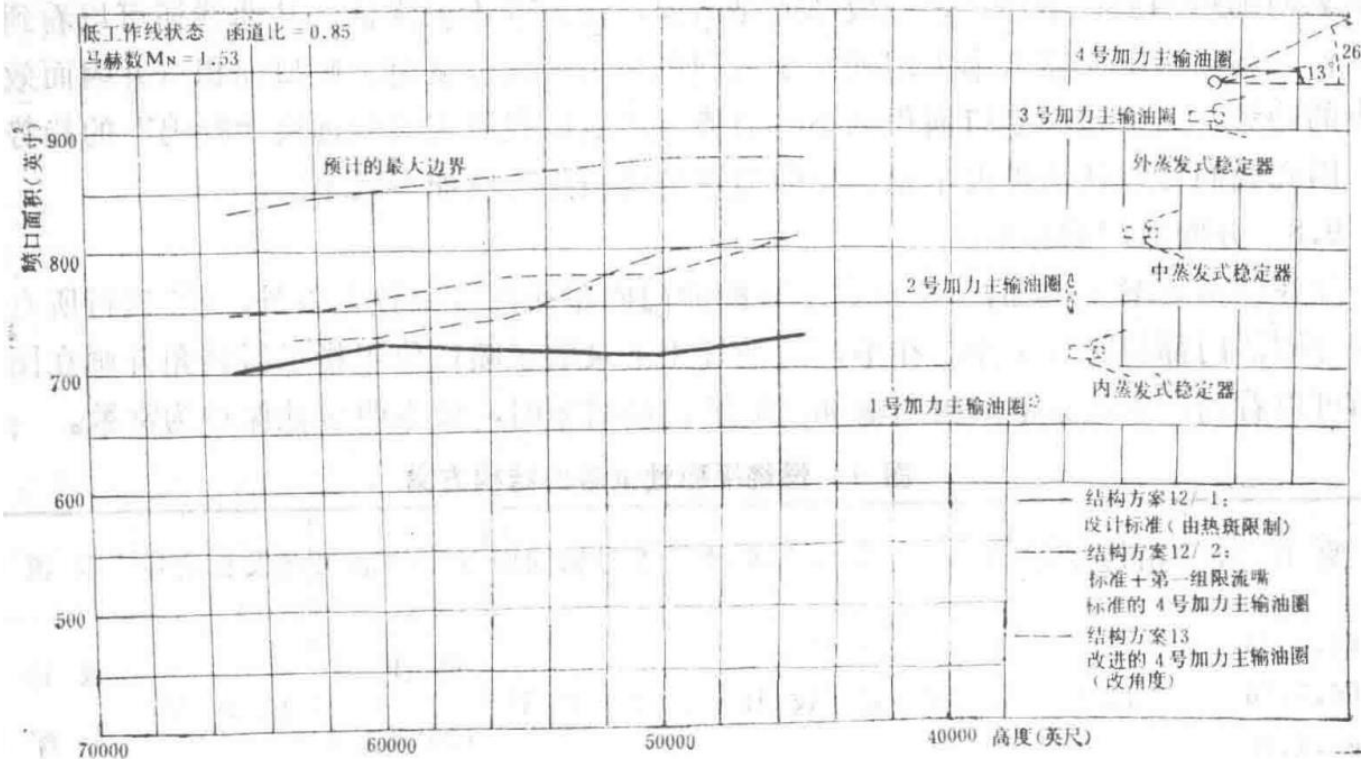


Figure 3: Afterburner Combustion Stability Test Results

Graph showing the relationship between nozzle area and altitude for different configurations, illustrating the stable combustion boundary.

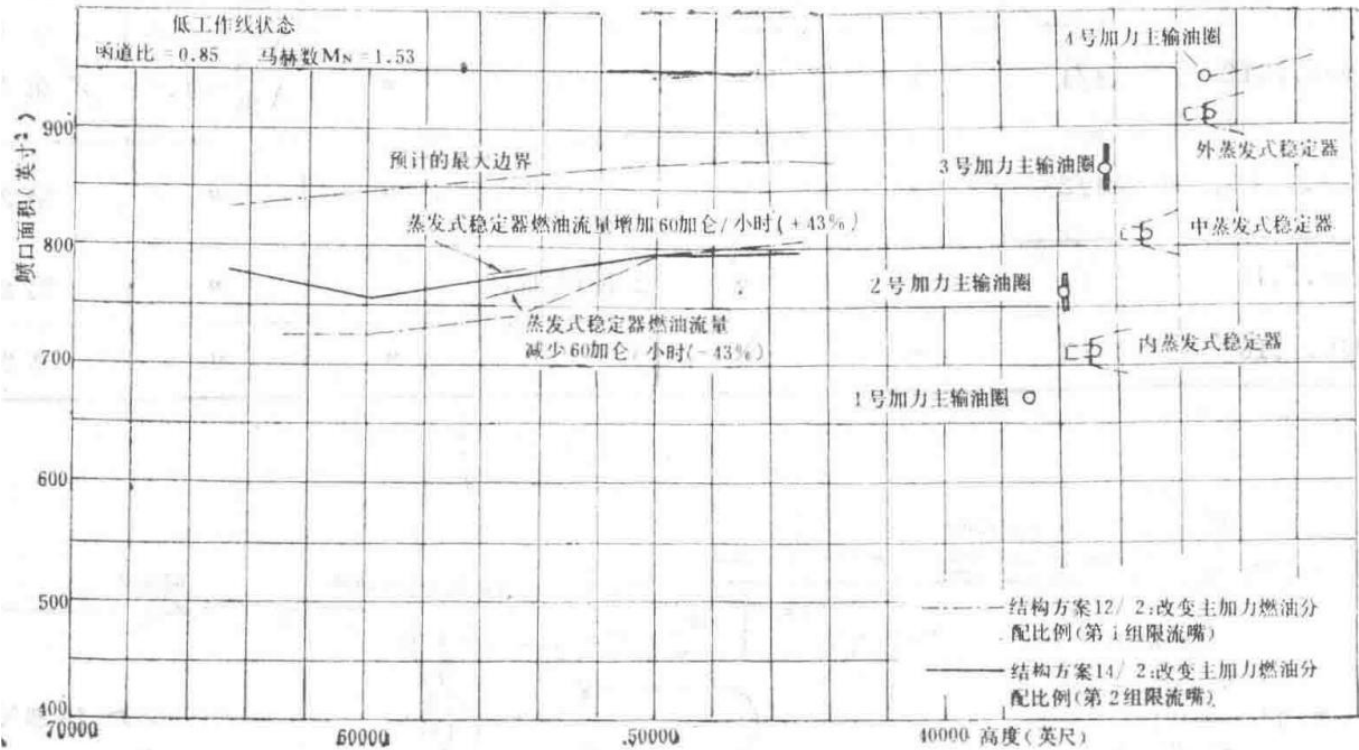


Figure 4: Afterburner Combustion Stability Test Results

Graph showing the effect of vaporizer stabilizer fuel flow adjustments on the stable combustion boundary.

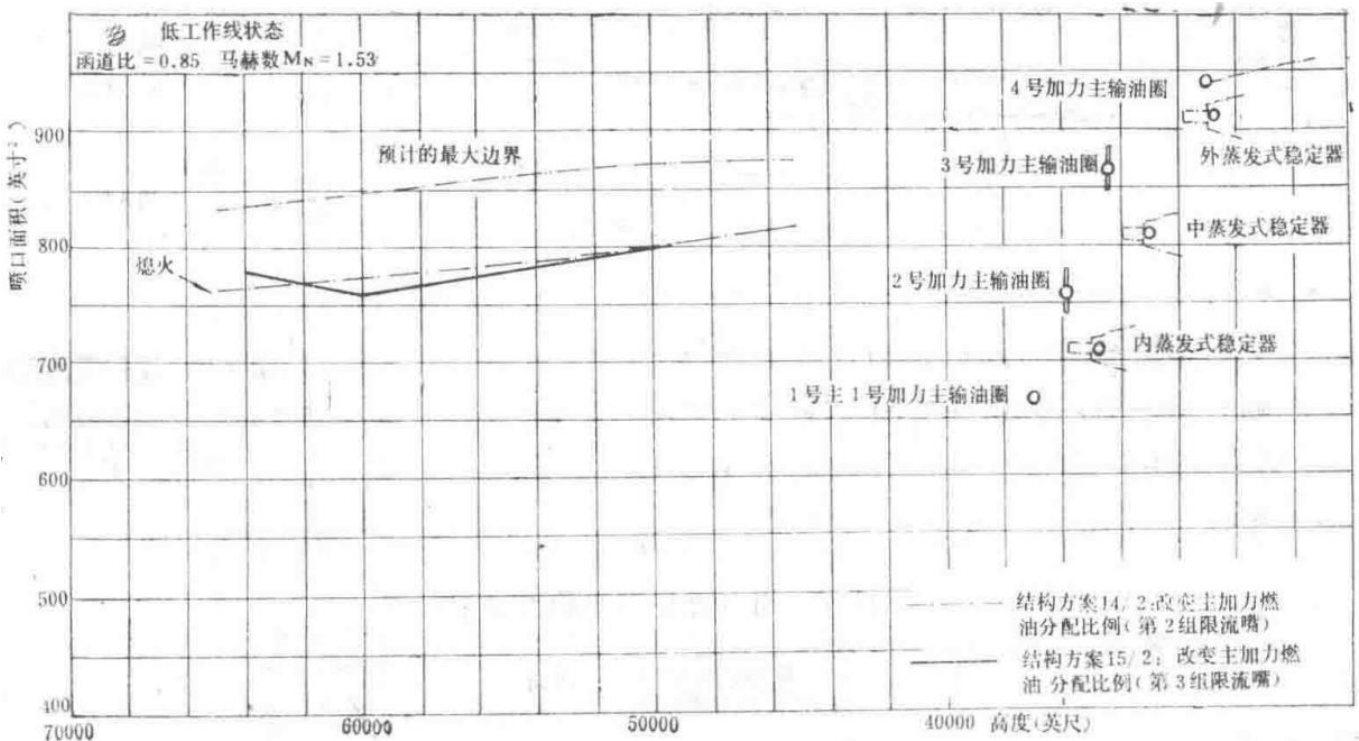


Figure 5: Afterburner Combustion Stability Test Results

Graph comparing the stable combustion boundaries for different restrictor groups.

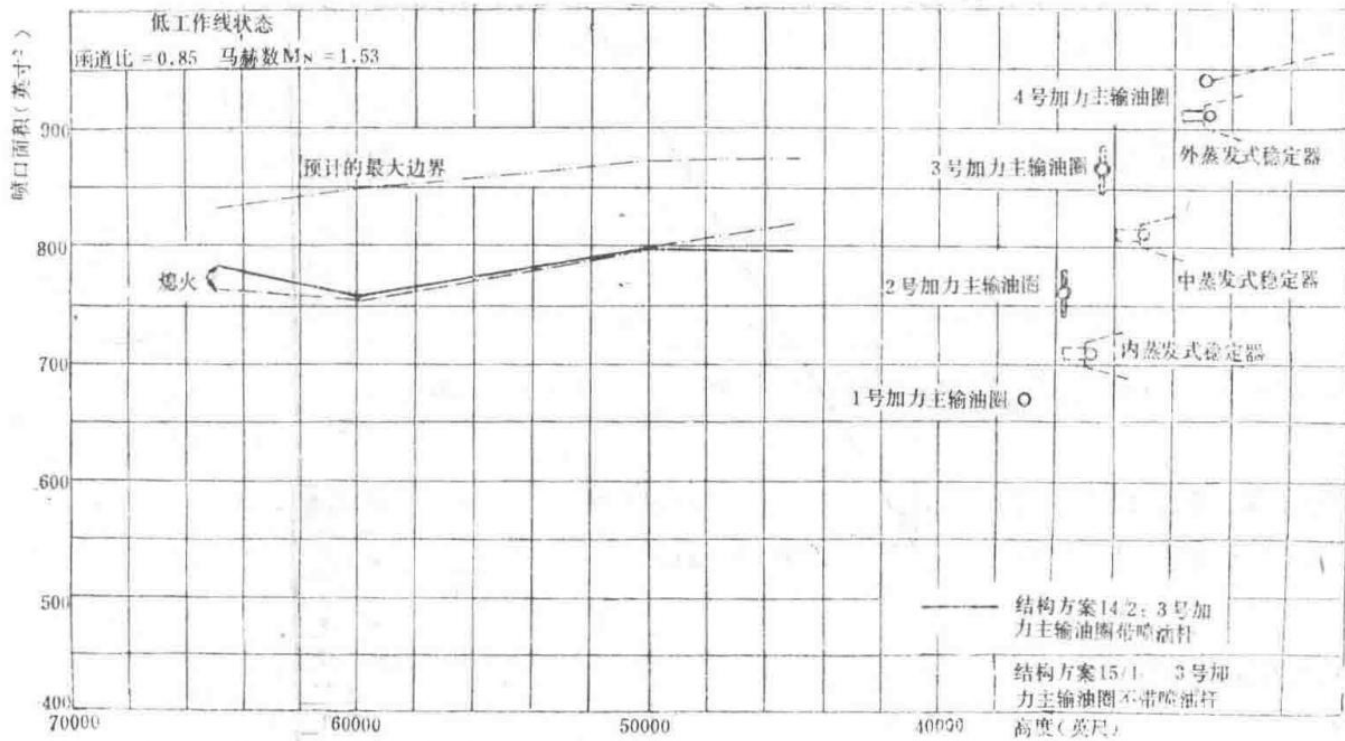


Figure 6: Afterburner Combustion Stability Test Results

Graph comparing the effect of removing spray rods from the No. 3 manifold on combustion stability.

— Section 19 —  
Content from Original Document (Pages 91-95)

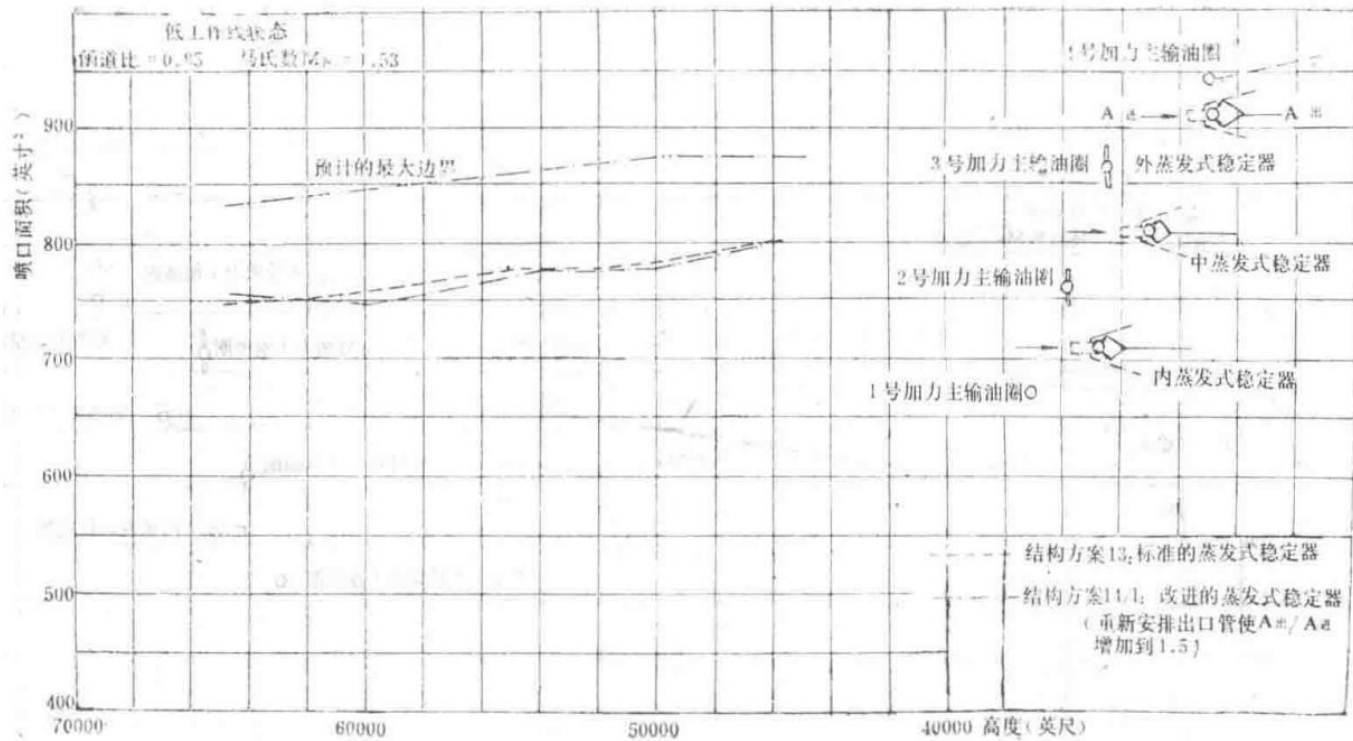


Figure 7: Afterburner Combustion Stability Test Results

Graphical representation of afterburner combustion stability test results for the Spey MK202 engine.

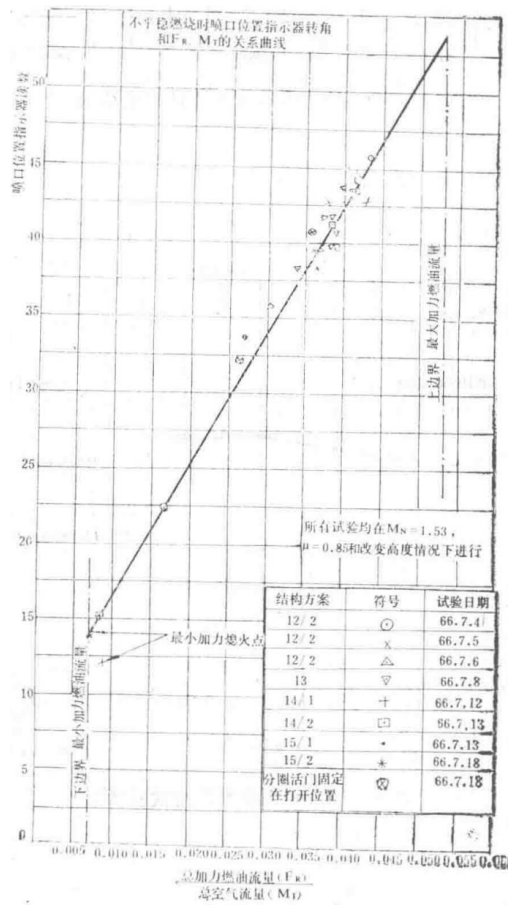


Figure 8: Afterburner Combustion Stability Research

# Development Technical Report DTR 86020

Spey MK202 Afterburner System Afterburner Ignition Tests on the High-Altitude Test Bed (Catalytic Igniter Installed in the Afterburner Combustion Chamber Center)

First Edition, July 24, 1967

## Introduction

Since November 1966, extensive ignition tests of the Spey afterburner system have been conducted on the high-altitude test bed.

Initial tests were performed using a developmental catalytic igniter installed in the afterburner combustion chamber center. Later (after April 1967), a design-type igniter was adopted. The tests ultimately achieved reliable ignition at an altitude of 40,000 feet and Mach 0.9, meeting the early operational standard.

1. Summarize the relatively important results obtained using the design-type catalytic igniter installed in the afterburner combustion chamber center.
2. Report the results of engine tests conducted according to the early operational standard.
3. Identify further improvements required for the existing afterburner combustion system and catalytic igniter to meet technical specifications.

## Conclusions

1. The early operational afterburner combustion chamber achieved reliable ignition at 40,000 feet and Mach 0.9 with the nominal fuel flow of the vaporizer stabilizer.
2. Increasing the total fuel flow of the vaporizer stabilizer at high altitudes improved afterburner ignition performance through the following aspects:
  3. (a) Reduced fuel-filling time – When using a vaporizer stabilizer with increased flow, at 52,000 feet and Mach 0.9, the fuel-filling time was reduced from 2.3 seconds to 1.3 seconds.
  4. (b) Improved flame propagation – For example, at 52,000 feet and Mach 0.9, the time for flame propagation from the inner-ring stabilizer to the outer-ring stabilizer decreased from 3.5 seconds (nominal flow) to 0.1 seconds (increased flow).
  5. (c) Enhanced afterburner ignition capability.
6. This report details the minimum pre-set fuel quantity required for the vaporizer stabilizer to achieve good flame propagation.
7. (a) Above 40,000 feet at Mach 0.9, the catalytic igniter fuel ring operates below its known lean limit, as verified by both test rig and engine tests.
8. (b) At 52,000 feet and Mach 0.9, a minimum fuel flow of 20 gallons/hour for the fuel ring is required to achieve stable catalytic igniter flame and thus improve ignition timing. The current fuel ring only provides approximately 5 gallons/hour at this altitude.
9. The venturi fuel supply system of this catalytic igniter operates above its known rich limit, with a 0.025 restrictor upstream of the venturi nozzle acting as a buffer.
10. Due to variations in vaporizer stabilizer flow, the ignition capability of early production engines will also vary.
11. Increasing the flow of the vaporizer stabilizer or fuel ring enables ignition completion within approximately 2 seconds up to 52,000 feet at Mach 0.9.

## Next Steps in Testing

1. Use an afterburner regulator with increased vaporizer stabilizer flow to improve ignition and flame propagation. This regulator will be available in August 1967.

2. Increase the fuel ring flow rate by using an enlarged external restrictor to maintain the existing catalytic igniter flow.
3. Determine the lean and rich limits of the catalytic igniter and fuel ring at sea level conditions.
4. Conduct afterburner ignition tests above 52,000 feet at Mach 0.9 after removing the engine inlet pressure (P1) limitation.
5. Study the catalytic igniter fuel system.

## Preface

Since November 1966, numerous afterburner ignition tests have been conducted on the high-altitude test bed to evaluate the afterburner catalytic ignition system installed in the afterburner combustion chamber center.

Early tests were performed using a developmental catalytic igniter. At 52,000 feet and Mach 0.9, fully automatic afterburner ignition was achieved within 14 seconds. This excessive delay was due to poor flame propagation from the inner-ring stabilizer to the outer-ring stabilizer.

Subsequent tests of the early design-type catalytic igniter installed in the afterburner combustion chamber center at sea level were not very successful. Extensive combustion tests were conducted before identifying inherent fuel supply faults in the design.

Starting from April 1967, further engine tests were conducted on the high-altitude test bed using a modified design-type catalytic igniter installed in the afterburner combustion chamber center. This modified catalytic igniter featured a "parallel" fuel supply system similar to that used in the developmental afterburner combustion chamber center, supplying fuel to both the venturi and the fuel ring simultaneously.

This report summarizes the relatively important results obtained from tests of the later design-type catalytic igniter installed in the afterburner combustion chamber center and recommends further improvements to the combustion chamber to meet current ignition technical requirements.

## Test Results

### [Test 5 \(A\), January 19, 1967, Engine 38 – Afterburner Combustion Chamber H348, Refer to Figure RHD863](#)

Figure RHD863 illustrates the final configuration with a developmental catalytic igniter installed in the afterburner combustion chamber center. This configuration also included a richer inner-ring vaporizer stabilizer, flame propagation slots, and a pyrophyllite catalyst. The absolute ignition limit was determined to be at 52,000 feet and Mach 0.9 ( $P_8 = 7.8$  psi absolute), although the ignition time was 14 seconds due to: (1) delayed ignition of the inner-ring stabilizer; (2) poor flame propagation.

If the catalytic igniter was fueled via a 3-second timer, the ignition time was too long to achieve ignition above 40,000 feet at Mach 0.9.

### [Test 9, April 6, 1967, Engine 41 – Afterburner Combustion Chamber H366, Refer to Figure RHD1007](#)

An early design of the catalytic igniter installed in the afterburner combustion chamber center with a parallel fuel supply system was tested during combustion instability studies using a wide-slot V-shaped stabilizer combustion chamber. The ignition limit was reached at approximately  $P_8 = 20.8$  psi absolute (30,000 feet, Mach 0.9).

### [Test 10, April 10, 1967, Engine 41 – Afterburner Combustion Chamber H348, Refer to Figure RHD1007](#)

The above configuration was modified with: (a) 5 flame propagation slots, (b) granular ceramic catalyst (split ceramic catalyst), and (c) a 0.025 diameter restrictor installed inside the venturi connector.

This configuration improved ignition time, achieving ignition at 35,000 feet within 2.6 seconds at Mach 0.9. However, the engine could not ignite at higher altitudes. The 0.025 restrictor later improved in-flight ignition capability.

## Test 11, April 18, 1967, Engine 20006 – Afterburner Combustion Chamber H348

This configuration featured a design-type catalytic igniter installed in the afterburner combustion chamber center with a parallel fuel supply system and a 0.025 diameter venturi restrictor (dual-satellite catalytic igniter). This wide-slot stabilizer afterburner combustion chamber reached its ignition limit at  $P_8 = 20.8$  psi absolute, rather than at  $P_8 = 18.5$  psi absolute (33,000 feet, Mach 0.9).

## Test 12, April 22/23, 1967, Engine 20006, Afterburner Combustion Chamber H348, Refer to Figures RHD1027 and 1028

- The engine was equipped with two separate fuel supply systems to independently supply fuel to the venturi and fuel ring of the catalytic igniter installed in the afterburner combustion chamber center, to determine their fuel requirements. The 0.035 diameter external restrictor was removed from the existing catalytic igniter fuel delivery pipeline, and the 0.025 restrictor was also removed from the venturi fuel supply pipeline.
- No attempt was made to ignite the afterburner combustion chamber; only the catalytic igniter operated independently. Its characteristics were observed at  $P_8 = 10$  psi absolute and  $P_8 = 15$  psi absolute across a range of fuel flows.
- Under these two conditions, the most stable and intense flame was achieved with a fuel flow range of 0.00015 lb/sec to 0.0005 lb/sec, confirming previous test rig results.
- When the catalytic igniter venturi was continuously supplied with a preset fuel flow, ignition attempts were made from maximum military power to minimum afterburner state via normal throttle selection. Initial tests at 36,000 feet and Mach 0.9 (with the fuel ring inoperative) found that increasing the catalytic system fuel flow reduced combustion chamber ignition time. However, introducing fuel ring fuel (for a given venturi flow) also reduced ignition time, with higher fuel ring flow resulting in faster ignition.
- At 46,000 feet and Mach 0.9, the afterburner combustion chamber could not ignite if the fuel ring had no flow (refer to Figure RHD1028). Increasing the fuel ring flow improved overall afterburner combustion chamber ignition time when the venturi flow was set to 0.00015 lb/sec.
- At 52,000 feet and Mach 0.9, similar results as described in (4) were obtained. The entire vaporizer stabilizer ignited immediately upon fuel introduction.
- Due to the engine inlet pressure ( $P_i$ ) limitation, the afterburner combustion chamber could not be ignited at higher altitudes.

## Test 13, April 27, 1967, Engine 20006 – Afterburner Combustion Chamber H348

- This configuration was the same as Test 12 but modified with a narrow V-slot and a 0.07 side nozzle installed at the catalytic igniter venturi throat. The test procedure studied was the same as described in Test 12.
- In this case, the catalytic igniter exhibited a strong flame with a fuel flow range of 0.0001 lb/sec to 0.0007 lb/sec, again confirming previous test rig results.
- At 36,000 feet and Mach 0.9:
  - (a) If the fuel ring was not supplied with fuel, the afterburner combustion chamber could not ignite.
  - (b) Increasing the fuel ring flow improved ignition time.
  - (c) Although the inner-ring stabilizer ignited within 4-5 seconds, generally 6-7 seconds were required from afterburner activation to full ignition of the entire afterburner chamber.
- At 45,000 feet and Mach 0.9, although the catalytic igniter produced a good flame, the afterburner combustion chamber could not ignite.

## Test 14, May 2, 1967, Engine 20006 – Afterburner Combustion Chamber H348 (Vaporizer Stabilizer Flow Variation with Continuous Catalytic Igniter Combustion), Refer to Figures RHD1024, 1025, 1026

This configuration included a fuel supply system that separately delivered fuel to the venturi and fuel ring of the catalytic igniter installed in the afterburner combustion chamber center, as well as an auxiliary fuel system for the vaporizer stabilizer.

Note: For this specific configuration, all quoted ignition times are measured from the rise in vaporizer stabilizer pressure (after afterburner activation) to the pressure rise due to ignition at S503.

- At 36,000 feet and Mach 0.9 (refer to Figure RHD1024): Before activating the afterburner, fuel continuously flowed through the venturi and fuel ring at rates of 0.00013 lb/sec and 30 gallons/hour, respectively. Attempts were made to ignite at minimum afterburner state by selecting vaporizer stabilizer fuel quantity. Although poor flame propagation was a major issue, ignition time significantly increased when vaporizer stabilizer flow was below nominal (214 gallons/hour). The inner-ring stabilizer ignited 2 seconds earlier than the second and third ring stabilizers. With nominal vaporizer stabilizer flow, ignition time was 2.5 seconds. When the flow was increased by 28%, ignition time reduced to 1.4 seconds. Additionally, flame propagation from the inner to outer V-slots no longer exhibited measurable delay.
- At 45,000 feet and Mach 0.9 (refer to Figure RHD1025): With a venturi flow of 0.00013 lb/sec and fuel ring flow of 30 gallons/hour, when the preset vaporizer stabilizer flow was below the nominal 137 gallons/hour, the entire combustion chamber could not ignite. Even at nominal vaporizer stabilizer flow, flame propagation issues were encountered, with the inner two rows of vaporizer stabilizers igniting approximately 1.0-1.5 seconds earlier than the outer stabilizers. An overall vaporizer stabilizer fuel flow exceeding 180 gallons/hour was required for instantaneous flame propagation in the afterburner combustion chamber. Further increasing the vaporizer stabilizer flow reduced ignition time even more. A vaporizer stabilizer flow of 210 gallons/hour was considered the minimum allowable flow to achieve sufficiently fast afterburner ignition and flame propagation at this altitude, representing a 53.7% increase over the nominal flow. Further ignition tests were conducted with various fuel ring fuel flows (with constant venturi and stabilizer flows), showing that increasing fuel ring flow reduced ignition time. Due to limitations in the auxiliary fuel supply, the flow could not exceed 40 gallons/hour. Increasing the venturi fuel flow to 0.00052 lb/sec had no significant effect except for increasing the afterburner ignition time to 1.25 seconds at the recommended higher stabilizer flow (with a flow of 0.00013 lb/sec).
- At 52,000 feet and Mach 0.9 (refer to Figure RHD1026): With a venturi fuel flow of 0.00013 lb/sec and fuel ring flow of 30 gallons/hour, when the vaporizer stabilizer flow was at or near the nominal 92 gallons/hour, afterburner ignition was very slow due to: (1) longer ignition times for the inner and middle vaporizer stabilizers (3-4 seconds); (2) delayed flame propagation to the outer-ring vaporizer stabilizer (3-4 seconds). Increasing the total vaporizer stabilizer flow to 150 gallons/hour improved overall afterburner ignition time, reducing it from 6-8 seconds to 2 seconds, although the outer-ring vaporizer stabilizer still ignited 1 second later than the inner two rings. Almost simultaneous flame propagation was achieved at 170 gallons/hour, representing an 84% increase over the nominal flow. Further studies with varying fuel ring flows found that a minimum flow of 20 gallons/hour was necessary to achieve a stable catalytic flame.

## Test 15 (a) and (b), May 24 to June 6, 1967 - Engine 41 with Afterburner H366 (Early Production Engine) (Refer to Figure RHD1023)

Since the current control system does not allow the total vaporizer stabilizer flow rate to exceed 30, it was necessary to redistribute the vaporizer stabilizer fuel to increase the flow to the inner-ring vaporizer stabilizer—a region likely favorable for ignition.

This test configuration included a vaporizer stabilizer with an increased (+75%) fuel flow rate, belonging to the general early production type. (Refer to Figure RHD1023).

At 50,000 feet and Mach 0.9 ( $P_8 = 8.5$  psia), consistent ignition was achieved, although the ignition time was 7 to 8 seconds. However, observations indicated that the inner-ring vaporizer stabilizer ignited 2.5 to 3.0 seconds after afterburner activation. At this altitude, before optimizing the total vaporizer stabilizer flow, this ignition device exhibited ignition characteristics similar to those obtained in Test 14 (Engine 20006 and Afterburner H348).

To rapidly ignite the combustion chamber, it was necessary to further increase the total vaporizer stabilizer fuel flow rate.

## Test 16 (A), June 6, 1967 - Engine 43 with Afterburner AU6 (Refer to Figure RHD1023)

Although this configuration was similar to Engine 41 and belonged to the early production type, the consistent ignition limit was only 38,500 feet at Mach 0.9 ( $P_8 = 14.1$  psia). Further investigation revealed that the preset flow rate of the vaporizer stabilizer for this engine was below the nominal value, and it was confirmed that when the vaporizer stabilizer fuel supply was low, ignition characteristics deteriorated.

## Test 16 (B), June 9, 1967 - Engine 43 with Afterburner AU6

The configuration was the same as in Test 16 (A), but with a steatite cup-shaped catalyst. Only limited ignition tests were conducted, and it appeared that this catalyst provided little or no improvement to ignition.

## Test 17, June 17, 1967 - Engine 507 with Afterburner H370 (Refer to Figure RHD1023)

Apart from a 6-second catalytic igniter timer and artificially increased afterburner fuel flow (achieved by mechanically fixing the  $P_3$  splitter in the open position), the afterburner configuration was the same as in Tests 15 and 16, belonging to the early production type.

At 52,000 feet and Mach 0.9 ( $P_8 = 7.65$  psia), successful ignition was achieved within 4 to 5 seconds after afterburner activation, even though the vaporizer stabilizer and catalytic igniter fuel pressures were zero for the first 1.5 seconds. At this condition, flame propagation was nearly instantaneous (1/10 second). Visual inspection in the test chamber could not identify the ignition status of individual vaporizer stabilizers.

Above this altitude, due to the engine inlet pressure  $P_1$  being limited to 5 psia, afterburner ignition could not be achieved.

## Discussion of Results

- Design-type afterburner with centrally mounted catalytic igniter—featuring a parallel fuel supply system.
- Initially, the early design could ignite up to 30,000 feet at Mach 0.9, but flow test results compared with previously determined test limits indicated that the catalytic igniter was operating above its known rich-fuel limit. To mitigate this issue, a 0.025-inch diameter restrictor was installed upstream of the Venturi nozzle to "buffer" the catalytic igniter fuel flow. This modification enabled ignition at 35,500 feet and Mach 0.9 (2.6 seconds). Although engine failure later prevented testing at higher altitudes.
- Installing the 0.025-inch restrictor improved the in-flight ignition limit by approximately 5,000 feet.
- Design-type afterburner with centrally mounted catalytic igniter—featuring an auxiliary fuel system supplying both the catalytic igniter and the fuel manifold.
  - (a) Early tests were conducted with a standard vaporizer stabilizer fuel distribution system and a 0.035-inch central hole supplying fuel to the catalytic igniter.
  - When the catalytic igniter was continuously supplied with fuel (but the fuel manifold was not), it was possible to maintain a stable catalytic igniter flame above its known rich-fuel limit. Clearly, when fuel was excessive, the catalytic igniter exceeded the rich-fuel boundary, and the excess fuel acted as a supply for the fuel manifold. Therefore, when using the catalytic igniter system, it is crucial to ensure that the catalytic igniter fuel supply is actually within the limit range to achieve successful reignition. Although only catalytic igniter fuel was used, ignition at 36,000 feet and Mach 0.9 was possible; however, without supplying fuel to the fuel manifold, the ignition time was too long to be practically feasible.
  - Above this altitude, flame propagation typically took 3 to 4 seconds. Although increasing the fuel manifold supply could reduce this delay, the ignition time of the inner-ring stabilizer still depended on the time required to establish the overall vaporizer stabilizer fuel flow, approximately 3 seconds at 45,000 feet and Mach 0.9. However, this could be significantly improved by several vaporizer stabilizer fuel-filling methods.
  - (b) Subsequent tests were conducted with a 0.07-inch side nozzle inside the Venturi tube wall and standard vaporizer stabilizer fuel distribution. The ignition times obtained were worse than in (a), and above 40,000 feet (Mach 0.9), ignition failed completely. Since the catalytic igniter flame was established before activation, poor ignition was due to the nominal flow rate of the vaporizer stabilizer. Thus, when the fuel manifold supply was increased to obtain a stronger and more stable catalytic igniter flame, ignition and flame propagation times were reduced again.
- Design-type afterburner with centrally mounted catalytic igniter—featuring an auxiliary fuel supply system for the vaporizer stabilizer.
  - This configuration also included an auxiliary fuel supply system for the catalytic igniter and fuel manifold, as well as a 0.07-inch side nozzle inside the Venturi tube wall.
  - At all altitudes up to the engine's limit of 52,000 feet at Mach 0.9, when the vaporizer stabilizer fuel flow was at or below nominal, the afterburner experienced flame propagation issues. In practice, this problem could be eliminated by increasing the vaporizer stabilizer fuel supply and/or increasing the fuel manifold flow. The required values are listed in the "Test Results" section.
  - Additionally, increasing the vaporizer stabilizer fuel supply could reduce the ignition time of the inner-ring vaporizer stabilizer, thereby improving the fuel-filling time.
  - For a given vaporizer stabilizer fuel flow, studies of different fuel manifold flow rates showed that "ignition" time and flame propagation improved with increased fuel supply. However, it was impossible to supply sufficient fuel to the catalytic igniter and inner-ring stabilizer area using only the current fuel manifold. This study also indicated that increasing the vaporizer stabilizer fuel would be necessary to provide optimal ignition conditions.
  - Increasing the Venturi fuel supply close to its known rich-fuel limit, under the larger vaporizer stabilizer flow rates suggested above, increased the combustion chamber ignition time.
- Early Production Engines
- Engine 41 with Afterburner 366, Afterburner AU6, and Engine 507 with Afterburner H370 are compared in Figures RHD952 and RHD1023 for automatic ignition results across three engines.
- With nominal vaporizer stabilizer fuel flow, this type of engine could reliably ignite at 40,000 feet and Mach 0.9. However, when introducing more total vaporizer stabilizer fuel (e.g., Engine 507), ignition was possible at higher states than the current maximum testable state of 52,000 feet, Mach 0.9 ( $P_1 = 5$  psia).
- On this engine (equipped with a 6-second timer), the total afterburner ignition time achieved was 4 to 5 seconds. This time could be further reduced with several vaporizer stabilizer fuel-filling methods and a

3-second timer. When the vaporizer stabilizer fuel flow reached the level of Engine 507, no combustion chamber flame propagation issues remained. Further validation was conducted in Test 14. The differences between Engines 43 and 41 were likely due to their different vaporizer stabilizer fuel flow rates.

## Recommendations

The current ignition system, including a 3-second timer device, can be further developed to potentially achieve an afterburner ignition limit with a total pressure of 6 psia. Two improvements are needed:

1. Increase the vaporizer stabilizer fuel flow rate.
2. Increase the fuel manifold fuel flow rate while maintaining the existing Venturi fuel flow rate.

The minimum vaporizer stabilizer fuel flow rate required for successful ignition and flame propagation is as follows:

Required Vaporizer Stabilizer Fuel Flow Rates

Altitude (feet)	Mach Number	Total Vaporizer Stabilizer Flow (gallons/hour)	Current	Required	Increase %
36000	0.9	214	214	274	28
45000	0.9	137	137	210	53.7
52000	0.9	92	92	170	84.8

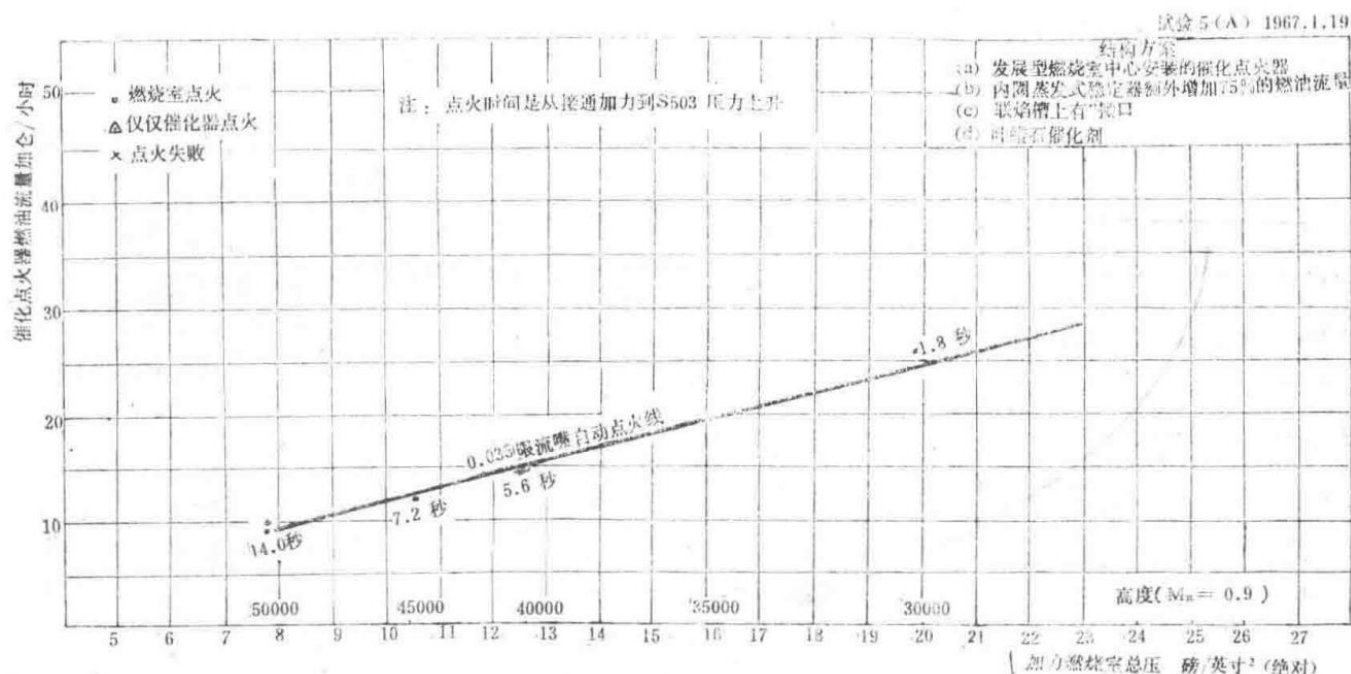


Figure RHD863: Ignition Test of Centrally Mounted Catalytic Igniter in Afterburner (Engine: 38, Afterburner: H348)

Test 9, April 6, 1967; Test 10, April 10, 1967.

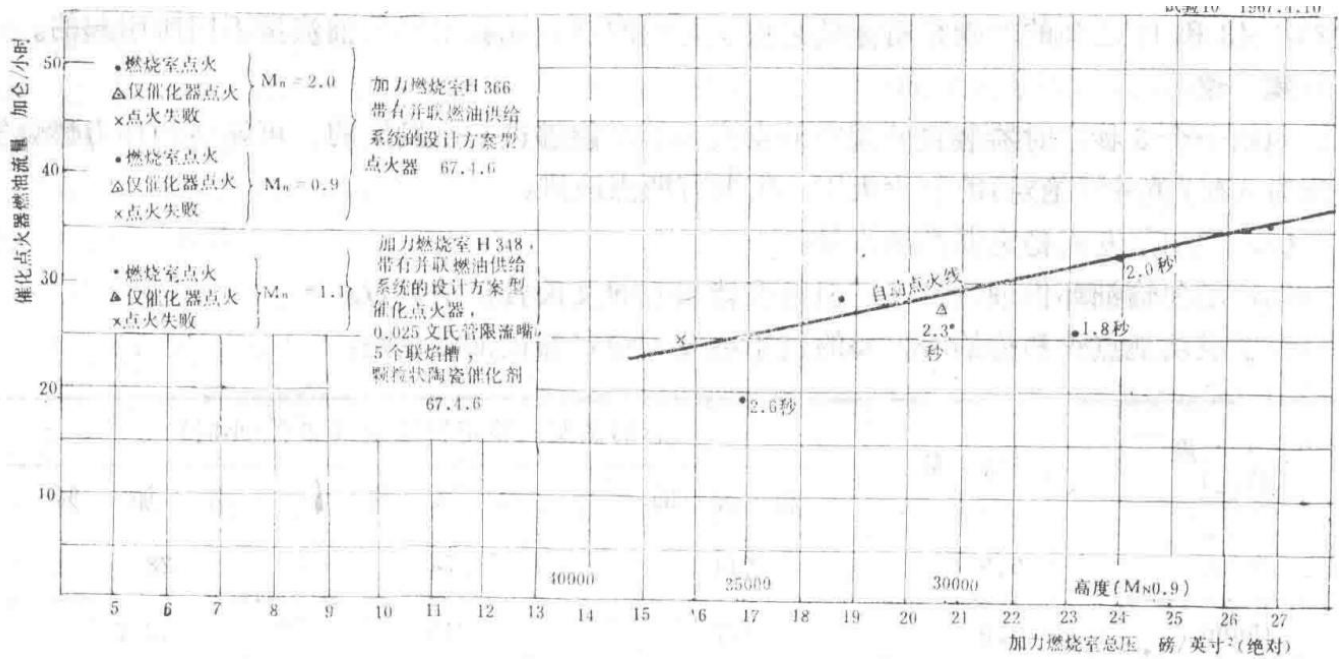


Figure RHD1007: Ignition Test of Centrally Mounted Catalytic Igniter in Afterburner (Engine: 41, Afterburner: H368 and H348)

Test 12(i), April 22, 1967, 36,000 feet, Mach 0.9, P<sub>s</sub> = 16.5 psia.

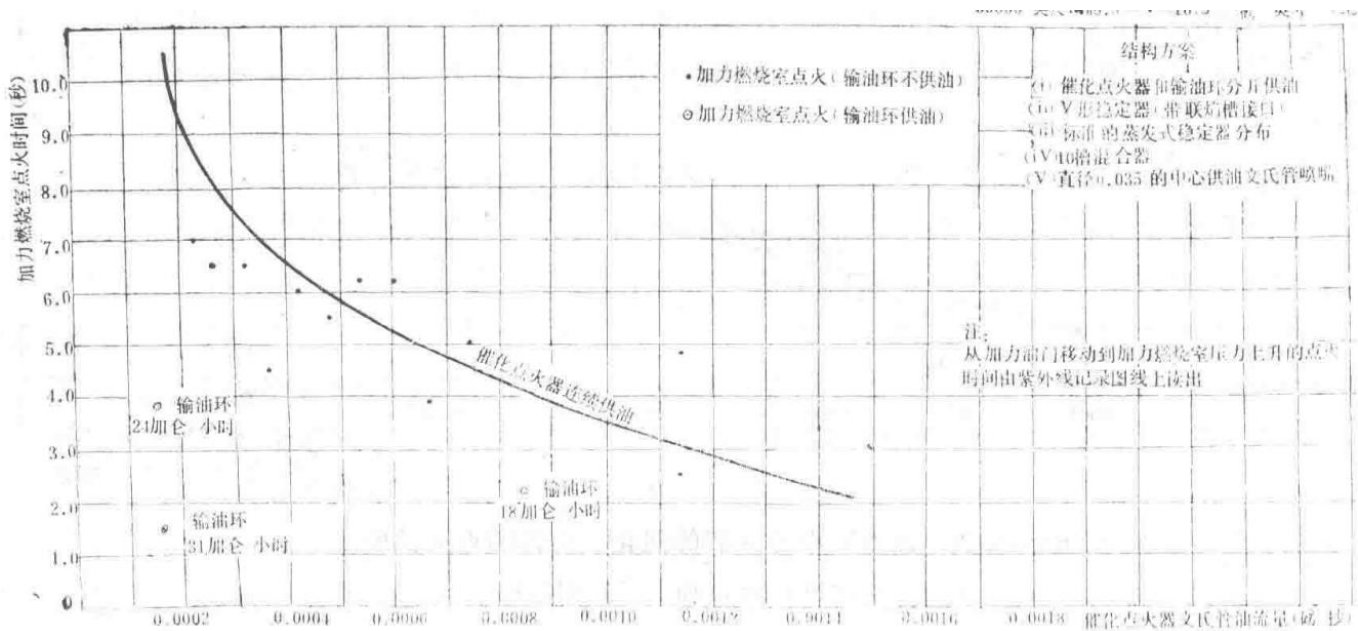


Figure RHD1027: Afterburner Ignition Test (Engine: 20006, Afterburner: H348)

Test data for afterburner ignition performance.

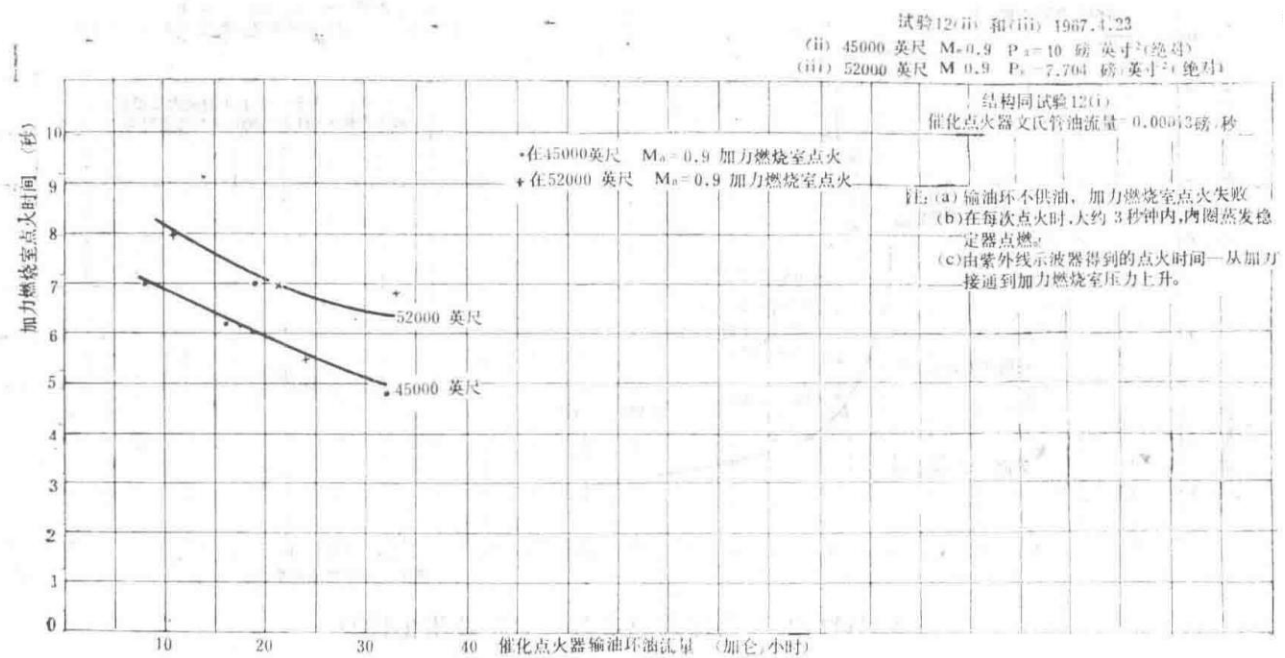


Figure RHD1028: Afterburner Ignition Test (Engine: 20006, Afterburner: H348)

Test data for afterburner ignition performance.

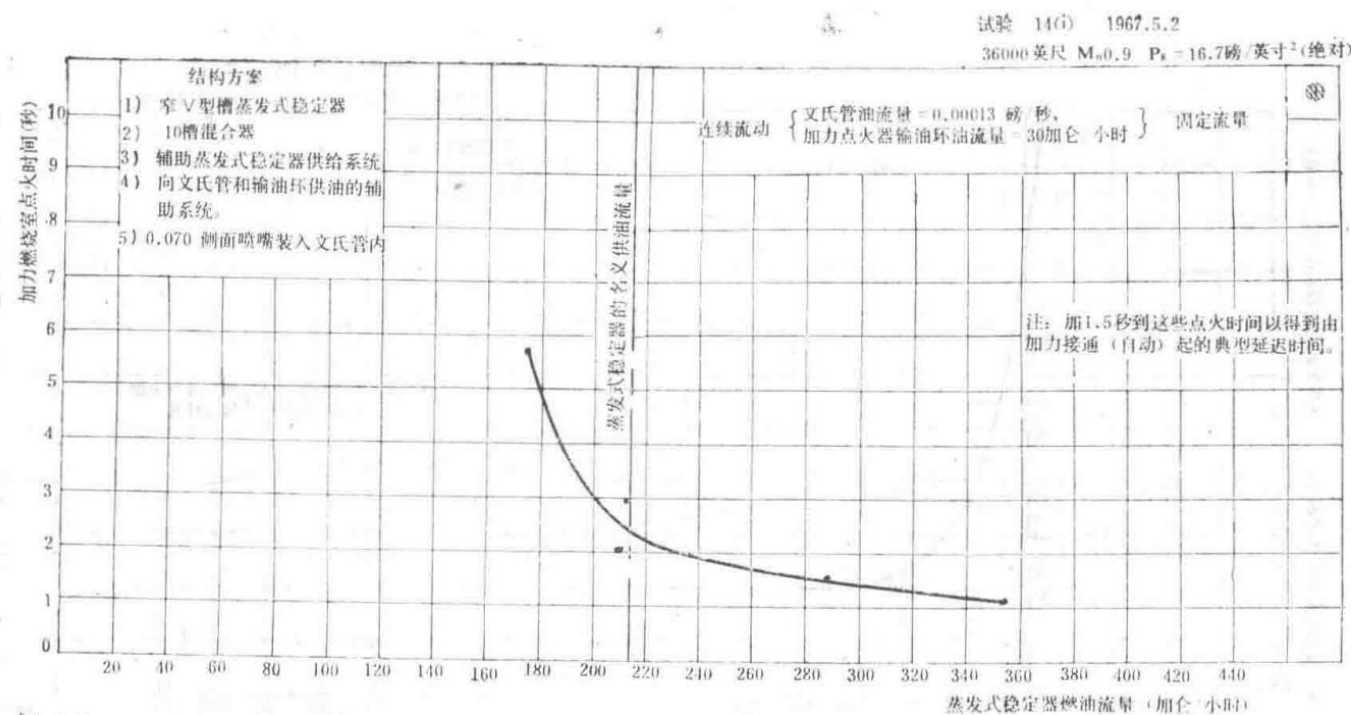


Figure RHD1024: Optimization Test of Vaporizer Stabilizer Fuel Supply

Test data for optimizing vaporizer stabilizer fuel flow rates.

— Section 21 —  
Content from Original Document (Pages 101-105)

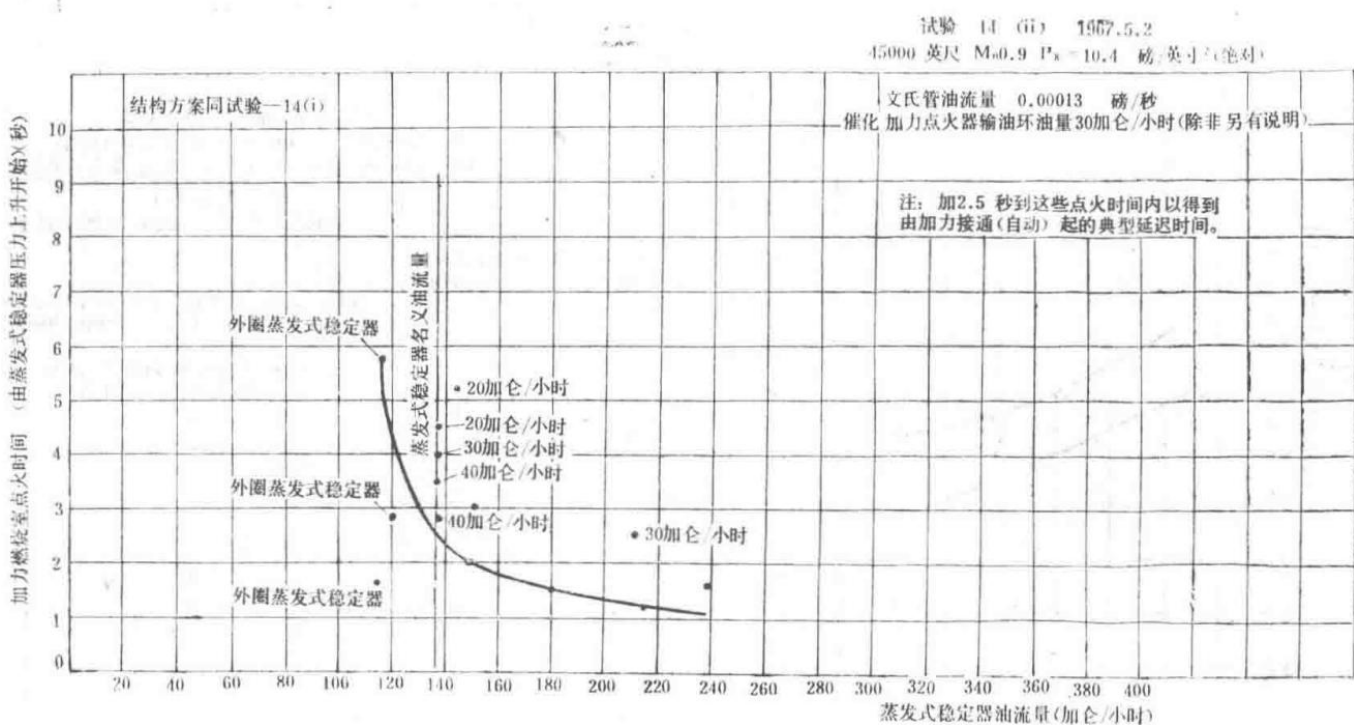


Figure RHD1025 Optimization Test of Evaporative Stabilizer Fuel Supply

Test results for optimizing the fuel supply to the evaporative stabilizer on engine 20006 with afterburner H348.

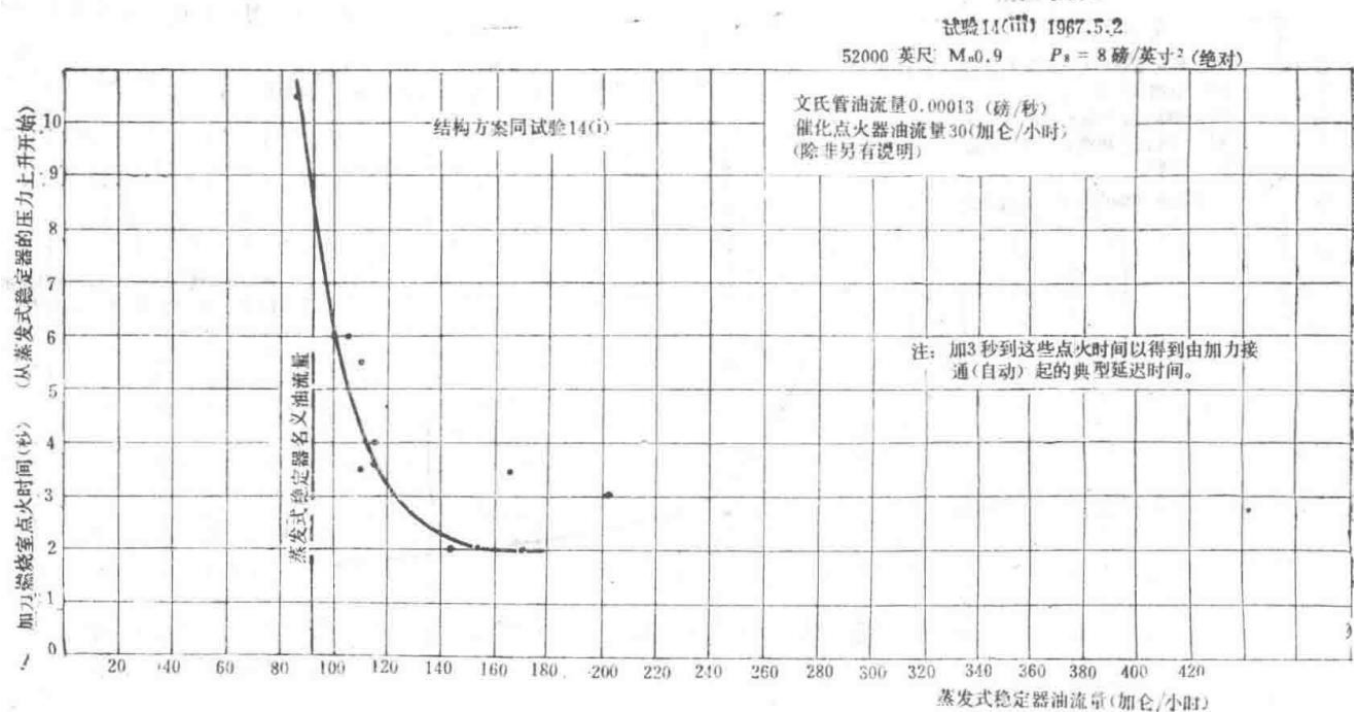


Figure RHD1026 Optimization Test of Evaporative Stabilizer Fuel Supply

Additional test results for optimizing the fuel supply to the evaporative stabilizer.

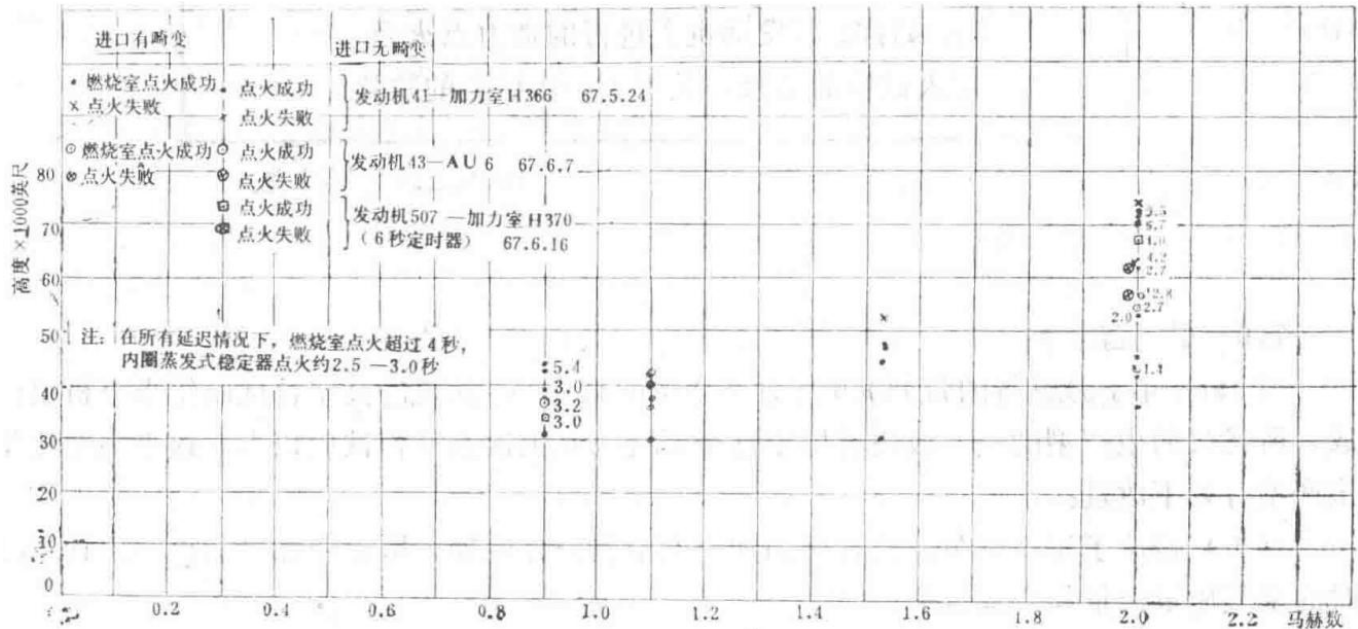
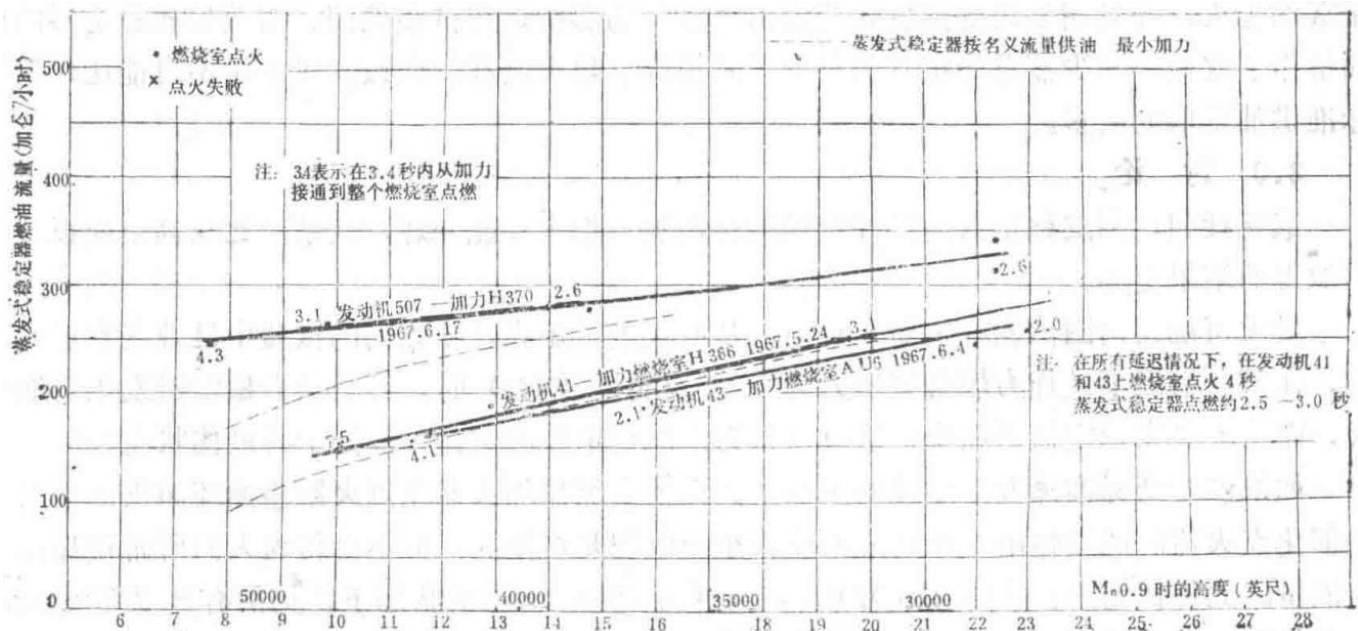


Figure RHD1023 High-Altitude Test Bench Afterburner Ignition Test

High-altitude test bench results for afterburner ignition using an early-type engine.



Fuel supply characteristics of the evaporative stabilizer under minimum afterburner conditions.

First Edition, February 1, 1968

Development Technical Report	DTR86052
Results of afterburner ignition and flameout tests conducted on engines 41/51, recommendations for the next phase of testing	

## 1.0 Introduction

The analysis of high-altitude test bench results from the 41 engine with the H366 afterburner, conducted in January 1968, has been completed. Several recommended improvements for the production version have been applied to this system. Since the last high-altitude test, this system has seen the following improvements compared to earlier production models:

1. Modified the pressure ratio regulator needle valve and the afterburner regulator splitter to increase engine air mass flow and fuel flow at Mach number (Mn) 2.0.
2. Increased the fuel supply to the evaporative stabilizer at high altitudes, approximately by 90% at 50,000 feet and Mn 0.9.
3. Redirected 2.8% of the total main afterburner fuel to the inner fuel manifold, as used in earlier production models.

## 2.0 Results

1. The afterburner ignition altitude increased by approximately 9,000 feet compared to earlier production models, reaching about 47,500 feet at Mn 0.9. In this test, 47,500 feet was the flameout altitude. As previously reported, the fuel-filling time of the catalytic igniter at such altitudes is a critical factor.
2. Compared to earlier production models, the afterburner flameout characteristics worsened by approximately 8,000 feet. Observations indicate this is a rich-oil flameout, significantly influenced by the fuel supply to the evaporative stabilizer. During testing, adjustments were made to the evaporative stabilizer fuel supply; reducing the fuel supply increased the flameout altitude, but the fuel supply could not be reduced significantly below the recommended standard.

## 3.0 Discussion

There is no doubt that increasing the fuel supply to the evaporative stabilizer worsens the afterburner flameout performance, with results being worse than those obtained on high-altitude simulation devices.

The most likely reason is that the inner ring evaporative stabilizer is too fuel-rich, promoting flameout. Visual observations from previous tests indicate that in some cases, when the afterburner combustion chamber pressure is 5 psi (absolute), other evaporative stabilizers experience lean-oil flameout while the inner ring stabilizer continues to burn. This suggests that the inner ring stabilizer load is likely at its optimal condition.

If reverting to the standard evaporative stabilizer fuel supply, it would be necessary to increase the fuel supply to the catalytic igniter's fuel ring to boost the catalytic igniter's energy output. Minor improvements in this area are possible but will not provide the desired energy levels. Additionally, at conditions exceeding the predicted Mn 0.9 and altitude of 48,000 feet, there remains the issue of fuel-filling delay in the evaporative stabilizer. The fuel system department is currently investigating the fuel-filling delay problem.

Two scenarios are considered:

- A(1) Restore the predefined fuel supply to each ring of the evaporative stabilizer as in the early production model. (2) Improve the catalytic ignition device to increase output energy and enhance fuel-filling of the catalytic igniter. (3) Improve the fuel-filling delay of the evaporative stabilizer.
- B(1) Maintain the increased fuel supply to the evaporative stabilizer but cut off fuel to the inner ring evaporative stabilizer. (2) Implement improvements to the catalytic ignition device as in A(2). (3) Eliminate the fuel-filling issue of the evaporative stabilizer at high altitudes.

From the perspective of afterburner ignition, increasing the fuel supply to the evaporative stabilizer remains highly advantageous. Tests on engine 41 demonstrated this, with all ignitions propagating instantaneously before reaching the flameout condition. It is crucial to determine a system compatible with production improvements and conduct further high-altitude test bench trials.

## 4.0 Recommended High-Altitude Test Bench Trials

- A(1) Adopt the new pressure ratio regulator needle valve and afterburner regulator splitter. (2) Implement the mentioned improvements to the catalytic igniter, combined with any measures to improve the fuel-filling delay of the evaporative stabilizer. (3) Verify performance, flameout, and ignition characteristics.
- B(1) Use the aforementioned changes to the evaporative stabilizer fuel distribution and supply fuel to the evaporative stabilizer via an auxiliary pump. (2) Retain improvements to the catalytic igniter. (3) Adjust the evaporative stabilizer fuel supply and verify flameout and ignition.

## Development Technical Report

Summary of afterburner ignition and flameout tests conducted on engine 20003 with H366T afterburner in the high-altitude test bench.

### 1.0 Introduction

#### 1.1

In February 1968, engine 20003 equipped with the H366T afterburner underwent afterburner ignition and flameout tests on the high-altitude test bench. The tests aimed to evaluate the effectiveness of improvements to the catalytic igniter and the evaporative stabilizer fuel supply system.

#### 1.2

Three standards of afterburner combustion chambers were tested:

1. Early production type.
2. Early production type but with a catalytic igniter system featuring increased fuel supply.
3. Early production type but with improved catalytic igniter, increased fuel flow, and distribution to the evaporative stabilizer.

### 2.0 Conclusions

1. During testing of the early production type on engine 20003 with the H366T afterburner, the combustion chamber ignition altitude reached 46,500 feet at Mn 1.1. Additionally, using AVCAT fuel at Mn 0.52, the ignition altitude reached 38,500 feet.
2. Improving the catalytic igniter enhanced the combustion chamber ignition boundary, reaching 50,500 feet at Mn 1.1 and 65,500 feet at Mn 2.0. The latter corresponds to an afterburner combustion chamber pressure of 8 psi (absolute). At these altitudes, ignition time remained long due to poor flame propagation in the evaporative stabilizer.
3. Increasing the evaporative stabilizer fuel supply by 60 gallons/hour resulted in nearly instantaneous flame propagation within the combustion chamber.
4. These results further confirm the necessity of the two improvement measures for enhancing afterburner ignition as outlined in report DTR86020: increasing the fuel supply to the catalytic igniter's fuel ring to boost output energy and increasing the fuel supply to the evaporative stabilizer to accelerate flame propagation in the combustion chamber.
5. Based on these tests, there is sufficient evidence to conclude that under high-altitude conditions, poor flame propagation in the combustion chamber with the early production type evaporative stabilizer fuel supply is determined by the fuel-filling characteristics of the evaporative stabilizer.
6. As mentioned in report DTR86052, modifying the fuel distribution of the evaporative stabilizer can increase its fuel supply without deteriorating afterburner flameout performance.
7. As confirmed by tests on engine 20003, the early production type afterburner flameout at Mn 0.9 occurred at 50,000 feet with an afterburner combustion chamber pressure of 7.2 psi (absolute). During tests on engine 43 last June, flameout occurred at a pressure of 5 psi (absolute), corresponding to Mn 0.9 and an

altitude of 55,000 feet. This performance degradation is attributed to the reintroduction of fuel into the inner fuel manifold.

8. Recommendations for the next high-altitude test bench trial include: (1) Improve the afterburner regulator to increase the evaporative stabilizer fuel supply by 60 gallons/hour across the entire operating range. (2) Adjust the distribution of the evaporative stabilizer fuel supply under a total test bench flow number of 32. (3) Improve the catalytic ignition system based on current high-altitude test bench results.

## 3.0 Improvements

### 3.1

Improvements to the catalytic igniter include:

1. Increasing the fuel supply to the fuel ring (catalytic igniter fuel ring orifice diameter: 0.046 inches).
2. Replacing the simple 0.025-inch restrictor in the venturi fuel line with an attenuator.
3. Increasing the restrictor diameter in the main fuel line to 0.04 inches.
4. Reducing the opening pressure of the check valve from 200 psi to 120 psi to increase the fuel supply to the catalytic igniter at high altitudes.

### 3.2

The third part of the test involved modifying the fuel distribution to the evaporative stabilizer to reduce the load on the inner ring evaporative stabilizer.

### 3.3

For automatic ignition, the fuel supply to the evaporative stabilizer was increased by 40 gallons/hour. During ignition with the auxiliary fuel supply system, the fuel supply could vary between the early production standard value and the early production standard value plus 100 gallons/hour.

## 4.0 Tests and Results

### 4.1

The test sequence was as follows:

1. Ignition tests of the early production type using AVTUR fuel at Mn 1.1.
2. Ignition and flameout tests of the early production type using AVCAT fuel at Mn 0.52.
3. Ignition and flameout tests at Mn 1.1 using AVTUR fuel and an improved catalytic ignition system.
4. Ignition and flameout tests at Mn 2.0 under the same conditions as (3).
5. Flameout and auxiliary fuel supply ignition tests at Mn 1.1 and 2.0 using AVTUR fuel, with modified evaporative stabilizer fuel distribution and fuel supplied through an auxiliary fuel system.
6. Final automatic ignition tests at Mn 1.1 using all improvements from item (5).

### 4.2

Figures 1 to 5 illustrate the automatic ignition scenarios. Figures 6 to 8 show the relationship between altitude, Mach number, and ignition time. The results of flameout optimization tests with varying evaporative stabilizer fuel supplies are shown in Figure 9. Figure 10 depicts the variation of evaporative stabilizer fuel supply with Mach number. Figure 11 illustrates the effect of automatic afterburner engagement and the establishment of evaporative stabilizer fuel supply on ignition time.

## 5.0 Observations

### 5.1

Analysis of dynamic curves recorded by the ultraviolet recorder during automatic ignition indicates three types of pressure rise patterns in the afterburner combustion chamber pressure oscillogram: single-stage, two-stage, and three-stage pressure rise patterns.

### 5.2

The three-stage pattern shown in Figure 1 is limited to automatic ignition in early production models. This suggests that...

— Section 22 —  
Content from Original Document (Pages 106-110)

When the fuel supply to the evaporative stabilizer is low, the flame propagation time is longer. Figure 1 also shows that after the catalytic igniter ignites, the inner ring ignites first, followed by full ignition.

### 5.3 Improvement of Catalytic Igniter

The improvement of the catalytic igniter has made ignition a two-stage process. However, at higher altitudes, the flame propagation time does not significantly shorten.

### 5.4 Effect of Increased Evaporative Stabilizer Fuel Supply

When the fuel supply to the evaporative stabilizer is increased, both single-stage and two-stage ignition occur. However, in the two-stage ignition mode, the flame propagation time is significantly reduced. In all cases, full ignition occurs immediately after the initial ignition.

### 5.5 Ignition Performance at Low Afterburner Pressures

At lower afterburner pressures, specifically below 15 psi (absolute), the ignition time of the catalytic igniter increases rapidly, regardless of improvements to the igniter. The high-altitude ignition capability of the catalytic igniter is limited by the timer.

### 5.6 Flameout Optimization Test at Mach 2

A flameout optimization test was conducted at Mach 2 using an improved fuel distribution scheme for the evaporative stabilizer (see Figure 9). The test results showed that, compared to the baseline flameout data at  $P_s = 7.2$ , the highest flameout altitude occurred when the evaporative stabilizer fuel supply was increased by 60 gallons/hour over the early production model, at  $P_s = 7.0$ .

$P_s = 7.2$

Baseline pressure for flameout comparison

$P_s = 7.0$

Pressure at which highest flameout altitude was observed with increased fuel supply

## 6.0 Discussion

### 6.1 Relationship Between Afterburner Pressure and Ignition Time

Figures 1 to 5 show that as the afterburner pressure decreases, the ignition time of the catalytic igniter increases significantly. This cannot be attributed solely to increased fuel filling time but appears to be related to the activation capability of the catalyst and afterburner pressure, or issues with fuel preparation.

#### 6.1.1 Catalyst Activation Capability

Regarding the catalyst activation capability, Btn, AEP, and other laboratory personnel attempted to derive a theoretical relationship between pressure and catalytic rate from test results, but no conclusive results were obtained. Only qualitative observations could be made, indicating that flame propagation on the catalyst surface deteriorates as pressure decreases.

## 6.1.2 Optimization of Fuel Preparation and Catalytic Igniter Fuel Supply

A series of tests were conducted on the combustion test rig to optimize fuel preparation and the fuel supply to the catalytic ignition system. These tests involved varying the size of the restrictor orifices, fuel types, and fuel ring dimensions.

## 6.2 Measurement of Evaporative Stabilizer Fuel Flow

A fuel flow meter for the evaporative stabilizer was installed on the engine and afterburner, enabling precise flow measurements. It confirmed that at a given afterburner pressure, different Mach numbers result in different fuel supply rates to the evaporative stabilizer. The variation is shown in Figure 10. At Mach 2.0, the fuel supply increases significantly, which positively impacts ignition at this Mach number. In terms of flame propagation during afterburner ignition, the nominal fuel supply adjustment of the early production afterburner is critical. This explains the inconsistency in previous high-altitude afterburner ignition test results, where better results were consistently obtained at Mach 2.0. Since the reserve engines operate at  $P_1$  below 5 psi (absolute), ignition tests were previously conducted at Mach 2.0.

$P_1$   
Pressure parameter for engine operation

## 6.3 Flame Propagation and Internal Fuel Filling of the Evaporative Stabilizer

It is evident that the flame propagation issue in the combustion chamber is related to the internal fuel filling of the evaporative stabilizer, based on two observations:

- The final part of the tests on Engine No. 20003 and Afterburner No. H366T was conducted using an auxiliary fuel supply system for the evaporative stabilizer, with results shown in Figure 11. It was noted that when the fuel supply to the evaporative stabilizer was fully established before afterburner activation, flame propagation was instantaneous and independent of the fuel supply rate to the evaporative stabilizer.
- Tests were conducted on a heated test rig with water injection at Hucknall. The results showed that flameout occurred within seconds after boiling in the restrictor of the evaporative stabilizer with a fixed flow rate. The fuel supplied to the evaporative stabilizer during the test was AVTUR and AVTAG.

## 6.4 Results of Increased Evaporative Stabilizer Fuel Supply

The results of tests with increased fuel supply to the evaporative stabilizer indicate that previous tests, using the early production model's predetermined fuel supply rates for each ring of the evaporative stabilizer, were too low for high-altitude afterburner ignition (see reports DTR86020 and DTR86052). An increase in the fuel supply to the evaporative stabilizer should be implemented, especially if this improves fuel filling. If no modifications are planned to fully open the evaporative stabilizer rotary valve, this increase is essential.

## 6.5 High-Altitude Test Results with Increased Fuel Supply

During high-altitude tests in January 1968 using Engine No. 41 and Afterburner No. H366, the fuel supply to the evaporative stabilizer was doubled at high altitudes while maintaining the original distribution ratio. Despite good flame propagation during afterburner ignition, the combustion chamber experienced flameout at a pressure of 8.5 psi (absolute). In contrast, during high-altitude tests in July 1967 using Engine No. 43 and Afterburner No. AU6, flameout occurred at 5 psi (absolute).

After the tests on Engine No. 41, it was decided to maintain the early production fuel supply rate for the inner ring of the evaporative stabilizer while increasing the fuel supply to the middle and outer rings to achieve a more

uniform load on each stabilizer (see report DTR86052). The table below lists the fuel supply load per inch of circumference for various evaporative stabilizer models.

Fuel Supply Load per Inch of Circumference for Different Evaporative Stabilizer Models

Configuration	Increased Fuel Supply at High Altitude	Inner Ring Stabilizer (gal/in)	Middle Ring Stabilizer (gal/in)	Outer Ring Stabilizer (gal/in)	Flameout Condition
Original Design		0.169	0.178	0.175	At $P_8 = 5.5$ psi (absolute), the inner ring experiences lean flameout first.
Early Production Model 43/10, July 1967		0.295	0.158	0.155	At $P_8 = 5$ psi (absolute), the middle and outer rings experience lean flameout first.
Early Production Model 20003/6, February 1968		0.295	0.158	0.155	At $P_8 = 7.2$ psi (absolute), all stabilizers experience flameout.
Proposed Improved Model 41/15, January 1968	100%	0.590	0.316	0.310	At $P_8 = 8.5$ psi (absolute), all stabilizers experience rich flameout.
Improved Fuel Distribution 20003/6, February 1968	60%	0.309	0.244	0.241	At $P_8 = 7.0$ psi (absolute), all stabilizers experience flameout.

## 6.6 Analysis of Flameout Pressure Variation

From the table above, it can be seen that for Engine No. 20003/6 as an early production model, the flameout pressure of the combustion chamber worsened, with flameout occurring at 7.2 psi (absolute) compared to 5 psi (absolute) in the previous year's test on Engine No. 43. This may be due to the resupply of the inner fuel ring. It is reasonable to consider the influence of fuel concentration at the center of the combustion chamber and to avoid burning the stabilizer of the catalytic igniter by directing the spray toward the edge of the inner ring evaporative stabilizer. If the afterburner can be ignited at high altitudes using a larger fuel supply from the catalytic igniter fuel ring, it could reduce the load on the inner ring evaporative stabilizer and further compensate for the fuel supply to the inner fuel ring. The effect of the inner fuel ring's fuel supply on flameout will be verified in future high-altitude test rig trials.

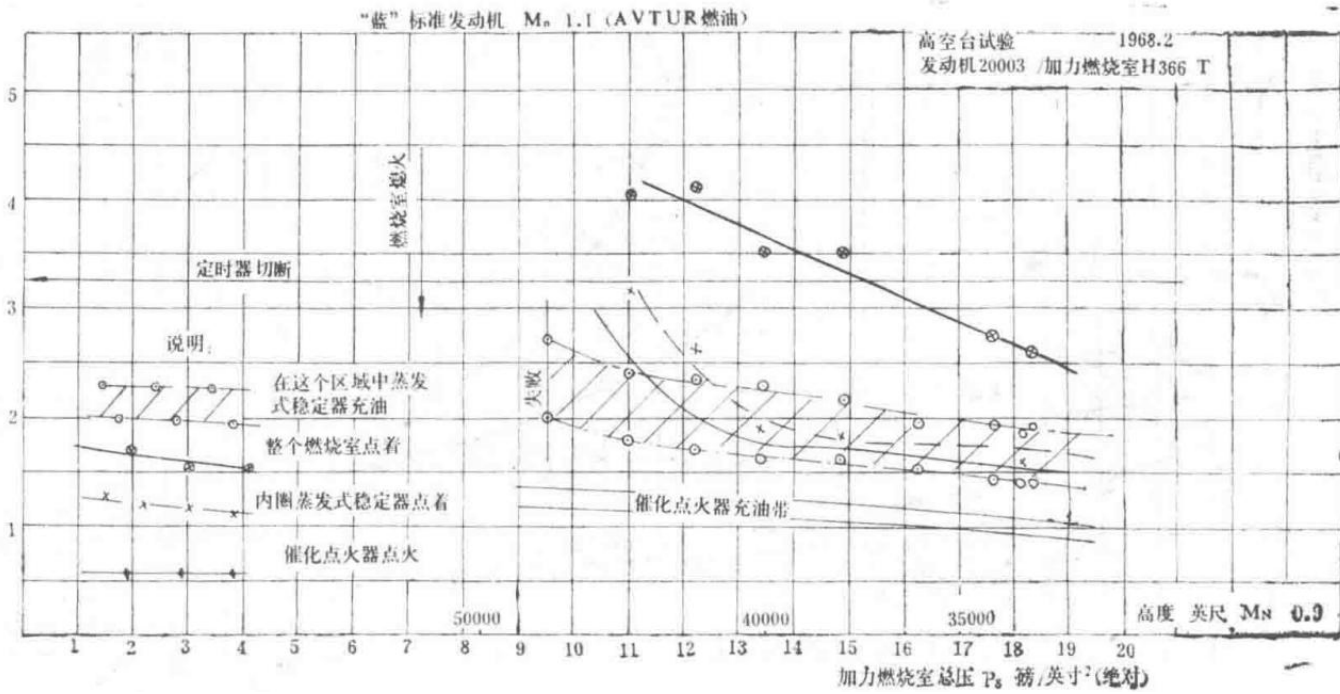


Figure 1: Afterburner Ignition Test Conducted on High-Altitude Test Rig

Graphical representation of afterburner ignition test results at various conditions.

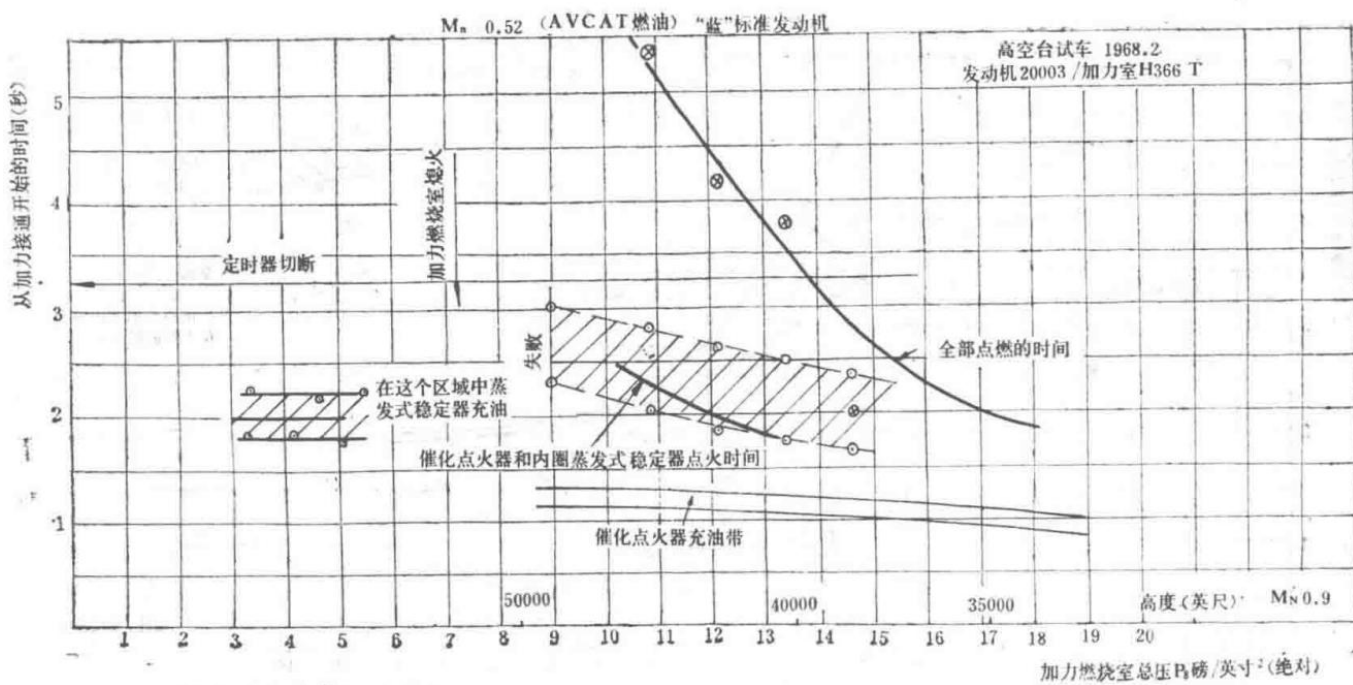


Figure 2: Afterburner Ignition Test Conducted on High-Altitude Test Rig

Graphical representation of afterburner ignition test results at various conditions.

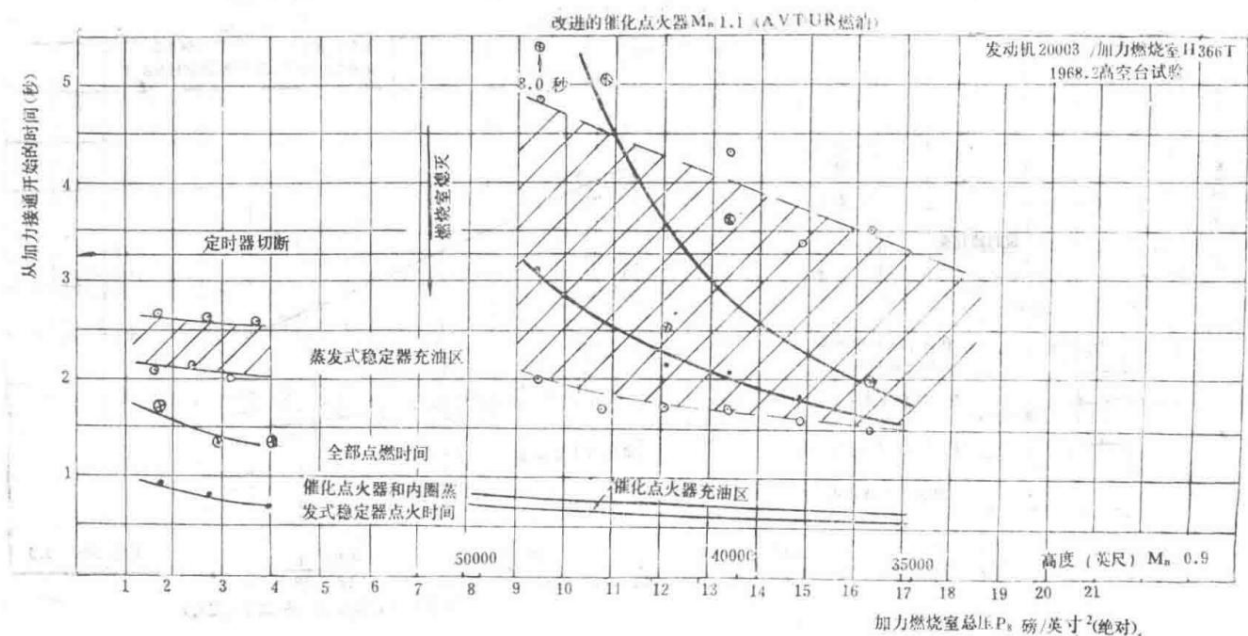


Figure 3: Afterburner Ignition Test Conducted on High-Altitude Test Rig

Graph showing flameout boundaries and ignition performance under different fuel supply conditions.

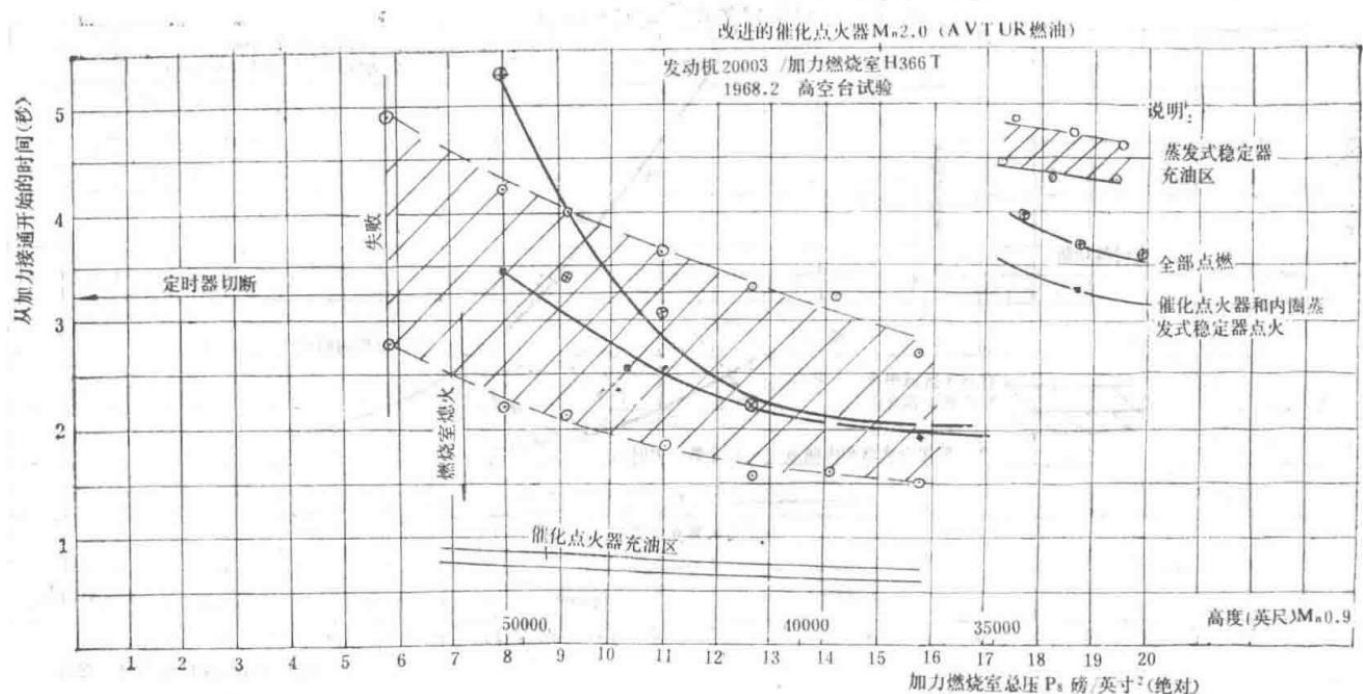


Figure 4: Afterburner Ignition Test Conducted on High-Altitude Test Rig

Graphical representation of ignition performance with varying fuel supply and altitude conditions.

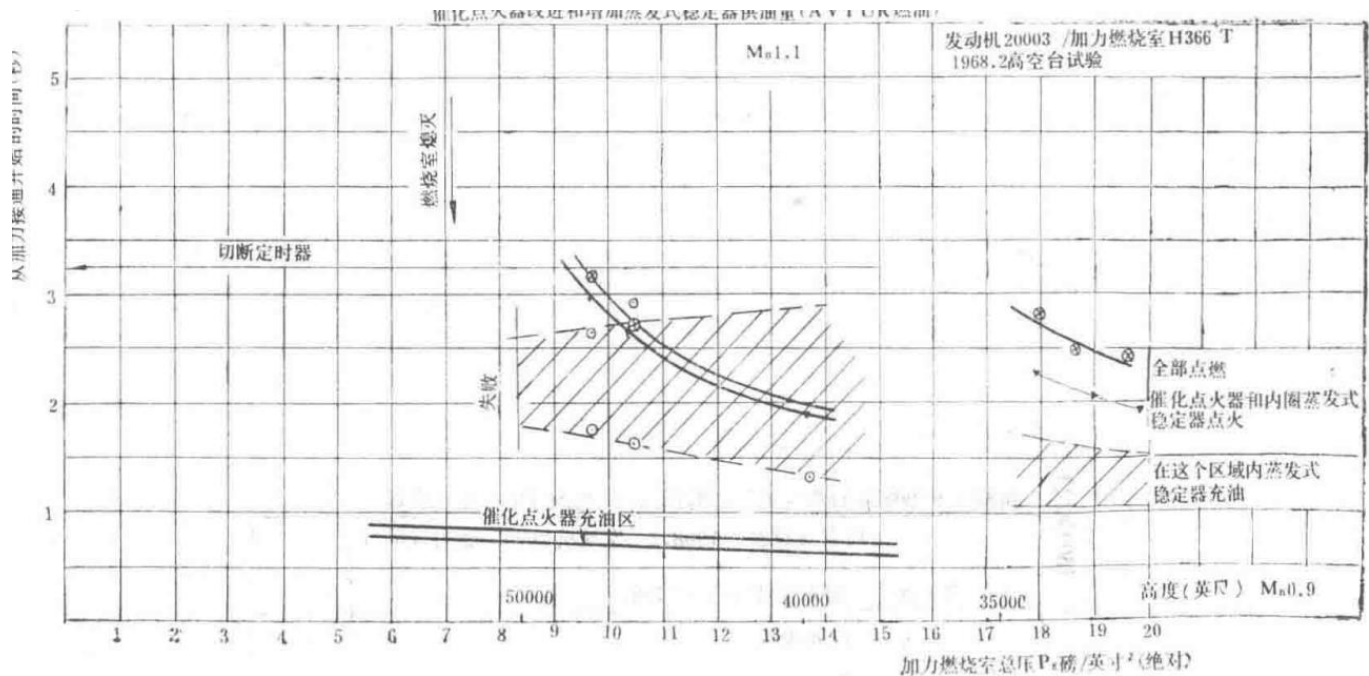


Figure 5: Afterburner Ignition Test Conducted on High-Altitude Test Rig

Graph showing the relationship between afterburner pressure and ignition time.

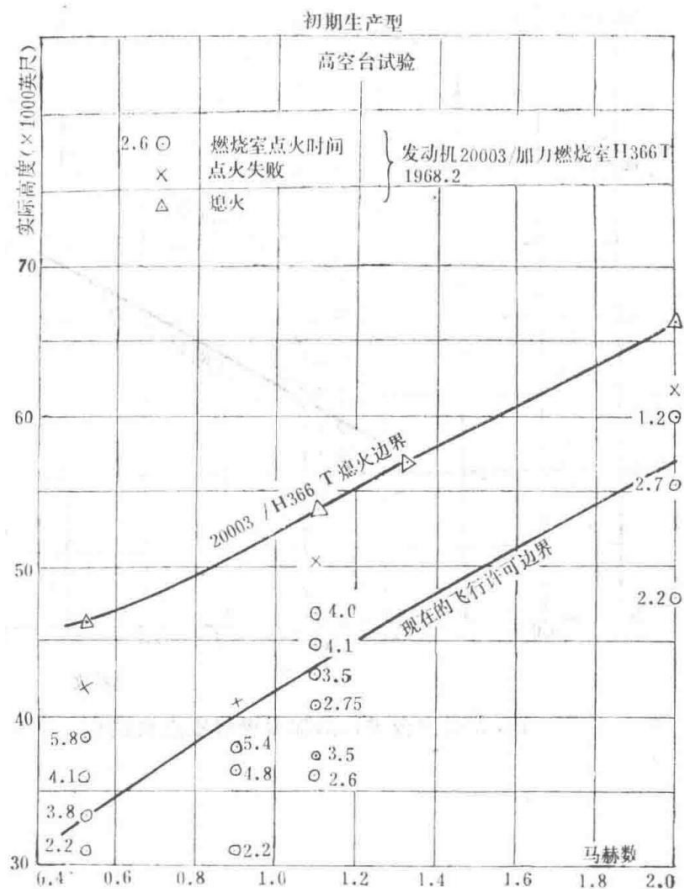


Figure 6: Afterburner Ignition Test Conducted on High-Altitude Test Rig

Graphical representation of flame propagation and ignition performance under different test conditions.

— Section 23 —  
Content from Original Document (Pages 111-115)

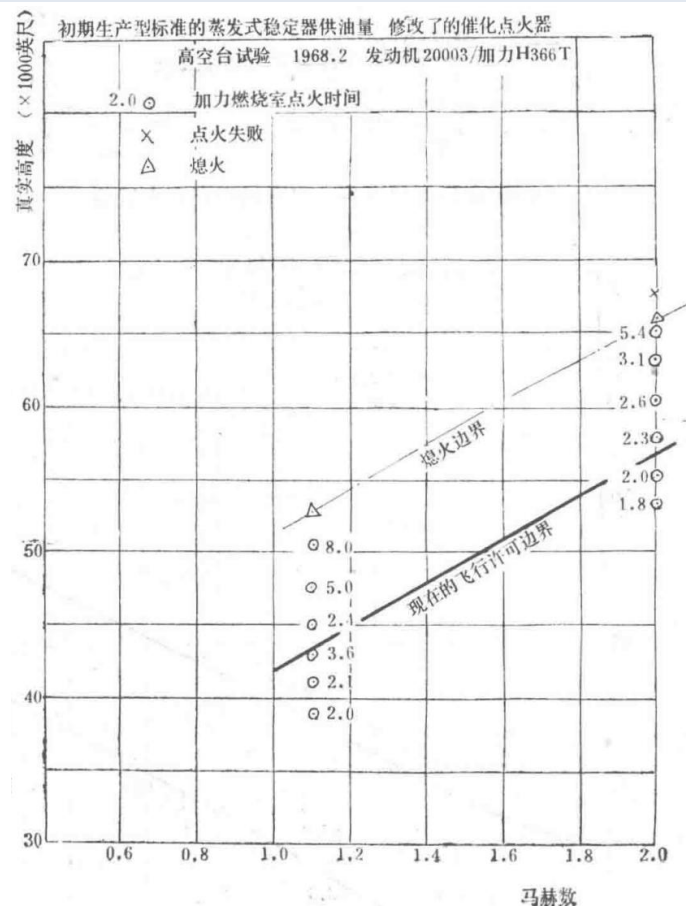
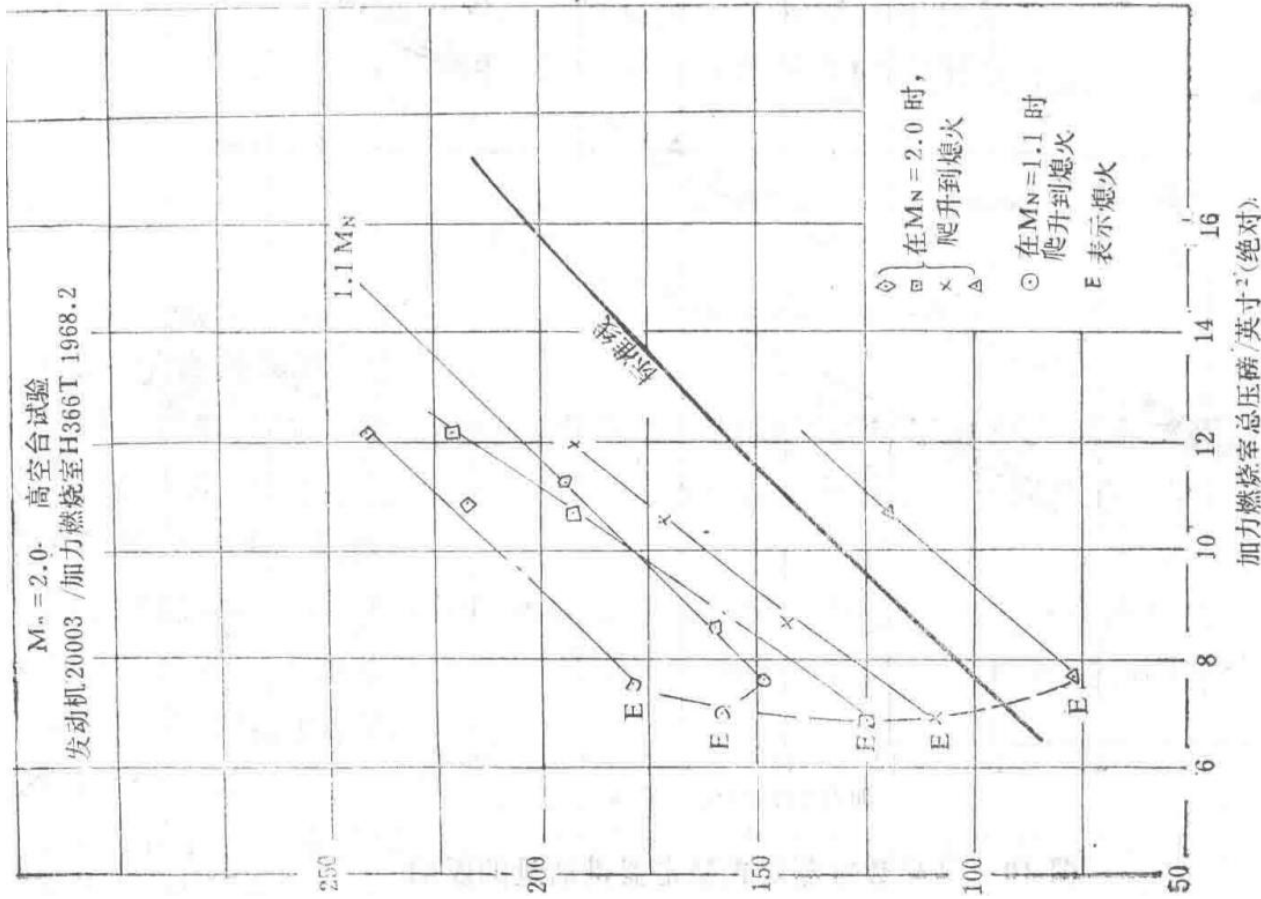


Figure 7: Afterburner ignition test conducted on the high-altitude test bed

Image showing the setup and results of afterburner ignition testing for the Spey MK202 engine on a high-altitude test rig.



Technical component or apparatus related to the Spey MK202 engine testing.



Additional technical diagram or component image.

图 8 在高空台进行的加力燃烧室点火试验  
图 8 加力燃烧室总压磅/英寸<sup>2</sup>(绝对)

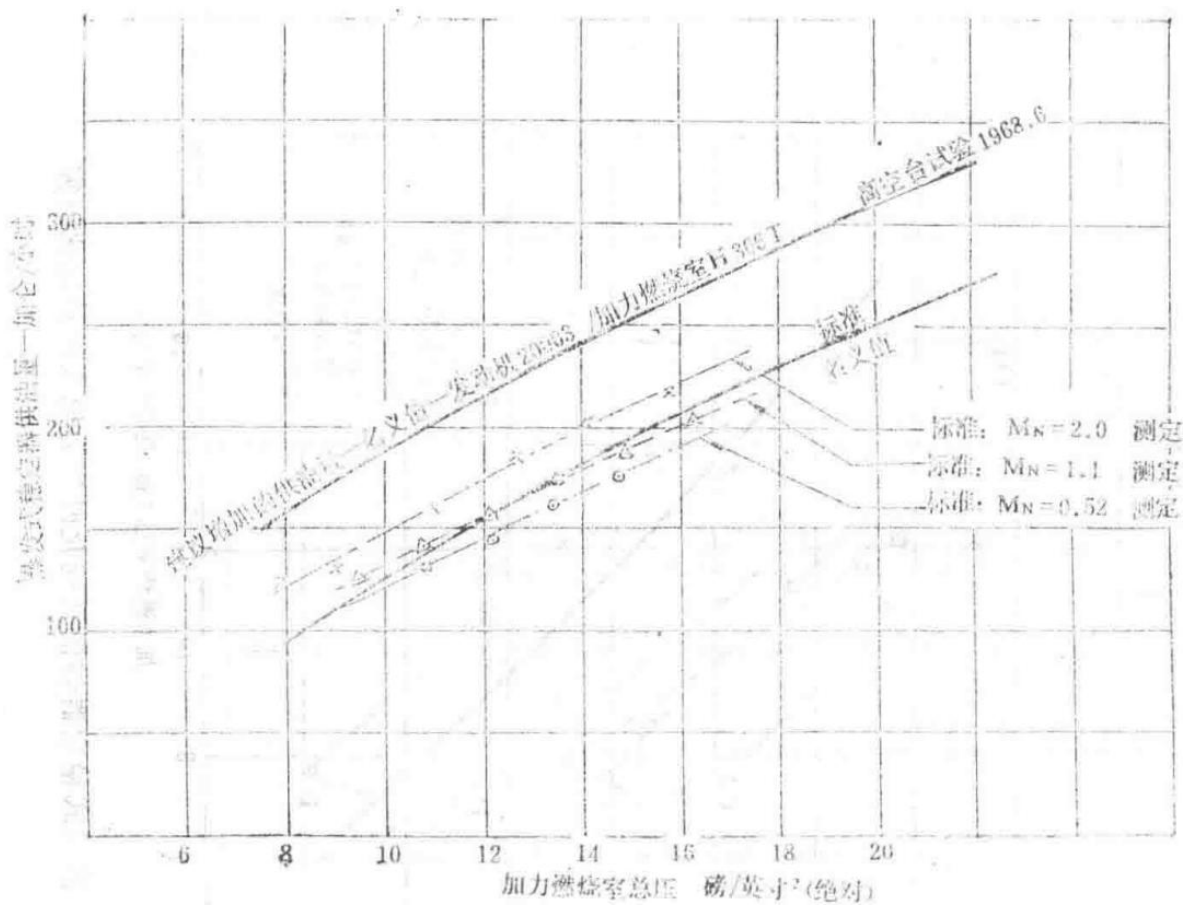


Figure 10: Effect of Mach number on fuel supply for the vaporizing stabilizer

Graph depicting how Mach number influences the fuel supply quantity for the vaporizing stabilizer in the Spey MK202 engine.

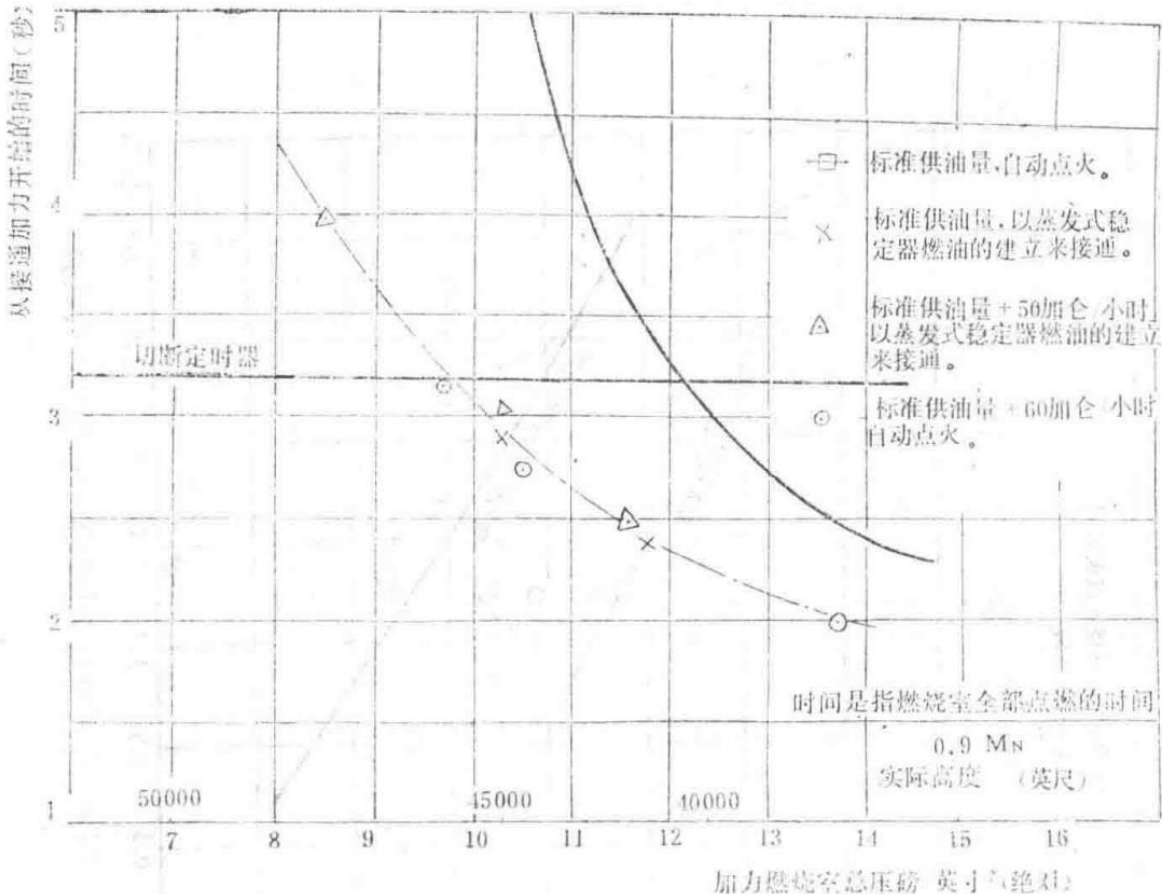


Figure 11: Comparison of afterburner ignition with and without fuel supply established for the vaporizing stabilizer

Graph comparing the performance of afterburner ignition when initiated simultaneously with vaporizing stabilizer fuel supply versus after fuel supply establishment.

#### Performance Technical Report

Performance Technical Report	PTR12257
H346 Afterburner Chamber Test Results and Discussion on the Spey MK202 Simulator at the High-Altitude Test Bed	

## 1966.8.5 First Edition

### 1.0 Introduction and Summary

Prior to the afterburner tests, the simulator was calibrated using two auxiliary nozzles with throat diameters of 21.25 inches and 22.75 inches to simulate high and low working lines, respectively. The results of this calibration are presented in DTR12169, which established the 'adjusted' state of the afterburner test setup.

Climb-to-flameout tests were conducted using the standard combustion chamber, which featured a modified No. 3 fuel manifold with or without a fuel shield. Other variations included the number of fuel manifolds and the fuel distribution among them. This report presents the results of these afterburner tests.

### 2.0 Conclusions

- Reducing the pitch circle diameter of the outer spray bars on the No. 3 fuel manifold improved fuel distribution, enabling a higher afterburning ratio before encountering unstable combustion.

- Removing the fuel shield and relocating the No. 4 fuel manifold downstream to the edge of the heat shield reduced the afterburning ratio by approximately 2%, equivalent to the afterburning ratio for a given fuel flow with standard fuel distribution using three manifolds.
- Over-fueling with the No. 1, No. 2, and No. 3 fuel manifolds while reducing the fuel flow to the No. 4 manifold improved afterburning performance.
- During simulator testing, it is essential to ensure the reliable operation of the nozzle position indicator, as thrust measurement is unreliable and this is the only method to determine the afterburning ratio.

## 3.0 Discussion

### 3.1 Measurements

#### 3.1.1 Determination of Afterburning Ratio

PTR12169 discusses the calibration of the test setup without afterburning, noting that thrust measurements are insufficiently precise for determining the afterburning ratio. Figure 1 illustrates some afterburning ratio values derived from standard combustion chamber tests, highlighting the degree of scatter. Thus, the only method to obtain the afterburning ratio is through estimation, using the nozzle position indicator readings and the theoretical relationship between the afterburning ratio and the change in effective area from non-afterburning to afterburning states. In high-altitude test beds, engine thrust measurements are highly reliable. Based on experience with the Spey 37 engine, the afterburning ratio can be determined simultaneously by thrust and nozzle position indicators, with the latter method proving highly satisfactory. This lends greater reliability to using the nozzle position indicator method for determining the afterburning ratio in setup tests.

#### 3.1.2 Fuel Flow

Before testing, all turbine flowmeters used were carefully calibrated against an Avery-Hardoll (a positive displacement flowmeter brand) and were found to provide consistent measurements for individual manifolds when compared to the total flow measured simultaneously by both turbine flowmeters and the Avery-Hardoll. Thus, the fuel flow distribution was precisely known.

These flow rates are compared to the required flow rates in technical documents, as shown in Figures 3, 5, and 6.

#### 3.1.3 Pressure Measurements

During simulator calibration, the measured pressures were well plotted and proportional to  $P\Box$ , as expected. When afterburning, if the nozzle controller (microjet) functions correctly to restore the setup to the non-afterburning state, this relationship should remain consistent. During standard combustion chamber tests, until duct damage occurred, S14 /  $P\Box$  varied by +2.5% (see Figure 7), and S503 varied by +4.25% (equivalent to two-thirds of the high working line corresponding value). After duct repair, the low working line calibration showed a -0.25% change in the S503 -  $P$  relationship, as shown in Figure 8. This change in S503 is likely a calibration shift due to repositioning of the S503 probe mounting during duct repair, rather than a significant change in the afterburner chamber state. With sufficient data to verify that the setup was adjusted to the non-afterburning calibration state, the setup should have the correct inlet state for the afterburner chamber.

## 4.0 Results

The goal was to achieve maximum afterburning using four fuel manifolds on the standard combustion chamber, but unstable combustion was encountered. It was hypothesized that reducing the pitch circle diameter of the outer spray bar orifices on the No. 3 fuel manifold could improve lateral fuel distribution. Comparison with the unstable combustion boundary indicated an improvement in the stable combustion boundary, as shown in

Figures 4, 5, and 6. Removing the fuel shield slightly reduced the afterburning ratio (by approximately 2%) but improved high-altitude stability, allowing the afterburner chamber to operate stably at a total pressure drop of 2 psi lower, achieving the design total pressure of 5 psi for the afterburner chamber. This was compared to the standard fuel distribution using three manifolds. All subsequent tests were conducted without the fuel shield. It should be noted that after removing the fuel shield, the outer fuel manifold was moved downstream to the plane of the heat shield edge to prevent fuel from falling behind the shield.

Over-fueling the No. 1, No. 2, and No. 3 fuel manifolds by approximately 15% increased the afterburning ratio by about 5%. Further over-fueling tests with three manifolds were not conducted. However, it was found that using four manifolds, with the No. 1, No. 2, and No. 3 manifolds over-fueled by the same amount (~15%) and the No. 4 manifold with reduced flow to maintain the same total flow, increased the afterburning ratio by approximately 7% relative to the standard distribution. No optimization tests for fuel distribution were conducted.

## 5.0 Figures

Figures 1 through 8 present the results of various tests conducted with the H346 afterburner chamber paired with the MK202 simulator on the high-altitude test bed.

Appendix Tables A, B, C, D, E, and F summarize the test results, but are omitted here due to unclear original text (Publisher's Note).

Figure 8: Changes in High-Altitude Test Fuel Supply Pressure Afterburning Time (Legend)

Symbol	Condition
○	Afterburner ignition at the same time as fuel supply
×	Lean flameout
△	Rich flameout

$S_{14} / P\Box$

Ratio of pressure measurement S14 to inlet pressure  $P\Box$ .

$S_{503}$

Pressure measurement S503.

— Section 24 —  
Content from Original Document (Pages 116-120)

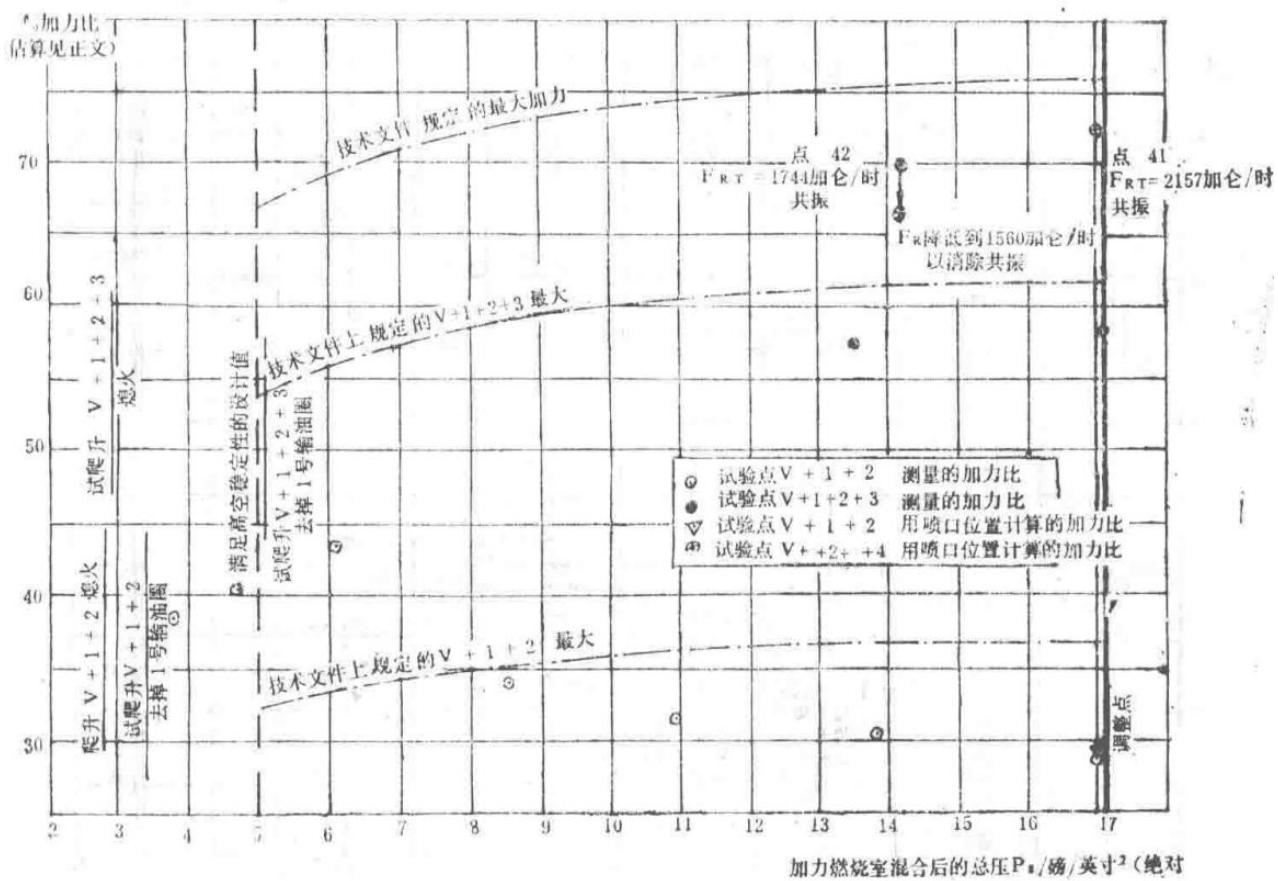


Figure 1 Relationship Between Augmentation Ratio and Mixed Total Pressure in Afterburner (Standard Afterburner)

Graph showing how the augmentation ratio varies with the mixed total pressure in the standard afterburner of the Spey MK202 engine.

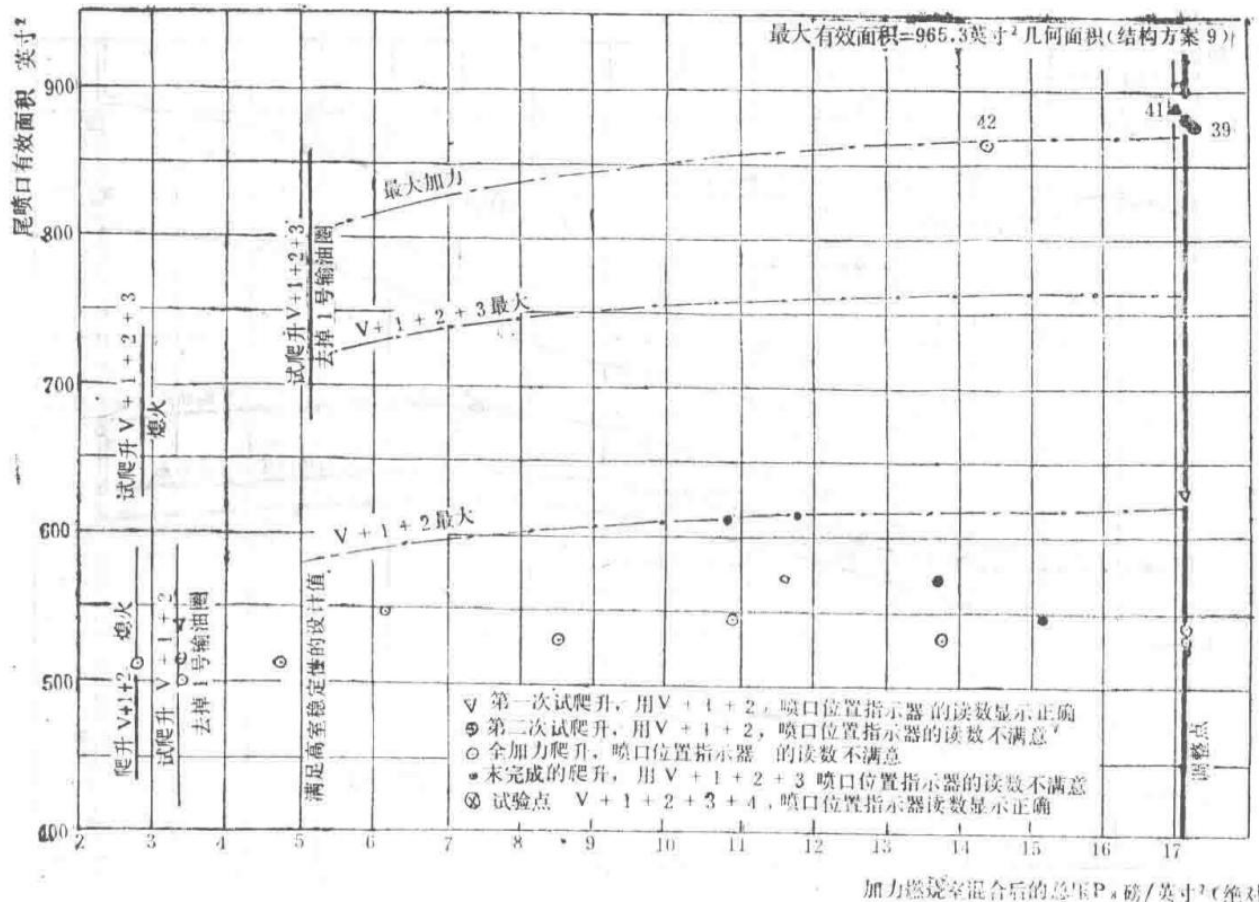


Figure 2 Relationship Between Nozzle Area and Mixed Total Pressure in Afterburner (Standard Afterburner)

Graph depicting the relationship between the tail nozzle area and the mixed total pressure in the standard afterburner.

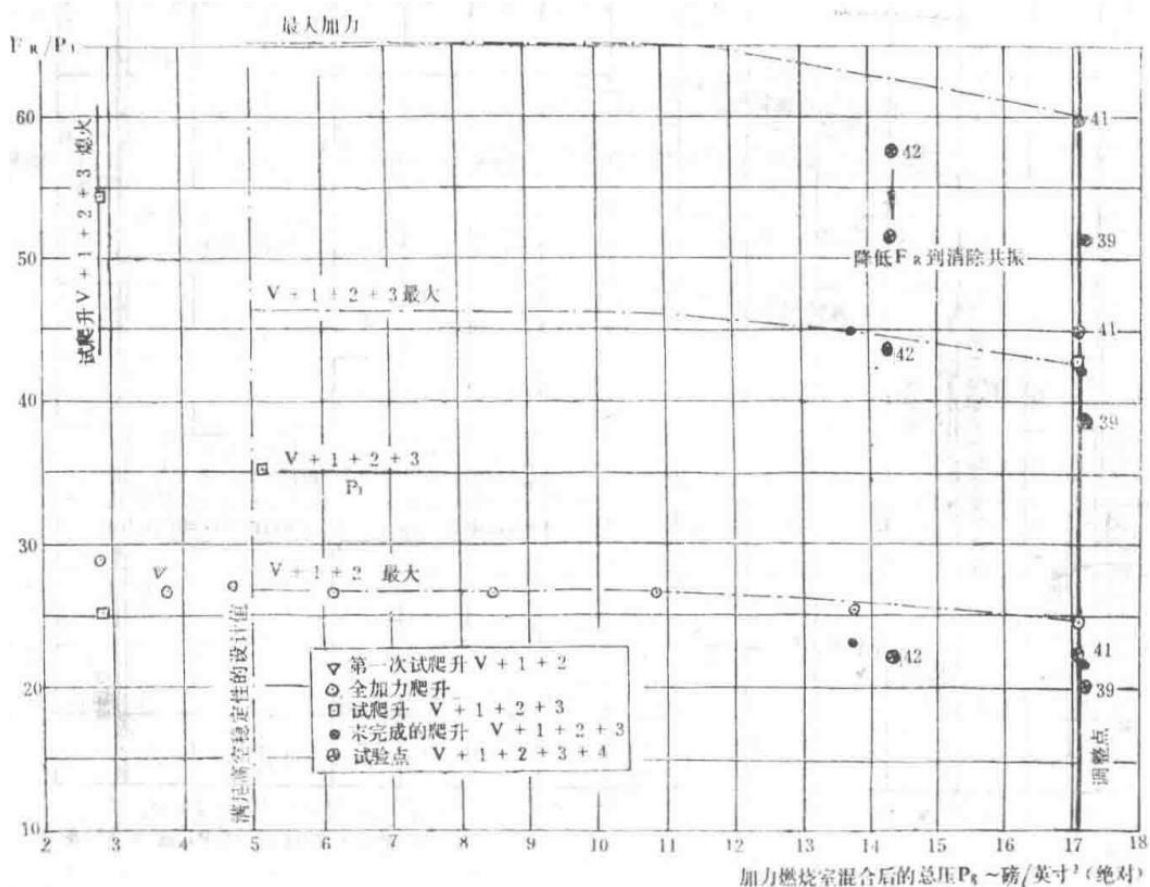


Figure 3 Fuel Flow Distribution (Standard Afterburner)

Diagram illustrating the fuel flow distribution in the standard afterburner configuration.

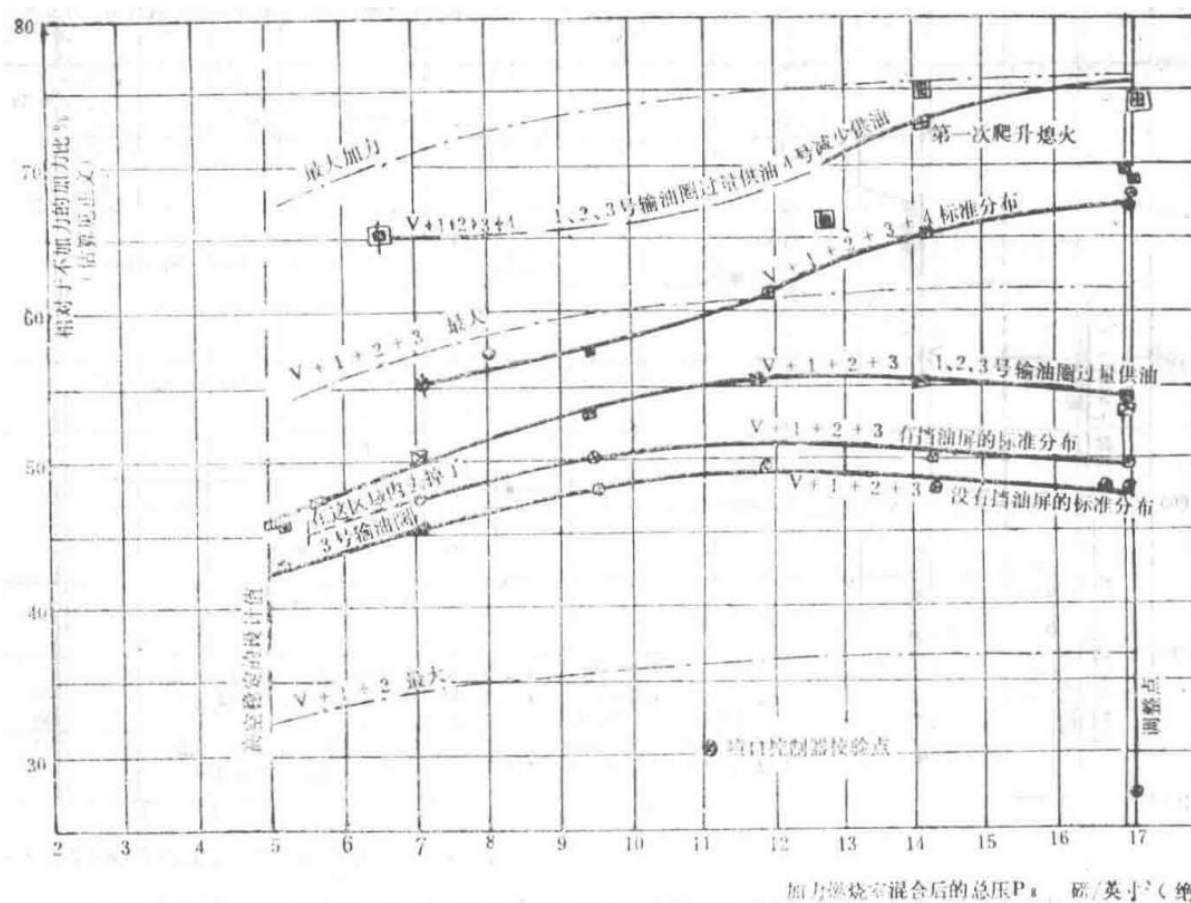


Figure 4 Relationship Between Augmentation Ratio and Mixed Total Pressure in Afterburner (Improved Afterburner)

Graph showing the relationship between augmentation ratio and mixed total pressure for an improved afterburner design.

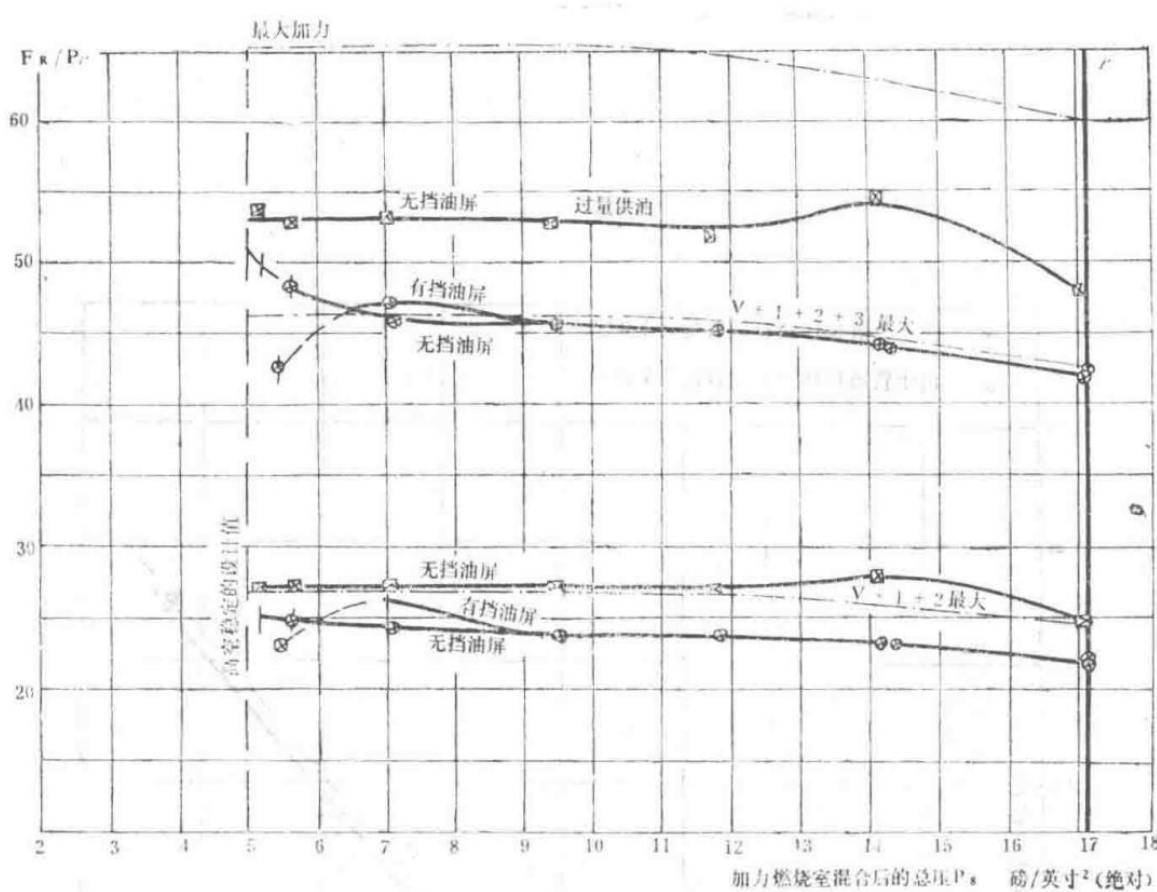


Figure 5 Fuel Flow Distribution (Improved Afterburner, 3 Fuel Manifolds)

Diagram showing fuel flow distribution in an improved afterburner with three fuel manifolds supplying fuel.

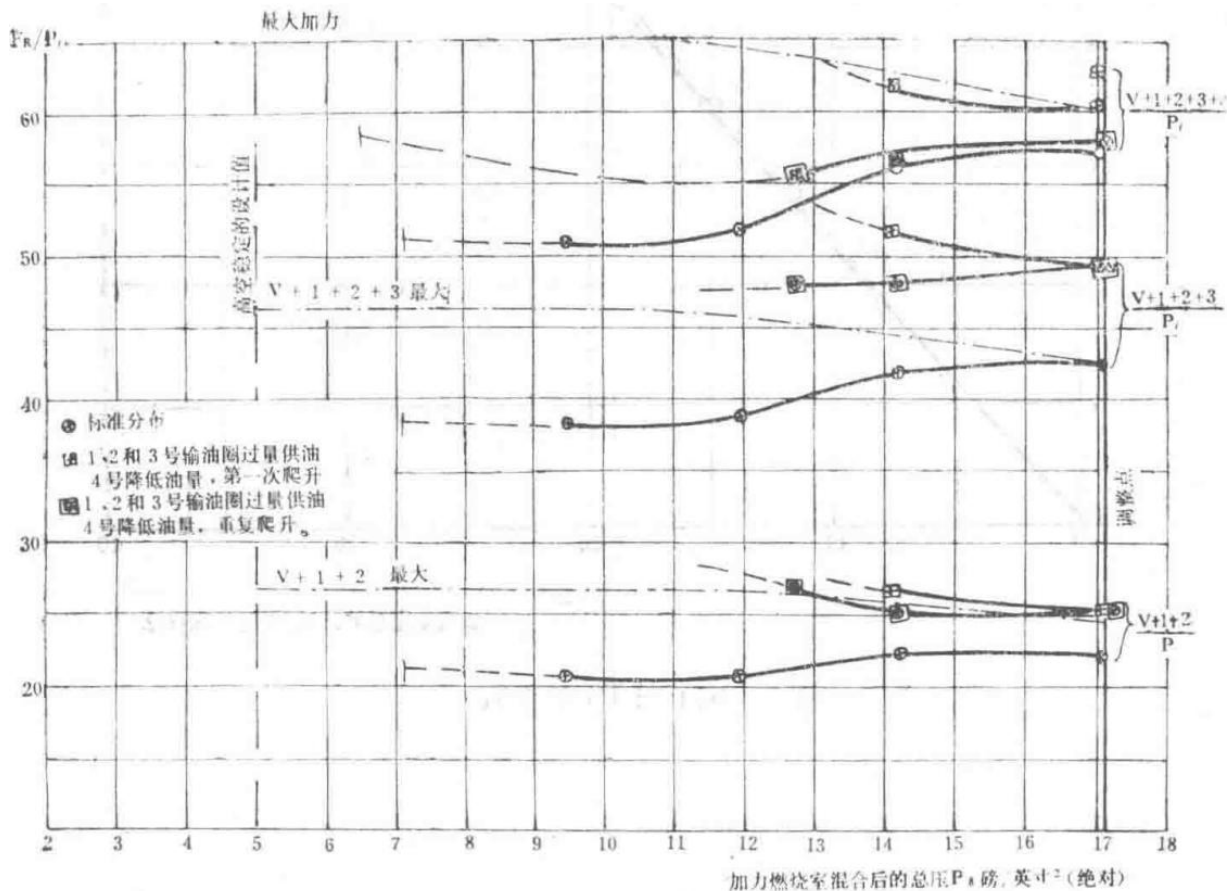


Figure 6 Fuel Flow Distribution (Improved Afterburner, 4 Fuel Manifolds, Without Fuel Baffle)

Diagram illustrating fuel flow distribution in an improved afterburner with four fuel manifolds and no fuel baffle.

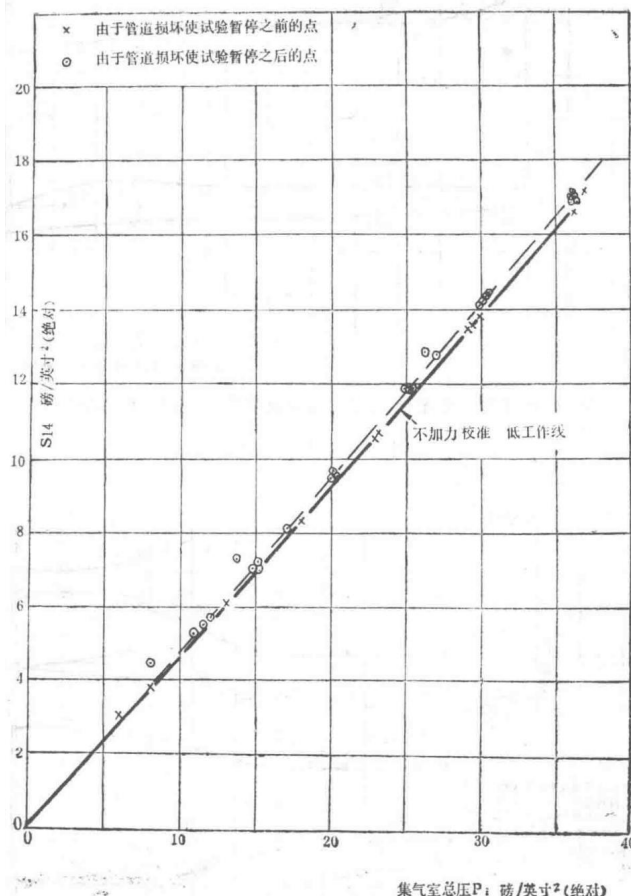


Figure 7 Relationship Between S14 and Pi

Graph showing the relationship between parameter S14 and Pi (pressure ratio) under various conditions.

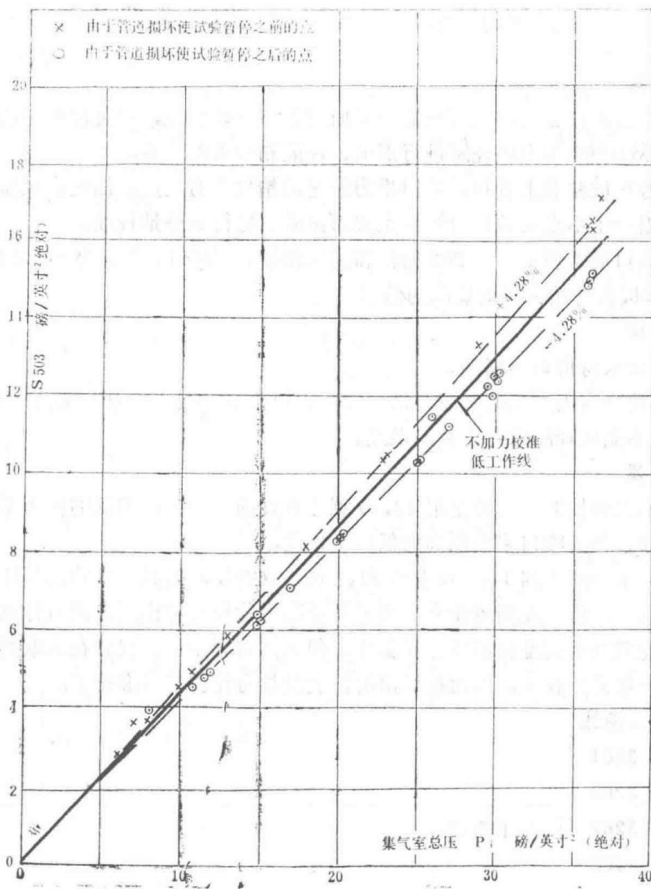


Figure 8 Relationship Between S503 and Pi

Graph depicting the relationship between parameter S503 and Pi (pressure ratio) under different operational states.

## Analysis of Afterburner Performance Parameters

This section analyzes the key performance parameters of the Spey MK202 engine's afterburner, focusing on the relationship between augmentation ratio, fuel flow distribution, nozzle area, and mixed total pressure ( $P_6^*$ ). The following graphs and data illustrate the performance characteristics under various test conditions.

Test Conditions and Symbols for Afterburner Performance Analysis

Symbol	Description
▽	Test point with V + 1 + 2, successful ignition at front section of combustion zone, stable combustion
△	Test point with V + 1 + 2 + 3, successful ignition at front section, unstable combustion at rear section
○	Test point with V + 1 + 2, successful ignition at rear section of combustion zone, unstable combustion
×	Test point with no ignition
⊗	Test point with V + 1 + 2 + 3 + 4, successful ignition at front section, combustion unstable at standard fuel supply
●	Test point with V + 1 + 2 + 3, successful ignition at front section, stable combustion at reduced fuel supply

The first graph (top) shows the relationship between augmentation ratio ( $F$ ) and mixed total pressure ( $P_6^*$ ) under maximum afterburner conditions. The augmentation ratio increases with  $P_6^*$  and varies based on the fuel supply strategy (e.g.,  $V + 1 + 2 + 3$ ).

The second graph (middle) illustrates the ratio of thrust ( $F$ ) to low-pressure turbine pressure ratio ( $P_4/P_1$ ) against  $P_6^*/\theta$  ( $\theta$  represents temperature correction). It highlights regions of no afterburner operation, partial afterburner operation, and full afterburner operation.

The third graph (bottom) presents the relationship between parameter S14 (specific fuel consumption indicator) and  $P_6^*/\theta$ . The data points are categorized based on test conditions, showing trends for both low and high augmentation configurations.

## Fuel Flow Distribution and Combustion Stability

The fuel flow distribution significantly impacts combustion stability in the afterburner. The diagrams in Figures 3, 5, and 6 compare fuel distribution strategies for standard and improved afterburners. The improved afterburner configurations (3 and 4 fuel manifolds) aim to optimize fuel mixing and reduce combustion instability.

- Standard afterburner: Single fuel distribution strategy with potential uneven mixing.
- Improved afterburner (3 manifolds): Enhanced fuel distribution but retains fuel baffle for flow control.
- Improved afterburner (4 manifolds, no baffle): Optimized fuel distribution with reduced flow resistance.

The graphs in Figures 7 and 8 show the relationships between parameters S14/S503 and  $P_i$  (pressure ratio). These parameters are critical for evaluating the thermodynamic efficiency and stability of the afterburner under varying operational conditions.

$$F = f(P_6^{*}, \theta, V)$$

Equation representing the augmentation ratio ( $F$ ) as a function of mixed total pressure ( $P_6^*$ ), temperature correction ( $\theta$ ), and fuel supply strategy ( $V$ ).

The maximum augmentation area ratio is specified as  $965.3 \text{ cm}^2$ , corresponding to the structural limit of the nozzle (Component No. 9). This constraint is critical for ensuring safe and efficient afterburner operation.

## Conclusion

The performance analysis of the Spey MK202 afterburner highlights the importance of optimized fuel flow distribution and mixed total pressure management. The improved afterburner designs demonstrate enhanced combustion stability and efficiency, particularly under high augmentation conditions.

Performance Technical Report	PTR 12169
Results and Discussion of Non-Afterburning High and Low Working Line Calibration Tests Conducted on the Spey MK202 Simulator in the Altitude Test Facility	

First Edition, December 30, 1965

## 1.0 Introduction

It was intended to install an afterburner behind the engine simulator in the altitude test facility to conduct ignition, performance, and flameout tests on the Spey MK202 afterburner using a method similar to that of the RB153-61.

Previous models had significant issues with thrust measurement accuracy during simulator testing. Therefore, prior to testing the MK202 afterburning system, the test facility was thoroughly calibrated using a non-ignited afterburner.

Two auxiliary nozzles were used to simulate the low and high working lines of the MK202, with nozzle diameters of 22.75 inches and 21.25 inches, respectively. This report presents and discusses the calibration results.

## 2.0 Conclusions

1. Thrust determination remains imprecise.
2. The measurements used to determine drag terms are satisfactory, but some "drag" terms appear to have been omitted.
3. The errors in the load cell readings still cannot be explained.

## 3.0 Summary

Two calibrations were conducted: one using a 22.75-inch diameter nozzle to simulate the low low-pressure working line, and another using a 21.25-inch diameter nozzle to simulate the high low-pressure working line.

The calibration results are shown in Figures 1 to 12 and Tables A and B. Comparison of these test results with theoretical values suggests that the drag term measurements are satisfactory but indicates that one or more drag terms may have been omitted. The errors in the load cell readings, first observed in previous altitude test facility simulator tests, remain unexplained. Despite careful recording of load cell readings, these anomalies persist, making it difficult to accurately derive performance and afterburning ratios.

## 4.0 Tables and Figures

- Figure 1: RH3264
- Figure 2: RH3265
- Figure 3: RH3267 Low Working Line Calibration
- Figure 4: RH3268
- Figure 5: RH3365
- Figure 6: RH3368
- Figure 7: RH3269
- Figure 8: RH3271 High Working Line Calibration
- Figure 9: RH3369

- Figure 10: RH3367
- Figure 11: RH3272
- Figure 12: RH3384 Preheater Combustion Efficiency
- Figure 13: RH3400 Schematic Diagram of Test Facility Design

$$X_D = KPi - \sum A_p p_0$$

Figure 3: Low Working Line Calibration (RH3267)

Graphical representation of calibration results for the low working line.

	低 工 作 线	高 工 作 线
计算的	0.466	0.480
测量的	0.474	0.490
计算的/测量的	0.985	0.980

Figure 8: High Working Line Calibration (RH3271)

Graphical representation of calibration results for the high working line.

低 工 作 线	调整状态 45000英尺 Mn 1.53	
	技术文件上的	实际的
外涵流量 $M_s$ 磅/秒	45.91	45.87
预热器质量流量 $M_p$ 磅/秒 (包括燃油流量)	54.70	54.63
加力燃烧室质量流量 $M_s$ 磅/秒	100.61	100.5
加力燃烧室混合后的总压 $P_s$ 磅/英寸 <sup>2</sup> (绝对)	17.10	× 17.103 + 16.83
$M_s/P_s$	5.88	× 5.876 + 5.97
$T_e$ °K	935	934

Figure 12: Preheater Combustion Efficiency (RH3384)

Graph showing preheater combustion efficiency.

$$A_{B1} = 108.4 = A_{B2}$$

Figure 13: Schematic Diagram of Test Facility Design (RH3400)

Schematic of the test facility setup.

## 5.0 Discussion

### 5.1 Determination of Gross Thrust

Gross thrust is determined by the net thrust measured by the load cell and corrections for "drag" terms, which include inlet momentum and pressure drops across seals. In this specific setup, these drag terms occur at the preheater inlet and the inlets of the two ducts supplying bypass air. The complete calculation formula is provided in Section 7.4.

## 5.2 Drag Terms

Theoretically, drag terms should form a set of straight lines passing through the origin when plotted against the plenum total pressure  $P\Box$ . The momentum term should form a single curve (Figures 1 and 6), and the pressure drop term, and thus the total drag, should vary with the ram pressure ratio  $P\Box / p_0$ . This was found to be the case (see Figures 2 and 7).

## 5.3 Comparison of Test Results with Theory

Section 7.0 explains that  $XG / p_0$  (gross thrust /  $p_0$ ),  $XD / p_0$  (total drag /  $p_0$ ), and  $X\Box / p_0$  (load cell reading /  $p_0$ , i.e.,  $(XG - XD) / p_0$ ) should form straight lines when plotted against  $P\Box / p_0$ . Figures 4 and 9 show that the  $XD / p_0$  points align well, but  $X\Box / p_0$  exhibits significant scatter, which is also reflected in the  $\Delta XG / p_0$  values. Due to this scatter, the test results were analyzed using average lines drawn through these scattered points. These average lines indicate discrepancies between theory and test results, believed to be due to omitted terms. The scatter around the average line reflects inaccuracies in net thrust measurement.

The slope of the  $\Delta X\Box$  versus  $\Delta p_0$  curve in Figures 5 and 10 provides the effective area value, at which the experimentally determined thrust/ $p_0$  curve intersects the ordinate. Under the condition that  $X\Box = XG - XD$ , average lines were drawn through the experimental values of  $XG / p_0$  and  $X\Box / p_0$ .

The gross thrust calculated from the afterburner inlet conditions was compared with the measured gross thrust values, where the inlet conditions were determined by measurements of airflow, fuel flow, and  $T_e$  in the test setup. The comparison results show that the calculated (or theoretical) thrust is higher than the average line obtained from the measured  $(X\Box + XD) / p_0$  values. The difference is  $18 P\Box / p_0 - 42.8$  for the low working line and  $13.5 P\Box / p_0 - 42.8$  for the high working line. These differences may represent the unaccounted drag terms.

Determination of the afterburner conditions indicates that the calculated total pressure ratio of the afterburner is approximately 2% lower than the average value measured by the total pressure rake upstream of the nozzle. This discrepancy may be due to the influence of total pressure distribution within the duct, making the measurement not a true average. However, they do suggest that the calculated  $P_s$  is at least reasonable.

Values of  $P_s / p\Box$

	Low Working Line	High Working Line			
Calculated	Measured	Calculated/Measured	Calculated	Measured	Calculated/Measured
0.466	0.474	0.985	0.480	0.490	0.980

## 5.4 Load Cell Readings

As mentioned in Section 5.3, the deviations in load cell readings  $X\Box$  cause scatter in  $XG$ . These deviations were observed during low working line calibration and recurred during high working line calibration. To investigate this issue, some verification points were taken at the high working line using  $I_s^2$ ,  $P\Box$ , and  $X\Box$ . The  $X\Box$  readings for some verification points differed from those of corresponding previous operating points. However, it is noteworthy that when a series of points were run at constant  $p\Box$  and varying  $p_0$ , the load cell readings formed a smooth curve, whereas previous readings taken at the same  $p\Box$  could not be connected smoothly (see Figures 11 and 9). Nevertheless, the  $\Delta X\Box / \Delta p_0$  values on this curve varied around an average of 110, while the

theoretical value is 67.2, representing the difference between the inlet and outlet flow areas of the setup.

It should be emphasized that during these calibrations, load cell readings were taken very carefully to ensure accurate measurements. Despite multiple checks and considerations before recording, these anomalies persisted.

## 5.5 Afterburner Nozzle Controller (Microjet) Adjustment

The pressure connected to the nozzle controller is the plenum total pressure and the static pressure in the bypass flow of the mixer. The static pressures measured by S2, S10, and S14 in the bypass flow of the mixer were very consistent, as shown in Tables A and B. S10 is connected to the nozzle controller, and its pressure is read on S14.

The nozzle controller is adjusted based on  $P_{\infty} / S14$ . When reverting to the low working line, the ratio  $P_{\infty} / S14$  should be 2.15, derived from a set of readings. Given sufficient time for analysis, the average value was found to be 2.155, confirming that the initial value of 2.15 is satisfactory.

To revert the engine to the high working line, the ratio  $P_{\infty} / S14$  should be adjusted to 2.135.

## 6.0 Afterburner Inlet Conditions

Afterburner Inlet Conditions for Low Working Line (Adjusted Condition: 45,000 ft, Mach 1.53)

	Technical Document	Actual
Bypass Flow Rate $M_a$ lb/s	45.91	45.87
Preheater Mass Flow Rate $M_{\infty}$ lb/s (including fuel flow)	54.70	54.63
Afterburner Mass Flow Rate $M_a$ lb/s	100.61	100.5
Afterburner Mixed Total Pressure $P_a$ lb/in <sup>2</sup> (absolute)	17.10	$\times 17.103 + 16.83$
$M_a / P_a$	5.88	$\times 5.876 + 5.97$
$T_a$ K	935	934

Afterburner Inlet Conditions for High Working Line (Adjusted Condition: 36,089 ft, Mach 1.1)

	Technical Document	Actual
Bypass Flow Rate $M_a$ lb/s	37.768	37.84
Preheater Mass Flow Rate $M_{\infty}$ lb/s (including fuel flow)	64.71	63.40
Afterburner Total Flow Rate $M_a$ lb/s	102.48	101.24
Afterburner Mixed Total Pressure $P_a$ lb/in <sup>2</sup> (absolute)	20.09	$\times 20.11 + 19.80$
$M_a / P_a$	5.1	$\times 5.00 + 5.12$
$T_a$ K	935	936

× Measured on the  $P_7$  pressure rake inside the afterburner. + Calculated from test facility measurements.

Afterburner conditions for test points 6–19 are given in Table A.

Afterburner conditions for test points 20–34 are given in Table B.

Table A (Low Working Line)

Reading No.	T <sub>0</sub> K	P <sub>0</sub> lb/in <sup>2</sup> abs	p <sub>0</sub> lb/in <sup>2</sup> abs	P <sub>0</sub> / p <sub>0</sub>	F <sub>000</sub> lb/s	η <sub>000</sub> %	T <sub>6</sub> K	MB lb/s	M <sub>000</sub> lb/s	μ (Bypass Ratio)
6	422	36.183	2.0832	17.368	0.740	95.8	934	45.87	53.89	0.851
7	422	25.068	1.535	16.33	0.521	94.4	937	32.13	37.10	0.865
8	422	28.967	1.741	16.638	0.596	95.7	936	38.86	43.05	0.902
9	422	32.979	1.946	16.945	0.679	95.5	937	41.73	48.97	0.852
10	405.5	5.984	0.9824	6.091	0.141	84.4	935	7.83	8.74	0.894
11	411	15.006	1.224	12.26	0.326	91.5	933	19.17	22.24	0.861
12	411	11.987	1.933	6.201	0.266	89.6	936	15.57	17.66	0.881
13	419.5	19.005	3.115	6.101	0.400	93.1	934	25.56	28.09	0.910
14	419	27.004	4.426	6.101	0.564	94.5	935	34.15	40.21	0.850
15	420.5	36.006	5.918	6.084	0.738	95.7	933	46.00	53.62	0.857
16	421	36.016	2.992	12.037	0.741	96.0	936	45.41	53.63	0.845
17	421	29.998	2.503	11.985	0.625	89.0	938	37.00	41.85	0.885
18	420.5	24.959	2.087	11.959	0.517	94.6	933	31.44	37.13	0.849
19	420	20.003	1.696	11.794	0.420	93.5	935	25.37	29.59	0.858

Table B (High Working Line)

Reading No.	T <sub>0</sub> K	P <sub>0</sub> lb/in <sup>2</sup> abs	p <sub>0</sub> lb/in <sup>2</sup> abs	P <sub>0</sub> / p <sub>0</sub>	F <sub>000</sub> lb/s	η <sub>000</sub> %	T <sub>6</sub> K	MB lb/s	M <sub>000</sub> lb/s	μ (Bypass Ratio)
20	387.5	41.297	4.163	9.920	0.910	96.7	935	37.84	62.49	0.605
21	388.5	10.984	1.077	10.199	0.257	87.8	934	11.02	16.11	0.684
22	387	19.981	2.007	9.620	0.455	94.0	941	18.81	29.88	0.630
23	389	29.996	2.956	10.148	0.668	95.6	939	28.66	45.05	0.636
24	389.5	15.031	1.456	10.324	0.343	91.7	933	14.75	22.53	0.655
25	389.5	10.994	0.989	11.116	0.324	70.6	937	10.38	16.22	0.640
26	387	10.994	1.112	9.887	0.256	86.8	934	10.42	15.84	0.658
27	382.5	6.004	0.721	8.327	0.155	80.9	933	6.44	8.84	0.729
28	388	15.006	1.895	7.919	-	935	14.69	22.46	0.653	
29	391	25.034	3.141	7.970	0.371	142.0	937	23.33	37.68	0.618
30	391	41.106	5.098	0.063	0.900	96.8	985	37.42	62.20	0.601
31	391.5	41.13	8.229	4.998	0.894	98.0	933	37.35	62.20	0.600
32	389	24.983	5.063	4.936	0.557	94.2	935	33.13	37.47	0.883
33	392	15.002	3.047	4.924	0.346	90.8	937	14.26	22.41	0.636
34	387	6.015	1.181	5.093	0.151	82.7	934	5.57	8.87	0.628

## 7.0 Theoretical Formulas

## 7.1 Nozzle Exit Geometric Area

The nozzle exit geometric area is 356 in<sup>2</sup> for the high working line and 406 in<sup>2</sup> for the low working line. The flow coefficient is taken as 1, which is entirely appropriate for expansion ratios > 2.0.

## 7.2 Test Facility Inlet Area

The inlet areas of the test facility are as follows: - Preheater flow area  $A_d = 186.2$  - Preheater seal area  $A_s = 12$  - Left bypass flow area  $AB_1 = 108.4 = AB_2$  - Left bypass seal area  $AB_{1d} = 4.1 = AB_{2d}$

## 7.3 Nozzle Choking Conditions

Under nozzle choking conditions, all pressure relationships except  $p_o$  should be fixed and dependent only on geometric areas.

## 7.4 Inlet Drag XD

$$XD = (\sum MV)/(g) + \sum A_d (p_d - p_o) + \sum Ad (pd - po)$$

General formula for inlet drag calculation.

$$XD = (M V)/(g) + (MB_1 VB_1)/(g) + (MB_2 VB_2)/(g) + A_d (P_d - p_o) + A_d (pd - po) + AB_{1d} (PB_1 - p_o) + AB_1 (PB_1 - po) + AB_{2d} (PB_2 - p_o) + AB_2 (PB_2 - po)$$

Expanded formula for inlet drag calculation.

$$XD = K P_d - \sum A p_o$$

Simplified formula for inlet drag.

From Section 7.3:

$$\sum A = 186.2 + 12 + 2 (108.4 + 4.1) = 423.2$$

Summation of inlet areas.

From Figures 4 and 9: -  $K = 365$  for the low working line -  $K = 345.5$  for the high working line

## 7.5 Gross Thrust XG

$$XG = f(Y) P_s AF_d - AF_d p_o$$

Formula for gross thrust calculation.

Where: -  $f(Y) = 1.26$  for the temperatures used -  $P_s / P_d^{**} = 0.466$  for the low working line (see Section 5.3) -  $P_s / P_d^{**} = 0.48$  for the high working line (see Section 5.3)

Thus: -  $XG = 240 P_d - 406 p_o$  for the low working line -  $XG = 216 P_d - 356 p_o$  for the high working line

**— Section 26 —**  
**Content from Original Document (Pages 126-130)**

Afterburner Inlet					Nozzle Control H				Thrust		
M <sub>8</sub> (lb/s)	T <sub>8</sub> (K)	P <sub>8</sub> (psia)	S503 (psia)	M <sub>8</sub> /P <sub>8</sub>	S2 (psia)	S10 (psia)	S14 (psia)	Pi/S14	XG/P <sub>0</sub>	X□/P <sub>0</sub>	XD/P <sub>0</sub>
100.50	711	16.83	15.806	5.97	16.76	16.76	16.76	2.159	5910	2520	3390
69.75	711	11.68	10.954	5.97	11.678	11.678	11.678	2.147	5545	2202	3344
82.51	716	13.84	12.537	5.95	13.437	13.434	13.434	2.156	5670	2342	3307
91.38	713	15.33	14.412	5.95	15.342	15.342	15.342	2.150	5760	2425	3335
16.71	697	2.765	2.618	6.04	2.815	2.829	2.829	2.115	1822	641	1182
41.74	704	6.95	6.591	6.01	7.05	7.05	7.05	2.129	4070	1695	2215
33.49	704	5.58	5.236	6.00	5.628	5.628	5.643	2.124	1857	817	1040
53.05	709	8.88	8.276	5.98	8.893	8.893	8.897	2.136	1814	825	989
74.93	711	12.52	11.789	5.99	12.568	12.597	12.362	2.146	1680	829	853
100.36	710	16.80	15.717	5.99	11.616	11.638	11.338	3.002	1795	855	943
99.78	714	16.78	15.762	5.99	16.764	16.739	16.739	2.152	3960	1761	2199
—	—	—	13.158	—	13.95	13.95			3950	1660	2290
69.09	712	11.58	10.908	5.97	11.602	11.617	11.641	2.144	3940	1603	2337
55.38	711	9.25	8.751	5.99	9.335	9.344	9.359	2.137	3882	1574	2308

101.23	740	19.80	18.914	5.12	19.329	19.344	19.339	2.135	2960	1252	1702
27.39	724	5.29	5.088	5.18	5.27	5.279	5.279	2.081	3130	1016	2112
49.16	739	9.60	9.316	5.12	9.629	9.609	9.609	2.079	3020	1275	1745
74.38	737	14.43	13.924	5.15	14.203	14.194	14.194	2.113	3077	1300	1777
37.62	730	7.29	6.959	5.15	7.153	7.153	7.153	2.101	3160	1333	1827
—	—	—	5.074	—	5.172	5.148	5.148	2.136	3114	1397	2027
26.51	728	5.12	5.025	5.17	5.172	5.172	5.172	2.126	2980	1178	1602
15.43	714	2.96	2.751	5.21	2.823	2.817	2.847	2.109	2478	1053	1425
—	—		6.885	—	7.101	7.104	7.104	2.112	2315	1012	1303
—	—		11.455	—	11.727	11.727	11.727	2.135	2335	1012	1323
100.72	743	19.70	18.748	5.11	19.083	19.083	19.031	2.160	2320	1087	1233
100.45	744	19.68		5.10	19.133	19.108	19.084	2.155	1290	604	666
71.15	691	13.42	11.563	5.30	11.737	11.707	11.737	2.129	1267	576	669

37.01	736	7.19	6.886	5.15	7.099	9.074	9.074	1.653	1266	574	684	
14.59	735	2.84	2.737	5.14	2.871	2.871	2.881	2.088	1333	592	741	

## 7.6 Net Thrust Term X□

$$X\Box = XG - XD$$

Equation for net thrust term, where  $X\Box$  is net thrust,  $XG$  is gross thrust, and  $XD$  is drag term.

## 7.7 Subscript Definitions

- p: Preheater
- B<sub>1</sub>: Left bypass inlet
- B<sub>2</sub>: Right bypass inlet
- d: Connecting duct
- S: Sealing surface
- F<sub>1</sub>: Nozzle exit

Figures 1 to 12 present the results of a series of afterburner-related tests conducted on the Spey MK202 simulation device in place of the engine on a high-altitude test stand.

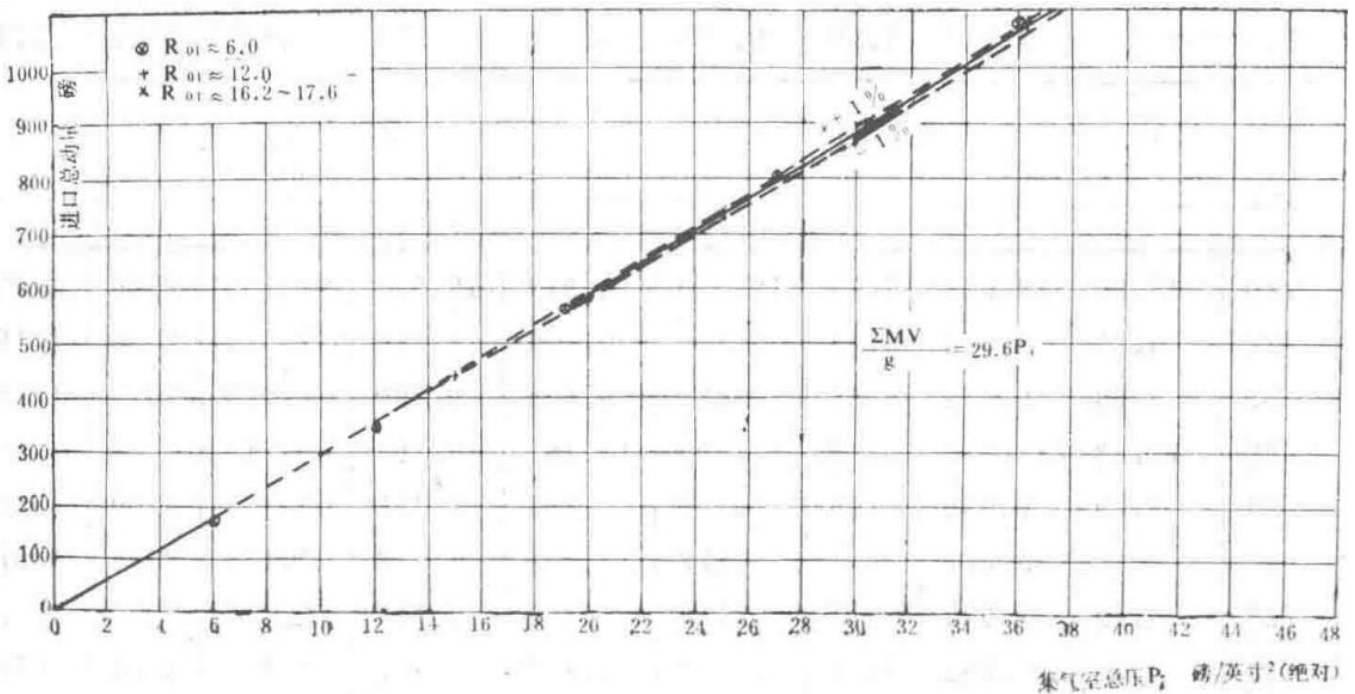


Figure 1 Relationship between Inlet Total Momentum and Pi (Low Operating Line Calibration)

Graph showing the correlation between inlet total momentum and Pi under low operating line calibration conditions.

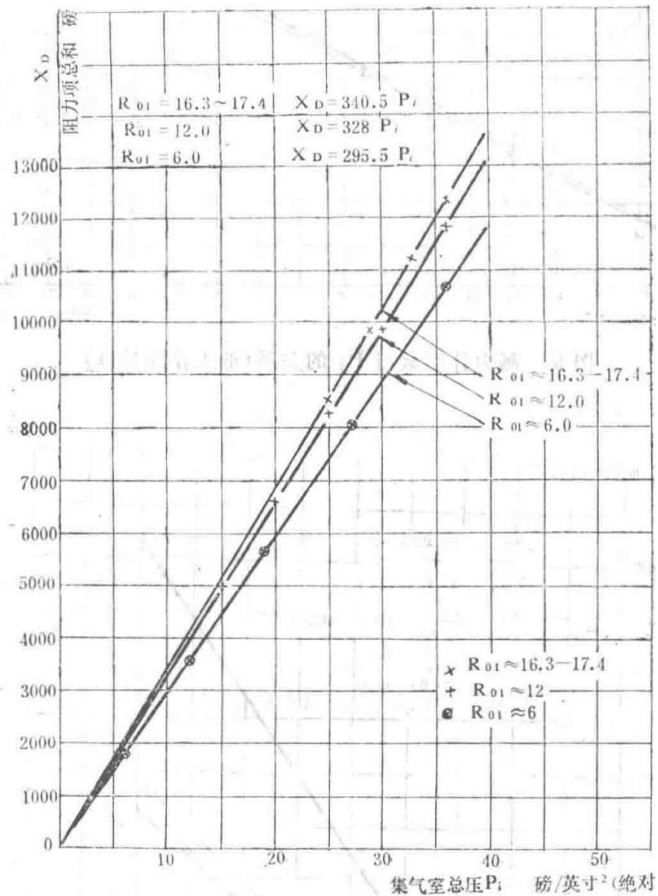


Figure 2 Relationship between Total Drag Term and  $P_i$  (Low Operating Line Calibration)

Graph depicting the relationship between the total drag term and  $P_i$  under low operating line calibration conditions.

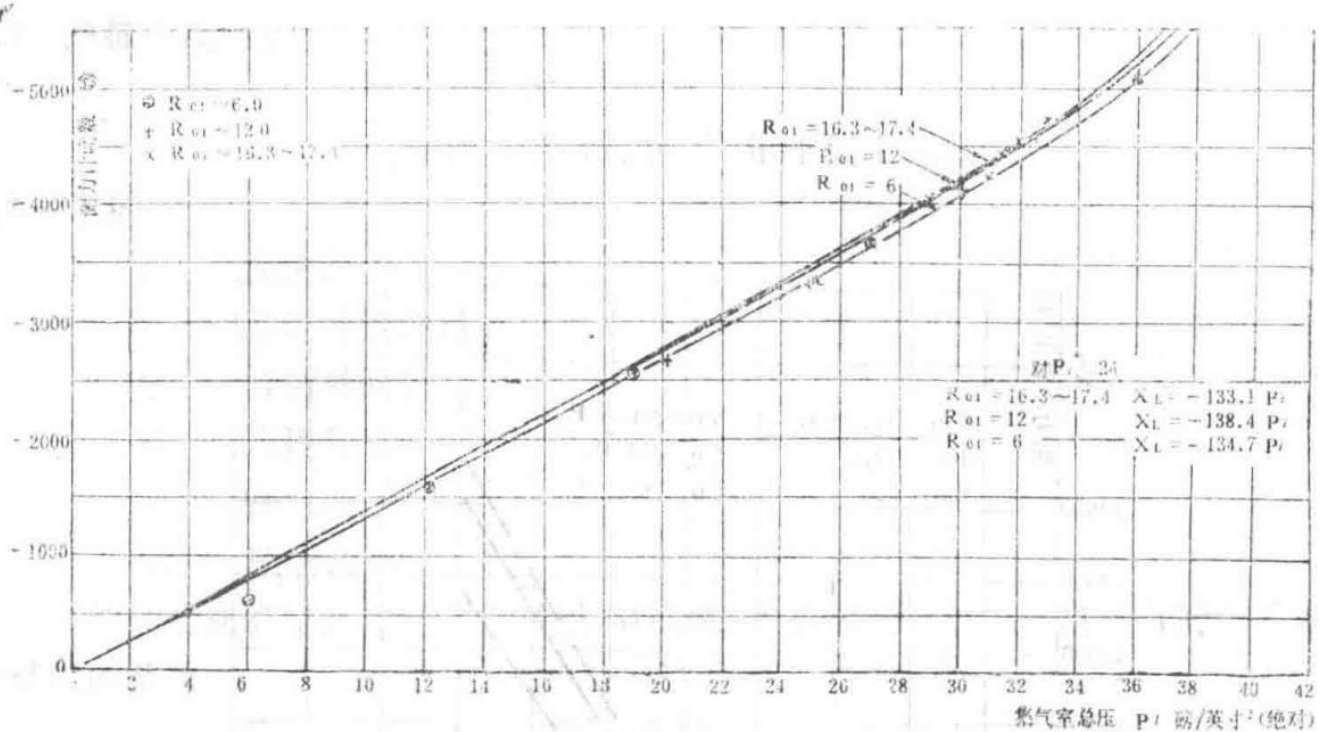


Figure 3 Relationship between Dynamometer Reading and  $P_i$  (Low Operating Line Calibration)

Graph illustrating the relationship between dynamometer readings and  $P_i$  under low operating line calibration conditions.

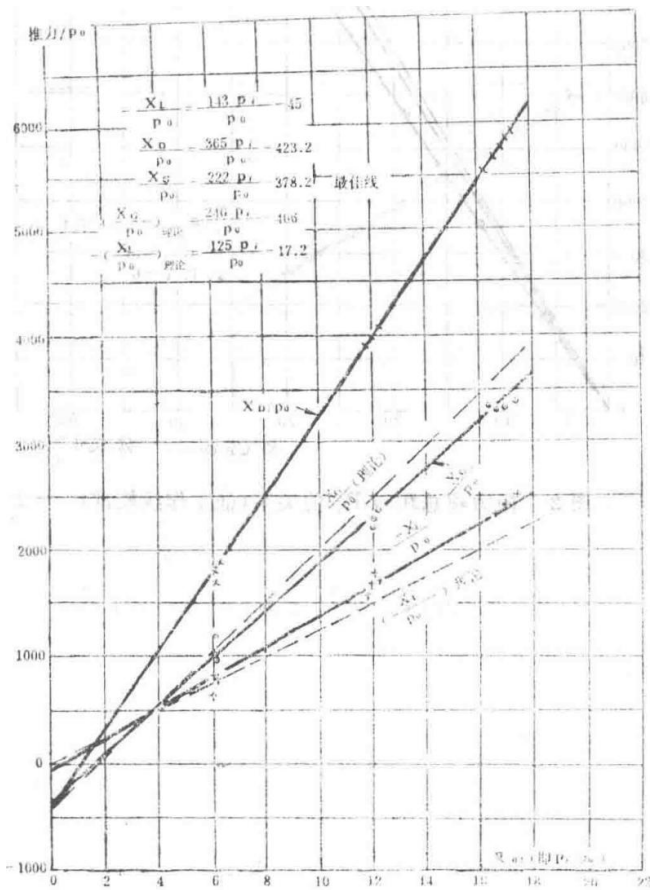


Figure 4 Relationship between Thrust/ $P_0$  and  $\dot{P}_i/P_0$  (Low Operating Line)

Graph showing the relationship between thrust normalized by  $P_0$  and  $\dot{P}_i$  normalized by  $P_0$  under low operating line conditions.

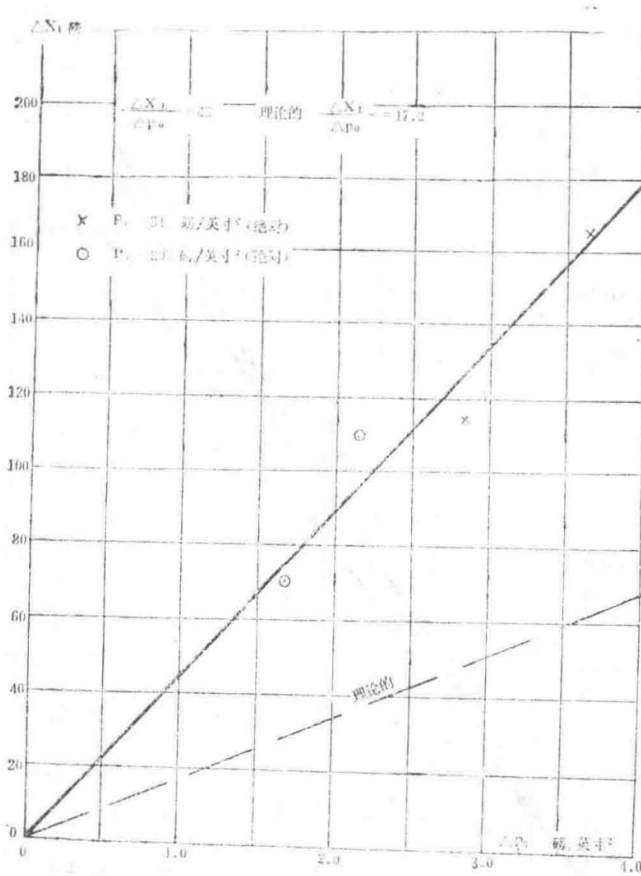


Figure 5 Relationship between  $\Delta X\Box$  and  $P_o$  (Low Operating Line)

Graph depicting the relationship between changes in net thrust term ( $\Delta X\Box$ ) and changes in  $P_o$  under low operating line conditions.

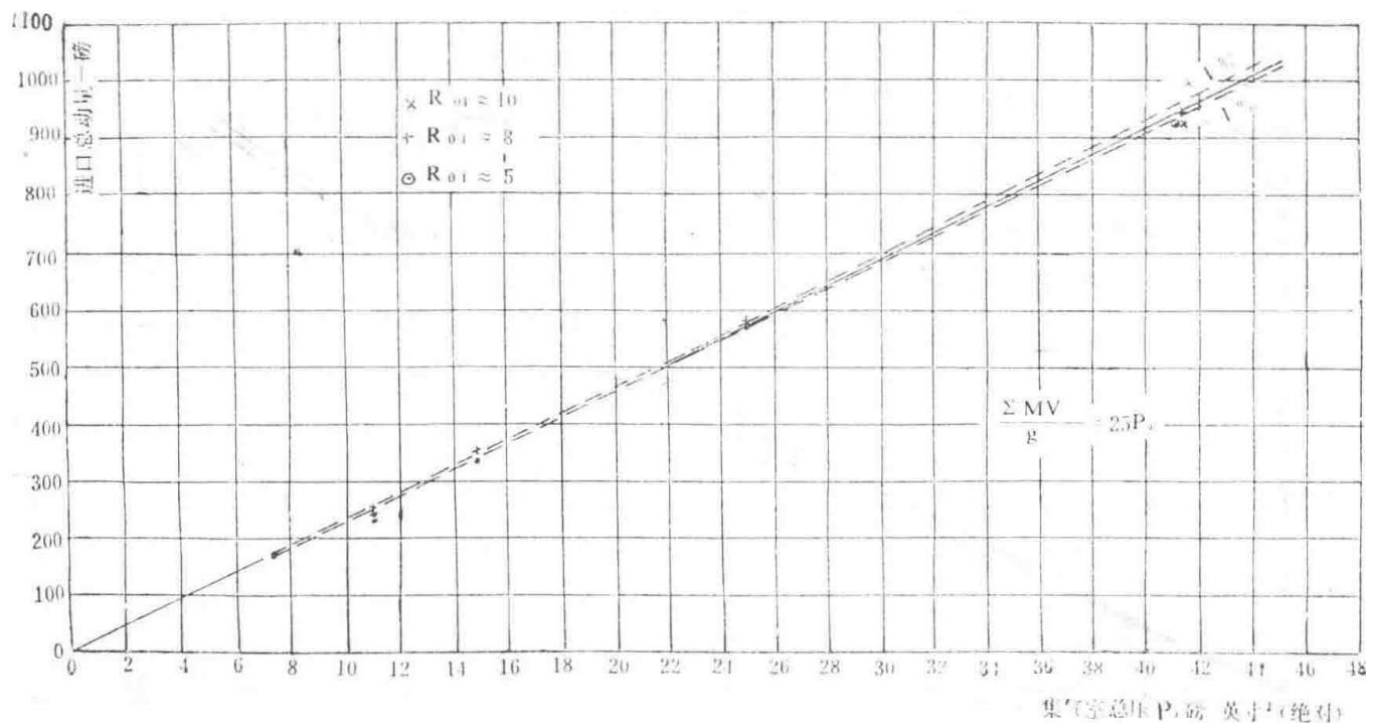


Figure 6 Relationship between Inlet Total Momentum and  $P_i$  (High Operating Line Calibration)

Graph showing the correlation between inlet total momentum and  $P_i$  under high operating line calibration conditions.

— Section 27 —  
Content from Original Document (Pages 131-135)

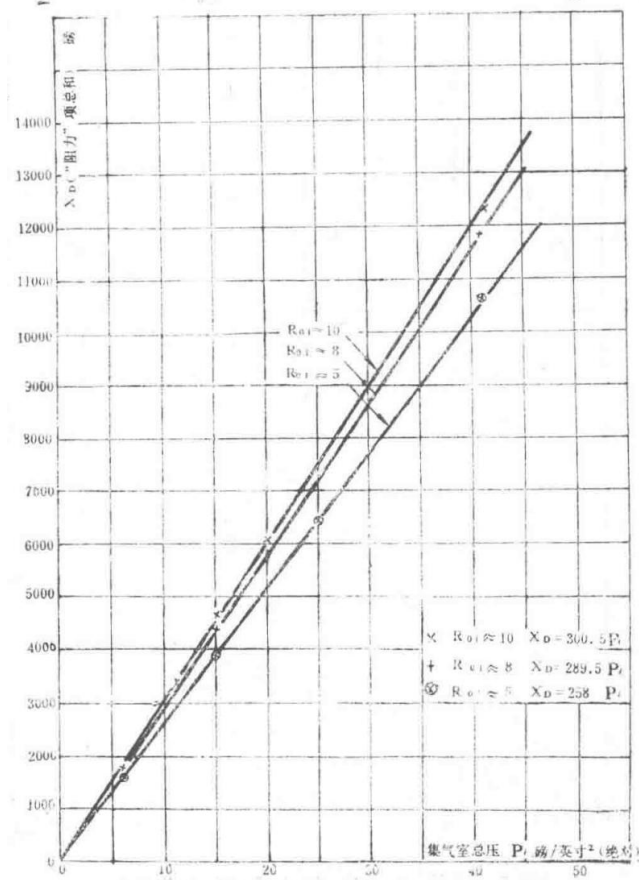


Figure 7 Relationship between Total Drag Term and Pi (High Work Line Calibration)

Graph showing the correlation between the total drag term and the parameter  $P_i$  under high work line calibration conditions.

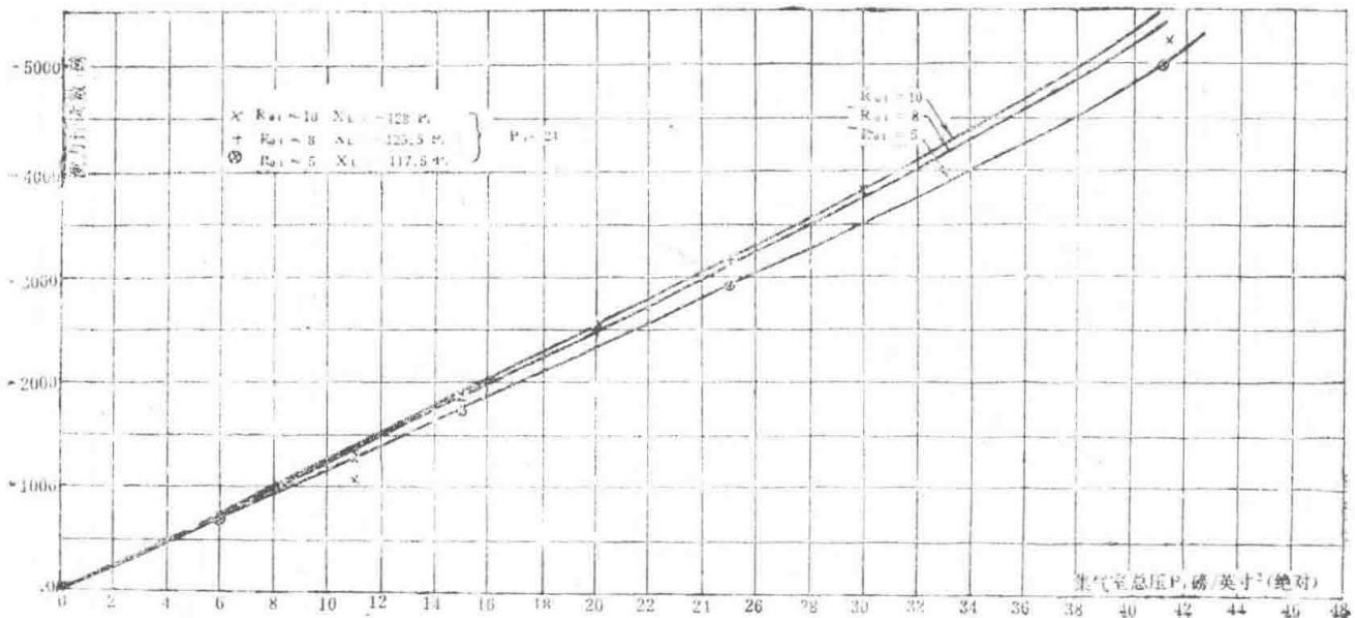


Figure 8 Relationship between Dynamometer Reading and Pi (High Work Line Calibration)

Graph depicting the relationship between dynamometer readings and the parameter  $P_i$  under high work line calibration conditions.

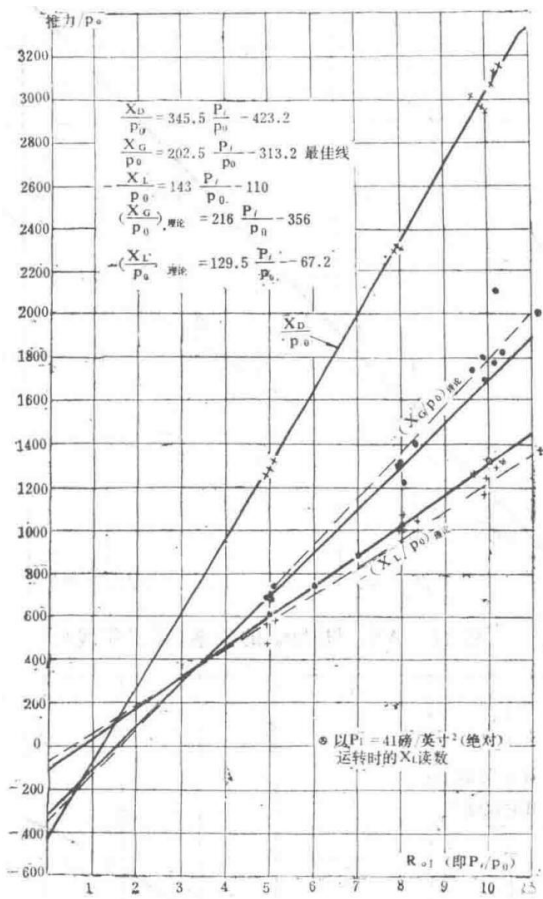


Figure 9 Relationship between Thrust  $\square \text{arp}_0$  and  $P \square / p_0$  (High Work Line)

Graph illustrating the relationship between thrust parameter  $\square \text{arp}_0$  and the ratio  $P \square / p_0$  under high work line conditions.

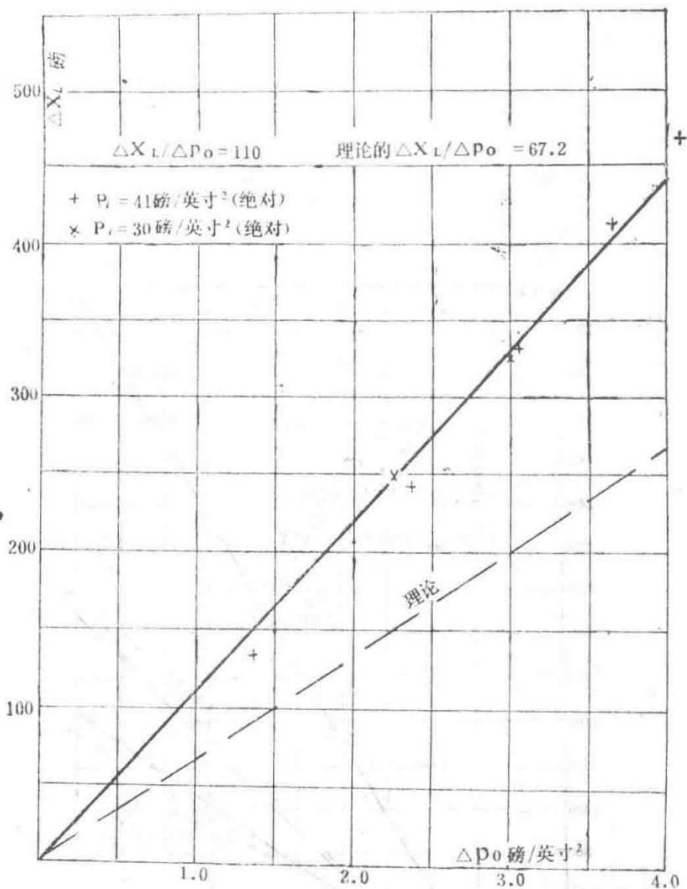


Figure 10 Relationship between  $\Delta X\Box$  and  $\Delta p_0$  (High Work Line)

Graph showing the relationship between  $\Delta X\Box$  and  $\Delta p_0$  under high work line conditions.

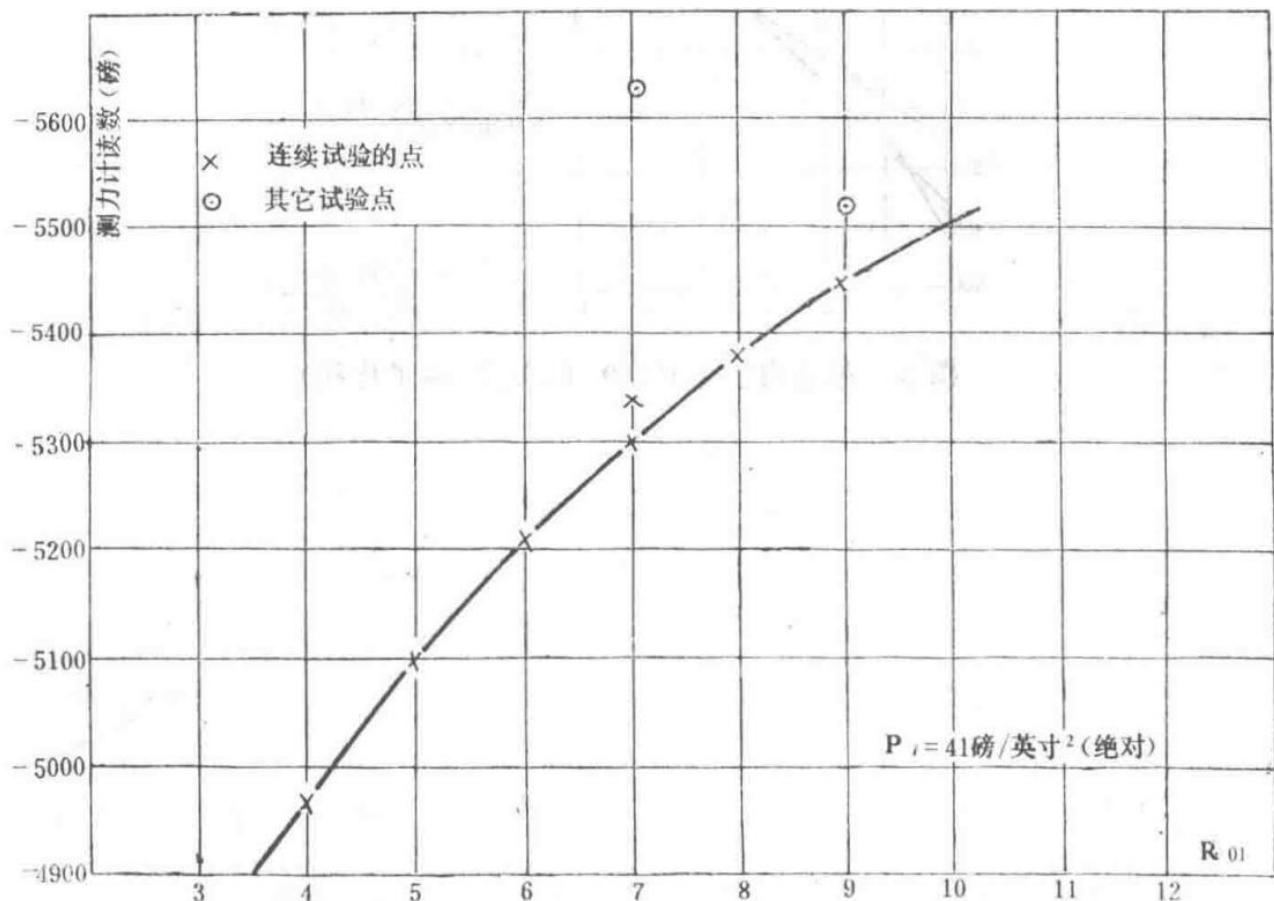


Figure 11 Relationship between Dynamometer Reading and  $P \square / p_0$  (High Work Line Calibration)

Graph depicting the relationship between dynamometer readings and the ratio  $P \square / p_0$  under high work line calibration conditions.

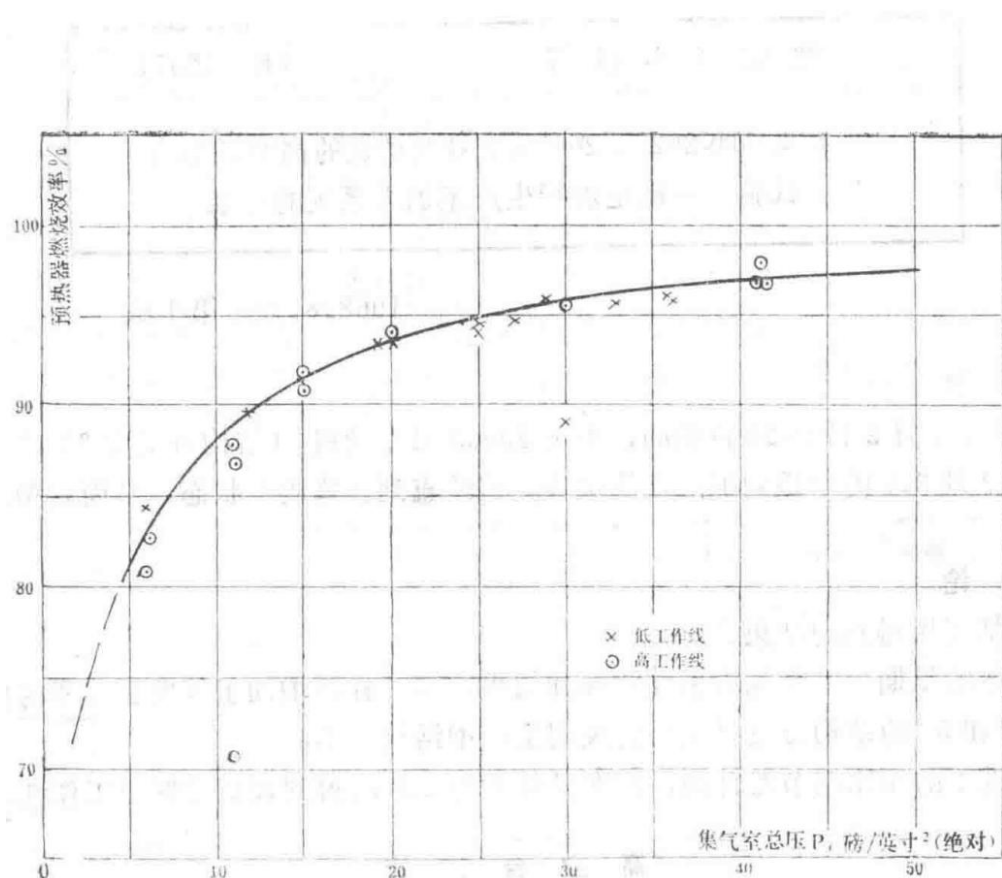


Figure 12 Relationship between Preheater Efficiency and  $P \square$

Graph showing the relationship between preheater efficiency and the parameter  $P \square$ .

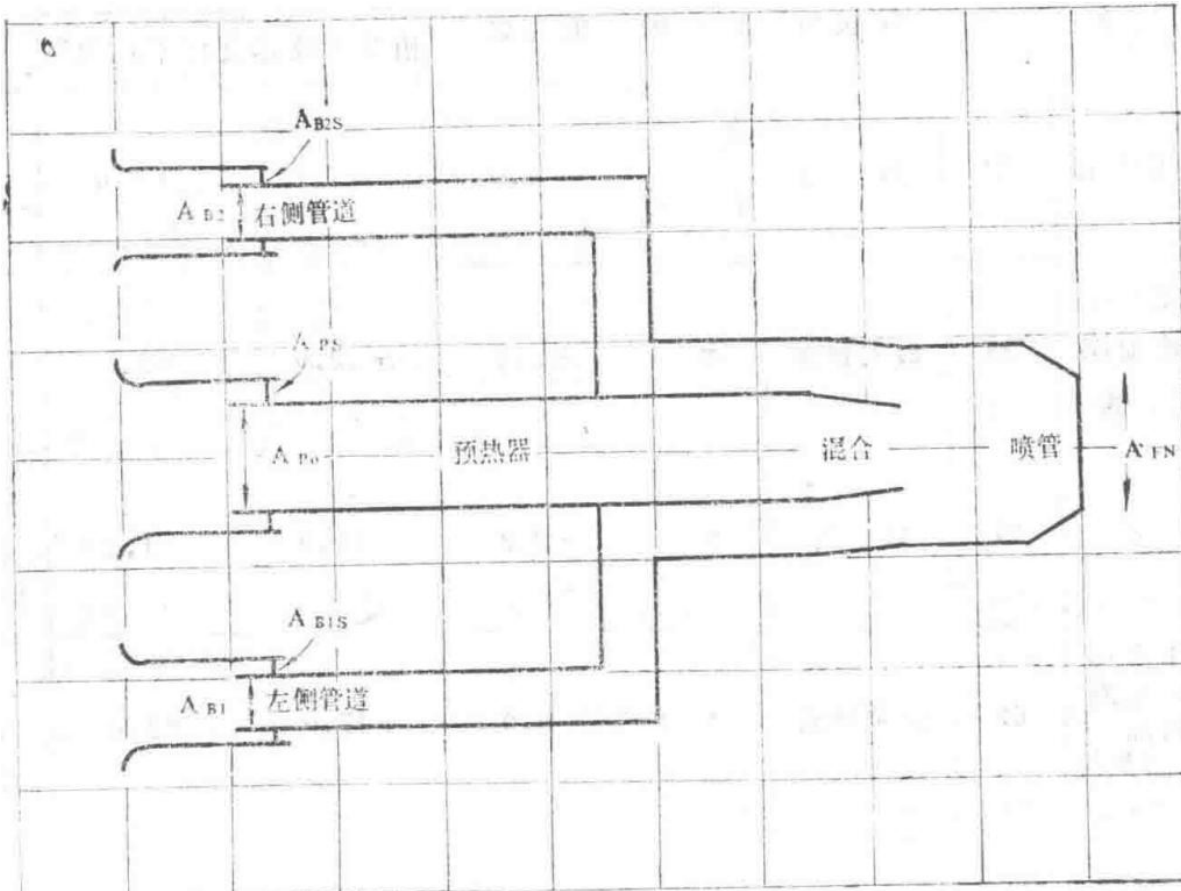


Figure 13 Schematic Diagram of Spey MK202 Engine Simulator for High-Altitude Test Facility

Schematic diagram illustrating the Spey MK202 engine simulator used in the high-altitude test facility.

Technical Performance Report	PTR 12571
Spey MK202 High-Altitude Test Facility Test for Engine No. 20003/7 – Establishing Standards for Current Production Afterburning System	

## 1.0 Abstract

From July 2 to July 24, 1968, the Spey engine No. 20003 (configuration 20003/7) underwent a series of afterburning performance tests at Mach numbers ranging from 0.9 to 2.0. The tests were conducted up to the 'buzz' condition to finalize the standards for the current production afterburning system.

## 2.0 Conclusions

The table below summarizes the results obtained. The early production afterburning combustor mentioned above, similar to the current production type, increased the fuel supply to the vaporizing stabilizer.

Configurations 4\* and 5\* represent the final current production type, specifically:

- An improved pressure ratio regulator needle valve to achieve a lower low-pressure work line at Mach 2.0.

### High-Altitude Facility Performance

Table 1

No.	Afterburning Combustor Configuration	Record No.	Afterburning Combustor State	Low-Pressure Work Line	XN (Ejector) % Relative to Specified Value	Fuel Supply Change Relative to Technical Document Average %	Airflow Change Relative to Technical Document Average % ΔML	Remarks
1	Early production type	24	Buzz	Current production type	+1.0	+7.0	+1.0	MN = 2.0, 36089 feet, International Standard Atmosphere
2	Early production type, No. 1 fuel ring not supplying fuel	25	Maximum fuel supply	Same as above	+3.5	+12.0	+2.4	MN = 2.0, 36089 feet, International Standard Atmosphere
3	Same as 2	27	Buzz	Same as above	-2.8	-10.0	-1.2	MN = 0.9, 36089 feet, International Standard Atmosphere
4	Early production type, No. 1 fuel ring not supplying fuel with drilled heat shield	69	Maximum fuel supply	Same as above	+4.0	+17.0	+1.0	MN = 2.0, 36089 feet, International Standard Atmosphere
5	Same as 4	94	Buzz	Same as above	-1.4	-5.0	-1.0	MN = 1.1, 36089 feet, International Standard Atmosphere

- b. Drilling holes in the heat shield.
- c. Fuel distribution for the afterburner of the "Red" standard engine:
- 'type': 'list', 'ordered': False, 'items': ['No. 1 fuel manifold: No fuel supply', 'No. 2 fuel manifold: 22%', 'No. 3 fuel manifold: 55%', 'No. 4 fuel manifold: 23%']
- d. The fuel supply for the vaporizer stabilizer is 12% of the main afterburner fuel manifold supply.

The "buzz" point mentioned in item 5 is an average value, with the lowest "buzz" point aligning with the desired minimum thrust point of the current production model.

Table 2: Test Bench Performance

	Without Boundary Layer Control Bleed	Boundary Layer Control Bleed from 7th Stage, Bleed Rate 7.49 lb/sec		
	Non-Afterburning	Afterburning	Non-Afterburning	Afterburning
Total Thrust XG (lbf)	12450	20416	11210	18151
Afterburner Temperature TRK (°K)		2040		2020

## 3.0 Introduction

A series of tests were conducted on the Spey 20003/7 engine to finalize the afterburner system for the current production model.

Most of the testing was performed with the current production-type afterburner, which features no fuel supply to the No. 1 fuel manifold and a drilled heat shield. Some verification was also done on the earlier model (where all fuel manifolds supplied fuel, the heat shield was not drilled, but the vaporizer stabilizer fuel supply was increased, and a lower low-pressure operating line was used, similar to the current model).

In all tests, no ejector air was introduced into the ejector nozzle, but the results were corrected for the ejector airflow specified for each flight condition.

## 4.0 Engine and Afterburner Standard Configuration

### 4.1 Structural Scheme of Spey 20003 Engine

The standard production engine's structural scheme features a single-inflection  $X_2$  needle valve in the pressure ratio regulator, providing a lower low-pressure operating line at Mach number ( $M \square$ ) 2, resulting in a higher airflow rate. This is a technical characteristic of the current production model.

### 4.2 Afterburner H366T

Initially, similar to the earlier model, all four fuel manifolds supplied fuel. During later performance tests of the current model, the No. 1 fuel manifold was not supplied with fuel, and a drilled heat shield was installed.

The main afterburner fuel flow distribution ratios (derived from test bench tests) for the two afterburners are as follows:

	Early Model	Current Model
--	-------------	---------------

No. 1 Fuel Manifold	2.7%	0
No. 2 Fuel Manifold	21.5%	22.0%
No. 3 Fuel Manifold	53.6%	55.0%
No. 4 Fuel Manifold	22.2%	23.0%

The fuel supply for the vaporizer stabilizer is as follows:

- Inner ring: 17.4%
- Middle ring: 31.0%
- Outer ring: 51.6%

The nozzle is equipped with a saddle stop device to limit the maximum usable area, with nominal sizes of 700, 800, and 900 square inches.

The nozzle position indicator system includes a 7000-ohm resistor to improve indication accuracy.

### 4.3 Afterburner Fuel Supply Control

The afterburner regulator adjustments were fundamentally suitable for providing the fuel supply required by the earlier model and could meet the additional fuel supply needed for the current model's performance. Sufficient fuel supply was also ensured for verifying the "buzz" boundary. For this purpose, a small valve (Kidder) was installed to allow controlled leakage of fuel from upstream to downstream of the main metering valve, but this only altered the fuel supply to the main fuel manifold.

During testing, to further increase the fuel supply, the afterburner regulator's air diverter was replaced and fine-tuned, allowing simultaneous adjustment of the fuel supply to both the main fuel manifold and the vaporizer stabilizer.

The current model's vaporizer stabilizer fuel supply is 60 gallons/hour higher than the earlier model. The nominal fuel distribution for the vaporizer stabilizer is:

- Outer ring: 56%
- Middle ring: 31%
- Inner ring: 14%
- Total flow rate  $F\Delta$ : 32.0

The nominal fuel distribution for the main fuel manifold is:

- No. 1 manifold: No fuel supply
- No. 2 manifold: 22.5%
- No. 3 manifold: 55.6%
- No. 4 manifold: 22.9%

## 5.0 Testing of the Blue Standard Engine

Initial verification was conducted at  $M\Delta = 2$ , primarily using the early-type combustion chamber. The main differences from the early production model were an increased vaporizer stabilizer fuel supply (+60 gallons/hour) and the use of the current production model's pressure ratio regulator needle valve, which provided a lower low-pressure operating line at  $M\Delta = 2$ . Performance was verified up to the nominal maximum fuel supply and the "buzz" limit.

## 6.0 Verification of the Current Production Model System

After verification of the early model, all further tests were conducted with no fuel supply to the No. 1 fuel manifold and with the heat shield modified to a drilled type.

A small valve was used to increase the afterburner fuel supply, and further increases were achieved by fine-tuning the afterburner fuel regulator's diverter.

M $\square$	P <sub>1</sub>	T <sub>1</sub>	Remarks
0.9	5.43	251.5	Guarantee point, 36,089 feet
1.1	6.83	269.7	
1.53	5.0	317.7	
1.53	7.0	317.8	
1.53	12.0	317.8	
2.0	7.0	389.8	
2.0	11.0	389.8	
2.0	18.0	389.8	
2.0	22.88	389.8	Guarantee point, 36,089 feet

## 7.0 Test Log

Test Log

Date	Record No.	Remarks
1968.7.2	*	Installed 710 in <sup>2</sup> saddle piece
	7, 8	Maximum military, non-afterburning, sea level condition, P <sub>1</sub> = 14.8, P <sub>0</sub> = 14.8
	9, 10	Afterburning operation to 710 in <sup>2</sup> saddle piece limited area, P <sub>1</sub> = 14.8, P <sub>0</sub> = 14.8
	13	Maximum military, non-afterburning, P <sub>1</sub> = 14.8, P <sub>0</sub> = 7.5
	14, 17	Afterburning operation to 710 in <sup>2</sup> saddle piece limited area, P <sub>1</sub> = 14.8, P <sub>0</sub> = 7.5
1968.7.3	18	M $\square$ = 2.0, P <sub>1</sub> = 23, T <sub>1</sub> = 389, maximum military
	19	M $\square$ = 2.0, P <sub>1</sub> = 23, T <sub>1</sub> = 389, maximum afterburning, no "buzz"
	21	Repeat 19, maximum afterburning, no "buzz"
	22	Repeat 19, maximum afterburning, no "buzz"
	23	M $\square$ = 2.0, P <sub>1</sub> = 23, T <sub>1</sub> = 389, "buzz" point
	24	Repeat 23
	*	No. 1 fuel manifold not supplied
	25	M $\square$ = 2.0, P <sub>1</sub> = 23, T <sub>1</sub> = 389, maximum fuel supply, no "buzz"

	26	$M\Delta = 0.9, P_1 = 5.4, T_1 = 252$ , maximum military
	27	$M\Delta = 0.9, P_1 = 5.4, T_1 = 252$ , "buzz" point
	28-31	$M\Delta = 2.0, P_1 = 23, T_1 = 389$ , afterburning
	*	Installed 710 in <sup>2</sup> saddle piece
	38	Maximum military, non-afterburning, sea level condition, $P_1 = 14.8, P_0 = 14.8$
	39-41	Afterburning operation point, sea level condition, $P_1 = 14.8, P_0 = 14.8$
	43	$M\Delta = 2.0, P_1 = 23, T_1 = 389$ , afterburning
	44, 53	At different altitudes, verified operating line without afterburning
	*	Installed drilled heat shield
1968.7.11	61	$M\Delta = 2.0, P_1 = 23.0, T_1 = 389$ , maximum military
	62	$M\Delta = 2.0, P_1 = 23.0, T_1 = 389$ , maximum afterburning, no "buzz"
	63	$M\Delta = 0.9, P_1 = 5.4, T_1 = 252$ , maximum military
	64	$M\Delta = 0.9, P_1 = 5.4, T_1 = 252$ , maximum afterburning limited by silencer howling
	65	$M\Delta = 2.0, P_1 = 23.0, T_1 = 389$ , maximum fuel supply to fuel manifold without small valve, no "buzz"
1968.7.15	66-67	$M\Delta = 2.0, P_1 = 23.0, T_1 = 389$ , maximum fuel supply to fuel manifold with small valve, no "buzz"
	*	Increased fuel supply by adjusting the afterburner regulator diverter
	68	$M\Delta = 2.0, P_1 = 23.0, T_1 = 389$ , maximum fuel supply to fuel manifold without small valve, no "buzz"
	69	$M\Delta = 2.0, P_1 = 23.0, T_1 = 389$ , maximum fuel supply to fuel manifold with small valve, no "buzz"
	70	$M\Delta = 2.0, P_1 = 18.0, T_1 = 389$ , maximum fuel supply to fuel manifold without small valve
	71	$M\Delta = 2.0, P_1 = 18.0, T_1 = 389$ , "buzz" point; $M\Delta = 2.0, P_1 = 11, T_1 = 389$ , maximum fuel supply to fuel manifold without small valve
	72	$M\Delta = 2.0, P_1 = 11, T_1 = 389$ , "buzz" point

	73	$M\Delta = 2.0, P_1 = 7.0, T_1 = 389$ , maximum fuel supply to fuel manifold without small valve
	74	$M\Delta = 2.0, P_1 = 7.0, T_1 = 389$ , maximum fuel supply to fuel manifold with small valve
	75	During record No. 75, engine condition was changed
	79	$M\Delta = 2.0, P_1 = 7.0, T_1 = 389$ , maximum fuel supply to fuel manifold without small valve
	80	$M\Delta = 2.0, P_1 = 7.0, T_1 = 389$ , "buzz" point
	81	$M\Delta = 1.53, P_1 = 12, T_1 = 320$ , maximum fuel supply to fuel manifold without small valve, no "buzz"
	82	$M\Delta = 1.53, P_1 = 12, T_1 = 320$ , maximum fuel supply to fuel manifold with small valve, no "buzz"
	83	$M\Delta = 1.53, P_1 = 7.0, T_1 = 320$ , maximum fuel supply to fuel manifold without small valve
	84	$M\Delta = 1.53, P_1 = 7.0, T_1 = 320$ , "buzz" point
	85	$M\Delta = 1.53, P_1 = 5.0, T_1 = 320$ , maximum fuel supply to fuel manifold without small valve, no "buzz"
	86	$M\Delta = 1.53, P_1 = 5.0, T_1 = 320$ , maximum fuel supply to fuel manifold with small valve, no "buzz"
	87	$M\Delta = 1.53, P_1 = 2.5$ , afterburner flameout; $M\Delta = 1.1, P_1 = 6.8, T_1 = 270$ , maximum fuel supply to fuel manifold without small valve
	88	$M\Delta = 1.1, P_1 = 6.8, T_1 = 270$ , "buzz" point
1968.7.18	*	Re-fine-tuned afterburner regulator diverter
	90	$M\Delta = 2.0, P_1 = 23, T_1 = 389$ , maximum afterburning, no "buzz"
1968.7.19	91	Repeated without "buzz"
	92, 93	$M\Delta = 1.1, P_1 = 6.8, T_1 = 270$ , maximum fuel supply to fuel manifold without small valve
	94	$M\Delta = 1.1, P_1 = 6.8, T_1 = 270$ , "buzz" point
	95	$M\Delta = 2.0, P_1 = 23, T_1 = 389$ , maximum fuel supply to fuel manifold without small valve, no "buzz"; Installed 800 in <sup>2</sup> saddle piece

1968.7.22	*	$M\Delta = 2.0, P_1 = 23, T_1 = 389$ , operated to 800 in <sup>2</sup> saddle piece limited area
1968.7.23	130	$M\Delta = 2.0, P_1 = 18, T_1 = 389$ , "buzz" point
	131	$M\Delta = 2.0, P_1 = 18, T_1 = 389$ , maximum fuel supply to fuel manifold without small valve
	132	Installed 710 in <sup>2</sup> saddle piece for test items of records 134-137; Repeated afterburning operation points of records 39-41
	134-136	Repeated maximum military of record 38
1968.7.24	137	$M\Delta = 1.1, P_1 = 6.8, T_1 = 269$ , maximum fuel supply to fuel manifold without small valve
	138	$M\Delta = 1.1, P_1 = 6.8, T_1 = 269$ , "buzz" point

## 8.0 Performance Verification Overview

### 8.1 Sea Level Condition

During tests simulating sea level conditions, several afterburner operating points were obtained. The initial curves were acquired at R01 values of 1.0 and 2.0, while later curves were obtained only at R01 = 1.0. Figure 16 compares these curves with the engine performance obtained on the test bed prior to high-altitude test cell trials. The peak points of all curves were limited by a 710 in<sup>2</sup> saddle stop. This is the reason why the thrust obtained was lower than the results from the test bed.

Tests on two current engines at different R01 values showed a thrust difference of 250 lbf, which can be attributed to pressure differences acting on the engine surface—as mentioned in Section 8.8. This adjustment raises the curves for records 9–12 to the same level as records 14–16. Even then, the high-altitude test cell performance was still approximately 300 lbf lower than the test bed results.

Comparing the afterburner performance curves at the same R01 value reveals that during testing, performance improved for a given F<sub>0</sub> / M<sub>1</sub>.

### 8.2 M<sub>0</sub> = 0.9, 36,089 ft

Fewer tests were conducted at M<sub>0</sub> = 0.9. These included one 'buzz' condition point with No. 1 fuel manifold not supplying fuel and equipped with a standard heat shield, and two test points with a drilled heat shield. The limiting condition for this state was the maximum available fuel supply (see Figure 1).

### 8.3 M<sub>0</sub> = 1.1, 36,089 ft

Initial verification at M<sub>0</sub> = 1.1 indicated a state limited by 'buzz.' Further verification showed that engine performance continued to deteriorate during 'buzz' operation.

Corresponding test points obtained during high-altitude test cell trials for engines 20003/6 and 20006/6 showed higher thrust at a given F<sub>0</sub> / M<sub>1</sub>. However, these tests used an early-type afterburner with No. 1 fuel manifold supplying fuel. Additionally, engine 20006 had a higher low-pressure operating line (+0.06 pressure ratio), resulting in approximately 2.5% higher net thrust.

### 8.4 M<sub>0</sub> = 1.53, Varying P<sub>1</sub> Values

At M<sub>0</sub> = 1.53 and 36,089 ft, P<sub>1</sub> values were varied. All tests were conducted with No. 1 fuel manifold not supplying fuel and with a drilled heat shield installed. The afterburner system experienced 'buzz' at P<sub>1</sub> = 5 and 7, but no 'buzz' occurred at P<sub>1</sub> = 12.0 with maximum fuel supply.

### 8.5 M<sub>0</sub> = 2.0, Varying P<sub>1</sub> Values

Here, P<sub>1</sub> varied from 7 to 22.88 psi (absolute). Except for 22.88 psi (absolute), all other P<sub>1</sub> values reached the 'buzz' point.

Table 3 summarizes the conditions at 36,089 ft.

Table 3 Summary of Conditions at 36,089 ft

Mach Number	P <sub>1</sub> (psi, absolute)	T <sub>1</sub> (°K)	XN (Ejector) Reference Value	Achieved Result	Remarks

0.9	5.43	251.5	7750	-0.65%	Fuel supply limit
1.1	6.83	269.7	9290*	+0.2% to -5.1%	'Buzz' limit
1.53	12.0	317.8	13260	+0.98%	Maximum afterburner fuel limit
2.0	22.88	389.8	15960*	+0.94%	Maximum afterburner fuel limit

\* Results at  $M\infty = 1.53$  and 2.0 were obtained after readjusting the afterburner fuel regulator splitter.

Figure 9 also compares the points obtained from the final test of engine 20003 with those from an early-type combustion chamber (where all fuel manifolds supplied fuel). Individual tests on the early-type combustion chamber used both early-type and current-type pressure ratio regulator needle valves. When these results were corrected for flow differences (taken from Figure 9a), it was shown that the early-type and current-type combustion chambers operated with the same efficiency.

## 8.6 Pressure Ratio Regulator Performance

Figures 12 and 13 illustrate the operating lines of the pressure ratio regulator across test conditions with Mach numbers ranging from 0.9 to 2.0, showing  $P_3 / P_6$  vs.  $P_3 / P_2$ ,  $P_3 / P_6$  vs.  $M \sqrt{T_1} / P_1$ , and  $P_2 / P_1$  vs.  $M \sqrt{T_1} / P_1$ . Figure 12 clearly shows the single inflection point characteristic of the needle valve and the corresponding  $M \sqrt{T_1} / P_1$  value at the inflection point. Figure 13 demonstrates the effect of the current-type needle valve on the low-pressure operating line.

## 8.7 Nozzle Calibration

For the first time in a high-altitude test cell, the true area of the engine nozzle assembly was determined using stops mounted on the nozzle.

During testing, three area stops—700, 800, and 900 in<sup>2</sup>—were used, and comparison curves were plotted between the nozzle area and nozzle position indicator readings under cold static calibration and hot operating conditions.

Near maximum conditions, the true nozzle area was approximately 40 in<sup>2</sup> smaller than the nozzle position indicator reading.

Figure 14 also shows the relationship between  $C_d$  and nozzle pressure ratio, from which the effective area can be derived.

## 8.8 Engine Surface Pressure

In total thrust calculations, the pressure acting on the engine surface was considered. For example, under sea level conditions with a ram pressure ratio nearly equal to 1, as mentioned in Section 8.1, thrust increased by 200–300 lbf. This increment was sufficient to align the two simulated sea level afterburner operations ( $R01 = 1.0$  and 2.0) with records 9–16. A more detailed technical document considering surface pressure measurements is being prepared.

The thrust values quoted throughout this report do not account for pressures acting along the engine's outer surface. Therefore, they are comparable to thrust values from other engines in previous reports.

## 9.0 Figures

- Figure 1:  $X\infty\infty\infty$  vs.  $F\infty / M_1$ ,  $M\infty = 0.9$ ,  $P_1 = 5.43$

- Figure 2:  $X_{NEI}$  vs.  $F_R / M_1$ ,  $M_1 = 1.1$ ,  $P_1 = 6.83$
- Figure 2a:  $\Omega_1$  vs.  $F_R / M_1$ ,  $M_1 = 1.1$ ,  $P_1 = 6.83$
- Figure 3:  $X_{NEI}$  vs.  $F_R / M_1$ ,  $M_1 = 1.53$ ,  $P_1 = 5.0$
- Figure 4:  $X_{NEI}$  vs.  $F_R / M_1$ ,  $M_1 = 1.53$ ,  $P_1 = 7.0$
- Figure 5:  $X_{NEI}$  vs.  $F_R / M_1$ ,  $M_1 = 1.53$ ,  $P_1 = 12.0$
- Figure 6:  $X_{NEI}$  vs.  $F_R / M_1$ ,  $M_1 = 2.0$ ,  $P_1 = 7.0$
- Figure 7:  $X_{NEI}$  vs.  $F_R / M_1$ ,  $M_1 = 2.0$ ,  $P_1 = 11.0$
- Figure 8:  $X_{NEI}$  vs.  $F_R / M_1$ ,  $M_1 = 2.0$ ,  $P_1 = 18.0$
- Figure 9:  $X_{NEI}$  vs.  $F_R / M_1$ ,  $M_1 = 2.0$ ,  $P_1 = 22.88$
- Figure 9a:  $M_1$  vs.  $F_R / M_1$ ,  $M_1 = 2.0$ ,  $P_1 = 22.88$
- Figure 10:  $P_1$  vs.  $F_R / M_1$ ,  $M_1 = 1.53$  (Buzz Point)
- Figure 11:  $P_1$  vs.  $F_R / M_1$ ,  $M_1 = 2.0$  (Buzz Point)
- Figure 12:  $S637 / S629$  vs.  $M_1 \sqrt{T_1} / P_1$
- Figure 13:  $P_{200} / P_1$  vs.  $M_1 \sqrt{T_1} / P_1$
- Figure 14: Nozzle Area vs. Nozzle Position Indicator Angle
- Figure 15: Hot Nozzle Area vs. Cold Nozzle Area
- Figure 16:  $X_c$  vs.  $F_R / M_1$  Test Bed Performance

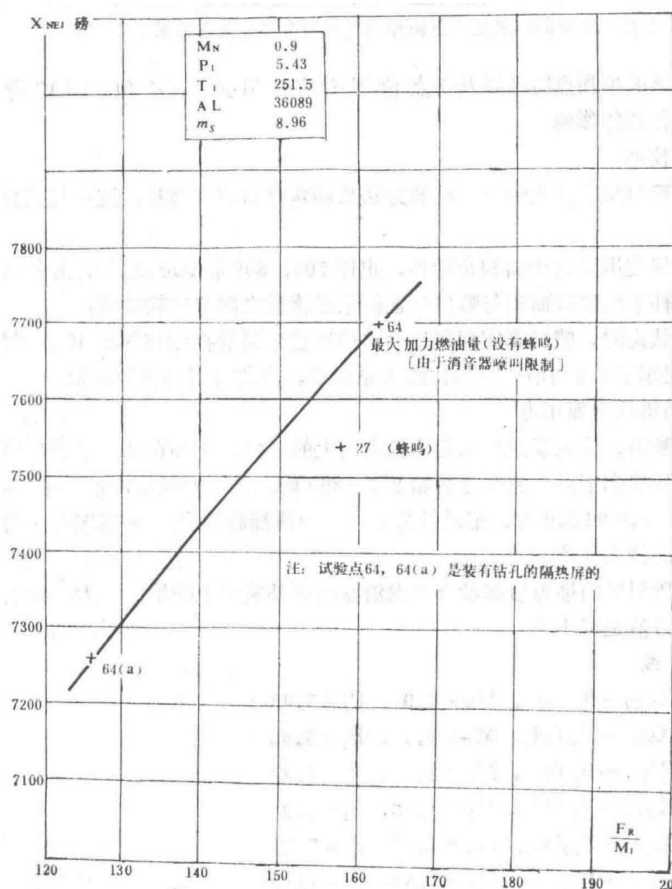


Figure 1 Afterburner Performance of Spey MK202 Engine 20003/7

Graph showing the afterburner performance characteristics of the Spey MK202 engine (serial 20003/7) under specified conditions.

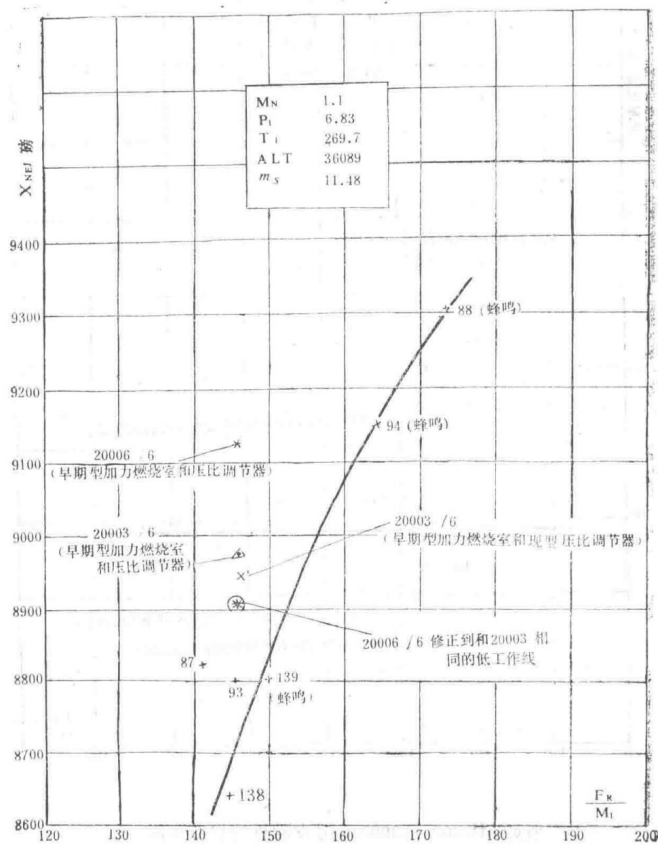


Figure 2 Afterburner Performance of Spey MK202 Engine 20003/7

Graph depicting the afterburner performance of the Spey MK202 engine (serial 20003/7) at  $M_\infty = 1.1$ .

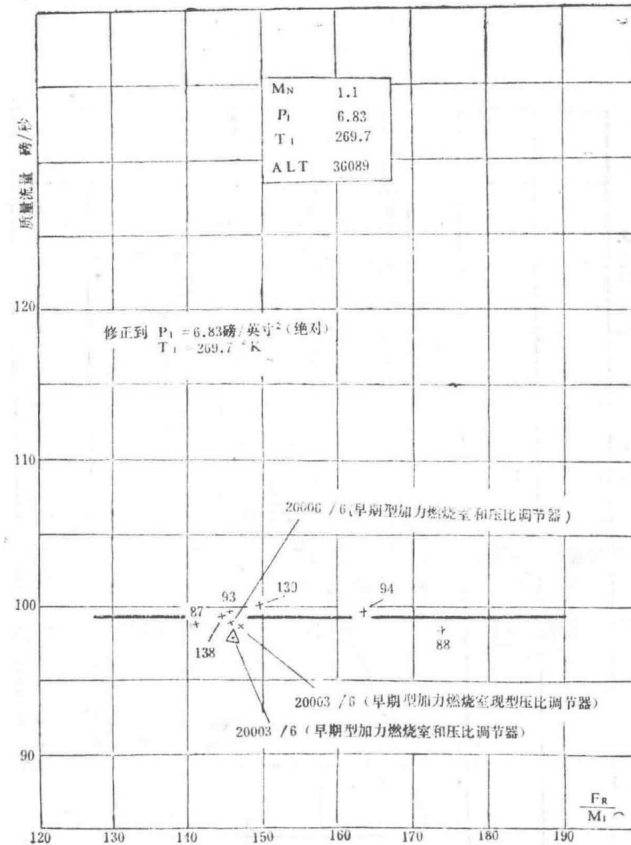


Figure 2a Afterburner Performance of Spey MK202 Engine 20003/7

Graph showing additional afterburner performance data for the Spey MK202 engine (serial 20003/7) at  $M_\infty = 1.1$ .

— Section 30 —  
Content from Original Document (Pages 146-150)

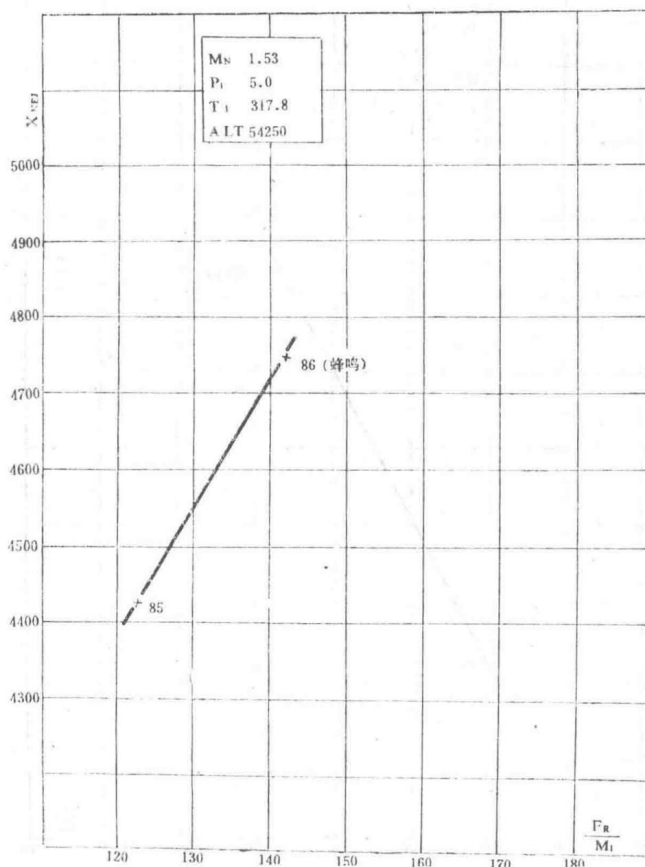


Figure 3 Afterburning Performance of Spey MK202 Engine No. 20003/7  
Graphical representation of afterburning performance parameters for Spey MK202 engine No. 20003/7.

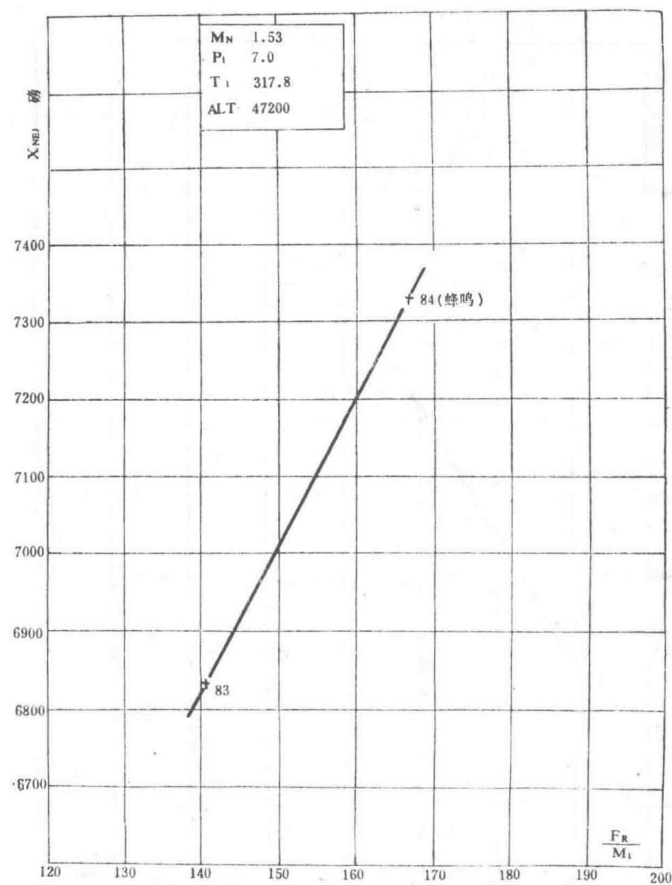


Figure 4 Afterburning Performance of Spey MK202 Engine No. 20003/7

Graphical representation of afterburning performance parameters for Spey MK202 engine No. 20003/7.

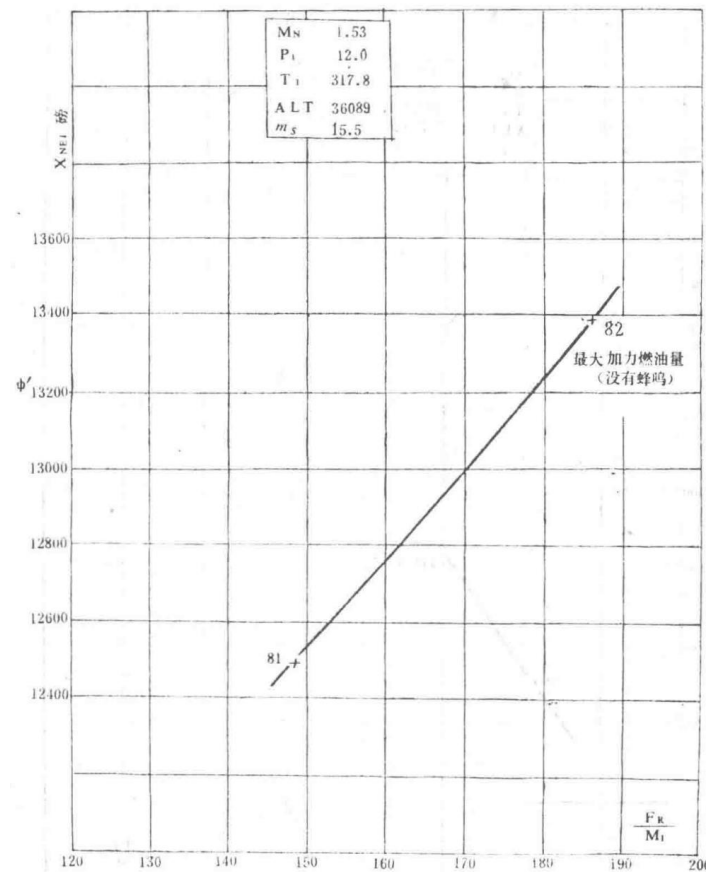


Figure 5 Afterburning Performance of Spey MK202 Engine No. 20003/7

Graphical representation of afterburning performance parameters for Spey MK202 engine No. 20003/7.

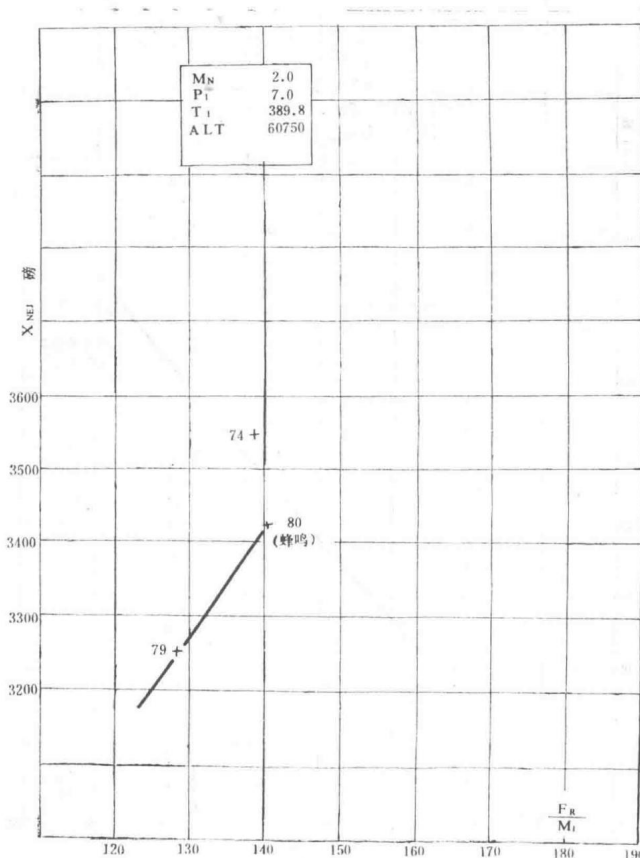


Figure 6 Afterburning Performance of Spey MK202 Engine No. 20003/7

Graphical representation of afterburning performance parameters for Spey MK202 engine No. 20003/7.

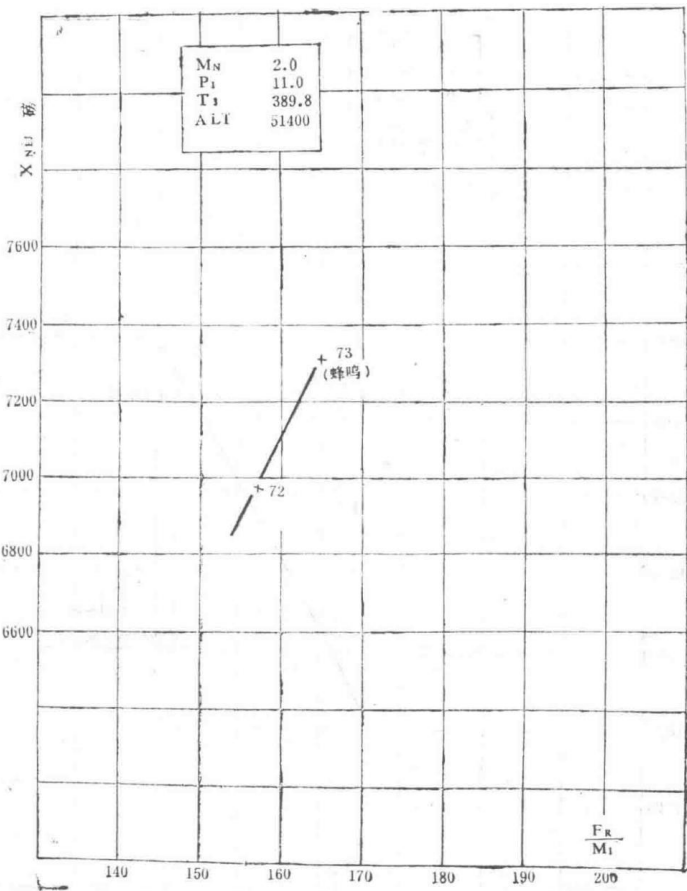
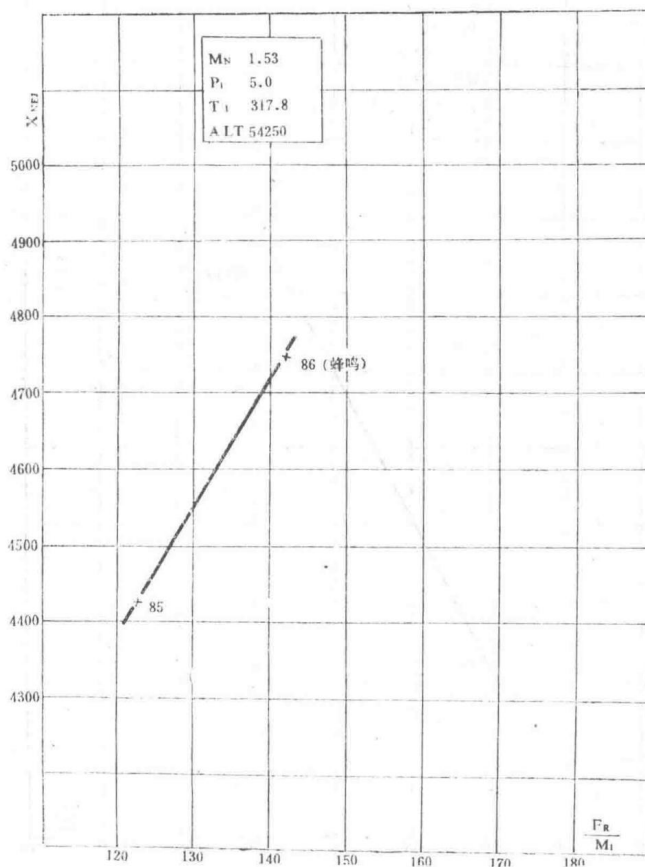


Figure 7 Afterburning Performance of Spey MK202 Engine No. 20003/7

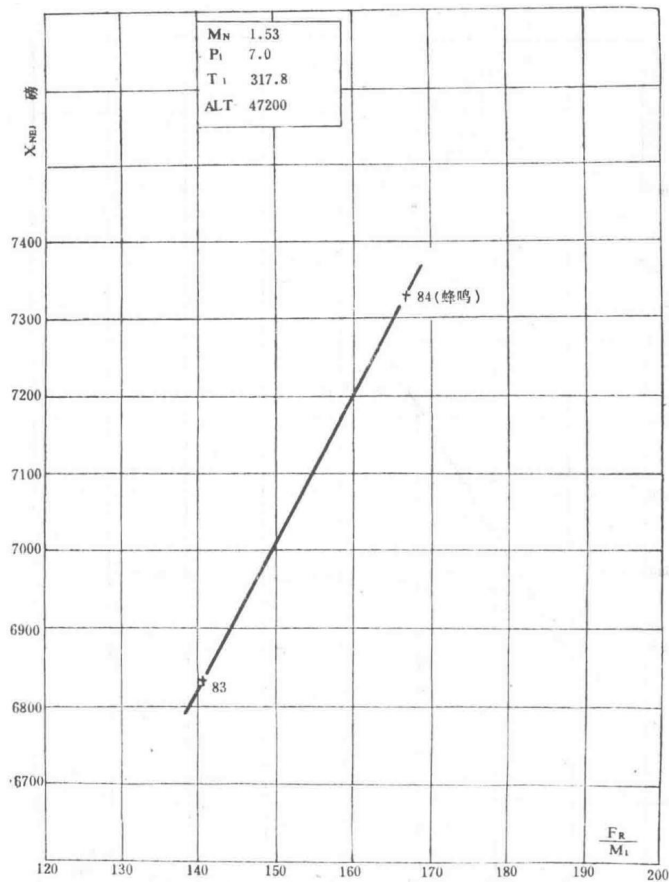
Graphical representation of afterburning performance parameters for Spey MK202 engine No. 20003/7.

## Afterburning Performance Analysis



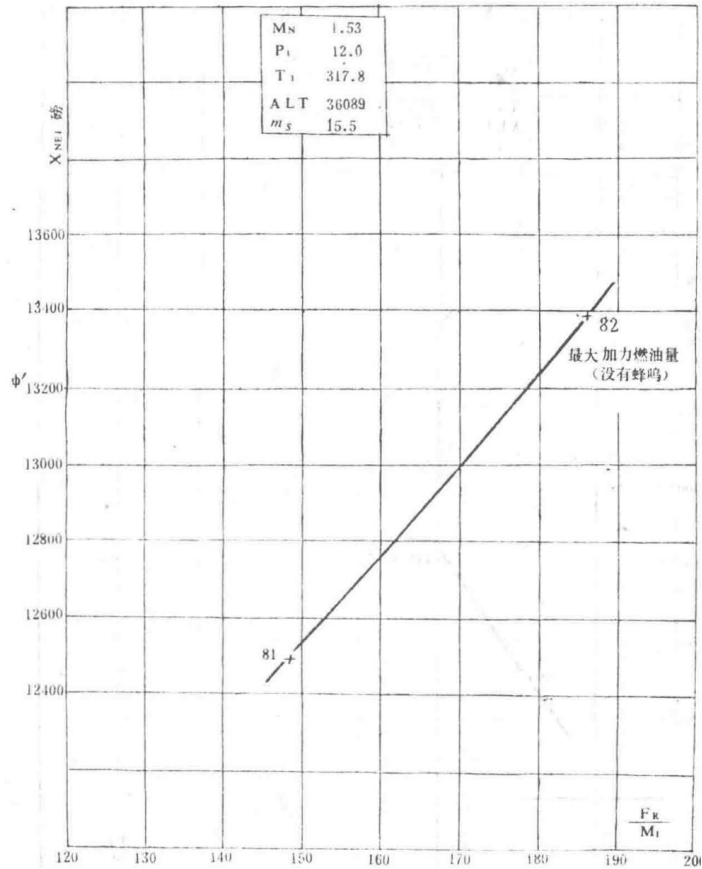
Conditions:  $M_N = 2.0$   $P_1 = 11.0$   $T_1 = 389.8$  K  $ALT = 51400$

The graph illustrates the variation of engine rotational speed ( $X\Box L$ ) with respect to the Mach number ( $M_1$ ). Data points 72 and 73 indicate specific performance values under these conditions.



Conditions:  $M_N = 1.53$   $P_1 = 12.0$   $T_1 = 317.8$  K  $ALT = 36089$   $m_s = 15.5$

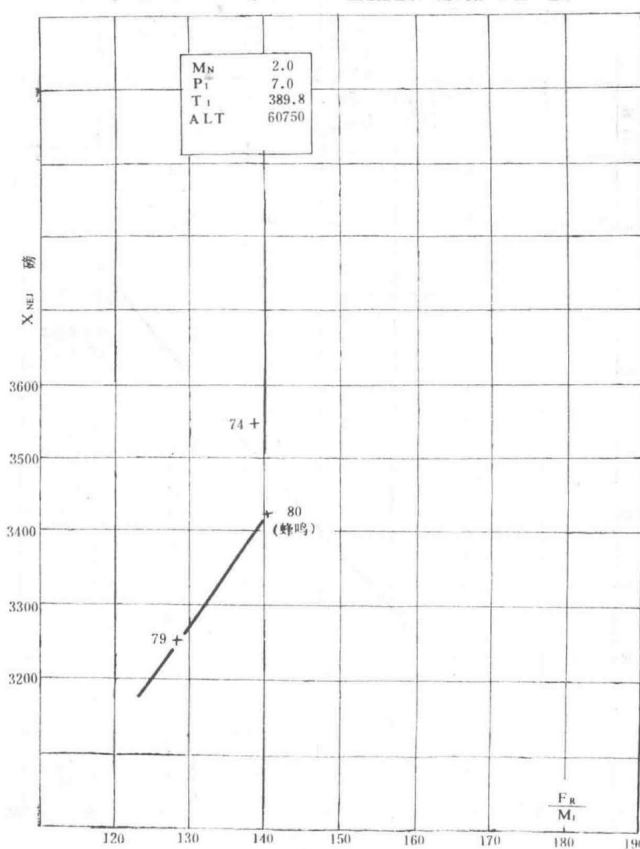
This graph depicts the fuel flow ratio ( $\Phi$ ) as a function of the Mach number ( $M_1$ ). The maximum afterburner fuel flow (with nozzle fully open) is indicated by data points 81 and 82.



Graph showing the relationship between net thrust ( $X\Box ET$ ) and Mach number ( $M_1$ ) under specified conditions:  $M_N = 1.53$ ,  $P_1 = 7.0$ ,  $T_1 = 317.8$  K,  $ALT = 47200$ .

Conditions:  $M_N = 1.53$   $P_1 = 7.0$   $T_1 = 317.8$  K  $ALT = 47200$

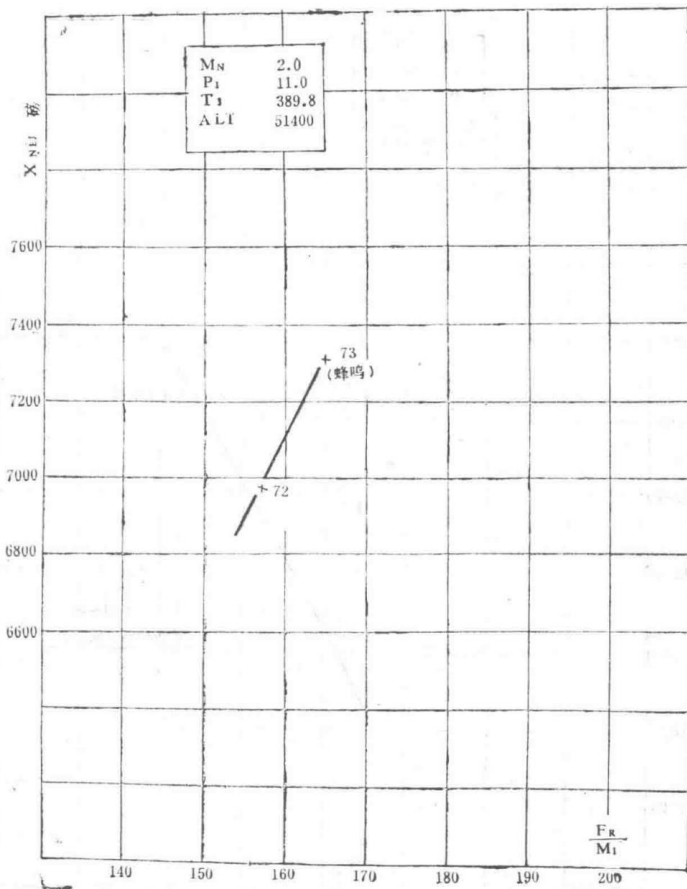
The graph shows the net thrust ( $X\Box ET$ ) variation with respect to the Mach number ( $M_1$ ). Data points 83 and 84 represent specific thrust values under these conditions.



Graph showing the relationship between engine rotational speed ( $X\Box L$ ) and Mach number ( $M_1$ ) under specified conditions:  $M_N = 2.0$ ,  $P_1 = 7.6$ ,  $T_1 = 389.8$  K,  $ALT = 60750$ .

Conditions:  $M_N = 2.0$   $P_1 = 7.6$   $T_1 = 389.8$  K  $ALT = 60750$

This graph illustrates the engine rotational speed ( $X\Box L$ ) as a function of the Mach number ( $M_1$ ). Data points 74, 79, and 80 indicate specific performance values under these conditions.



Graph showing the relationship between net thrust ( $X\Box ET$ ) and Mach number ( $M_1$ ) under specified conditions:  $M_N = 1.53$ ,  $P_1 = 5.0$ ,  $T_1 = 317.8$  K,  $ALT = 54250$ .

Conditions:  $M_N = 1.53$   $P_1 = 5.0$   $T_1 = 317.8$  K  $ALT = 54250$

The graph depicts the net thrust ( $X\Box ET$ ) variation with respect to the Mach number ( $M_1$ ). Data points 85 and 86 represent specific thrust values under these conditions.

— Section 31 —  
Content from Original Document (Pages 151-155)

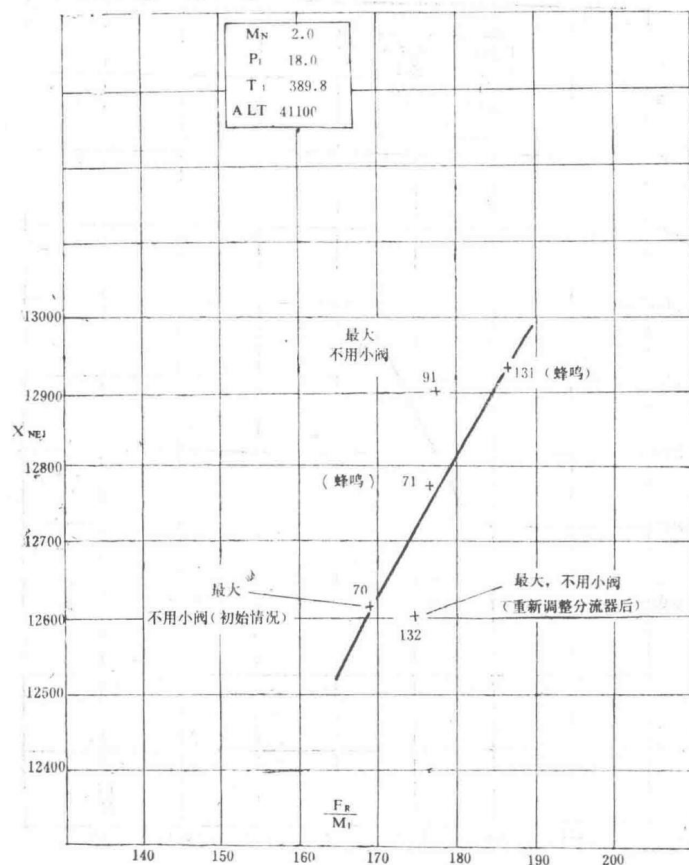
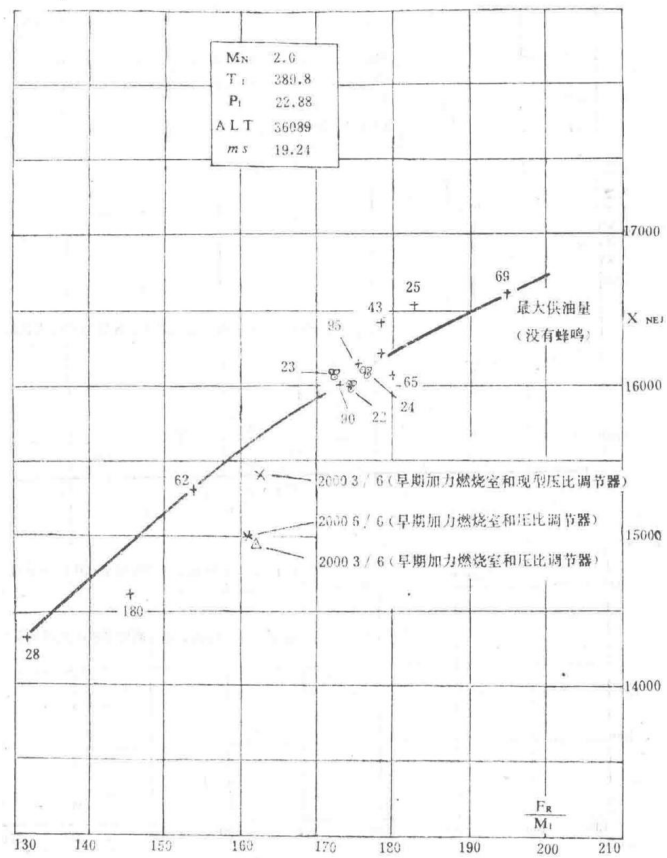


Figure 8 Afterburning Performance of Spey MK202 Engine No. 20003/7

Graph showing the afterburning performance characteristics of the Spey MK202 engine (No. 20003/7).



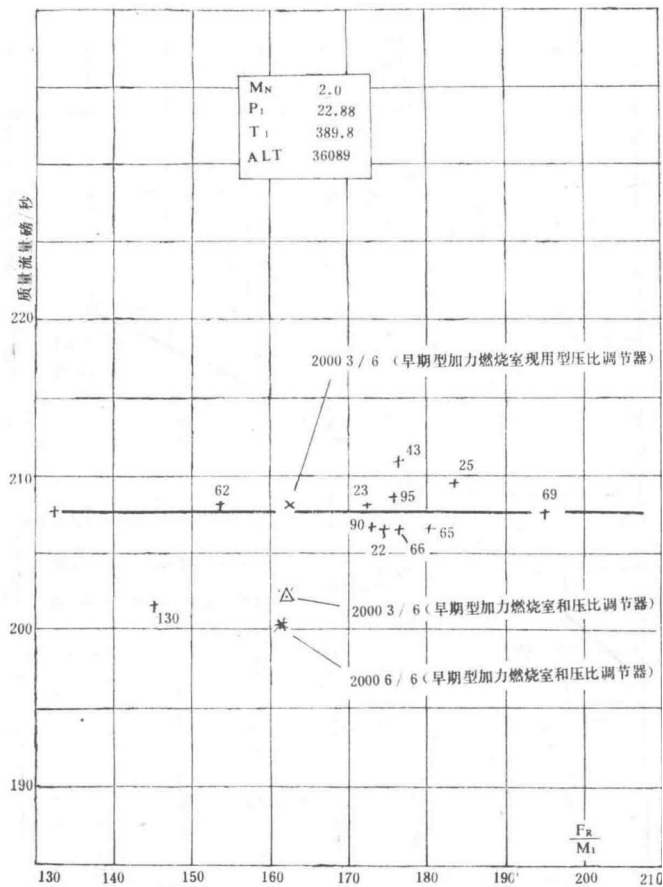


Figure 9a Afterburning Performance of Spey MK202 Engine No. 20003/7

Additional graph detailing the afterburning performance of the Spey MK202 engine (No. 20003/7).

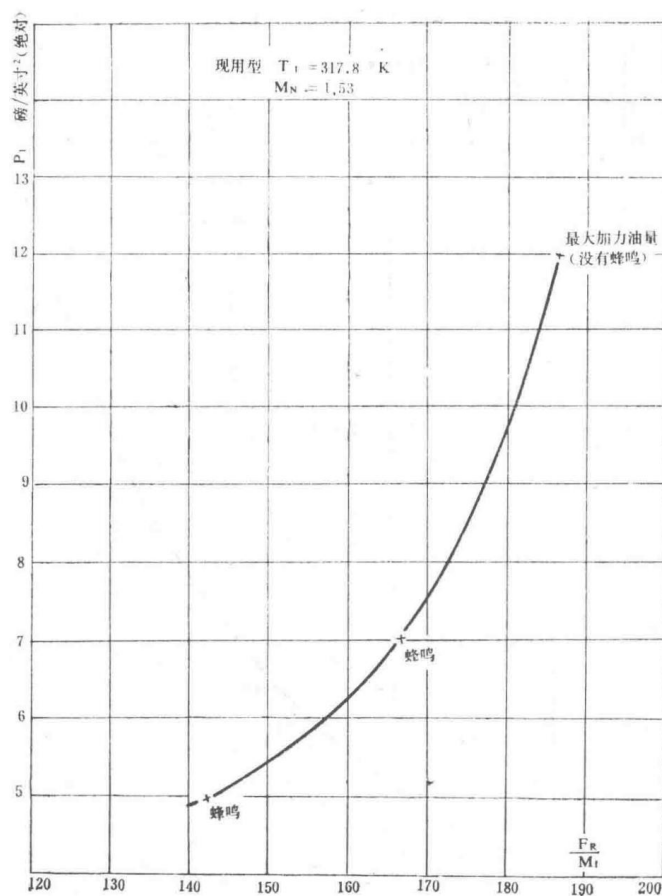


Figure 10 Variation of Buzz Boundary with  $P_1$  for Spey MK202 Engine No. 20003/7 ( $M\Delta = 1.53$ )

Graph showing how the buzz boundary of the Spey MK202 engine (No. 20003/7) varies with inlet pressure  $P_1$  at a Mach number of 1.53.

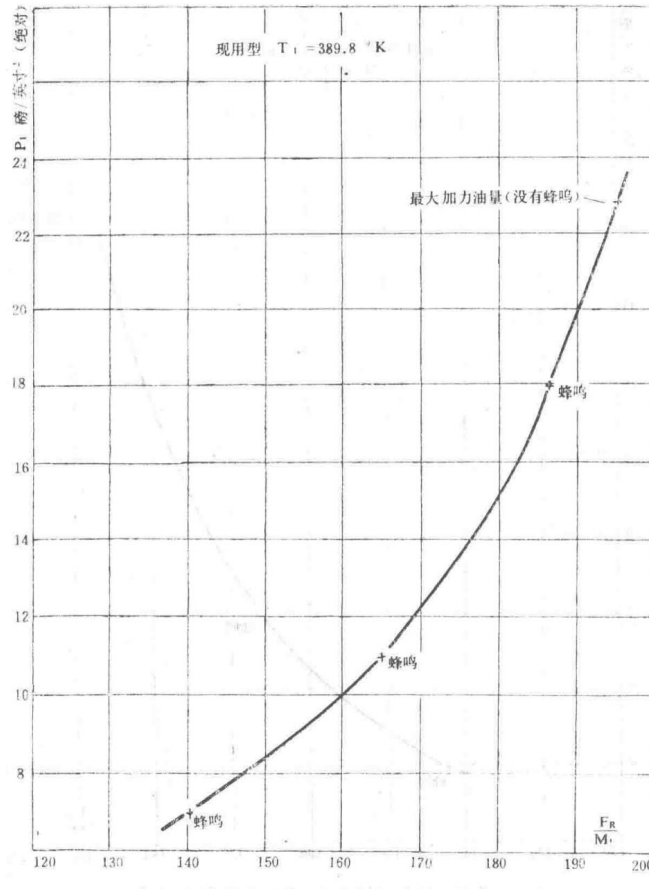


Figure 11 Variation of Buzz Boundary with  $P_1$  for Spey MK202 Engine No. 20003/7 ( $\Delta M\Delta = 2.0$ )

Graph showing how the buzz boundary of the Spey MK202 engine (No. 20003/7) varies with inlet pressure  $P_1$  at a Mach number difference of 2.0.

## Performance Analysis

The following section presents the performance characteristics of the Spey MK202 engine (No. 20003/7), focusing on afterburning performance and buzz boundary variations under different conditions.

Test Conditions for Afterburning Performance (First Graph)

Parameter	Value
$M\Delta$	2.0
$T_1$ (K)	389.8
$P_1$ (kPa)	22.88
ALT (m)	36039
$m\Delta$ (kg/s)	19.24

The first graph illustrates the relationship between engine parameters under specific test conditions. The key observations include the maximum afterburning thrust limits and the occurrence of buzz phenomena.

- The line labeled '最大加力油量 (没有蜂鸣)' indicates the maximum afterburning fuel flow without buzz occurrence.

- The '蜂鸣' (buzz) boundary is marked at various points along the thrust curve.
- Early afterburner fuel control and current adjusted models are compared at different thrust settings.

Test Conditions for Afterburning Performance (Second Graph)

Parameter	Value
M <sub>1</sub>	2.0
P <sub>1</sub> (kPa)	18.0
T <sub>1</sub> (K)	389.8
ALT (m)	41100

The second graph provides further insights into the engine's performance at a higher altitude of 41,100 meters. The buzz boundary and maximum afterburning limits are again highlighted.

- The '新调整分流器后' (after new flow divider adjustment) shows improved performance without buzz.
- The '蜂鸣' (buzz) points are plotted to indicate the operational limits.

Test Conditions for Pressure Ratio Performance

Parameter	Value
Model Type	Current
T <sub>1</sub> (K)	317.8
M <sub>1</sub>	1.53

The graph of pressure ratio (P<sub>1</sub>) versus corrected thrust (F<sub>1</sub> / M<sub>1</sub>) demonstrates the engine's buzz boundary at a Mach number of 1.53. The '蜂鸣' (buzz) points are critical for understanding the operational envelope.

Test Conditions for Pressure Ratio at Higher P<sub>1</sub> (Fourth Graph)

Parameter	Value
Model Type	Current
T <sub>1</sub> (K)	389.8
M <sub>1</sub>	2.0

The final graph shows the pressure ratio performance at a higher inlet temperature of 389.8 K, illustrating the buzz boundary and maximum afterburning limits.

— Section 32 —  
Content from Original Document (Pages 156-160)

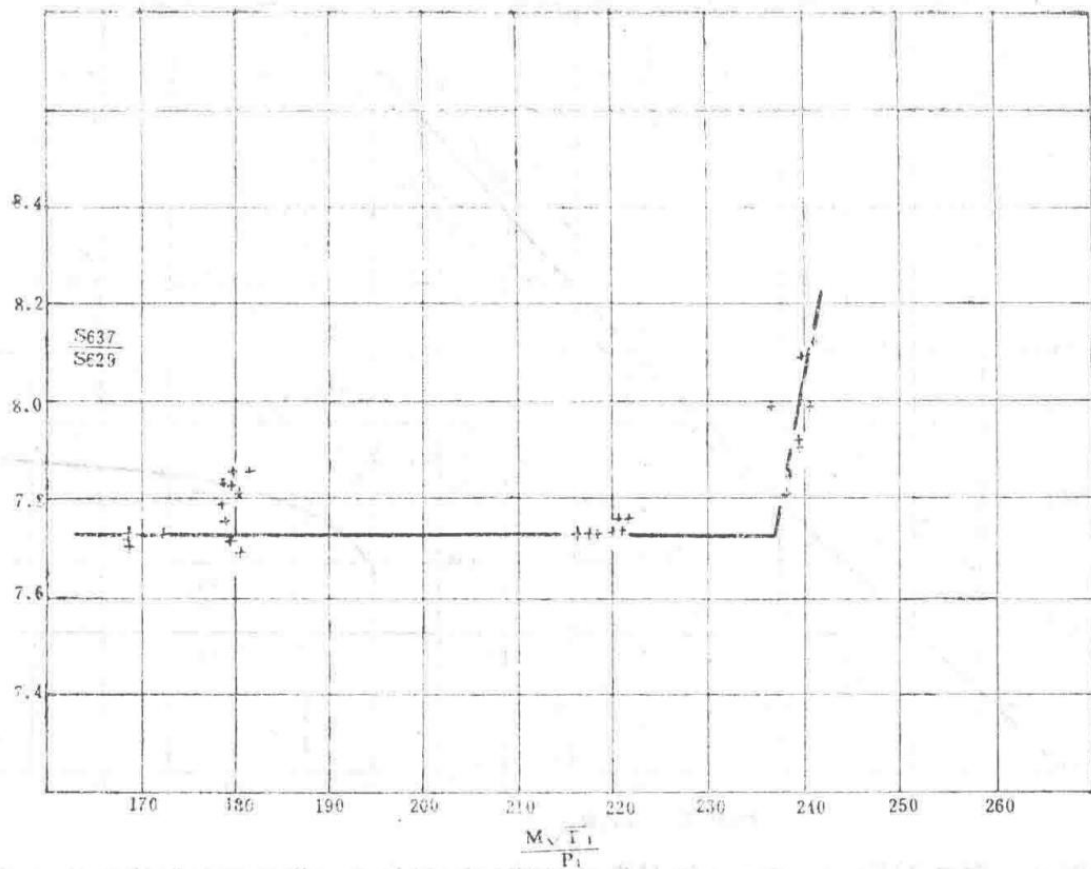


Figure 12: Inflection Points and Characteristics of the Pressure Ratio Regulator with Current-Type Needle Valve for Spey MK202 Engine No. 20003/7

Graph showing the inflection points and operational characteristics of the pressure ratio regulator equipped with the current-type needle valve for the Spey MK202 engine.

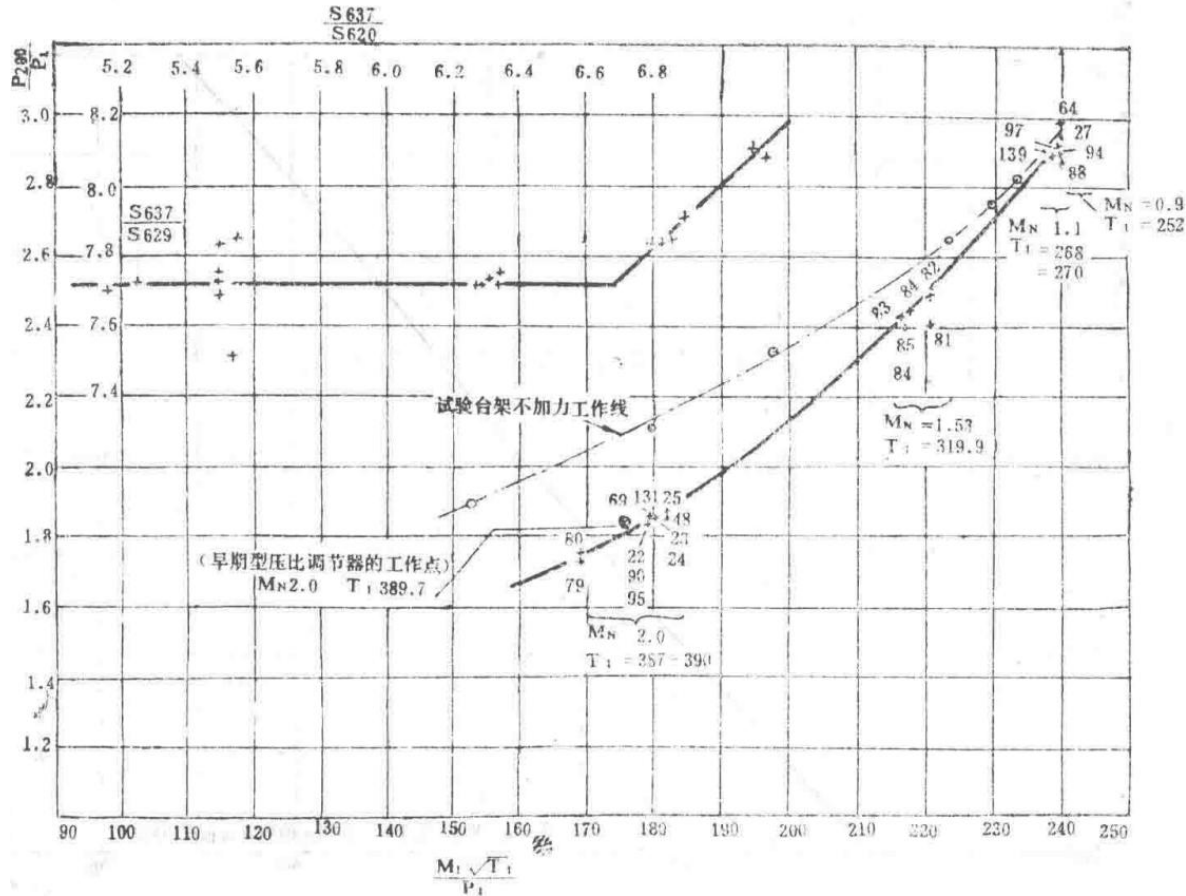


Figure 13: Low-Pressure Operating Lines and Pressure Ratio Regulator Operating Lines at Different Mach Numbers ( $M\Box$ ) for Spey MK202 Engine No. 20003/7

Graph depicting the low-pressure operating lines and the pressure ratio regulator operating lines at various Mach numbers for the Spey MK202 engine.

$M\Box$

Mach number notation used in the graphs.

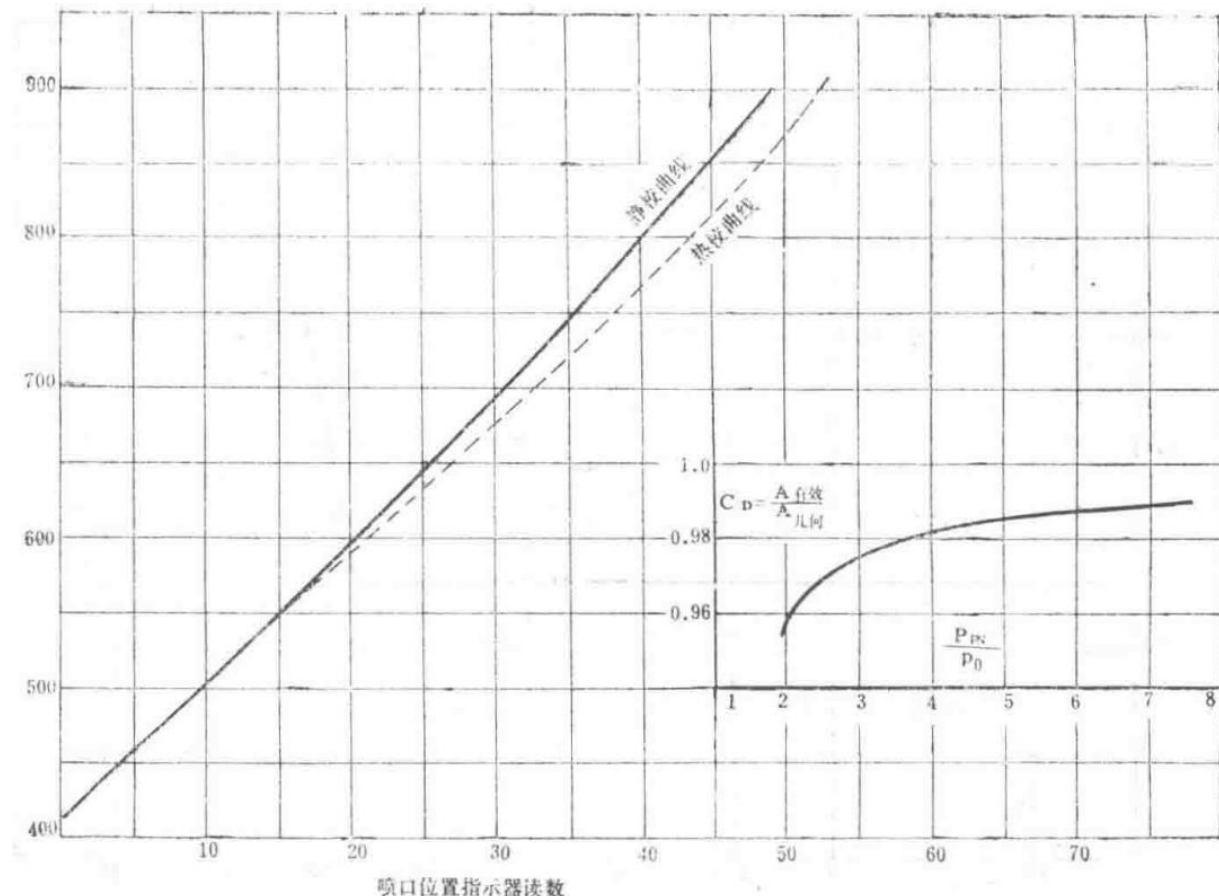


Figure 14: Relationship Between Nozzle Area and Nozzle Position Indicator Reading for Spey MK202 Engine No. 20003/7

Graph showing the correlation between the nozzle area and the nozzle position indicator readings for the Spey MK202 engine.

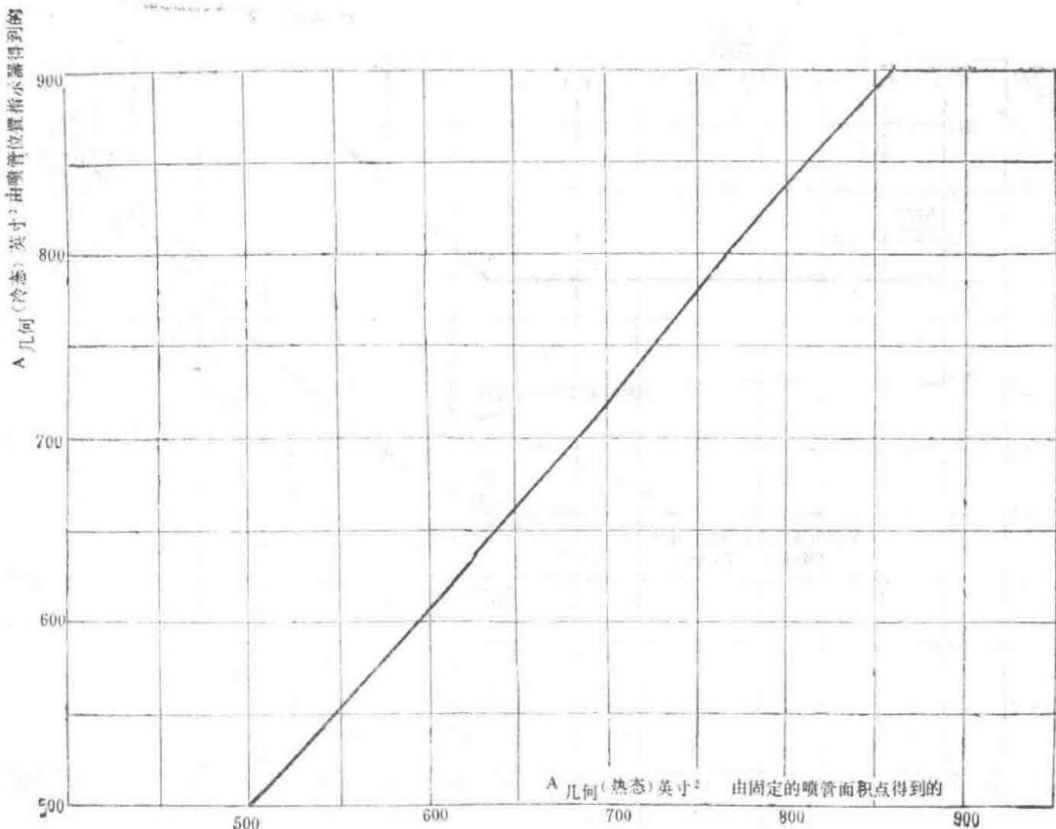


Figure 15: Relationship Between Cold Nozzle Area and Hot Nozzle Area for Spey MK202 Engine No. 20003/7 (with Afterburner H366T)

Graph illustrating the relationship between cold and hot nozzle areas for the Spey MK202 engine equipped with afterburner H366T.

Uncaptioned image, potentially related to engine components or test setup.

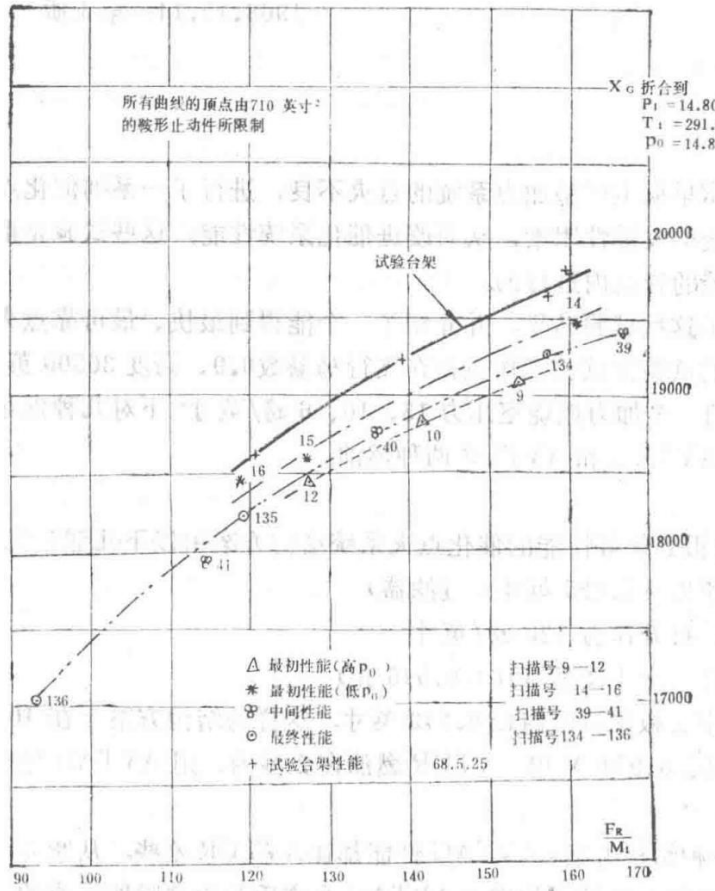


Figure 16: Comparison of Afterburning Performance at Sea Level Test Stand and Sea Level Condition in Altitude Test Facility for Spey MK202 Engine No. 20003/7

Graph comparing the afterburning performance of the Spey MK202 engine at sea level test stand and sea level condition in an altitude test facility.

### Combustion Research Report

Report Title	Report Number
Combustion Research Report	CRR 12043
Spey MK202 Afterburner - Ignition Tests of Centrally Mounted Catalytic Igniter	

Version 1, dated 14 October 1968.

## 1.0 Abstract

Due to poor ignition performance of the early production afterburning system of the RB168-25R, a series of catalytic ignition system rig tests were conducted to investigate key factors affecting system performance, thereby improving the catalytic system's performance. These tests involved installing a complete ignition system in an 8-inch diameter duct.

This report outlines the test results and introduces an improved system that achieves the fastest and most reliable ignition.

The rig test work discussed in this report includes tests conducted at flight Mach numbers of 0.9, altitudes of 36,500 feet, 44,500 feet, and 53,000 feet, corresponding to afterburner pressures of 15, 10, and 6 psi, respectively, for various catalytic igniter configurations. Both AVTAG and AVTUR fuels were tested.

## 2.0 Conclusions

1. The recommended catalytic ignition system configuration for optimal performance consists of the following components:
  2. 1) Venturi flow restrictor (0.025-inch + filter)
  3. 2) Check valve with an opening pressure of 120 psi
  4. 3) Production-type fuel distribution ring with conical spray ( $16 \times 0.046\text{-inch holes}$ )
  5. 4) Afterburner strut restrictor with an inner diameter of 0.043 inches. This configuration can reliably ignite within 2 seconds using AVTUR fuel and within 3 seconds using AVTAG fuel at a pressure of 10 psi (absolute) (44,500 feet, 0.9 M $\square$ ).
1. For each configuration, AVTAG performance was slightly inferior to AVTUR. Ultraviolet recorder oscillograms indicated that this was due to the more volatile AVTAG fuel boiling within the Venturi tube.
2. With a 120 psi check valve, the size of the afterburner strut restrictor was not as critical as when using the earlier production-type 200 psi check valve.
3. The 120 psi check valve is superior to the 200 psi check valve. Under certain engine conditions, using the 120 psi check valve increases S635 by 80 psi, improving ignition time with the optimal afterburner strut restrictor size.
4. Testing with both fuels showed that the early production-type fuel distribution ring improved the performance of the early production system.
5. For any specific catalytic igniter arrangement, the optimal afterburner strut restrictor size depends on the afterburner pressure. For a defined configuration, the optimal restrictor sizes at pressures of 15, 10, and 6 psi (absolute) are 0.051, 0.047, and 0.041 inches, respectively.
6. The effect of inlet temperature variation was studied, concluding that within the S635 range encountered in aircraft, changes in inlet temperature have minimal impact on ignition time. The temperature variation range was from 720 K to 930 K.

## 3.0 Test Equipment

Atmospheric tests were conducted from March 15, 1968, to April 24, 1968, on Combustion Rig 'A' No. 7.

Tests at pressures of 10 psi and 6 psi were conducted from May 8, 1968, to May 31, 1968, at the Lucas Company's Burnley altitude test facility.

## 4.0 Introduction

The centrally mounted catalytic igniter on the early production engines consisted of a 200 psi check valve, a 0.036-inch afterburner strut restrictor, and a 0.025-inch Venturi restrictor. This system could reliably ignite at a Mach number of 0.9 and an altitude of 40,000 feet using AVTUR fuel, and at 32,000 feet using AVTAG fuel. To improve the fuel filling time, which was considered to occupy a significant portion of the ignition time, the hole size in the catalytic fuel distribution ring was increased from 0.039 inches to 0.046 inches, and a 120 psi check valve was installed. This check valve provided an additional 80 psi fuel pressure at the catalytic igniter inlet for given pump pressure and altitude conditions. The 0.025-inch Venturi restrictor was replaced with a  $7 \times 0.035\text{-inch damper}$ , which had the same flow coefficient in cold tests, to prevent blockage from gum deposits caused by fuel boiling. For a given pump pressure, increasing the afterburner strut restrictor to 0.040 inches increased flow and reduced fuel filling time.

However, tests conducted on the production-type configuration in the altitude test facility showed deteriorated ignition performance.

## 5.0 Test Objectives

The objective of this series of tests was to investigate the ignition capabilities of both the early production and production-type catalytic systems. Further tests were conducted to study the influence of key system factors and

thereby improve ignition performance.

From these results, an improved catalytic ignition system was developed that enhances ignition performance for both AVTUR and AVTAG fuels.

## 6.0 Test Rig

As shown in Figure 1, the catalytic igniter was installed in an 8-inch diameter duct. Air was supplied through a preheater to achieve airflow Mach numbers representative of those at the leading edge of the catalytic igniter on the engine. Most tests were conducted at 850 K, approximately 80 K lower than the temperature required at the center of the afterburner on the engine, to prevent overheating of the test rig. However, some tests were conducted at 930 K to observe the effect of temperature on ignition.

Sensors were used to record the transient pressure rise at various points in the catalytic igniter fuel system, and a fuel flow meter of the measuring flask type recorded fuel flow. An event marker connected to the fuel solenoid valve circuit provided a mark on the ultraviolet recorder oscillogram when the solenoid valve was activated. Successful ignition was recorded by changes in pressure within the 8-inch duct, sensed by a pressure transducer designated S503. A typical oscillogram is shown in Figure 2.

A camera was installed to observe the ignition through the test rig's exhaust silencer, focusing on the catalytic igniter cone. Activating the solenoid valve produced a light spot, marking the ignition event on the photosensitive paper.

The fuel system of the test rig is shown in Figure 1. An ejector formed the overflow system on the afterburner, used to clear fuel from the catalytic system supply lines after the catalytic system was shut down, preventing gumming and subsequent restrictor blockage. An exhaust pipe was used to reduce the pressure in the duct to approximately 50 psi before the catalytic system was activated, matching the back pressure required in the main fuel supply line encountered on the engine. All piping and components downstream of the check valve were identical to those on the engine.

## 7.0 Test Procedure

The duct mass flow rate, temperature, and pressure were adjusted, and the fuel system upstream of the check valve was filled. The exhaust pipe solenoid valve was operated to reduce the pressure in the fuel line to approximately 50 psi. The constant pressure pump was then set to 1000 psi, and ignition was initiated.

$$CD = (A_{ff}c) / (Ag \cdot c)$$

Discharge coefficient equation shown in the graph.

$$(P_2)/(P_1)$$

Pressure ratio equation shown in the graph.

$$M_1 \sqrt{((T_1)/(P_1))}$$

Non-dimensional mass flow parameter used in the graphs.

— Section 33 —  
Content from Original Document (Pages 161-165)

Activate the ultraviolet recorder and start the camera 1 to 2 seconds before engaging the catalytic igniter. A 6-second ignition window is permitted when the chamber pressure is 15 psi, and an 8-second window is allowed at lower chamber pressures.

Repeat the tests for different pump pressures, performing two ignition attempts at each pressure.

In Burnley, photography was impossible due to the closed-loop suction-type test setup.

Tests for different structural configurations and fuels are shown in Figure 4.

The test results are analyzed by plotting a set of ignition time versus S635 pressure curves. For a given structural configuration, a single curve is provided on the graph. From these curves, ignition time versus restrictor R1 plots can be derived for a given S635 pressure.

## 8.0 Test Conditions

### Derby Tests (Atmospheric Pressure)

Parameter	Value 1	Value 2
Chamber Pressure (psi, absolute)	15	15
Chamber Temperature (°K)	850	720
Mass Flow Rate (lb/s)	5.09	5.53
Mach Number at Catalytic Igniter Leading Edge	0.35	0.35
Ultraviolet Recorder Speed (in/s)	8	-

### Burnley Tests (Below Atmospheric Pressure)

Parameter	Value 1	Value 2	Value 3	Value 4
Chamber Pressure (psi, absolute)	10	10	6	6
Chamber Temperature (°K)	850	930	850	930
Mass Flow Rate (lb/s)	3.46	3.30	2.07	1.99
Mach Number at Catalytic Igniter Leading Edge	0.35	0.35	0.35	0.35
Ultraviolet Recorder Speed (in/s)	4	-	-	-

#### Instrumentation and Measurement Ranges

Instrumentation	Derby Range	Burnley Range
Flowmeter Pressure Transducer (S1)	100 gal/h	100 gal/h
(S2)	15 psi	10 psi
(S3)	15 psi	10 psi

(S635)	300 psi	100 psi
(S635)	1000 psi	300 psi
(S503)	10 psi	5 psi

## 9.0 Discussion

Given the extensive work conducted, presenting all results would make this report overly lengthy. Therefore, only relevant graphs are included, which are:

- Effect of afterburner pressure – See Section 9.1
- Effect of afterburner temperature – See Section 9.2
- Effect of fuel – See Section 9.3
- Effect of fuel manifold – See Section 9.4
- Catalytic igniter stability boundary – See Section 9.5
- Effect of check valve – See Section 9.6
- Effect of 0.025-inch restrictor + filter – See Section 9.7

### 9.1 Effect of Afterburner Chamber Pressure

Figure 5 shows the ignition time variation with afterburner strut restrictor at three different chamber pressures for a constant S635 pressure line.

It is observed that smaller restrictors reduce ignition time at all chamber pressures by increasing fuel pressure (S635). However, larger restrictors show intersecting curves, where higher fuel pressure results in longer ignition times, likely due to over-rich conditions at the cone.

For this specific configuration, as chamber pressure decreases from 15 psi to 10 psi and then to 6 psi (absolute), the optimal restrictor size decreases from 0.051 inches to 0.047 inches and then to 0.041 inches.

At an afterburner pressure of 15 psi (absolute), the predetermined S635 is approximately 170 psi (absolute); at 10 psi (absolute), it is approximately 130 psi (absolute). When the chamber pressure is 6 psi (absolute) with a 120 psi (absolute) check valve, the S635 is approximately 110 psi (absolute). For a 0.040-inch restrictor configuration using AVTUR fuel, the ignition times are:

Chamber Pressure $p_0$ (psi)	Ignition Time (seconds)
15	1.10
10	2.65
6	3.10

It is also noted that as chamber pressure decreases, the curves become steeper due to reduced stability limits, making the selection of R1 more critical. This is confirmed by the catalytic igniter stability curves in Figure 9.

The same effects were observed for AVTAG fuel.

### 9.2 Effect of Afterburner Chamber Temperature

Figure 6 illustrates the effect of temperature on ignition time using AVTUR fuel. At lower fuel pressures, higher temperatures result in longer ignition times, likely due to fuel vaporization. At higher pressures, this effect diminishes as fuel flow increases.

At a predetermined S635 pressure of 170 psi, the effect of temperature is not significant for a specific chamber pressure of 10 psi (absolute). Temperature variation does not affect the optimal afterburner strut restrictor size.

Tests were also conducted at a lower temperature of 720 °K. Although results were limited, reducing temperature increased ignition time. The effect of lowering temperature to 720 °K appears more pronounced than increasing it to 930 °K.

## 9.3 Effect of Fuel

Figure 7 shows the effect of fuel on ignition. For this specific configuration, using AVTAG fuel increases ignition time by approximately 1 second. AVTAG fuel results in longer ignition times across all test configurations. However, the difference in ignition times between AVTUR and AVTAG varies among configurations, indicating that both fuels should be tested for each specific configuration to properly evaluate performance. The increase in ignition time is likely due to fuel boiling and vaporization, with AVTAG being a more volatile fuel. Fuel boiling and vaporization reduce flow within the catalytic igniter and cause vapor lock and Venturi blockage in the cone fuel manifold.

## 9.4 Effect of Fuel Manifold

Figure 8 illustrates the effect of early-production and production-type fuel manifolds on a specific configuration. With the optimal R1 restrictor, the production-type fuel manifold reduces ignition time by approximately 0.5 seconds compared to the early-production type. AVTAG fuel tests showed a similar trend, with ignition time reduced by approximately 0.75 seconds. This improvement is likely due to a better "match" achieved by readjusting the fuel ratio between the Venturi and fuel manifold. It is possible that the increased orifice size is not yet optimal. Further tests confirmed that increasing the fuel manifold orifice size to further reduce the Venturi fuel ratio is appropriate.

## 9.5 Catalytic Igniter Ignition Curves

Figure 9 shows the catalytic igniter ignition curves using AVTUR fuel with an early-production fuel manifold. These curves are essentially independent of fuel type, fuel manifold, afterburner strut restrictor, and Venturi restrictor sizes. However, AVTAG fuel slightly lowers the rich limit. Near the rich limit, ignition time increases, similar to when chamber pressure is reduced. Special fuel flow variation curves for specified afterburner strut restrictors are overlaid on this graph. It is observed that higher ignition altitudes (lower pressure) require smaller restrictor sizes. Figure 5 fully illustrates this point. However, reducing restrictor size to facilitate high-altitude ignition increases ignition time at higher afterburner pressures, as the predetermined fuel flow shifts toward the lean limit of the catalytic igniter. Thus, the optimal restrictor size for high-altitude conditions is smaller than that for sea-level ignition. For a 7 psi (absolute) ignition limit, the required afterburner strut restrictor size is approximately 0.043 inches, regardless of Venturi restrictor size.

## 9.6 Effect of Check Valve

Figure 10 compares 120 psi and 200 psi check valves. The 120 psi check valve produces a flatter set of curves, though ignition time is only slightly improved. This valve is less sensitive to afterburner strut restrictor size and thus less sensitive to afterburner pressure. The pressures cited are downstream of the check valve (S635). For a true comparison at a given engine condition (fixed upstream fuel pressure), approximately 80 psi should be subtracted from the 120 psi check valve line. Thus, a 125 psi S635 line with a 200 psi check valve should be compared to a 200 psi S635 line with a 120 psi check valve. It is evident that the 120 psi check valve is superior in two aspects:

- It provides a flatter set of ignition curves.
- For a given engine condition, it achieves approximately an 80 psi increase in fuel pressure.

## 9.7 Effect of 0.025-inch Restrictor + Filter with AVTUR Fuel

A helical filter was added to the Venturi restrictor to prevent blockage of the 0.025-inch orifice by gum deposits caused by fuel boiling in the afterburner strut fuel supply line.

Figure 11 compares ignition test results using AVTUR fuel with a 0.025-inch restrictor + filter Venturi to a similar configuration with a simple 0.025-inch restrictor. With a predetermined S635 pressure of 170 psi and a 0.048-inch afterburner strut restrictor, an ignition time of 1.4 seconds was achieved at 10 psi (absolute). This is well within the 3-second timer limit. Successful ignition at low S635 pressure (6 psi absolute) was achieved, though ignition time approached 4 seconds. This configuration represents the best performance in this test series.

## 9.8 Effect of 0.025-inch Restrictor + Filter with AVTAG Fuel

Figure 12 shows test results for the same configuration using AVTAG fuel. Ignition times are longer than those with AVTUR fuel (Figure 7). However, with a predetermined S635 pressure of 130 psi and a 0.048-inch afterburner strut restrictor, ignition within 2.6 seconds was possible at 10 psi (absolute), also within the 3-second timer limit.

At a chamber pressure of 6 psi (absolute), ignition was possible, but with this size of afterburner strut restrictor, ignition time was very long, potentially causing ignition failure in the engine.

## 9.9 Summary

The best test configuration consists of a Venturi restrictor with a 0.025-inch + filter and an early-production fuel manifold. Unfortunately, due to insufficient test time, this Venturi restrictor with a production-type fuel manifold was not tested, but improvements in ignition time are expected based on Section 9.4. For this reason, the early-production fuel manifold is included in the recommended configuration, which comprises:

1. Venturi restrictor (0.025-inch + filter)
2. 120 psi check valve
3. Catalytic igniter cone fuel manifold (16 × 0.046-inch orifices)
4. Afterburner strut restrictor = 0.043 inches

The Venturi restrictor installed on the actual early-production configuration (i.e., 7 × 0.035-inch dampers) exhibited poor ignition performance, achieving ignition only with large afterburner strut restrictor sizes and high S635 fuel pressures. This is likely due to fuel boiling in the damper channels, restricting Venturi nozzle flow. For this reason, results are not presented.

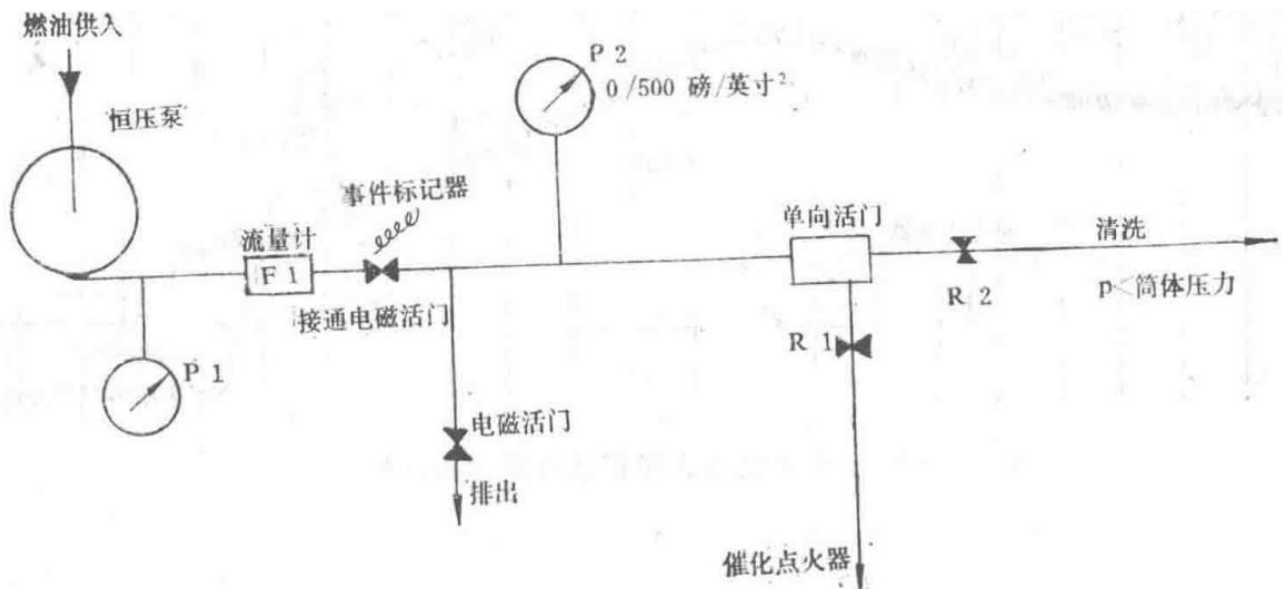


Figure 1: Fuel System of the Catalytic Igniter

Schematic diagram of the catalytic igniter fuel system, showing components such as the fuel pump, pressure gauges, flowmeter, solenoid valve, check valve, restrictors (R1, R2), and catalytic igniter.

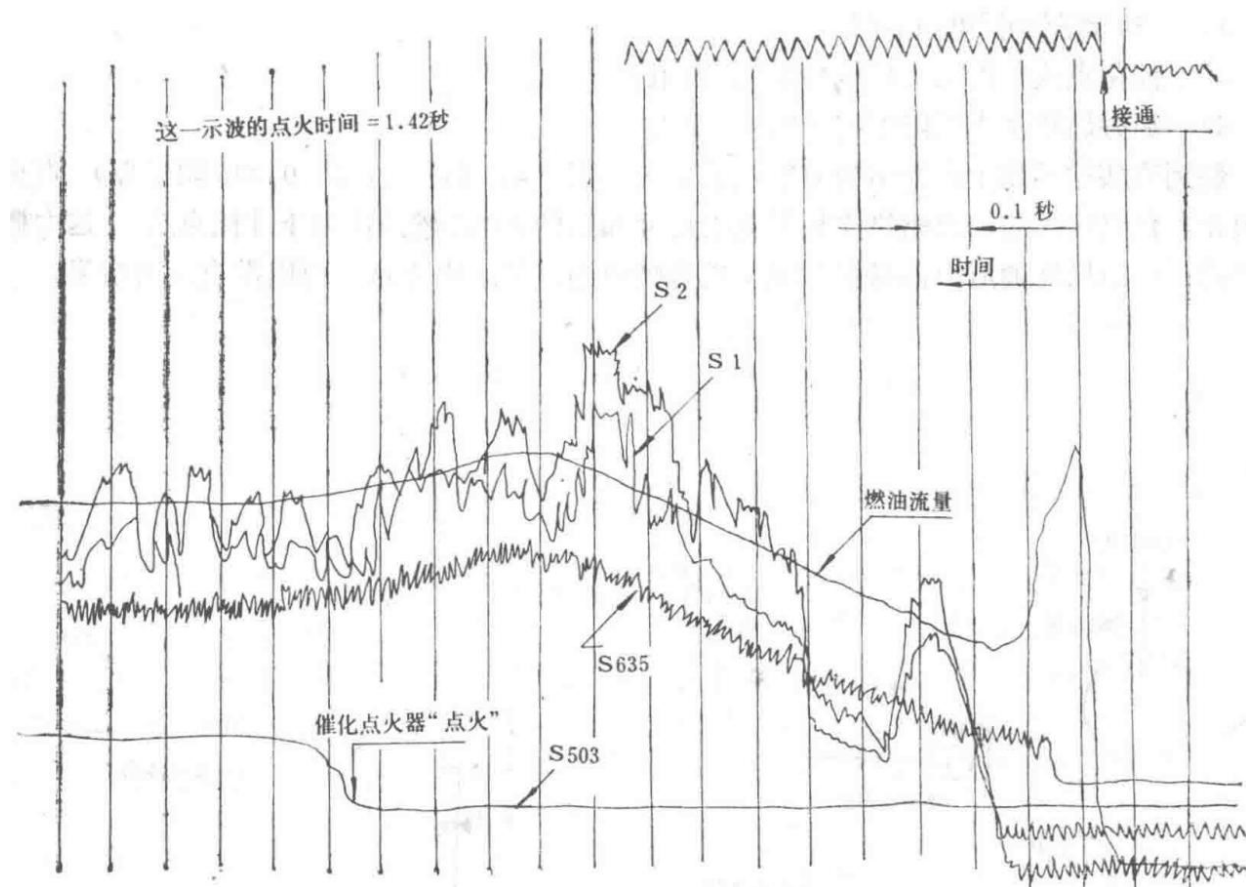


Figure 2: Typical Ultraviolet Oscillogram of the Ignition Process

Ultraviolet recorder trace showing the ignition process, including signals for catalytic igniter "ignition," fuel flow rate, and various sensor readings (S1, S2, S635, S503) over time.

## Figure 3 Test Configuration Scheme

Test Parameters for Figure 3 Configuration

R3 Venturi Restrictor	R1 Afterburner Support Plate Restrictor	P <sub>a</sub> psi <sup>2</sup> (absolute)	T <sub>a</sub> K	Fuel	Check Valve psi <sup>2</sup> (absolute)	Fuel Manifold Holes × Size	
0.025	0.035	15	850	AVTUR	200	16 × 0.039	
0.025	0.041	15	850	AVTUR	200	16 × 0.039	
0.025	0.048	15	850	AVTUR	200	16 × 0.039	
0.025	0.048	15	850	AVTUR	200	16 × 0.039	
7 × 0.035	0.040	15	850	AVTUR	120	16 × 0.046	
7 × 0.035	0.040	15	850	AVTUR	120	16 × 0.046	
7 × 0.035	0.055	15	850	AVTUR	120	16 × 0.046	
7 × 0.035	0.055	15	850	AVTAG	120	16 × 0.046	
0.025	0.055	15	850	AVTAG	200	16 × 0.039	
0.025	0.048	15	850	AVTAG	200	16 × 0.039	
0.025	0.041	15	850	AVTAG	200	16 × 0.039	
0.025	0.036	15	850	AVTAG	200	16 × 0.039	
0.025	0.036	15	850	AVTAG	200	16 × 0.039	
0.025	0.040	15	850	AVTUR	120	16 × 0.039	
0.025	0.048	15	850	AVTUR	120	16 × 0.039	
0.025	0.055	15	850	AVTUR	120	16 × 0.039	
0.025	0.036	15	850	AVTUR	120	16 × 0.046	
0.025	0.040	15	850	AVTUR	120	16 × 0.046	
0.025	0.048	15	850	AVTUR	120	16 × 0.046	
0.025	0.055	15	850	AVTUR	120	16 × 0.046	
0.025	0.040	15	850	AVTUR	120	16 × 0.046	
0.025	0.048	15	850	AVTAG	120	16 × 0.046	
0.025	0.055	15	850	AVTAG	120	16 × 0.046	
0.025	0.036	15	850	AVTAG	120	16 × 0.046	
0.025	0.040	15	850	AVTAG	120	16 × 0.039	
0.025	0.048	15	850	AVTAG	120	16 × 0.039	
0.025	0.055	15	850	AVTAG	120	16 × 0.039	

0.025	0.036	1515		850850	AVTAGAVT AG	120120	16 × 0.03916 × 0.039
0.025	0.045						

## Figure 4 Test Configuration Scheme

Test Parameters for Figure 4 Configuration

R3 Venturi Restrictor	R1 Afterburner Support Plate Restrictor Nozzle	P psi <sup>2</sup> (absolute)	T K	Fuel	Check Valve psi <sup>2</sup> (absolute)	Fuel Manifold Holes × Size
0.030	0.040	15	850	AVTUR	120	16 × 0.039
0.030	0.048	15	850	AVTUR	120	16 × 0.039
0.030	0.055	15	850	AVTUR	120	16 × 0.039
0.030	0.036	15	850	AVTUR	120	16 × 0.039
0.030	0.048	15	850	AVTAG	120	16 × 0.039
7 × 0.061	0.048	15	850	AVTUR	120	16 × 0.039
7 × 0.061	0.048	15	850	AVTUR	120	16 × 0.039
7 × 0.061	0.055	15	850	AVTUR	120	16 × 0.039
7 × 0.061	0.036	15	850	AVTUR	120	16 × 0.039
0.025 + Filter	0.040	15	850	AVTUR	120	16 × 0.039
0.025 + Filter	0.048	15	850	AVTUR	120	16 × 0.039
0.025 + Filter	0.055	15	850	AVTUR	120	16 × 0.039
0.025 + Filter	0.036	15	850	AVTUR	120	16 × 0.039
0.025 + Filter	0.036	15	850	AVTAG	120	16 × 0.039
0.025 + Filter	0.040	15	850	AVTAG	120	16 × 0.039
0.025 + Filter	0.048	15	850	AVTAG	120	16 × 0.039
0.025	0.036	10	850	AVTUR	120	16 × 0.039
0.025	0.041	10	850	AVTUR	120	16 × 0.039
0.025	0.048	10	850	AVTUR	120	16 × 0.039
0.025	0.055	10	850	AVTUR	120	16 × 0.039
0.025	0.036	10	930	AVTUR	120	16 × 0.039
0.025	0.041	10	930	AVTUR	120	16 × 0.039
0.025	0.048	10	930	AVTUR	120	16 × 0.039
0.025	0.055	10	930	AVTUR	120	16 × 0.039
0.025	0.036	6	850	AVTUR	120	16 × 0.039
0.025	0.041	6	850	AVTUR	120	16 × 0.039
0.025	0.048	6	850	AVTUR	120	16 × 0.039
0.025	0.055	6	850	AVTUR	120	

0.025						16 × 0.039
0.025	0.048	6	850	AVTUR	120	16 × 0.039
0.025	0.036	10	850	AVTAG	120	16 × 0.039
0.025	0.041	10	850	AVTAG	120	16 × 0.039
0.025	0.048	10	850	AVTAG	120	16 × 0.039
0.025	0.055	10	850	AVTAG	120	16 × 0.039
0.025	0.048	10	930	AVTAG	120	16 × 0.039
0.025	0.036	6	850	AVTAG	120	16 × 0.039
0.025	0.041	6	850	AVTAG	120	16 × 0.039

Continuation of Test Parameters for Figure 4 Configuration

R3 Venturi Restrictor	R1 Afterburner Support Plate Restrictor	P psi <sup>2</sup> (absolute)	T <sub>s</sub> K	Fuel	Check Valve psi (absolute)	Fuel Manifold Holes × Size
0.025	0.048	6	850	AVTAG	120	16 × 0.039
7 × 0.061	0.048	10	850	AVTAG	120	16 × 0.039
7 × 0.061	0.048	10	980	AVTAG	120	16 × 0.039
7 × 0.061	0.036	6	850	AVTAG	120	16 × 0.039
7 × 0.061	0.041	6	850	AVTAG	120	16 × 0.039
7 × 0.061	0.048	6	850	AVTAG	120	16 × 0.039
7 × 0.061	0.048	6	850	AVTUR	120	16 × 0.039
7 × 0.061	0.048	10	930	AVTUR	120	16 × 0.039
7 × 0.061	0.048	6	850	AVTUR	120	16 × 0.039
0.025 + Filter	0.048	10	850	AVTUR	120	16 × 0.039
0.025 + Filter	0.048	6	850	AVTUR	120	16 × 0.039
0.025 + Filter	0.048	10	850	AVTAG	120	16 × 0.039
0.025 + Filter	0.041/0.048	6	850	AVTAG	120	16 × 0.039
0.025	0.036	10	850	AVTUR	120	16 × 0.039
0.025	0.041	10	850	AVTUR	120	16 × 0.039
0.025	0.048	10	850	AVTUR	120	16 × 0.046
0.025	0.055	10	850	AVTUR	120	16 × 0.046
0.025	0.041	10	930	AVTUR	120	16 × 0.046
0.025	0.041	6	930	AVTUR	120	16 × 0.046
0.025	0.036	850	6	AVTUR	120	16 × 0.046
0.025	0.041	850	6	AVTUR	120	16 × 0.046
0.025	0.048	850	6	AVTUR	120	16 × 0.046
0.025	0.055	850	6	AVTUR	120	16 × 0.046
0.025	0.036	850	10	AVTAG	120	16 × 0.046

0.025	0.041	850	10	AVTAG	120	$16 \times 0.046$
0.025	0.048	850	10	AVTAG	120	$16 \times 0.046$
0.025	0.055	850	10	AVTAG	120	$16 \times 0.046$
0.025	0.036	850	6	AVTAG	120	$16 \times 0.046$
0.025	0.041	850	6	AVTAG	120	$16 \times 0.046$
0.025	0.048	850	6	AVTAG	120	$16 \times 0.046$
0.025	0.055	850	6	AVTAG	120	$16 \times 0.046$
0.025	0.041	930	10	AVTAG	120	$16 \times 0.046$
0.025	0.041	930	6	AVTAG	120	$16 \times 0.046$

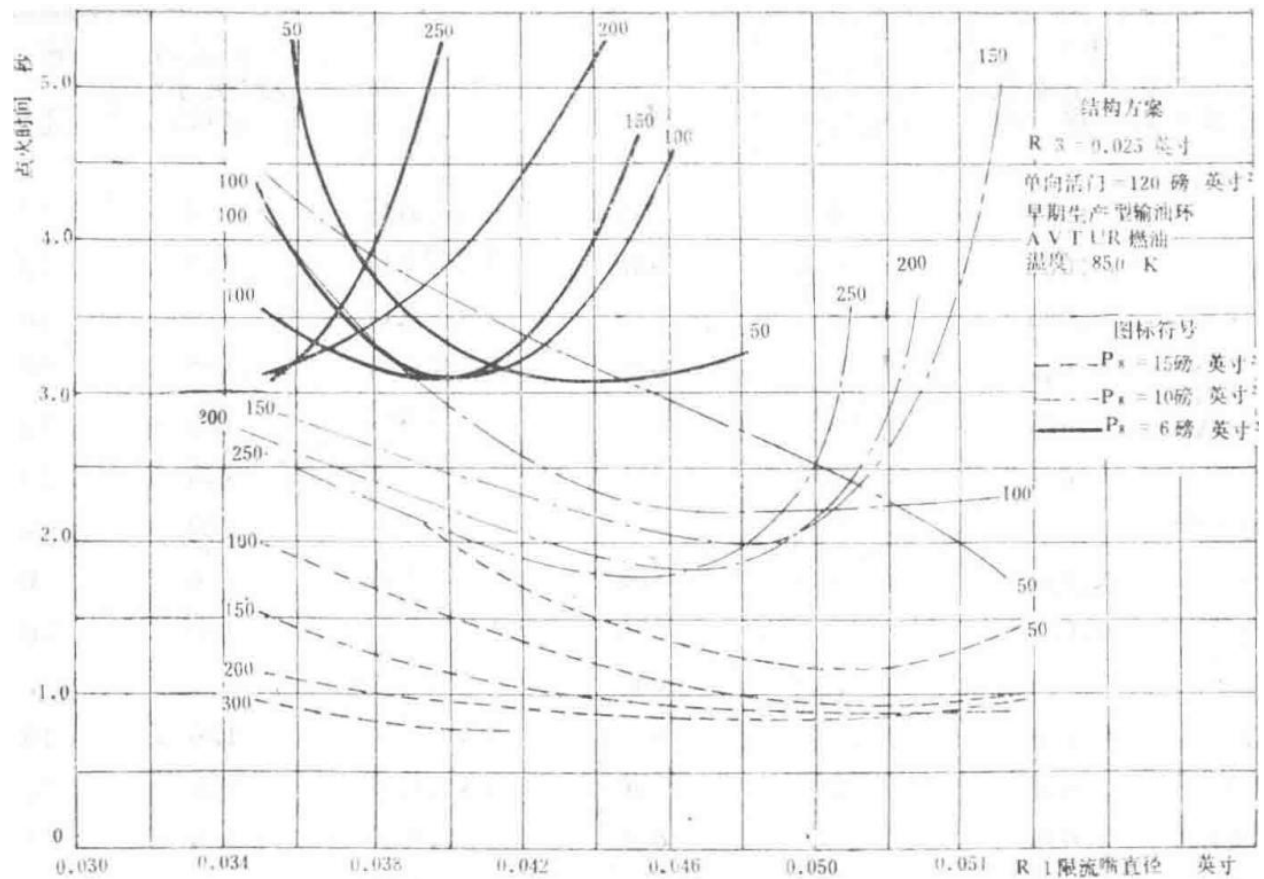


Figure 5 Influence of Afterburner Pressure

Graph showing the effect of afterburner pressure on fuel system performance parameters.

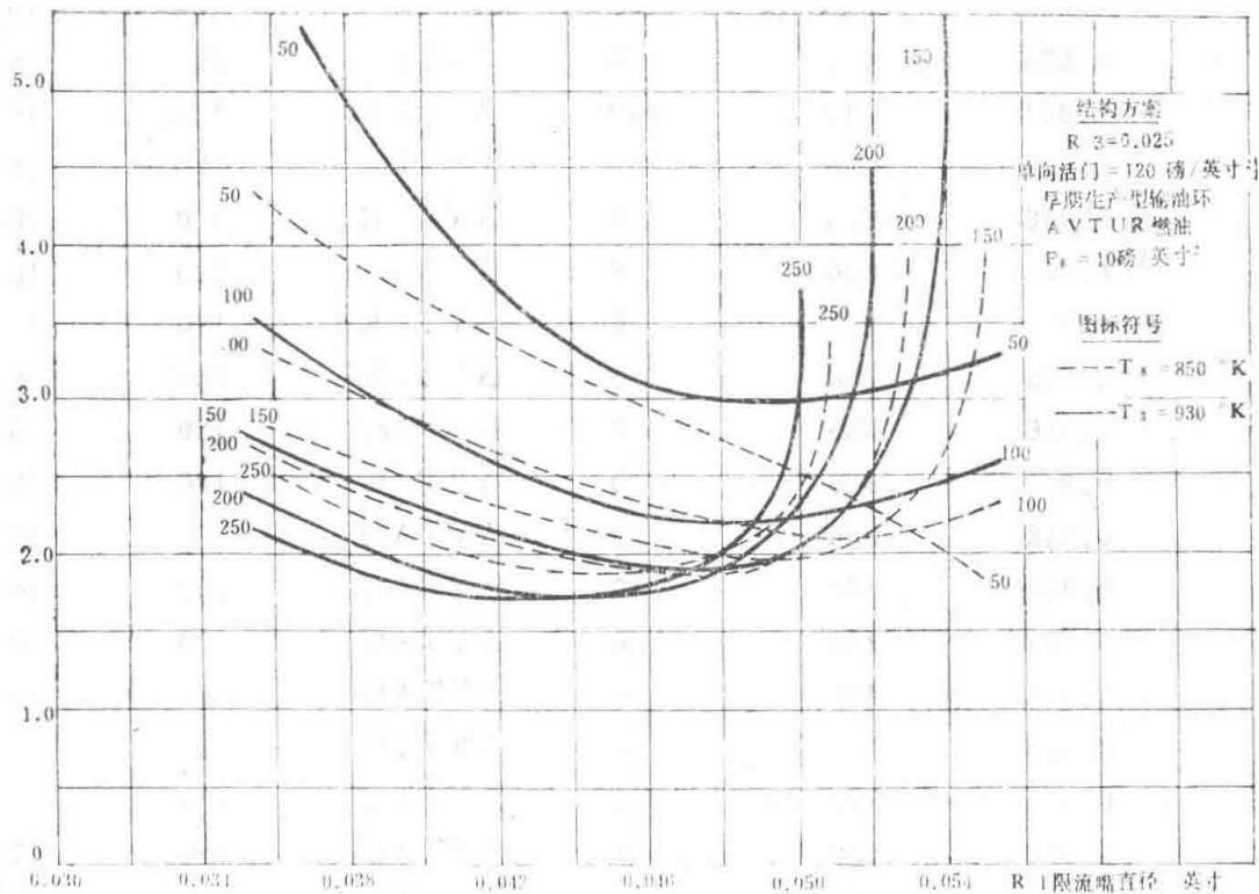


Figure 6 Influence of Inlet Temperature

Graph showing the effect of inlet temperature on fuel system performance parameters.

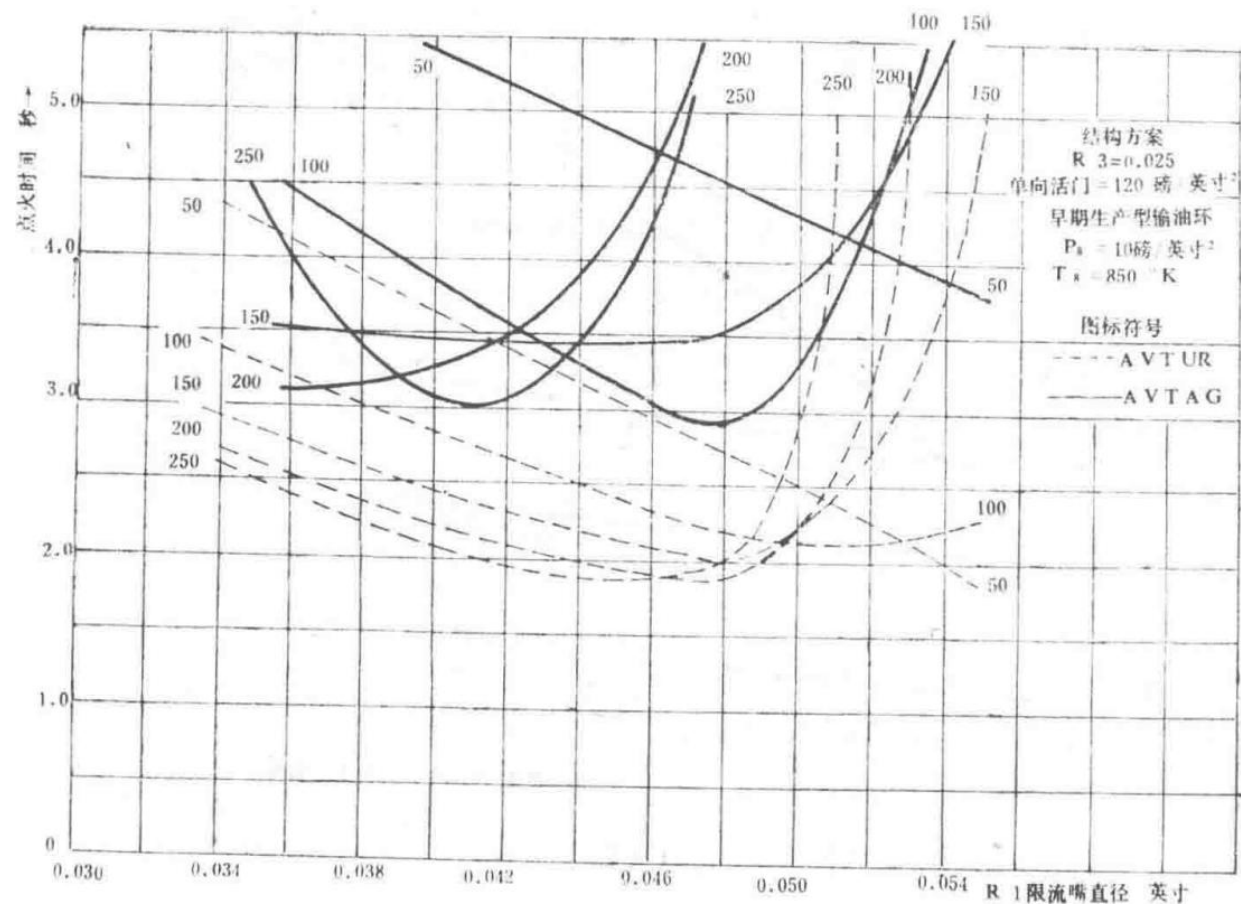


Figure 7 Influence of Fuel Type

Graph comparing the effects of different fuel types (AVTUR vs AVTAG) on fuel system performance.

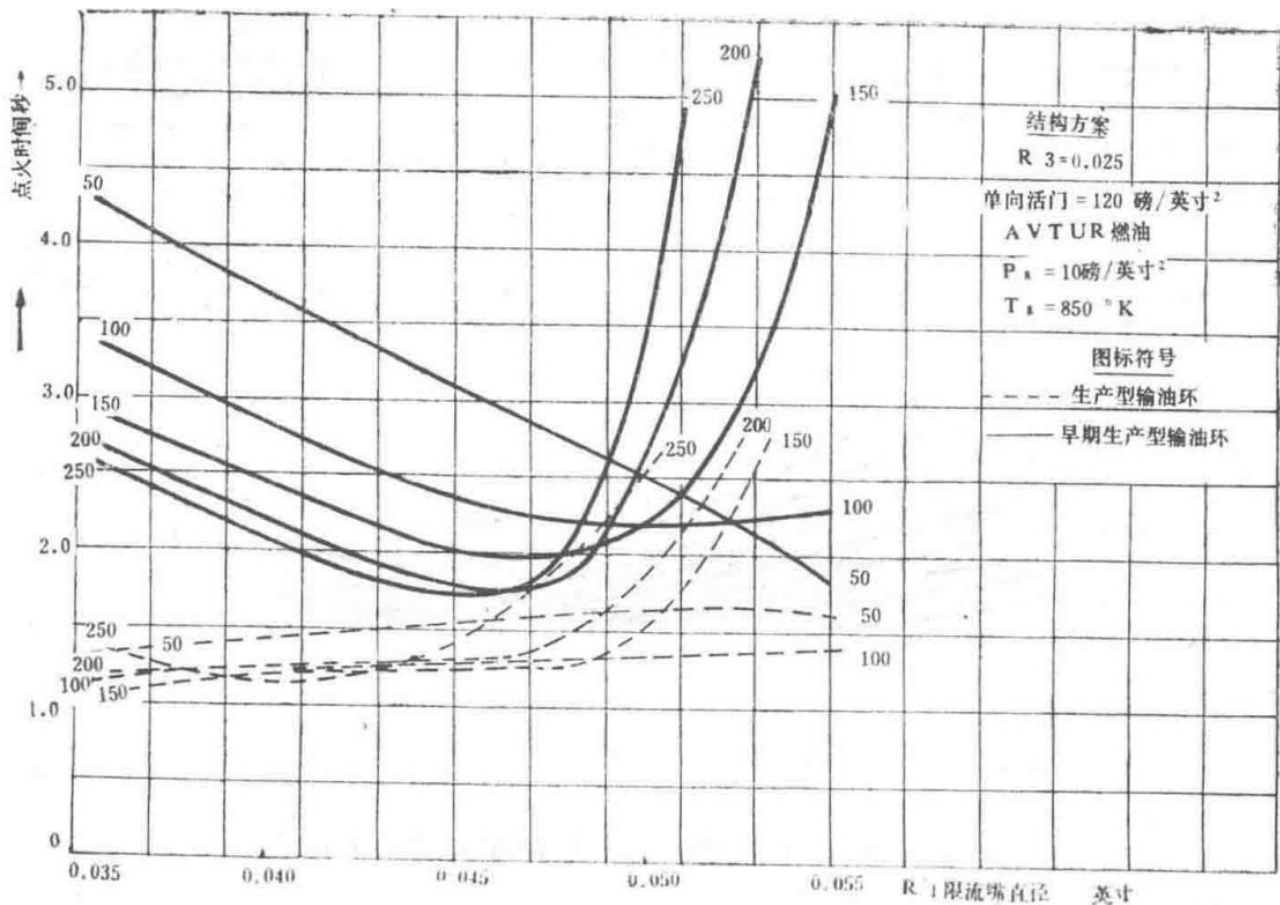


Figure 8 Influence of Early Production and Production-Type Fuel Manifolds

Graph comparing the performance differences between early production and production-type fuel manifolds.

— Section 35 —  
Content from Original Document (Pages 171-175)

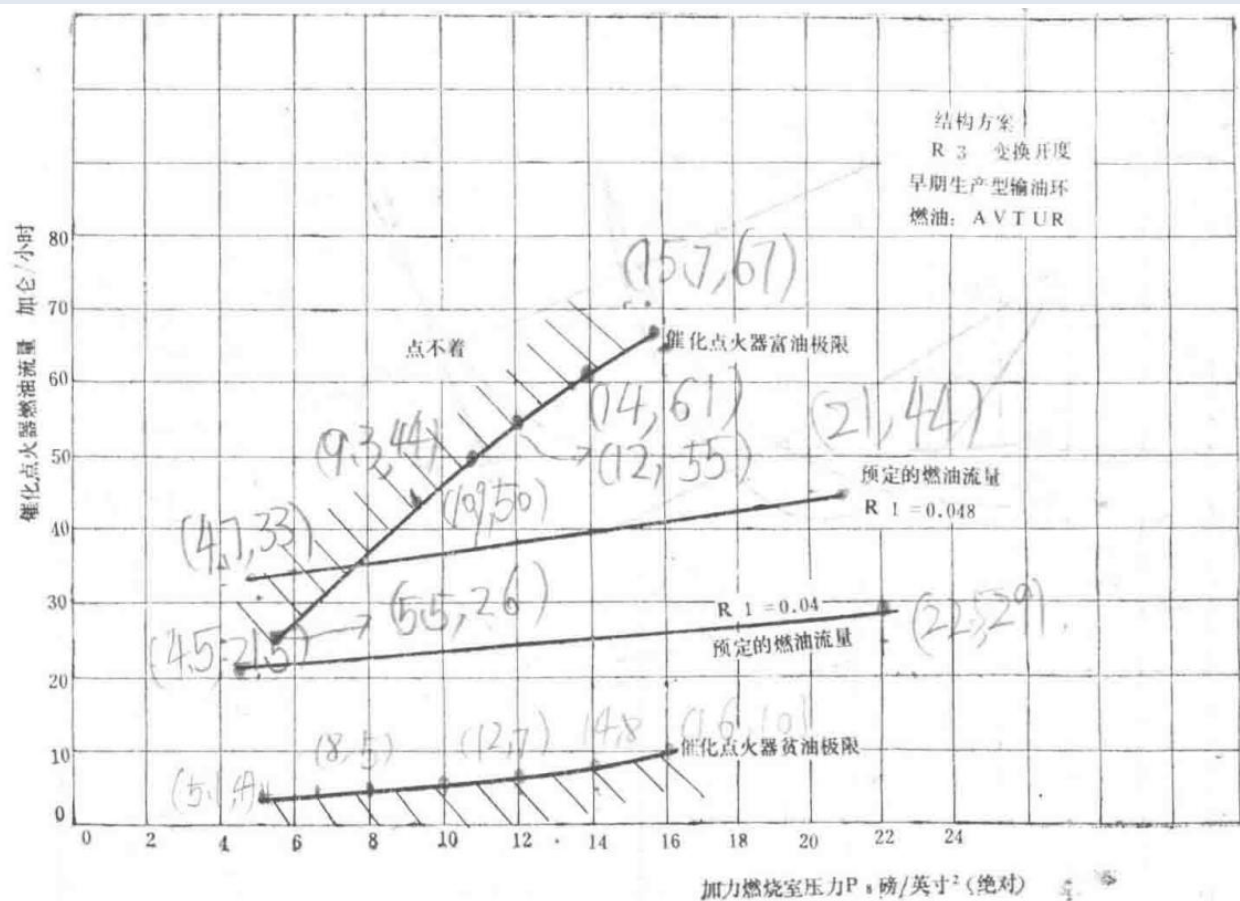


Figure 9: Ignition Limits of Catalytic Igniter

Diagram showing the ignition limits of the catalytic igniter used in the Spey MK202 afterburner system.

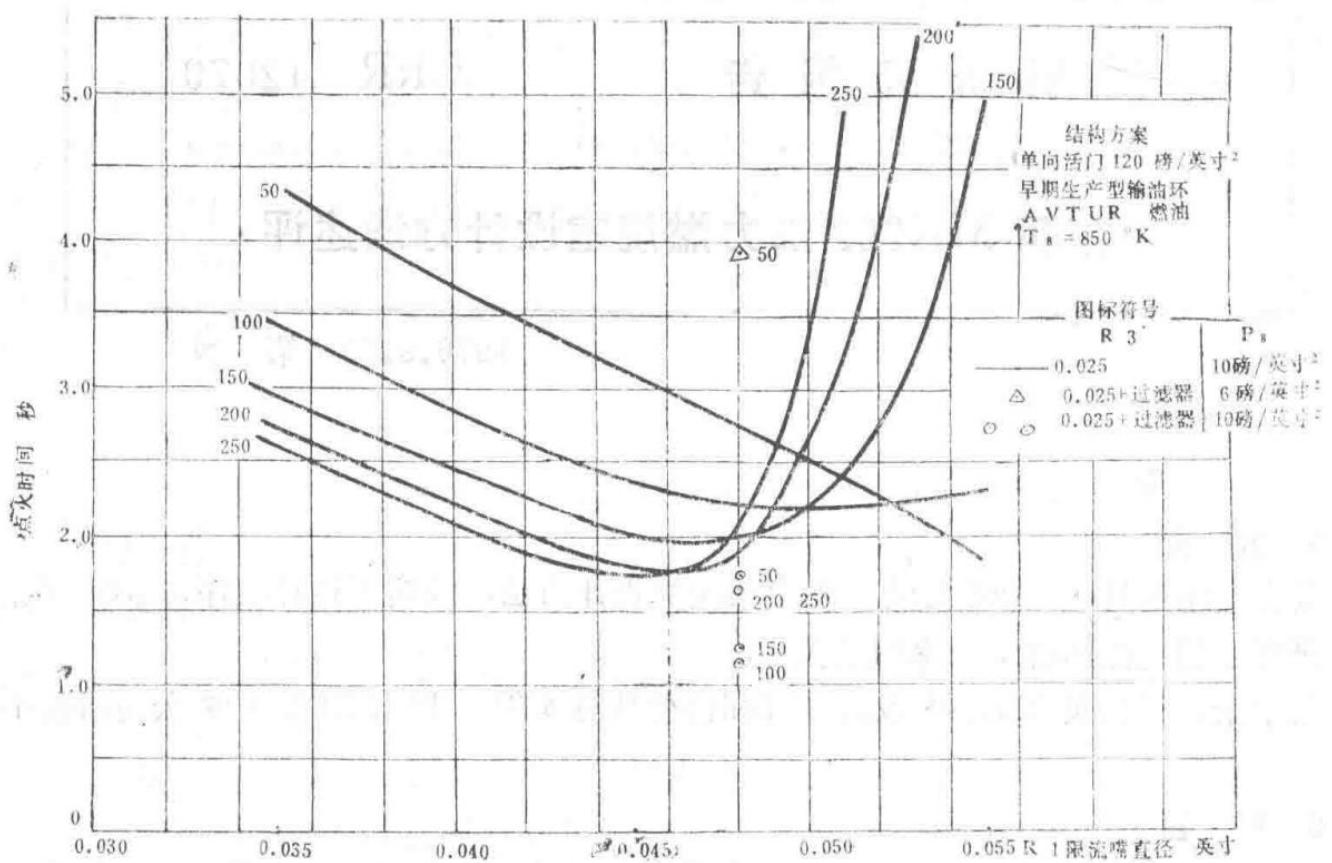
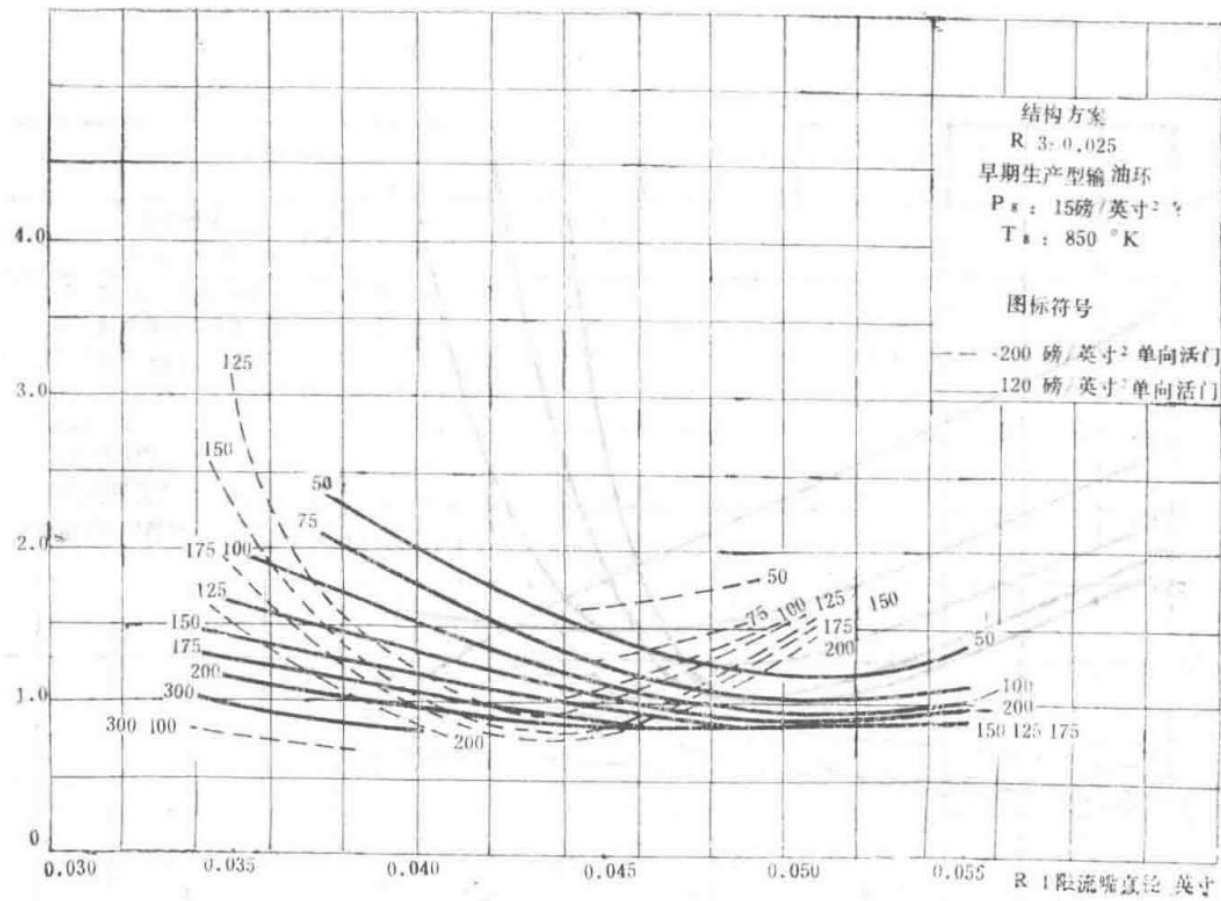


Figure 11: Influence of R3 Restrictor with 0.025 and 0.025+ Filters

Diagram illustrating the influence of the R3 restrictor with 0.025 and 0.025+ filters on afterburner performance.

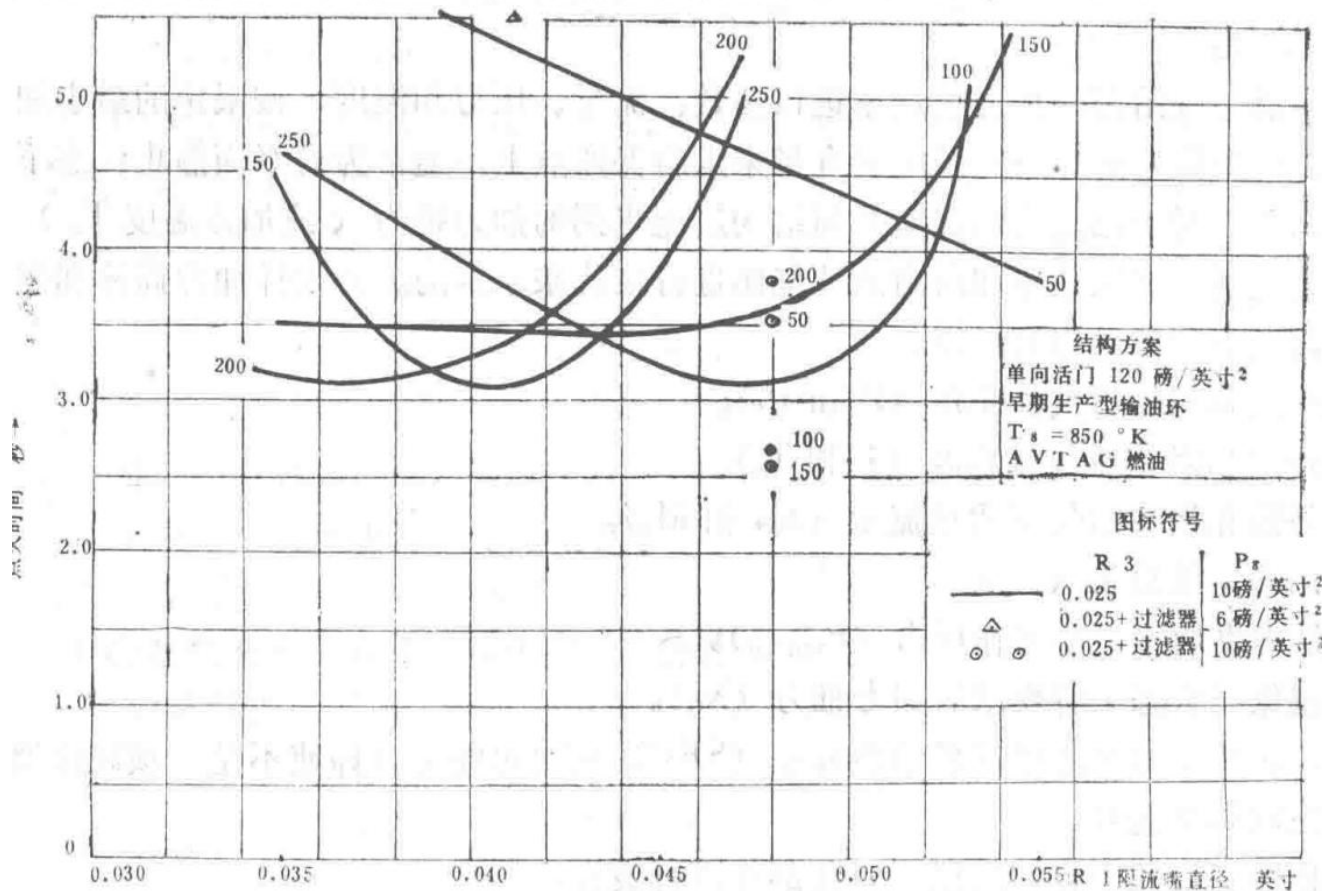


Figure 12: Influence of R3 Restrictor with 0.025 and 0.025+ Filters

Further analysis of the R3 restrictor's influence with 0.025 and 0.025+ filters on afterburner performance parameters.

## Review of Spey MK202 Afterburner Design Methodology

CRR 12079 First Edition, September 29, 1976

### 1.0 Abstract

This report describes the design methodology of the Spey MK202 engine afterburner system. It outlines the design procedures, estimates system performance, and investigates the relationship between stability and combustion efficiency.

The appendices provide examples of Spey MK202 design calculations and performance estimations to illustrate the methods used by Rolls-Royce.

### 2.0 Introduction

The Spey engine is the first British turbofan engine equipped with a full afterburner system. Naturally, its design principles are largely derived from previous turbojet engines, such as Rolls-Royce's Avon engine, as well as from scaled test rig experiments. While these design principles are constrained by empirical experience, they are sufficient for preliminary design and performance estimation.

## 3.0 Afterburner Design Procedure

Figure 1 presents a flowchart of the design procedure for a full afterburner system like the Spey MK202. The symbols used in the figure are listed in Table I.

The fundamental approach involves determining the required thrust ( $X_G$ ) at a specified guarantee point—typically sea-level static conditions—based on given afterburner inlet parameters (flow rate, pressure, and temperature), a defined minimum afterburner operating pressure, and constrained combustion chamber length and diameter. For a fixed combustion chamber geometry, the achievable afterburner thrust (or afterburner temperature  $T_{\infty}$ ) is determined iteratively based on the amount of air available for combustion, combustion efficiency, and the fuel-air ratio. The following parameters are assumed to be known for the design calculations of the afterburner casing and combustion chamber:

- Total pressure of the bypass and turbine exit flows ( $P_2$  and  $P_6$ ).
- Total temperature of the bypass and turbine exit flows ( $T_2$  and  $T_6$ ).
- Mass flow rates of the bypass and turbine exit flows ( $M_2$  and  $M_6$ ).
- Total length of the afterburner system ( $L_0$ ).
- Minimum operating pressure of the afterburner ( $P_{\text{min}}$ ).
- Required afterburner thrust at the guarantee point ( $X_G$ ).

Additionally, the afterburner should aim for the lowest possible specific fuel consumption (SFC), even if not a strict requirement, and the lightest possible weight. The design procedure is divided into several stages, each addressing the design of specific components.

### 3.1 Determination of Mixer Geometry

The Spey MK202 employs a high-combustion-efficiency "mixed" afterburner system, achieved by introducing radial velocity into the inner flow with minimal pressure loss.

Due to limited experience with two-stream mixed afterburners, the actual design method remains immature. However, for engine matching requirements, it is critical that the areas of the bypass and turbine exit flows at the mixer plane are designed to ensure equal static pressures for both streams. Given the total mixer area determined by the engine outlet geometry and the number of mixing funnels, the jet angle  $\theta$  can be derived. Figure 2 illustrates the overall arrangement of the mixer jet configuration, with performance relationships validated through test rig experiments within the following ranges:

Thus, the mixer design must not exceed these limits and must align with the primary requirement of equal static pressures for the bypass and turbine exit flows at their mixing point.

### 3.2 Mixer Performance

The pressure loss of the jet mixer, commonly referred to as mixing funnel loss, is a function of the jet angle  $\theta$  and the total pressure ratio  $P_6 / P_2$ , as demonstrated by test rig results. Figure 3 shows the variation of the flow coefficient  $CD$  (baseline value of 0.6) with  $\theta$  and the pressure ratio  $P_8 / P_2$ . The mixing funnel loss for the two streams is a function of the mixing diameter and the mixing funnel perimeter, represented in terms of dynamic pressure head at the mixer plane in Figure 4. The total pressure of each stream is then determined.

The mixed flow pressure  $p_8$  can be estimated using the momentum equation:

$$(M_2 V_2)/(g) + A_2 p_2 + (M_6 V_6)/(g) + A_6 p_6 = (M_8 V_8)/(g) + A_8 p_8$$

Momentum equation for estimating mixed flow pressure in the afterburner.

The average temperature  $T_8$  is estimated from the sum of the thermal content of the two streams:

$$M_2 C_{p_2} T_2 + M_6 C_{p_6} T_6 = M_8 C_{p_8} T_8$$

Equation for estimating the average temperature of the mixed flow based on thermal content.

Since the system is considered "mixed," these average or "bulk" parameters are used for the combustion chamber design.

Mixing the two streams can yield a thrust gain. Generally, the length from the mixer to the nozzle in the afterburner system is insufficient to ensure complete mixing. Therefore, a mixing efficiency relationship is used to determine the magnitude of partial mixing thrust. Figure 5 shows the variation of mixing efficiency  $\eta$  with a combined parameter representing mixer geometry and mixing length, where:

$$\eta = (X_{mix} - X_{unmixed})/(X_{fully mixed} - X_{unmixed})$$

Mixing efficiency equation, where  $X_{mix}$  is partial mixing thrust,  $X_{unmixed}$  is the sum of thrusts for unmixed flows, and  $X_{fully mixed}$  is the thrust for fully mixed flows.

### 3.3 Selection of Afterburner Diameter and Length (D, LB)

The weight of the afterburner system is proportional to the product of the square of the afterburner diameter (D) and the total length ( $L_o$ ):

$$W \propto D^2 L_o$$

Relationship between afterburner weight and its geometric parameters.

Thus, reducing these parameters is crucial for weight considerations. The total length consists of the mixing length (L $\square$ ) and the combustion length (LB):

$$L_o = L\square + LB$$

Total length of the afterburner system as the sum of mixing and combustion lengths.

To achieve maximum performance, the total length  $L_o$  should be as large as possible, but it is typically constrained by aircraft geometry. For preliminary performance iterations, the minimum mixing length is set to one times the afterburner diameter. If performance allows for a reduction in combustion length, the mixing length can be increased beyond this value.

The diameter directly determines the magnitude of the free-stream Mach number within the afterburner and thus affects combustion stability (i.e., larger nozzle diameters result in more stable combustion). Initially, the afterburner diameter is usually constrained by aircraft geometry. If no specific constraints exist, the total diameter of the afterburner (including the nozzle and actuators) is designed not to exceed the engine's maximum diameter. This ensures that the afterburner does not increase the engine's frontal area, thereby avoiding additional installation drag. After preliminary calculations of stability and efficiency, the afterburner diameter may be adjusted during the design phase based on performance reassessment.

### 3.4 Determination of Stabilizer Slot Width (W)

The selection of the stabilizer slot width depends on the required minimum operating pressure of the afterburner, as well as the inlet temperature and flow velocity of the afterburner. This can be expressed using the stability parameter (S), derived from early test rig results, with a minimum operating value of 12, where:

$$S = (p \cdot W)/(V \cdot A)$$

Stability parameter equation, where  $p$  is the static pressure at the stabilizer lip (psi absolute),  $W$  is the slot width, and  $V$  is the flow velocity at the stabilizer lip.

For these calculations, a stabilizer blockage ratio ( $\beta$ ) of 30% is assumed when computing the stabilizer lip conditions. If the afterburner geometry deviates from this value during preliminary calculations, the stability parameter must be recalculated. Equation (6) is derived from Figure 6, which shows the stable combustion region behind the flame stabilizer used in the Spey MK202. A value of  $S = 12$  appears to provide a suitable

operating range, ensuring sufficient stability for the determined stabilizer slot width.

### 3.5 Stabilizer Quantity

At this design stage, an assumption must be made regarding the amount of cooling air required for the afterburner. In preliminary calculations, a cooling air quantity can be arbitrarily assumed (e.g., 10% for a full afterburner system). The magnitude of this value depends on the cooling efficiency of the heat shield design and its performance at maximum afterburner temperatures. Detailed calculations of heat shield design and performance are provided in Reference [1]. Any corrections to the assumed combustion air quantity derived from heat shield design analysis require recalculation of the combustion chamber structure. Given the assumed combustion air quantity and afterburner diameter, the inner radius of the heat shield ( $R_{\square \square}$ ) can be calculated.

There is a clear relationship between the number of stabilizers ( $N$ ), slot width, and blockage ratio, as shown in Figure 7 and expressed by the following equation:

$$(R_{\square \square})/(W) = (1)/(\beta_{\square}) \sqrt{(N^2 + N - N \beta_{\square})}$$

Relationship between stabilizer quantity, slot width, and blockage ratio, where  $\beta_{\square}$  is the stabilizer blockage ratio within the heat shield.

Since the number of stabilizers must be an integer, adjustments to the blockage ratio may be necessary to satisfy Equation (8).

Table I: Symbols Used in Afterburner Design Procedure

Symbol	Description
XG	Required afterburner thrust at guarantee point
T <sub>□</sub>	Afterburner temperature
P <sub>2</sub> , P <sub>6</sub>	Total pressure of bypass and turbine exit flows
T <sub>2</sub> , T <sub>6</sub>	Total temperature of bypass and turbine exit flows
M <sub>2</sub> , M <sub>6</sub>	Mass flow rates of bypass and turbine exit flows
L <sub>o</sub>	Total length of afterburner system
P <sub>s</sub> □□□	Minimum operating pressure of afterburner
D	Afterburner diameter
LB	Combustion length
L <sub>□</sub>	Mixing length
W	Stabilizer slot width
S	Stability parameter
p <sub>□</sub>	Static pressure at stabilizer lip
β	Stabilizer blockage ratio
N	Number of stabilizers
R <sub>□□</sub>	Inner radius of heat shield
η□□□	Mixing efficiency
X <sub>□□</sub>	Partial mixing thrust
X <sub>□□</sub>	Sum of thrusts for unmixed flows
XF <sub>□</sub>	Thrust for fully mixed flows

Recalculating the stabilizer slot width ( $W$ ) derived from Equation (6) is necessary when Equation (9) is modified. Therefore, iterative calculations between  $W$  and  $N$  are required to simultaneously satisfy both Equation (6) and Equation (8).

## 3.6 Radial Spacing of Stabilizers

In the afterburner, the radial position of the stabilizers is arranged according to the Equal Slot Load (E.G.L) principle. This means that the radial flame extension distance at each stabilizer lip is equal. The stabilizer positioned radially inward is placed upstream along the flow line of the outer stabilizer, with an axial distance of twice the stabilizer slot width.

The "Equal Slot Load" is defined as:

$$(A\Delta's)/(P\Delta) = (2w)/(11)z \times 4 = (x)/(2)$$

Definition of Equal Slot Load (E.G.L)

Where:

- $\Delta A/\Delta$  = Flow cross-sectional area between adjacent stabilizers
- $\Delta P/\Delta$  = Perimeter of the stabilizer lip
- $x$  = Radial distance between adjacent stabilizers

Referring to Figure 8, it can be seen that:

$$N W + N x_1 + x_0 = R\Delta : s$$

Radial spacing relationship among stabilizers

Where:

- $W$  = Stabilizer slot width
- $x_0$  = Radial distance between the outer stabilizer lip and the heat shield, as seen in Figure 9, approximately  $(x_1)/2$

Therefore, the average radius for each stabilizer is:

$$R_1 = x_1 + (W)/2$$

Average radius of the first stabilizer

$$R_2 = 2x_1 + (3)/2W$$

Average radius of the second stabilizer

$$R_3 = 3x_1 + (5)/2W$$

Average radius of the third stabilizer

## 3.7 Diffuser Design and Axial Spacing of Stabilizers

Section 3.6 described the method for radial arrangement of stabilizers, assuming they are coplanar. If the stabilizers are staggered, the local blockage ratio decreases, reducing the local velocity at the stabilizer lip. This improves stability for a given stabilizer slot width.

For a 30° V-shaped stabilizer, the wake decay behind it shows that static pressure is not fully recovered at 5 times the slot width downstream, and aerodynamic effects still exist. Upstream, blockage affects the flow at 2

times the slot width. Therefore, in diffuser design, the stabilizers are moved 2 slot widths upstream, but it is assumed that the influence of each stabilizer still exists at the coplanar position (i.e., 4 slot widths downstream). The diffuser section containing the stabilizers is then designed with a constant equivalent flow area.

When stabilizers are moved upstream into the diffuser, their relative positions are maintained by moving along flow lines according to the "area rule" method. After diffuser design, even if it is of constant area, it is necessary to verify that the diffuser operates stably.

It is assumed that each stabilizer divides the diffuser into annular flow channels of different diameters. First, consider the upstream diffuser formed by the inner stabilizer, assuming a fully developed boundary layer displacement thickness  $\delta^*/(W_1) = 0.0625$ . The maximum effective wall angle  $\phi_1$  for non-separated flow can then be estimated from Figure 10. Considering the boundary layer growth rate from Figure 11, this calculation is repeated for each subsequent channel. As a precaution, the growth rate is typically doubled to ensure stable channels.

The maximum allowable angle for each channel is then compared with the actual design value to ensure the diffuser is stable and has the minimum total length.

The Spey MK202 afterburner structure consists of individually fueled flame stabilizers and a main afterburner fuel manifold located upstream of these flame stabilizers. The design of the pilot flame stabilizer is introduced in Reference [2], and the arrangement and design of the main afterburner fuel manifold are detailed in Reference [3].

## 4.0 Performance Estimation

Section 3 outlined the basic design of the afterburning system. It is now necessary to estimate the performance achievable with this design. Performance evaluation determines whether the required thrust has been achieved or if design modifications are needed.

### 4.1 Cold Pressure Loss Estimation

The cold pressure loss of the afterburning system is determined by the diffuser structure, stabilizer blockage ratio, fuel manifold blockage ratio, struts, delivery pipes, connectors, and ignition devices. At the initial design stage, most of these factors are not yet determined. Thus, for preliminary estimation, cold loss is considered to depend only on the stabilizer blockage ratio.

Therefore:

$$(\Delta P / D)_1 = 2 CD (\beta) / (1 - \beta)^2$$

Cold pressure loss equation

Where:

- $\Delta P$  = Cold pressure loss (psi)
- $D$  = Dynamic pressure head corresponding to the full cross-section of the afterburner (psi)
- $CD$  = Stabilizer drag coefficient = 1.0 for 30° V-gutter or vaporizer stabilizers
- $\beta$  = Blockage ratio of stabilizers in the full cross-section

The pressure after loss  $P'$  can be determined by:

$$P' = P - (\Delta P / D) \times D$$

Pressure after cold loss

Figure 12 shows  $(\Delta P / D)$  considering only the V-gutter, where:

$$\Delta P / D = CD (\beta) / (1 - \beta)^2$$

### Pressure loss ratio due to V-gutter

Cold loss is sometimes considered as a function of total pressure  $\Delta P / P$ .

$$\Delta P / P = ((\Delta P) / (D))_1 \times (D) / (P_s) \times 100\%$$

Cold loss as a percentage of total pressure

## 4.2 Combustion Efficiency ( $\eta_c$ ) Calculation

The combustion efficiency at a given condition is estimated using a modified form of King's efficiency relation (Reference [4]). King's original work was for a single flame stabilizer and did not account for flame extension distance. To apply this relation to multiple stabilizer systems, a width factor (WF) is added to the combustion length (L) term. This modification redefines the correlation parameter ( $\epsilon$ ) as:

$$\epsilon = (P_c^{10.6324} T_s^{-1.07} (750 - V)^{0.6252}) / (e^{(3)/(1)} \times (w_c^{1.0})^{(2.71)})$$

Modified King's efficiency correlation parameter

Where:

- $P_c$  = Total pressure after cold loss (psia)
- $T_s$  = Mixed temperature (K)
- $V$  = Flow velocity within the heat shield (ft/s)
- $L$  = Combustion length (inches)

For this calculation, it is assumed that all stabilizers are coplanar. The graph derived from King's data, showing the relationship over a range of "unburned" fuel-air ratios, is presented in Figure 13. The "unburned" fuel-air ratio is defined as:

Where:

- $f_a r$  = Total fuel-air ratio used (engine plus afterburning system)
- $f_a r g c$  = Theoretical engine fuel-air ratio required to increase temperature from  $T_i$  to  $T_s$

It should also be noted that the combustion efficiency used in this relation is defined as:

$$\eta_c = (T_c - T_s) / (T_c - T_i)$$

Definition of combustion efficiency

Where:

- $T_c$  = Actual hot core flow temperature (°K)
- $T_i$  = Theoretical hot core flow temperature (°K)

Thus, the combustion efficiency at a given fuel-air ratio and condition can be estimated.

## 4.3 Afterburning Temperature ( $T_c$ ) Calculation

The theoretical hot core flow temperature  $T_c$  is calculated from the theoretical total fuel-air ratio ( $f_a r g c$ ) and the engine inlet temperature  $T_i$ , using temperature rise curves. With Equation (21), the hot core flow temperature  $T_c$  can be determined, and the afterburning temperature is then calculated from the hot core flow temperature and mixed temperature using the following equation:

$$M_f \sqrt{T_c} = (1 - (x)/(100)) M_3 \sqrt{T_s} + M_{air} \sqrt{T_i}$$

Afterburning temperature calculation

Where:

- $\dot{M}_F$  = Total mass flow through the nozzle (lb/s)
- $\mu = (1 + f \cdot a \cdot r) M_a$
- $x$  = Percentage of air used for combustion
- $\dot{M}_{HC}$  = Hot core mass flow through the nozzle (lb/s) =  $(x)/(100) M_a (1 + f \cdot a \cdot r) C$

## 4.4 Combustion Zone Heat Loss Calculation

The total pressure loss due to combustion, i.e., heat loss, depends on the inlet Mach number and the square root of the temperature ratio, as shown in Figures 14 and 15. The loss also depends on the specific heat ratio, which varies with temperature and fuel-air ratio. Using appropriate heat loss curves (for maximum heat release rate in afterburning calculations,  $(\gamma)/(y - 1)$  is approximately 5), the total pressure of the hot core flow nozzle  $(P_{1F})$  can be determined.

## 4.5 Total Afterburning Thrust (XGL) Calculation

The total afterburning thrust  $(X_G)$  consists of the thrust from two airflows:  $(X_C)$  and  $(X_H)$ . Thus:

### 4.5.1 Cooling Air Thrust (XCA)

The cooling air thrust  $(X_C)$  is obtained from the thrust curves in Figures 16(A) to (L), i.e., the relationship between  $(X)/(M \sqrt{T})$  and  $P$ , using appropriate values.

Where:

- $P_v$  =  $P_a$  (psia)
- $T = T_a$  ( $^{\circ}$ K)
- $p_o$  = Ambient pressure at the nozzle (14.696 psia, sea level static condition)

### 4.5.2 Hot Core Flow Thrust (XHC)

The hot core flow thrust  $(X_H)$  is similarly obtained from the thrust curves using the appropriate  $(X)/(y - 1)$  value.

Where:

- $T = T_H$

The calculated total thrust is compared with the required thrust at the design condition. Typically, at this stage, the thrust is designed to be approximately 4% higher than required to ensure a safety margin. This accounts for errors in estimating cold losses or situations where the engine's turbine exit pressure and temperature are lower than the specified performance. If the designed thrust is insufficient, design modifications are necessary. If it exceeds requirements, the design can be adjusted to reduce the size or weight of the afterburner.

## 4.6 Impact of Design Parameter Variations on Performance

### 4.6.1 Length (LB)

Variations in combustion length affect combustion efficiency and thus performance. The impact is significant at high-altitude conditions because  $\eta_c$  varies greatly with altitude. At higher afterburner pressures (sea level), this effect is smaller. The system weight directly depends on the total length.

### 4.6.2 Afterburner Diameter (D)

Variations in afterburner diameter affect both stability and combustion efficiency. Increasing the diameter reduces airflow velocity, thereby improving stability. The effect is substantial; for the Spey MK202 afterburner, increasing the diameter by 1 inch increases the stability parameter ( $S$ ) by over 8%. The impact on combustion efficiency is less certain because reduced velocity improves efficiency, but greater flame extension distance may reduce it. The net result is that efficiency is not significantly affected, but each case must be evaluated for its pros and cons. Additionally, weight must be considered, as the afterburner system weight is a function of the diameter squared.

#### 4.6.3 Stabilizer Slot Width ( $W$ )

Increasing the stabilizer slot width improves both combustion stability and efficiency. The slot width directly affects the stability parameter, and Reference [2] indicates that the impact is significant under high loads (i.e., at low afterburner pressures). However, care must be taken to ensure that the blockage ratio of the combustion chamber is not too large, as increased blockage raises the velocity at the stabilizer lip. Beyond a certain blockage ratio, stability begins to decrease, as demonstrated in Figure 17. This figure shows the variation of the stability parameter with blockage ratio for various inlet Mach numbers of the afterburner. It illustrates that the optimal blockage ratio depends on the inlet Mach number and confirms the significant impact of Mach number (afterburner diameter) on stability, as mentioned in Section 4.6.2.

The impact of stabilizer slot width on combustion efficiency is less pronounced, primarily due to reduced flame extension distance caused by smaller spacing between stabilizers. However, increasing the blockage ratio of the combustion chamber increases cold losses, reducing both non-afterburning and afterburning thrust. Afterburning thrust may be compensated by improvements in other performance aspects, but the non-afterburning pressure loss is a constant penalty on engine specific fuel consumption, which may be a critical issue.

#### 4.6.4 Number of Stabilizers ( $N$ )

Increasing the number of stabilizers improves combustion efficiency by reducing flame extension distance. However, if the blockage ratio is to be maintained, as reasoned above, the stabilizer slot width must be reduced. This reduction decreases stability, leading to flameout at higher afterburner pressures (lower altitudes).

#### 4.6.5 Percentage of Air Used for Combustion ( $x$ )

This report suggests that for preliminary calculations of a full afterburning system using mixed air as cooling air, 90% of the air is assumed to be used for combustion. Reducing the cooling air increases  $\text{F}_{\text{combustion}}$ , thereby increasing thrust. However, reducing cooling air may cause mechanical strength issues for the heat shield. Thus, the required air quantity is determined by the heat shield design and the maximum hot core flow temperature that may occur within the flight envelope.

### 4.7 Performance Limitations

At this stage of calculation, it is necessary to check for possible limitations on maximum performance. These limitations can be categorized into two items:

- (a) Hot core flow temperature
- (b) Mach number after hot core flow combustion

During the design phase, the hot core flow temperature is limited to 2175°K because exceeding this value may cause mechanical failure of the heat shield tail and nozzle flaps due to high radiative heat flux. Additionally, this temperature is close to the stoichiometric fuel-air ratio temperature, approaching the limit of combustion performance. However, due to potential poor fuel-air distribution in practical scenarios, further considerations are necessary.

There is little margin for adjustment. If this limit is exceeded in the design calculations, the percentage of air used for combustion must be increased to reduce this temperature.

The Mach number after combustion in the hot core flow at the nozzle must be kept below 0.6. Figure 18 shows the relationship between the thrust of a typical afterburning engine and the post-combustion Mach number. It can be seen that beyond approximately 0.7, the thrust increase is minimal. This is because as the Mach number increases, heat losses become a more dominant factor. Therefore, the Mach number is limited to 0.6 to avoid this situation.

As long as these specified limits are not exceeded, other performance parameters can be calculated.

## 4.8 Calculation of Non-Afterburning Gross Thrust and Nozzle Area

The non-afterburning gross thrust ( $X_{GD}$ ) is calculated by comparing the partially mixed thrust and the fully mixed thrust, taking into account the degree of mixing ( $K$ ) calculated in Section 3.2.

### Fully Mixed Case ( $X_{FM}$ ext and $A_{FM}$ )

The fully mixed thrust  $X_{FM}$  is calculated using the pressure  $P^*$  after cold-state losses and the "mixed" state temperature and flow ( $T_m$ ,  $M_m$ ) with the thrust curve corresponding to the -1 value in Figure 16. Similarly, the nozzle area  $A_{FM}$  is calculated under the assumption of fully mixed conditions.

### Unmixed Case ( $X_{UM}$ ext and $A_{UM}$ )

The thrust in the unmixed case is calculated using the Mach number, temperature, and pressure at the mixer outlet, considering the cold-state pressure losses for each flow. It is assumed that the loss for each flow is the same as calculated in the mixed case in Section 4.1, but expressed as  $\Delta P / P$ .

Thus, the thrust ( $X_2'$  and  $X_6'$ ) and nozzle area for each flow are calculated using the pressure after losses for each flow ( $P_2'$  and  $P_6'$ ) from the thrust curves.

$$P_2' = P_2 - ((\Delta P)/(P))_1 \times P_2$$

Pressure after loss for the first flow

$$P_{\delta_6}' = P_{\delta_6} - ((\Delta P)/(P))_{\delta_1} \times P_{\delta_6}^{**}$$

Pressure after loss for the second flow (corrected notation)

The thrusts  $X_2'$  and  $X_6'$  are summed to obtain the unmixed thrust  $X_{UM}$ .

$$\Delta X_{UM} = X_2' + X_6'$$

Summation of thrusts for unmixed case

Similarly, since

$$K = (X_{FM} - X_{UM})/(X_{FM} - X_{UM})$$

Definition of mixing degree K for thrust

it is also assumed that

$$K = (A_{FM} - A_{UM})/(A_{FM} - A_{UM})$$

Definition of mixing degree K for nozzle area

Thus, the partially mixed thrust  $X_{\text{part}}$  and area  $A_{\text{part}}$  are calculated. Here,

$$AD = A_{\text{part}}$$

Nozzle area for non-afterburning case

## 4.9 Calculation of Afterburning Ratio (B)

The afterburning ratio B is defined as

$$B = (X_{\text{part}} - X_{\text{GD}})/(X_{\text{GD}})$$

Definition of afterburning ratio B

## 4.10 Calculation of Afterburning Nozzle Area ( $A_{\text{eff}}$ )

The afterburning nozzle area  $A_{\text{eff}}$  consists of the sum of the cooling air nozzle outlet area and the hot core flow outlet area.

$$A_{\text{eff}} = AC + A_{\text{core}}C (all \text{ effective areas})$$

Total effective nozzle area for afterburning

The cooling air nozzle outlet area is obtained from the thrust curve  $X / A P_0 PF / P_0$  in Figure 16.

Here,

$$PF = P_s'^*$$

Pressure for cooling air nozzle

$$X = XC$$

Thrust for cooling air

$$A = AC$$

Area for cooling air nozzle

Similarly, the hot core flow area is calculated as

$$PF = P_{\text{core}}C$$

Pressure for hot core nozzle

$$X = X_{\text{core}}C$$

Thrust for hot core flow

$$A = A_{\text{core}}C$$

Area for hot core nozzle

Thus, the total effective nozzle area for afterburning can be determined.

## 4.11 Calculation of Nozzle Geometric Area

Sections 4.8 and 4.10 provide the calculations for the effective nozzle areas under non-afterburning and afterburning conditions. The mechanical design to achieve the required geometric area must be calculated using a flow coefficient, which depends on the nozzle flap angle that is not yet known at this stage. Therefore, iteration between the flap angle and geometric area is required using Figures 19 and 20 to obtain the necessary effective area.

## 5.0 Discussion

This report describes the method used for designing the Spey MK202 afterburning system. Using this method, the position, size, and number of flame stabilizers, as well as the diffuser in which the stabilizers are placed, can be determined. The calculation results in this report allow mechanical design to proceed, but due to practical design difficulties and unconsidered strength issues, performance must be re-evaluated after the preliminary design. For completeness, the Spey MK202 design calculations are listed in Appendix A.

This report does not consider the ignition system for the Spey afterburning system. The selection and design of the ignition system are detailed in Reference [5].

## 6.0 References

1. CRR 12082
2. CRR 12084
3. CRR 12083
4. CRR 12080
5. CRR 12081

## Appendix A

### Mixer Geometry

The following conditions were assumed in the calculations:

Bypass flow:

$$T_2 = 406.3 \text{ } ^\circ\text{K}$$

Temperature of bypass flow

Turbine flow:

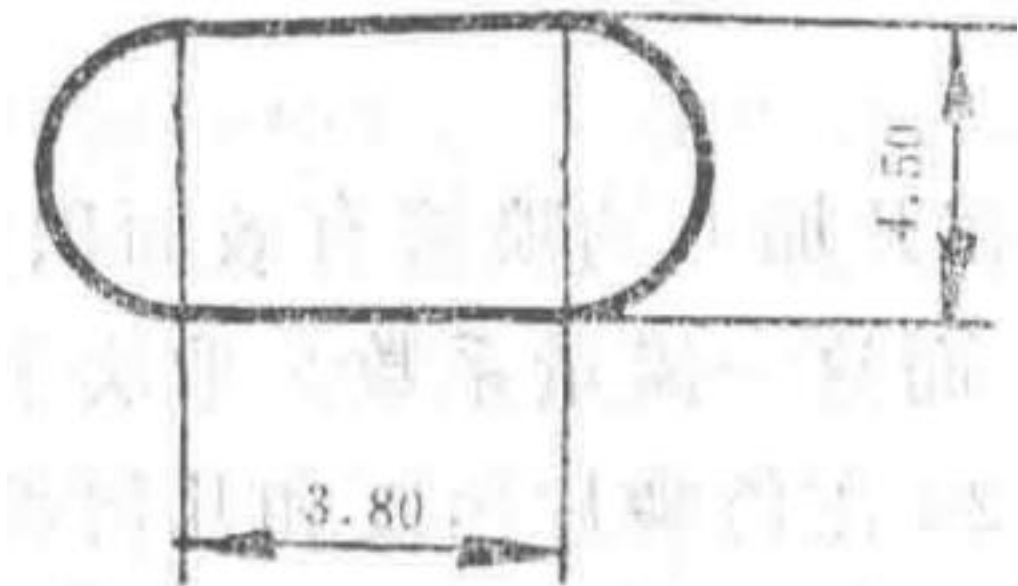
Total area (at mixer plane) = 951 in<sup>2</sup>, geometric area = 570.6 in<sup>2</sup>, effective area CD = 0.6. The total effective area is allocated to ensure equal static pressures for both flows:

Effective area  $A_2 = 202.6 \text{ in}^2 \equiv 337.7 \text{ in}^2$  geometric area

Effective area  $A_6 = 368 \text{ in}^2 \equiv 613.3 \text{ in}^2$  geometric area

And  $p_2 = p_8 = 36.978 \text{ psi (absolute)}$

The mixer is designed with 10 mixing funnels and  $L / W = 2.0$ ,  $A_2 = 330 \text{ in}^2$ .



Schematic of a mixing funnel

Diagram showing the geometry of a single mixing funnel used in the mixer design.

Each mixing funnel is of the form shown above, thus:

$$\text{Perimeter EP} = (2 \times 3.8 + \pi \times 4.5) \times 10 = 217.4 \text{ in}$$

Mixer length  $L = 75$  in, and  $D = 28$  in.

For  $P_e / P_2 = 1.052$  and  $\theta = 30^\circ$ , from the graph:  $CD = 0.576$ .

$$(\sqrt{CD} \times EP) / D = (\sqrt{0.576} \times 217.4) / (28) = 5.89$$

Calculation of mixing funnel parameter

Figure 4 gives a mixing funnel loss of 12.5%.

To achieve effective mixing at the nozzle,  $D = 28$  in must be corrected. Although  $D = 28$  in at the mixer, at 45 in along the 75 in mixing length, the mixing diameter is 35 in. Thus, a mixing diameter of 34 in is used.

$$(\sqrt{CD} \times EP \times L) / ((D)^2) = (\sqrt{(0.576 \times 217.4 \times 75)}) / ((34)^2) = 10.70$$

Corrected mixing parameter

Thus,  $\eta = 83\%$ .

## State Estimation After Mixer

Given:

Therefore,

$$\Delta P / P = 12.5\%, P_2' = 39.518 - 0.318 = 39.200 \text{ psi (absolute)}$$

Similarly,

Therefore,

$$\text{Given } \Delta P^* / P = 12.5\%, P_s' = 41.590 - 0.578 = 41.012 \text{ psi (absolute)}$$

## Calculation of Mixed State

Given:

$$Q_2' = (79.4 \times \sqrt{406.3}) / (202.6 \times 39.200) = 0.2015$$

Flow parameter for bypass flow

Thus,

$$(V) / (\sqrt{T}) = 20.3$$

Velocity parameter

Therefore,

Similarly,

Thus,  $V_6' = 827.3 \text{ ft/s}$

Momentum:

$$(\sum (MV)/(g) + Ap), (\text{see Equation 16.c.7}) = [\text{complex momentum balance calculation}]$$

Momentum balance equation (simplified for clarity)

## Enthalpy Balance: ( $\sum MC\Delta T$ )

$$79.4 \times 0.2396 \times 406.3 + 127.5 \times 0.2527 \times 938.8 = 206.9 \times C_{\Delta} \times T_s$$

Enthalpy balance equation

Thus, iteration for  $T$  and  $C_{\Delta}$  yields  $T = 744 \text{ K}$ .

Given  $p_s = 36.75$ ,

$$= (206.9 \times \sqrt{744}) / (570.6 \times 36.75^{**}) = 0.2691$$

Flow parameter for mixed state

From (1),  $p_s = 36.748 \text{ psi (absolute)}$ . Thus,

$$T_s = 744 \text{ K}$$

Temperature after mixing

## Determination of Flame Stabilizer Slot Width

Let the minimum  $P_s = 5 \text{ psi (absolute)}$ .

Given:

Assume  $\beta = 30\%$ .

Thus,

$$(P)/(p) = 1.0569$$

Pressure ratio for stabilizer calculation

At  $P_s = 5 \text{ psi (absolute)}$ ,

$$(pWT)/(V) = (5) / (1.0569) \times (\sqrt{744}) / (18.4) \times W = 7.013 \times W$$

Parameter for stabilizer slot width

Thus, if the limit  $(DWT \cdot (pWT)/(V)) = 12.0$ , then  $W = 1.711 \text{ in}$ . Therefore, in the calculations, it is assumed that:

## Number of Flame Stabilizers

Assume 90% of the air is used for combustion (i.e., 90% of the area of 1075 in<sup>2</sup>).

Equivalent radius inside the heat shield = 17.549 in.

Solving the above equation yields  $N = 2.68$ , thus 3 rings of stabilizers are used.

## Flame Stabilizer Spacing

Equal groove loading (E.G.L.):

Here,  $x$  = distance between stabilizers = 3.54.

Thus, the inner stabilizer radius  $R_1 = x + (W)/(2) = 4.42$  in.

The area for each stabilizer is as follows:

Thus,

## Diffuser (Oil Shield) Design

The Spey is designed with a diffuser (inside the heat shield) having a constant effective flow area. The stabilizers are staggered upstream by twice the slot width, as shown in Figure 21.

Effective flow area = 647.31 in<sup>2</sup>, inside the oil shield.

Thus, when taking the stabilizer area into account, the oil shield area is:

$$A_2 f/\square = 647.31 + 41.23 + 106.66$$

Calculation of free flow area at plane 2.

Therefore, at plane 1, the free flow area is calculated accordingly.

Therefore, at plane 0, which is twice the groove width upstream of the No. 1 stabilizer.

In these calculations, it is assumed that the area of each stabilizer is equal to its area at the common plane position. In reality, when moving upstream, the stabilizer is required to move along the streamline, so the area slightly decreases.

The position of the upstream stabilizer must be calculated, and the diameter of the diffuser wall must be precisely determined based on the actual stabilizer area.

## Radial Position of Staggered Stabilizers

No. 3 stabilizer radius = 15.00 inches (unchanged).

At plane 2:

Let the radius of the No. 2 stabilizer be  $R_2^2$ , and the radius of the No. 1 stabilizer be  $R_1^2$ . Then:

$$((9.70)^2)/((17.55)^2) = ((R_2^2)^2)/((15.985)^2)$$

Relationship between stabilizer radii at plane 2.

Therefore,  $R_2^2 = 8.835$  inches.

Stabilizer area  $^2_2 = 97.15 \text{ in}^2$ .

Similarly:  $R_1^2 = 4.026$  inches.

Stabilizer area  $^2_1 = 44.27 \text{ in}^2$ .

Let the radius of the No. 1 stabilizer be  $R_1^1$  (at plane 1). Then:

$R_1 = 3.75$  inches.

Stabilizer area  $^1_1 = 41.23 \text{ in}^2$ .

## Recalculation of the Oil Baffle

Since the airflow area at each stabilizer plane is equal,

$$D_{28,1,8} = 31.69 \text{ inches}$$

Diameter at a specific plane.

And  $A_1 f/\square = 647.31 + 41.23 = 688.54 \text{ in}^2$ ,  $D_{5/5} = 29.61 \text{ inches}$ ,  $D_0 f/\square^*$  remains equal to 28.71 inches (as before).

## Determination of Diffuser (Inside Oil Baffle) Stability

First, estimate the diffuser (0–1) between the inner stabilizer centerline and the oil baffle. Treat as an angled annular channel.

Length ( $L$ )  $\tau = 2 \times W = 3.5$  inches.

At the inlet, diffuser width ( $W_1$ ) =  $(28.71 - 7.50)/(2) = 10.605$  inches.

However, assuming  $(\delta)/(W_1) = 0.0625$ , so  $\Phi' = 16^\circ 30'$ , which is the maximum allowable effective angle for airflow without separation.

Now assume the diffuser has an angle  $\beta$ . Then,

Here,  $\varphi$  is the actual diffuser angle.

Now, the average radius ( $R$ ) =  $(28.71 - 7.50)/(2 \times 2) + 3.75 = 9.052$ .

Since for small angles,  $\beta = (\text{with small inner wall angle})$ . Therefore,

Thus,

5.858

Intermediate calculation result.

Let the actual wall angle be  $\alpha$ .

Therefore, wall angle  $\beta + (\Phi)/(2) = 10^\circ 26'$  maximum.

Thus,

$$\alpha = (0.90)/(2 \times 3.5) = 0.1286$$

Calculation of wall angle  $\alpha$ .

Converting radians to degrees:  $0.1286 \times 57.3 = 7.37^\circ$ .

Given  $Q = 720 \text{ g/s}$ ,  $1.88a = 8.11$ ,  $18.18 = 14$ .

## Cold Loss Estimation and Post-Cold Loss Pressure

The cold loss of the afterburner system ( $\Delta P/D$ ) is given as follows:

Since  $\beta = 30\%$ ,  $\Delta P / D = 1.22$ .

$$Q_s = (206.9 \times \sqrt{744})/(1075 \times 40.765) = 0.1288$$

Calculation of flow parameter  $Q_s$ .

$$(P / p)_s = 1.0260$$

Pressure ratio at station 8.

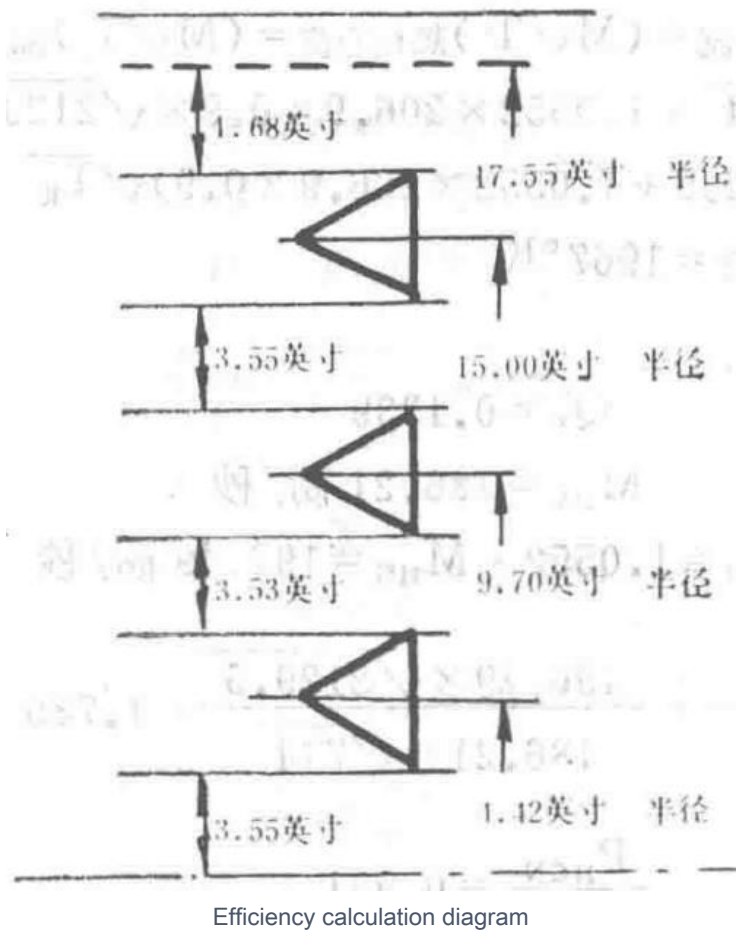
Given  $P_s = 40.765$ , so  $D = 1.033$ ,  $(\Delta P)/(D) = 1.22$ , and  $(\Delta P)/(P) = 3.80\%$ . Therefore,  $P_s' = 39.216 \text{ psi}$ .

## Efficiency Calculation

Width factor:

Thus,  $W \times F = 3.039 \text{ inches}$ .

Therefore,



Efficiency calculation diagram

Diagram related to efficiency calculation parameters.

Given  $P_{\infty}^{*} = 39.216 \text{ psi} = 5647.0 \text{ psf}$ ,

$$P_{\infty}^{10.324} = 16.428$$

Pressure raised to the power of 0.324.

$$T = 744 \times 1339 \times R, T^{1.07} = 2216.4$$

Temperature conversion and calculation.

Ideal condition.

Therefore:

$$\square = (16.428 \times 2216.4 \times 4.513) / (2.452) = 67015.8$$

Efficiency calculation result.

Note: The original text mistakenly wrote  $\Gamma_{\infty}$ .

## Afterburner Temperature

Since

$$BED = 7A = 288 = 456 \times K$$

Temperature calculation in the afterburner.

But

Therefore,

$$0.0663 = (f \square \square \square \square a \square \square \square \square r \square \square \square \square - 0.0112)/(0.0112)$$

Correction factor calculation.

Efficiency

Given  $t_e = 80.0 = W$ ,

But

Therefore,

$$\eta \square = 92\%$$

Efficiency of the system.

$$0.92 (2250 - 744) = T \square C - 744$$

Temperature rise calculation.

$$T \square C = 2129.5 \square \square^r K$$

Final temperature after combustion.

$$0.1 \times 206.9 \times \sqrt{744} + 1.0552 \times 206.9 \times 0.9 \times \sqrt{2129.5} = (0.1 \times 206.9 + 1.0552 \times 206.9 \times 0.9) \sqrt{T \square}$$

Heat addition calculation.

## Heat Loss Calculation

$$((M \sqrt{T}) d \square f_f) / ((M \sqrt{T}) d \square f_f) = (196.49 \times \sqrt{2129.5}) / (186.21 \times \sqrt{744}) = 1.785$$

Heat loss ratio calculation.

$$(P \square C \square) / (P \square C) = 0.931$$

Pressure ratio after heat loss.

## Thrust Calculation (Non-Afterburning)

### (A) Fully Mixed Thrust ( $X_F \square$ ) and Area ( $A_F \square$ )

$$(P_F \square) / (P_0) = (P_s') / (P_0) = 2.668,$$

Pressure ratio for fully mixed thrust.

Therefore,  $X_F \square = 12782 \text{ lbf}$ .

$$(X) / (A p_0) = 2.37$$

Thrust per unit area calculation.

Similarly,  $A_F \square = 367 \text{ in}^2$ .

### (B) Unmixed Thrust ( $X_U \square$ ) and Area ( $A_U \square$ )

Outer flow:

Given  $P_2 = 39.518$  psi (absolute) and  $\Delta P / P = 3.8\%$ ,

$$\Delta P = 1.502$$

Pressure loss calculation.

Therefore,  $P_2' = 38.016$  psi (absolute).

$$(P_F \square) / (P_0) = (P_2') / (P_0) = 2.587$$

Pressure ratio for outer flow thrust.

Therefore,

$$(X) / (M \sqrt{T}) = 2.222$$

Thrust parameter for outer flow.

$X_2' = 3556$  lbf.

Similarly,  $A_2' = 106.0$  in<sup>2</sup>.

Turbine flow:

Given  $P_8 = 41.590$  psi (absolute),

Therefore,  $P_6' = 40.010$  psi (absolute).

$$(P_F \square) / (P_0) = (P_6') / (P_0) = 2.722$$

Pressure ratio for turbine flow thrust.

Therefore,

$$(X) / (M \sqrt{T}) = 2.295$$

Thrust parameter for turbine flow.

Check and thus,

Therefore,  $X \square \square = X_2' + X_6' = 12622$  lbf, and

### (C) Partially Mixed Thrust ( $X \square \square$ ) and Area ( $A \square \square$ )

Mixing coefficient  $K = 83\%$ .

$$K = (X \square \square - X \square \square) / (X_F \square - X \square \square)$$

Mixing coefficient calculation.

## Thrust Calculation (Afterburner Operation)

### Cold Flow

$$(P_{\infty} / P_0) = (P_s / P_0) = 2.668$$

Pressure ratio of cold flow at mixed state (before cold loss)

Similarly, for the hot core flow:

$$P_F / P_0 = P_C / P_0 = 2.484$$

Pressure ratio of hot core flow

$$X M_{YT} = 2.23$$

Ratio of thrust parameter X to mass flow parameter MYT

$$(X) / (A p_0) = 2.1$$

Ratio of thrust parameter X to product of area A and reference pressure  $p_0$

Therefore, the Mach number after combustion is checked as follows:

$$Q_{HCN} = 196.49 \times \sqrt{(2129.5^*)} 968 \times 36.510 = 0.2566$$

Calculation of flow parameter Q for hot core flow (Note: Original text missing square root symbol)

Thus, the hot core flow Mach number  $M_{N} = 0.439$ , which is below the maximum permissible value.

Table I

Symbol	Unit	Definition
P	lb/in <sup>2</sup>	Total pressure
p	lb/in <sup>2</sup>	Static pressure
T	K	Total temperature
V	ft/s	Velocity
M	lb/s	Mass flow rate
MN		Mach number

\* Note: The original text omitted the square root symbol in the equation.

### Nomenclature

- N - Number of stabilizers
- W - Inches, Stabilizer slot width
- Lc - Inches, Combustion length
- W.F. - Inches, Width factor
- X - Percentage of air used for combustion (%)
- S.F.C. - lb/hr/lb, Specific fuel consumption rate
- ΔP/D - Stabilizer loss expressed in dynamic pressure head

- $\Delta P/D_1$  - Total cold loss in combustion chamber
- DP - Afterburner diameter (inches)
- $\eta_c$  - Combustion efficiency
- $P_{min}$  - lb/in<sup>2</sup>, Minimum operating pressure of afterburner
- A - Inches<sup>2</sup>, Area of mixer main duct
- AG g - Inches<sup>2</sup>, Mixing funnel outlet area perpendicular to outlet airflow
- $\theta$  - Mixer jet angle (degrees)
- L - Inches, Mixing funnel length
- W - Inches, Mixing funnel width
- CD - Flow coefficient
- $\beta$  - %, Stabilizer blockage ratio
- $L_m$  - Inches, Mixing length (from mixer to stabilizer)
- $T \square - K$ , Gas temperature at nozzle (thrust average)
- $T \square C - K$ , Hot core flow outlet temperature
- AcAN - Inches<sup>2</sup>, Cooling air outlet area at nozzle
- XGL - lb, Total thrust with afterburner
- XGD - lb, Total thrust without afterburner
- Cp - Specific heat at constant pressure

## Subscripts

- 2 - Bypass outlet
- 6 - Turbine exhaust flow outlet
- 8 - Mixed state (before cold loss)
- 8' - After cold loss
- L - Stabilizer edge

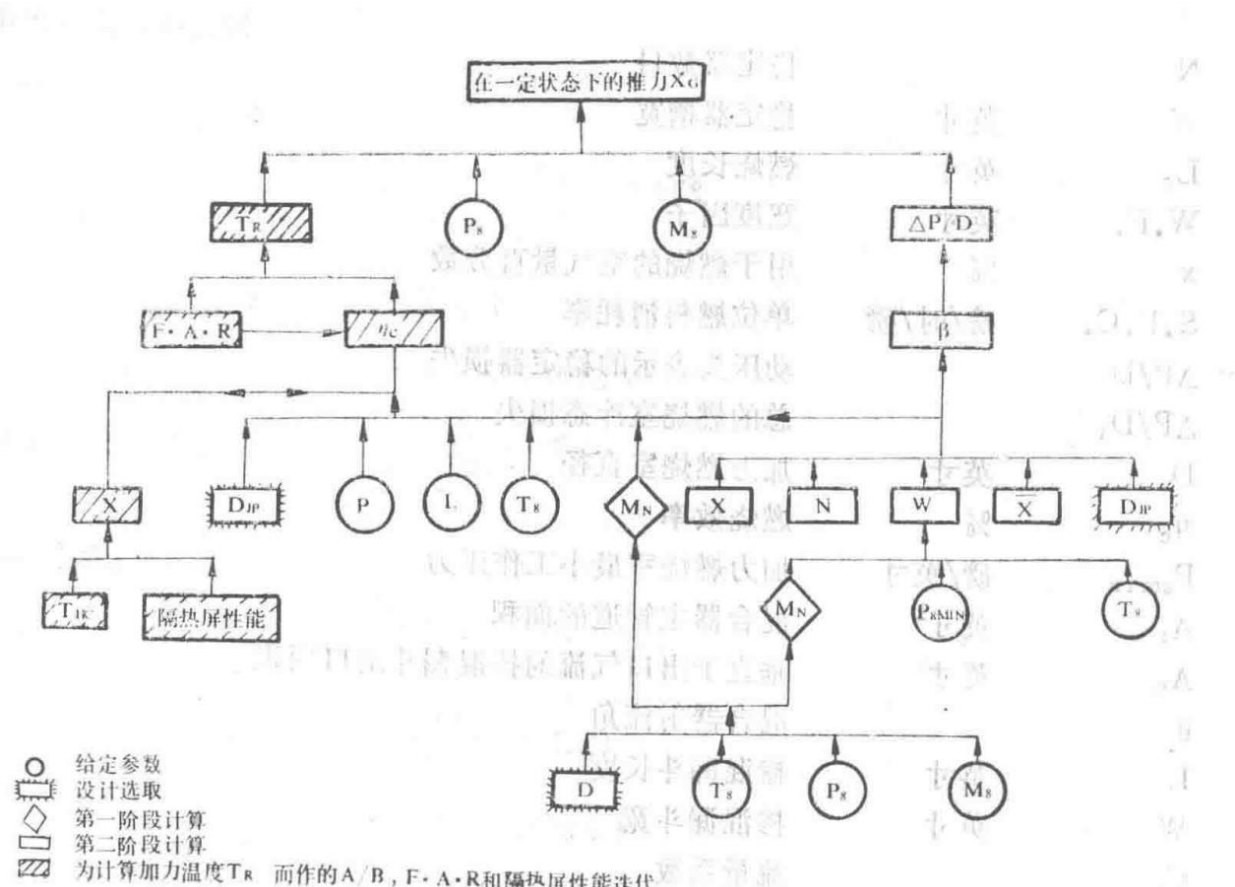


Figure 1: Afterburner Design Performance Optimization

Diagram illustrating the optimization process for afterburner design performance.

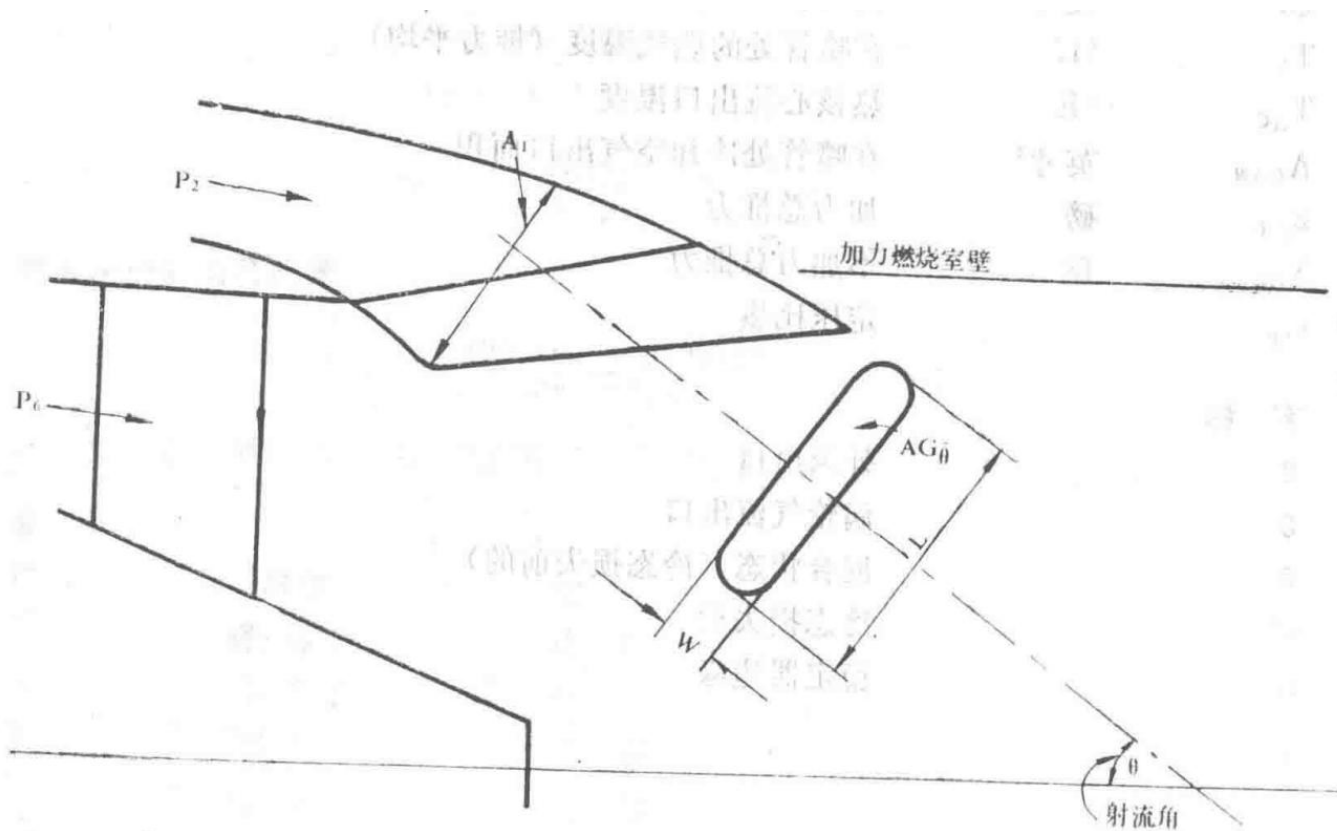


Figure 2: Jet Mixer Schematic Diagram

Schematic representation of the jet mixer used in the Spey MK202 engine.

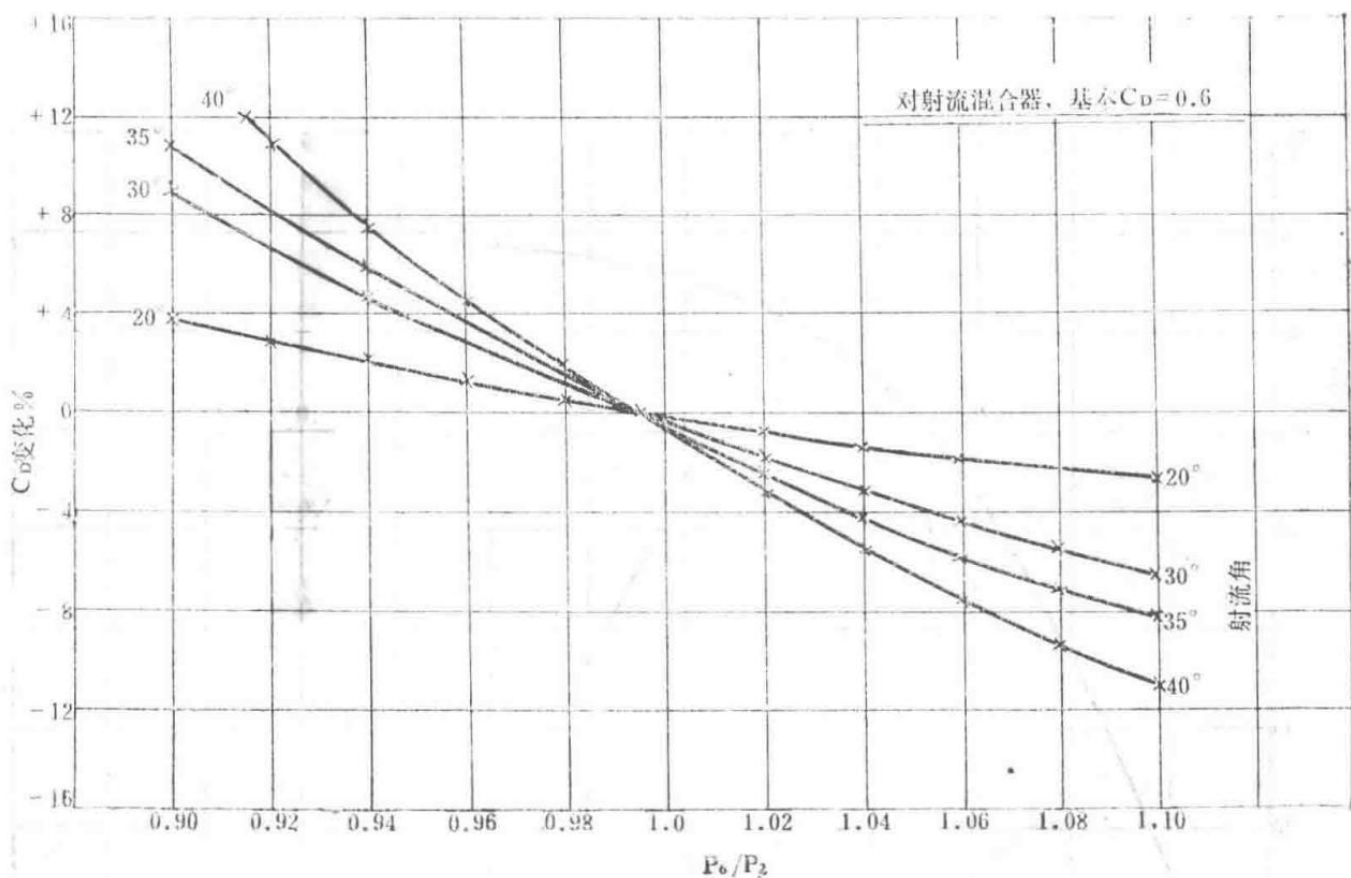


Figure 3: Effect of  $\theta$  and  $P_8/P_2$  on Basic Flow Coefficient CD

Graph showing the influence of mixer jet angle  $\theta$  and pressure ratio  $P_8/P_2$  on the basic flow coefficient CD.

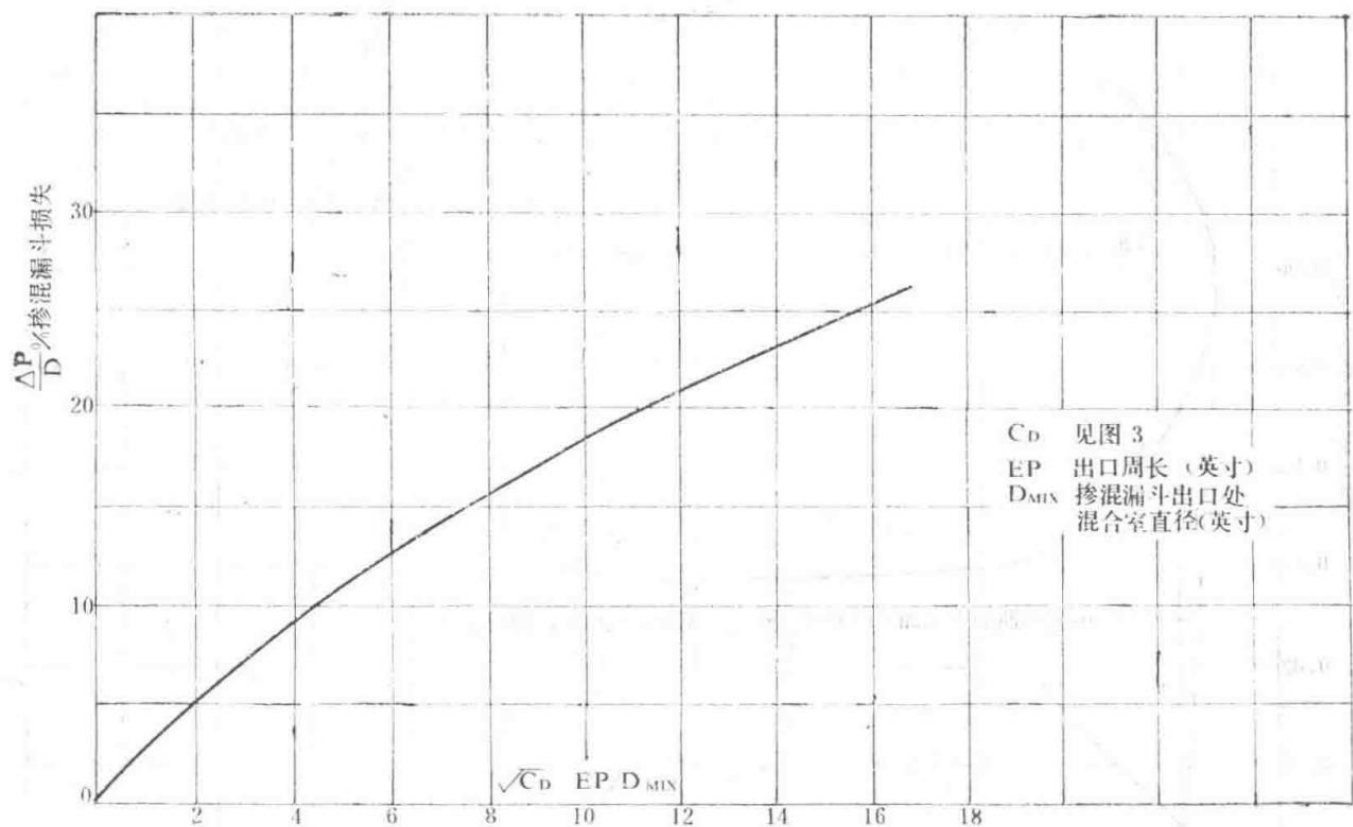


Figure 4: Mixer Loss (Mixing Funnel Loss)

Diagram depicting the losses associated with the mixing funnel in the engine.

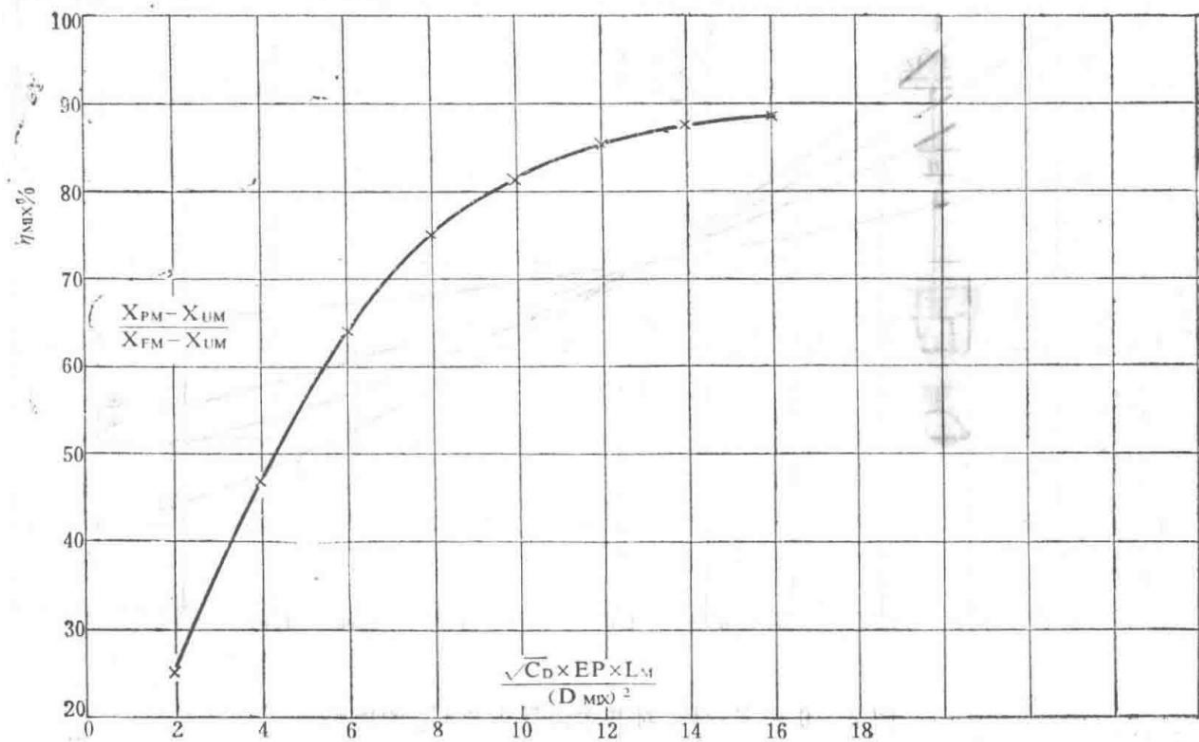


Figure 5: Mixer Performance Relationship Curves

Performance relationship curves for the mixer component of the engine.

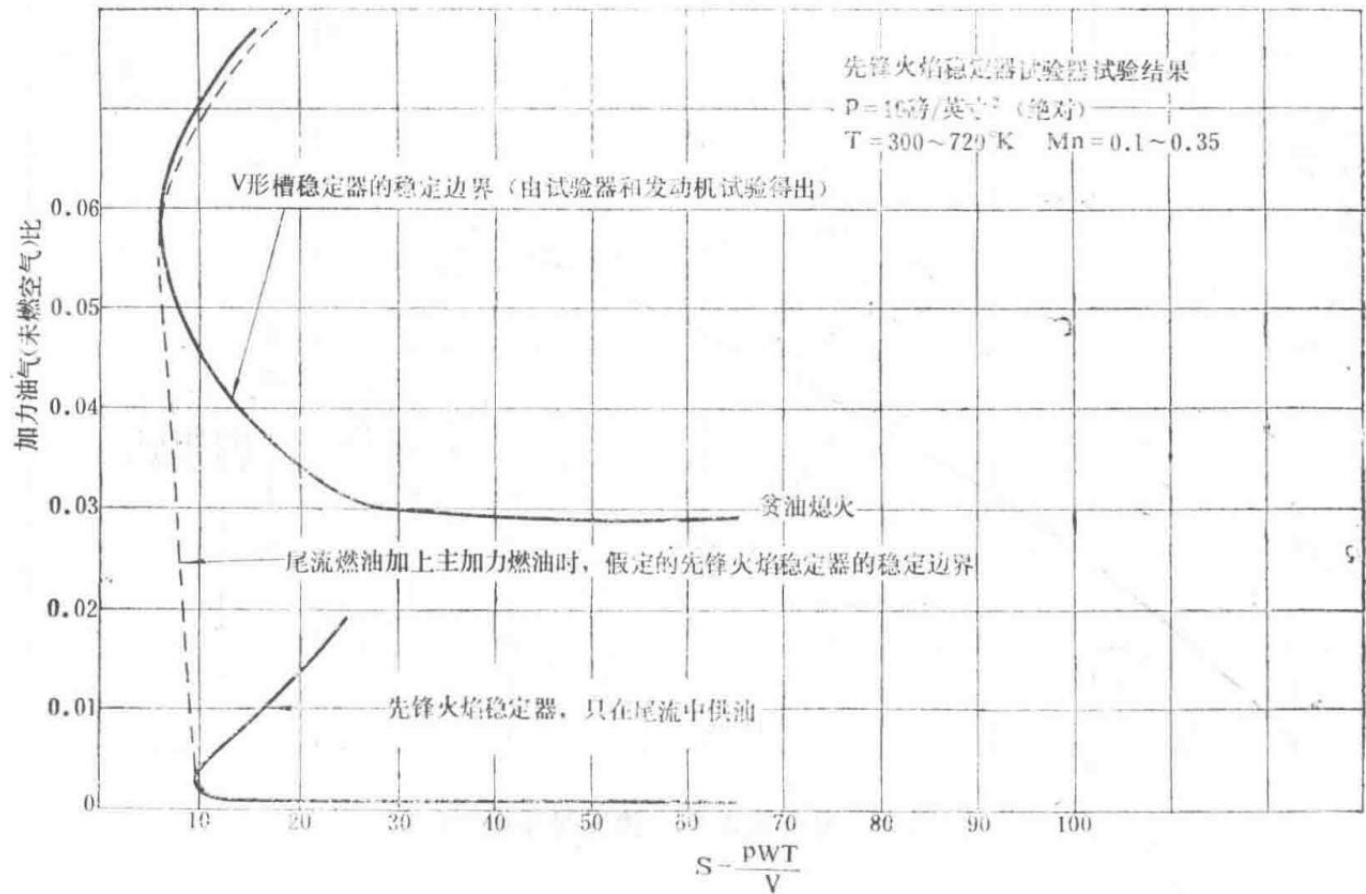


Figure 6: Stability Comparison Between V-Gutter Stabilizer and Pioneer Flame Stabilizer

Comparison of stability characteristics between V-gutter stabilizers and pioneer flame stabilizers.

— Section 40 —  
Content from Original Document (Pages 196-200)

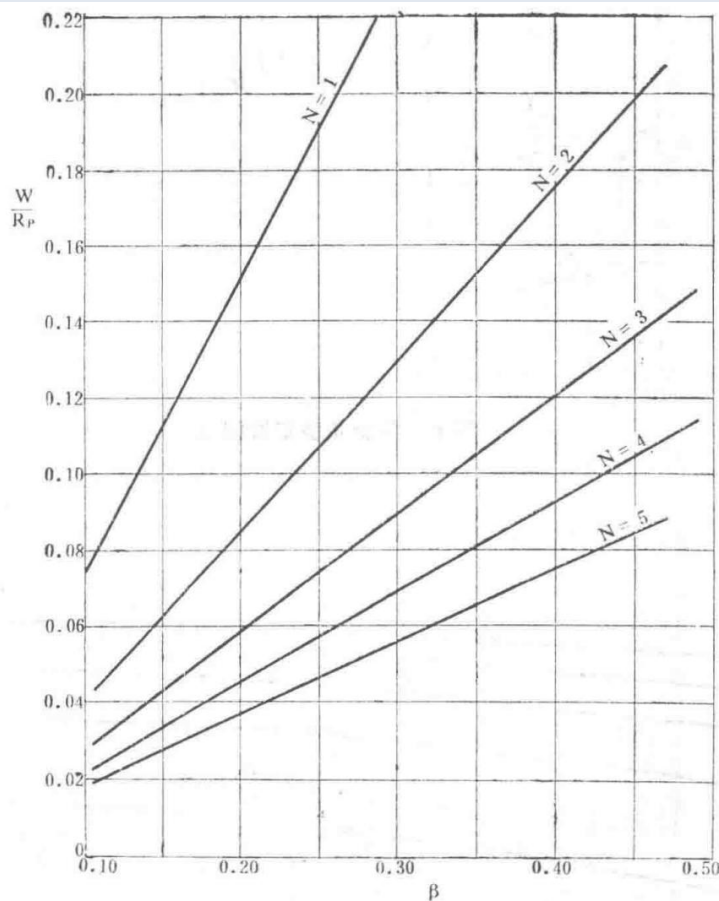


Figure 7: Relationship between  $N$ ,  $R\Box$ ,  $W$ , and  $\beta$  under equal slot load

Graph showing the interdependencies of parameters  $N$  (number of slots),  $R\Box$  (pressure ratio),  $W$  (mass flow rate), and  $\beta$  (flow angle) under equal slot load conditions.

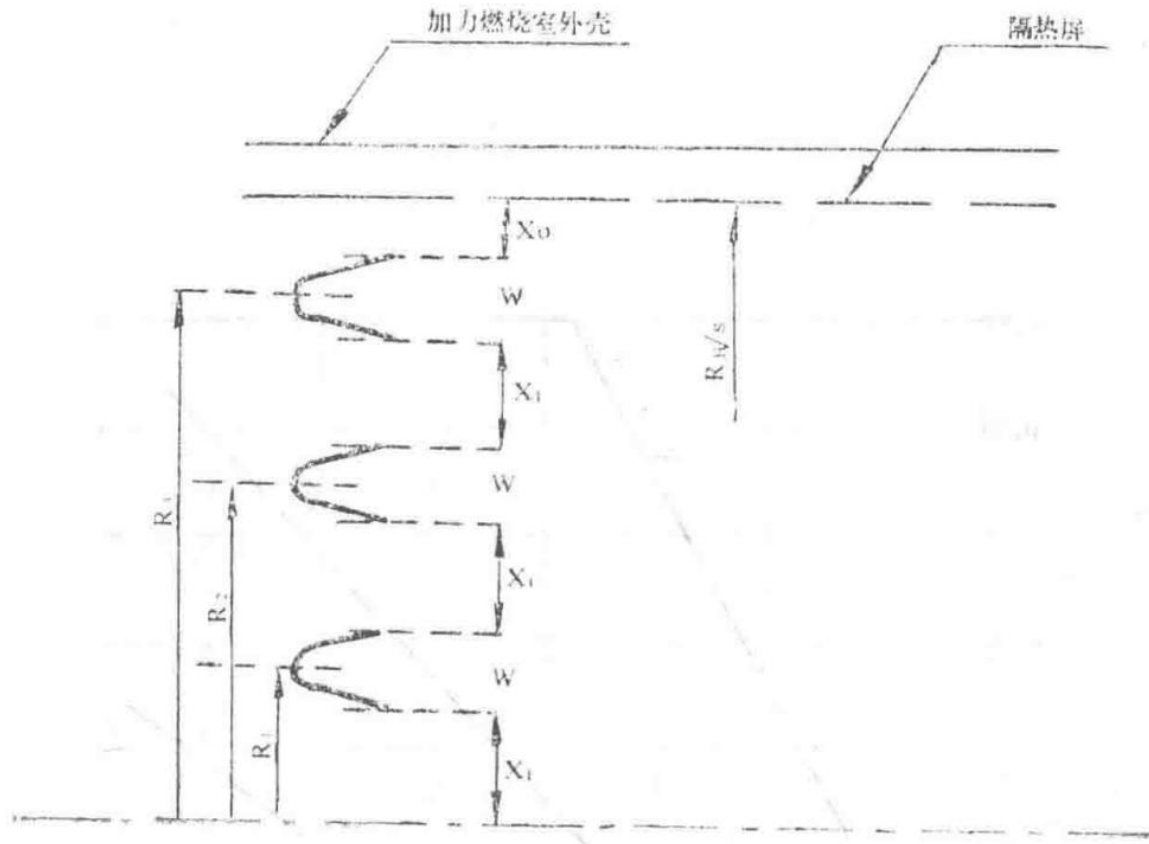


Figure 8: Equal slot load stabilizer spacing

Diagram illustrating the spacing between stabilizers under equal slot load conditions.

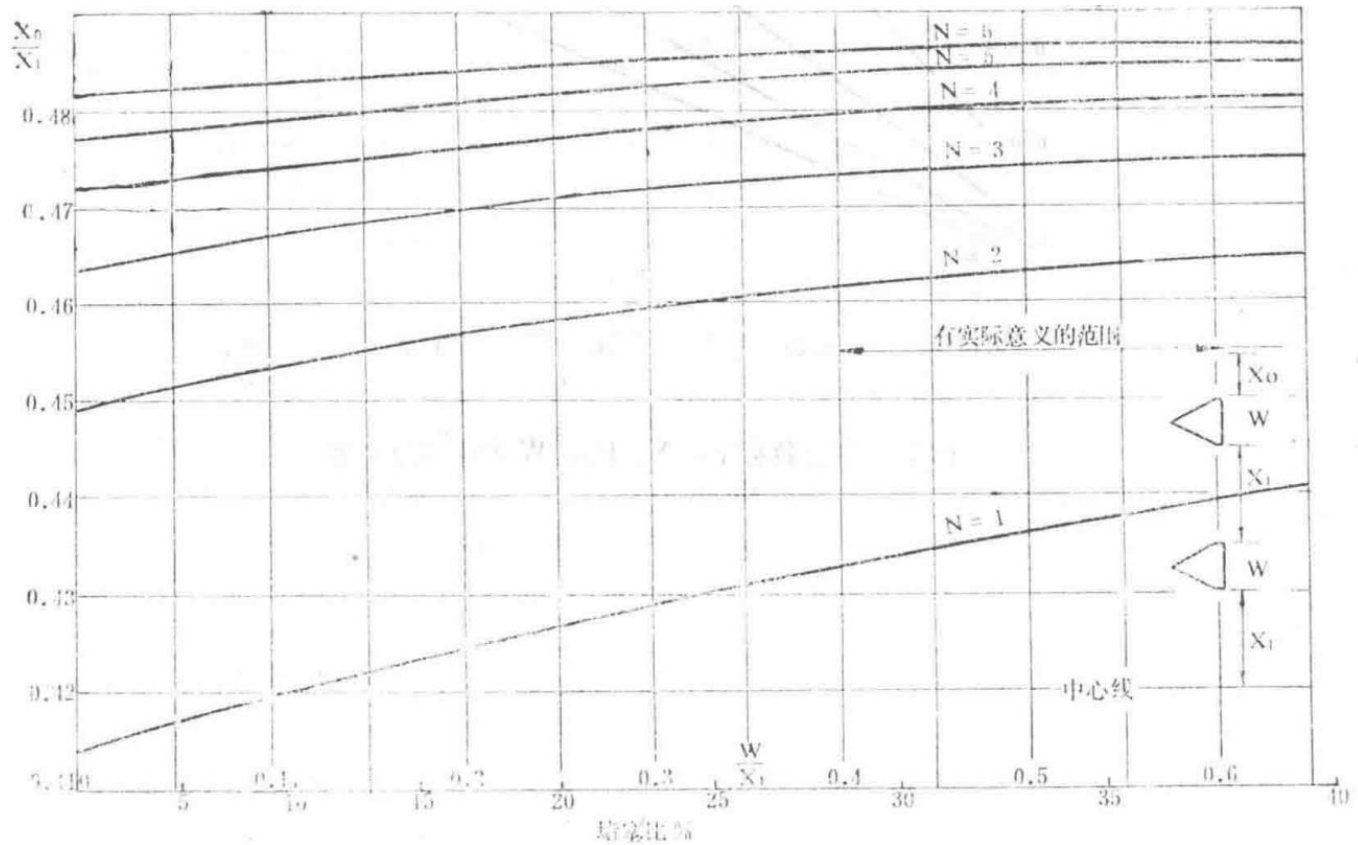


Figure 9: Equal slot load stabilizer spacing relationship curves

Curves depicting the relationship between stabilizer spacing parameters under equal slot load conditions.

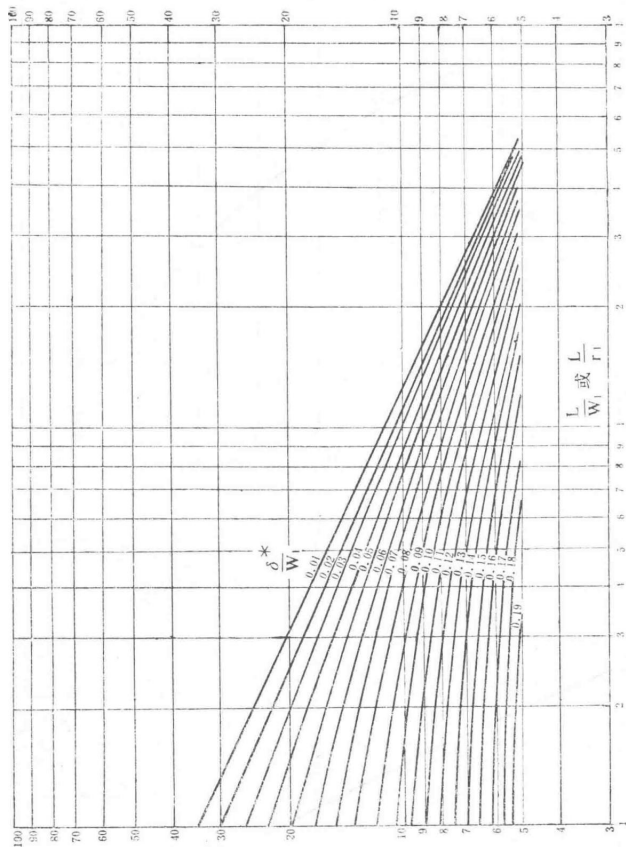
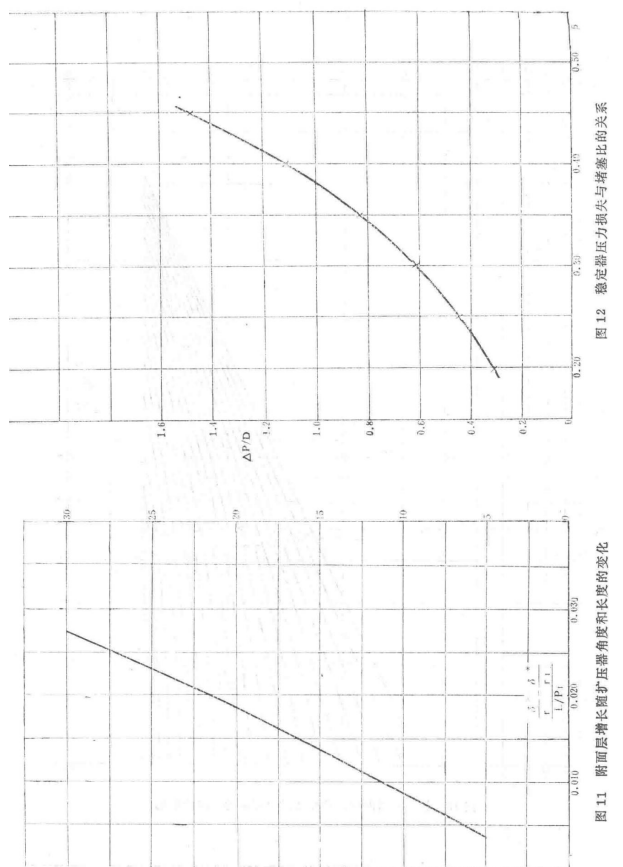


Figure 10: Influence of length and boundary layer displacement thickness on stable flow limit

Graph showing how the length of the combustion chamber and boundary layer displacement thickness affect the stable flow limit.



Unlabeled diagram (possibly a schematic or intermediate graph related to combustion parameters).

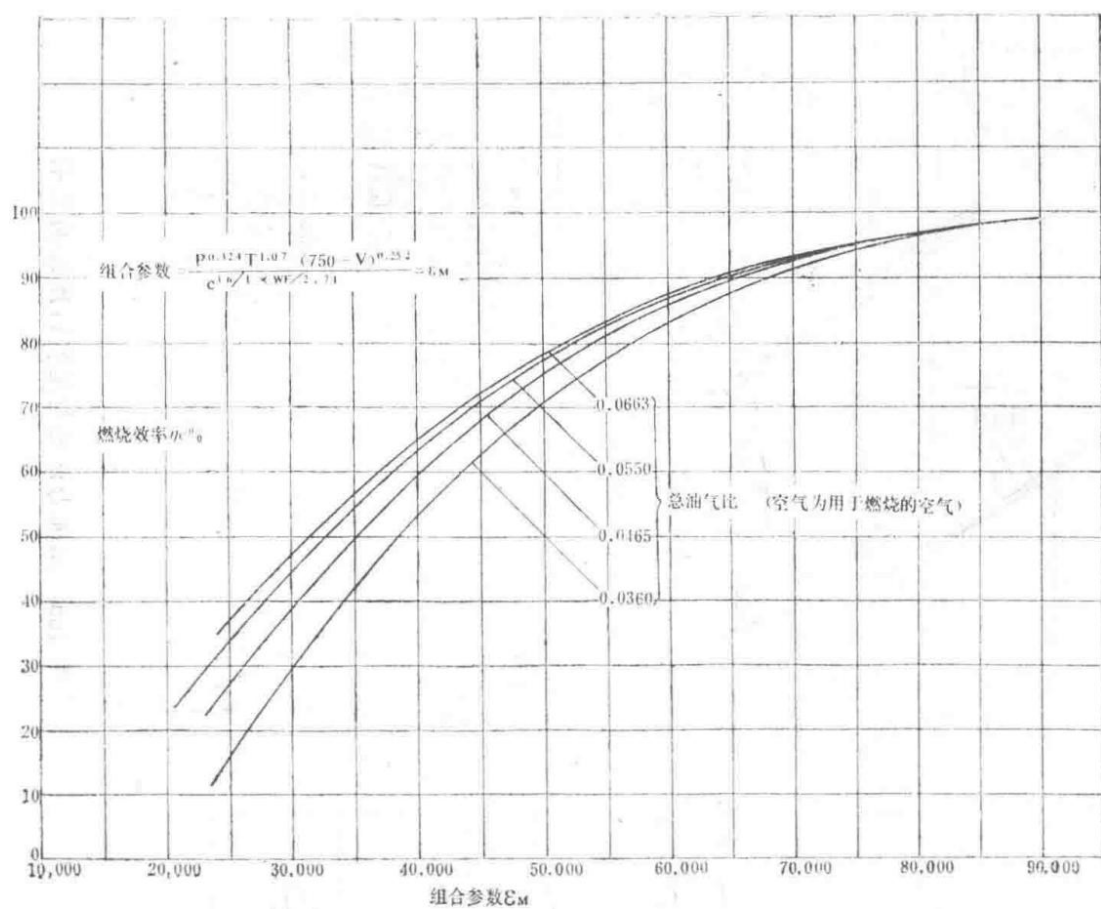


Figure 13: Combustion efficiency versus combined parameter  $\square$  relationship curve

Curve showing the relationship between combustion efficiency and the combined parameter □.

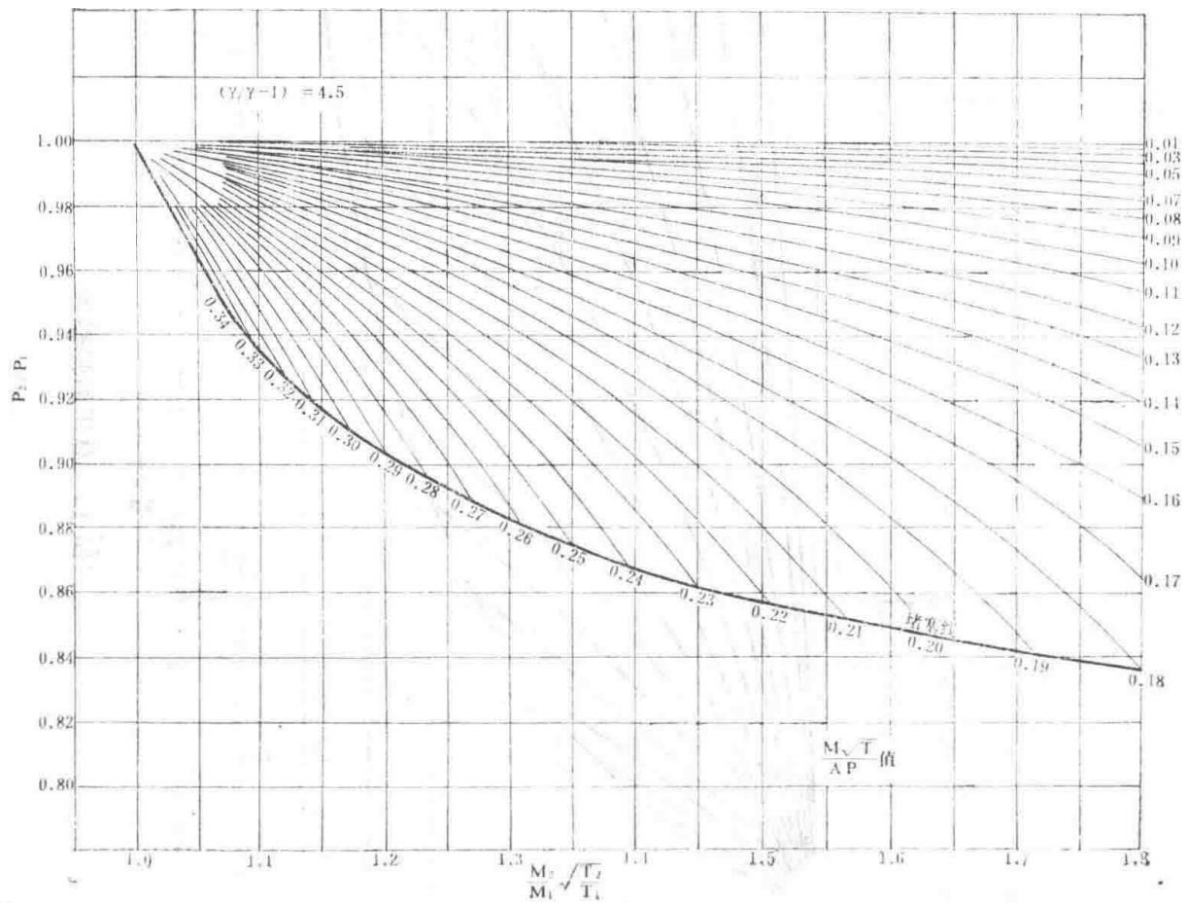


Figure 14: Thermal loss of total pressure

Graph depicting the thermal loss of total pressure in the engine system.

Parameter Relationship Table (from Figure 7 diagram)

L/W <sub>1</sub>	$\delta/W_1$	W <sub>1</sub>
1	0.01	0.01
2	0.02	0.02
3	0.03	0.03
4	0.04	0.04
5	0.05	0.05
6	0.06	0.06
7	0.07	0.07
8	0.08	0.08
9	0.09	0.09
10	0.10	0.10
11	0.11	0.11
12	0.12	0.12
13	0.13	0.13
14	0.14	0.14
15	0.15	0.15

16	0.16	0.16
17	0.17	0.17
18	0.18	0.18
19	0.19	0.19

Stable Combustion Boundary Parameters (from Figure 8 diagram)

X <sub>0</sub> /X <sub>1</sub>	N	θ
0.12	1	0.42
0.13	2	0.44
0.14	3	0.45
0.15		0.46
0.16		0.47

$$p_0^{0.42} T_0^{1.0} (750)/(V^{0.254})$$

Equation for combined parameter calculation under specific inlet conditions (pressure p<sub>0</sub>, temperature T<sub>0</sub>, and velocity V).

Combustion Efficiency vs. Combined Parameter ε□ (from Figure 13 diagram)

Combined Parameter ε□	Combustion Efficiency ηΓ <sub>0</sub>
20,000	20
30,000	40
40,000	60
50,000	70
60,000	80
70,000	90
80,000	95

$$(r)/(r_1) = f((L)/(P_1))$$

Relationship between normalized radius (r)/(r<sub>1</sub>) and normalized length (L)/(P<sub>1</sub>) for flame stabilization.

Total Pressure Loss vs. Mach Number and Temperature Ratio (from Figure 14 diagram)

M√(T <sub>0</sub> /T <sub>1</sub> )	P <sub>2</sub> /P <sub>1</sub> (for ΔP/P)
1.0	1.00
1.1	0.98
1.2	0.96
1.3	0.94
1.4	0.92
1.5	0.90
1.6	0.88
1.7	0.86

1.8	0.84
-----	------

Relationship between  $(W)/(R\Delta)$  and  $\beta$  for Different N Values (from Figure 7 diagram)

$\beta$	$W/R\Delta$ (N=1)	$W/R\Delta$ (N=2)	$W/R\Delta$ (N=3)	$W/R\Delta$ (N=4)	$W/R\Delta$ (N=5)
0.10	0.02	0.04	0.06	0.08	0.10
0.20	0.04	0.08	0.12	0.16	0.20
0.30	0.06	0.12	0.18	0.24	0.30
0.40	0.08	0.16	0.24	0.32	0.40
0.50	0.10	0.20	0.30	0.40	0.50

The diagrams and tables above illustrate the key relationships between various aerodynamic and thermodynamic parameters in the Spey MK202 engine's combustion system under equal slot load conditions. These include the effects of stabilizer spacing, boundary layer displacement thickness, combustion efficiency, and total pressure loss on engine performance.

— Section 41 —  
Content from Original Document (Pages 201-205)

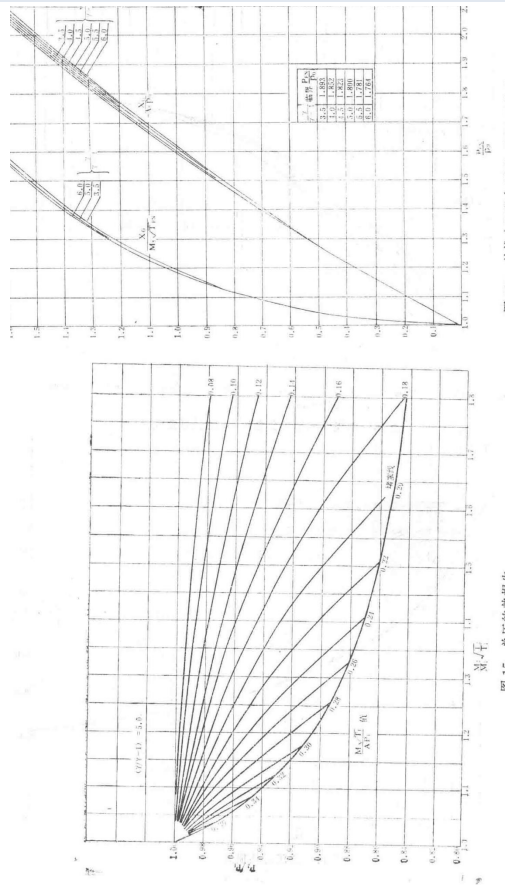
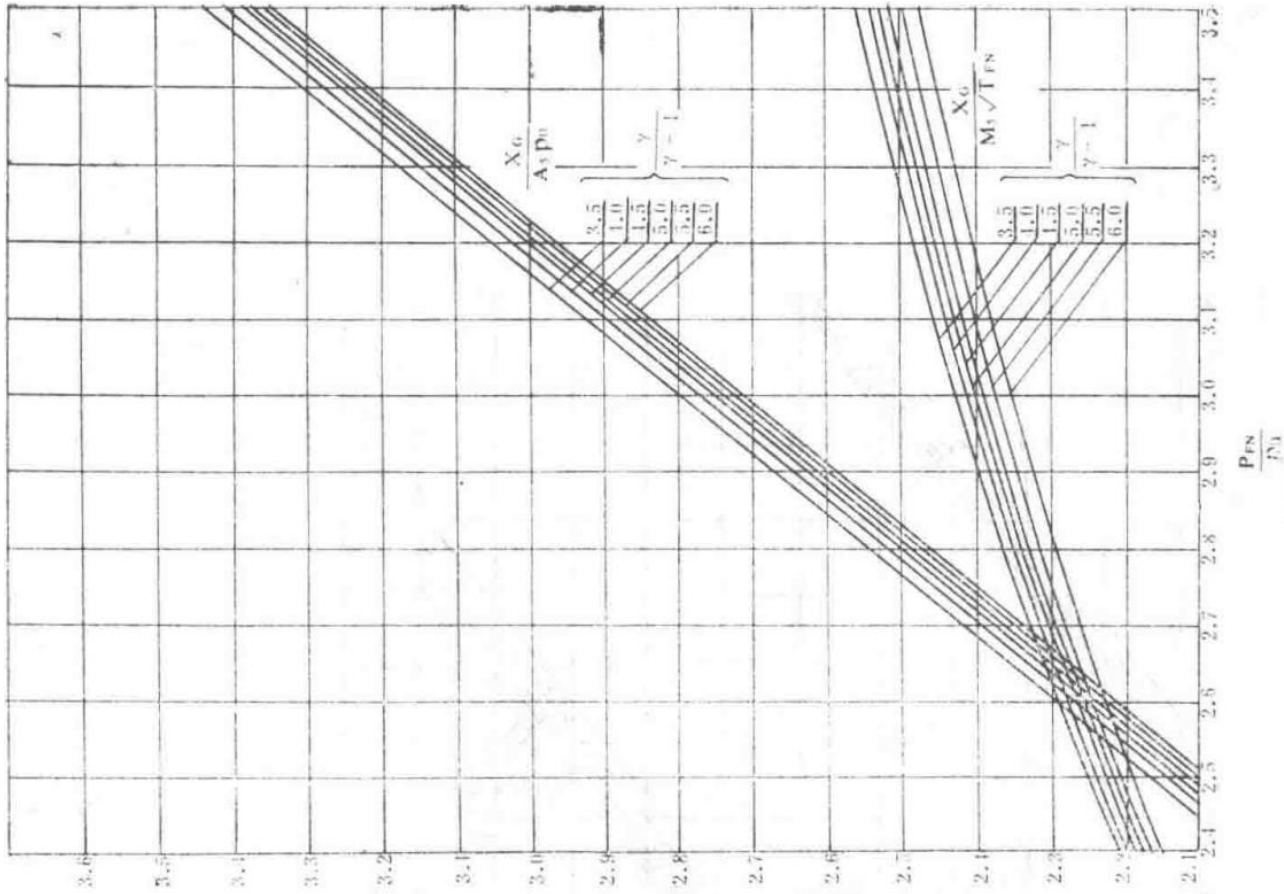


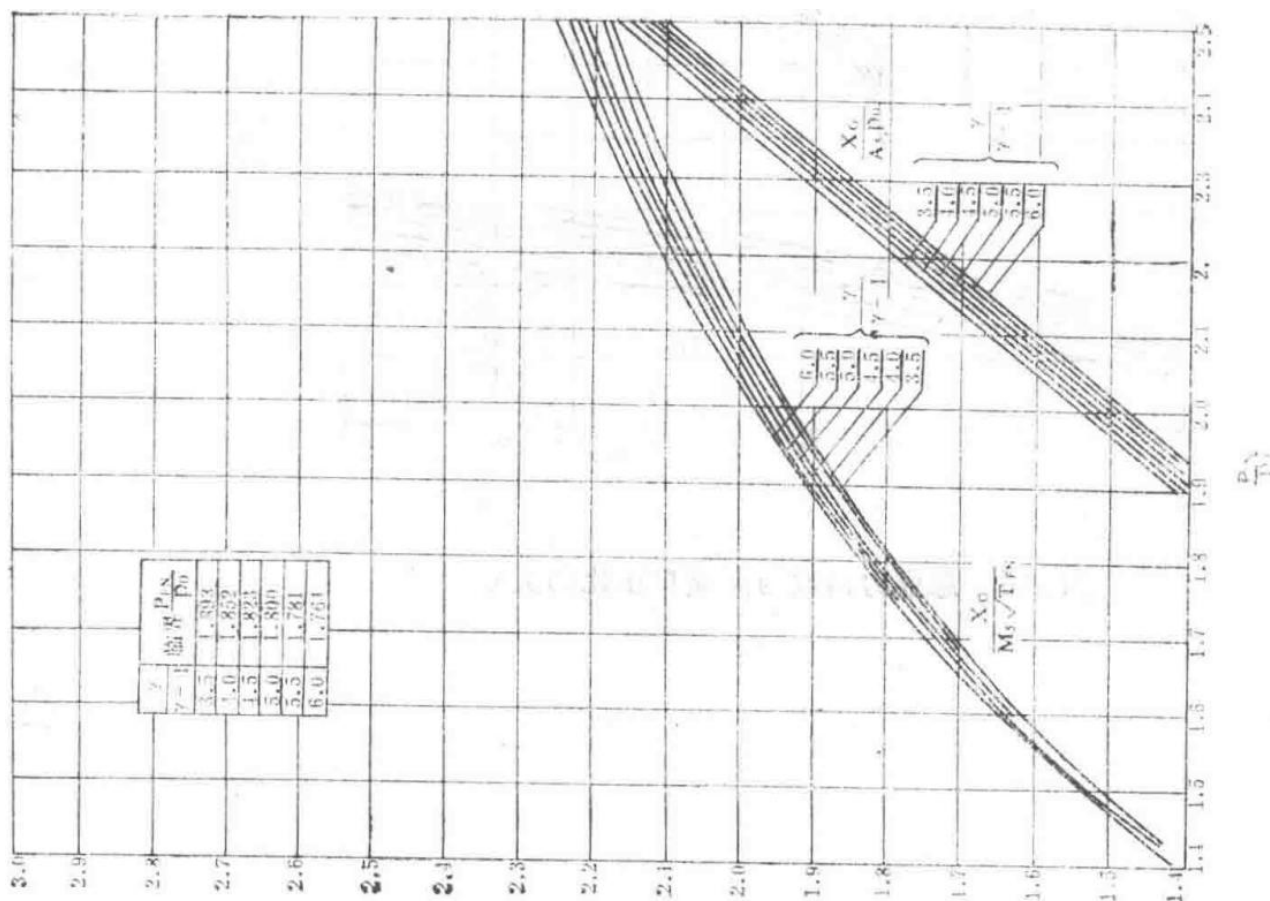
图 16a 燃油热效率与总温比之间的关系

图 15 比压的热损失

Technical diagram related to Spey MK202 aircraft engine performance characteristics.



Technical diagram related to Spey MK202 aircraft engine performance characteristics.



Technical diagram related to Spey MK202 aircraft engine performance characteristics.

图 16c 总推力函数与尾喷口压比的关系

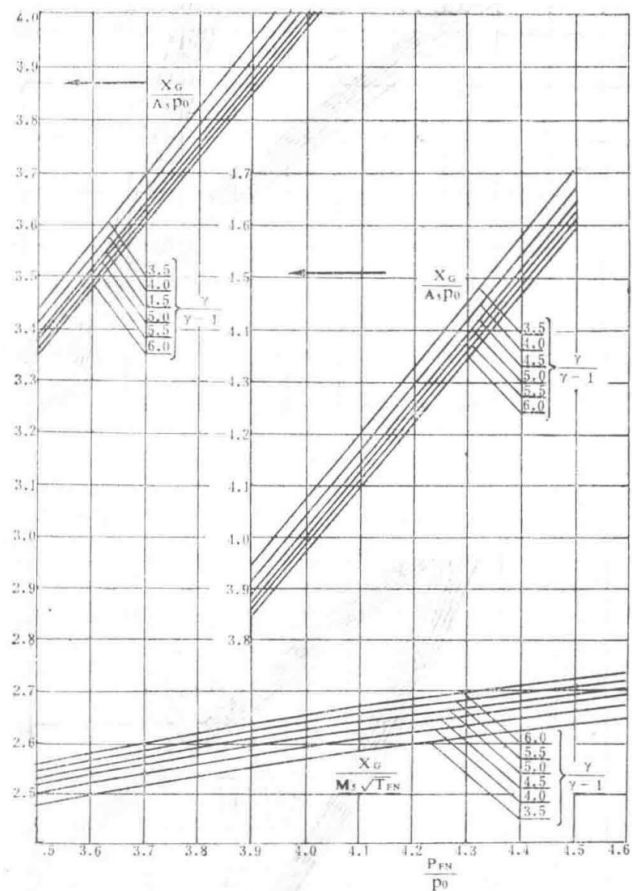


Figure 16d: Relationship between total thrust function and nozzle pressure ratio

Graph showing the relationship between the total thrust function and the nozzle pressure ratio for the Spey MK202 engine.

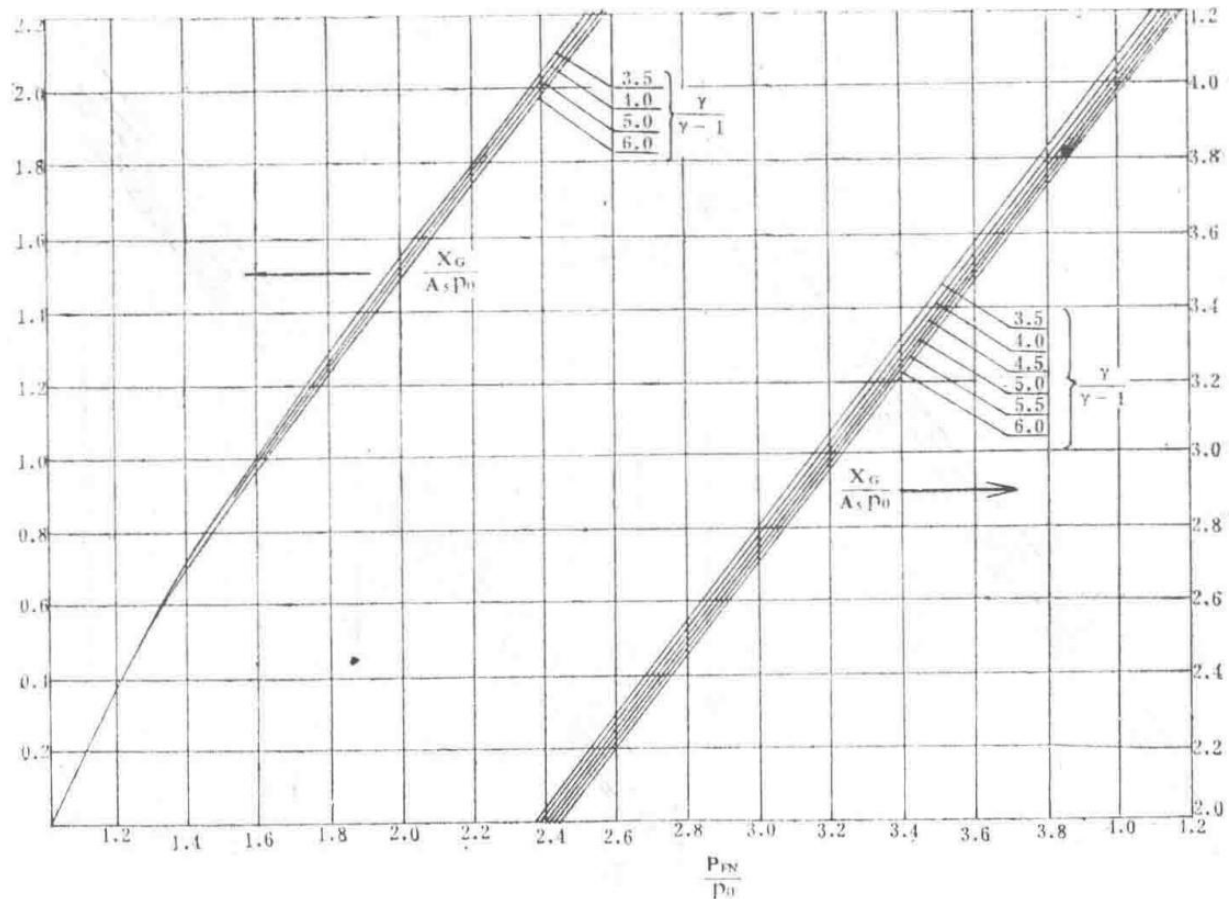


Figure 16e: Relationship curve of  $\text{rac}XGA_8p_{08}$   $\text{rac}P_7p_7$  for a convergent nozzle

Graph depicting the relationship between  $\text{rac}XGA_8p_{08}$  and  $\text{rac}P_7p_7$  for a convergent nozzle in the Spey MK202 engine.

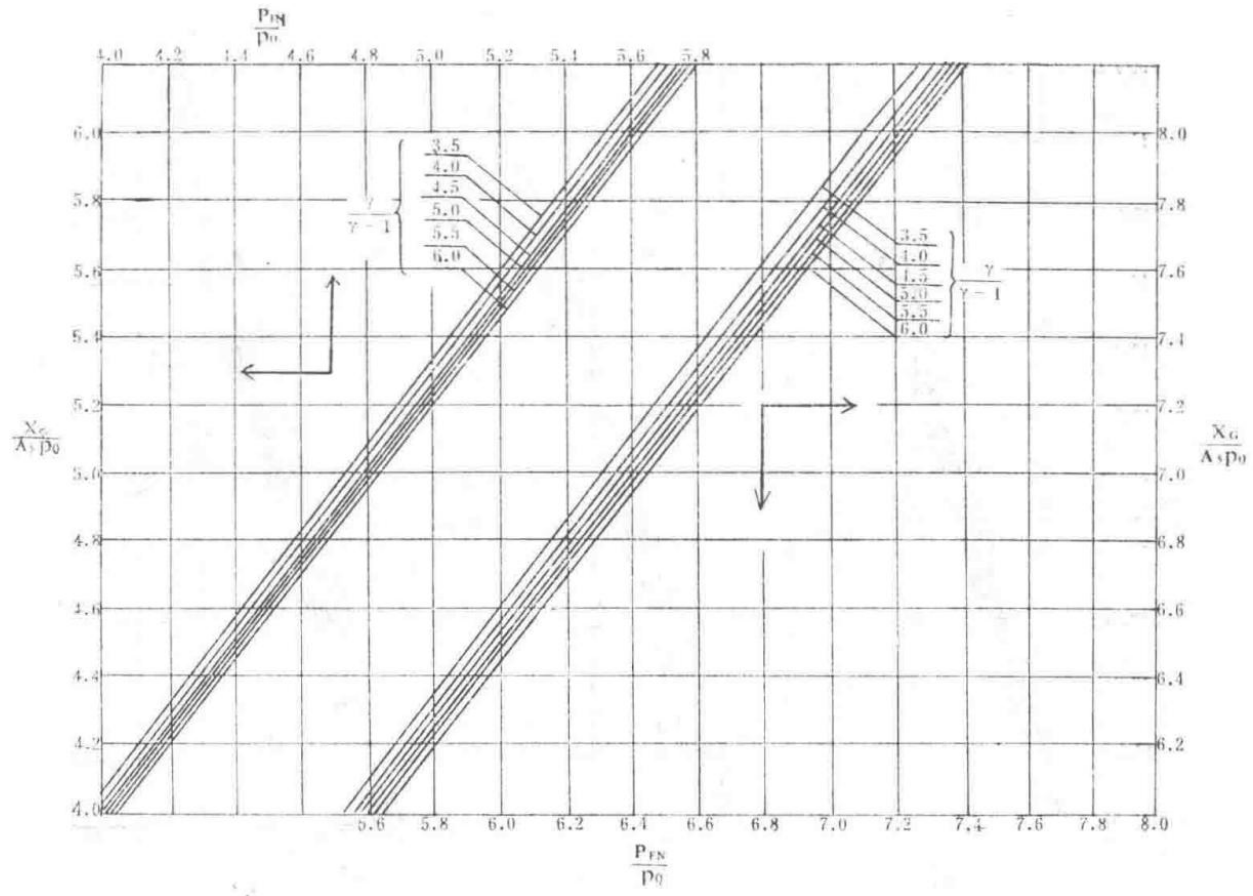


Figure 16f: Relationship curve of  $\text{rac}XGA_8p_0$   $\text{rac}P_7p_7$  for a convergent nozzle

Graph depicting the relationship between  $\text{rac}XGA_8p_0$  and  $\text{rac}P_7p_7$  for a convergent nozzle in the Spey MK202 engine.

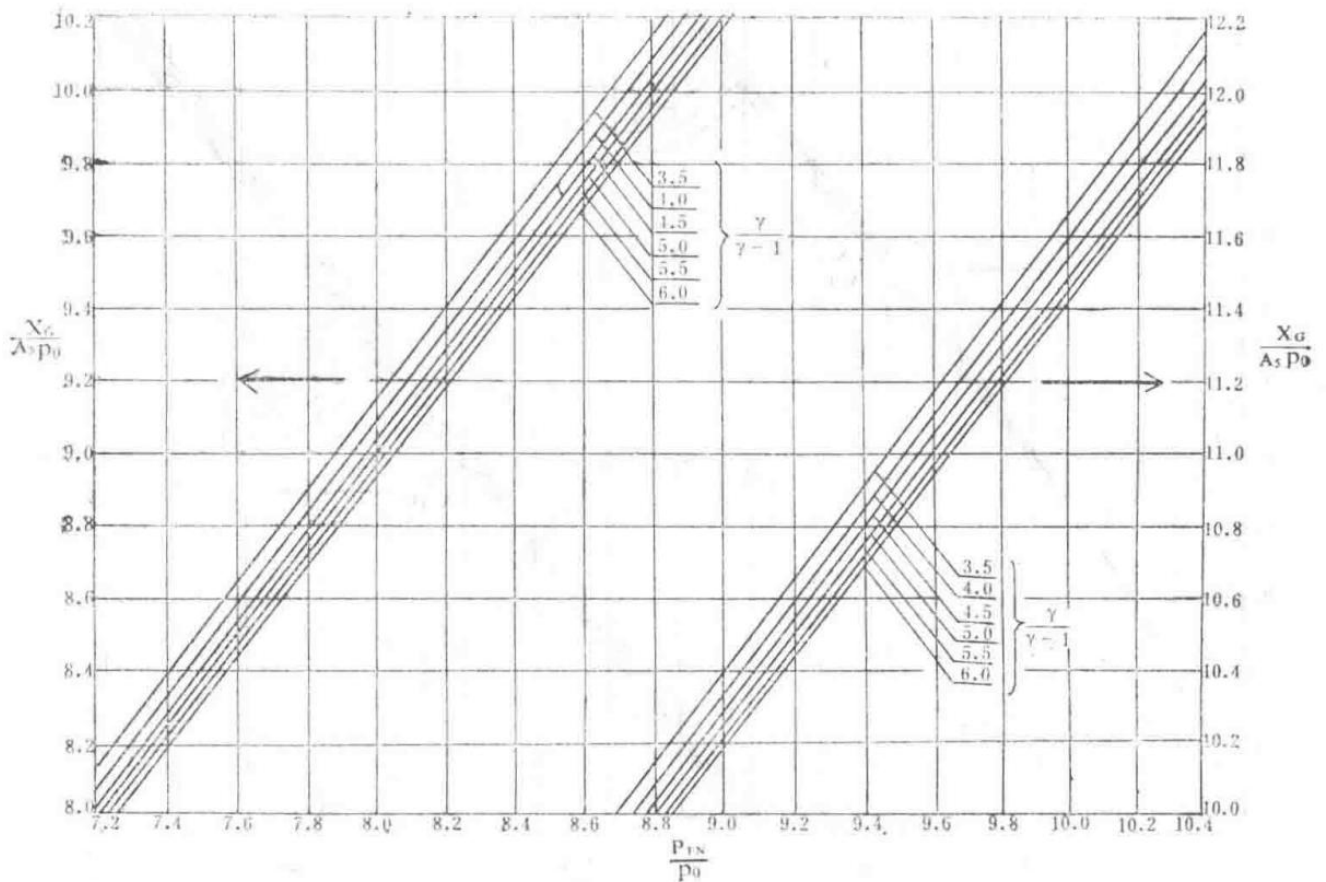


Figure 16g: Relationship curve of  $\frac{racXGA_8p_0}{racP_7p_7}$  for a convergent nozzle

Graph depicting the relationship between  $\frac{racXGA_8p_0}{racP_7p_7}$  and  $\frac{racP_7p_7}{racXGA_8p_0}$  for a convergent nozzle in the Spey MK202 engine.

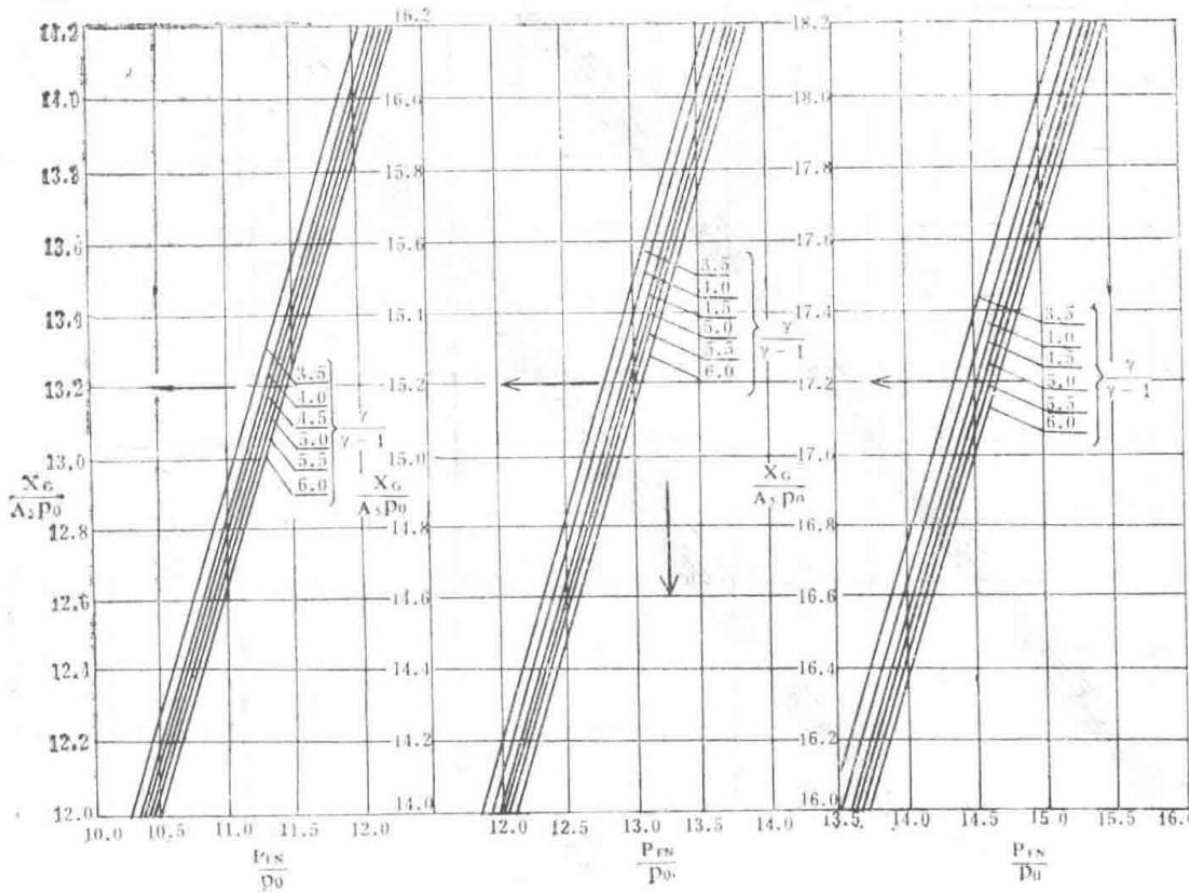
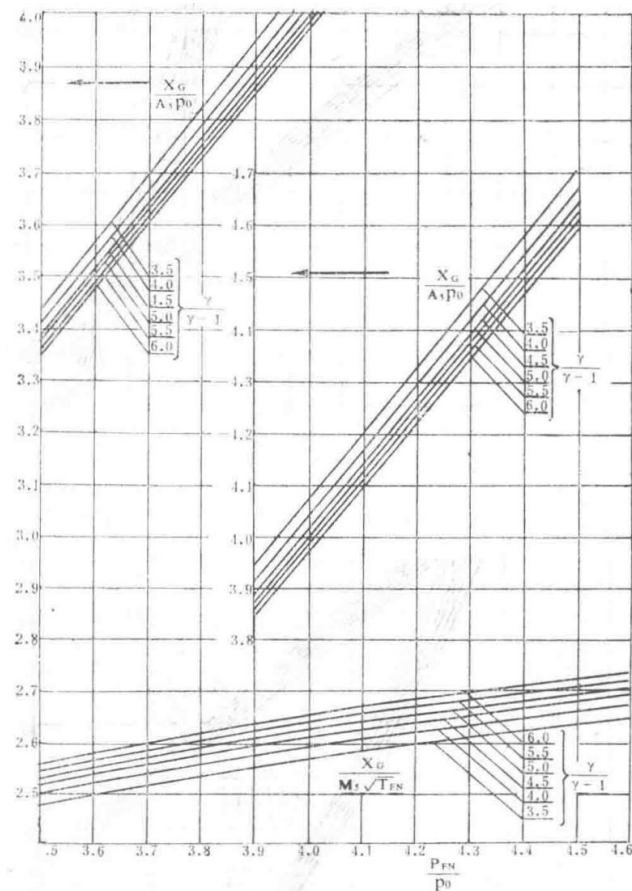


Figure 16h: Relationship curve of  $\text{racXGA}_8p_0$  vs  $\text{racP}_7p_7$  for a convergent nozzle

Graph depicting the relationship between  $\text{racXGA}_8p_0$  and  $\text{racP}_7p_7$  for a convergent nozzle in the Spey MK202 engine.

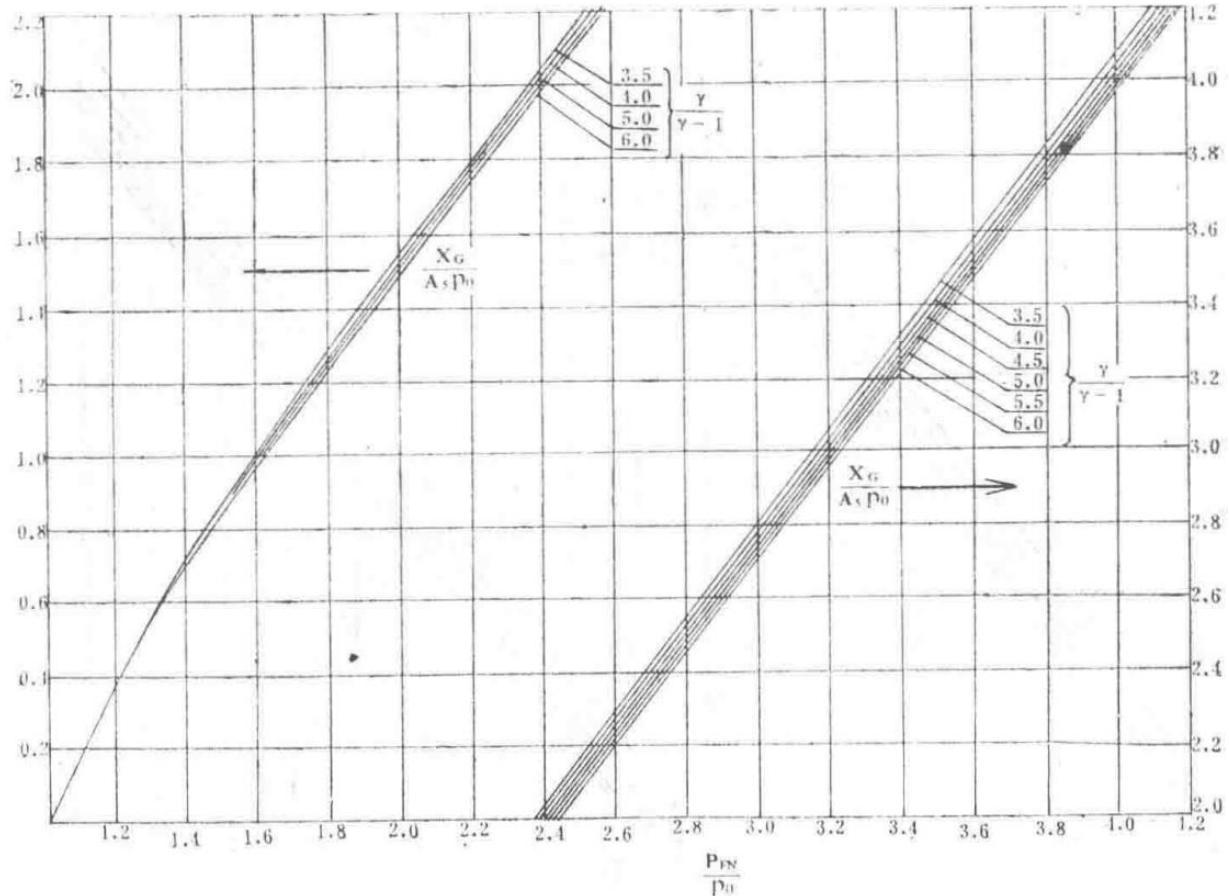
## Performance Characteristics of the Spey MK202 Engine Nozzle

The following diagrams illustrate various performance characteristics of the Spey MK202 engine, particularly focusing on the relationships between different aerodynamic parameters and nozzle pressure ratios.



Graph of  $\text{racXGA}_8 p_0$  vs.  $\text{racPF} \Delta p_0$

This graph shows the relationship between the thrust function parameter  $\text{racXGA}_8 p_0$  and the nozzle pressure ratio  $\text{racPF} \Delta p_0$  for different values of the specific heat ratio  $\gamma$ .



Graph of  $\frac{X_G}{A_8 p_0}$  vs.  $\frac{P_{7N}}{P_0}$  for various  $\gamma$  values

This graph illustrates how  $\frac{X_G}{A_8 p_0}$  varies with  $\frac{P_{7N}}{P_0}$  for different specific heat ratios  $\gamma$  in a convergent nozzle configuration.

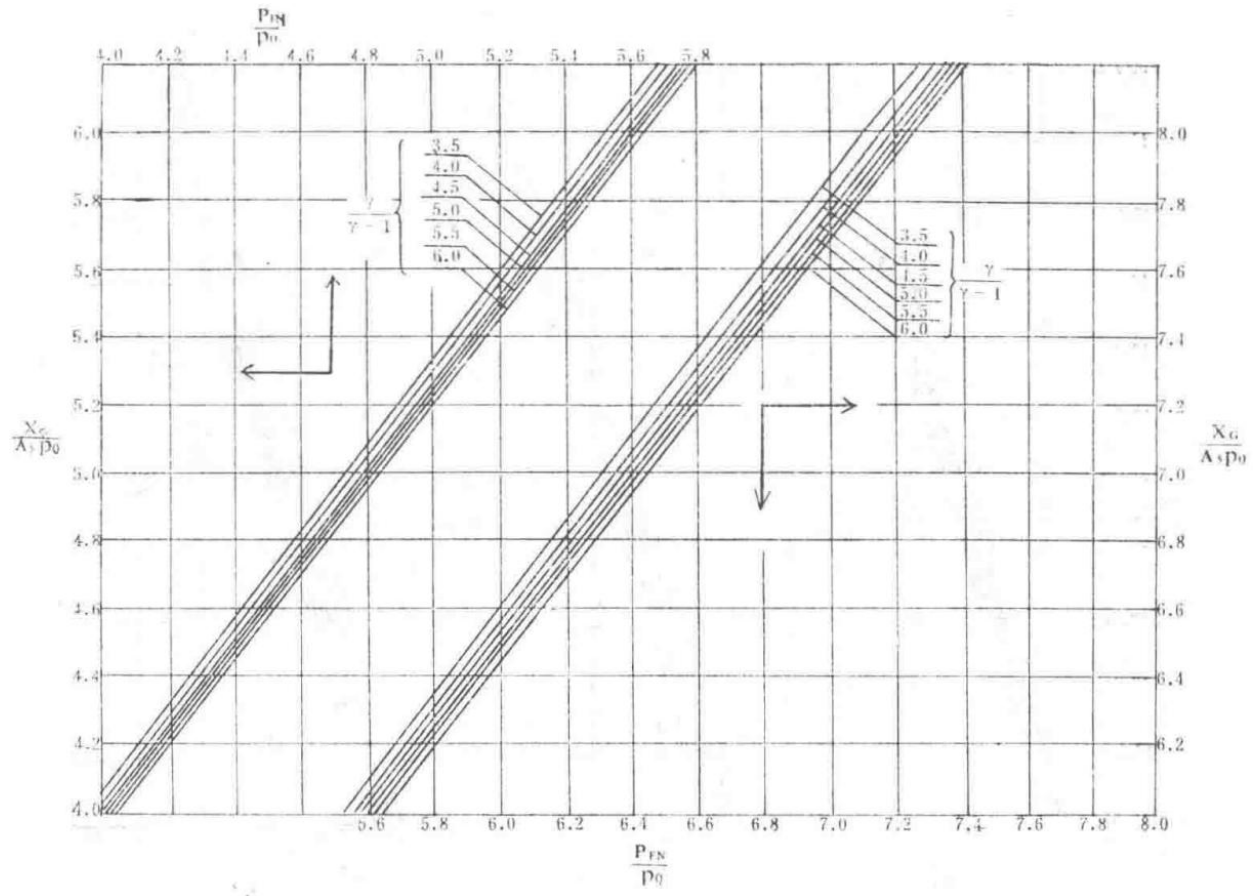
$$(XG)/(A_8 p_0)$$

Thrust function parameter where  $XG$  is the gross thrust,  $A_8$  is the nozzle throat area, and  $p_0$  is the ambient pressure.

$$(P_7)/(p_7)$$

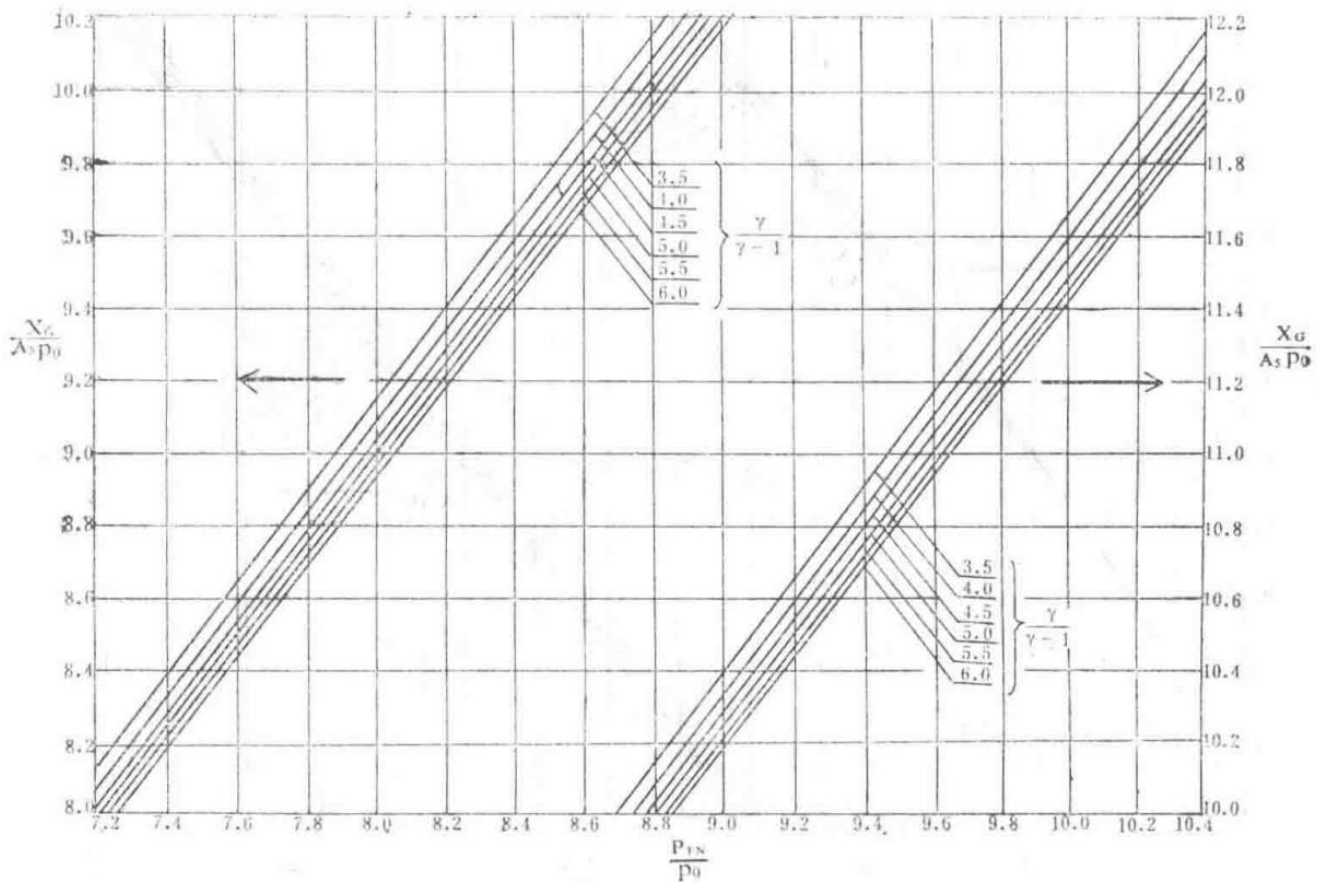
Nozzle pressure ratio where  $P_7$  is the total pressure at the nozzle inlet and  $p_7$  is the static pressure at the nozzle inlet.

The above figures provide critical insights into the performance of the convergent nozzle under various operating conditions. The specific heat ratio  $\gamma$  plays a significant role in determining the behavior of these parameters.



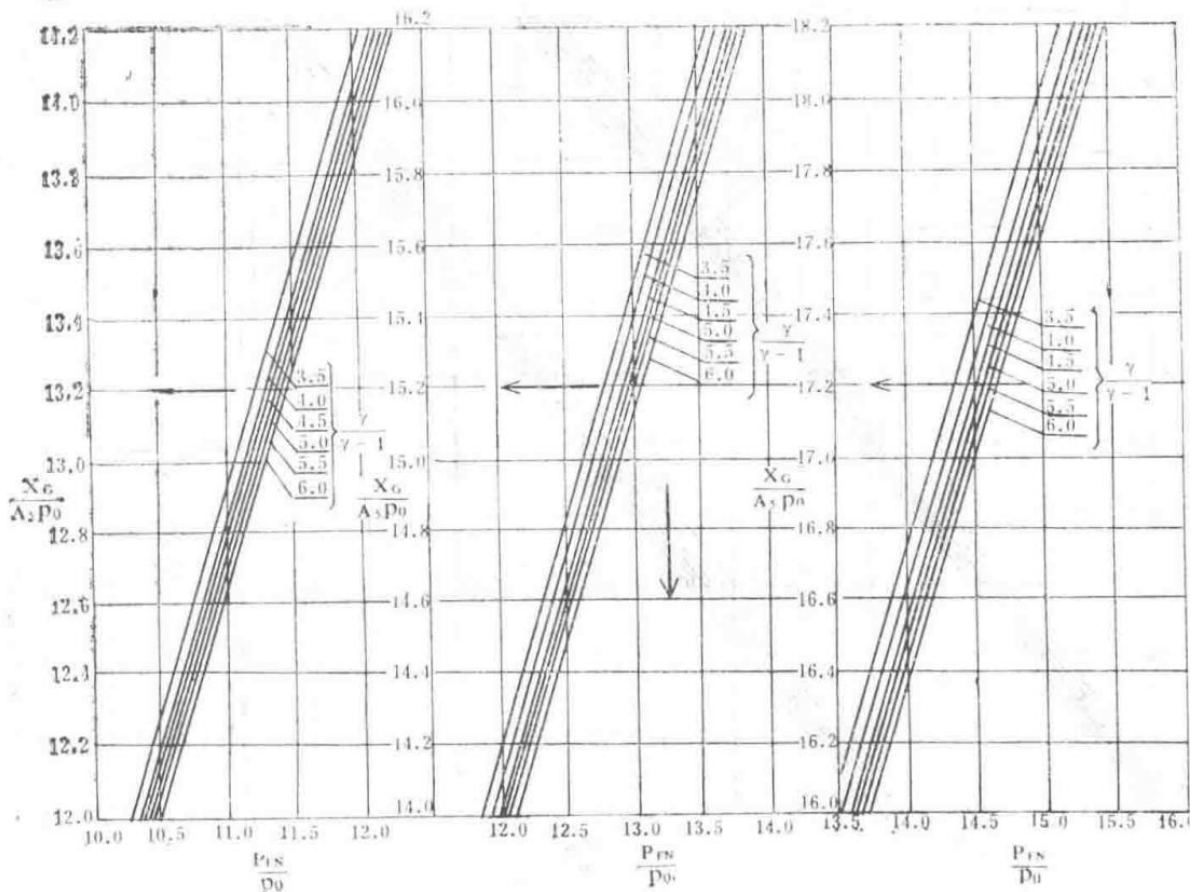
Detailed relationship of  $racXGA_8p_0$  and  $racP_7p_0$

This detailed graph shows the relationship between  $racXGA_8p_0$  and  $racP_7p_0$  for a convergent nozzle, highlighting the influence of different  $\gamma$  values.



Graph of  $\text{rac}X_a A_e p_0$  vs.  $\text{rac}P_{\text{exit}} p_0$

This graph depicts the relationship between  $\text{rac}X_a A_e p_0$  and the turbine exit pressure ratio  $\text{rac}P_{\text{exit}} p_0$  for different  $\gamma$  values.



Graph of thrust parameter relationships under varied conditions

This graph provides a comprehensive view of the thrust parameter  $\frac{X_G}{A_s p_0}$  under various pressure ratios and specific heat ratios.

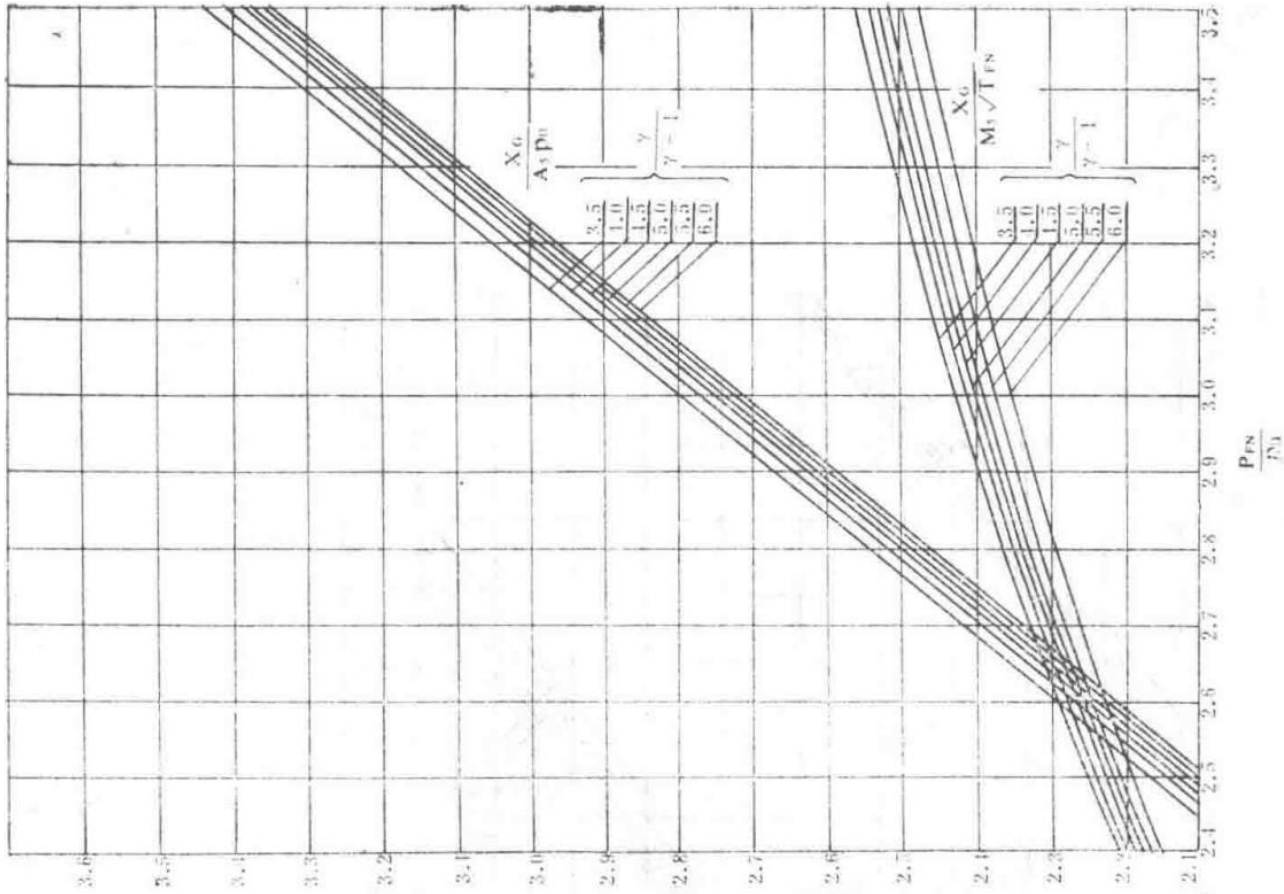


Figure 16a: Relationship between corrected flow function and nozzle parameters

Graph showing the relationship between the corrected flow function and other nozzle parameters, including Mach number and pressure ratios.

The diagrams and graphs collectively provide a detailed analysis of the aerodynamic performance and efficiency of the Spey MK202 engine's nozzle system under different operational scenarios.

图 16c 总推力函数与尾喷口压比的关系

— Section 42 —  
Content from Original Document (Pages 206-210)

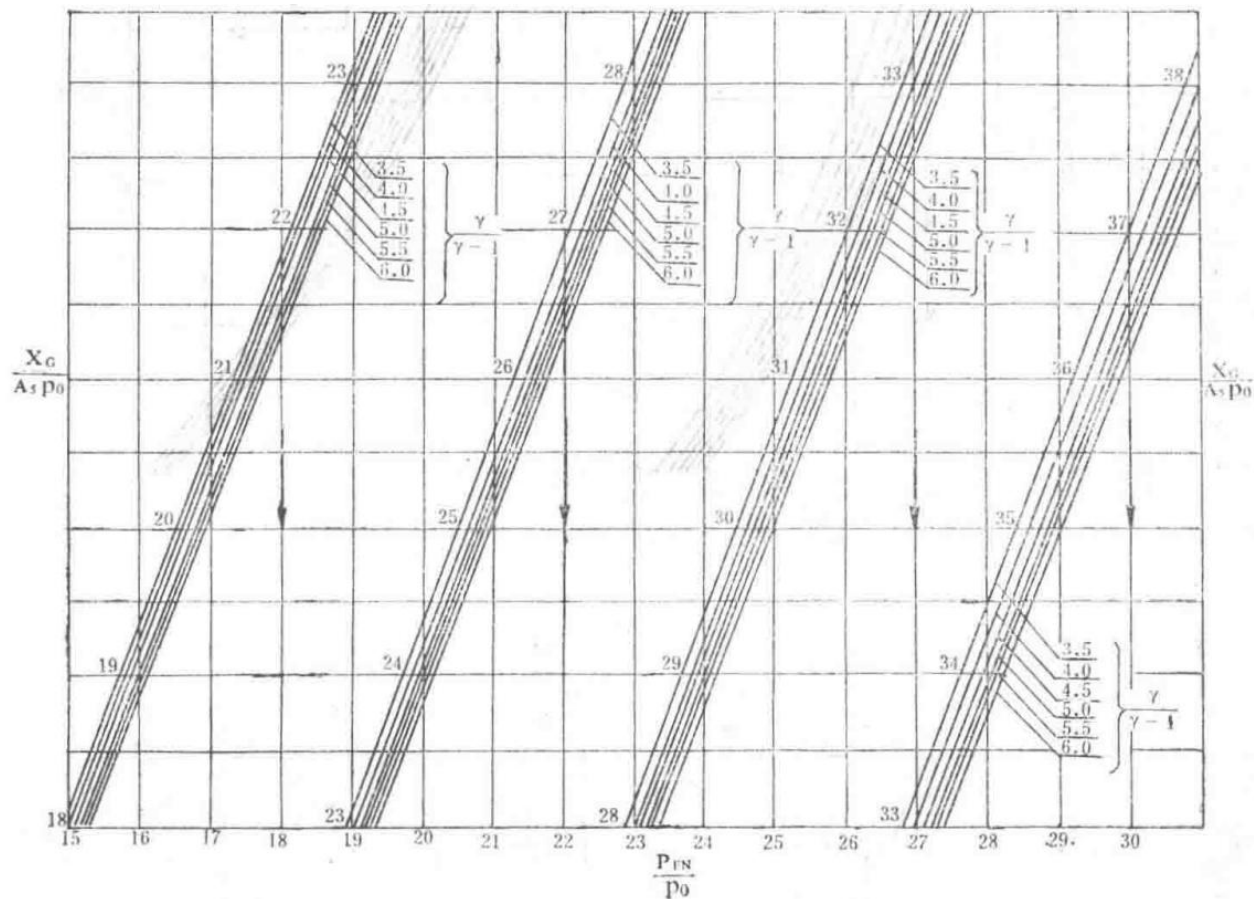
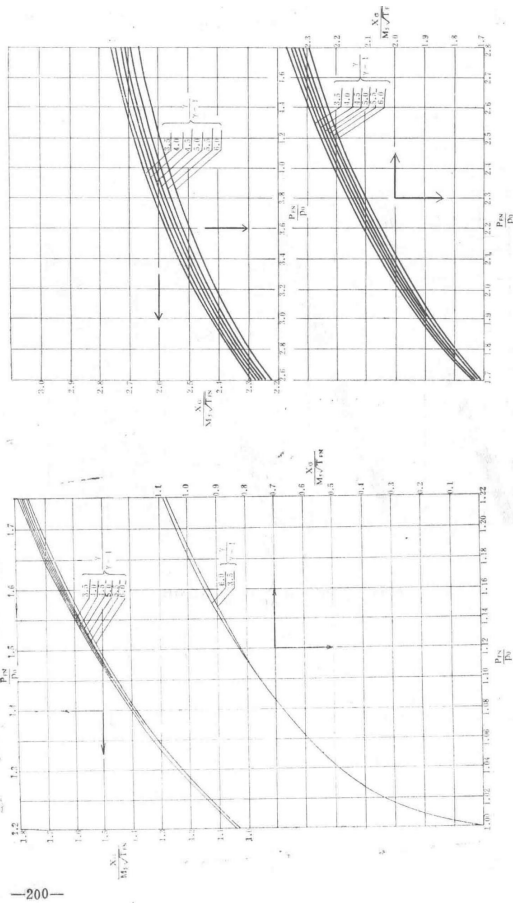


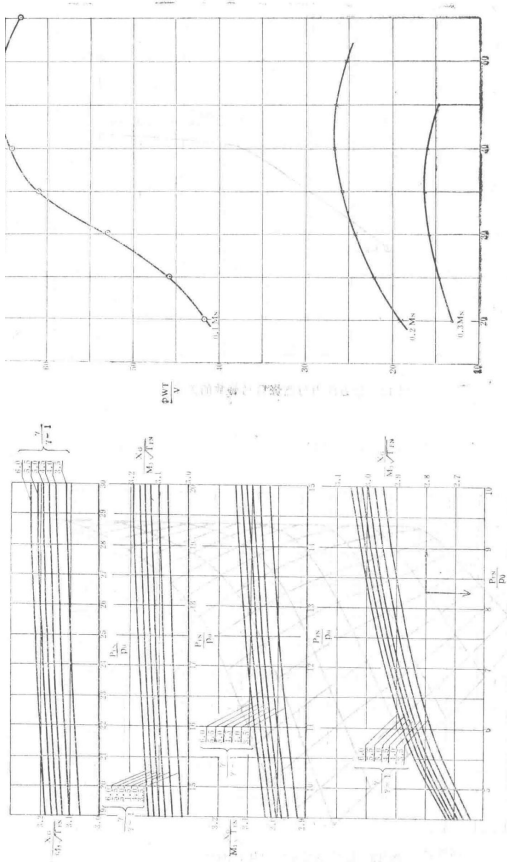
Figure 16i Relationship curve of  $\frac{X_G}{A_5 P_0}$  vs  $\frac{P_{FN}}{P_0}$  for a convergent nozzle

Graph showing the relationship between the normalized position parameter  $\frac{X_G}{A_5 P_0}$  and the pressure ratio  $\frac{P_{FN}}{P_0}$  for a convergent nozzle in the Spey MK202 engine.



-200-

Technical diagram related to the Spey MK202 engine, details not specified in the source text.



Technical diagram related to the Spey MK202 engine, details not specified in the source text.

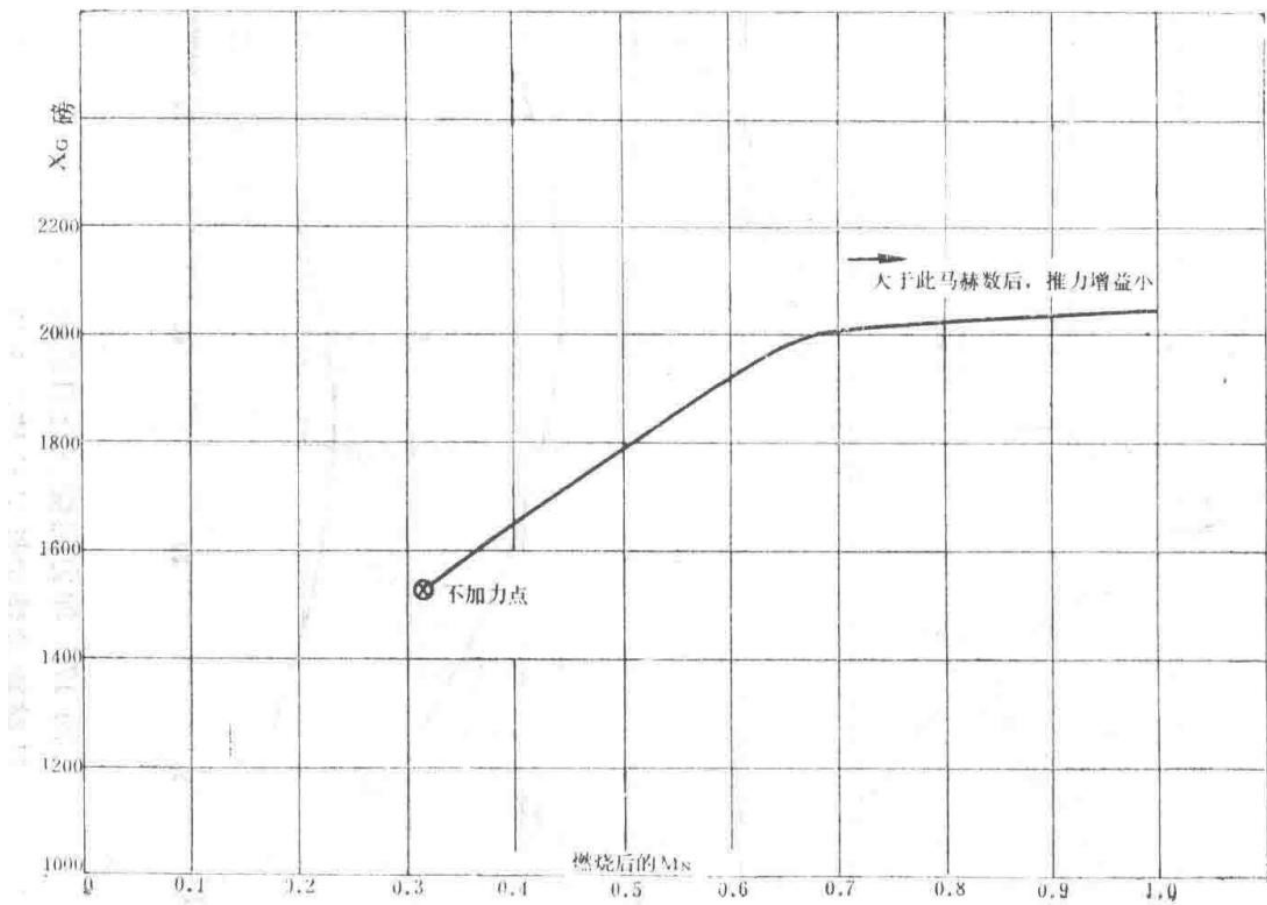


Figure 18 Relationship between afterburning thrust and post-combustion Mach number

Graph depicting the variation of afterburning thrust with the Mach number after combustion in the Spey MK202 engine.

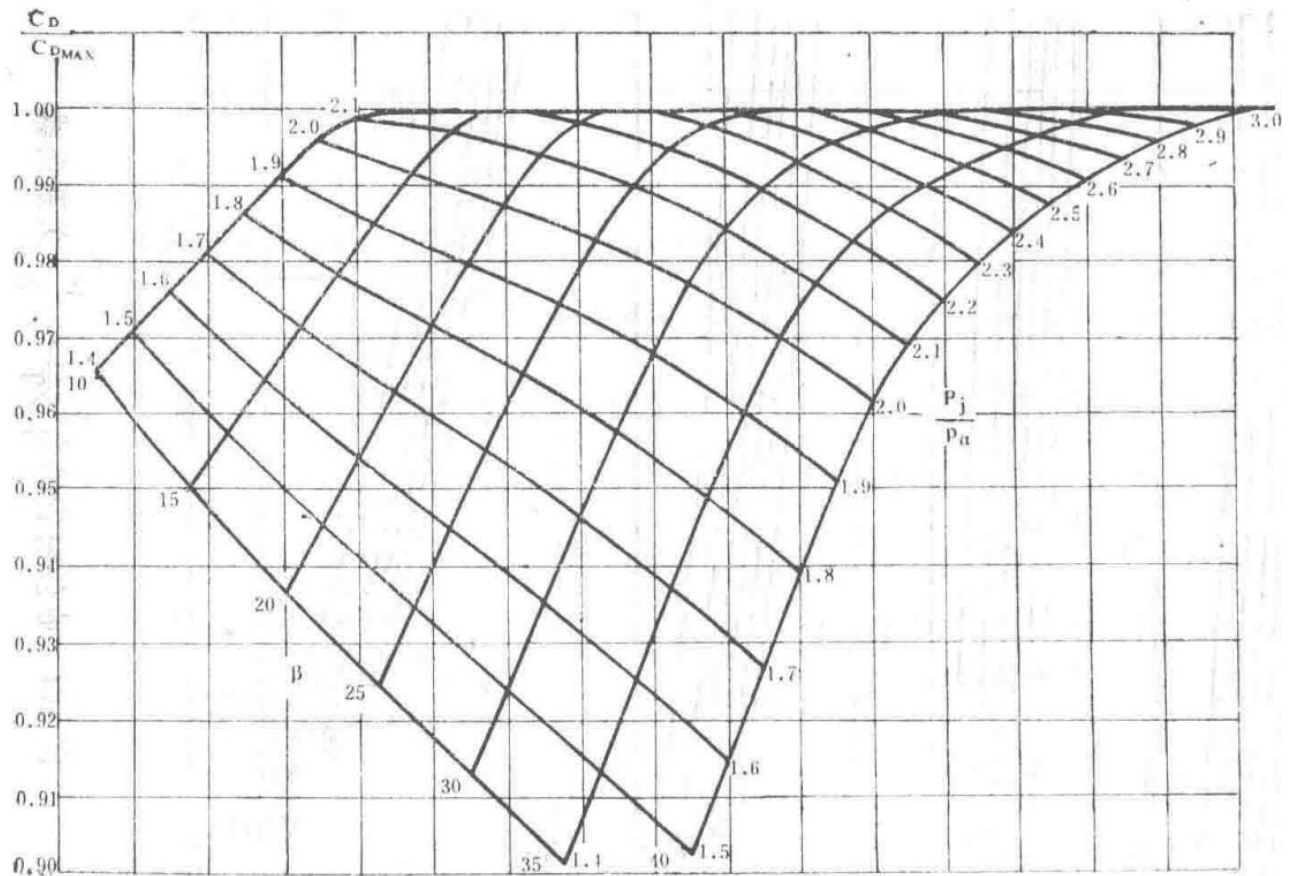


Figure 19 Variation of flow coefficient with nozzle pressure ratio

Graph showing how the flow coefficient changes with the nozzle pressure ratio in the Spey MK202 engine.

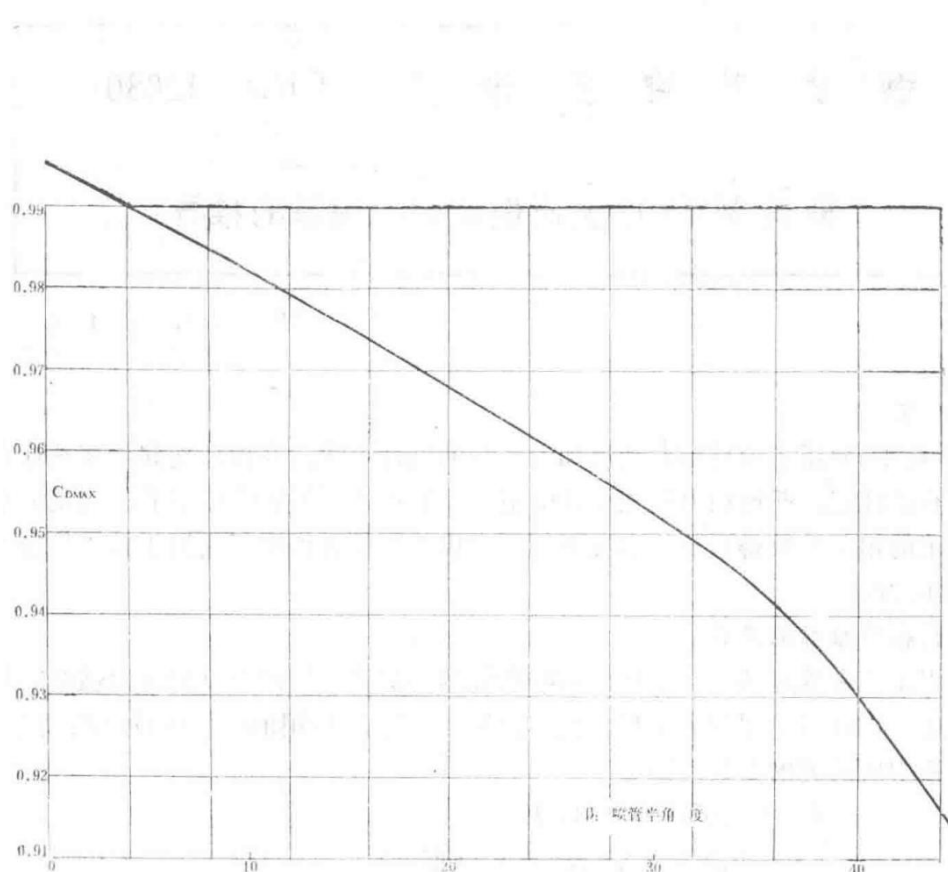


Figure 20 Variation of flow coefficient with convergent nozzle angle for a fully choked convergent nozzle

Graph illustrating the relationship between the flow coefficient and the convergence angle of a fully choked convergent nozzle in the Spey MK202 engine.

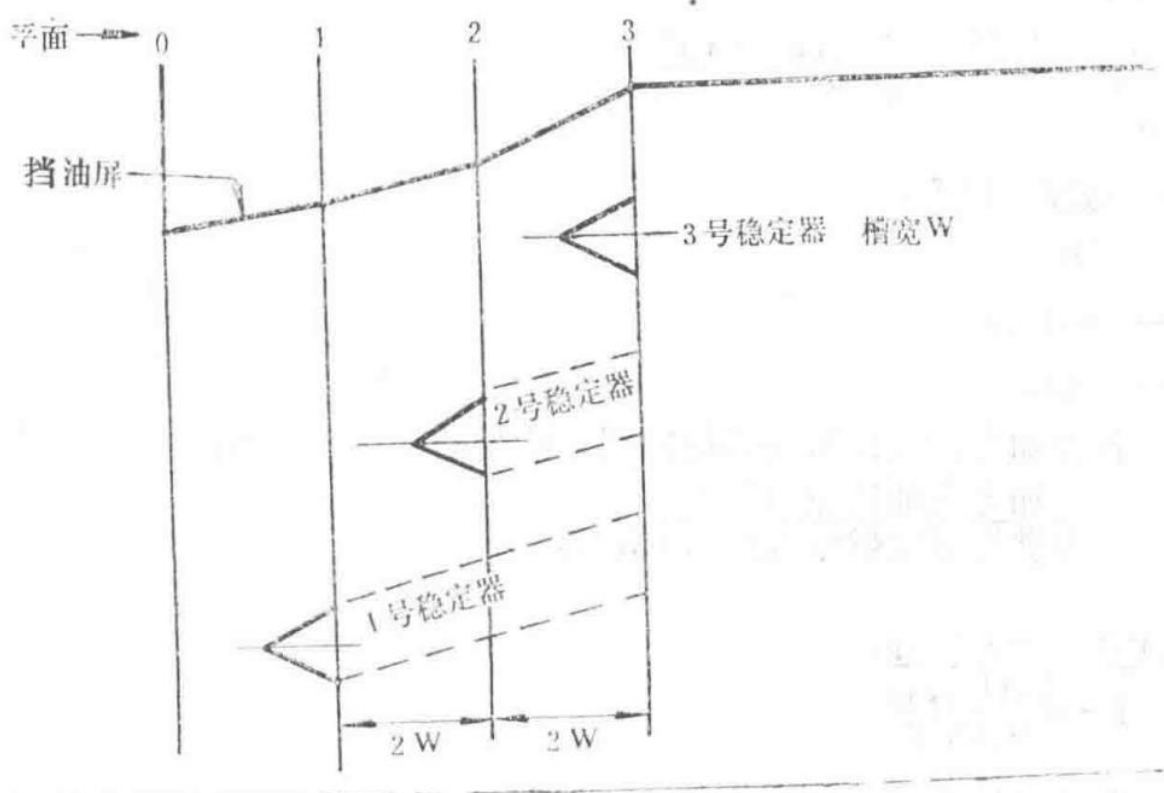


Figure 21 Schematic diagram of offset stabilizers in the diffuser (oil shield)

Diagram showing the arrangement of offset stabilizers within the diffuser (oil shield) section of the Spey MK202 engine.

$$(X)/(A\square) (P)/(p)$$

Equation representing the relationship between the normalized position parameter  $X/A\square$  and the pressure ratio  $P/p$  for a convergent nozzle.

Tabulated Data for Convergent Nozzle Characteristics (from Figure 16i)

$X/A\square$	$P/p$ (Pressure Ratio)	$M_3$ (Mach Number)	Notes
0.1	1.0	0.2	Initial condition
0.2	1.2	0.4	
0.3	1.5	0.6	
0.4	1.8	0.8	
0.5	2.0	1.0	Critical condition
0.6	2.2	1.2	
0.7	2.4	1.4	
0.8	2.6	1.7	
0.9	2.8	2.0	
1.0	3.0	2.2	Fully choked

Flow Coefficient Variation with Nozzle Pressure Ratio (from Figure 19)

Nozzle Pressure Ratio ( $P_{\square s}/P_s$ )	Flow Coefficient (CD)	Notes
1.1	0.92	
1.2	0.94	
1.4	0.96	
1.6	0.97	
1.8	0.98	
2.0	0.985	
2.2	0.99	
2.5	0.992	
3.0	0.995	Maximum flow coefficient

Flow Coefficient vs. Convergent Nozzle Angle (from Figure 20)

Convergence Angle (degrees)	Flow Coefficient (CD)	Notes
10	0.99	
15	0.98	
20	0.97	
25	0.95	
30	0.93	
35	0.91	
40	0.90	Fully choked condition

The diagrams and graphs presented in this section illustrate key performance characteristics of the Spey MK202 engine's nozzle and afterburning systems. These include the relationship between pressure ratios and normalized position parameters, the impact of nozzle pressure ratios on flow coefficients, and the effect of convergence angles on choked nozzle flow. The stabilizer arrangement in the diffuser section is also depicted to highlight its role in combustion stability.

— Section 43 —  
Content from Original Document (Pages 211-215)

Report Title	Report Number
Combustion Research Report	CRR12080
	Derivation of the King's Combustion Efficiency Relationship for the Spey MK202

First Edition, September 13, 1976

## 1.0 Introduction

Reference [1] introduces the design methodology for the afterburning systems of internal and external combustion engines. During the design phase, it is necessary to predict the performance achievable at various guarantee points. The method used in the Spey afterburning system design to calculate achievable combustion efficiency is based on a correlation parameter derived from a modified King's relationship. This document summarizes King's work and explains the modifications required to the correlation parameter when applied to multi-stage stabilizer systems.

## 2.0 Derivation of King's Correlation Parameter

The parameter derived by King is based on tests conducted on a combustor with a specific configuration, ensuring a relatively uniform fuel-air ratio throughout the afterburner test section. Combustion efficiency is expressed in terms of afterburner inlet total temperature, total pressure, flow velocity, fuel-air ratio used, and combustion length. The parameter ranges studied in this relationship are as follows:

- Total temperature T: 700 °K to 1033 °K
- Total pressure P: 5.2 to 12.5 psi (absolute)
- Flow velocity V: 400 to 650 ft/s
- Fuel-air ratio (F<sub>□</sub> / M<sub>□</sub>B): 0.034 to 0.0676
- Combustion chamber length L: 30 to 66 inches

$$= P^{0.9324} \times T^{1.07} \times (750 - V)^{0.262}, e^3/l,$$

Definition of King's correlation parameter  $\xi$

The units used are:

- P: lb/ft<sup>2</sup>
- T: °R
- V: ft/s
- L: ft

图 1 燃烧效率随  $\xi$  的变化

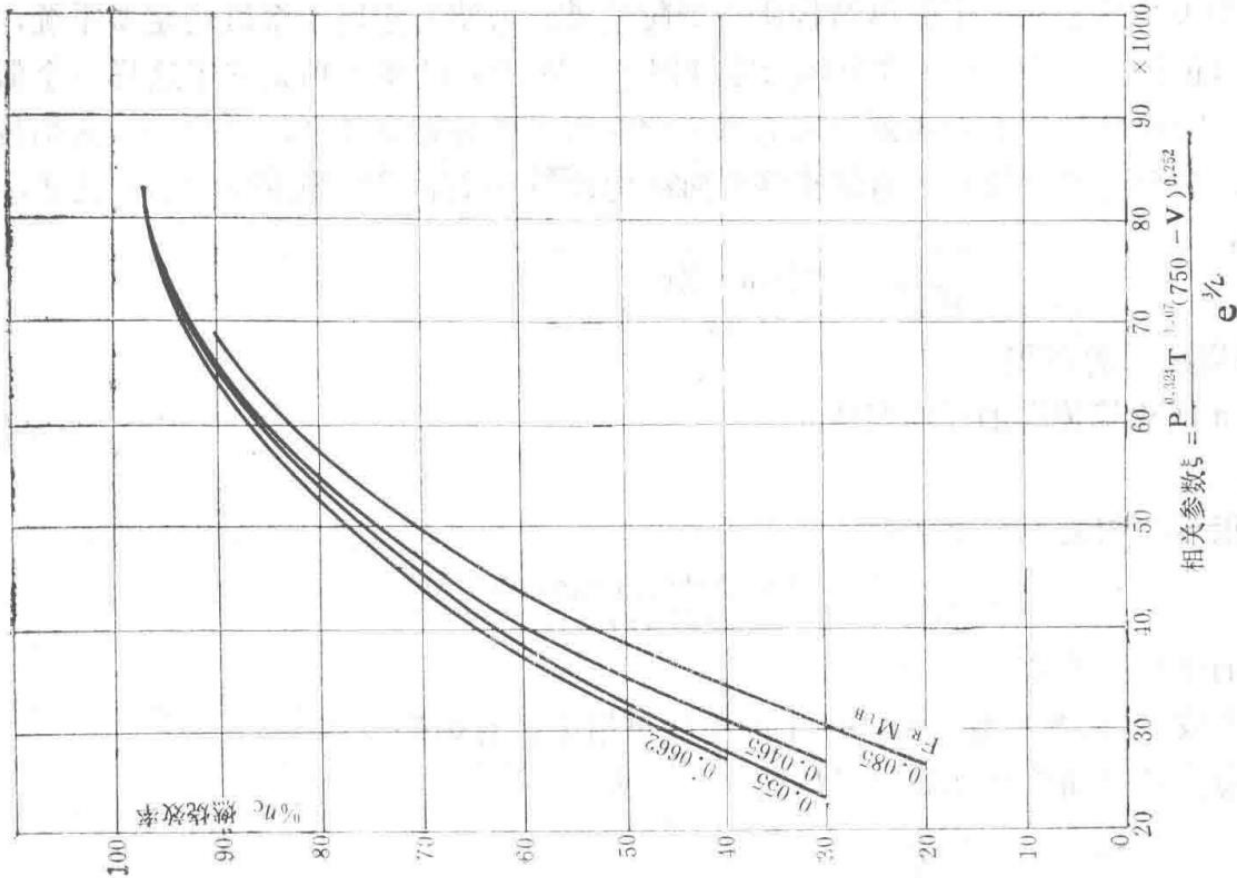


Figure 1: Combustion efficiency curves for various afterburner fuel-air ratios

Curves showing combustion efficiency as a function of the correlation parameter  $\xi$  for different fuel-air ratios in the afterburner.

Here, the fuel-air ratio is defined as:

$$F \square, M \square B = \text{Afterburner fuel flow (F)} \square / \text{Unburned air mass flow in afterburner (M)} \square B,$$

Definition of fuel-air ratio in the afterburner

Thus,

$$F \square, M \square B = FAR \square - FAR \square \cdot \square D, 1 - FAR \square \cdot \square D, 0.0676,$$

Expression for fuel-air ratio in terms of overall and ideal fuel-air ratios

Where:

- $FAR \square$  = Overall fuel-air ratio of the engine plus afterburner
- $FAR \square \cdot \square D$  = Ideal fuel-air ratio for engine temperature rise

### 3.0 Modification of Efficiency Relationship for Multi-Stage Systems

Since this relationship is based on results from a simple configuration, a correction term must be included in the combustion length term to apply it to multi-stage stabilizer systems. This new term, called the Width Factor (W.F.), is based on the assumption that the combustion length required to achieve a certain combustion efficiency under a given set of inlet conditions depends on the radial distance of flame propagation. For the test rig geometry used to determine the original relationship, the calculated W.F. value is 2.71 inches. The W.F. is

defined as:

$$W.F. = \sum A_n \times Z_n / \sum A_n,$$

Definition of Width Factor (W.F.)

- $A_n$  = Area of combustion zone n
- $Z_n$  = Radial distance of flame propagation in zone n

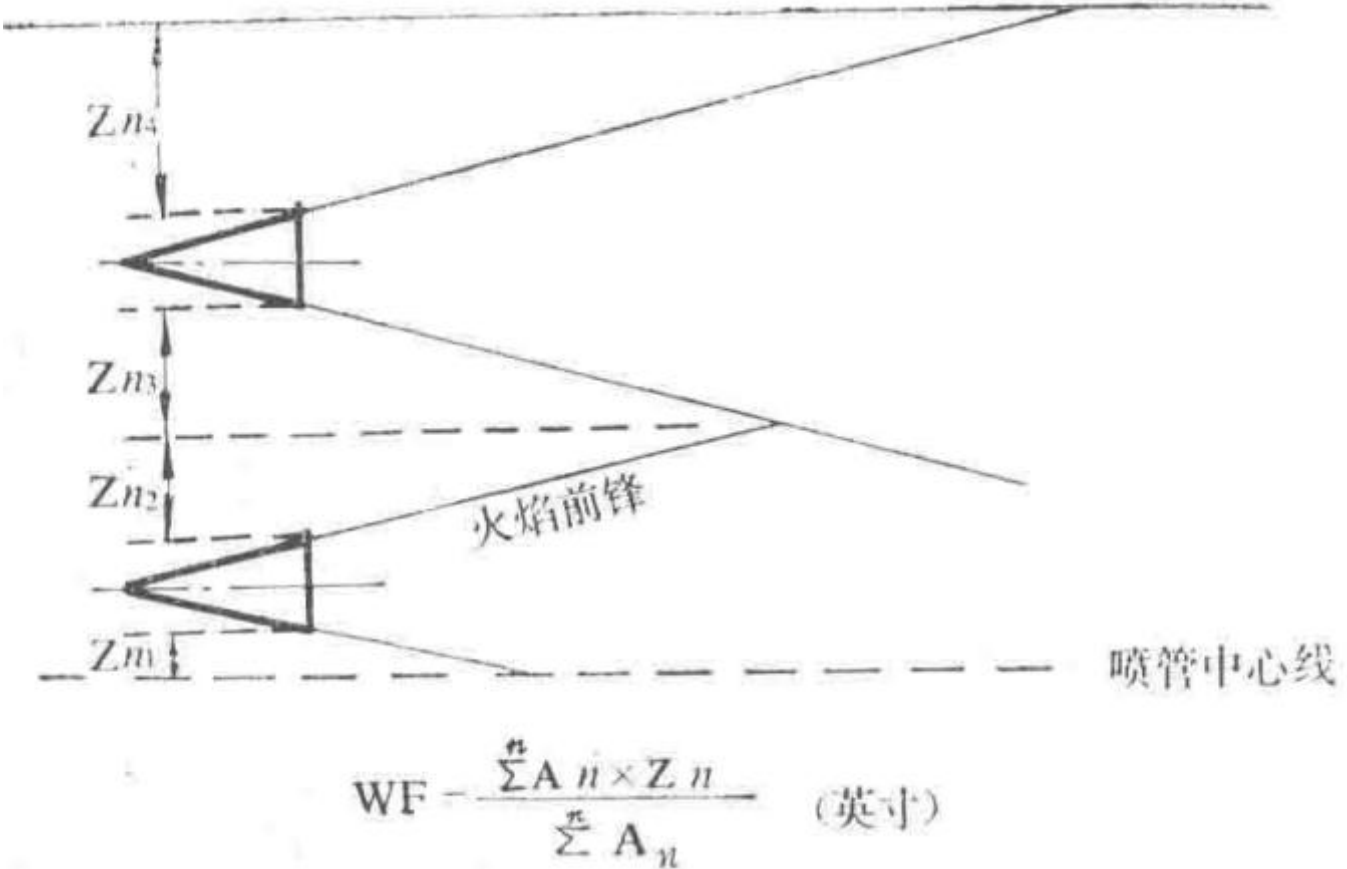


Figure 2: Definition of Width Factor

Diagram illustrating the calculation of the Width Factor (W.F.) for flame propagation in a multi-stage stabilizer system.

The modified correlation parameter is then defined as:

$$\xi = P^{0.9324} \times T^{1.07} \times (750 - V)^{0.252} e^{(3/1 \times w_n / 2.71)},$$

Modified correlation parameter  $\xi$  for multi-stage systems

The unit for W.F. is inches.

By replacing the parameter  $\xi$  with the modified parameter  $\xi$ , the curves in Figure 1 can be used to estimate combustion efficiency.

It should be noted that the combustion efficiency calculated from these curves is defined as:

$$\eta_c = T_{outlet} - T_{inlet}, T_{outlet} D - T_{inlet} D,$$

Definition of combustion efficiency  $\eta_c$

Where:

- $T_{outlet}$  = Afterburner temperature achieved at the outlet

- $T_{\square}$  = Afterburner inlet temperature
- $T_{\square}D$  = Ideal temperature rise in the afterburner

## 4.0 References

- Reference [1] CRR12079

Document Title	Report Number
Spey MK202 Afterburner Catalytic Ignition System Design	CRR 12081

First Edition, September 15, 1976

## 1.0 Summary

This report introduces the various ignition systems commonly used in afterburner combustion chambers. The characteristics of each system are compared, and their advantages and disadvantages are analyzed.

The catalytic ignition system currently used in the Spey MK202 is presented, and its design and performance are discussed.

## 2.0 Ignition Systems

There are three basic types of afterburner ignition systems in common use. They are:

1. Hot-shot ignition
2. Electric spark ignition
3. Catalytic ignition

No single ignition system is superior in all aspects for every application. The most suitable system must be selected based on specific requirements. Factors to consider include:

- Performance, ignition range, and speed
- Blockage and weight
- Impact on engine-specific fuel consumption (and mechanical conditions)
- System lifespan
- Applicability
- Ancillary requirements (high-energy ignition box and fuel supply, etc.)

The following sections describe the commonly used ignition systems and their advantages and disadvantages.

### 2.1 Hot-Shot Ignition

The principle of hot-shot ignition involves injecting a stream of fuel into the engine combustion chamber, typically in the primary combustion zone, to generate a hot gas jet that passes through the turbine into the afterburner system (see Figure 1). This method enables very short afterburner ignition times, and with further development, the system achieves highly reliable ignition.

The main disadvantage of this method is the potential overheating of the turbine outlet guide vanes. One remedy is to reduce the amount of fuel injected into the engine combustion chamber (i.e., lower the hot-shot temperature) and use a relay nozzle downstream of the turbine to increase the jet temperature. However, this complicates the fuel system, as the timing coordination between the main nozzle and the relay nozzle is critical. Another method to avoid overheating the turbine guide vanes is to inject the hot-shot into the third zone of the combustion chamber, achieving full temperature rise only after passing through the guide vanes. However, if the residence time is less than the ignition delay time, the fuel may not ignite at all, making the nozzle arrangement crucial.

Additional issues with this system may arise due to the very low fuel flow requirements at high altitudes and the tendency for nozzles to coke in high-temperature environments, as well as potential engine damage from nozzle failures.

The main advantages of this system are its short ignition time and high operational altitude. Furthermore, installing this system does not compromise engine performance or affect the engine-specific fuel consumption rate.

## 2.2 Electric Spark Ignition

Electric spark ignition was used in early turbojet engine afterburner systems. The igniter is installed in the wake of the combustion chamber center cone or V-gutter stabilizer. Fuel is supplied separately or, more commonly, existing afterburner fuel is ignited by the electric spark.

The main advantage of this system is its simplicity, requiring no auxiliary air or fuel, only a high-energy ignition box.

This system should be capable of igniting the afterburner at altitude limits, as electric spark ignition can still ignite when the main combustion chamber pressure drops to 3.5 psi (absolute). However, this may not be achievable in afterburner systems with poor fuel preparation, necessitating more sophisticated fuel preparation devices and possibly separate fuel supply.

The high-energy ignition box commonly used in the main combustion chamber produces sparks at a rate of approximately 60 sparks per minute. To achieve rapid ignition in the afterburner system, the high-energy ignition box needs to be upgraded to achieve a higher spark rate.

The main disadvantage of the electric spark ignition system is the poor mechanical integrity of the igniter. The optimal ignition position is almost always in a location that causes the igniter to overheat during afterburner combustion. This can be mitigated by immediately shutting off the ignition fuel supply after ignition, but this compromises the system's primary advantage of simplicity.

## 2.3 Catalytic Ignition

The Spey MK202 selected the catalytic ignition system due to its simple fuel control system, low blockage, light weight, and suitability for use. Although the system's performance was not fully determined during the design phase, it was believed that further development could meet the requirements of the Spey MK202.

Platinum is an efficient catalyst for the oxidation reaction between hydrocarbons and oxygen. The platinum catalytic ignition system is installed in the afterburner and supplied with a metered amount of fuel via a timer. The resulting flame is used to ignite the main afterburner fuel, after which the catalytic system fuel supply is cut off. This system achieves combustion within 3 seconds of ignition initiation. Although it requires a separate fuel supply, the controller is simple.

The lifespan of the ignition device depends on the number of ignition cycles and engine vibration, making it difficult to determine. However, the igniter can be designed to allow easy replacement of potentially damaged components.

# 3.0 Spey Catalytic System Design

## 3.1 Discussion

The early design of the Spey catalytic igniter consisted of a catalytic assembly housed in a sleeve mounted on the engine exhaust cone within the turbine exhaust flow. The catalytic system fuel was injected via a multi-hole spray bar located upstream of the catalytic assembly. This design imposed strict requirements on the size and arrangement of the fuel nozzles, providing a small fuel flow to trigger the catalytic assembly and a much larger flow to stabilize the flame on the igniter cone. The resulting flame had to be sufficient to extend into the

afterburner combustion chamber.

The high Mach number and varying swirl of the gas flow increased the difficulty of fuel supply and caused igniter vibration, leading to rapid failure of the catalytic assembly within a short operating time.

Due to these challenges, the catalytic igniter was repositioned to the center of the combustion chamber (see Figure 2).

### 3.2 Operating Principle

Fuel is supplied through a feed pipe inside a strut and splits into two streams near the ignition device for the catalytic system. An attenuator and filter regulate a small proportion of the total fuel flow (approximately 1/300), as described in Section 3.5. This fuel stream is directed into a downstream-facing nozzle located at the throat of a Venturi tube. The fuel mixes with air flowing through the Venturi tube, and the resulting stoichiometric mixture is then directed through holes in a plate upstream of the catalytic assembly into a platinum satellite drum. The drum increases the temperature, producing a 'cigar-shaped' flame.

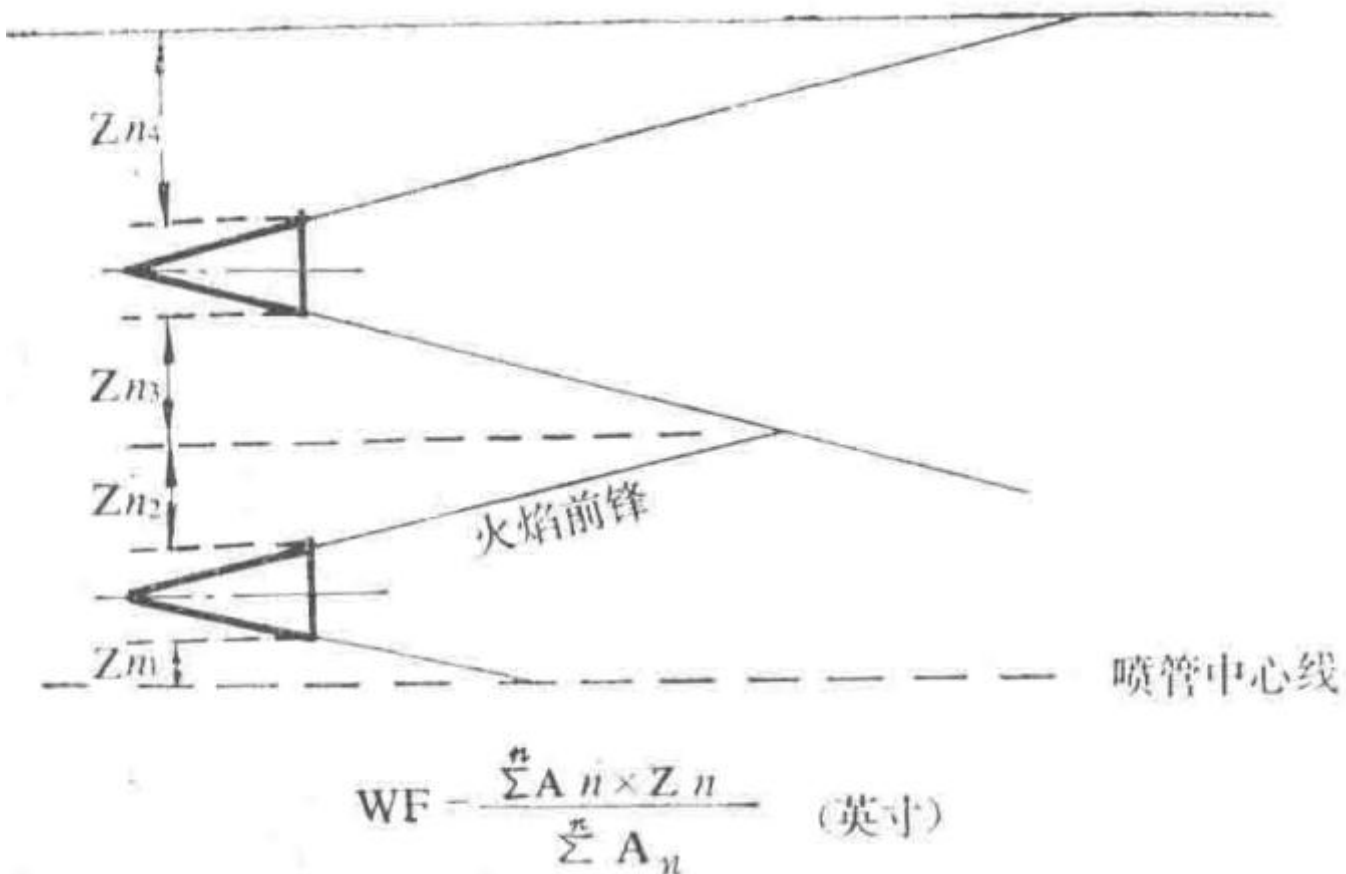


Figure 2: Spey MK202 Catalytic Igniter Positioning

Diagram showing the repositioned catalytic igniter in the center of the combustion chamber.

The flow ignites the remaining fuel (299/300 of the total fuel quantity) that passes through the fuel distribution ring around the tail cone and enters the wake of the cone. This forms a flame that ignites the inner-circle vaporizing stabilizers, and the flame then propagates to other stabilizers via the inter-flame channels.

## 3.3 Design

### 3.3.1 Catalytic Igniter Tail Cone

The tail cone diameter determines the stability of the catalytic igniter after ignition and may define the minimum combustion pressure. It does not affect the ignition timing.

The stability of the tail cone is determined by the parameter  $(pDT)/(V)$ .

$$p = \text{Afterburner static pressure lb/in}^2$$

Definition of static pressure in the afterburner.

$$V = \text{Gas flow velocity ft/s}$$

Definition of gas flow velocity.

$$T = \text{Gas temperature } ^\circ\text{K}$$

Definition of gas temperature.

$$D = \text{Tail cone diameter ft}$$

Definition of tail cone diameter.

As shown in Figure 3a, the parameter value at the flameout point is 10. For the Spey engine:

$$V = 680 \text{ ft/s } T = 720 \text{ } ^\circ\text{K } D = 3 \frac{1}{4} \text{ in}$$

At the flameout point, the pressure  $p$  is calculated as:

$$p = (10 \times 680)/(3(1)/(4) \times 720) = 2.91 \text{ lb/in}^2 \text{ (absolute)}$$

Calculation of static pressure at flameout point.

Thus, as long as the predetermined fuel supply is appropriate, the Spey tail cone can still operate at an afterburner pressure of 3 lb/in<sup>2</sup> (absolute).

Tests with small-scale experimental devices indicate that the tail cone length can affect the operational range. If the recirculation zone is too long, the primary fuel in the system may fail to ignite due to insufficient heating from the catalytic component, leading to ignition failure. If too short, the fuel residence time decreases, narrowing the stability boundary.

A tail cone angle of 60° is recommended, as this angle has been proven suitable for conical stabilizers.

### 3.3.2 Catalytic Assembly

The parameters shown in Figure 3b define the operational range of the catalytic assembly. Here:

$$M = \text{Afterburner mass flow rate lb/s}$$

Definition of afterburner mass flow rate.

$A$  = Afterburner area in<sup>2</sup>

Definition of afterburner area.

$p$  = Afterburner static pressure lb/in<sup>2</sup> (absolute)

Definition of afterburner static pressure.

$T$  = Gas temperature ^K

Definition of gas temperature.

The catalytic assembly reaction rate limit is  $7.5 \times 10^{-4}$ . The operational pressure limit for the Spey catalytic assembly is  $P = 2.11$  lb/in<sup>2</sup> (absolute).

### 3.3.3 Fuel Introduction to the Catalytic Assembly

When the catalytic assembly is installed on the turbine exhaust tail cone, significant variations in fuel supply to the catalytic assembly were observed. This is due to changes in the swirl intensity of the turbine airflow under different flight conditions. To avoid this issue during system rearrangement and to ensure a fixed and known fuel quantity reaches the catalytic assembly, a Venturi fuel introduction device was installed upstream of the catalytic assembly. This ensures the system is insensitive to swirl. Additionally, since fuel is introduced at the throat of the pipe, fuel preparation is improved.

## 3.4 Structure and Materials

The structure of the catalytic assembly is shown in Figure 4. The assembly itself consists of two rows of 20 satellite rollers, spaced apart and surrounding a central body, embedded in a silicon carbide catalytic bed cup. The satellite rollers are made of platinum-rhodium (20% rhodium) mesh plated with platinum, with a thickness of 0.01 inches. The central body support is made of similar material but thicker (0.030 inches). The I-C silicon carbide catalytic bed cup exhibits excellent thermal shock resistance and oxidation resistance. This material contains some free silicon, which can diffuse into platinum under reducing conditions and affect its performance. Prior to use, the catalytic bed cup is oxidized at 1400°C to reduce the silicon diffusion rate.

The fuel-air mixture enters the catalytic assembly through holes in an upstream plate made of pyrophyllite. This material is naturally soft in its mineral state, making it easy to machine and drill. Upon heat treatment at 800°C, the material hardens.

Between the upstream plate and the satellite rollers is a turbulence plate, also made of platinum-rhodium alloy wire mesh (30% rhodium), with a thickness of 0.020 inches.

## 3.5 Fuel System

Fuel supplied to the catalytic igniter passes through a timer located outside the afterburner, allowing fuel flow for 3 seconds, as shown in Figure 5. Consequently, the catalytic igniter must ignite the afterburner fuel within 3 seconds of afterburner activation. Fuel is supplied via a check valve, with a bypass oil hole on the valve allowing the working fuel line downstream (inside the afterburner) to connect to an external flushing line during non-afterburning operation. The total fuel flow to the catalytic igniter is regulated by a restrictor at the inlet of the fuel supply line, where the fuel is entirely in liquid form. After passing through the restrictor, the flow is divided between the Venturi nozzle and the tail cone fuel distribution ring. The required nozzle fuel flow rate is very small (measured as low as 0.0002 lb/s to achieve maximum catalytic assembly heat release). At such low flow rates, the fuel in the pipeline vaporizes, making the system particularly sensitive to the fuel's volatility characteristics. The flow rate with AVTAG fuel differs from that with AVTUR fuel. The system is adjusted to favor the most commonly used AVTUR fuel; if AVTAG fuel is used, performance may degrade.

## 3.6 Performance

It has been demonstrated that, as long as the predetermined fuel flow rate is appropriate (see Section 3.3.2), the catalytic assembly can operate down to 2.1 lb/in<sup>2</sup> (absolute).

The stability range of the tested tail cone is shown in Figure 6. The igniter can operate at a pressure of 5 lb/in (absolute), whereas the theoretical calculation in Section 3.3.1 predicted 3 lb/in (absolute). In practice, data confirming the upper portion of the experimental curve is limited, and it can be considered that the experimental and theoretical predictions are essentially consistent. The predetermined fuel supply for the Spey MK202 engine's catalytic igniter lies within the stability boundary, and ignition has been proven possible with AVTUR or AVCAT fuel up to 7 lb/in (absolute). Although the total predetermined fuel flow rate is the same when using AVTAG fuel, differences in volatility, as previously mentioned, cause the catalytic assembly to fail at approximately 14 lb/in<sup>2</sup> (absolute).

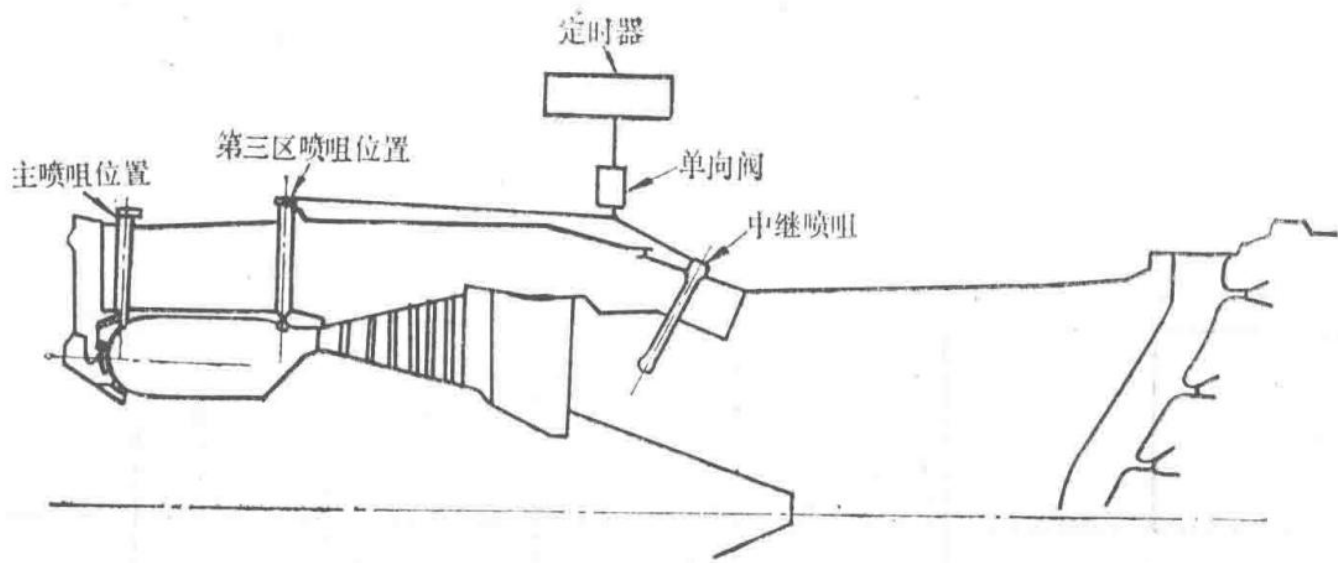


Figure 1: Hot Jet Afterburner Ignition

Diagram illustrating the hot jet afterburner ignition system.

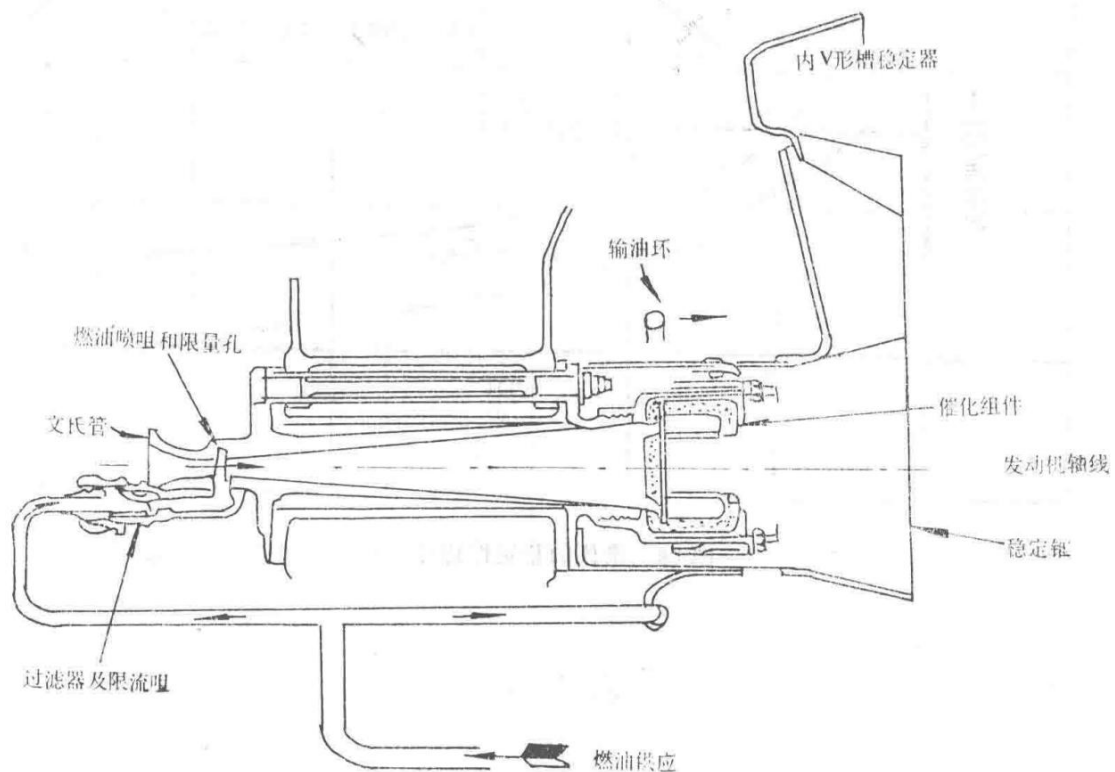


Figure 2: Spey Catalytic Ignition System with Venturi Fuel-Air Supply

Schematic of the Spey engine's catalytic ignition system using a Venturi for fuel-air supply.

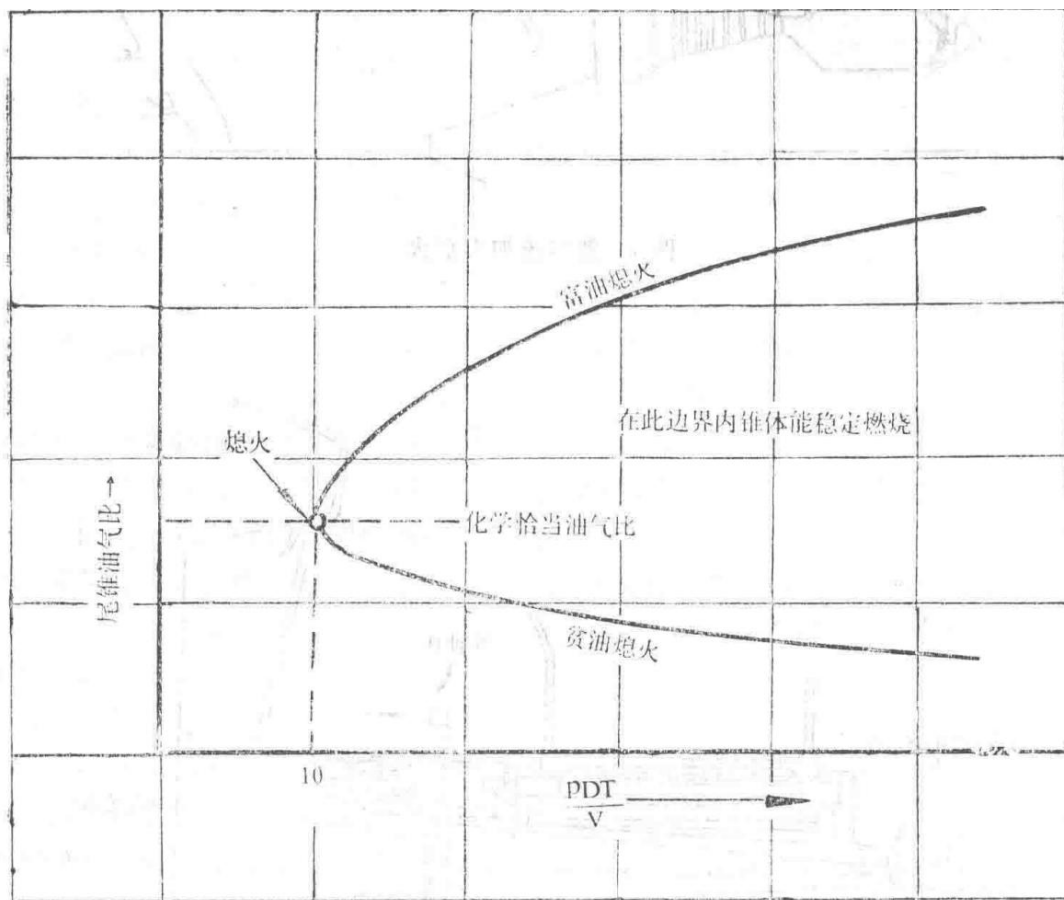


Figure 3a: Stability Boundary of the Cone

Graph depicting the stability boundary of the tail cone in terms of the parameter  $(pDT)/(V)$ .

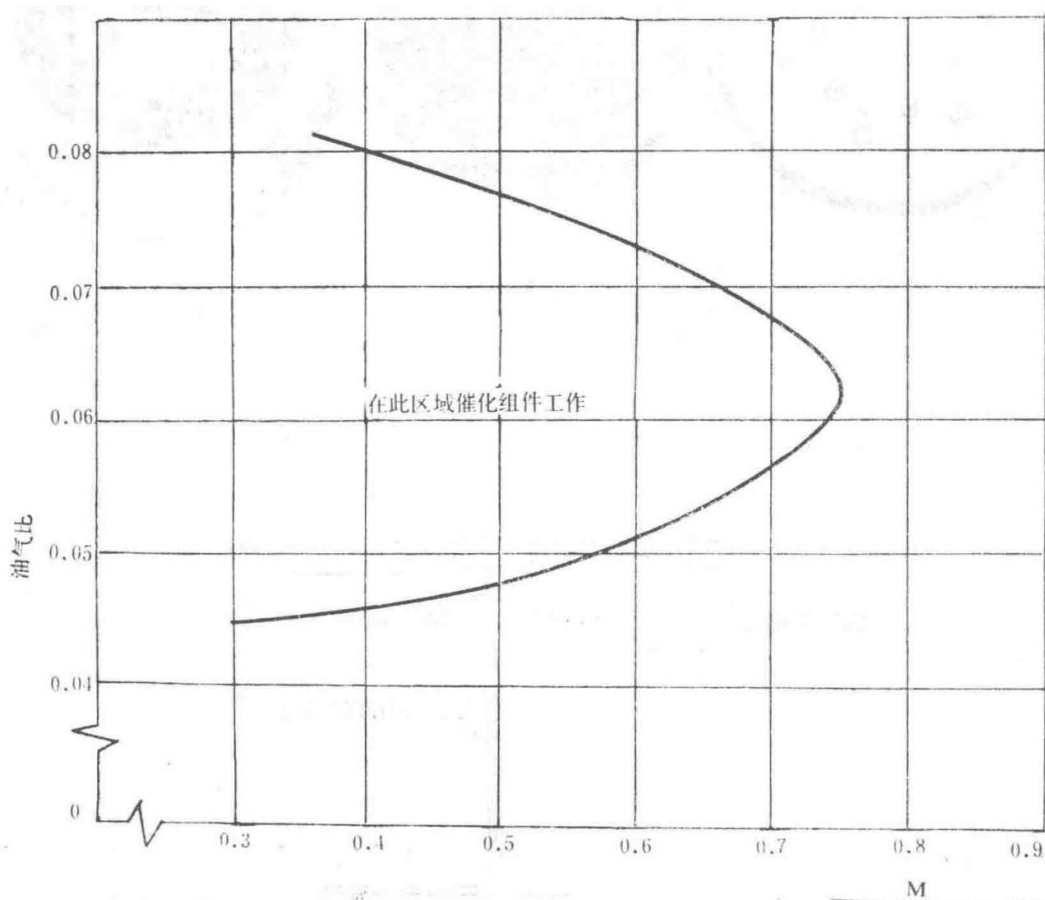


Figure 3b: Performance of the Catalytic Assembly

Graph showing the operational performance range of the catalytic assembly.

$$D = 3(1)/(4)$$

Tail cone diameter specification.

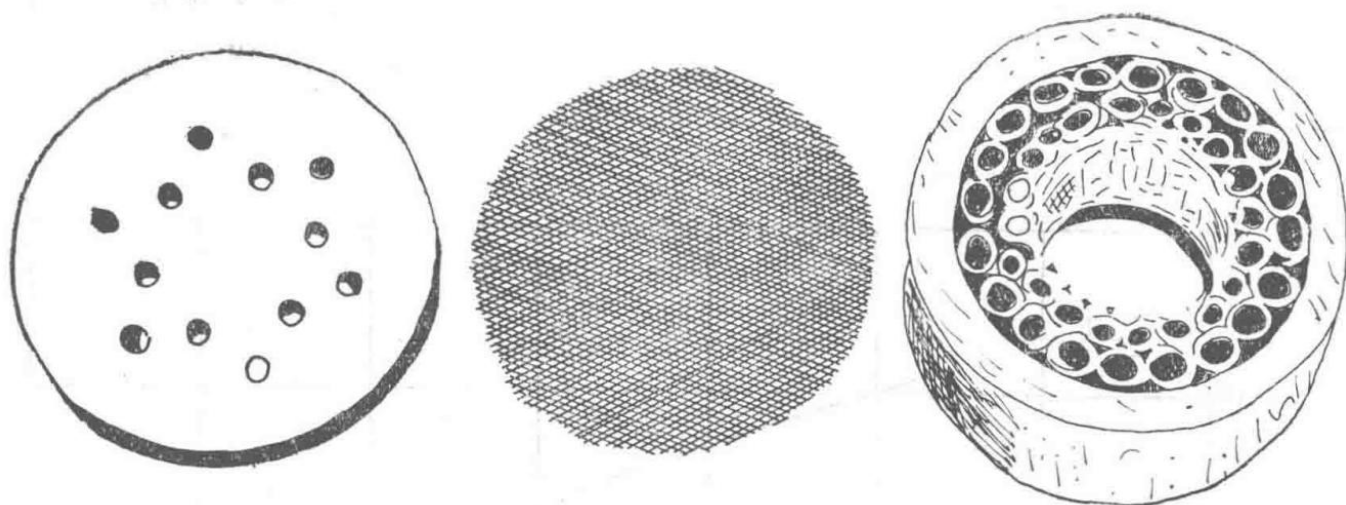
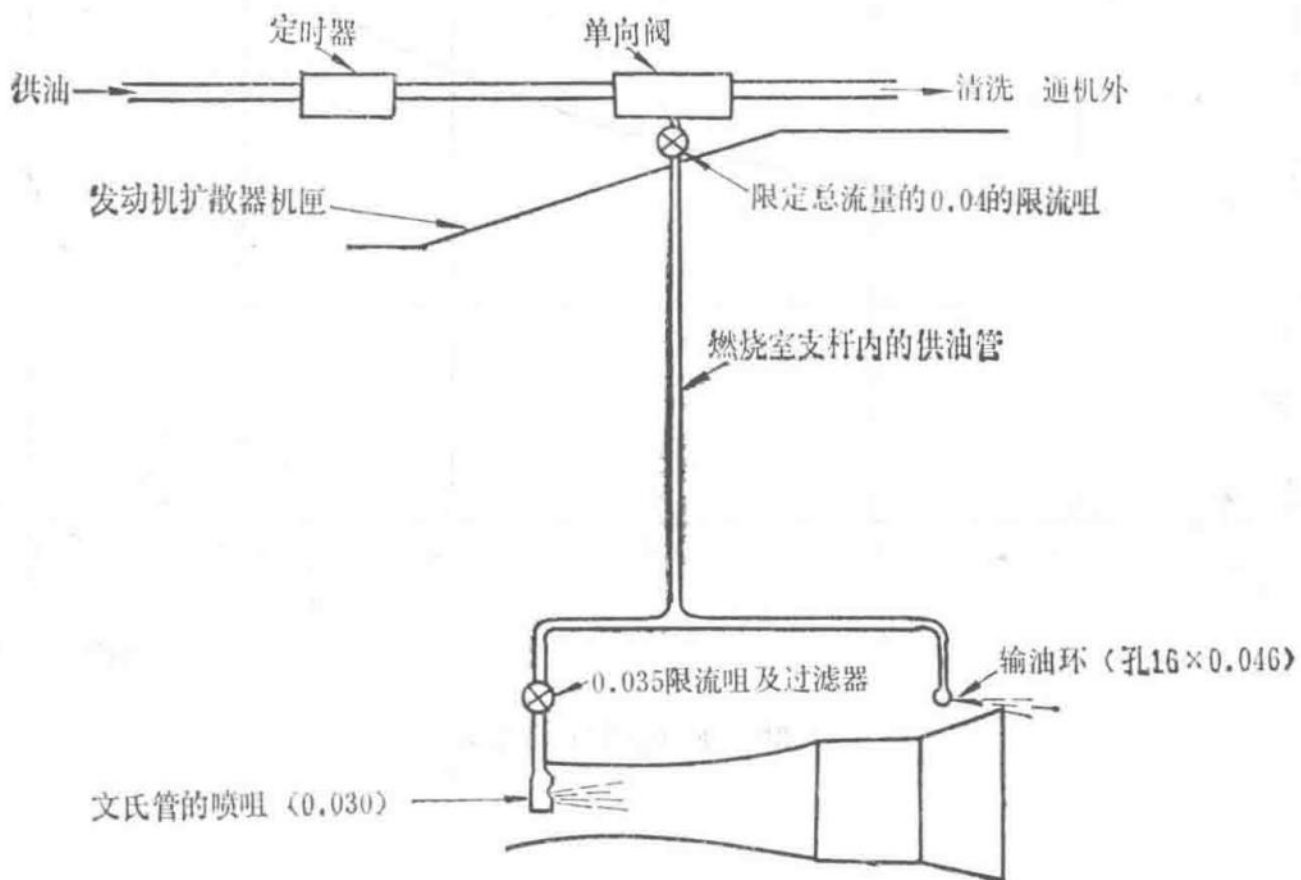


Figure 4

Technical diagram referenced in the document (specific content not described in text).



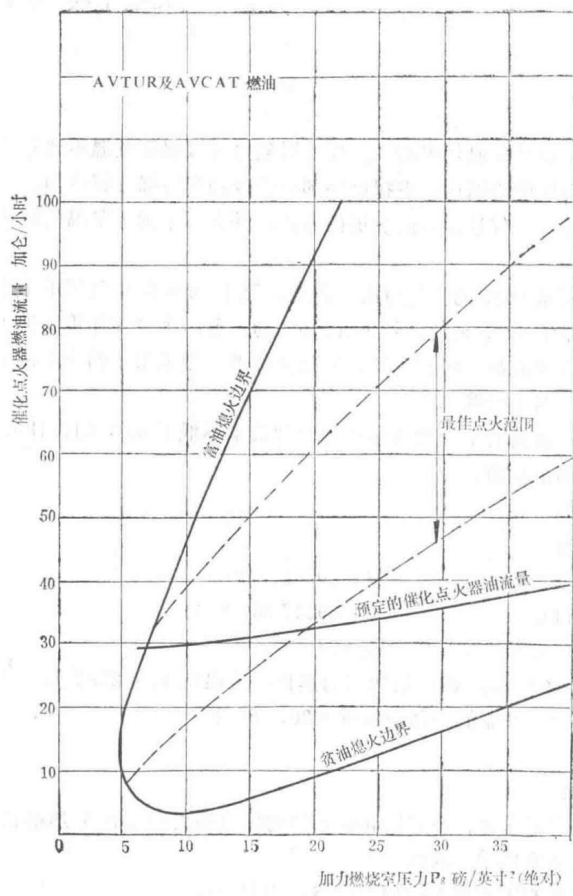


Figure 6 Operating Range of Catalytic Igniter

Graph depicting the operational range of the catalytic igniter.

#### Combustion Research Report Header

Report Title	Report Number
Combustion Research Report	CRR 12082
Spey MK202 Afterburner Heat Shield Design	

First Edition, September 22, 1976

## 1.0 Abstract

Due to the high gas temperatures in the afterburner, heat shields are required to ensure that wall temperatures do not exceed the maximum allowable values. The heat shield is supplied with air from the mixer outlet to provide external convective cooling and internal film cooling. This section describes the method for designing heat shields based on the required cooling airflow and introduces the heat transfer calculations used to determine wall temperature.

## 2.0 Introduction

At maximum afterburning conditions, 90% of the airflow is used for combustion, leaving 10% for cooling. The heat shield is designed using 15% of the total inlet airflow, with 5% reintroduced into the main combustion flow through the first four cooling rings. The afterburner is designed for sea-level static conditions, with four single-corrugated simple cooling rings in the front section of the heat shield and four double-wall segments in the rear section. The heat shield wall temperature is maintained below the material's maximum allowable value by

using high convective airflow velocities in the cooling channels and a cooling efficiency of no less than 50%.

## 3.0 Design Conditions

Sea-level static conditions:

- Total gas flow rate  $M = 207 \text{ lb/s}$
- Afterburner inlet total pressure  $P = 39.17 \text{ psi}$
- Afterburner inlet total temperature  $T_c = 740 \text{ K}$
- Temperature of the hot core flow after 90% of the air is burned with 99% efficiency  $T_{\square} = 2182 \text{ K}$
- Cooling airflow at  $T_c = 740 \text{ K}$  (10% of total) =  $20.7 \text{ lb/s}$

## 4.0 Assumptions

### 4.1 Hot Gas Flow

1. Pressure losses from the afterburner diffuser, stabilizer, and fuel manifold occur at the trailing edge of the V-gutter stabilizer.
2. Stabilizer blockage ratio  $\square\eta = 30\%$ .
3. Pressure losses due to heating are uniformly distributed along the afterburner.

### 4.2 Cooling Airflow

1. A 5% total pressure loss occurs along the outer surface of the heat shield in the cooling air channel, uniformly distributed along the afterburner casing.
2. Flow coefficient for corrugated cooling slots  $CD = 0.66$ ; flow coefficient for double-wall cooling slots  $CD = 0.8$ .

## 5.0 Heat Shield Design Procedure

The heat shield is designed based on a cooling airflow of 10% of the total airflow at an inlet temperature  $T_c = 740 \text{ K}$ . The high-temperature gas temperature after 90% of the air is burned is calculated as  $T = 2182 \text{ K}$ . The heat shield temperature  $T_{\square}$  depends on the size of the cooling air slots, which are calculated using the following method:

### 5.1 Cooling Air Slot Dimensions

1. Calculate the cold-state pressure loss based on stabilizer blockage plus diffuser losses:
2. 'type': 'equation', 'latex': ' $(\Delta P)/(D) = 2 \times (\beta)/((1 - \beta)^2)$ ', 'inline': False, 'description': 'Equation for cold-state pressure loss calculation.'
3. Calculate the cooling air total pressure  $P_c$ , assuming a 5% pressure loss in the cooling channel.
4. Calculate the pressure loss due to heating using Figure 1.
5. Calculate the post-heating total pressure  $P_{\square}$ ,  $Q_{\square}$ ,  $P/p$ , and static pressure  $p_{\square}$  from steps 2 and 3.
6. Calculate  $P_c / p_{\square}$  from steps 2 and 4, and find  $Q_c$  from the Q-curve.
7. Assuming  $CD = 0.8$  for double-wall segments and  $CD = 0.66$  for corrugated segments, calculate  $A_{\square}$ ,  $A_c$ , and  $W$  from  $Q_c$ .
8. To compensate for reduced pressure differential in the cooling rings due to surface friction losses in the cooling air channels, increase the cooling slot area. The pressure loss due to surface friction is given by:
9. 'type': 'equation', 'latex': ' $\Delta P = 4 (f l)/(D \square) (\rho V^2)/(2 g \times 144)$ ', 'inline': False, 'description': 'Equation for pressure loss due to surface friction.'
10. Where:

11. 'type': 'equation', 'latex': ' $D = (4 \pi d W) / (2 \pi d)$ ', 'inline': False, 'description': 'Hydraulic diameter calculation.'
12. 'type': 'equation', 'latex': ' $\rho = (p \times 144) / (R t)$ ', 'inline': False, 'description': 'Density calculation for cooling air.'
13. Calculate corrected values for  $P_c$ ,  $P_c / p_y$ , and  $W$  from steps 5 and 6.
14. Calculate the corrected  $\Delta P$  and iteratively solve for  $W$ .

Appendix 1 provides a calculation example for the first row of cooling slots in the double-wall segment, where the cooling airflow  $M_c = 3.81 \text{ lb/s}$  and slot height  $W = 0.120 \text{ inches}$ .

## 6.0 Heat Shield Temperature

The heat shield temperature  $T_s$  is calculated based on the balance between the heat transferred from the hot gas to the wall and the heat removed by the cooling airflow. Referring to Figure 2, the relevant radiation and convection terms are:

$$C_1 = h_1 (T_w.g. - T_s)$$

Convective heat transfer from hot gas to heat shield.

$$R_1 + C_1 = R_2 + C_2$$

Heat balance equation for the heat shield.

### 6.1 Calculation Method for Heat Shield Temperature $T_s$

1. Specify the maximum allowable temperature for C263 material  $T_{allow} = 1165 \text{ K}$ .
2. Determine the required cooling efficiency  $\eta_c$  from Figure 3 to ensure  $T_s \leq 1165 \text{ K}$ .
3. Calculate the gas-side wall temperature  $T_w.g$  from  $T-T$  and find  $T = 2182 \text{ K}$ ,  $T_0 = 740 \text{ K}$  from Figure 4.
4. Find  $X$  from  $\eta_c$  and Figure 5.
5. Calculate the cooling length  $l$  using the following equation:
6. 'type': 'equation', 'latex': ' $X = (m / (mc))^0.8 (Ac / (A))^{0.8} ((T_s) / (T_c))^{0.6} (l^{0.8}) / (W)$ ', 'inline': False, 'description': 'Equation for cooling length calculation.'
7. Calculate  $T_s$  based on the heat balance equation  $R_1 + C_1 = R_2 + C_2$ , where:
8. 'type': 'equation', 'latex': ' $R_1 = 3.94 \times 10^{-4} [1 - ((T_s) / (T_c))^{2.5}]$ '  $R_2 = 0.55 \times 10^{-8} (T_s^4 - T_c^4)$ '  $C_1 = h_1 (T_w.g. - T_s)$ '  $C_2 = h_2 (T_s - T_c)$ '  $C_3 = h_3 (T_w - T_c)$ ', 'inline': False, 'description': 'Heat balance components for radiation and convection.'
9. The values of  $h_2$  and  $h_3$  depend on the temperature and flow rate of the cooling air through the cooling channel and thus vary with axial position. Typical values for the first and last segments are:

Typical Heat Transfer Coefficients

	First Segment	Last Segment
$h$	44.5	44.5
$h_2$	131.7	138.6
$h_3$	54.7	16.6

1. Calculate the heat loss of the cooling air using:
2. 'type': 'equation', 'latex': ' $m C \Delta T = A (C_2 + R_2)$ ', 'inline': False, 'description': 'Equation for cooling air heat loss.'
3. Calculate the corrected  $T_c$ ,  $T_w.g$ , and  $T_s$ .
4. Check if  $T_s < T_{allow}$ .

5. If  $T_w > T_{\text{outer}}$ , increase  $W$  and reduce the cooling length for the same cooling flow rate  $m_c$ , then recalculate  $T_w$ .

6. If  $T_w < T_{\text{outer}}$ , reduce  $W$  to decrease  $m_c$  and increase  $T_w$ .

Appendix 3 provides a calculation example for the first row of cooling slots in the double-wall segment, where the inner wall temperature  $T_w$  of the heat shield is calculated as 1106 K. This increases the cooling air temperature  $T_c$  from 740 K to 794 K, with the outer wall temperature  $T_{\text{outer}}$  calculated as 806 K.

## 7.0 Cooling Efficiency

The gas-side wall temperature  $T_{w,g}$  and cooling segment length  $l$  are calculated from the cooling efficiency  $\eta_c$  and  $X$ , where:

$$\eta_c = (T_w - T_{w,g}) / (T_w - T_c)$$

Equation for cooling efficiency.

$$X = ((m_w)/(mC))^{0.8} ((A_c)/(A_w))^{0.8} ((T_w)/(T_c))^{0.6} (l^{0.18})/(W)$$

Equation for cooling efficiency parameter  $X$ .

At the initial end of the double-wall segment of the heat shield,  $\eta_c = 50\%$  is obtained from Figure 3, and  $X = 39.7$  is obtained from Figure 5.

— Section 46 —  
Content from Original Document (Pages 226-230)

$$m = 195.8 \text{ lb/s}, A = \pi \cdot 951 / 144 = 6.6 \text{ ft}^2, T = 2182^\circ \text{ K}$$

Given parameters for hot gas flow: mass flow rate, area, and temperature.

$$m_c = 3.81 \text{ lb/s}, A_c = (34.8) / (12) \times \pi \times (0.120) / (12) = 0.0911 \text{ ft}^2, T_c = 740^\circ \text{ K}$$

Given parameters for cooling air flow: mass flow rate, area, and temperature.

$$39.7 = (195.8^\circ \text{ K}) / (3.81) (0.0911^\circ \text{ K}) / (6.6) (2182^\circ \text{ K}) / (740) (l^\circ \text{ K}) / (0.120)$$

Equation for calculating a parameter related to cooling efficiency using given flow properties.

$$T_{\text{cal}} = 1461^\circ \text{ K}$$

Calculated temperature value for a specific parameter (possibly virtual reference outlet gas temperature).

## 8.0 Cooling Ring Spacing

The relationship between cooling air gap dimensions, spacing between gaps, cooling flow rate, and temperature is given by:

$$X = ((m_h) / (m_c))^{0.8} ((A_c) / (A_h))^{0.8} ((T_c) / (T_h))^{0.6} (l^\circ \text{ K}) / (W)$$

Equation defining the parameter X, which relates cooling air gap dimensions and flow properties.

Where: - l = cooling length - W = cooling gap height Subscripts H and C denote hot gas and cooling air, respectively.

Figure 5 shows the relationship between cooling efficiency and this parameter.

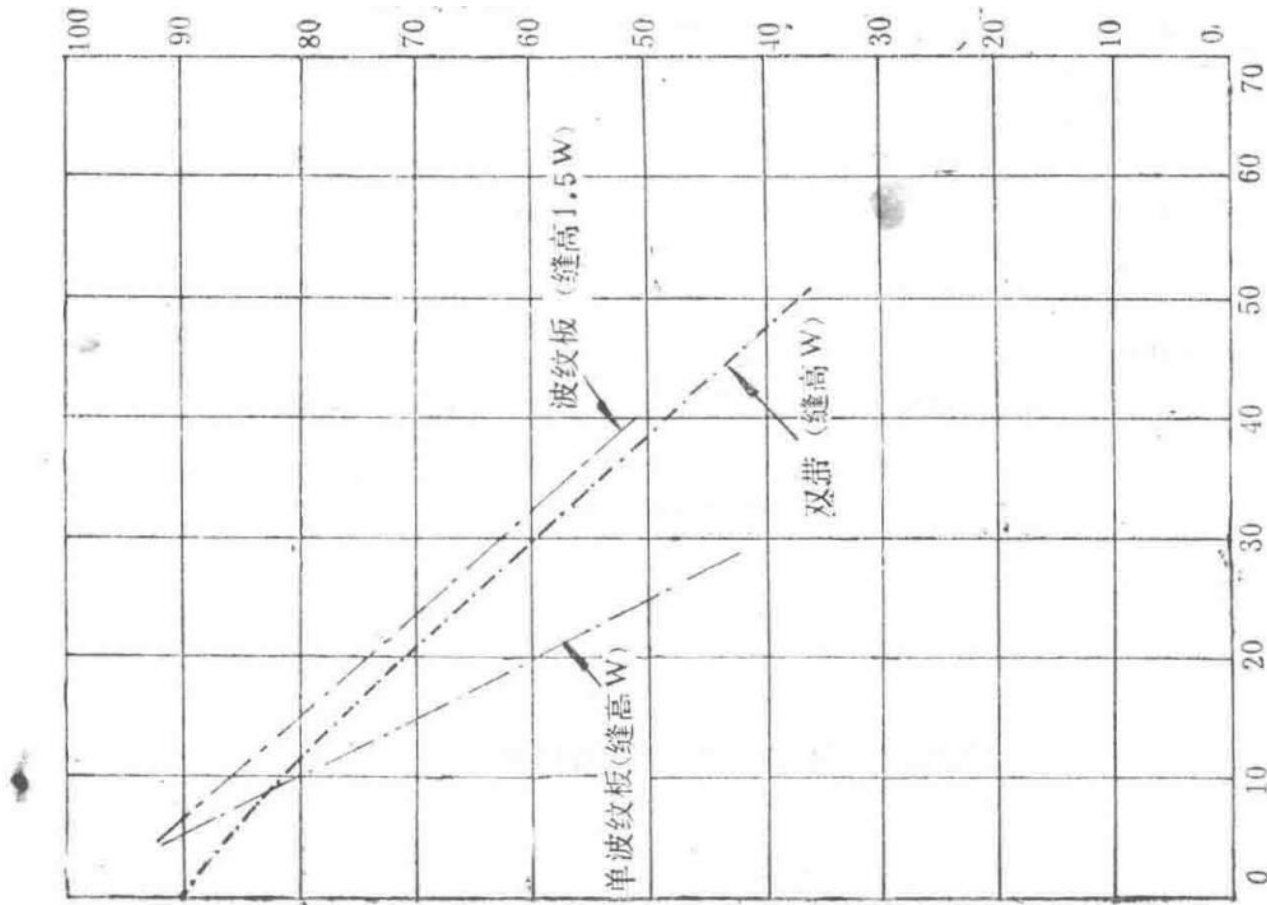


Figure 5 Cooling efficiency curve

Graph depicting the relationship between cooling efficiency and the parameter X.

## Nomenclature

### Symbols and their descriptions

Symbol	Description	Unit
$T\Box$	Hot core gas temperature	^K
$T_c$	Inlet cooling air temperature	^K
$T_c'$	Outlet cooling air temperature	^K
$T\Box$	Heat shield inner wall temperature	^K
$T\Box.\Box$	Heat shield outer wall temperature	^K
$T_{w.g}$	Wall gas temperature	^K
$T_w$	Afterburner casing wall temperature	^K
$A_c$	Cooling gap area	ft <sup>2</sup>
$A\Box$	Hot gas flow area	ft <sup>2</sup>
$M_c$	Cooling airflow mass flow rate	lb/s
$M\Box$	Hot gas flow mass flow rate	lb/s
$l$	Cooling length	ft
$W$	Cooling gap height	ft
$e\Box$	Heat shield emissivity	-

图 5 冷却效率曲线

$e\Box$	Gas emissivity	-
$\epsilon_w$	Afterburner casing emissivity	-
$a_g$	Gas absorptivity	-
$\beta$	Stabilizer blockage ratio	-
$P_c$	Cooling channel total pressure	lb/in <sup>2</sup>
$P_h$	Heated total pressure	lb/in <sup>2</sup>
$p_h$	Heated static pressure	lb/in <sup>2</sup>
$f$	Surface friction coefficient	-
$L$	Cooling air channel length	ft
$V$	Cooling air velocity	ft/s
$D_h$	Hydraulic mean diameter = $4 \times \text{Area} / \text{Wetted Perimeter}$	-
$\rho$	Cooling air density	lb/ft <sup>3</sup>
$R$	Gas constant = 96.0	ft-lb/lbK

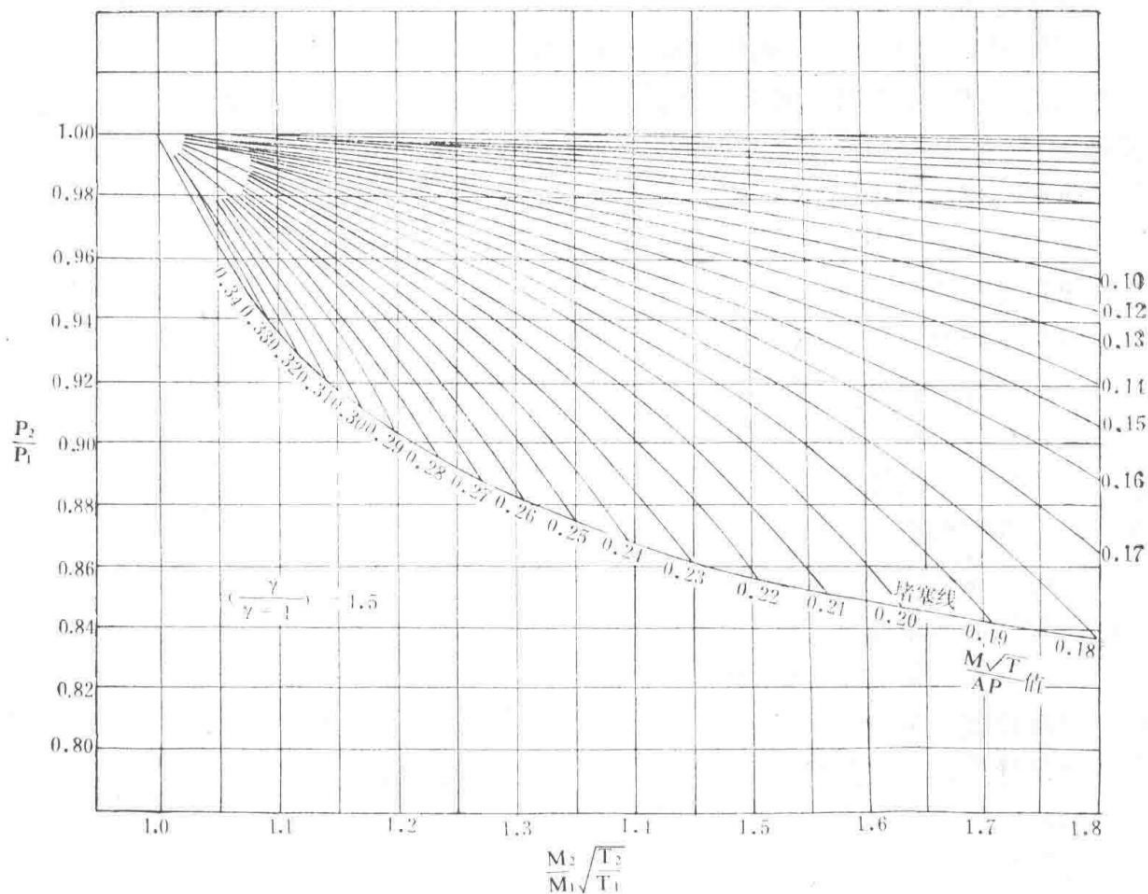
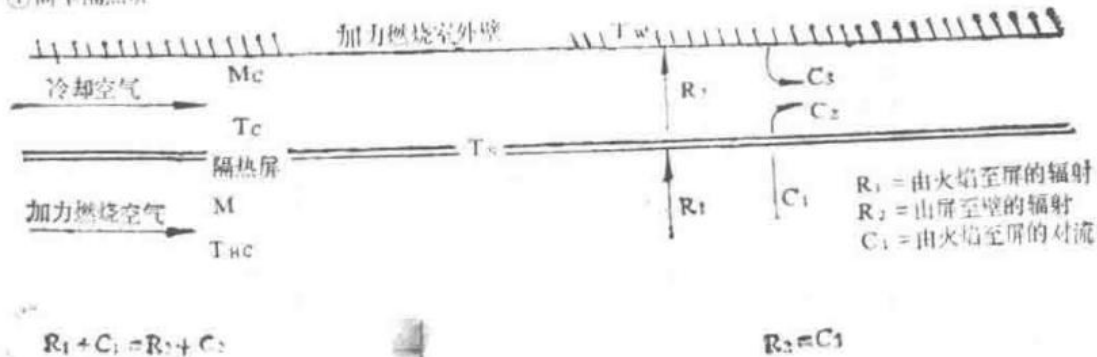


Figure 1 Total pressure loss due to heating

Graph showing the total pressure loss as a function of heating in the engine.

① 简单隔热屏



② 双面气膜冷却隔热屏

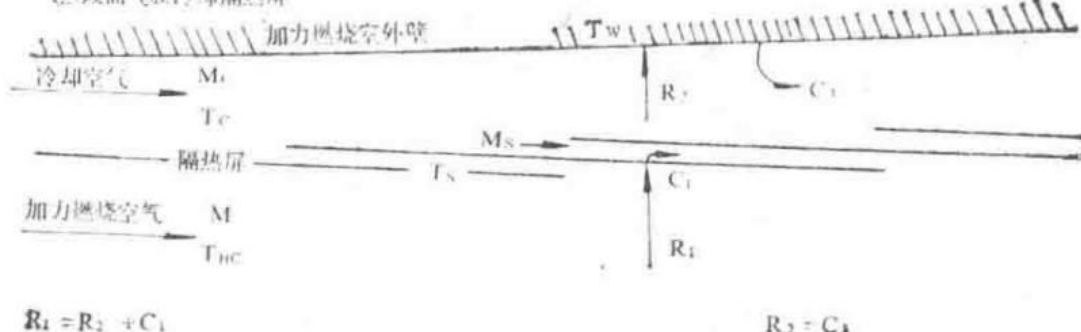


Figure 2 Heat transfer subprocesses used in afterburner temperature calculations

Diagram illustrating the subprocesses involved in heat transfer calculations for the afterburner.

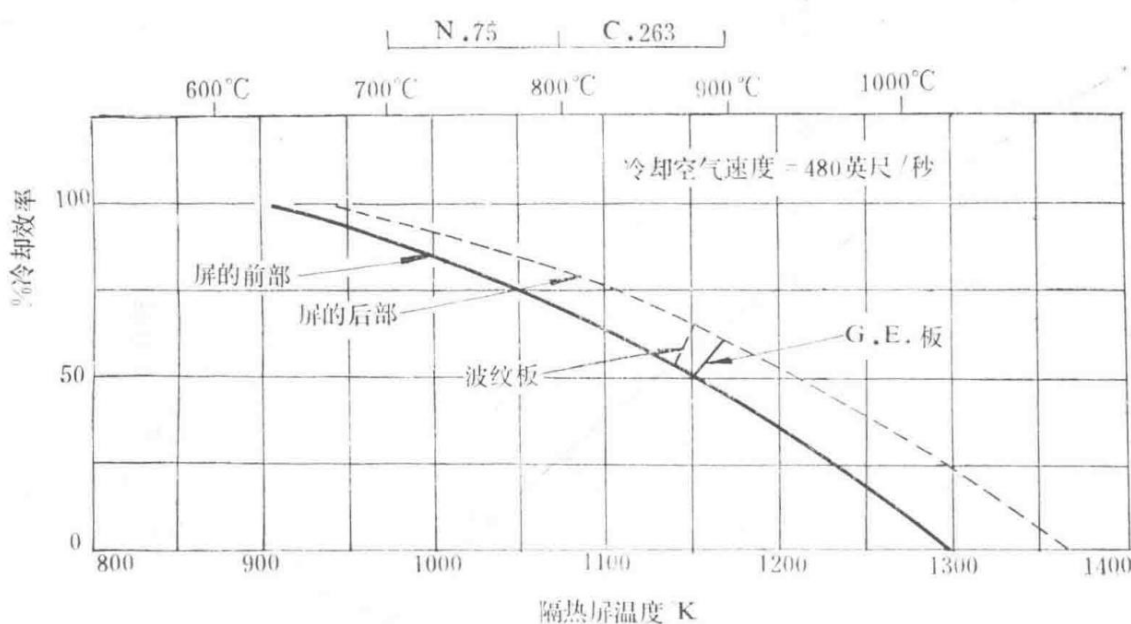
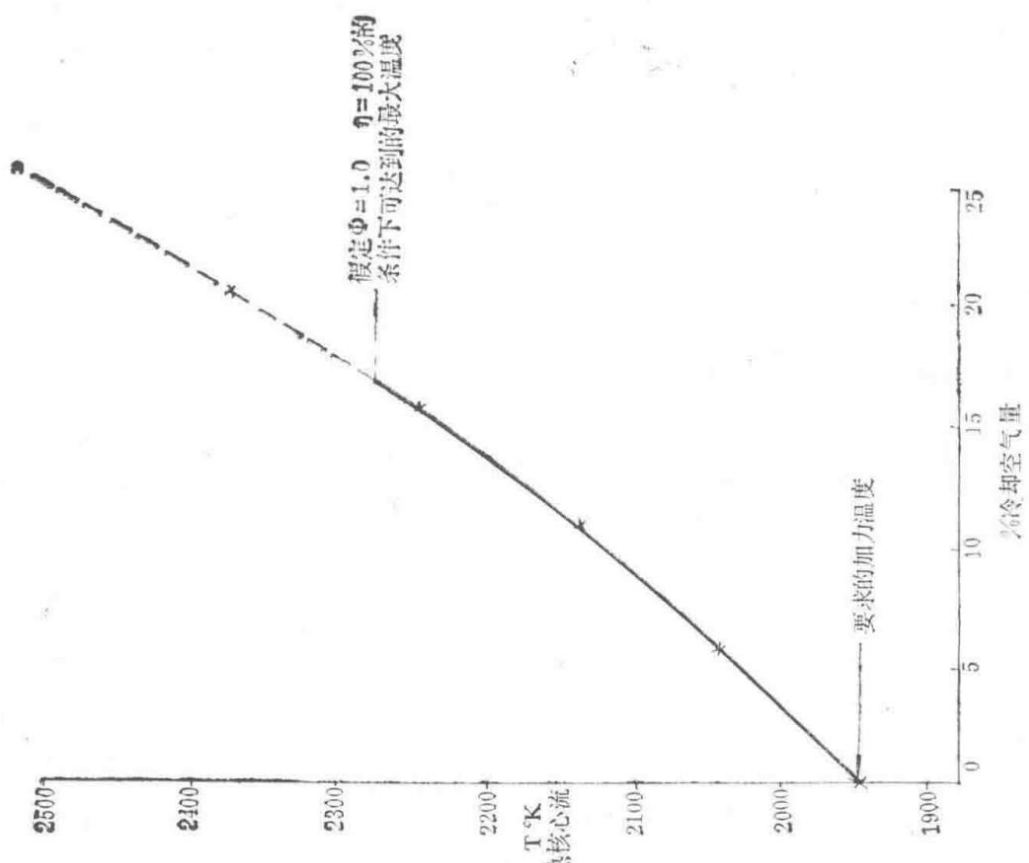


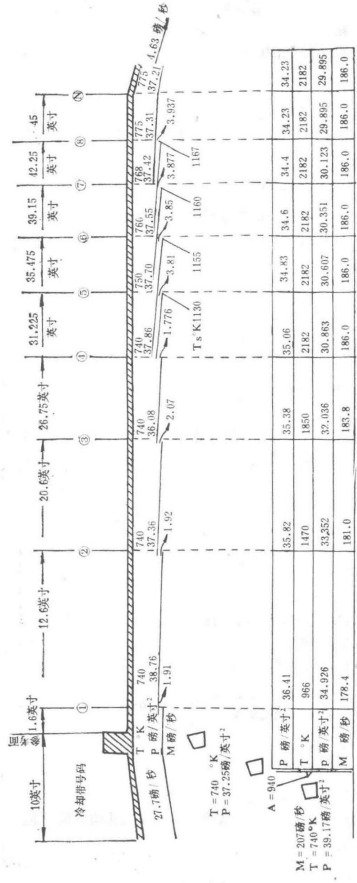
Figure 3 Heat shield temperature

Graph or diagram showing temperature distribution in the heat shield.



Unlabeled diagram 4

Technical diagram without a specific caption.



## Unlabeled cooling efficiency-related graph

## Graph related to cooling efficiency parameters.

## Appendix 1

### Aerodynamic Calculation for Cooling Gap Dimensions

#### Operating Conditions of Afterburner at Sea Level Static State

Mass flow rate  $M = 207 \text{ lb/s}$

$$T_c = 740^{\circ}\text{K} M \sqrt{(T), A P = Q}$$

Definition of flow parameter  $Q$

$Q = 0.134$

Pressure  $P = 39.17 \text{ psi (absolute)}$   $P_p = 1.028$

Area  $A = 1075 \text{ in}^2$   $p = 38.103 \text{ psi}$   $P - p = 1.067 \text{ psi}$

#### Cold Pressure Loss

Stabilizer blockage ratio  $\beta = 0.30$

$$\Delta P_D = 2 \beta (1 - \beta)^2,$$

Pressure loss coefficient due to blockage

$\Delta P_D = 1.22$

$$\Delta P = 1.22 \times 1.067$$

Calculation of cold pressure loss

Pressure after cold loss  $P = 37.87 \text{ psi (absolute)}$

After cold loss  $Q = 0.138$

#### Pressure Loss Due to Heating

Assumed cooling air flow = 10%  $M = 186.3 \text{ lb/s}$  (plus fuel flow)

Overall fuel-air ratio = 0.0615 Engine fuel-air ratio = 0.011 Afterburner fuel-air ratio = 0.0505

Combustion efficiency  $\eta_c = 99\%$  Therefore, actual fuel-air ratio = 0.0510

Afterburner fuel flow = 9.5 lb/s Total flow  $M = 186.3 + 9.5 = 195.8 \text{ lb/s}$

$$M_2, M_1 \sqrt{(T_2, T_1)} = 195.8, 186.3 \sqrt{(2182, 740)} = 1.805$$

Flow parameter after heating

From Figure 1,  $P_2, P_1 = 0.923$

Pressure after heating =  $0.923 \times 37.87 = 34.95 \text{ psi}$

Total  $\Delta P = 2.92 \text{ psi}$ , assumed to be uniformly distributed along the afterburner liner.

At the first cooling ring position  $I, L = 0.668$

Therefore,  $P = 0.668 \times 2.92 = 1.95 \text{ psi}$

Thus,  $P_1 = 35.92$  psi

$$Q = 195.8 \times \sqrt{(2182),951 \times 35.92},$$

Calculation of Q at the first cooling ring

$$Q = 0.2677, P_1, p_1 = 1.143, p_2 = 31.43 \text{ psi}$$

## Cooling Ring Duct Pressure

A uniform 5% pressure loss is assumed along the duct.

## Cooling Air Gaps

Pressure ratio across the heat shield:

$$P_{c,p} = 37.86, 31.43 = 1.204 Q_c = 0.3040$$

Pressure ratio and flow parameter for cooling air

Cooling air mass flow  $M_c = 3.81 \text{ lb/s}$  Effective area  $A_1 = 3.81 \sqrt{(740),0.304 \times 37.86} = 9.00 \text{ in}^2$

Discharge coefficient  $CD = 0.80$  Therefore,  $AC = 11.25 \text{ in}^2$  Gap width  $W = 11.25, \pi \times 34.8 = 0.103 \text{ in}$

However, due to surface friction in the cooling air passage between the two walls of the heat shield,  $P_{c,p}$  will decrease.

$$\Delta P = 4 f l, D \rho V^2, 2 g,$$

Pressure loss due to friction

Where  $f = \text{surface friction coefficient} = 0.006$  (from Figure 7 for  $Re = 4.3 \times 10^4$ )

$$\rho = p, R T = 31.31 \times 144,96 \times 740 = 0.0635 \text{ lb/ft}^3$$

Density calculation

Segment length  $l = 4.5 \text{ in}$

$$D = 4 \times \pi \times 34.8 W, 2 \times \pi \times 34.8 W = 2 W$$

Hydraulic diameter calculation

$$\Delta P = 2 f l, W \rho V^2, 2 \times 32.17 \times 144 = 2 \times 0.006 \times 4.5 \times 0.0635 \times 914^2, 0.102 \times 64.34 \times 144,$$

Detailed pressure loss calculation

Thus,  $P_c$  reduces to 34.83 psi

$$P_{c,p} = 34.83, 31.31 = 1.112 Q = 0.2445 A_1 = 12.17 \text{ in}^2$$

Updated pressure ratio and flow parameter

Area  $A = 15.21 \text{ in}^2$  Gap width  $W = 0.139 \text{ in}$ . Repeating calculations for  $W$  and  $\Delta P$  yields  $W = 0.120 \text{ in}$ .

Cold loss  $\Delta P, D = 1.22$  at the first row of cooling gaps in the double-wall section. Duct loss and heat loss are assumed linear:  $P_2 / P_1 = 0.92$ , 5% loss.

Summary:  $P_c = 37.86$ ,  $p_1 = 31.31$ ,  $m_c = 3.81$ ,  $\rho = 0.0635$

Cooling Gap Calculation Results

Pc (psi)	Pc/pH	Q	Ae (in <sup>2</sup> )	A (in <sup>2</sup> )	W (in)	V/√T	V (ft/s)	pV <sup>2</sup> /(2g × 144) (psi)	2fl/W	ΔP (psi)
37.86	1.209	0.3055	8.96	11.2	0.102	33.6	914	5.73	0.529	3.03
34.83	1.112	0.2445	12.17	15.21	0.139	25.4	691	3.27	0.388	1.27
36.59	1.169	0.2855	9.92	12.4	0.113	30.8	838	4.8	0.478	2.29
35.57	1.136	0.264	11.04	13.8	0.126	28.0	762	3.98	0.428	1.71
36.15	1.155	0.277	10.35	12.9	0.118	29.6	805	4.44	0.458	2.03
35.83	1.144	0.2695	10.73	13.4	0.123	28.7	781	4.18	0.440	1.84
35.93	1.147	0.2715	10.62	13.28	0.121	29.0	789	4.27	0.444	1.90

W converges to 0.121 in, ΔP converges to 1.9 psi.

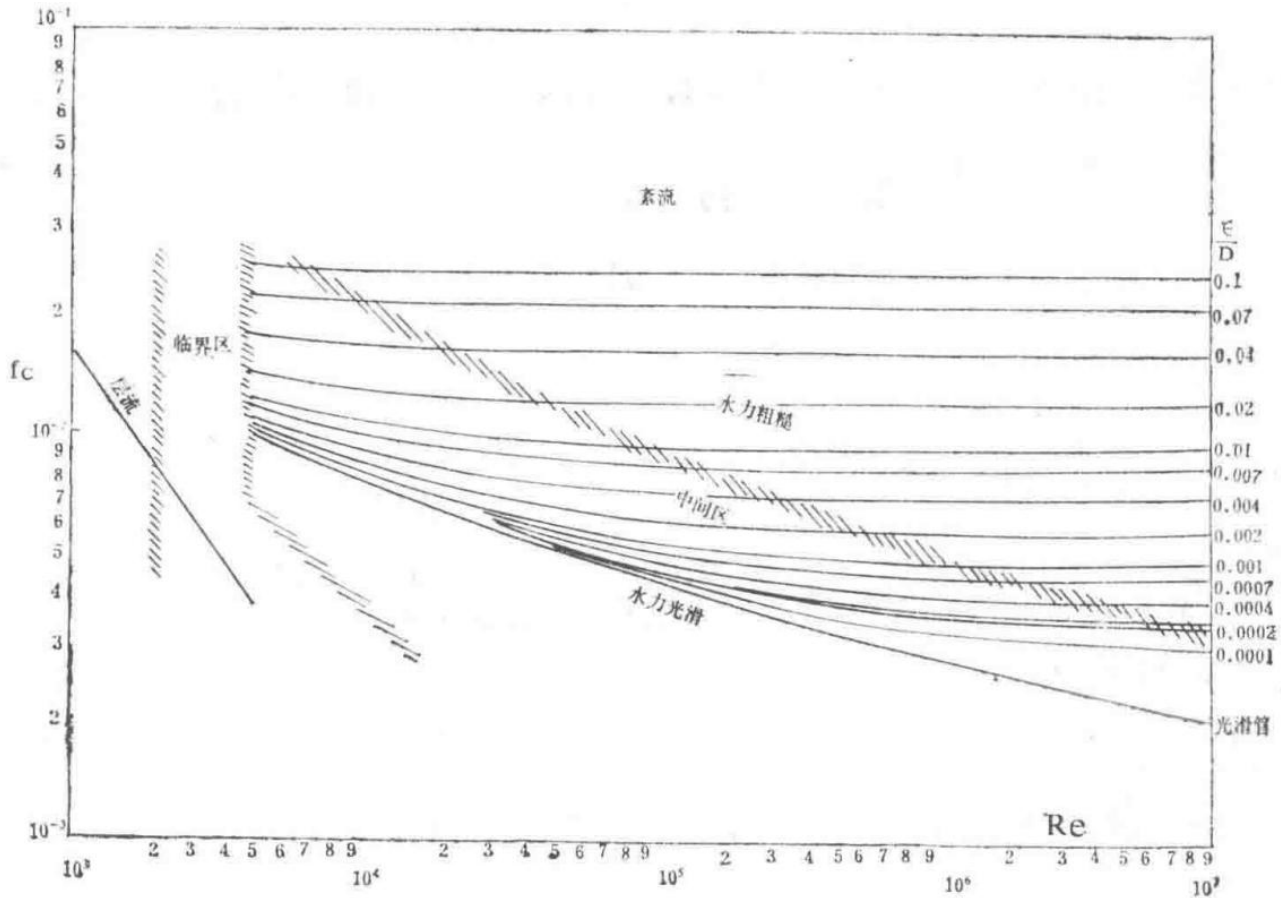


Figure 7: Friction Factor for Straight Pipes

Graph showing the friction factor for straight pipes as a function of Reynolds number.

## Appendix 2

### Heat Transfer Coefficients

Radiative heat transfer from hot gas to the heat shield is  $R_1$ , and convective heat transfer is  $C_1$ . Under equilibrium conditions,  $R_1$  and  $C_1$  must be balanced by convective heat transfer  $C_2$  and radiative heat transfer  $R_2$  from the heat shield to the cooling air and afterburner casing wall.

## Radiative Heat Transfer from Gas to Shield $R_1$

This is given by the Stefan-Boltzmann equation:

$$R_1 = 1.01 \times 10^{-8} [1 + e^{\frac{1}{T}} (e^{\frac{1}{T}} T^4 - a g T^4)]$$

Stefan-Boltzmann equation for radiative heat transfer

Where  $e^{\frac{1}{T}} = e_w = 0.7$

$$a g = e^{\frac{1}{T}} (T^4 - T^4)^{1.5},$$

Absorptivity of gas

Beam length  $l_B = 0.6$  D = 1.7 ft

$$R_1 = 39400 [1 - (T^4 - T^4)^{2.6}],$$

Simplified radiative heat transfer equation

## Internal Convection $C_1$

From gas to heat shield:

$$C_1 = 0.02 (K, \mu^{0.8}) (M^{0.8}, d^{0.2} A^{0.8}) (Twg - T) 3600^{0.8},$$

Convective heat transfer equation

Where K = thermal conductivity of gas,  $\mu$  = viscosity, d = hydraulic mean diameter, A = cross-sectional area.

At  $Twg = 1461^\circ$ ,  $K, \mu^{0.8} = 0.263$

Mass flow M = 195.8 lb/s  $M^{0.8} = 68.0$   $3600^{0.8} = 700$

$$C_1 = 0.02 \times 0.263 \times 68.0 \times 700, 1.238 \times 4.54 (Twg - T)$$

Detailed convective heat transfer calculation

$$C_1 = 44.5 (Twg - T)$$

Simplified convective heat transfer equation

## Convective Heat Transfer $C_2$

Between inner and outer walls of the heat shield:

$$C_2 = 0.02 (K, \mu^{0.8}) (m^{0.8}, d^{0.2} A^{0.8}) (T - T_c) 3600^{0.8},$$

Convective heat transfer equation for heat shield walls

At  $T_c = 740^\circ$ ,  $K, \mu^{0.8} = 0.218$

$$C_2 = 131.7 (T - T_c)$$

Simplified convective heat transfer equation

When cooling air temperature increases from  $T_c$  to gap outlet temperature  $T_{c\Delta}$ ,  $C_2$  increases to  $C_2 = 134.1 (T - T_{c\Delta})$

## External Radiative Heat Transfer $R_2$

From heat shield to afterburner casing wall:

$$R_2 = 1.01 \times 10^{-8} [ e_c e_w, e_w + e_w (1 - e_w) d_w, d_w ] (T_w^4 - T_c^4)$$

Radiative heat transfer from shield to casing

Where  $e_w$  = shield emissivity = 0.7,  $e_w$  = wall emissivity = 0.7,  $d_w$  = shield diameter = 34.8, 12 = 2.9 ft,  $d_w$  = wall diameter = 37.0, 12 = 3.08 ft

$$R_2 = 0.55 \times 10^{-8} (T_w^4 - T_c^4)$$

Simplified radiative heat transfer equation

## External Convective Heat Transfer $C_3$

From outer wall of heat shield to cooling air:

$$C_3 = 0.02 (K, \mu^{0.8}) (m^{0.8}, d^{0.2} A^{0.8}) (T_w, \square - T_c) \times 3600^{0.8},$$

Convective heat transfer from shield outer wall to cooling air

$$K, \mu^{0.8} = 0.218$$

Thermal conductivity to viscosity ratio

$$C_3 = 54.7 (T_w, \square - T_c)$$

Simplified convective heat transfer equation

## Appendix 3

### Heat Shield Temperature Calculation Example

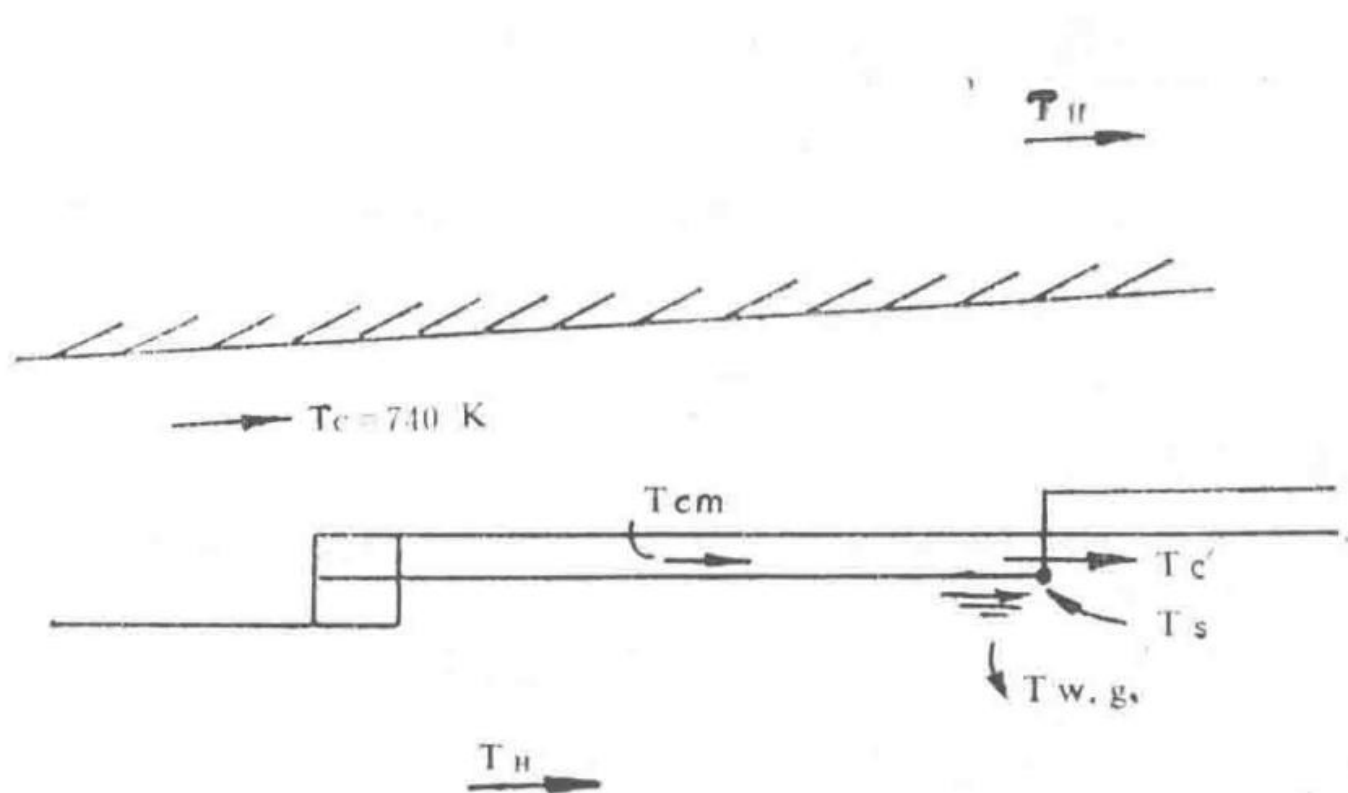


Diagram illustrating the first cooling gap in the double-wall section of the heat shield.

At the first cooling gap in the double-wall section:

$$mC = 3.81 \text{ lb/s},$$

Cooling air mass flow rate.

$$T_c = 740^{\circ}\text{K},$$

Cooling air temperature.

$$W = 0.120 \text{ inches},$$

Width of the cooling gap.

$$T_H = 2182^{\circ}\text{K},$$

Hot core gas temperature.

$$\eta C = 50\% = T_H - T_w \quad \text{and} \quad g., T_H - T_c,$$

Cooling efficiency.

$$T_w \quad \text{and} \quad g. = 1461^{\circ}\text{K},$$

Calculated gas-side wall temperature.

Let  $T = 1150^\circ\text{K}$ . Then:

$$C_1 = 44.5 (T_w.g. - T)$$

Convective heat transfer coefficient term.

$$C_1 = 13839 \text{ CHU} / \text{ft}^2 \cdot \text{hour},$$

Calculated value of  $C_1$ .

$$R_1 = 39400 [ 1 - ( T, T )^{2.5} ],$$

Radiative heat transfer coefficient term.

$$R_1 = 31455 \text{ CHU} / \text{ft}^2 \cdot \text{hour},$$

Calculated value of  $R_1$ .

$$C_2 = 131.7 (T - T_c)$$

Convective heat transfer to cooling air.

$$C_2 = 53997 \text{ CHU} / \text{ft}^2 \cdot \text{hour},$$

Calculated value of  $C_2$ .

$$R_2 = 0.55 \times 10^{-8} (T^4 - T_c^4)$$

Radiative heat transfer to cooling air.

It is observed that:

$$(R_1 + C_1) < (R_2 + C_2)$$

Heat transfer balance condition.

When  $T = 1075^\circ\text{K}$ :

$$R_1 + C_1 = 49865 \quad R_2 + C_2 = 49815$$

Heat transfer balance at  $T = 1075^\circ\text{K}$ .

Thus,  $(R_1 + C_1) \approx (R_2 + C_2)$ .

Heat absorbed by the cooling air:

$$A = 6.83 \text{ ft},$$

Area parameter for heat absorption.

Heat absorbed =  $C_2 + R_2$ . When  $T = 1075^\circ\text{K}$ ,  $C_2 + R_2 = 49815 \text{ CHU} / \text{ft}^2 \cdot \text{hour}$ .

$$m C \Delta T = A (C_2 + R_2)$$

Heat balance equation for cooling air temperature rise.

$$3.81 \times 3600 \times 0.2467 \times \Delta T = 6.83 \times 49815$$

Calculation of temperature rise  $\Delta T$ .

$$\Delta T = 101^\circ\text{K},$$

Temperature rise of cooling air.

The average temperature  $T_{c\Delta}$  is given by:

$$\text{Log mean temperature difference } \Delta T = (1075 - 740) - (1075 - 841), \quad (1075 - 740, 1075 - 841),$$

Logarithmic mean temperature difference calculation.

$$\Delta T = 101, \quad 1.4316 = 281, \quad K,$$

Calculated log mean temperature difference.

$$T_{c\Delta} = 1075 - 281 = 794, \quad K,$$

Average cooling air temperature.

Recalculate  $T$  using the increased cooling air temperature  $T_{c\Delta} = 794, \quad K$ :

Let  $T = 1150, \quad K$ . With higher thermal conductivity at  $T_{c\Delta} = 794, \quad K$ , the  $C_2$  term increases. Given  $A, 14^\circ = 0.222$ ,  $C_2$  becomes:

$$C_2 = 134.1 (T - T_{c\Delta})$$

Updated convective heat transfer term.

$C_1$  and  $R_1$  remain unaffected. With the increase in  $T_{c\Delta}$ ,  $R_2$  decreases.

Let  $T = 1100, \quad K$ :

- $R_1 = 32290$
- $C_1 = 16065$
- $R_1 + C_1 = 48355$
- $R_2 = 5867$
- $C_2 = 41035$
- $R_2 + C_2 = 46902$

When  $T = 1106, \quad K$ :

- $R_1 = 32193$
- $R_1 + C_1 = 47991$
- $R_2 = 6044$
- $R_2 + C_2 = 47883$
- $(R_1 + C_1) \approx (R_2 + C_2)$
- $C_2 = 41839$

Recalculate the temperature rise of the cooling air:

$$m \cdot C \cdot \Delta T = A (R_2 + C_2)$$

Heat balance equation for recalculated temperature rise.

$$3.81 \times 3600 \times 0.2479 \Delta T = 6.83 \times 47883$$

Calculation of updated temperature rise  $\Delta T$ .

$$T'c = 836, \quad K,$$

Updated cooling air exit temperature.

$$\text{Log mean temperature difference } \Delta T = 96, \quad 1.356,$$

Recalculated log mean temperature difference.

$$T_{\Delta} = 315 \text{ K}$$

Log mean temperature difference value.

$$T_{c\Delta} = 1106 - 315 = 791 \text{ K}$$

Updated average cooling air temperature.

## Calculation of Heat Shield Outer Wall Temperature $T_{w\Delta}$ .

Let  $T_{w\Delta} = 800 \text{ K}$ .

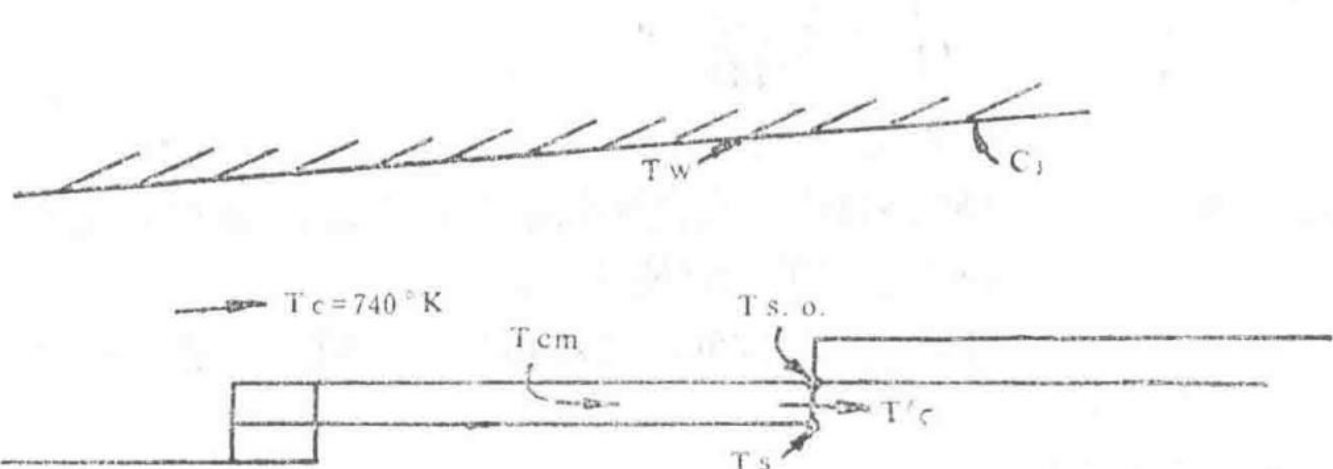


Diagram illustrating the temperature distribution for the outer wall of the heat shield.

$$C_1 = 134.1 (794 - 800)$$

Convective heat transfer term for outer wall.

$$C_1 = -805 \text{ CHU} / \text{ft}^2 \cdot \text{hour},$$

Calculated value of  $C_1$  for outer wall.

$$R_1 = 0.55 \times 10^{-8} (1106^4 - 800^4)$$

Radiative heat transfer term for outer wall.

$$R_1 = 5977 \text{ CHU} / \text{ft}^2 \cdot \text{hour},$$

Calculated value of  $R_1$  for outer wall.

$$C_2 = 54.7 (800 - 740)$$

Convective heat transfer to cooling air for outer wall.

$$C_2 = 3282 \text{ CHU} / \text{ft}^2 \cdot \text{hour},$$

Calculated value of  $C_2$  for outer wall.

$$R_2 = 0.55 \times 10^{-8} (800^4 - 740^4)$$

Radiative heat transfer to cooling air for outer wall.

$$R_2 = 603 \text{ CHU} / \text{ft}^2 \cdot \text{hour},$$

Calculated value of  $R_2$  for outer wall.

$$R_1 + C_1 = 5172 \text{ CHU / ft}^2 \cdot \text{hour},$$

Total heat transfer to outer wall.

$$R_2 + C_2 = 3885 \text{ CHU}^\square / \text{ft}^2 \cdot \text{hour},$$

Total heat transfer from outer wall to cooling air.

Since  $(R_1 + C_1) > (R_2 + C_2)$ , T $\square.\square.$  is too low.

Let  $T_{\square.\square.} = 820 \text{ K}$ . At  $T_{\square.\square.} = 806 \text{ K}$ :

Calculate the temperature rise of the cooling air:

Cross-sectional area =  $34.8 \pi \times 4.5,144$ ,

Cross-sectional area of the cooling channel.

Heat absorbed =  $(R_2 + C_2) = 4282 \text{ CHU} / \text{ft}^2 \cdot \text{hour}$  (at  $T_{\square.\square.} = 806^{\circ}\text{F}$  K).

$$m \cdot C_{\square} \cdot \Delta T = A (R_2 + C_2)$$

Heat balance equation for cooling air temperature rise.

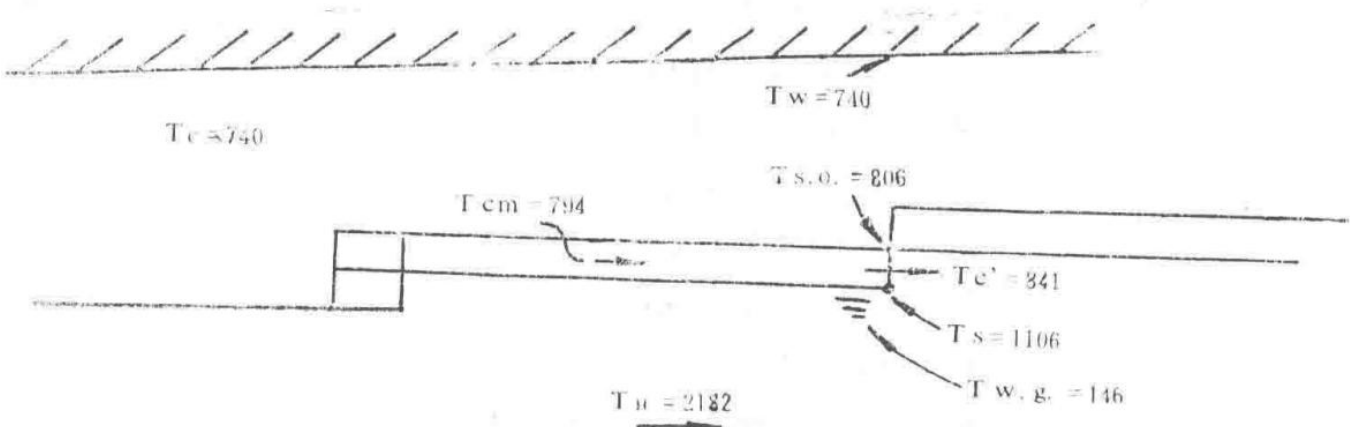
$$\Delta T = 3.42 \times 4282$$

#### Calculation of temperature rise $\Delta T$ .

$$\Delta T = 1 / \square \square^r \square,$$

Temperature rise of cooling air, negligible.

The afterburner liner is insulated, and it is assumed that there is no heat loss through the insulation material. The wall temperature  $T_w = T_c = 740^\circ\text{K}$ .



Summary diagram of temperature calculations at the first cooling gap in the double-wall section of the heat shield.

All temperatures are in Kelvin.

With a hot core flow temperature  $T_{\text{in}} = 2182 \text{ K}$  and cooling efficiency  $\eta_c = 50\%$ , the gas-side wall temperature  $T_{w,g}$  at the exit of the first cooling gap in the double-wall section is  $1461 \text{ K}$ . This results in heat shield inner and outer wall temperatures of  $T_{\text{in}} = 1106 \text{ K}$  and  $806 \text{ K}$ , respectively.

The cooling air temperature between the two walls increases from  $T_c = 740^\circ\text{K}$  at the inlet of the cooling gap to  $T_c = 841^\circ\text{K}$  at the outlet, yielding an average value of  $T_c = 794^\circ\text{K}$  along this section. The heat shield temperature at the exit of each cooling channel can be calculated similarly, with appropriate

adjustments to the heat transfer coefficients to account for the increased cooling air temperature in each segment.

The coefficients used in the radiative heat transfer terms remain constant, but in the convective heat transfer terms, the coefficients vary with temperature due to changes in the thermal conductivity  $K$  and viscosity  $\mu$  of the gas. However, within the temperature range used, these changes are minimal.

Document	Reference
Combustion Research Report	CRR12083
	Spey MK202 Afterburner Fuel Manifold Design

## 1.0 Summary

This report presents the design and layout method for the main afterburner fuel manifold used in conjunction with Rolls-Royce vaporizer stabilizers. It explains the determination of the fuel manifold dimensions and the assessment of the potential for fuel boiling. The appendices include a set of typical calculations for the Spey MK202 as examples of the method's application.

## 2.0 Introduction

Reference [1] outlines the general design methodology for a full afterburning system in turbofan engines. For variable afterburning ratio systems, the recommended combustion chamber consists of vaporizer V-gutter stabilizers with independent fuel supply (see Reference [2]) and an associated main afterburner fuel system. The latter system injects fuel into the combustion zone through annular manifolds located upstream of the stabilizers and between them. This report describes the arrangement of these main afterburner fuel manifolds and the process for determining the manifold diameter and spray hole sizes.

When the fuel manifold is exposed to hot gas flow, particularly at low fuel flow rates, there is a risk of fuel boiling. This boiling can lead to fuel cracking, causing carbon deposits and clogging in the manifold and nozzles. If left unchecked, it can result in poor fuel distribution from the manifold and eventually complete blockage of the manifold or nozzles. This document presents a method for estimating the potential for boiling and includes typical calculations for the Spey MK202.

## 3.0 Design Procedure

The design procedure for the fuel manifold is illustrated in Figure 1, assuming the system consists of plain orifice nozzles on the manifold supplied by a pressure-controlled fuel flow regulator.

### 3.1 Fuel Flow Requirements

Since the inlet parameters of the afterburner at off-design conditions are often unknown during the early design stages, calculations are performed for sea-level static conditions, which are commonly specified as the guarantee point. Since this condition is not the maximum fuel flow state for the afterburner, the calculations include a margin to account for potential higher flow requirements (e.g., during low-altitude, high-speed flight). The fuel-to-air ratio  $FAR \square C$  for the maximum afterburning hot core flow is known (see Reference [1]), as is the mass flow rate of the hot core flow  $M \square C$ . The fuel flow rate  $F \square$  can then be calculated using the following equation:

$$F \square = FAR \square \times M \square C,$$

Fuel flow rate calculation.

— Section 49 —  
Content from Original Document (Pages 241-245)

$$F.NO \square \square \square \square = Q / \sqrt{(\Delta P)},$$

Flow number equation where Q is fuel flow rate.

Where Q is the fuel flow rate in gallons per hour.

$\Delta P$  is the pressure drop across the nozzle in pounds per square inch.

Thus, the required total flow number for the main afterburner fuel manifold can be calculated using the following equation:

$$FN_T = F \square c \square \square \square \square c \square \square \square \square y \square \square \square / \sqrt{400},$$

Total flow number calculation for the main afterburner fuel manifold.

### 3.3 Flow Numbers for Each Manifold

The main afterburner fuel manifold is used to distribute fuel to achieve an appropriate constant fuel-air ratio in the combustion zone. Therefore, fuel is distributed in proportion to the airflow in the afterburner combustion chamber. Assuming the mass flow rate per unit area through the combustion chamber is constant, the fuel flow rate should evidently be distributed proportionally to the area.

Since the Spey afterburning system's pilot flame is stabilized on an annular stabilizer, the afterburner fuel supply pipes are chosen in an annular form. The areas between the centerlines of each stabilizer are calculated, and the total flow number ( $\square$ ) is distributed according to the size of each area.

	面积 英寸 <sup>2</sup>	%	输油圈流量数
中心线到内侧稳定器(1号)	60.13	6.32	17.70
1号到2号稳定器	230.91	24.28	67.98
2号到3号稳起器	406.42	42.73	119.64
3号稳定器到隔热屏	253.69	26.67	74.68
总的	951.50		280.00

Figure 2: Three rows of planar stabilizers combined with four main afterburner fuel manifolds.

Diagram showing the arrangement of three rows of planar flame stabilizers integrated with four main afterburner fuel manifolds.

These fuel supply devices can use single-path or multi-path fuel supply, but for calculation convenience, they are treated as single-path fuel supply.

The flow numbers for each manifold are  $1, 2, 3$  and  $4$ . It is assumed that each manifold is connected in parallel to the main fuel supply pipe outside the afterburner combustion chamber. Therefore:

$$\text{array,rl} \& FN \square = FN_1 + FN_2 + FN_3 + FN_4 \& FN_1 = A_1 / A \square, FN_2 = A_{12} / A \square, FN_3 = A_{23} / A \square, FN_4 = A_{34} / A \square \text{ array},$$

Flow number distribution equations for each manifold.

$$A \square = A_1 + A_{12} + A_{23} + A_{34},$$

Total area calculation for the manifolds.

Thus, the flow numbers for each manifold positioned between the stabilizers are determined.

## 3.4 Nozzle Diameter and Number

The flow number for a single-hole nozzle is expressed by the following equation:

$$FN = 1000 \times D^2,$$

Flow number equation for a single-hole nozzle.

Where D is the nozzle diameter in inches.

The flow number FN for a manifold with N nozzles is:

$$FN = N \times 1000 \times D^2,$$

Flow number equation for a manifold with multiple nozzles.

Therefore, there can be an infinite number of combinations of nozzle numbers and diameters that satisfy the manifold flow number requirements. However, there are usually some basic requirements that limit the selection range.

- Nozzle diameter should not be less than 0.025 inches. Below this size, nozzles are prone to clogging unless the fuel is strictly filtered. Additionally, manufacturing tolerances for holes smaller than this size will constitute a significant proportion of the small hole area, thereby affecting the required manifold flow number and fuel distribution.
- Nozzle diameter should not exceed 0.04 inches to ensure good fuel preparation (droplet size is proportional to the square of the hole diameter), especially when the pressure drop across the nozzle is low.
- The circumferential spacing of nozzles on each manifold (proportional to  $1 / N^{1/2}$ ) should be as close as possible to the radial spacing between nozzles or the radial distance from the nozzle to the stabilizer centerline.
- If strut arrangements divide the manifold into annular segments, the number of nozzles should be an integer multiple of the number of struts. This allows each annular segment to be fueled by the same number of nozzles.

## 3.5 Manifold Diameter (Same Plane)

To meet the third requirement in Section 3.4, the diameter of the manifold (i.e., the radial position of the nozzles) must be determined.

As previously mentioned, the design requirement for the manifold is to achieve a uniform and constant fuel-air ratio across the afterburner combustion chamber cross-section. Therefore, the manifolds should be positioned at the area centers of each fuel supply zone. Thus, in Figure 2, Manifold 1 is placed at the center of area  $A_1$ , Manifold 2 at the center of  $A_2$ , and so on. Here, it is assumed that the manifolds and stabilizers are coplanar. The designer can then check the manifold positions to determine if multiple manifold rings are needed in each annular passage. For example, in the Spey afterburning system, using a single manifold ring in areas  $A_{12}$  and  $A_{23}$  would result in a radial distance exceeding 5 inches. If a 5-inch circumferential spacing is used to determine the number and diameter of nozzles, the nozzle hole diameter would exceed the maximum allowable diameter (approximately 0.084 inches). Therefore, in such cases, multiple manifold rings must be used to reduce the hole spacing. In the Spey engine, this is achieved by installing fuel rods on the positioned manifolds. Strictly speaking, these fuel rods should have different lengths on the inner and outer sides to spray fuel toward the area center between the manifold and the V-gutter centerline. However, for manufacturing convenience, the fuel rods on the Spey manifold are made equal in length.

## 3.6 Axial Position of the Manifold

From Sections 3.4 and 3.5, the nozzle diameter and number, as well as the radial positions of the manifolds assumed to be in the same plane, can be determined. To achieve better fuel preparation before the fuel enters the combustion zone, the manifold is placed at a suitable distance upstream of the stabilizer. The greater the distance, the better the fuel preparation and the more uniform the distribution. However, it is necessary to avoid fuel sprayed from the afterburner manifold entering the wake region of the stabilizer, as this would affect the operating range of the flame stabilizer. Spey's experience indicates that a distance of 6 to 10 inches yields optimal performance.

The manifold is moved upstream from the coplanar position along the streamline using the 'area rule' method, assuming no stabilizer blockage.

## 3.7 Manifold Cross-Sectional Diameter

As mentioned earlier, a primary requirement for the manifold is to ensure a uniform and constant fuel-air ratio across the afterburner combustion chamber cross-section. Therefore, fuel sprayed from each manifold must be uniformly distributed circumferentially (i.e., the flow rate from each nozzle should be equal). The inner diameter of the manifold must be large enough to avoid flow throttling. The manifold is made from a pipe with an inner cross-sectional area not less than 75% of the total geometric area of the nozzles to ensure this. Thus:

Since manifold blockage affects the cold loss of the combustion chamber, and cold loss must be kept to a minimum, the manifold cross-sectional area should be minimized while satisfying Equation (8). For an annular manifold with only one fuel inlet, the fuel flow rate through the manifold decreases with distance from the inlet. Therefore, the inner diameter of the manifold can be gradually reduced according to the decrease in fuel flow rate. This can still be handled using Equation (8), where when the remaining downstream nozzle hole area is only half of the total nozzle area,  $\Delta A_{\text{nozzles}}$  is used instead of  $A_{\text{nozzles}}$  in Equation (8).

## 3.8 Fuel Boiling Criteria

### 3.8.1 Introduction

When the manifold is in a high-temperature gas flow, especially at low fuel flow rates, there is a possibility of fuel boiling. This can cause fuel cracking, leading to manifold coking and carbon deposits, resulting in deteriorated fuel distribution and even nozzle blockage. The following describes a method for estimating the possibility of fuel boiling.

Fuel boiling is most likely to occur at high altitudes with low fuel flow rates and when using high-volatility fuels (such as JP4-type fuels). Therefore, it is necessary to know the afterburner conditions and fuel flow rates at the altitude limits of the flight envelope. Since it is uncertain where the limiting conditions occur, calculations must be performed for various flight states along the flight envelope.

### 3.8.2 Calculation Method

The method essentially involves calculating the heat exchange from the gas to the fuel to estimate the fuel inlet temperature at which boiling begins for each fuel flow rate. This is then compared with the temperatures that may be encountered in that flight state.

Assume the following parameters are known:

- M: Afterburner mass flow rate, lb/s
- T: Afterburner gas temperature, °K
- P: Afterburner total pressure, psi (absolute)
- F: Manifold fuel flow rate, lb/s
- FN: Manifold fuel flow number
- D: Manifold diameter, inches
- XD: Manifold cross-sectional diameter, inches

- N: Number of nozzle holes on the manifold
- D<sub>s</sub>: Nozzle diameter, inches
- A: Afterburner area, square inches

The fuel pressure ( $P_f$ ) in the manifold can be calculated from the flow number, since:

$$FN = F_c \sqrt{(\Delta P) / 360, SG},$$

Flow number equation for calculating fuel pressure.

Here, SG is the specific gravity of the fuel, and

$$PF = \Delta P + P_f,$$

Equation for calculating fuel pressure in the manifold.

Thus, the value of  $\Delta P$  can be determined from Figure 3. For JP4 fuel, an equivalent pressure  $\Delta P^*$  must be used instead of at which fuel can vaporize at the same temperature. This can be obtained from Figure 4.

Since the manifold length L can be determined by:

$$L = \pi D_s L_0 / 12,$$

Equation for calculating manifold length.

And referring to Figure 5, the equivalent length  $L^*$  of the manifold can be determined.

Since

$$X_{D_s} = L^* / (M D_s A)^{0.6},$$

Equation for calculating  $X_{D_s}$ .

Thus,  $X_{D_s} / X_{288}$  can be determined.

Using Figure 6, the fuel inlet temperature at which boiling occurs in the manifold can be determined. When using the Figure 6 curve for JP4 fuel, the equivalent saturation vapor pressure ( $P_v$ ) must be used. Then, compare the actual fuel inlet temperature with the calculated boiling-limited inlet temperature for each flight state to determine if boiling will occur. Since each manifold has different boiling characteristics, each manifold should be calculated accordingly.

If boiling is likely to occur, the following measures must be taken:

1. Reduce the inner diameter of the manifold.
2. Implement segmented fuel supply in flight states where boiling may occur, i.e., supply fuel to certain manifolds only, thereby increasing the fuel flow rate in the supplied manifolds.
3. Shield the manifold.

The first measure is feasible as long as Equation (8) is still satisfied; if not, fuel distribution will deteriorate. Segmented fuel supply increases the fuel flow rate. A valve can be installed that cuts off fuel to certain manifolds as altitude increases, so a given amount of fuel flows at a higher rate through the remaining manifolds. This method can be applied to all manifolds, with only one manifold (usually the inner one) supplying fuel at extreme altitudes.

The last method to prevent fuel boiling is to shield the manifold from the hot gas flow. Calculations show that a fuel shield with a 0.1-inch gap can reduce the heat exchange rate to the fuel by a factor of 4, making this an effective method to prevent boiling. However, the shield increases the effective size of the manifold and the associated cold loss. Since cold loss must be kept to a minimum, the shielding method is not promising.

## 4.0 References

- JCRR12079 – Review of Spey MK202 Afterburner Design Method
- JCRR12084 – Development of Spey MK202 Afterburner Vaporizer Stabilizer

## Appendix A

The following calculations determine the manifolds for a combustion device with three-stage stabilizers arranged in the same plane, as shown in Figure 7.

### 1) Fuel Flow Rate at Sea Level Static Condition

The fuel-air ratio used = 0.0663 (hot core flow). Hot core flow mass flow rate =  $206.9 \times 0.9 = 186.21 \text{ lb/s}$ . Since  $M \square P = 206.9 \text{ lb/s}$ , the amount of air participating in combustion =  $0.9 M \square P$ . Therefore, the fuel flow rate ( $F \square$ ) = 5,593 gallons/hour.

### 2) Total Flow Number of the Manifold

Flow number =  $F \square / \sqrt{\Delta P} = 5593 / 20 = 280$ .

### 3) Flow Numbers for Each Manifold

Area calculations at the stabilizer plane yield the following areas and flow distribution proportions:

Area and flow number distribution for each manifold.

Region	Area (in <sup>2</sup> )	Percentage (%)	Manifold Flow Number
Centerline to Inner Stabilizer (No. 1)	60.13	6.32	17.70
No. 1 to No. 2 Stabilizer	230.91	24.28	67.98
No. 2 to No. 3 Stabilizer	406.42	42.73	119.64
No. 3 Stabilizer to Heat Shield	253.69	26.67	74.68
Total	951.50		280.00

### 4) Manifold Diameter (Same Plane)

Since the manifolds are positioned at the centers of the annular bands formed by the stabilizer centerlines, the area inside Manifold 1 =  $60.13 / 2 = 30.065 \text{ in}^2$ , diameter ( $D_1$ ) = 6.187 inches. The area inside Manifold 2 =  $60.13 + \frac{1}{2}(230.91) = 175.59 \text{ in}^2$ , diameter ( $D_2$ ) = 14.951 inches. Similarly,  $D_3 = 25.086 \text{ inches}$ ,  $D_4 = 32.397 \text{ inches}$ .

If a single manifold ring arrangement is used between No. 1, No. 2, and No. 3 stabilizers, the radial distance from the nozzle to the stabilizer centerline is 3.1 inches and 2.9 inches. The distance from Manifold 1 to Stabilizer 1 and from Manifold 4 to Stabilizer 3 is approximately 1.3 inches each. For such a configuration, radial fuel rods are installed on the inner and outer sides of Manifolds 2 and 3 to achieve two nozzle pitch circle diameters to coordinate radial spacing. The fuel rods are designed so that nozzles can be positioned along their length up to 1 inch from the manifold centerline to facilitate optimal design. An arbitrary nozzle position was chosen for the first test.

### 5) Actual Manifold Diameter

The manifolds are arranged at diameters  $D_1$ ,  $D_2$ ,  $D_3$ , and  $D_4$  in the same plane as shown in Figure 8. The inner three rings require upstream movement along the flow line into the fuel-shielded diffuser.

Thus:

$$(25.026)^2, (34.80)^2 = (D'_3)^2, (28.40)^2,$$

Equation for calculating the adjusted diameter of Manifold 3.

Therefore,  $D'_3 = 20.47$  inches.

The same method is used for Manifold 2. However, since the inner manifold (No. 1) is located upstream of the fuel shield leading edge, the calculation for Manifold 1 is based on the original diffuser dimensions.

$$(D_1)^2, (DD_4)^2 = (D'_1)^2, (DD_1)^2,$$

Equation for calculating the adjusted diameter of Manifold 1.

$$(6.187)^2, (37.00)^2 = (D'_1)^2, (29.70)^2,$$

Substituted values for Manifold 1 diameter calculation.

Thus,  $D'_1 = 4.97$  inches. The calculation for  $D_2$  yields  $D'_2 = 11.97$  inches.

## 6) Number and Diameter of Nozzles

During design, it was determined that the combustion chamber containing the manifolds has five struts, so the number of nozzles on each manifold should be divisible by 5.

For Manifold 3, the relationship between the number and size of nozzle holes corresponding to the required flow number is as follows:

Required flow number =  $120.0 = 1000 D^2 N$

Nozzle number and diameter combinations for Manifold 3.

Number of Nozzles (N)	50	60	70	80
Diameter (D)	0.0490	0.0447	0.0414	0.0387
				Nozzle holes too large

It is evident that at least 80 nozzles are required for this manifold, as fewer nozzles result in excessively large hole sizes. Further increasing the number of nozzles to reduce hole diameter has minimal effect (100 nozzles would have a diameter of 0.0346 inches), especially considering the added weight of the fuel rods.

Such calculations are performed for all manifolds to determine the minimum number of nozzles with hole diameters less than 0.04 inches.

Nozzle number and diameter for each manifold.

Manifold Number	Number of Nozzles	Nozzle Diameter (inches)
1	10	0.041
2	45	0.038
3	80	0.038
4	55	0.040

## 7) Fuel Boiling Criteria

The calculations provided are for a condition at an altitude of 60,000 feet and Mach number  $M\infty = 1.9$ , where the fuel flow rate is low. Both JP1 and JP4 fuels were considered, with calculations performed only for the No. 3 fuel manifold.

At an altitude of 60,000 feet and  $M\infty = 1.9$ , the estimated mixed afterburner inlet conditions are:

Mass flow rate  $M = 56.4 \text{ lb/s}$ , Pressure  $P = 10.85 \text{ psi (absolute)}$ , Temperature  $T = 721 \text{ K}$

No. 3 afterburner fuel manifold fuel flow rate  $F = 1.0583 \text{ lb/s}$

Flow number F.N. = 120

Number of nozzles N = 80

Manifold position parameter  $XD = 0.405$  (average)

Diameter  $D = 20.8 \text{ inches}$

Afterburner area  $A = 1075 \text{ square inches}$

Given the equation for flow number:

$$F.N. = F, \sqrt{(\Delta P)} 360, S.G.,$$

Flow number equation relating fuel flow rate, pressure drop, and specific gravity.

Substituting the values:

$$120 = 1.0583, \sqrt{(\Delta P)} \times 360, 0.78,$$

Thus,  $\Delta P = 16.57$ . For JP1 fuel,  $PF = 27.42 \text{ psi (absolute)}$ .

For JP4 fuel, from Figure 4, the equivalent saturation vapor pressure is  $3.50 \text{ psi (absolute)}$ .

Therefore, from Figure 3:

For JP1 fuel,  $X_{288} = 104.0$

For JP4 fuel,  $X_{288} = 42.5$

Since the manifold length  $L = \pi D / 12 = 5.445 \text{ feet}$

From Figure 5:  $L^* / L = 5.64$

Thus, the equivalent length  $L^* = 30.71 \text{ feet}$

$$X_0 = L^*, F ( M XD, A )^{0.8} = 30.71, 1.0583 ( 56.4 \times 0.405 \times 12, 1075 )^{0.8} = 12.78$$

Equation for calculating the parameter  $X_0$ .

Therefore, for JP1 fuel:

$$X_0, X_{288} = 12.78, 104.0 = 0.1229$$

From Figure 6, the inlet fuel temperature causing fuel boiling in the manifold is  $450 \text{ K}$ . For JP4 fuel:

$$X_0, X_{288} = 12.78, 42.5 = 0.301$$

The inlet fuel temperature is  $360 \text{ K}$ .

Thus, at an altitude of 60,000 feet and  $M\infty = 1.9$ , boiling will occur in the No. 3 fuel manifold if the inlet temperature exceeds  $177^\circ \text{C}$  for JP1 fuel and  $87^\circ \text{C}$  for JP4 fuel.

The maximum fuel outlet temperature of the Spey afterburner high-pressure pump is estimated to be 80 °C. Therefore, JP1 fuel will not boil in the manifold, while JP4 fuel is close to boiling. Further calculations are required for other manifolds under this condition, and additional flight conditions should be analyzed using the same method.

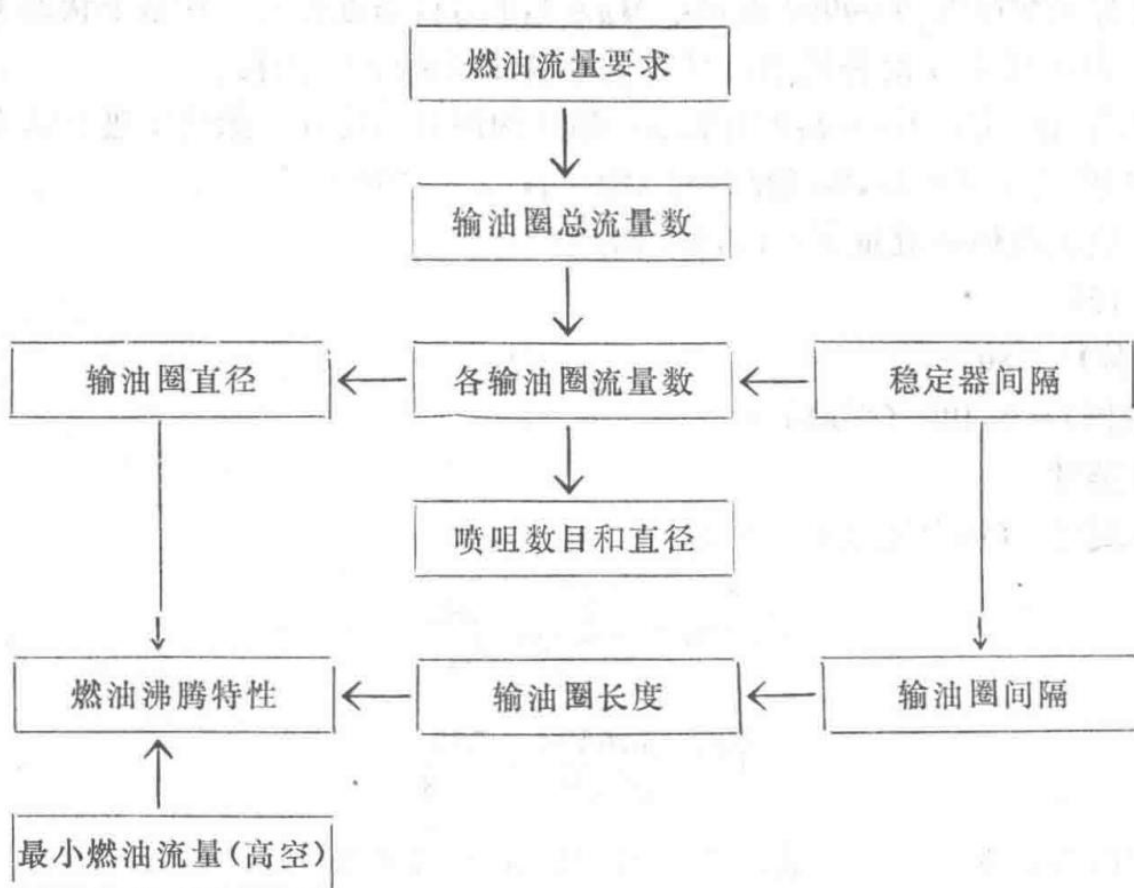


Figure 1: Afterburner Main Fuel Manifold Design Procedure

Flowchart detailing the design procedure for the afterburner main fuel manifold.

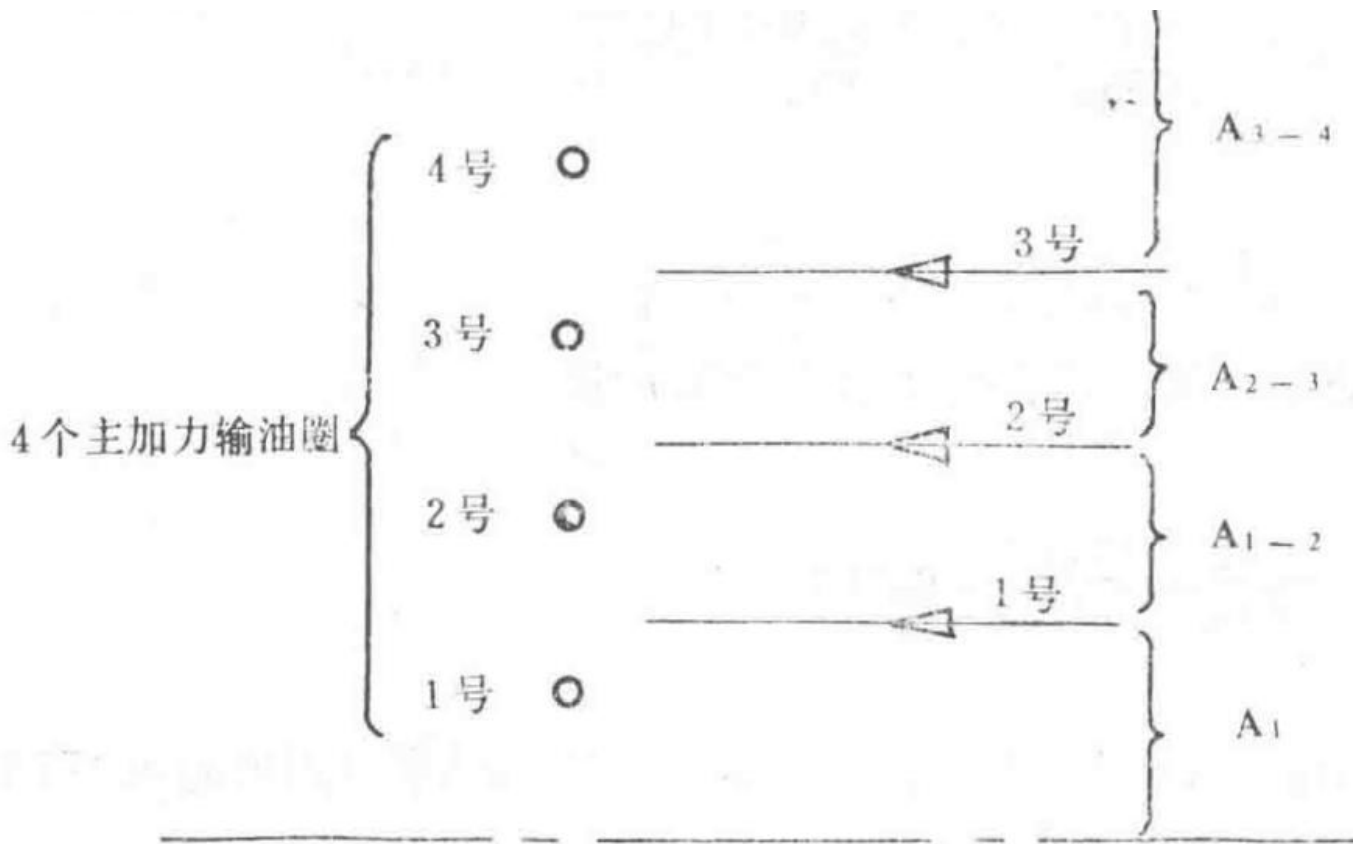


Figure 2: Typical Three-Stage V-Gutter Flame Stabilizer Structure

Diagram showing the structure of a typical three-stage V-gutter flame stabilizer.

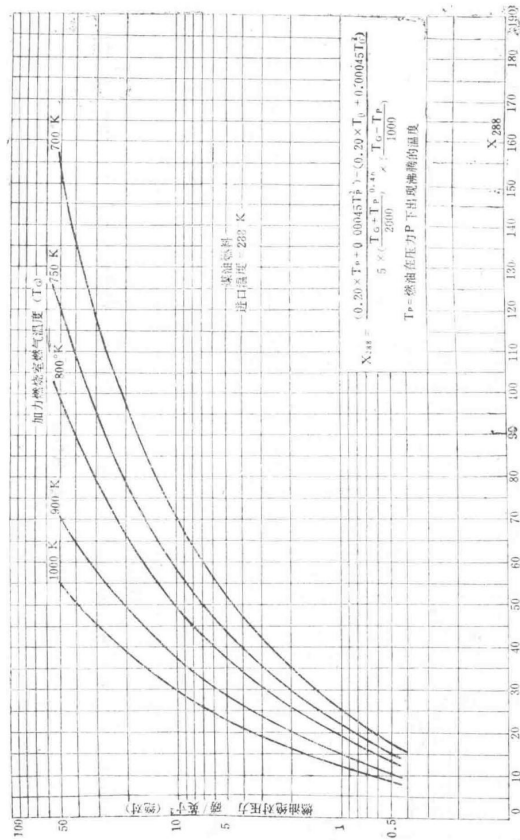
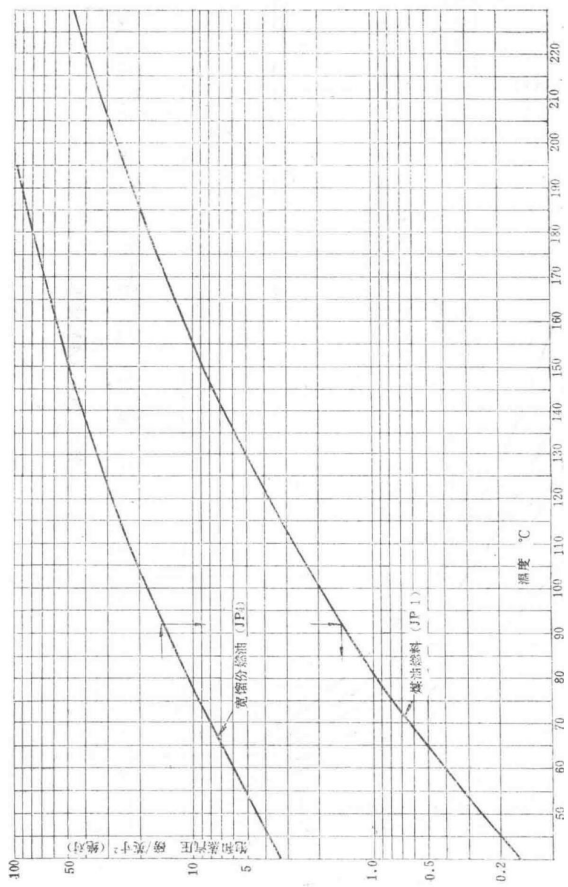
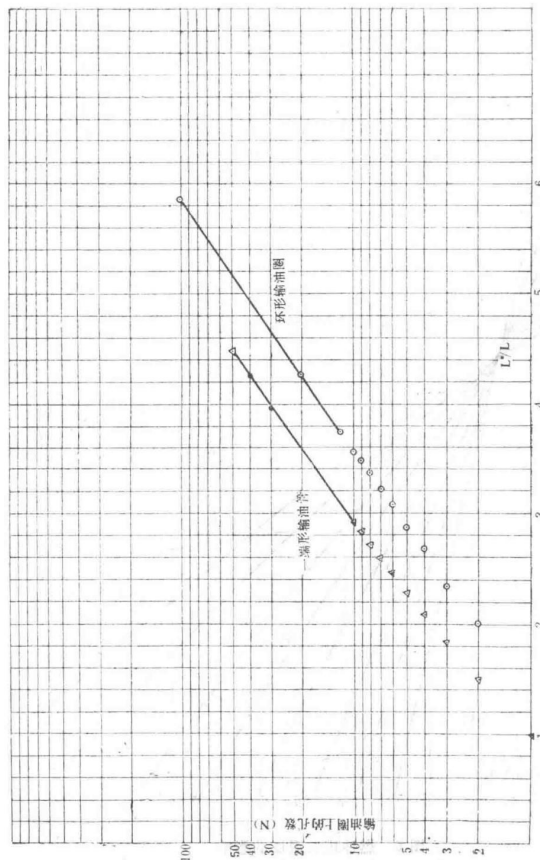


Diagram of a multi-stage fuel manifold layout.



Graph showing the relationship between  $L^*/L$  and some parameter (likely related to fuel flow characteristics).



Graph depicting the relationship between fuel temperature and vapor pressure for JP1 and JP4 fuels.

— Section 51 —  
Content from Original Document (Pages 251-255)

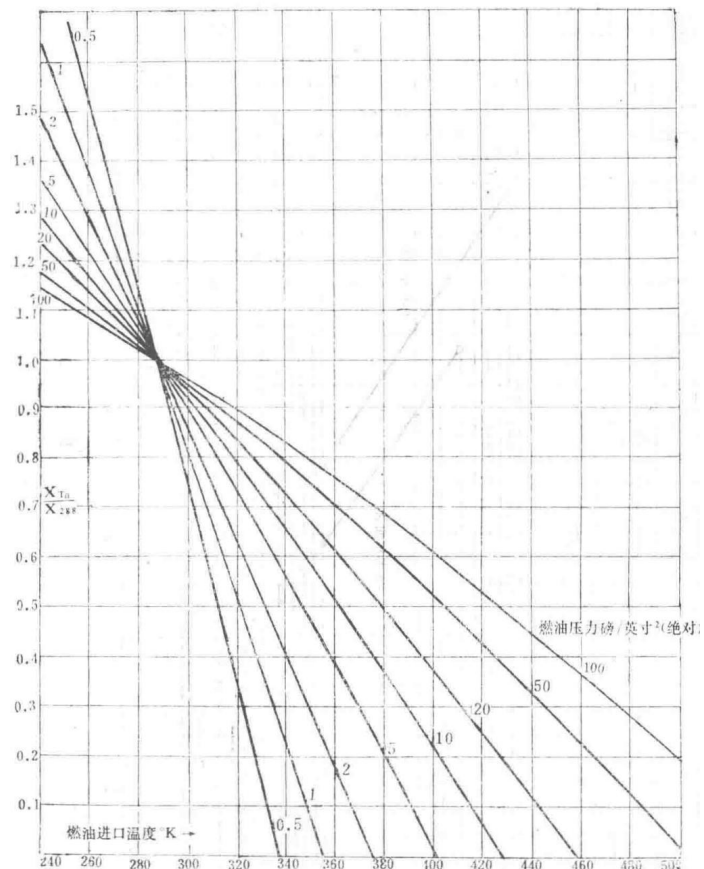


Figure 6: Effect of Fuel Inlet Temperature

Diagram illustrating the impact of fuel inlet temperature on the performance of the Spey MK202 afterburner system.

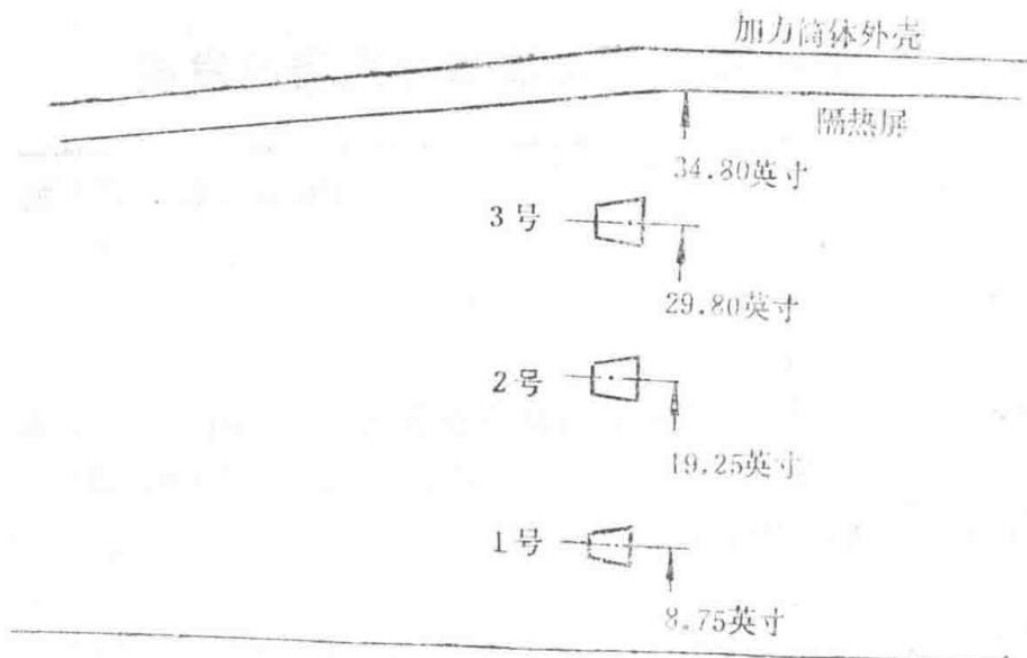


Figure 7: Schematic Diagram of Three-Stage Stabilizer Device

Schematic representation of the three-stage flame stabilizer used in the Spey MK202 afterburner.

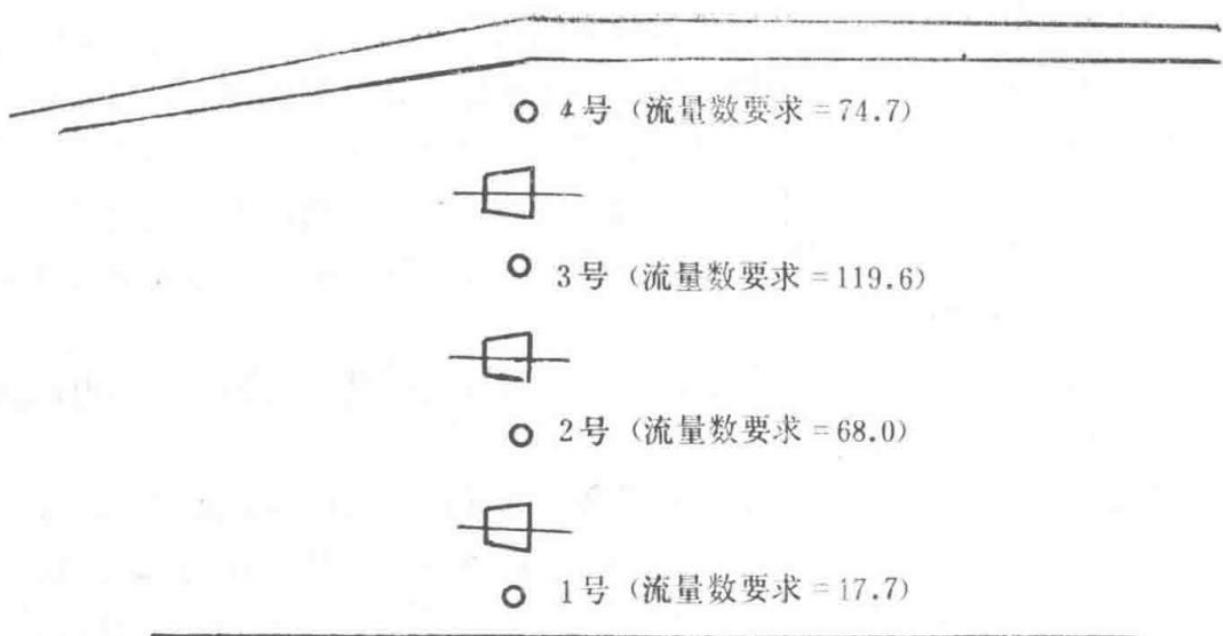


Figure 8: Sketch of Main Afterburner Fuel Manifold Matched with Figure 7 Stabilizer

Sketch showing the main afterburner fuel manifold designed to work in conjunction with the stabilizer depicted in Figure 7.

Document Header

Title	Report Number
Combustion Research Report	CRR12084
Development of Spey MK202 Afterburner Evaporative Stabilizer	

First Edition, September 22, 1976

## 1.0 Abstract

This report describes the benefits derived from using evaporative gutter-type flame stabilizers, which are superior to planar V-gutters. The design and sizing principles of Rolls-Royce's flame stabilizers are studied, and their working principles are explained. The performance of this flame stabilizer is presented and compared with that of simple V-gutters.

## 2.0 Introduction

Afterburning systems designed before 1960 used planar V-gutters as flame stabilizers, relying on upstream fuel manifolds to inject part of the fuel into the gutter wake region. Igniting this portion of fuel establishes a flame, which then propagates to the remaining fuel. Since this afterburning system is nearly a premixed system, the ignition limits of kerosene regrettably restrict the fuel-air ratio to no less than 0.03 for ignition. This fuel-air ratio corresponds to 30% of the afterburning ratio for a full afterburning turbofan engine.

During the ignition of a turbofan engine, pressure fluctuations in the afterburner can adversely affect the operation of the low-pressure compressor. Indeed, if excessive pressure changes occur, the engine may surge. Modern afterburning engines with low compressor surge margins avoid surging by designing the afterburning system to prevent excessive pressure fluctuations during ignition. This is achieved by ensuring the tailpipe responds as quickly as possible and that the afterburning system can ignite at the minimum afterburning fuel flow (i.e., low afterburning ratio). In V-gutter flame stabilizer systems, a method called zonal fuel supply can reduce the minimum usable afterburning ratio to below 30%. This method involves sequentially cutting off fuel supply from the outer manifolds until only the inner manifold supplies fuel, as shown in Appendix Figure 1. This allows for a low afterburning ratio but has two drawbacks: first, the afterburning thrust varies in a stepwise manner with fuel flow, as shown in Figure 2, with each step corresponding to a change in the number of fuel-supplying manifolds; second, the propulsion efficiency is low, meaning a significant thrust loss, as detailed in Appendix 1 of this report. In this context, propulsion efficiency is defined as the ratio of the fuel required to produce a given thrust with a uniform temperature at the nozzle to the fuel required to produce the same thrust with a non-uniform temperature distribution.

Consequently, an alternative system was designed and implemented, where fuel is locally supplied within the flame stabilizer, employing what is known as an evaporative gutter stabilizer.

The fuel supplied to the stabilizer ensures that the flame stabilizer operates near the chemically correct fuel-air ratio across the entire flight envelope. When only this portion of fuel is supplied, a small afterburning ratio of nearly 10% can be achieved, with high combustion efficiency due to the fuel-air ratio being close to the chemically correct value. Additionally, since combustion occurs across the entire cross-section of the afterburner, propulsion efficiency is also high. Using this method, temperature increases can be below 100% while maintaining good stability and high combustion efficiency.

Thrust augmentation is achieved by injecting fuel into the airflow between the upstream fuel manifolds and the flame stabilizer, as shown in Figure 3(a). This fuel can be gradually increased to allow completely smooth thrust adjustment up to the maximum achievable thrust, as shown in Figure 3(b). As long as the main afterburning fuel—referred to as primary afterburning fuel—does not enter the wake region of the flame stabilizer, the system's stability is not affected by the magnitude of the afterburning ratio.

## 3.0 Design of Evaporative Stabilizer

### 3.1 Working Principle

A schematic diagram of the evaporative stabilizer is shown in Figure 4.

Fuel is injected through fuel nozzles onto a splash plate installed in the stabilizer's air intake. The air intake of the stabilizer draws air from the gas flow, forming an emulsion-like mixture with the fuel that flows into the distribution pipes inside the stabilizer. Numerous pairs of small holes in the distribution pipes allow the fuel-air mixture to flow along the pipes into the stabilizer. The slots on the stabilizer's back, aligned with the small holes in the distribution pipes, serve three purposes: further atomizing the fuel with the main airflow, cooling the stabilizer walls, and enhancing the recirculation zone of the stabilizer.

### 3.2 Design Principles

The design of the evaporative stabilizer largely relies on water flow simulations and sector tests on test rigs. There is no direct experimental data available for specific designs, only empirical design limits. The design principles are listed below in order of importance:

#### 3.2.1 Stabilizer Gutter Width (W)

The gutter width of the stabilizer determines the final stability of the flame stabilizer and is established during the combustion chamber design phase, as referenced in [1]—CRR12079. All other dimensions are related to it.

#### 3.2.2 Air Slot Position

Structurally, the air slots should be positioned as close as possible to the stabilizer wall to ensure proper recirculation behind the stabilizer, as shown in Figure 5. Water flow simulation tests indicate that if the slots are positioned too far from the wall, the recirculation zone may be disrupted, potentially reducing stability.

#### 3.2.3 Slot Area ( $A_{\square}$ )

The ratio of the slot area to the total stabilizer blockage area (excluding slots) should be between 0.06 and 0.08. Although there are conflicting arguments regarding this relationship, early model stabilizer tests confirm that deviating from this rule can result in inefficient combustion of the pilot fuel.

#### 3.2.4 Stabilizer Cross-Sectional Area

To maintain the correct proportion of recirculation in the V-gutter stabilizer, a V-gutter with an axial length-to-width ratio of  $0.85 \pm 0.05$  is used. No data supports this exact ratio, but it is believed that significant deviations could reduce stability.

#### 3.2.5 Distribution Pipe Diameter

The ratio of the outer diameter of the distribution pipe to the stabilizer gutter width should be  $\leq 0.25$ . This ensures the proper form of recirculation. It is also important that the diameter of the distribution pipe ensures its area is no less than half the area of the air intake. This ensures the air intake draws the appropriate amount of air.

### 3.2.6 Air Intake Size

To ensure a fixed proportion of the fuel-air mixture enters each V-gutter from the distribution pipe, it is recommended that the inlet area of the air intake to the blockage area of the V-gutter ratio be  $0.016 \pm 0.004$ . The relatively wide range for this ratio is due to the lack of data confirming that such tolerances allow all V-gutters in the design to use the same air intake.

### 3.2.7 Distribution Pipe Hole Area

The ratio of the total area of the holes in the distribution pipe to the air intake area should be no less than 1.0. Considering the influence of the discharge coefficient (CD), a value of 1.5 is recommended. If this value is below 1.0, fuel may overflow from the air intake, causing the stabilizer to become overly fuel-rich at the air intake position.

### 3.2.8 Stabilizer Included Angle

A  $30^\circ$  wall included angle is typically used for V-gutters and evaporative V-gutters. Variations of  $\pm 10^\circ$  are considered acceptable without significant adverse effects on combustion performance. Increasing the angle too much, beyond  $40^\circ$ , as proven by test rig experiments, can cause internal separation and disrupt the recirculation zone. Changes in the included angle can also affect the cold-state pressure loss. A larger angle increases the coefficient CD.

### 3.2.9 Number of Distribution Pipes

The number of distribution pipes is usually determined by structural considerations such as stabilizer length and the number of supports. In Rolls-Royce designs, the length of the distribution pipes is typically 6 to 8 inches.

### 3.2.10 Distribution Pipe Outlet Hole Spacing

The spacing of the outlet holes in the distribution pipe should be selected so that the slots in the V-gutter align with each injection hole. If possible, the holes should be equally spaced around the circumference, and the gap between the ends of the distribution pipes should not be too large. If the gap is too large, it can cause connection issues.

### 3.2.11 Fuel Injection in Air Intake

To ensure pilot fuel enters the distribution pipe through the air intake, it is recommended that fuel be injected at a  $45^\circ$  angle downstream relative to the splash plate.

## 4.0 Performance

The stability of the pilot flame stabilizer, where only the fuel in the stabilizer wake region burns, is shown in Figure 6 and compared with the operating range of a simple V-gutter stabilizer. The stability parameter (S) is defined as:

$$S = pWT/V,$$

Stability parameter formula, where  $p$  is the static pressure at the stabilizer lip,  $W$  is the stabilizer gutter width,  $T$  is the airflow temperature at the stabilizer, and  $V$  is the airflow velocity at the stabilizer lip.

Here,  $p$  = static pressure of the airflow at the stabilizer lip,  $\text{lb/in}^2$  (absolute);  $W$  = stabilizer gutter width, inches;  $T$  = airflow temperature at the stabilizer,  $^\circ\text{K}$ ;  $V$  = airflow velocity at the stabilizer lip,  $\text{ft/s}$ .

It can be observed that the minimum operating fuel-to-unburned air ratio for the V-gutter stabilizer is 0.03, corresponding to approximately a 30% afterburning ratio. The corresponding stability for the pilot flame stabilizer

is around 0.003, allowing for a very small afterburning ratio when only the wake fuel is burned. Both stabilizer systems can operate down to an S range of 6 to 8.

As long as the main afterburning fuel is injected into the combustion chamber without entering the recirculation zone, there is no reason to believe that the pilot flame stabilizer cannot operate within the same stability range as that obtained from V-gutter stabilizer tests. Therefore, a third curve is drawn from the peak of the pilot flame stabilizer stability curve, extending to the rich blowout line of the V-gutter stabilizer system. Although no experimental data supports this assumption (other curves are derived from test rig or engine test data), it is considered reasonable from a stability perspective.

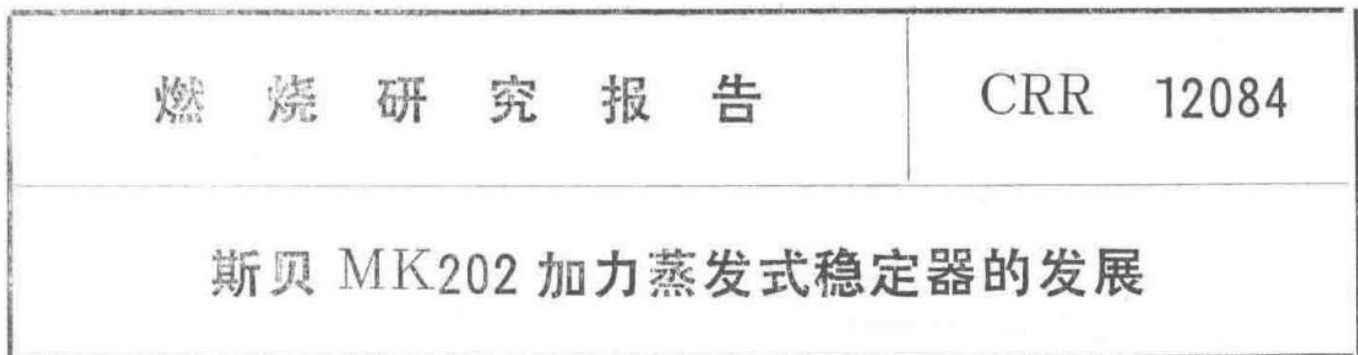
## 5.0 References

- [1] CRR12079—Review of Spey MK202 Afterburner Design Methods

## Appendix 1: Calculation of Propulsion Efficiency Loss Due to Non-Uniform Temperature Distribution at the Nozzle

Assumptions:

1. Combustion efficiency of chemical reactions is 100%
2. Engine inlet airflow temperature is 288°K
3. Engine afterburner conditions are as defined by AR.168, i.e.: Afterburner Mach number  $M\infty = 0.22$ , Afterburner temperature  $T\infty = 700^{\circ}\text{K}$



Temperature Distribution Diagram

Diagram showing the temperature distribution at different stages of the afterburner fuel supply system, illustrating the effect of non-uniform temperature on propulsion efficiency.

$$S = \frac{pWT}{V}$$

Propulsion Efficiency Loss Chart

Chart depicting the relationship between fuel-air ratio and temperature increase, used to calculate propulsion efficiency loss due to non-uniform temperature distribution.

$$p_t = 2 p_0,$$

Static pressure in the afterburner

$$Q = M \sqrt{T}, AP = 0.1382$$

Flow parameter in the afterburner

### a) Thrust in Non-Afterburning Mode

Main combustion chamber fuel-air ratio = 0.01012

Thus,  $\gamma / (\gamma - 1) = 3.8$

Since there is no heat loss in the afterburner, the following applies:

$$P_n = 2.00$$

Pressure ratio at the nozzle

Here,  $P_n$  is the nozzle pressure.

Therefore,  $M_T X, M = 1.946$ , and thrust  $X = 51.46 M$ .

### b) Thrust of Afterburning System with Uniform Nozzle Temperature Distribution

Assuming a uniform temperature rise in the afterburner of  $100^\circ\text{C}$ , and letting  $M$  equal the total air mass flow through the system, then  $T_n = 800^\circ\text{C}$  K and  $\Delta T = (T_n - T_1) = 512^\circ\text{C}$  K.

Thus, the total fuel-air ratio including the main combustion chamber and afterburning system = 0.01274.

The average temperature of the afterburning system =  $750^\circ\text{C}$  K, so  $\gamma / (\gamma - 1) = 3.85$ .

Afterburner fuel-air ratio =  $0.01274 - 0.01012 = 0.00262$ .

Calculation of heat loss in the afterburner:

$$M_n \sqrt{T_n}, M_4 \sqrt{T_4} = 1.01274, 1.0102 \sqrt{(800,700)} = 1.0717$$

Mass flow and temperature ratio in the afterburner

Obtaining  $p_n, p_4 = 0.996$ . Since  $p_4, p_0 = 2$ , thus  $P_n, p_0 = 1.992$  and  $X, M \sqrt{T} = 1.938$ . Therefore, thrust = 54.81 M.

Afterburning ratio =  $(54.81 - 51.46, 51.46) \times 100\% = 6.51\%$

### c) Thrust of Afterburning System with Combustion Concentrated in Central Core Region

Let  $M$  = total air mass flow rate.

$m$  = air mass flow rate participating in combustion in the core region, with the fuel-air ratio assumed to be 85% of the stoichiometric fuel-air ratio.

$M'$  = remaining air mass flow rate (assumed to flow through the afterburning system at  $700^\circ\text{C}$  K).

Thus,  $M = M' + m$ .

Core region fuel-air ratio =  $0.85 \times 0.0676 = 0.0575$ .

Therefore, temperature rise in the core region =  $1820^\circ\text{C}$  K.

Nozzle temperature in the core region =  $288 + 1820 = 2108$  K.

Thus,  $\gamma / (\gamma - 1) = 4.5$  (in the core region).

Afterburner fuel-air ratio in the core region =  $0.0575 - 0.01012 = 0.04738$ .

Heat loss pressure in the core region:

$$M \sqrt{T}, M_4 \sqrt{T_4} = 1.0575, 1.01012 \times \sqrt{2108,700} = 1.817$$

Mass flow and temperature ratio in the core region

Thus,

$$p, p_4 = 0.917, p, p_0 = 2 \times 0.917 = 1.834$$

Pressure ratio at the nozzle for core combustion

Therefore,

$$X, M \sqrt{T} = 1.840$$

Thrust parameter for core combustion

As in section a), the gas thrust in the non-core region can be calculated as  $51.46 M'$ . Thus, for the thrust in systems b) and c) to be equal:

$$54.81 M = 84.48 m + 51.46 M'$$

Thrust balance equation

And since  $M = M' + m$ ,

Thus,  $m = 0.1015 M$ .

Propulsive efficiency  $\eta$  = fuel consumption for uniform temperature rise to achieve the same thrust / fuel consumption for combustion only in the core region.

$$\eta = 0.00262, 0.0473 \times 0.1015 = 0.5453$$

Propulsive efficiency calculation

That is, the propulsive efficiency is 54%.

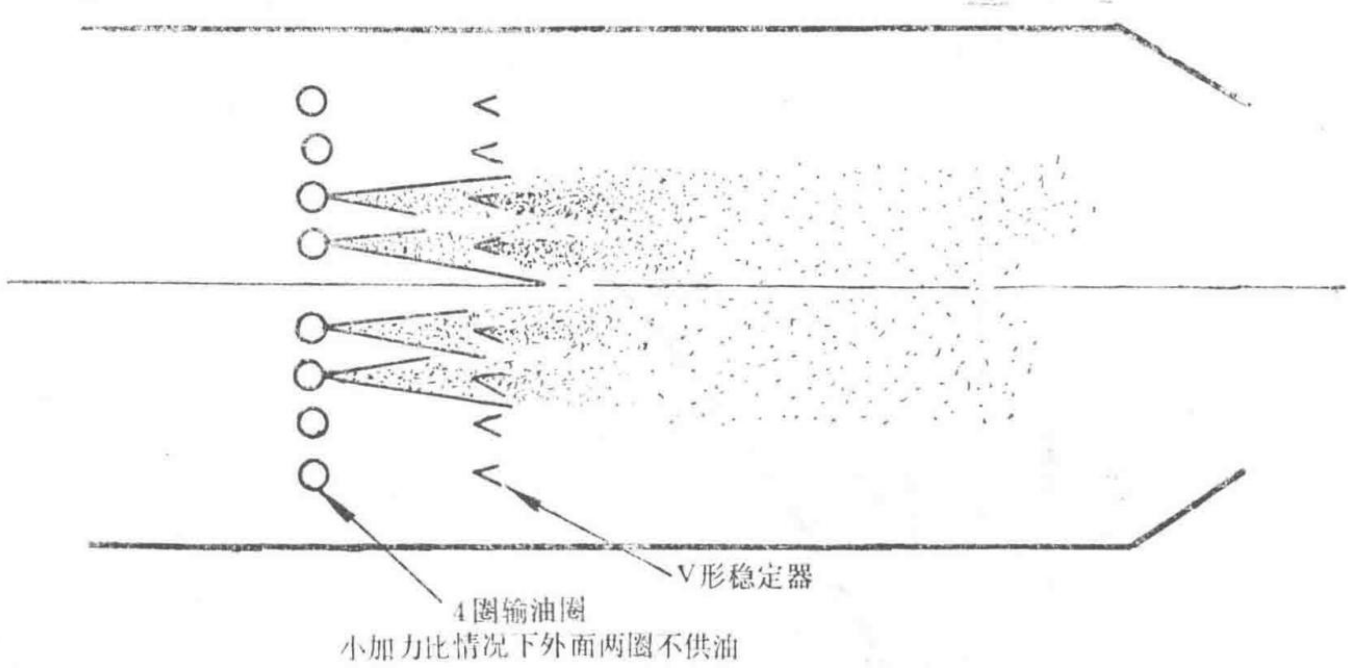


Figure 1: Reducing Afterburning by Closing Outer Fuel Circuits (i.e., Zoned Fuel Supply)

Diagram illustrating the method of reducing afterburning by selectively closing outer fuel circuits in a zoned fuel supply system.

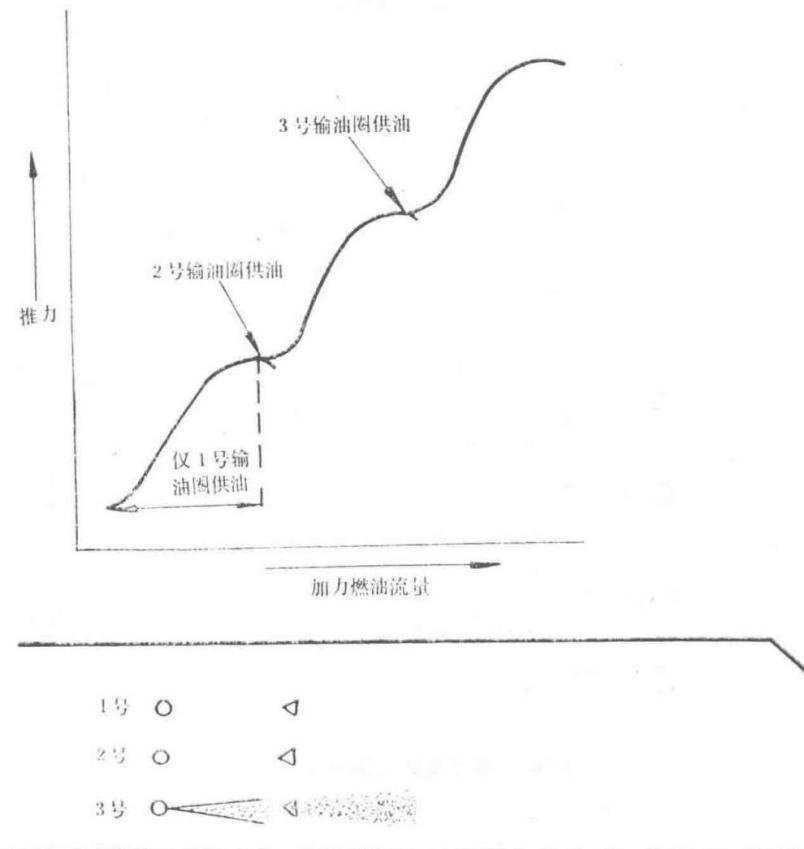


Figure 2: Typical Relationship Between Thrust and Fuel Flow in a Zoned Fuel Supply Afterburning System

Graph showing the relationship between thrust and fuel flow rate for different zones in an afterburning system.

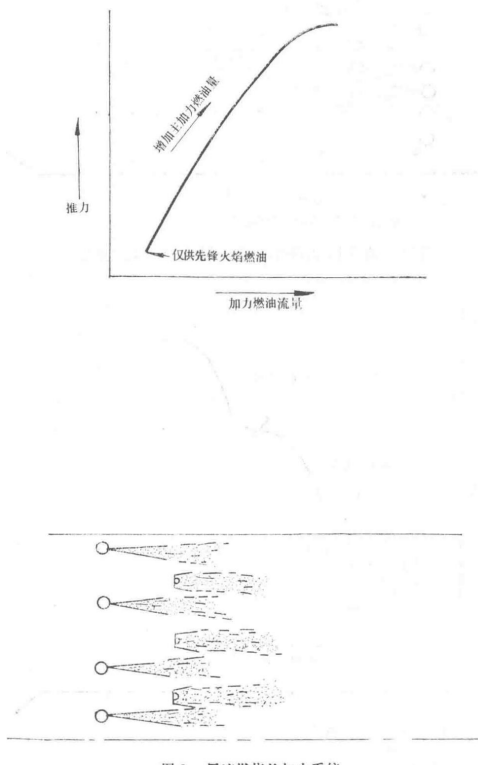


Figure 3: Afterburning System with Wake Combustion

Diagram of an afterburning system utilizing wake combustion.

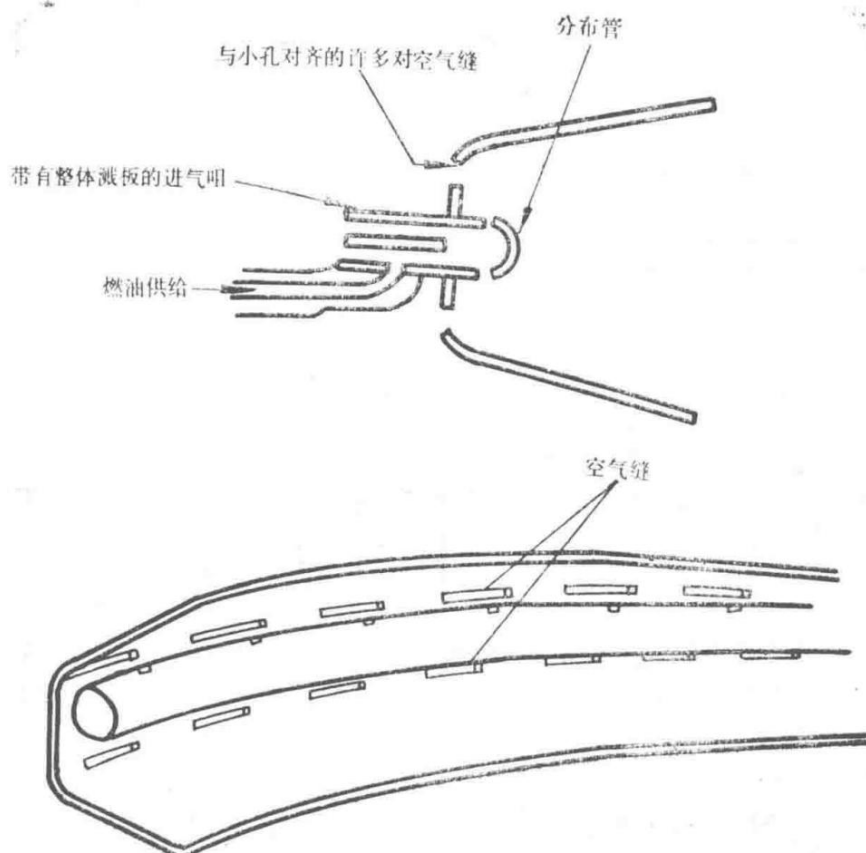


Figure 4: Schematic Diagram of an Vaporizer Stabilizer

Schematic of a vaporizer-type flame stabilizer used in afterburning systems.

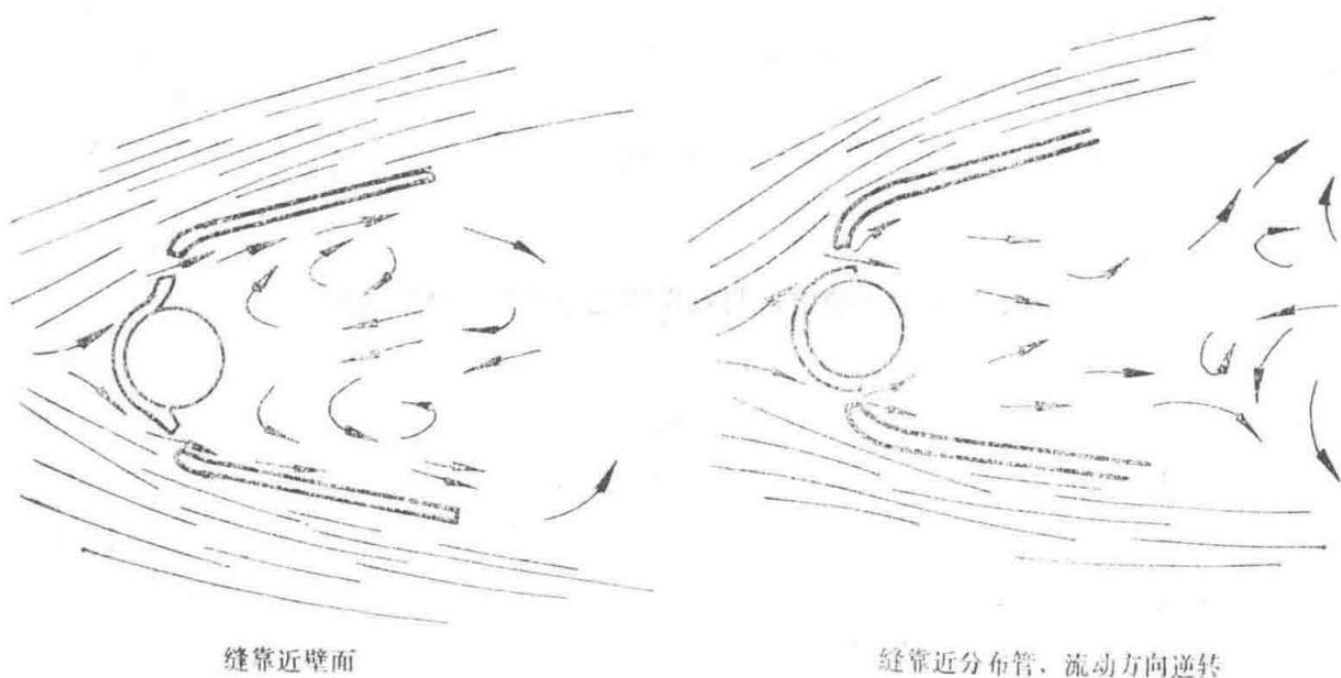


Figure 5: Water Flow Simulation Test Results of a Vaporizer Stabilizer

Results from water flow simulation tests illustrating the performance of a vaporizer stabilizer.

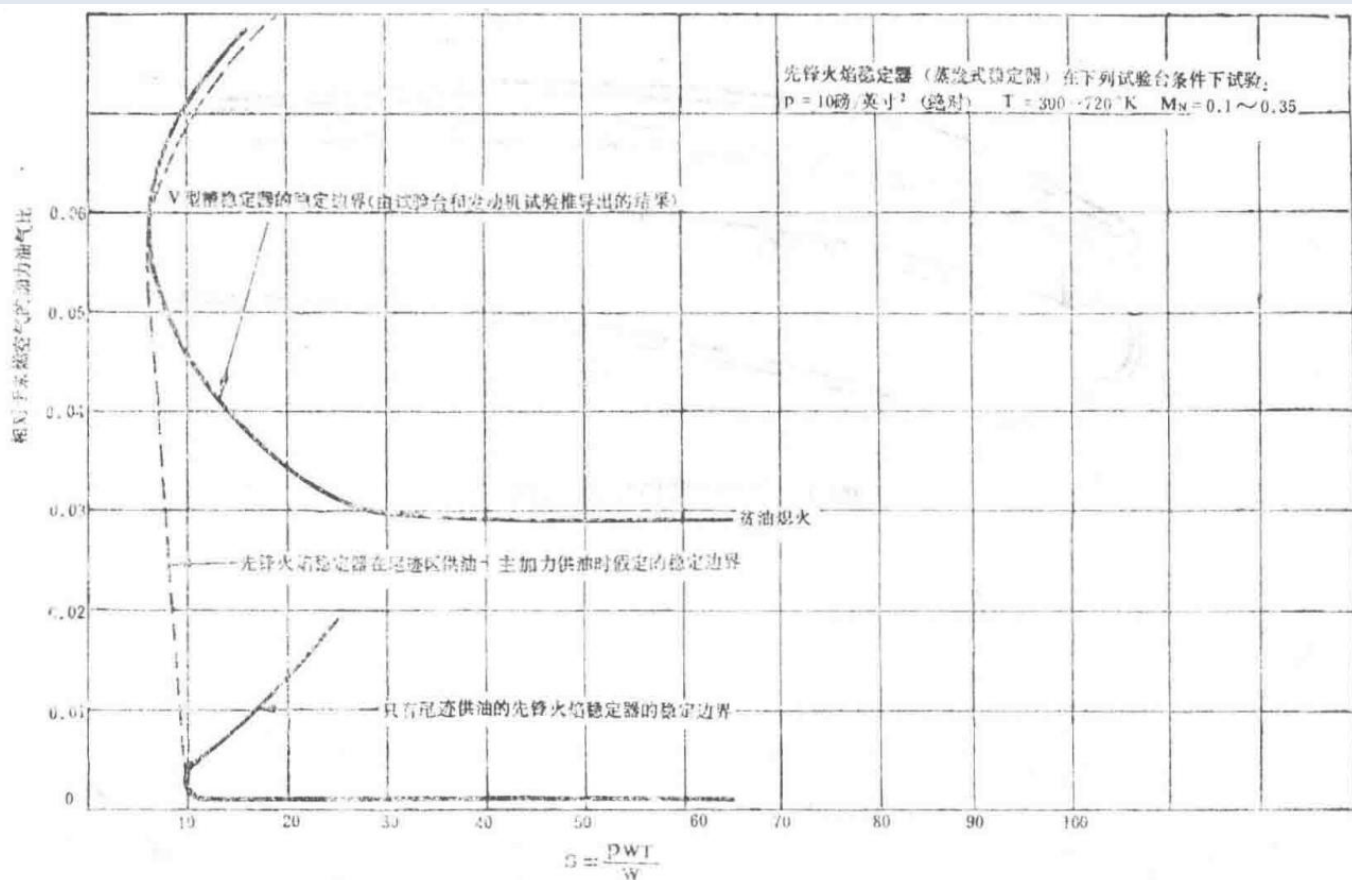


Figure 6: Comparison of Stability Between V-Groove Stabilizer and Vaporizer Stabilizer

Comparison of combustion stability characteristics between V-groove and vaporizer-type stabilizers in the Spey MK202 engine.

#### Combustion Research Report Header

Document	Report Number
Combustion Research Report	CRR 12051
	Development of Spey MK202 Mixer

First Edition, October 14, 1969

## 1.0 Abstract

This report presents the test results of various types of mixers. The tests were conducted on a Spey simulator in an altitude test facility. The current standard 10-slot 210 square inch mixer was developed from the original 185 square inch 10-funnel mixer.

## 2.0 Conclusions

2.1 Across all tested altitude ranges and at a flight Mach number of 1.53, the 210 square inch 10-funnel mixer achieved an afterburner temperature approximately 50°C higher before the onset of "buzz" compared to the 185 square inch 10-funnel mixer. However, the 185 square inch 10-funnel mixer, due to better matching, exhibited superior non-afterburning specific fuel consumption.

2.2 The 20-funnel civil Spey mixer with an afterburner casing tested at a flight Mach number of 1.53 did not experience "buzz," whereas the 10-funnel mixer produced "buzz" at similar afterburner temperatures.

2.3 Compared to the 10-funnel mixer, the 10-slot mixer achieved a higher afterburner temperature limited by "buzz." Under test conditions at a flight Mach number of 1.53, the temperature difference was approximately 80°C.

2.4 At a flight Mach number of 2.0, the 10-slot mixer achieved an afterburner temperature approximately 120°C higher before the onset of "buzz" compared to the 10-funnel mixer.

2.5 The 10-slot mixer with a streamlined fairing reduced its effective area from 210 square inches to 185 square inches. There was no difference in the achievable afterburner temperature.

## Discussion

Tests were conducted between January 30, 1967, and February 24, 1967, in the No. 2 chamber of the altitude test facility using an afterburner simulator. During this period, various structural types were tested in addition to mixer changes. However, similar structures were selected to compare the impact of mixers on performance. Thus, the readings from the test graphs cannot be directly compared across different figures. Table 1 shows the comparison of mixers.

Table 1: Mixer Comparison Summary

Figure	Compared Mixers	Results
1	185 sq in 10-funnel vs 210 sq in 10-funnel	210 sq in 10-funnel better, but 185 sq in better for engine matching
2	210 sq in 20-funnel vs 210 sq in 10-funnel	210 sq in 10-funnel (civil Spey) no "buzz"
3	210 sq in 10-funnel vs 210 sq in 10-slot	10-slot better
4	210 sq in 20-funnel vs 210 sq in 10-slot	10-slot better
5	210 sq in 10-slot vs 10-slot with streamlined fairing (185 sq in)	No change
6	10-slot with streamlined fairing (185 sq in) vs 210 sq in 10-funnel	10-slot with streamlined fairing better
7	Clockwise rotation of mixer	No change

## Figure 1 - Effect of Mixer Area

This figure compares the original 185 square inch 10-funnel mixer with the 210 square inch 10-funnel mixer. All points shown are "buzz" limited. The 210 square inch mixer achieves approximately 50°C higher afterburner temperature across the afterburner casing pressure range. However, tests indicate that the 185 square inch mixer has the best non-afterburning specific fuel consumption.

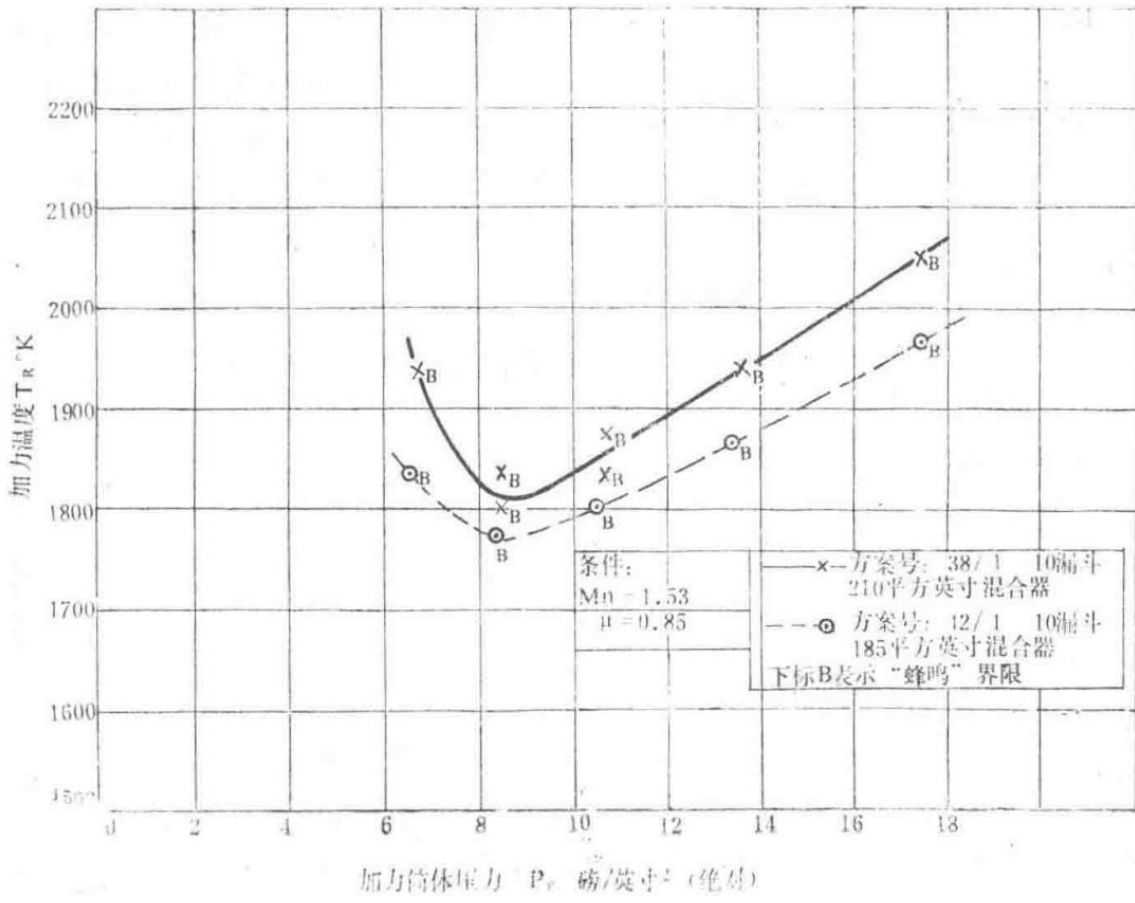


Figure 1: Effect of Mixer Area

Graph showing the comparison of afterburner temperature limits between 185 sq in and 210 sq in 10-funnel mixers under specified flight conditions.

## Figure 2 - Effect of 20-Funnel Mixer

The 20-funnel civil mixer did not experience "buzz" across the entire test altitude range at a flight Mach number of 1.53. However, despite using a higher fuel flow rate, the afterburner temperature did not increase compared to the 10-funnel mixer. Thus, although the 10-funnel mixer's performance was limited by "buzz," it proved to be a more efficient combustor.

Although referred to as funnel-type, the civil mixer is almost slot-type because the funnels are not inserted into the casing. Based on this and the system's "buzz"-free characteristics, a 10-slot mixer was tested. This mixer is the type used in the Phantom Spey after removing the funnels.

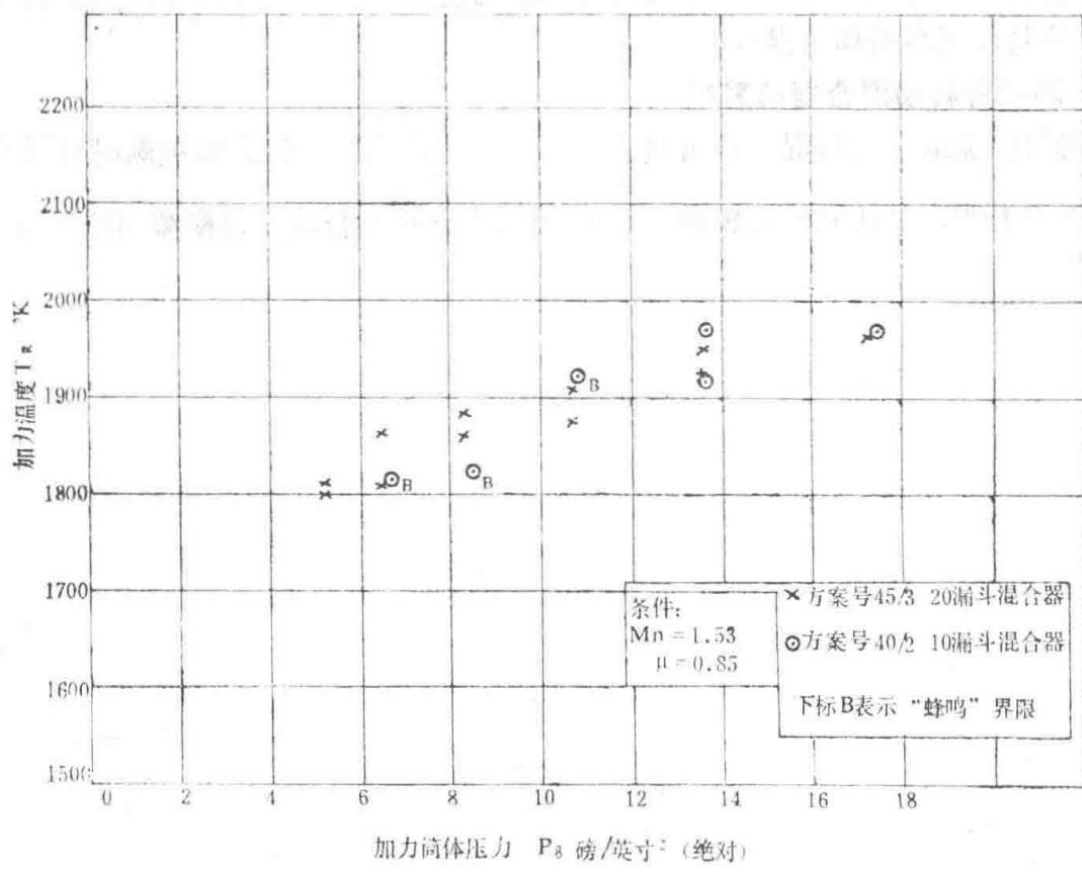


Figure 2: Effect of 20-Funnel Mixer

Graph showing the performance comparison between 20-funnel and 10-funnel mixers under specified flight conditions.

### Figure 3 - Effect of 10-Slot Mixer

This figure shows that across all test altitude ranges at a flight Mach number of 1.53, the 10-slot mixer achieves an afterburner temperature approximately 80°C higher than the 20-funnel mixer. However, both configurations were limited by "buzz."

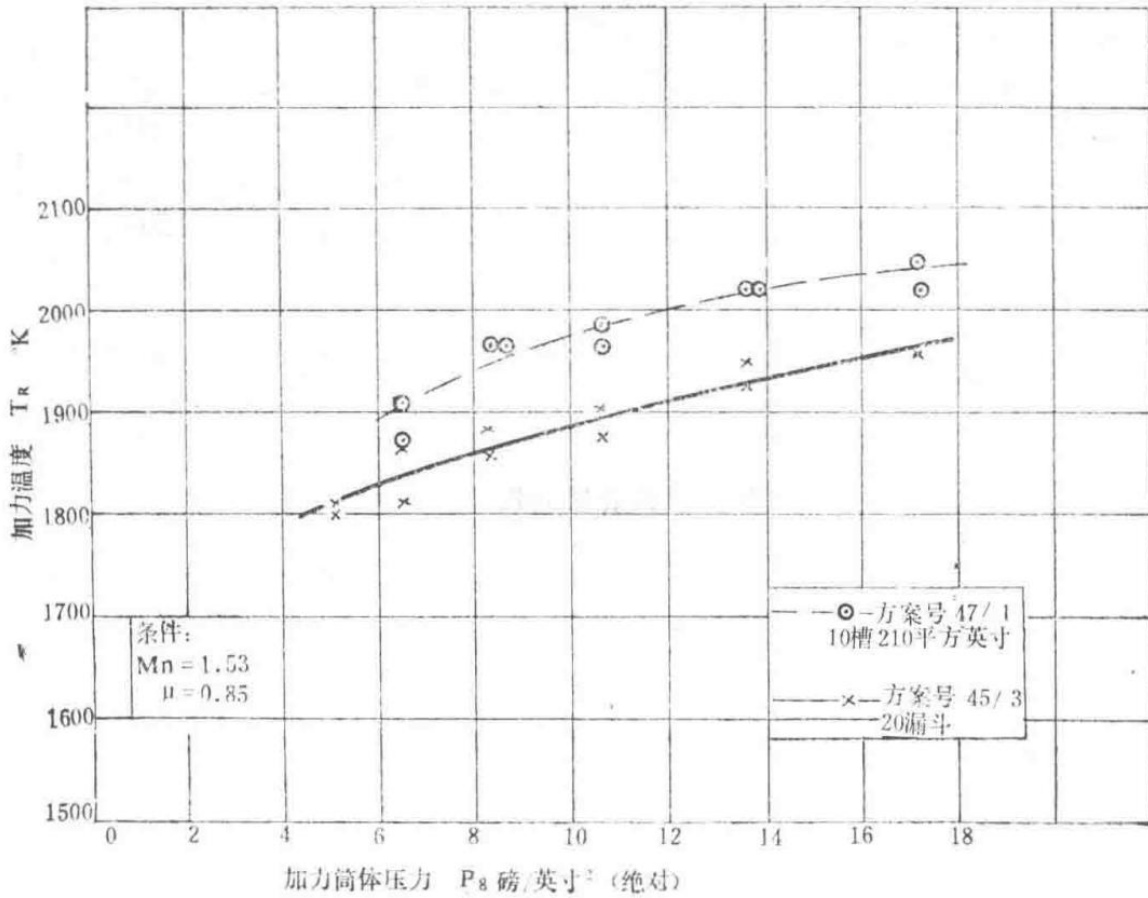


Figure 3: Effect of 10-Slot Mixer

Graph showing the performance comparison between 10-slot and 20-funnel mixers under specified flight conditions.

#### Figure 4 - Effect of 10-Slot Mixer

At a flight Mach number of 2.0, the 10-slot mixer achieved an afterburner temperature approximately 120°C higher than the 10-funnel mixer. This slot-type mixer is a funnel-type mixer structure with the funnels removed. It is the configuration now installed on production engines.

#### Figure 5 - Effect of 10-Slot Mixer with Streamlined Fairing

The area of the slot-type mixer is larger than the original 185 square inch funnel-type. In this test, adding a streamlined fairing reduced the effective area to 185 square inches. Across the test altitude range at a flight Mach number of 1.53, the 10-slot mixer with a streamlined fairing showed minimal change in afterburner temperature compared to the 10-slot mixer without the fairing. This test aimed to determine if there was any impact on afterburning performance, as earlier tests indicated that the 185 square inch mixer had the best non-afterburning engine specific fuel consumption.

#### Figure 6 - Effect of 10-Slot Mixer with Streamlined Fairing

Figure 6 compares the performance of two mixers: one with a 210 square inch 10-funnel configuration and the other with a 10-slot configuration plus a streamlined fairing. The graph shows that across most of the test altitude range, the 10-slot mixer with a streamlined fairing achieves a higher afterburner temperature than the 10-funnel mixer.

## Figure 7 - Effect of Clockwise Rotation of Mixer

Considering that the outlet flow pattern of the mixer relative to the combustion chamber might affect "buzz," the mixer was rotated clockwise by half a circumferential pitch. Observations indicated no impact on performance, suggesting that the combustion chamber is insensitive to changes in the mixer outlet cross-sectional flow pattern at an angle of 11°.

— Section 54 —  
Content from Original Document (Pages 266-270)

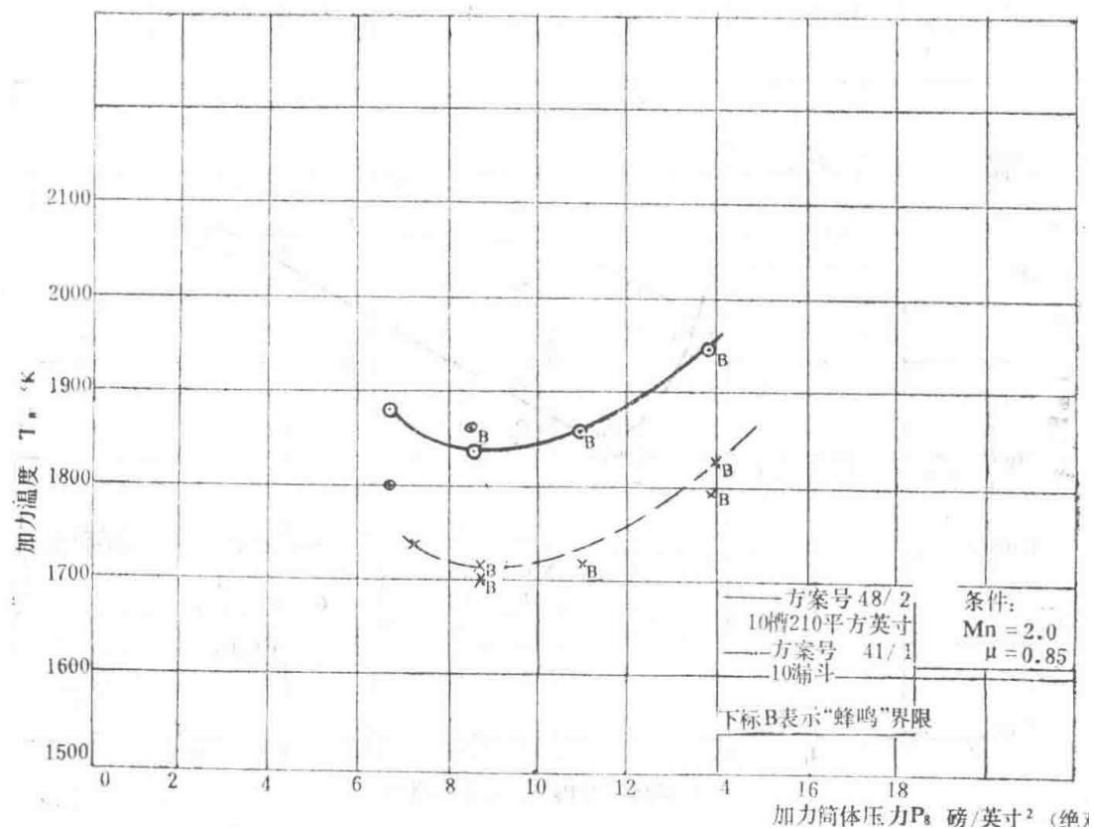


Figure 4: Influence of 10-Slot Mixer

Diagram showing the effect of a 10-slot mixer on engine performance parameters.

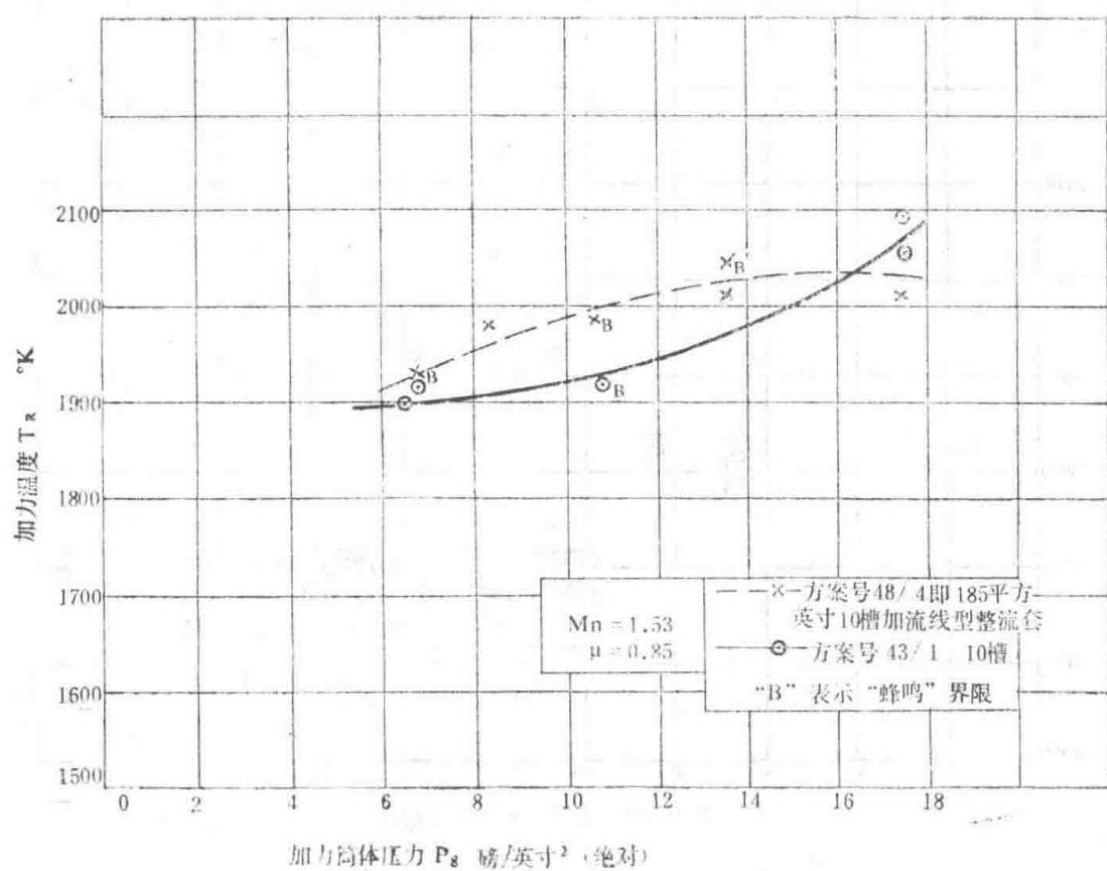


Figure 5: Influence of 10-Slot with Streamlined Fairing Sleeve

Diagram illustrating the impact of a 10-slot mixer combined with a streamlined fairing sleeve on engine performance.

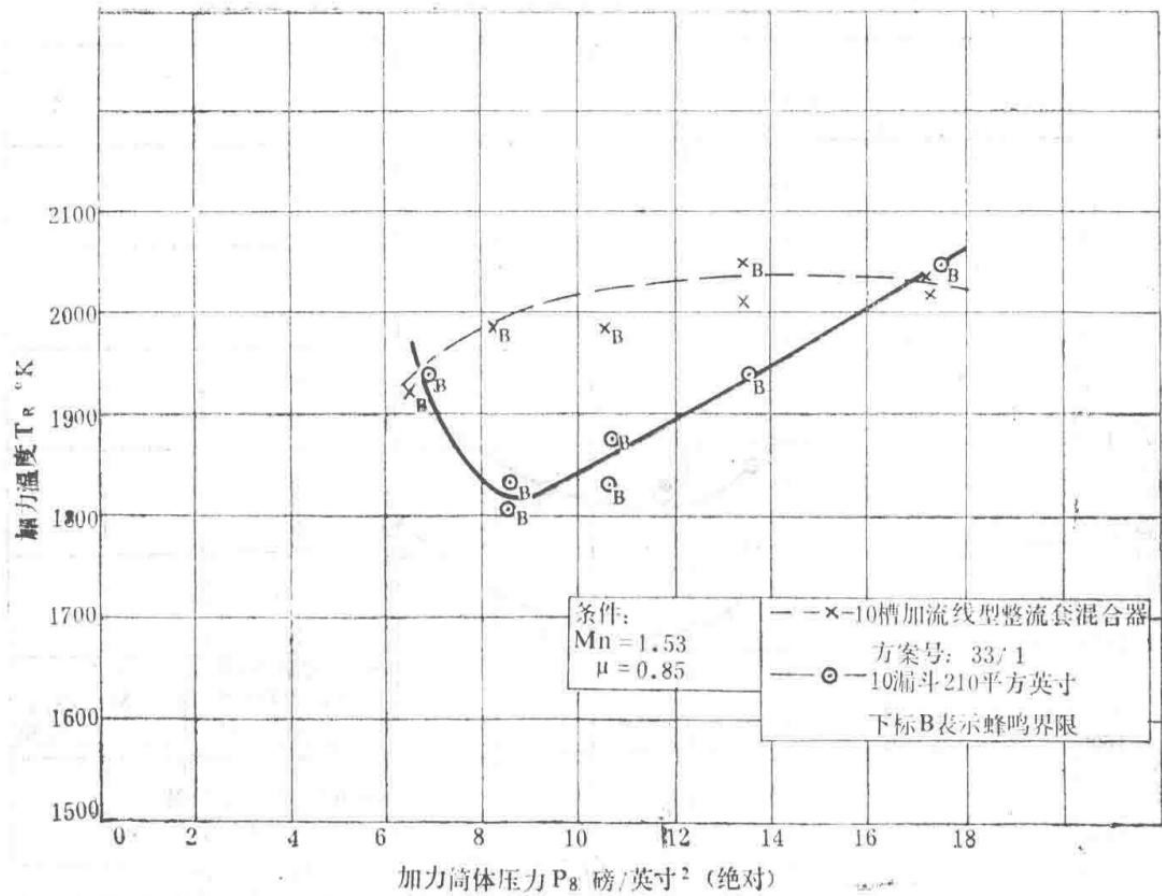


Figure 6: Influence of 10-Slot with Streamlined Fairing Sleeve

Further analysis of the 10-slot mixer with streamlined fairing sleeve effects on engine parameters.

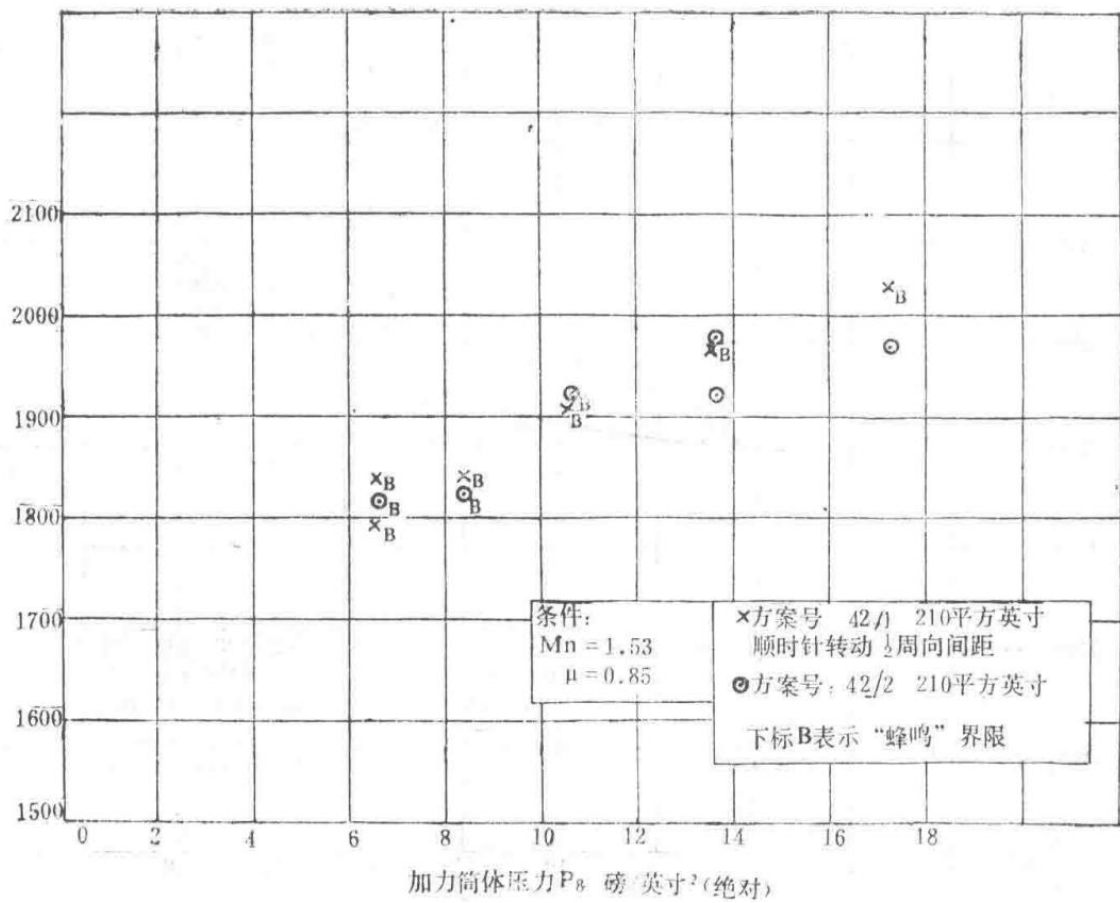


Figure 7: Influence of Clockwise Rotating Mixer

Diagram depicting the influence of a clockwise rotating mixer on engine performance.

Technical Design Report Header

Document Type	Section
Technical Design Report	Part TDR7787A
	Spey MK202 Fuel Control System - High Pressure Fuel Pump Design Documentation

First Edition, October 29, 1976

## Abstract

This report specifies the requirements for the high-pressure fuel pump and includes technical reports that materialize these requirements, as well as typical characteristics of the high-pressure fuel pump.

## 1. Introduction

The high-pressure fuel pump supplies fuel to the engine combustion chamber and injects fuel into the afterburner system during afterburner activation. Additionally, it provides fuel for cooling and servo mechanisms for accessories and afterburner devices.

This report describes the design requirements for the high-pressure fuel pump and provides relevant data.

## 2. Initial Technical Requirements for the High-Pressure Fuel Pump

### 2.1 Requirements

The pump shall supply the engine with the required amount of fuel at the necessary pressure.

### 2.2 Rated Speed

The pump is driven by the engine, with a speed ratio of 0.2318 relative to the high-pressure compressor speed. When the engine high-pressure rotor speed is 12,640 rpm, the mechanical drive output speed is 2,930 rpm. The maximum speed of the engine high-pressure rotor is 13,125 rpm.

### 2.3 Maximum Pressure

The pump shall include a device to limit the pressure within the control system to not exceed safe operating values.

### 2.4 Pumping Capacity

The pump shall have the capability to deliver fuel according to the dimensionless fuel flow versus dimensionless parameter  $N\bar{\square} / \sqrt{(\Omega T_1)}$  curves shown in Figures 1, 2, and 3 (non-afterburning) and Figure 4 (afterburning).

At high-altitude operation, the flow rates derived from these curves must be corrected using the fuel flow correction factor provided in Figure 5.

The maximum fuel flow occurs at sea level (when the T<sub>0</sub> limiter is active), with a maximum fuel temperature of 60°C. The minimum fuel density is 0.716.

When the 12-stage boundary layer control bleed is engaged, the maximum steady-state fuel flow required for a single engine at 11,800 rpm is 11,120 lb/hr (1,557 gallons/hr). Additionally, during engine acceleration, the pump shall be capable of supplying fuel according to the rich-oil characteristics shown in Figure 12.

Beyond meeting the engine's fuel requirements, the pump must also have sufficient capacity to satisfy additional flow demands for engine accessories. At 11,800 rpm, this flow rate is 450 gallons/hr.

## 2.5 Engine Pressure Ratio

The compressor pressure ratio of the engine versus speed, presented in dimensionless form, is shown in Figures 6 to 11.

## 2.6 Atmospheric Conditions

For this type of engine, the maximum and minimum atmospheric operating conditions are represented on a specialized chart with atmospheric temperature as the scale.

## 2.7 Aircraft Operating Conditions

For this type of engine, the operating conditions in terms of altitude versus Mach number M<sub>∞</sub> are plotted on a corresponding design limit flight envelope.

## 2.8 Nozzle Pressure

The nozzles are preliminarily determined to be dual-circuit nozzles with the following flow characteristics:

- Total pilot nozzle flow characteristic number = 2.5
- Total main nozzle flow characteristic number = 55
- Main nozzle flow characteristic number can vary between 50 and 60.

The flow characteristic number is given by the following equation:

$$\text{Fuel specific gravity used} = 0.79$$

Fuel specific gravity used in calculations.

## 2.9 Fuel Temperature Range

The fuel temperature range at the pump inlet shall be from -40°C to +135°C.

## 2.10 Low-Pressure Fuel Pressure

When fuel is supplied at the flow rates and pressures specified in the table below, the fuel pump shall not exhibit cavitation.

Flow Rate (gallons/hour)	Fuel Pressure at Pump Inlet
0	8 psi + fuel vapor pressure
500	9.5 psi + fuel vapor pressure
1000	12 psi + fuel vapor pressure
1500	17 psi + fuel vapor pressure

The maximum low-pressure fuel pressure values are:

- Steady-state: (i) 130 psi (gauge) at +120°C, (ii) 90 psi (gauge) at +135°C
- Transient: 180 psi (gauge) at 120°C

## 2.11 Filtration Performance

A low-pressure fuel filter is installed upstream of the fuel pump, with the following characteristics:

1. It shall filter out at least 95% of all particles 10 microns in size.
2. The maximum particle size passing through the filter shall not exceed 40 microns.

## 2.12 Fuel

The pump shall be designed to operate with any of the following fuels:

Civilian Fuel	Military Fuel
AVTUR	JP-1
AVTAG	JP-4
AVCAT	JP-5

The fuel may or may not contain 0.1% to 0.15% anti-icing additive (by volume).

## 2.13 Operation During Catapult Takeoff

During takeoff with longitudinal acceleration up to 5g and engine attitudes ranging from horizontal to 30° nose-up, the pump must operate smoothly without periodic fluctuations or power loss. If the throttle lever is rapidly advanced or retarded during catapult takeoff, the pump shall enable normal engine acceleration and deceleration.

## 2.14 Fuel Contamination

The designed pump shall operate without failure when using fuel specified in Section 2.12 that meets British Ministry of Defense contamination standards. However, for endurance testing, the contamination level of the fuel may follow standards mutually agreed upon by Rolls-Royce and the customer based on specific applications.

The internal components of the pump shall withstand seawater contamination.

## 2.15 Diagrams

The symbols used in Figures 1 to 11 are as follows:

Symbol	Description	Unit
F□	Engine fuel flow rate	gallons/hour
α□	Engine fuel flow correction factor	
N□	High-pressure shaft speed	rpm
R <sub>o1</sub>	Ram ratio	
P <sub>1</sub>	Low-pressure compressor inlet total pressure	psi (absolute)

$P_2$	Low-pressure compressor outlet total pressure	psi (absolute)
$P_3$	High-pressure compressor outlet total pressure	psi <sup>2</sup> (absolute)
$T_1$	Low-pressure compressor inlet total temperature	K
$T_2$	Low-pressure compressor outlet total temperature	K
$T_3$	High-pressure compressor outlet total temperature	K

— Section 55 —  
Content from Original Document (Pages 271-275)

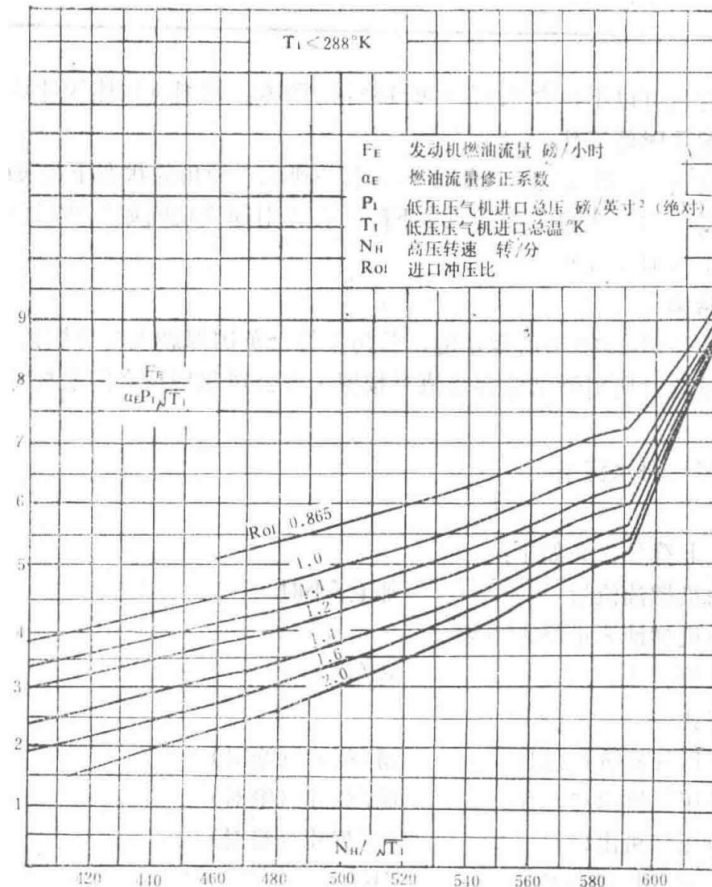


Figure 1 Fuel Flow of Spey MK202 Engine (Low Speed, Non-Afterburning)

Graph showing the fuel flow characteristics of the Spey MK202 engine at low rotational speeds without afterburner engagement.

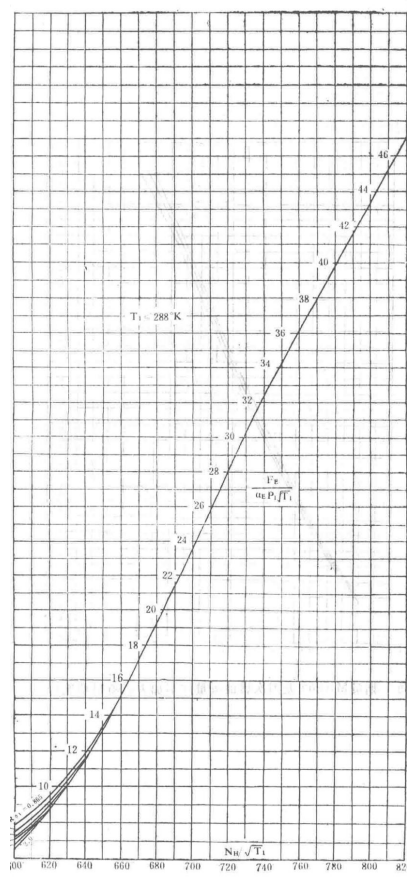


Figure 2 Fuel Flow of Spey MK202 Engine (Non-Afterburning)

Graph depicting the fuel flow of the Spey MK202 engine under non-afterburning conditions.

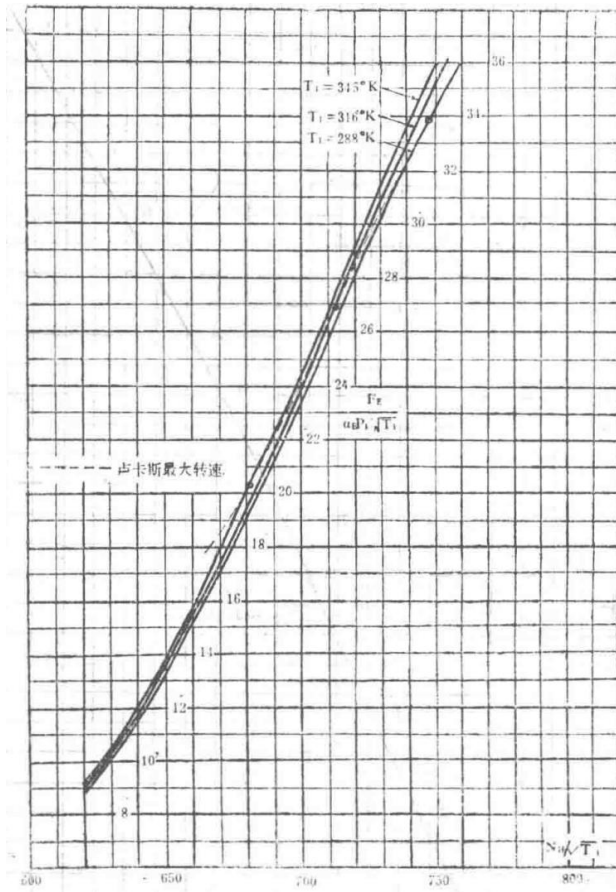


Figure 3 Dimensionless Fuel Flow of Spey MK202 Engine (Non-Afterburning, Choked Nozzle)

Graph illustrating the dimensionless fuel flow characteristics of the Spey MK202 engine with a choked nozzle and no afterburner.

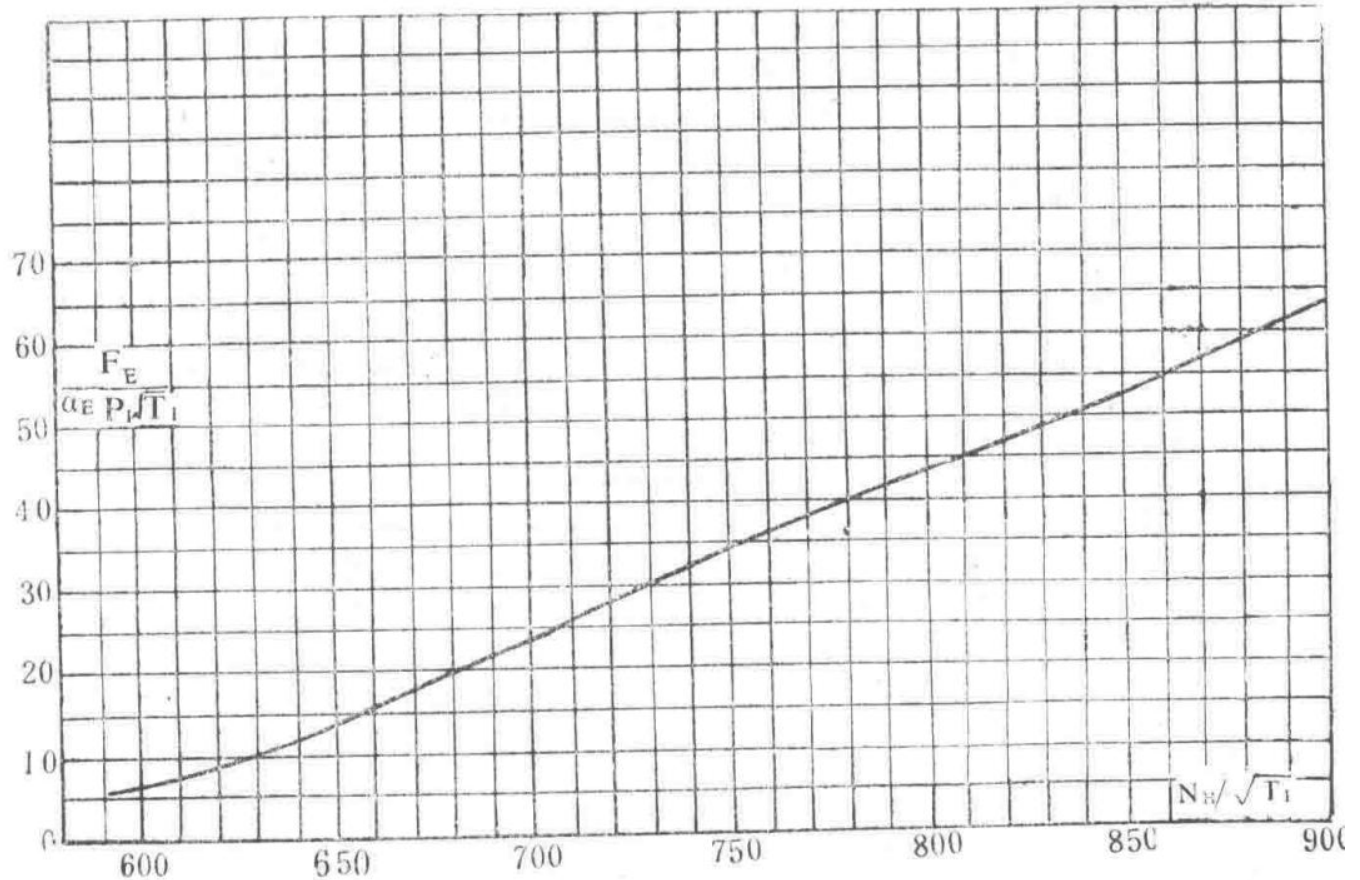


Figure 4 Dimensionless Fuel Flow of Spey MK202 Engine (Afterburning Only,  $N_E / \sqrt{T_1} = 900$ )

Graph showing dimensionless fuel flow for the Spey MK202 engine used exclusively in afterburning mode at maximum high-pressure rotor speed.

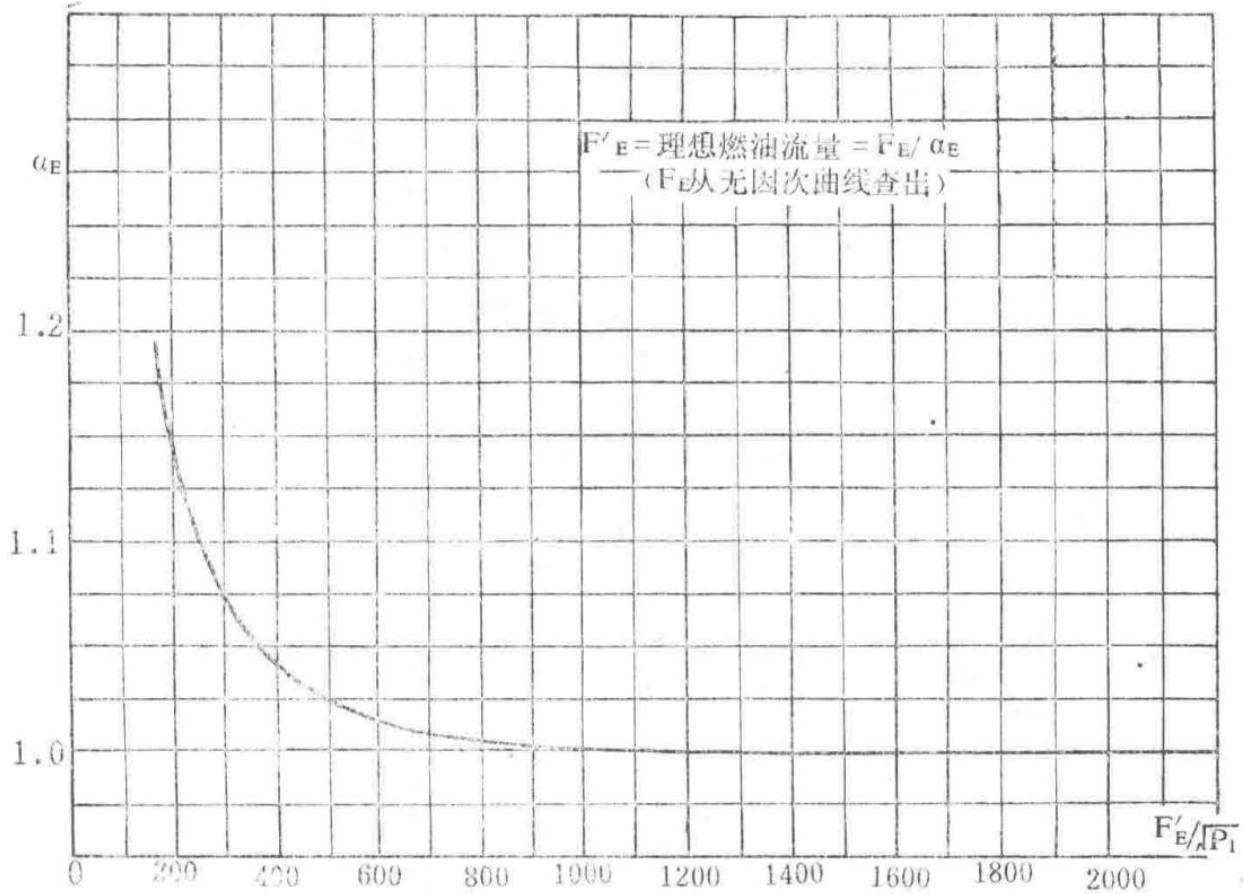


Figure 5 Spey MK202 Engine Fuel Flow Correction Coefficient -  $\alpha_E$

Graph depicting the fuel flow correction coefficient  $\alpha_E$  for the Spey MK202 engine.

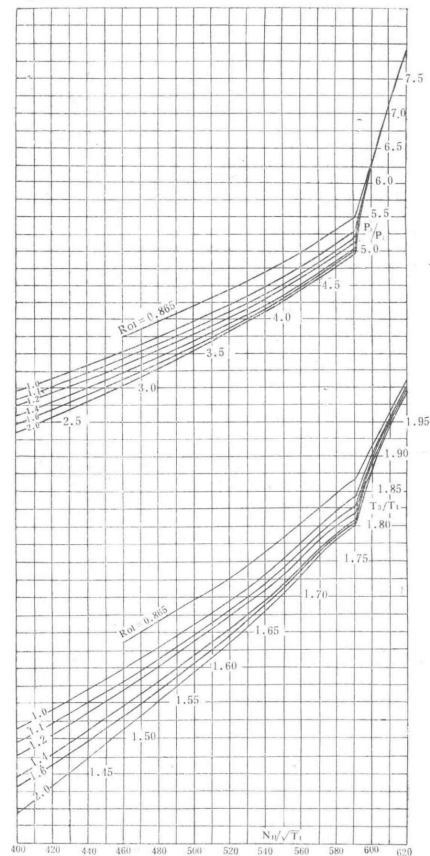


Figure 6 Dimensionless Total Temperature and Total Pressure at High-Pressure Compressor Outlet of Spey MK202 Engine  
(Applicable for Inlet Temperature  $T_1 \leq 288\text{ K}$ , Non-Afterburning)

Graph showing the dimensionless total temperature ( $T_3/T_1$ ) and total pressure ( $P_3/P_1$ ) at the high-pressure compressor outlet of the Spey MK202 engine for inlet temperatures up to 288 K without afterburner.

The following section details the fuel flow characteristics and correction factors for the Spey MK202 aircraft engine under various operational conditions. The graphs provide critical data for engine performance analysis, including fuel consumption rates, dimensionless parameters, and correction coefficients.

$$F' = \text{Actual fuel flow rate} = F \cdot \alpha$$

Equation defining the actual fuel flow rate  $F'$  as the product of the ideal fuel flow rate  $F$  and the correction coefficient  $\alpha$ .

#### Nomenclature for Engine Parameters

Symbol	Description	Unit
$F$	Actual fuel flow rate per unit time	-
$\alpha$	Fuel flow correction coefficient	-
$P_1$	Low-pressure compressor inlet total pressure	Pascals (Pa) or equivalent
$T_1$	Low-pressure compressor inlet total temperature	Kelvin (K)
$N$	High-pressure rotor speed	RPM
$R_{in}$	Inlet pressure ratio	-

The dimensionless parameters such as  $T_3/T_1$  (total temperature ratio) and  $P_3/P_1$  (total pressure ratio) are crucial for evaluating the thermodynamic performance of the high-pressure compressor stage. These ratios help in assessing the efficiency and operational limits of the engine under varying inlet conditions.

— Section 56 —  
Content from Original Document (Pages 276-280)

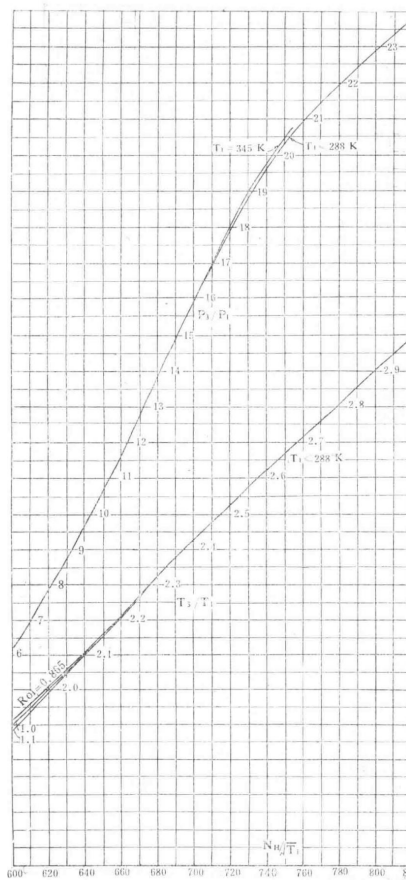


Figure 7 Spey MK202 Dimensionless High-Pressure Compressor Exit Total Pressure and Total Temperature (for Non-Afterburning Operation)

Graph showing the dimensionless total pressure and total temperature at the exit of the high-pressure compressor of the Spey MK202 engine under non-afterburning conditions.

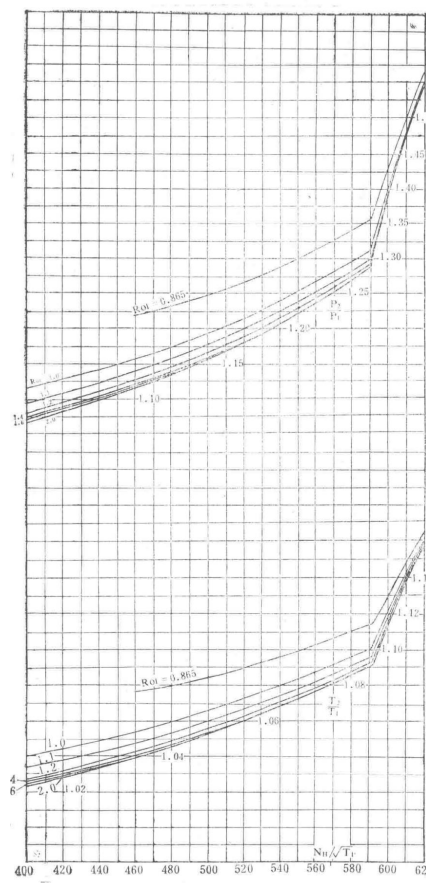


Figure 8 Spey MK202 Dimensionless Low-Pressure Compressor Exit Total Pressure and Total Temperature (Applicable for Inlet Total Temperature  $T_1 \leq 288^\circ\text{K}$ , Non-Afterburning Operation)

Graph showing the dimensionless total pressure and total temperature at the exit of the low-pressure compressor of the Spey MK202 engine for inlet total temperature  $T_1 \leq 288^\circ\text{K}$  under non-afterburning conditions.

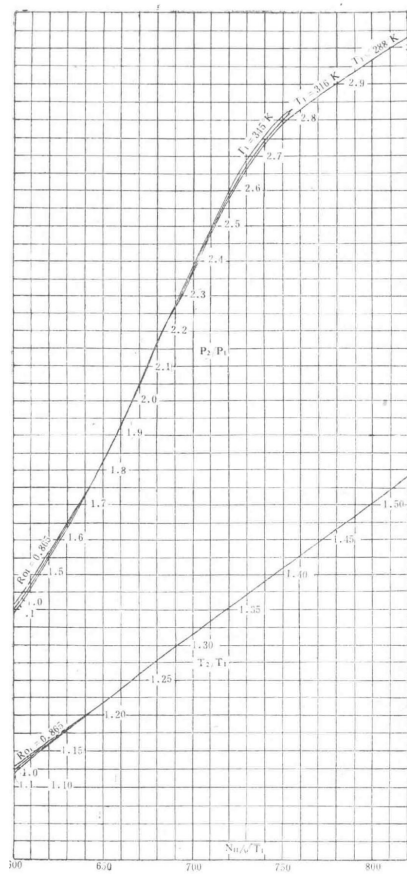
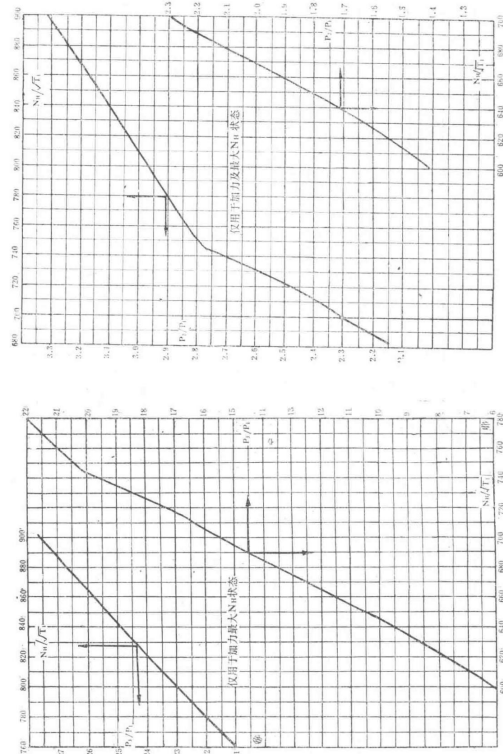


Figure 9 Spey MK202 Dimensionless Low-Pressure Compressor Exit Total Pressure and Total Temperature (for Non-Afterburning Operation)

Graph showing the dimensionless total pressure and total temperature at the exit of the low-pressure compressor of the Spey MK202 engine under non-afterburning conditions.



Uncaptioned image, possibly a schematic or graph related to the Spey MK202 engine.

$\frac{P_3}{P_2}$	以海平面静态国际标准大气不抽气稳态运转( $F/P_2 N_H$ )的%表示的加速控制装置的( $F/P_2 N_H$ )	
	海平面国际标准大气	40000英尺, 0.86 Mn 国际标准大气
2		174%
3		170%
4	125%	143%
5		138%
6		130%
7		125%

Figure 12 Spey MK202 Acceleration Control Device Control Line

Graph depicting the control line of the acceleration control device for the Spey MK202 engine.

### 3. Lucas P1001 High-Pressure Fuel Pump

This is a variable-stroke plunger pump. The outstanding advantage of this type of pump is its variable output flow, which can match a wide range of engine requirements. Unlike fixed-displacement pumps (such as gear pumps), it does not require a valve to spill excess fuel back to the low-pressure side. Because it uses a variable-stroke pump, the fuel heating caused by the recirculation of large amounts of fuel during high-altitude idle flight conditions can be kept to a minimum. Another major advantage is its minimal leakage, allowing the pump to provide higher output pressure. This ensures better fuel atomization during engine ignition, even at very low pump speeds.

The pump structure is similar to the Lucas "D" type pump used on civil Spey engines. The Spey MK202 engine's high-pressure fuel pump is driven by the high-speed gearbox through an appropriate gear train at 0.2318 times the high-pressure rotor speed. The plungers are axially positioned within the rotor and reciprocate as they rotate around the swashplate. By changing the angle of the swashplate, the pump's stroke can be adjusted. The swashplate is controlled by the force of a servo piston with unequal areas, which opposes the spring force. The servo piston senses changes in the fuel pressure difference between the fuel regulator (C.A.S.C) and the low-pressure shaft limiter. In practice, the stroke of the high-pressure fuel pump is adjusted to maintain a balance between the pump force, the force generated by the pressure difference on both sides of the servo piston, and the spring force.

The outlet pipeline of the pump includes a spill valve or limit valve, which can handle the pump's full flow if necessary. This valve is set to open at approximately 1800 psi (gauge pressure), though this pressure increases significantly with the flow through the valve. When the flow through the valve is 2200 gallons per hour, the required maximum pressure is 2800 psi (gauge pressure).

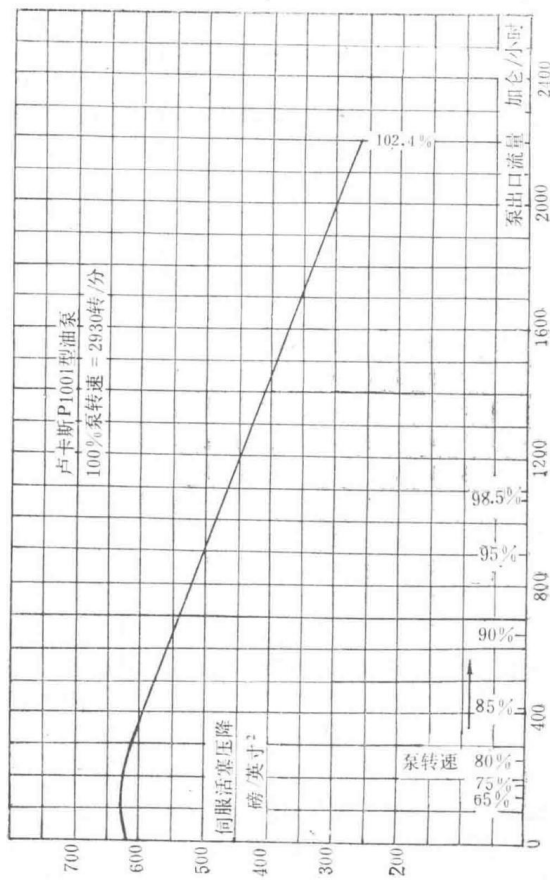
## 4. High-Pressure Fuel Pump (Lucas P1001) Data

For the Spey MK202,  $N_{\square} = 0.2318 N_{\square}$ , where:

Correction Factors for Sea-Level Static International Standard Atmosphere Non-Afterburning Operation ( $F/P_2N_{\square}$ )  
Percentage Table

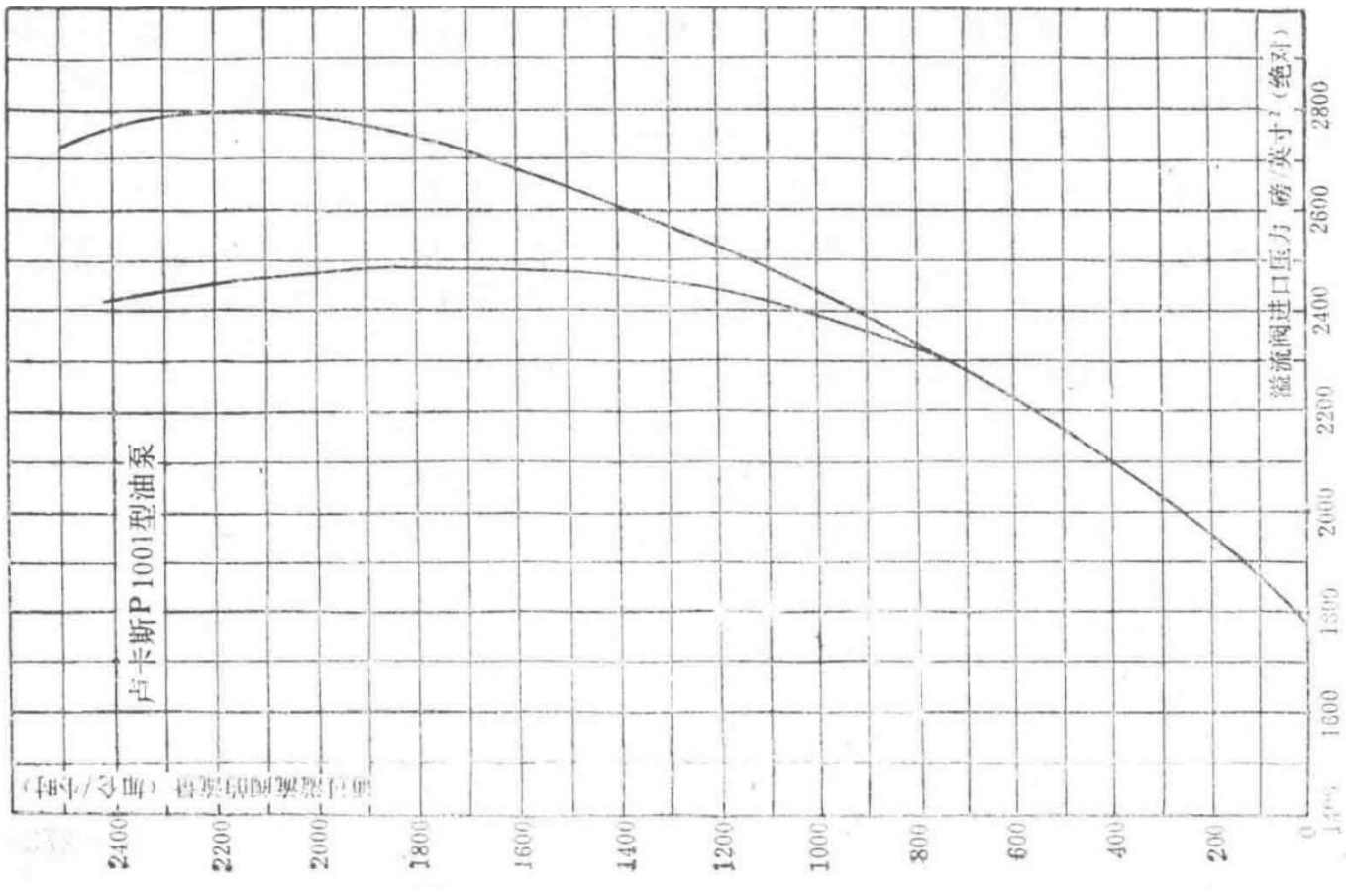
$P_3/P_2$	Sea-Level Static International Standard Atmosphere	40,000 Feet, 0.86 Mn International Standard Atmosphere
2	174%	
3	170%	
4	125%	143%
5		138%
6		130%
7		125%

— Section 57 —  
Content from Original Document (Pages 281-285)



Typical Relief Valve Characteristics

Graph showing the characteristics of the relief valve for the Spey MK202 engine.



Typical Servo Piston Characteristics

Graph showing the characteristics of the servo piston for the Spey MK202 engine.

N□

High-pressure rotor speed in revolutions per minute (rpm).

P□

Pump output pressure in pounds per square inch (psi), gauge pressure.

Typical characteristics of the relief valve and servo piston are shown in Figure 13 and Figure 14, respectively.

## 5. Estimation of Maximum Fuel Flow

Technical Design Report

Document	Report Number
Technical Design Report	TDR784
Spey MK202 Maximum Fuel Flow Estimation	

### Objective

To estimate the engine fuel flow, primarily to provide technical specifications for accessory design.

### Reason for Issue 5

The estimated maximum engine fuel flow has been revised due to changes in the boundary layer control flight envelope (maximum equivalent airspeed of 250 knots, with boundary layer control engaged, Mach number  $M \square$  of 0.38).

## References

- Engine performance based on the latest standards, including the supplementary regulation limiting  $N \square / \sqrt{T_1}$  to 810.
- A.I.A. inlet recovery coefficient.
- Temperature  $T_e$  control regulation as recommended by the Performance Department.
- Engine performance calculated by computer without extraction of 7th and 12th stage high-pressure air.
- $T_e / T_1$  control requirements derived from performance calculations and unpublished data.

## Boundary Layer Control Operating Envelope

Boundary layer control can be selected at an equivalent airspeed of 250 knots, at altitudes up to 15,000 feet, and at any rotor speed from idle to maximum. The engine inlet temperature range can be derived from the flight envelope and atmospheric temperature scale.

### Conclusions (Boundary Layer Control Disengaged)

It can be demonstrated that the maximum fuel flow occurs at sea level under conditions where  $N \square$  is maximized,  $N \square / \sqrt{T_1}$  is maximized, and  $(p_3 - p_0)$  is maximized, coinciding with ambient temperature.

At  $t_0 = 241.1 \text{ extK}$  (corresponding to  $M \square = 0.219$ ), the estimated maximum flow rate is 10,742 lb/hr. Under this condition, the estimated inlet temperature of the high-pressure fuel pump is  $60^\circ\text{xtC}$ . At this temperature, the minimum specific gravity of wide-cut fuel is 0.716. Therefore, the maximum volumetric flow rate for steady-state engine operation is 1,500 gallons/hour.

Since the engine operating line is the same at these low temperatures, the maximum flow rate obtained is identical regardless of whether afterburning is engaged.

For different inlet recovery coefficients, the maximum fuel flow remains unchanged but corresponds to different  $t_0$  and  $M \square$  values.

To illustrate how engine fuel demand varies near the maximum fuel flow condition, Tables 1, 2, and 3 provide fuel flow data for altitudes from sea level to 3,000 feet,  $M \square$  from 0.1 to 0.3, and ambient temperatures ranging from ISA  $-53^\circ\text{C}$  to ISA  $-43^\circ\text{C}$ .

### Conclusions (Boundary Layer Control Engaged, Aircraft Flaps Fully Deployed, Two Engines Operating, 14.3% Bleed Air)

With aircraft flaps fully deployed and 12th stage boundary layer control engaged, the  $T_s$  limiter controls the maximum fuel flow. Under these conditions, at  $t_0 = 221.9 \text{ extK}$  and  $t_0 = 240 \text{ extK}$ ,  $M \square$  up to 0.38,  $P_3$ , and  $N \square / \sqrt{T_1}$  limiters do not control fuel flow.

All fuel flow values given with boundary layer control engaged refer to the condition with 12th stage high-pressure compressor bleed air.

At  $t_0 = 221.9 \text{ extK}$  and  $M \square = 0.38$ , the estimated maximum fuel flow is 11,000 lb/hr. The  $t_0$  and  $M \square$  values represent the coldest sea-level weather and highest Mach number at which boundary layer control can operate. Under this condition, the estimated inlet temperature of the high-pressure fuel pump is  $60^\circ\text{C}$ , where the minimum specific gravity of wide-cut fuel is 0.716. Therefore, the maximum volumetric flow rate during steady-state engine operation at 11,800 rpm is 1,540 gallons/hour.

Since the engine operating line is the same at these low temperatures, the maximum fuel flow obtained is identical regardless of whether afterburning is engaged.

Given that the aircraft inlet recovery coefficient at  $M_\infty = 0.38$  is 0.98, the fuel flow at 11,800 rpm will decrease from 1,540 gallons/hour to 1,510 gallons/hour.

Table 4 provides the engine fuel demand at sea level,  $M_\infty$  from 0 to 0.38, and ambient temperatures of ISA -61.1°C and ISA -48°C.

### Single Engine Operation: 12th Stage High-Pressure Compressor Bleed Air at 16%

Flight condition:  $M_\infty = 0.38$ , sea level,  $t_0 = 221.9$  extK.

This condition also corresponds to  $T_e$  limited to 950 extK, with a maximum fuel flow of 11,120 lb/hr (1,557 gallons/hour) at 11,800 rpm.

### Boundary Layer Control Bleed Air

Boundary layer control air is obtained from the 7th or 12th stage of the high-pressure compressor.

Table 1: Engine Fuel Demand (lb/hr) at ISA -53°C (Boundary Layer Control Disengaged)

Altitude (ft)	Mach Number	0.1	0.15	0.20	0.25	0.3	$t_0$ (K)
0		10290	10394	10538	10497	10303	235
500		10084	10185	10327		10513	234
1000		9881	9980	10120	10302	10476	233
1500		9682	9779	9916	10094	10315	232
2000		9486	9581	9715	9890	10106	231
2500		9293	9386	9518	9689	9901	230
3000		9104		9324	9492	9700	229.1

Table 2: Engine Fuel Demand (lb/hr) at ISA -48°C (Boundary Layer Control Disengaged)

Altitude (ft)	Mach Number	0.1	0.15	0.20	0.25	0.3	$t_0$ (K)
0		10398	10503	10650	10608	10413	240
500			10191	10293	10437	10588	239
1000		9986	10086	10228	10412	10640	238
1500		9786	9884	10022	10202	10426	237
2000		9588	9684	9820	9996	10215	236
2500		9394	9488	9621	9794	10008	235
3000		9203	9295	9425	9595	9805	234.1

Table 3: Engine Fuel Demand (lb/hr) at ISA -43°C (Boundary Layer Control Disengaged)

Altitude (ft)	Mach Number	0.1	0.15	0.20	0.25	0.3	$t_0$ (K)
0		10360	10421	10507	10618	10520	245
500		10221	10282	10366	10476	10610	244
1000		10084	10143	10227	10335	10468	243
1500		9888	9987	10089	10196	10327	242

2000		9689	9786	9923	10058	10187	241
2500		9493	9588	9723	9897	10049	240
3000		9301	9394	9525	9697	9909	239.1

Operational procedures specify that 7th stage boundary layer control is always used during takeoff and possible single-engine landings, while 12th stage boundary layer control is used in all other conditions.

As reference data, the maximum fuel flow at  $t_0 = 247$  extK (equivalent to ISA -26°C, as required by the engine specification), sea level, and  $M \square = 0.38$  is 9,475 lb/hr (1,324 gallons/hour).

Tables 1, 2, and 3 provide the engine fuel demand (lb/hr) with boundary layer control disengaged, assuming the use of an A.I.A. inlet.

Table 4: Engine Fuel Demand (lb/hr) with Boundary Layer Control Engaged (Sea Level, A.I.A. Inlet)

$t_0$ (K)	Mach Number	0	0.2	0.38
221.9		10550	10500	11000
240		9325	9400	9820

## 6. Determination of High-Pressure Fuel Pump Output Pressure

Technical Design Report

Document	Report Number
Technical Design Report	TDR3934
Determination of High-Pressure Fuel Pump Output Pressure for Spey MK202	

Issue 3, dated 18 November 1965.

### Objective

To provide a formula for estimating the high-pressure pump output pressure under any flight condition.

### Introduction

To determine the performance of systems using high-pressure fuel as the servo mechanism power source, it is necessary to establish the output pressure values of the high-pressure pump.

### Results

The high-pressure pump output pressure is given by the following formula:

$$P \square = P_3 + 620 - 5.35 \times 10^{-3} F \times 0.79, S.G. + 5.13 \times 10^{-6} F^2 \times 0.79, S.G.,$$

Formula for calculating high-pressure pump output pressure.

Where: -  $P \square$  = High-pressure pump output pressure (psi, absolute) -  $P_3$  = High-pressure compressor outlet pressure (psi, absolute) -  $F$  = Engine fuel flow (lb/hr) - S.G. = Fuel specific gravity

The values of  $F$  and  $P_3$  can be determined based on engine performance data under specific flight conditions.

During sudden acceleration, it can be assumed that the fuel flow exceeds the steady-state fuel flow by 30%.

The high-pressure fuel pump is equipped with a relief valve set at a pressure 1,800 psi higher than the pump's low-pressure side. The maximum low-pressure of the pump is approximately 130 psi.

## Data Assumptions

- Main nozzle flow characteristic number: 55
- Secondary nozzle flow characteristic number: 2.5
- Flow characteristic number with shutdown switch fully open: 240
- Pressure differential through CASC: 620 psi at low flow, 200 psi at 2,600 gallons/hour.

# 7. Flow Requirements for High-Pressure Speed-Cleaning Filter and High-Pressure Fuel Pump

Issue: 2 Date: January 18, 1965

## Technical Design Report

Document Type	Report Number
Technical Design Report	TDR3954
Spey MK202 High-Pressure Speed-Cleaning Filter and High-Pressure Fuel Pump Flow Requirements	

## Abstract

It has been demonstrated that the existing fuel pump's supply capacity exceeds the engine's total fuel demand at maximum operating conditions (i.e., total temperature  $t_0 = 221.9$  K) by only a small margin, as specified in the brochure. When the engine operates at an inlet temperature of 247 K, there is sufficient fuel supply capacity available. The maximum flow rate through the speed-cleaning filter is provided in Table 1 of this report.

## Reasons for Issue 2

1. Revised estimation of the maximum fuel flow extracted by the high-pressure speed-cleaning filter from the fuel pump.
2. Comparison of maximum fuel demand and the fuel pump's supply capacity.
3. Estimated maximum flow rates for all devices, discussed in Section 7.1 of this report.

### 7.1 Summary of High-Pressure Speed-Cleaning Filter Flow

Table 1 lists the flow requirements for the engine's high-pressure speed-cleaning filter. This flow, combined with the fuel supply required by the engine combustion chamber, equals the flow demand for the engine's high-pressure fuel pump.

Table 1: Required Flow Rates for Engine High-Pressure Fuel System (gallons/hour)

	Device	Required Engine High-Pressure Fuel Flow (gallons/hour)	
1	Thermal jet or catalytic igniter	300 (instantaneous)*	
2	V-type afterburner fuel regulator	With afterburner Without afterburner	120* 50*
3	Afterburner nozzle system pressure ratio actuator	250 (instantaneous)* / 120 (steady-state)	
4	Cold-start fuel	136 (only at low fuel pressure)	
5	Low-pressure regulator cooling	20*	

6	N/ $\sqrt{T}$ device and inlet guide vane actuator	70*	
7	Nozzle release valve readjustment piston	Engine speed below 80%	5
		Engine speed above 80%	30*

The flow rates shown in Table 1 do not occur simultaneously. For example, cold-start fuel is not required when afterburner ignition is activated. The most severe combination occurs when these flows are superimposed, which happens during engine acceleration with an assumed fuel pressure of 1500 psi.

The flow rates marked with an asterisk (\*) are summed, as they occur simultaneously during afterburner ignition. Thus, the total additional flow requirement for the high-pressure speed-cleaning filter is 790 gallons/hour.

Since the instantaneous flow rate of the pressure ratio actuator lasts only about one second, only the steady-state flow rate of 120 gallons/hour is considered. Therefore, the total additional flow requirement for the speed-cleaning filter is reduced to 660 gallons/hour.

## 7.2 High-Pressure Fuel Pump Supply Capacity

The maximum engine fuel demand occurs at a high-pressure rotor speed of 11,800 rpm. The selected Lucas fuel pump (66P1001) operates at 0.2318 N□, with a rated flow of 1000 gallons/hour at a pump speed of 1000 rpm. Given the pump's estimated volumetric efficiency of 95%, the pump's output flow rate is 2544 gallons/hour.

## 7.3 Maximum High-Pressure Fuel Demand Including Servo and Leakage Flows

(a) The engine's maximum fuel demand occurs at sea level, with a Mach number M□ of 0.378 and 12-stage boundary layer control activated. This represents the maximum speed at which boundary layer control can be used at a temperature of 221.9 K. For normal operation, the calculated maximum fuel flow is 1540 gallons/hour (11,000 lb/hour at a fuel specific gravity of 0.716), and 1557 gallons/hour for single-engine operation.

(b) At sea level and a temperature of 247 K, the latest calculated maximum fuel demand for normal engine operation is 1310 gallons/hour (9380 lb/hour), and 1324 gallons/hour (9475 lb/hour) for single-engine operation.

In addition to steady-state engine requirements, the pump must also provide:

1. Servo flow and leakage for the fuel pump and C.A.S.C. mechanical devices.
2. Servo flow and leakage for other engine components such as bleed valves, afterburner, and catalytic ignition devices.

Table 2 assumes conditions with 12-stage boundary layer control activated, M□ = 0.378, sea level, wide-cut fuel with a specific gravity of 0.716, and a pump pressure of 1500 psi.

### 7.3.2 Single-Engine Operation – Boundary Layer Control Activated

At  $t_0 = 221.9$  K, the engine's steady-state fuel demand is 1557 gallons/hour. At  $t_0 = 247$  K, it is 1324 gallons/hour. Thus, at a maximum speed of 11,800 rpm, the pump requirements are as follows:

- $t_0 = 221.9$  K, engine acceleration (without afterburner) – 2479 gallons/hour
- $t_0 = 221.9$  K, afterburner – 2364 gallons/hour
- $t_0 = 247$  K, engine acceleration (without afterburner) – 2089 gallons/hour
- $t_0 = 247$  K, afterburner – 2131 gallons/hour

Margin for development and thrust improvement:

- $t_0 = 221.9$  K, engine acceleration (without afterburner) – 65 gallons/hour
- $t_0 = 221.9$  K, afterburner – 180 gallons/hour
- $t_0 = 247$  K, engine acceleration (without afterburner) – 454 gallons/hour
- $t_0 = 247$  K, afterburner – 412 gallons/hour

Table 2: Fuel Flow Rates (gallons/hour)

	Engine Acceleration (Without Afterburner)	Afterburner at Maximum Speed		
Device	$t_0 = 221.9 \text{ K}$	$t_0 = 247 \text{ K}$	$t_0 = 221.9 \text{ K}$	$t_0 = 247 \text{ K}$
Engine steady-state fuel demand	1540	1310	1540	1310
Thermal jet or catalytic igniter	—	—	300	300
Acceleration flow (25% of steady-state demand)	385	328	—	—
C.A.S.C. leakage and cooling flow	160	160	160	160
Afterburner fuel regulator	50	50	120	120
Afterburner nozzle system pressure ratio actuator (steady-state)	120	120	120	120
N/ $\sqrt{T}$ device and inlet guide vane actuator	70	70	70	70
Nozzle release valve readjustment piston	30	30	30	30
Shut-off switch	3	3	3	3
Fuel pump servo mechanism	Included in pump efficiency			
Total	2458	2071	2343	2113
Pump capacity	2544	2544	2544	2544
Margin for development and power improvement	86	473	201	431

## 7.4 Discussion

The engine's total maximum fuel flow requirements in Table 2 and Section 7.3.2 do not include any considerations for development or thrust improvement.

Under the two inlet temperature conditions mentioned above, the pump theoretically meets the requirements with the leakage rates shown in Table 2 (leakage specifications are included in the relevant fuel system specifications). However, under 221.9 K weather conditions, there is only a small margin (65 gallons/hour, which is 4% of the engine's maximum steady-state fuel demand), whereas under 247 K conditions, the margin is 412 gallons/hour.

Wherever possible, leakage should always be minimized.

## 7.5 Impact of Insufficient Fuel Supply on Engine Performance

In all conditions where the fuel pump can meet the engine's maximum fuel demand, the relationship between fuel flow and thrust loss is as follows:

At sea level,  $M_\infty = 0.378$ , with 12-stage boundary layer control and  $t_0 = 221.9$  K, the normal steady-state fuel demand is 1540 gallons/hour, and the net thrust is 13,060 lb. A reduction of 100 gallons/hour in steady-state fuel flow results in a thrust loss of 340 lb.

## 8. Explanation of Afterburner Acceleration Control System Utilizing Engine Main Pump Flow

Issue: 1 Date: January 5, 1966

### Technical Design Report

Document Type	Report Number
Technical Design Report	TDR 4167
Spey MK202 Explanation of Afterburner Acceleration Control Utilizing Engine Main Pump Flow	

## Abstract

To avoid low-pressure compressor surge during afterburner engagement, afterburner acceleration control is required. It is proposed that the existing afterburner high-pressure fuel serves as the servo power source, assuming that higher-pressure engine fuel is available at high altitudes. This report investigates whether the main pump has sufficient capacity to provide 100 gallons/hour of fuel and 5 gallons/hour of steady-state leakage during afterburner engagement.

## Results

For the engine specified in the brochure, the Spey MK202 engine's main fuel pump supply capacity was studied in Report TDR3954. Based on the latest C.A.S.C. leakage data, the capacity at maximum flow during afterburner engagement is as follows:

- (a) 221.9 K, cold day: 161 gallons/hour (10.5% of engine fuel demand).
- (b) 247 K, cold day: 391 gallons/hour (30% of engine fuel demand).

The above data also account for a 200 gallons/hour margin for C.A.S.C. leakage and cooling. This C.A.S.C. design includes an  $N \square T_1$  regulation mechanism.

In the current engine, this regulation mechanism has been phased out. Based on leakage and cooling flow measurements from previous C.A.S.C. designs, a margin of 55 gallons/hour is sufficient for the new C.A.S.C. design's anticipated leakage. Thus, if required, 145 gallons/hour is now available for the Afterburner Acceleration Control Unit (ACU) while maintaining the margins in (a) and (b).

Since the 100 gallons/hour flow demand for the afterburner acceleration control unit during afterburner engagement is only instantaneous, and the continuous leakage of this unit is approximately 5 gallons/hour, fuel extraction from the engine's high-pressure pump can be considered. The low-pressure return line should be located downstream of the flow meter.

Note: Early-manufactured C.A.S.C. units may retain the  $N \square T_1$  mechanism—though non-functional—and such regulators may have leakage up to 200 gallons/hour. In any case, the additional 5 gallons/hour steady-state leakage from the afterburner acceleration control unit will not excessively reduce the pump's supply capacity to the point of losing development and improvement potential.

## 9. Recommendation for Redesign of High-Pressure Pump Servo Piston

	Document Type	Report Number
	Technical Design Report	TDR7357
Spey MK202 Estimation of Servo Pressure Drop – Recommendation to Redesign High-Pressure Pump Servo Piston to Improve AVCAT Fuel Relight Capability		

Issue: 1 Date: December 5, 1969

## Purpose

This section presents the rationale for redesigning the high-pressure pump servo piston to estimate the impact of increased pressure on the afterburner system.

### 9.1 Introduction

Lucas Gas Turbine Equipment Limited has been investigating the possibility of using a newly designed high-pressure pump servo piston to improve AVCAT fuel relight capability. This proposal would increase the required pilot nozzle pressure at low and high speeds while ensuring that the maximum pressure of the existing system is not exceeded.

Estimations have been made of the servo pressure differential versus pump output pressure characteristics for both the existing and redesigned servo pistons.

Based on the additional data provided and referring to engine performance data, the impact of the proposed pressure changes on the afterburner system can be estimated.

## 9.2 Data

### 9.2.1 Pump Outlet Pressure

The pump outlet pressure is given by:

$$P_{\square} = 0.97 P_3 + 5.575 \times 10^{-6} F_{\square}^2 \times 0.79, S.G. + 6$$

Pump outlet pressure formula, where  $P_{\square}$  is the pump outlet pressure,  $P_3$  is the compressor delivery pressure,  $F_{\square}$  is the main nozzle fuel flow, and S.G. is the fuel specific gravity.

Where:

$$F_{\square} = (FB - 500) \text{ assuming a constant pilot nozzle fuel flow} = 500 \text{ lb/hour,}$$

Main nozzle fuel flow formula, where FB is the engine fuel flow.

FB = Engine fuel flow (lb/hour) S.G. = Fuel specific gravity

The estimated servo pressure differential is shown in Figure 1 and Figure 2 of this report.

### 9.2.2 Estimated Servo Pressure Differential vs. Pump Output Pressure Characteristics (See Figures 1 and 2 of this report)

A single operating line for the servo pressure differential versus pump output pressure has been plotted on the Lucas curve. This is approximate and assumes full stroke is reached at  $P_{\square} = 1900$  psi, meaning the pump

pressure  $P_{\square}$  only increases with flow, thus increasing the pump stroke. When afterburner is engaged, the servo pressure differential may tend to fall below the indicated characteristic, depending on aircraft flight conditions and engine speed. In any case, exceeding the indicated characteristic is unlikely.

技术设计报告

TDR 3954

## 斯贝 MK202

### 高压速度清洗过滤器和高压燃油泵的流量要求

Figure 1: Estimated Servo Pressure Differential vs. Pump Output Pressure Characteristics

Graph showing the relationship between servo pressure differential and pump output pressure for the existing and redesigned servo pistons.

技术设计报告

TDR 4167

## 斯贝 MK202

### 加力加速控制利用发动机主泵流量的说明

Figure 2: Estimated Servo Pressure Differential vs. Pump Output Pressure Characteristics

Additional graph showing the relationship between servo pressure differential and pump output pressure for the existing and redesigned servo pistons.

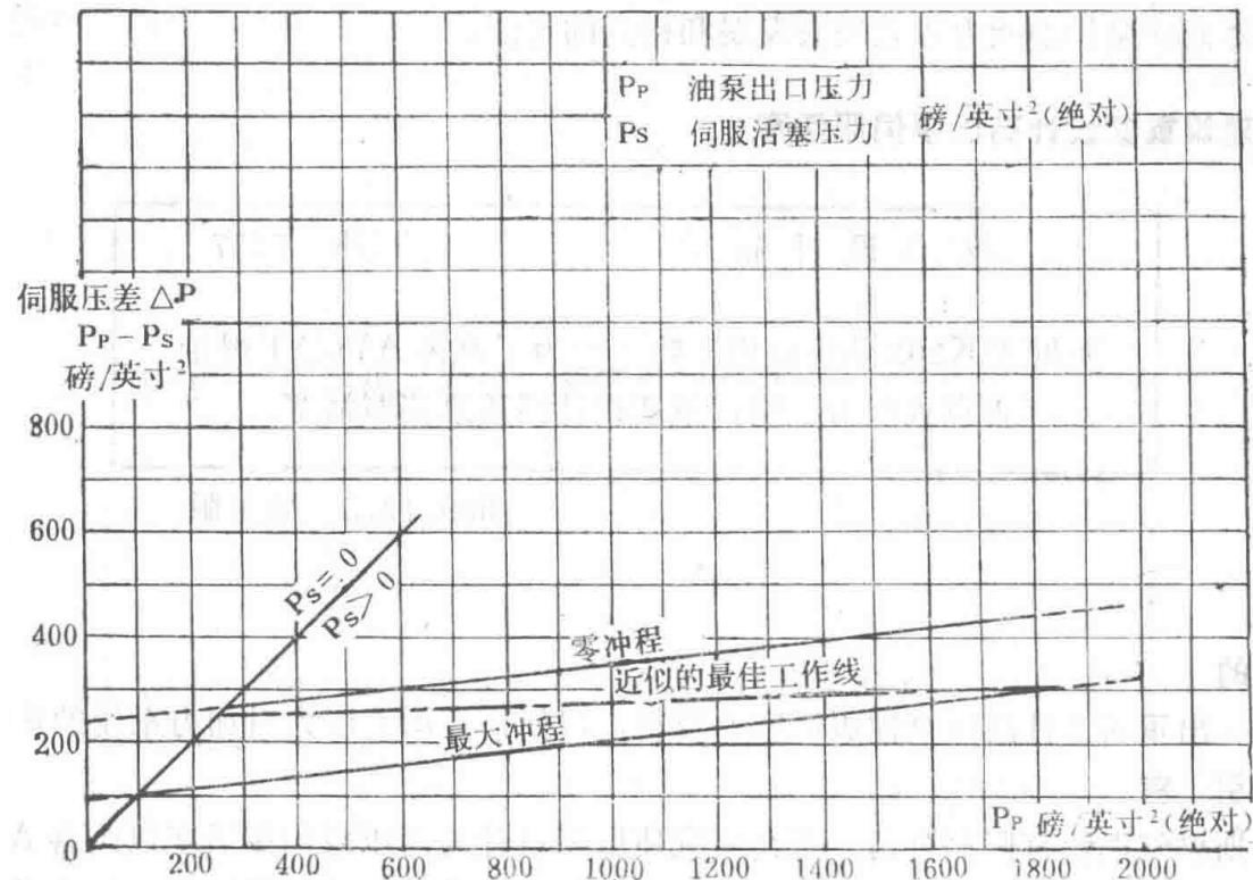


Figure 1 Approximate Estimated Servo Pressure Differential vs. Oil Pump Outlet Pressure Characteristic Curve for Spey MK202 (Existing Oil Pump Servo Piston)

Graph showing the relationship between servo pressure differential and oil pump outlet pressure for the existing servo piston design in the Spey MK202 engine.

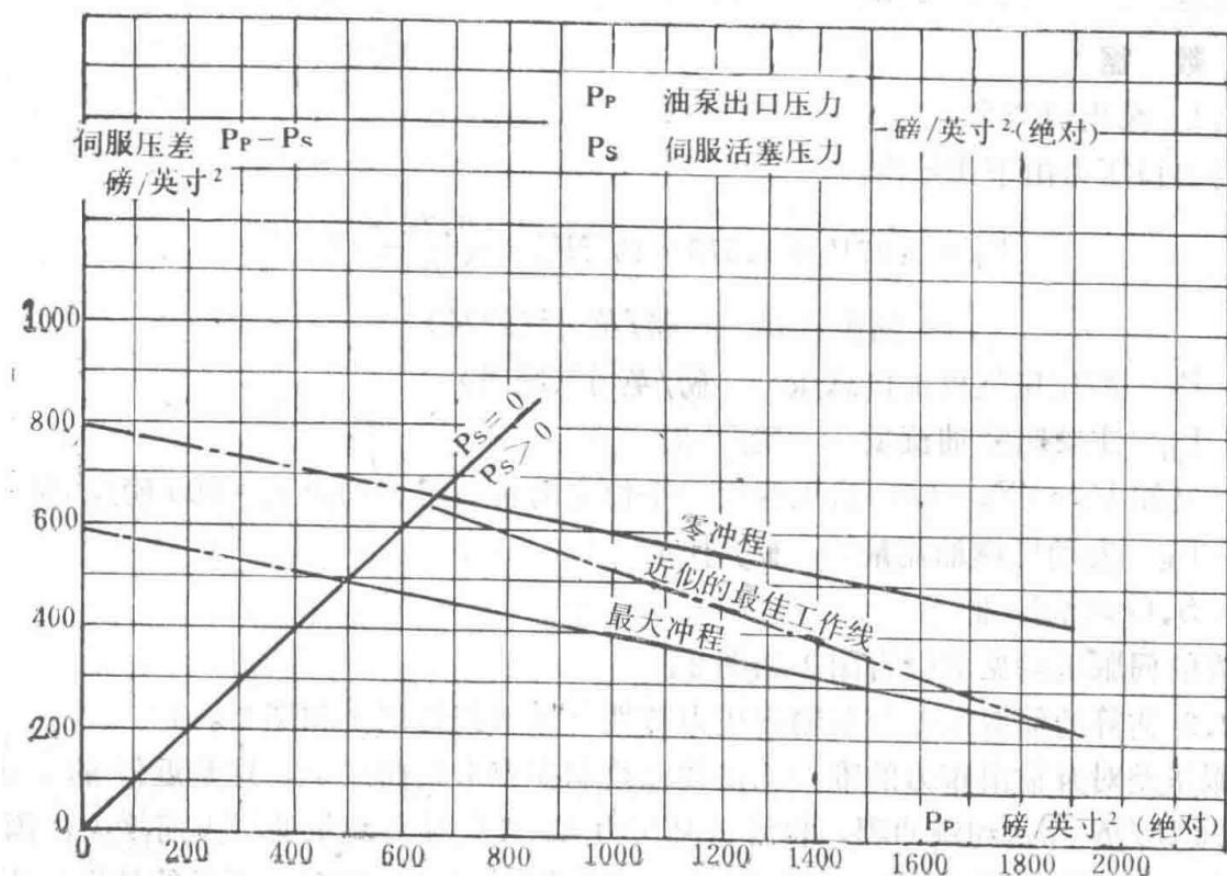


Figure 2 Approximate Estimated Servo Pressure Differential vs. Oil Pump Outlet Pressure Characteristic Curve for Spey MK202 (Recommended Redesigned Servo Piston)

Graph showing the relationship between servo pressure differential and oil pump outlet pressure for the recommended redesigned servo piston in the Spey MK202 engine.

#### Document Header

Document Type	Section
Technical Design Report	TDR7787B Section
	Spey MK202 Fuel Control System - CASC Design Documentation

First Edition, October 27, 1976

## Abstract

This report defines the requirements and design characteristics for CASC and includes technical reports that materialize these requirements.

## 1. Introduction

The fuel control system must determine the appropriate fuel flow for the engine across a wide range of conditions. During start-up, acceleration, and deceleration, the control system must meet engine requirements and enable continuous operation under any flight conditions within the specified flight envelope. Additionally, it must satisfy operational and safety requirements. Specifically, at any time, the pilot must be able to move the throttle lever slowly or rapidly to any position without endangering the engine, and no anticipated failure within the engine control system should pose a hazard to the aircraft.

This report outlines the general requirements for the fuel control system and applies these requirements to the Spey MK202 fuel system. It also includes the rationale for parameter selection, CASC principles and data, and related reference reports.

## 2. Original Technical Requirements for CASC Design

CASC – Combined Acceleration and Speed Control fuel flow regulator, abbreviated as fuel flow regulator.

### 2.1 Description of Requirements

- Control engine speed at all positions of the throttle lever between maximum and minimum.
- Control engine acceleration and deceleration to prevent surge and flameout with boundary layer control engaged or disengaged.
- Limit turbine exhaust temperature within specified ranges via mechanical output from an electrically actuated mechanism.
- Limit high-pressure compressor outlet pressure to a specified value.
- Limit the maximum speed of the high-pressure shaft.
- Limit the maximum fuel flow of the engine (related to high-pressure shaft speed) to a specified value.
- Supply the required fuel flow to the engine at the necessary pressure.
- Provide appropriate fuel atomization at the nozzles.
- Limit the high-pressure compressor outlet temperature to a specified value via mechanical output from an electrically actuated mechanism.
- Limit the maximum value of  $N \square / \sqrt{T_1}$  (for early production engines, this is achieved by setting appropriate  $T_e$  control curves).

### 2.2 Engine Description

The engine is a twin-spool, bypass-type engine designed as a powerplant for military aircraft. It is generally installed horizontally and features an afterburning system and variable geometry exhaust nozzle.

### 2.3 Atmospheric Conditions

The range of environmental atmospheric conditions considered in the engine design is represented on an atmospheric temperature scale chart applicable to this engine type.

### 2.4 Aircraft Operating Conditions

Flight Envelope

The engine's operating conditions, defined in terms of altitude vs. Mach number curves, are represented on an appropriate "Design-Limited Flight Envelope."

### 2.5 Engine Performance Curves

The dimensional and non-dimensional parameter curves of the engine are listed as follows: Curves in Figures 1 to 11 can be found in the "Original Technical Requirements" for the high-pressure fuel pump (TDR7787A Section, Chapter 2). The remaining curves are provided in this section. These curves closely approximate the performance of early production engines.

- Figure 1 Engine Fuel Flow  $N \square / \sqrt{T_1}$ , without afterburner and at low engine speed.
- Figure 2 Engine Fuel Flow  $N \square / \sqrt{T_1}$ , without afterburner and at high engine speed.
- Figure 3 Engine Fuel Flow  $N \square / \sqrt{T_1}$ , without afterburner and with supercritical nozzle.

- Figure 4 Engine Fuel Flow  $N \cdot \sqrt{T_1}$ , with afterburner.
- Figure 5 Engine Fuel Flow Correction Coefficient  $\alpha \cdot F' / \sqrt{P_1}$ .
- Figure 6 High-Pressure Compressor Outlet Pressure  $N \cdot \sqrt{T_1}$ , without afterburner,  $T_1 \leq 288$ , and at low engine speed.
- Figure 7 High-Pressure Compressor Outlet Pressure  $N \cdot \sqrt{T_1}$ , without afterburner and at high engine speed.
- Figure 8 Low-Pressure Compressor Outlet Pressure  $N \cdot \sqrt{T_1}$ , without afterburner,  $T_1 \leq 288$ , and at low engine speed.
- Figure 9 Low-Pressure Compressor Outlet Pressure  $N \cdot \sqrt{T_1}$ , without afterburner and at high engine speed.
- Figure 10 High-Pressure Compressor Outlet Pressure  $N \cdot \sqrt{T_1}$ , with afterburner.
- Figure 11 Low-Pressure Compressor Outlet Pressure  $N \cdot \sqrt{T_1}$ , with afterburner.
- Figure 12  $P_1 / P_0$  M Number.
- Figure 13  $T_1 / T_0$  M Number.
- Figure 14 Total Thrust High-Pressure Shaft Speed.
- Figure 15 Effects of Bleed Air and Power Extraction  $N \cdot \sqrt{T_1}$ .
- Figure 16 Effect of 7th Stage Bleed on  $F / P_1 \sqrt{T_1}$   $N \cdot \sqrt{T_1}$ .
- Figure 17 Effect of 7th Stage Bleed on  $P_2 / P_1 \sqrt{T_1}$ .
- Figure 18 Effect of 7th Stage Bleed on  $P_3 / P_1 \sqrt{T_1}$ .
- Figure 19 Effect of 12th Stage Bleed on  $F / P_1 \sqrt{T_1}$   $N \cdot \sqrt{T_1}$ .
- Figure 20 Effect of 12th Stage Bleed on  $P_2 / P_1 \sqrt{T_1}$ .
- Figure 21 Effect of 12th Stage Bleed on  $P_3 / P_1 \sqrt{T_1}$ .

## Symbol Table

Symbol	Description	Unit
$P_0$	Ambient Pressure	psi (absolute)
$P_1$	Low-Pressure Compressor Inlet Total Pressure	psi <sup>2</sup> (absolute)
$P_2$	Low-Pressure Compressor Outlet Total Pressure	psi (absolute)
$P_3$	High-Pressure Compressor Outlet Total Pressure	psi <sup>2</sup> (absolute)
$p_3$	High-Pressure Compressor Outlet Static Pressure	psi (absolute)
$t_0$	Ambient Temperature	K
$T_1$	Low-Pressure Compressor Inlet Total Temperature	K
$T_2$	Low-Pressure Compressor Outlet Total Temperature	°K
$T_3$	High-Pressure Compressor Outlet Total Temperature	°K
$T_6$	Low-Pressure Turbine Outlet Total Temperature	°K
$R_{01}$	Inlet Ram Ratio $R_{01} = P_1 / P_0$	
$F_e$	Actual Engine Fuel Flow	lb/hr
$F_e'$	Ideal Engine Fuel Flow	lb/hr

$\alpha$	Fuel Flow Correction Coefficient $\alpha = F / F'$	
$N$	High-Pressure Compressor Speed	rpm
$N$	Low-Pressure Compressor Speed	rpm
SHP	Extracted Power	horsepower
$M$	12th Stage Bleed Air Flow	lb/sec
$Ms_7$	7th Stage Bleed Air Flow	lb/sec
MD	Boundary Layer Control Bleed Air Flow	lb/sec
TD	Boundary Layer Control Bleed Port Total Temperature	$^{\circ}\text{K}$
PD	Boundary Layer Control Bleed Port Total Pressure	psi <sup>2</sup> (absolute)

## 2.6 Engine Maximum Operating Conditions

The engine's maximum operating conditions are typically controlled as follows:

### 2.6.1 Takeoff Condition

During takeoff, the high-pressure shaft speed regulator should operate normally.

When boundary layer control is used, the combustion chamber temperature is limited by the maximum temperature controller. This controller adjusts the high-pressure shaft full-range speed regulator to prevent the exhaust nozzle temperature from exceeding the limits specified in the amplifier's "Original Technical Requirements" diagram. Refer to Section 2 of TDR7787C.

### 2.6.2 Entire Flight Conditions

The high-pressure compressor outlet pressure and temperature limiters can also reduce engine speed (see Sections 2.7.2 and 2.7.3, respectively).

## 2.7 Fuel System Components

### 2.7.1 High-Pressure Shaft Full-Range Speed Regulator

For early production engines, the maximum high-pressure shaft speed is limited to 12,577 rpm to allow for future increases. When the inlet total temperature is between 244 $^{\circ}\text{K}$  and 340 $^{\circ}\text{K}$ , the regulator must control the speed within  $\pm 1/4\%$  of the maximum high-pressure shaft speed. Below 244 $^{\circ}\text{K}$  and above 340 $^{\circ}\text{K}$ , in addition to the above tolerance, the variation must not exceed  $\pm 1/2\%$  of the maximum regulated high-pressure shaft speed.

In addition to the above tolerances, the effects of fuel and fuel temperature variations on the maximum high-pressure shaft speed, as specified in Section 2.13, must not exceed  $\pm 1/4\%$  of the maximum speed.

Under standard atmospheric conditions at sea level, the high-pressure shaft ground idle speed is 6,500 rpm. Below 11,600 rpm, the allowable variation increases to  $+1/2\%$  of the maximum speed. Regardless of the engine's state, the control accuracy of the maximum high-pressure shaft speed must be achieved.

To maintain suitable engine oil temperature at  $M = 0.8$ , 45,000 feet, and hot weather conditions ( $\Delta t_o = 233^{\circ}\text{K}$ ), the minimum high-pressure shaft idle speed required is 10,400 rpm.

## 2.7.2 High-Pressure Compressor Outlet Pressure

To limit the high-pressure compressor outlet static pressure to 330 psi (gauge), the fuel system includes a pressure limiter. When the limiter is fully engaged, the pressure variation should not exceed  $\pm 1$  psi. During the transition between the high-pressure shaft speed regulator and the  $P_3$  limiter, the high-pressure compressor outlet pressure variation should not exceed  $\pm$  psi. The limiter should be easily adjustable within a range of  $\pm 35$  psi.

This device must be capable of resetting the high-pressure compressor outlet static pressure limit to 150 psi to allow for adjustments on the engine under hot and high-altitude operating conditions. Upon removal of the reset, the limiter should revert to its original setting and maintain the aforementioned accuracy.

High-pressure compressor outlet static pressure =  $0.97 \times$  high-pressure compressor outlet total pressure.

The maximum temperature of the high-pressure compressor outlet air supplied to this device is 350°C.

## 2.7.3 High-Pressure Compressor Outlet Temperature

The maximum high-pressure compressor outlet temperature is required to be controlled at  $806^{\circ}\text{K} \pm 3^{\circ}\text{K}$ . This control is achieved by the amplifier transmitting the  $T_3$  signal to operate the actuator (as described in Section 2.7.1) to adjust the high-pressure shaft full-range speed regulator. This adjustment should reduce the engine's high-pressure speed to a maximum of 11,320 rpm, with a mechanical stop pin preventing any further reduction. This stop pin is adjustable and can be set to any minimum speed between 11,200 and 12,200 rpm.

## 2.7.4 Low-Pressure Shaft Speed Regulator

The low-pressure shaft speed regulator is a safety device that does not limit the high-pressure shaft speed during normal operation.

## 2.7.5 Turbine Exhaust Temperature Limiter

The turbine exhaust temperature ( $T_6$ ) should be limited according to the program specified in the amplifier's "Original Technical Requirements." Refer to Section 2 of TDR7787C. The limiter receives the  $T_6$  expected value voltage error signal from the amplifier and controls the engine's high-pressure shaft speed as described in Section 2.7.3.

## 2.7.6 F/N Limitation

In the event of a failure in the compressor outlet pressure limiter, the fuel system is required to limit the fuel flow corresponding to the engine's high-pressure shaft speed.

This value should be easily adjustable within the range of 0.79 to 1.99.

## 2.7.7 Low-Pressure Compressor Surge Limitation

To avoid low-pressure compressor surge, it is necessary to limit the maximum value of  $N\sqrt{\Delta P} / \sqrt{T_1}$ . Early production engines achieved this by using an amplifier to control  $T_6 / T_1$  at  $T_6 / T_1 = 3.79$ . Later engines can control this by maintaining  $P_3 / P_2$  constant using a pneumatic method via a readjusted CASC bellows  $P_3 / P_2$  switch.

## 2.7.8 Flow Control Device

The 008 design of this device aims to meet the engine's required flow characteristics as specified in Section 2.5 within the high-pressure shaft speed range given in Section 2.7.1, while being influenced by environmental conditions (Section 2.6), flight envelope (Section 2.4), compressor outlet pressure (Section 2.7.2), compressor outlet temperature (Section 2.7.3), and turbine exhaust temperature (Section 2.7.5).

For a given rotational speed, bleed air extraction and power offtake alter the engine's required flow characteristics.

Maximum bleed air and power extraction are as follows:

## Aircraft Control Bleed

- Stage 12 bleed – 17.3 lb/sec at maximum power, sea level static, and  $t_0 = +50^\circ\text{C}$ .
- Stage 7 bleed – 6.25 lb/sec at maximum afterburner, sea level, 140 knots/hour, and  $t_0 = \text{standard atmosphere} +25^\circ\text{C}$ .

## Cabin and Auxiliary Equipment Cooling

- Stage 12 bleed – 1.083 lb/sec under International Standard Atmosphere (ISA) and sea level cruise conditions.
- Stage 7 bleed – 1.05 lb/sec at maximum power and maximum flight speed.

## Power Requirements

- Hydraulic pump: 48 horsepower.
- Constant speed drive: 48 horsepower continuous, 72 horsepower for 5 minutes, 96 horsepower for 5 seconds.

For cold starts, measures must be taken to increase idle flow, which is achieved by selecting a switch and setting a fuel bypass on the C.A.S.C.

When the engine is in the following state: boundary layer control bleed equals 16% of the high-pressure compressor mass flow, sea level  $M_\infty = 0.378$ , ambient temperature  $221.9^\circ\text{C}$ , and high-pressure compressor speed equals 11,800 rpm, the engine requires a maximum fuel flow of 11,120 lb/hour. The estimated pump inlet temperature at this condition is 60%, and the corresponding fuel specific gravity is 0.716.

### 2.7.9 High-Pressure Fuel Pump

Requirements for the high-pressure fuel pump are included in section TDR7787A. The pressure relief valve is adjusted to open at an inlet pressure above 1,800 lb/in<sup>2</sup>. The maximum low-pressure fuel pressures are:

- Steady-state operation: (1) 130 lb/in<sup>2</sup> (gauge) at  $+120^\circ\text{C}$ , (2) 90 lb/in<sup>2</sup> (gauge) at  $+135^\circ\text{C}$ .
- Transient: 180 lb/in<sup>2</sup> (gauge) at  $+120^\circ\text{C}$ .

### 2.7.10 Acceleration and Deceleration Control

The fuel system must protect the engine from surge during acceleration and from flameout during deceleration. Within the flight envelope (Section 2.4), using any fuel specified in Section 2.13, at any temperature and altitude, rapid movement of the power lever in either direction should not cause any abnormal engine operation.

Section 2.17 provides appropriate rich and lean fuel characteristics at sea level static, 41,000 feet  $M_\infty = 0.86$ , and 68,000 feet  $M_\infty = 2.0$  under International Standard Atmosphere conditions.

When boundary layer control is selected, the acceleration control device requires readjustment. The readjustment pressure is provided by the high-pressure compressor outlet pressure signal, with a minimum signal pressure of 30 lb/in<sup>2</sup> (gauge) for the readjustment device to operate. Section 2.17.3.3 also provides rich fuel characteristics when boundary layer control is engaged.

For International Standard Atmosphere sea level static conditions, concerning only the high-pressure compressor pressure ratio, the readjustment range should be easily adjustable between 115% to 190% of the

steady-state operating line (no bleed).

For International Standard Atmosphere sea level static conditions, the dimensionless quantity  $F / P_2 N$  for rich and lean fuel characteristics requires the following adjustment range:

- Acceleration control device rich fuel characteristic: 115% to 144% of the steady-state operating line at standard atmosphere sea level static conditions.
- Deceleration control device lean fuel characteristic: 50% to 70% of the steady-state operating line at International Standard Atmosphere sea level static conditions.

## 2.8 Throttle Lever Angle Characteristics

Under International Standard Atmosphere sea level static conditions, above a high-pressure shaft speed of 10,500 rpm, the relationship between thrust and CASC throttle lever angle should be essentially linear. Figure 14 shows the total thrust versus engine speed curve under International Standard Atmosphere sea level static conditions. The CASC throttle lever travel from idle to maximum should be  $58^\circ$ , with an idle dead zone of  $3^\circ \pm 1^\circ$ .

$P_3$ 磅/英寸 <sup>2</sup> (绝对)	$P_2$ 磅/英寸 <sup>2</sup> (绝对)	$N_c$ 转/分	流量 加仑/小时
51	10.7	3520	215~240
63	12.1	3650	255~290
74	12.3 *	3790	325 —
83	14.3	3920	375 —
91	15	4050	450 —
97	15.7	4190	500 —

Figure 14: Total Thrust vs. Engine Speed under International Standard Atmosphere Sea Level Static Conditions

Graph depicting the relationship between total thrust and engine rotational speed at sea level static conditions.

## 2.9 Power Lever Torque

The torque required to operate the power lever should not exceed 12 lb·in.

## 2.10 Nozzle

The nozzle is designed to work with a dual-circuit nozzle system having the following flow characteristic numbers:

- Total secondary nozzle flow characteristic number = 2.5.
- Total primary nozzle flow characteristic number = 55.

In subsequent developmental tests, the nozzle flow characteristic number may vary within the range of 50 to 60.

Flow characteristic number = Fuel flow (lb/hr),  $\sqrt{(}$ Pressure differential across nozzle (lb/in<sup>2</sup>) $)$ ,

Equation defining the flow characteristic number for the nozzle, with fuel specific gravity of 0.79.

A device must be included in the fuel control unit to ensure that the primary nozzle does not open until the secondary nozzle pressure reaches 300 lb/in<sup>2</sup> (Note: This value was later changed to 600 lb/in<sup>2</sup>).

## 2.11 Stability

Control throughout the engine operating range should be stable according to the following technical standards:

1. Under steady-state operating conditions, there should be no regular oscillations exceeding 0.1% of the maximum high-pressure shaft speed or irregular variations exceeding 0.2% of the maximum engine speed (peak-to-peak value).
2. When relevant limiters are engaged, the maximum overshoot should not exceed 1.13% of the maximum high-pressure shaft speed.

It should be noted that air contained within the engine control system should not impair control stability; otherwise, the system must automatically bleed air until stable operation is achieved.

## 2.12 Filtration

A low-pressure filter is installed upstream of the fuel pump. The filter has the following characteristics:

1. Filters out at least 95% of particles 10 microns or larger.
2. The maximum particle size passing through the filter does not exceed 40 microns.

## 2.13 Fuel

The control unit is designed to operate with any of the following fuels:

- AVTUR JP-1
- AVTAG JP-4
- AVCAT JP-5

The fuel may or may not contain 0.1% to 0.15% (by volume) of anti-icing additive.

The fuel temperature range at the control unit inlet is -40°C to +135°C.

## 2.14 Operation During Catapult Takeoff

During catapult takeoff, longitudinal acceleration can reach 5g. Under engine attitudes ranging from horizontal to 30° nose-up, the control unit must operate satisfactorily and ensure no thrust fluctuations.

During catapult takeoff and arrested landing, if the throttle lever is abruptly opened or closed, the control unit should ensure normal engine acceleration or deceleration.

## 2.15 Fuel Contamination

The control unit is designed to operate without failure using fuels specified in Section 2.13 that meet relevant British standards for contamination. However, endurance tests may be conducted according to standards mutually agreed upon by Rolls-Royce and the customer based on specific applications. Fuel may also be contaminated by seawater.

## 2.16 Gear Ratio

Regulator speed (Nc) = 0.3323 times engine high-pressure shaft speed.

## 2.17 Calibration of Acceleration and Deceleration Control Devices under International Standard Atmosphere Sea Level Static Conditions

### 2.17.1 Calibration of Acceleration Control Device at Sea Level Static Conditions

The acceleration control device should be calibrated according to the following data:

Calibration Data for Acceleration Control Device at Sea Level Static Conditions

$P_3$ (lb/in <sup>2</sup> absolute)	$P_2$ (lb/in <sup>2</sup> absolute)	Nc (rpm)	Flow (gallons/hour)
32.6	15.6	2160	170~205
52	17.1	2820	250~295
68	18.7	3320	330~375
105	23.4	3500	470~525
155	29.5	3720	695~760
207	35.8	3950	1000~1105
267	43.0	4200	1440~1500

Record the cooling flow at  $P_3 = 267$  lb/in<sup>2</sup> (absolute) and  $P_2 = 43$  lb/in<sup>2</sup> (absolute). It should not exceed 200 gallons/hour.

At  $P_3 = 267$  lb/in<sup>2</sup> (absolute), the flow can be adjusted upward to 480 gallons/hour and downward to 1350 gallons/hour.

Record the high-altitude idle flow at the fully closed position and at 3 and 6 turns outward from this position.

### 2.17.2 Calibration of Deceleration Control Device at Sea Level Static Conditions

Calibration Data for Deceleration Control Device at Sea Level Static Conditions

$P_3$ (lb/in <sup>2</sup> absolute)	$P_2$ (lb/in <sup>2</sup> absolute)	Nc (rpm)	Flow (gallons/hour)
32.6	15.6	2160	60~90
52	17.1	2820	90~125
68	18.7	3320	110~160
105	23.4	3500	160~205
155	29.5	3720	235~285
207	35.8	3950	335~420
267	43.0	4200	450~560

### 2.17.3 Calibration of Acceleration and Deceleration Control Devices at 41,000 Feet, $M\Delta = 0.86$

#### 2.17.3.1 Calibration of Acceleration Control Device at 41,000 Feet

Calibration Data for Acceleration Control Device at 41,000 Feet,  $M\Delta = 0.86$

$P_3$ (lb/in <sup>2</sup> absolute)	$P_2$ (lb/in <sup>2</sup> absolute)	Nc (rpm)	Flow (gallons/hour)
51	10.7	3520	215~240
63	12.1	3650	255~290
74	13.3	3790	325~
83	14.3	3920	375~
91	15.0	4050	450
97	15.7	4190	500

### 2.17.3.2 Calibration of Deceleration Control Device at 41,000 Feet

Calibration Data for Deceleration Control Device at 41,000 Feet,  $M\Delta = 0.86$

$P_3$ (lb/in <sup>2</sup> absolute)	$P_2$ (lb/in <sup>2</sup> absolute)	Nc (rpm)	Flow (gallons/hour)
51	10.7	3520	80~137
63	12.1	3650	95~140
74	13.3	3790	110~165
83	14.3	3920	130~190
91	15.0	4050	150~215
97	15.7	4190	165~235

### 2.17.3.3 Calibration with Boundary Layer Control Readjustment

Adding 30 lb/in<sup>2</sup> (gauge) air to the boundary layer control connection, the acceleration control curve at sea level static conditions must meet the following requirements:

Calibration Data with Boundary Layer Control Readjustment at Sea Level Static Conditions

$P_3$ (lb/in <sup>2</sup> absolute)	$P_2$ (lb/in <sup>2</sup> absolute)	Nc (rpm)	Flow (gallons/hour) Min	Flow (gallons/hour) Max
155	29.5	3720	910	1080
190	33.7	3870	1190	1250
207	35.8	3950	1340	1400

### 2.17.4 Calibration of Acceleration and Deceleration Control Devices at 68,000 Feet, $M\Delta = 2.0$

#### 2.17.4.1 Calibration of Acceleration Control Device at 68,000 Feet

Calibration Data for Acceleration Control Device at 68,000 Feet,  $M\Delta = 2.0$

$P_3$ (lb/in <sup>2</sup> absolute)	$P_2$ (lb/in <sup>2</sup> absolute)	Nc (rpm)	Flow (gallons/hour) Min	Flow (gallons/hour) Max
20	3.8	3650	96	137
24	4.1	3790	106	148
26	4.4	3920	113	157
29	4.55	4050	123	170
31	4.8	4190	133	180

#### 2.17.4.2 Calibration of Deceleration Control Device at 68,000 Feet

Calibration Data for Deceleration Control Device at 68,000 Feet,  $M\Delta = 2.0$

$P_3$ (lb/in <sup>2</sup> absolute)	$P_2$ (lb/in <sup>2</sup> absolute)	Nc (rpm)	Flow (gallons/hour)
20	3.8	3650	Nominal value – record

24	4.1	3790	Record
26	4.4	3920	Record
29	4.55	4050	Record
31	4.8	4190	Record

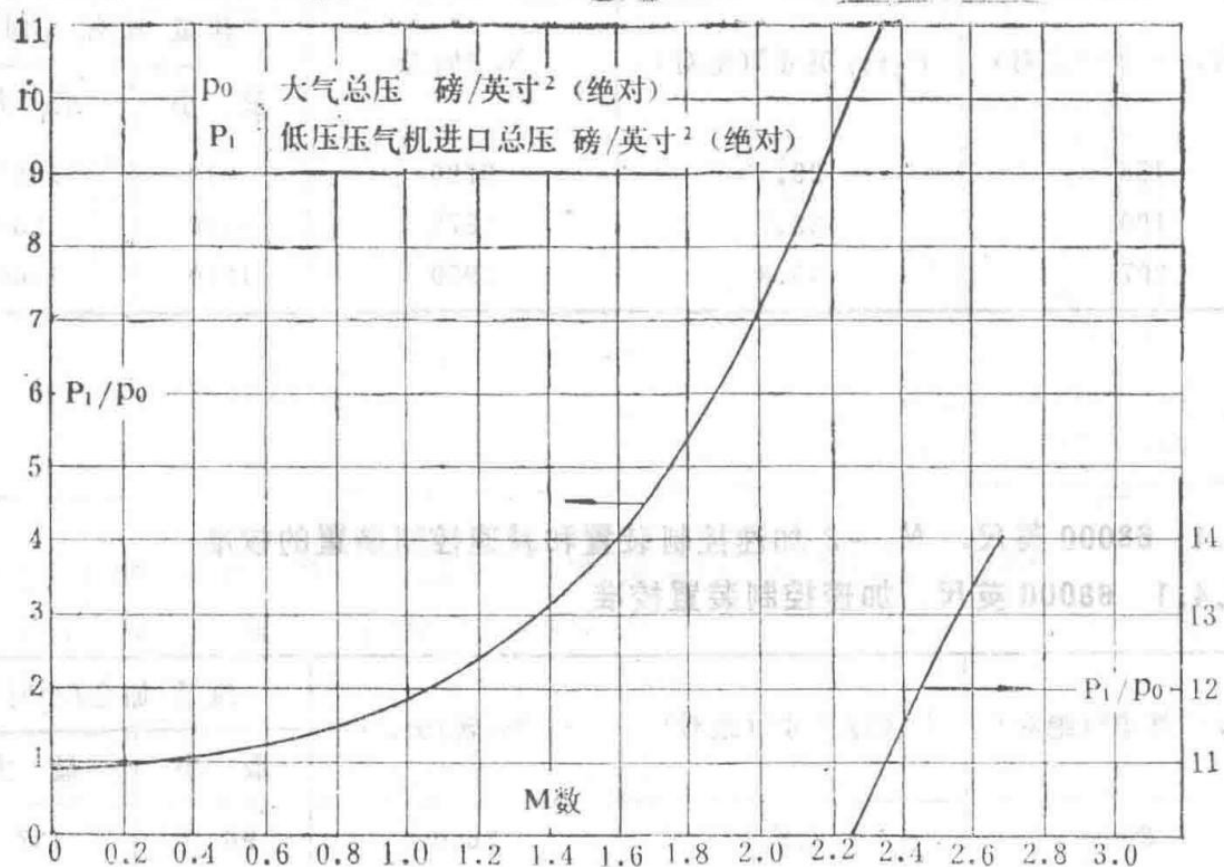


Figure 12 Engine Inlet Pressure Ratio

Graph showing the relationship between engine inlet pressure ratio ( $P_2/P_1$ ) and high-pressure shaft speed parameter ( $N\sqrt{\rho}/T_1$ ) under 12-stage maximum air extraction condition.

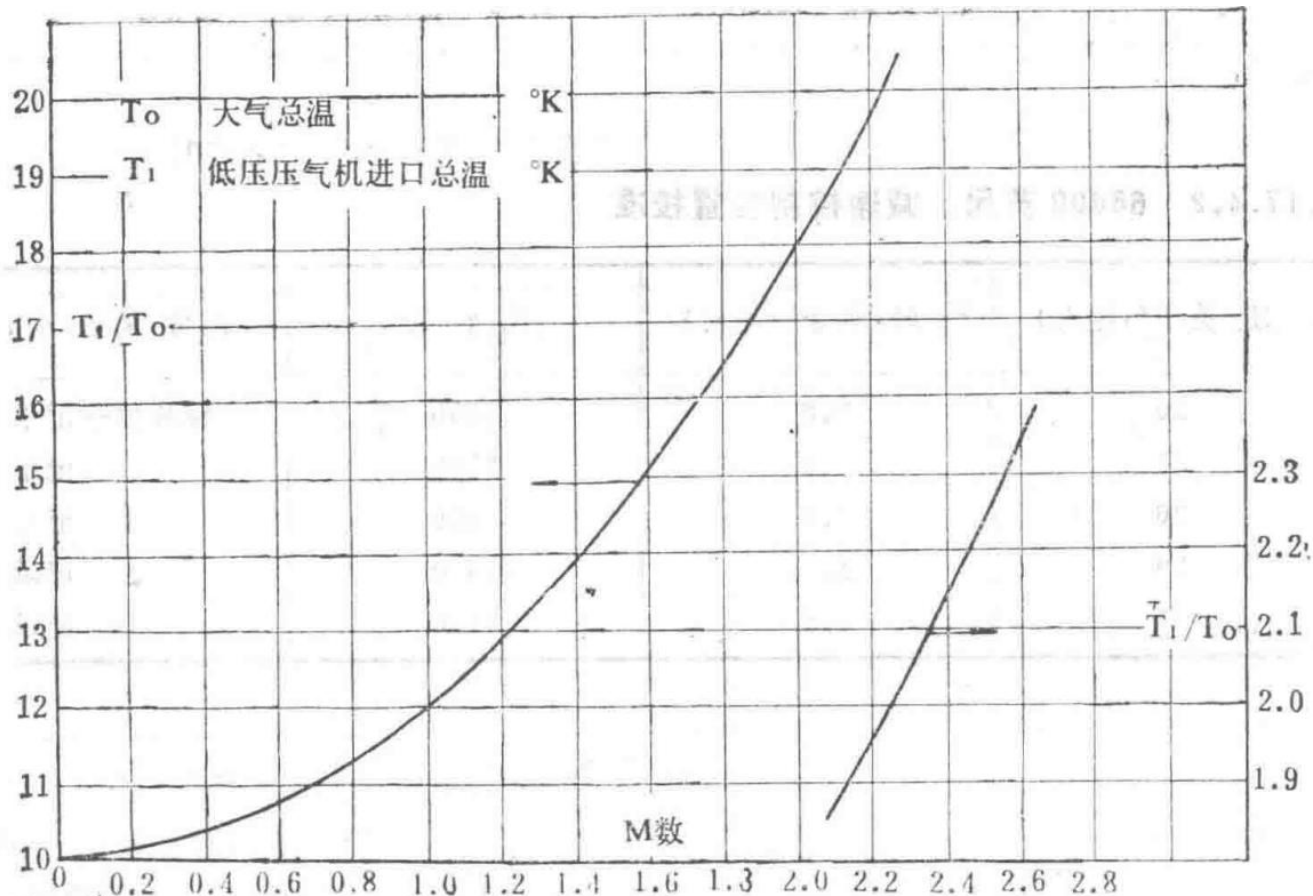


Figure 13 Engine Inlet Temperature Ratio

Graph depicting the effects of high-pressure compressor air extraction, 7th-stage air extraction, and power extraction on the relationship between corrected thrust ( $\Delta F_c$ ) and high-pressure shaft speed parameter ( $N \square / \sqrt{T_1}$ ).

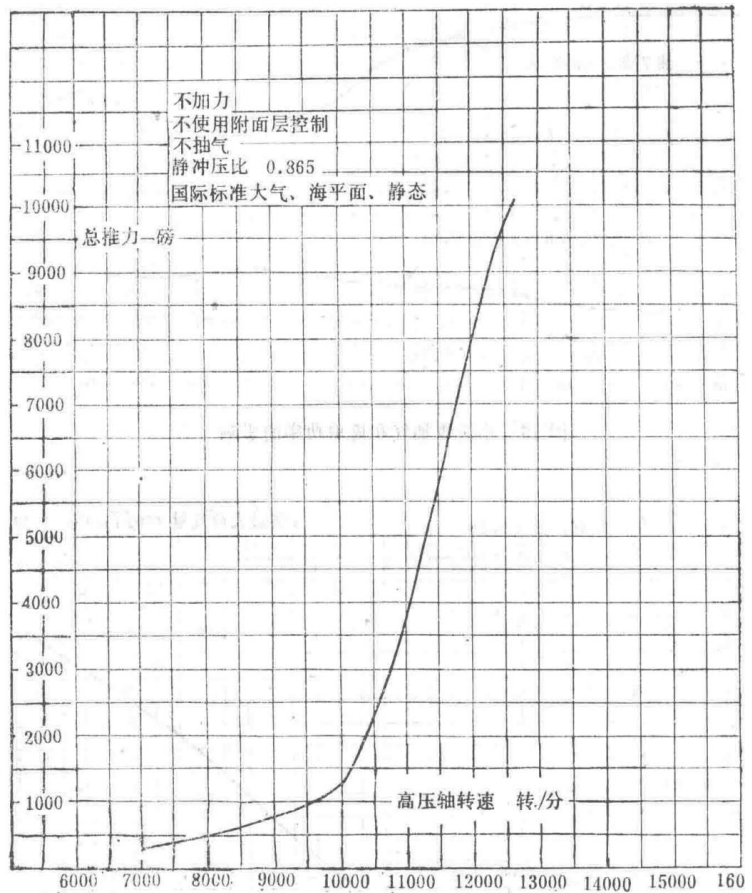


Figure 14 Relationship Between Thrust and High-Pressure Shaft Speed

Graph showing the relationship between thrust and high-pressure shaft speed under standard atmospheric conditions (International Standard Atmosphere, sea level, static).

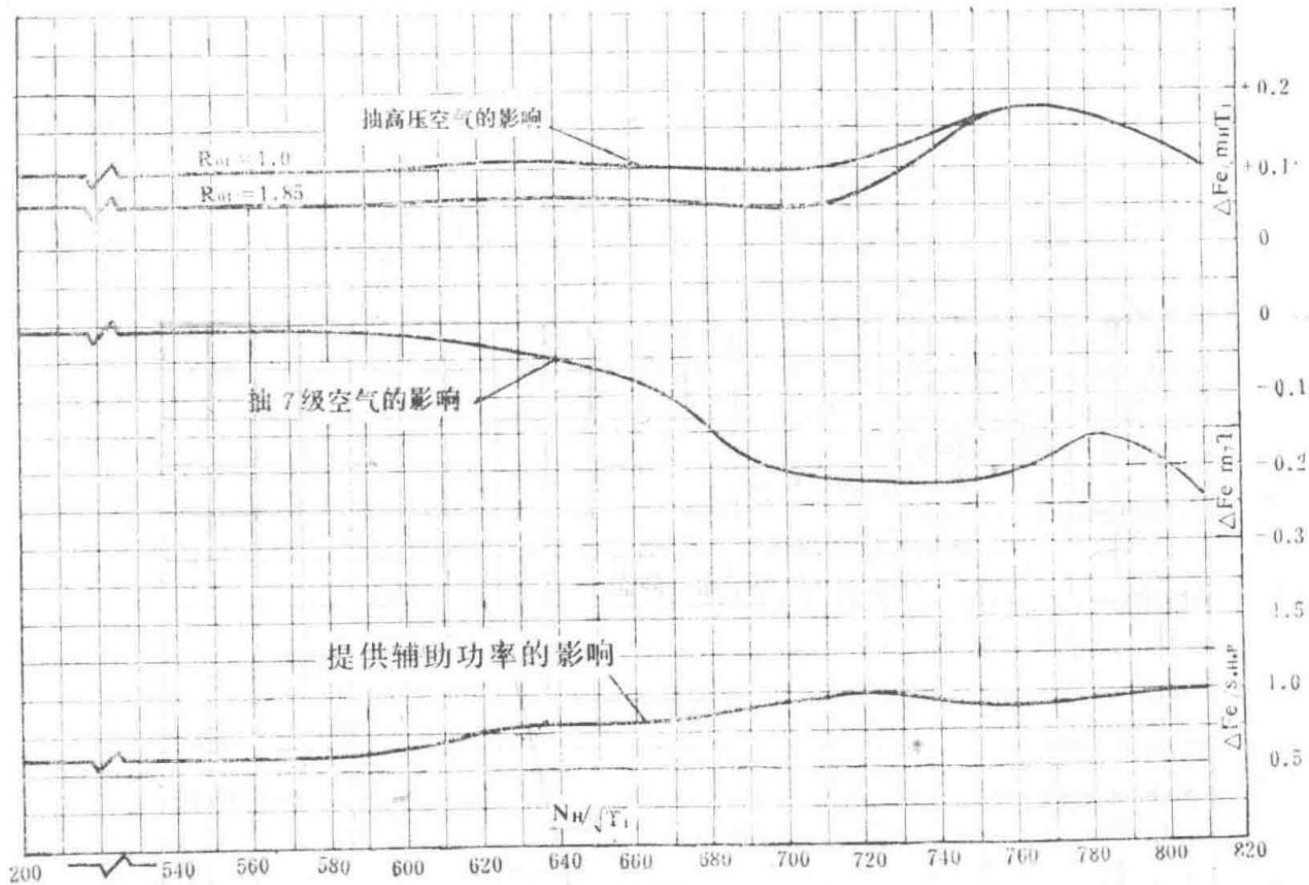


Figure 15 Effects of Low-Flow Air Bleed and Power Extraction

Graph illustrating the impact of low-flow air bleed and power extraction on engine performance parameters.

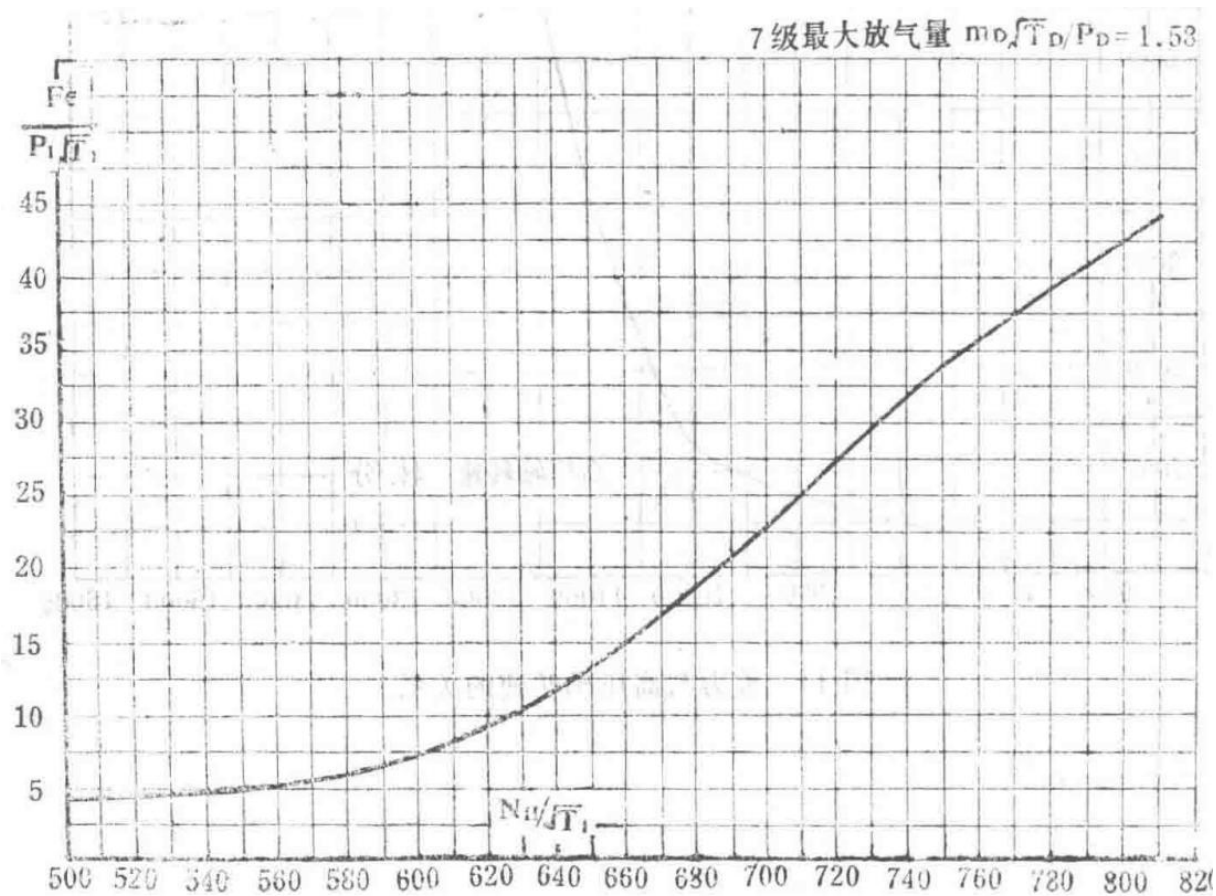


Figure 16 Effect of 7th-Stage Air Bleed on PT and N $\square$  Relationship

Graph showing the effect of 7th-stage air bleed on the relationship between turbine pressure ratio (PT) and high-pressure shaft speed parameter ( $N\square/\sqrt{T_1}$ ).

$$P_2, P_1 \text{ vs. } N\square, \sqrt{T_1},$$

Relationship between pressure ratio ( $P_2/P_1$ ) and high-pressure shaft speed parameter ( $N\square/\sqrt{T_1}$ ).

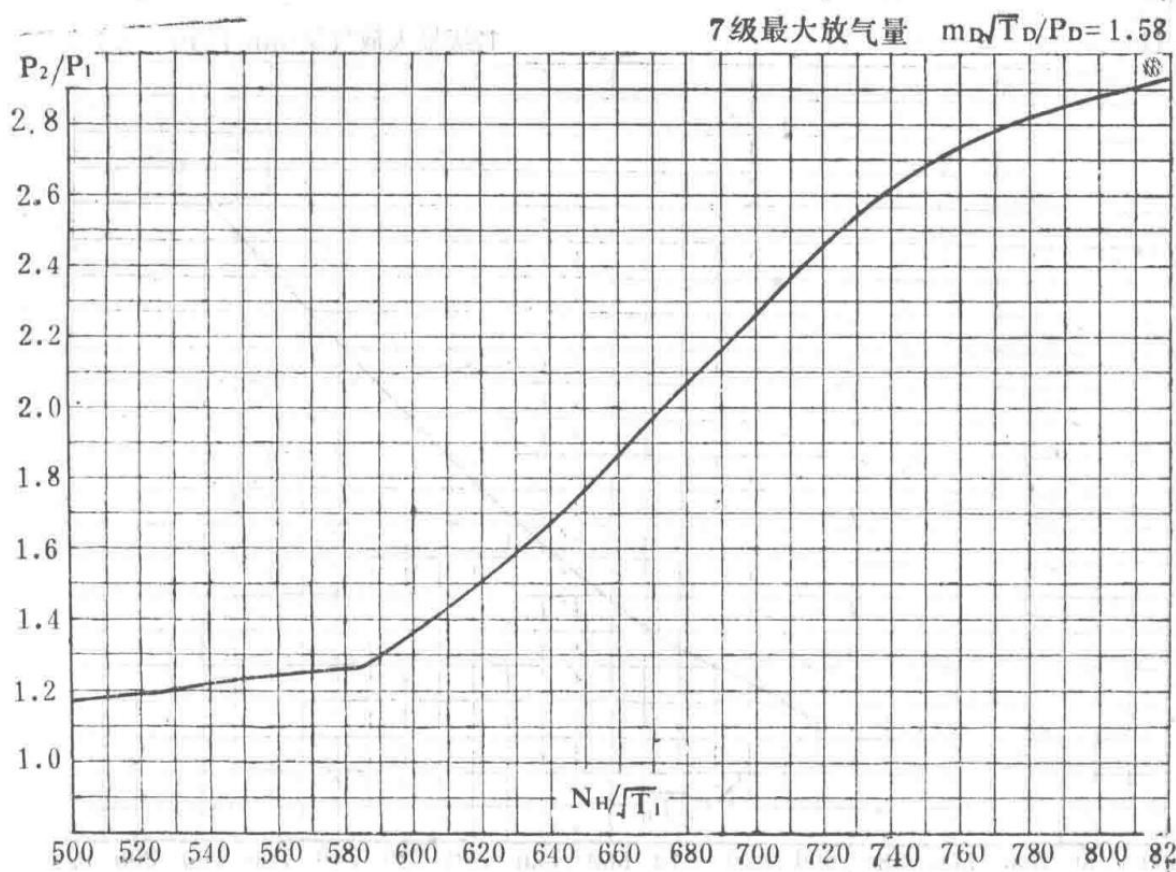


Figure 17 Effect of 7th-Stage Air Bleed on  $P_2/P_1$  vs.  $N\square/\sqrt{T_1}$  Relationship

Graph showing the effect of 7th-stage air bleed on the relationship between pressure ratio ( $P_2/P_1$ ) and high-pressure shaft speed parameter ( $N\square/\sqrt{T_1}$ ).

$$P_2, P_1 \text{ vs. } N\square, \sqrt{T_1},$$

Relationship between pressure ratio ( $P_2/P_1$ ) and high-pressure shaft speed parameter ( $N\square/\sqrt{T_1}$ ) under 7th-stage air bleed condition.

7 级最大放气量  $m_D \sqrt{T_D}/P_D = 1.58$

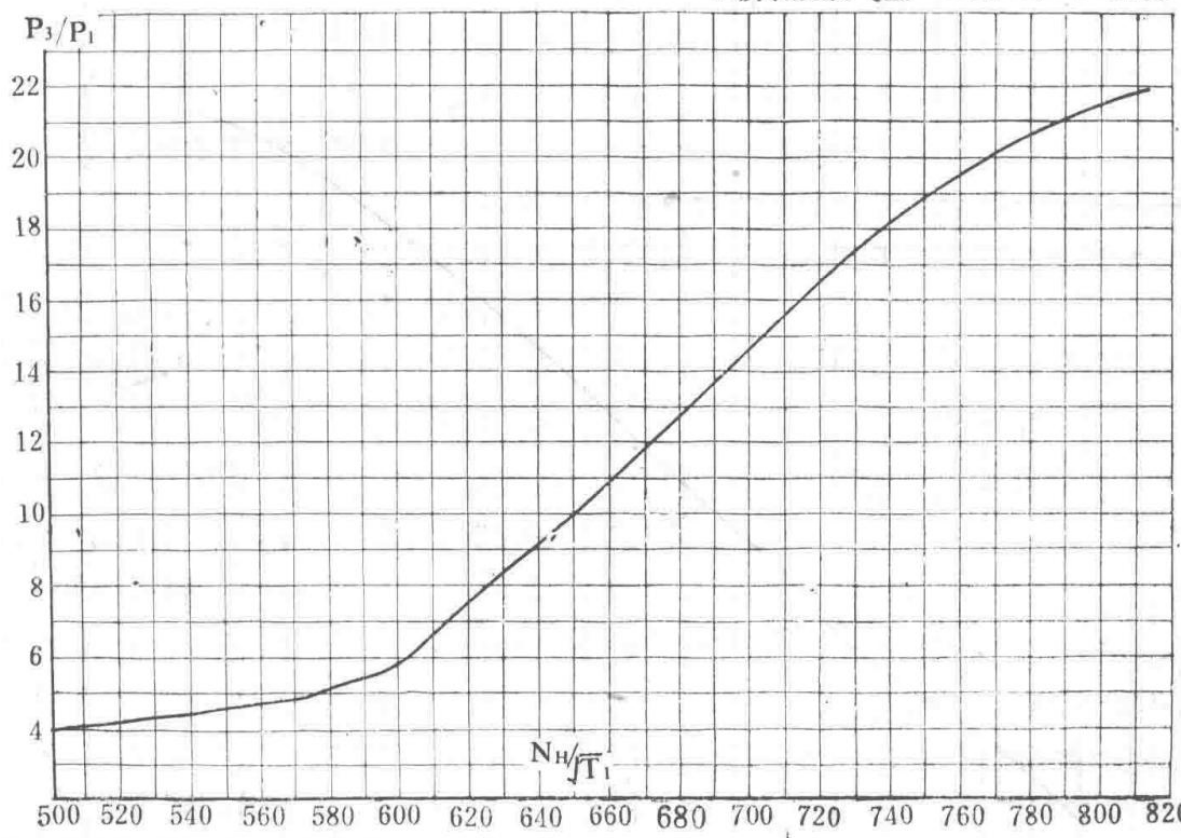
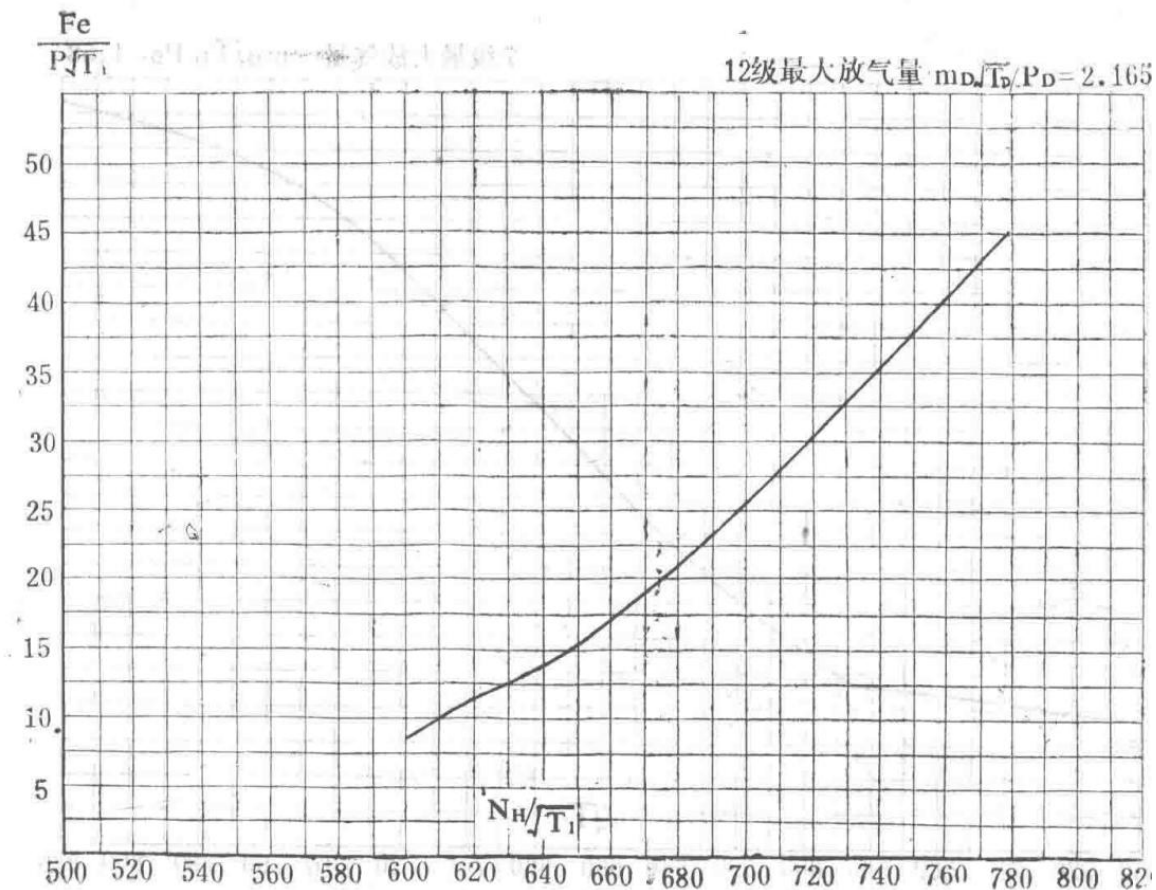


Figure 18 Effect of 7th-Stage Air Bleed on  $P_3/P_1$  vs.  $N\Box/\sqrt{T_1}$  Relationship

Graph showing the effect of 7th-stage air bleed on the relationship between pressure ratio ( $P_3/P_1$ ) and high-pressure shaft speed parameter ( $N\Box/\sqrt{T_1}$ ).

$P_3, P_1$  vs.  $N\Box, \sqrt{T_1}$ ,

Relationship between pressure ratio ( $P_3/P_1$ ) and high-pressure shaft speed parameter ( $N\Box/\sqrt{T_1}$ ) under 7th-stage air bleed condition.



Uncaptioned image, possibly a schematic or diagram related to engine components.

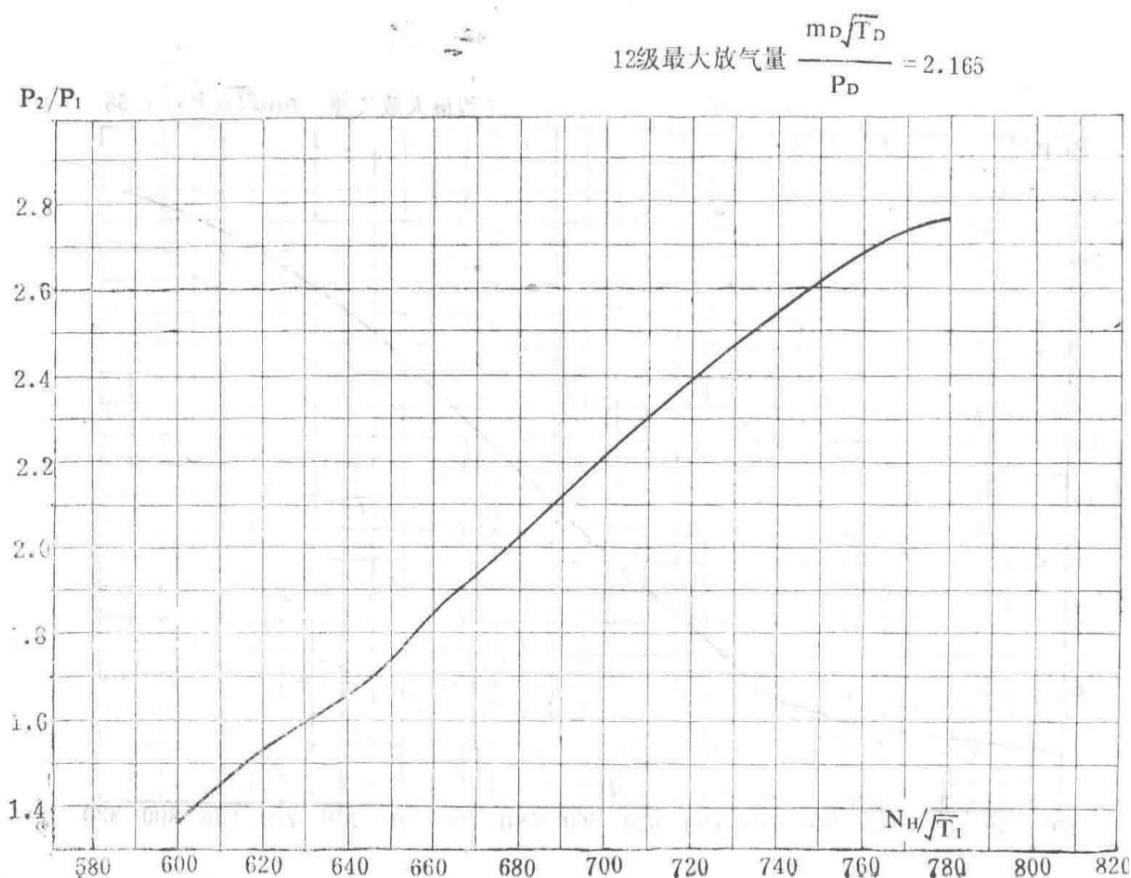


Figure 19 Effect of 12th-Stage Air Bleed on  $F \square / (P_1 \sqrt{T_1})$  vs.  $N \square / \sqrt{T_1}$  Relationship; Figure 20 Effect of 12th-Stage Air Bleed on  $P_2 / P_1$  vs.  $N \square / \sqrt{T_1}$  Relationship

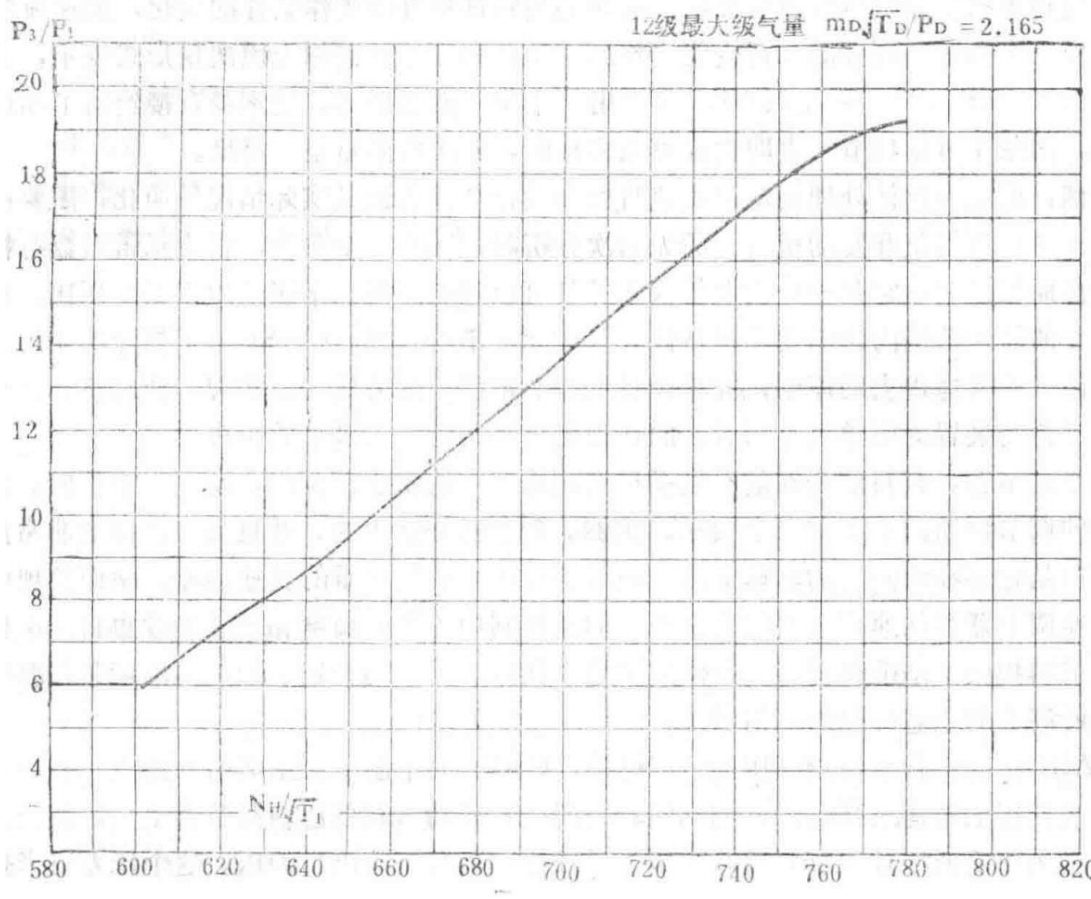
Graphs showing the effect of 12th-stage air bleed on the relationships between corrected thrust parameter ( $F \square / (P_1 \sqrt{T_1})$ ) and high-pressure shaft speed parameter ( $N \square / \sqrt{T_1}$ ), and between pressure ratio ( $P_2/P_1$ ) and high-pressure shaft speed parameter ( $N \square / \sqrt{T_1}$ ).

$F \square, P_1 \sqrt{T_1}$  vs.  $N \square, \sqrt{T_1}$ ,

Relationship between corrected thrust parameter ( $F \square / (P_1 \sqrt{T_1})$ ) and high-pressure shaft speed parameter ( $N \square / \sqrt{T_1}$ ) under 12th-stage air bleed condition.

$P_2, P_1$  vs.  $N \square, \sqrt{T_1}$ ,

Relationship between pressure ratio ( $P_2/P_1$ ) and high-pressure shaft speed parameter ( $N \square / \sqrt{T_1}$ ) under 12th-stage air bleed condition.



Effect of Stage 2 Bleed on the Relationship Between  $\frac{P_3}{P_1}$  and  $\frac{N\bar{\square}}{\sqrt{T_1}}$

Graph showing the influence of stage 2 bleed air on the relationship between the pressure ratio  $P_3/P_1$  and the corrected high-pressure spool speed  $N\bar{\square}/\sqrt{T_1}$ .

### 3. CASC Technical Requirements Notes

The primary requirement for the fuel flow control system is that the CASC (Combined Acceleration and Speed Control) must have very low hysteresis to achieve precise control of engine fuel flow. Secondly, variations in fuel temperature, density, and viscosity within normal ranges should not significantly affect acceleration control and speed regulation. The system is also required to be easily calibrated on the test bench.

Additionally, when the throttle lever is at the maximum position, the engine should be automatically controlled to limit the maximum values of various parameters such as  $N\bar{\square}$ ,  $T_6$ ,  $P_3$ , and  $N\bar{\square}$ . The engine's ultimate strength requirements dictate that these parameters must be kept within safe limits.

A further requirement for the Spey-type CASC system is to achieve rapid acceleration capability in a simple and direct manner, without relying on a large number of correction devices to overcome specific difficulties.

### 4. Design Principles

In the fuel flow regulator, acceleration control and the pilot's full-range speed regulator control are combined. Thus, the name CASC stands for "Combined Acceleration and Speed Control."

One of the fundamental principles of CASC is to control acceleration based on a dimensionless fuel flow function. This dimensionless fuel flow function precisely defines the permissible excess fuel supply at any operating condition.

The permissible excess fuel supply during acceleration is limited by the onset of stall or surge and varies with engine speed and inlet conditions. This variation is complex, making it difficult for a control system that reflects only a single parameter (such as the old air-fuel ratio type operating on compressor outlet pressure) to provide a satisfactory acceleration program. In fact, studies of engine characteristics near the stall boundary using well-known dimensionless analysis methods show that to compensate accurately for changes in operating conditions, the acceleration fuel flow program must respond to three parameters. The same analysis indicates that when fuel flow and operating conditions are expressed in dimensionless form, the relationship ( $\frac{\text{racF}_1}{\sqrt{T_2}} \frac{P_2}{\sqrt{P_1}}$ ) can be described by a single curve. This directly provides the basis for acceleration control. Appendix 1 (Section 14) shows that this can be achieved without measuring air temperature.

Of course, using the dimensionless method to handle engine stall characteristics and design acceleration control is a simplification of actual conditions and requires further explanation. In the dimensionless analysis of compressor and engine characteristics, there is another parameter representing the effect of Reynolds number on the characteristics. However, experience shows that it is a secondary factor and can be neglected. Another influencing factor is the ram pressure ratio, which affects engine characteristics only within a small speed range and is not difficult to handle in practice. CASC is based on the principle of considering all factors except secondary ones and is implemented in a very simple manner, achieving an unusually satisfactory compromise between control precision and device simplicity and reliability.

Regarding the regulator, its purpose is to develop a fast, stable, and accurate control loop across the wide range of conditions encountered by aero engines. For the first two requirements, a proportional regulator is appropriate and has the advantage of being mechanically very simple. However, it inherently exhibits speed droop, which, if uncorrected, can cause significant speed errors. Fortunately, CASC can combine the speed regulator with the acceleration controller. The altitude and speed parameters used in acceleration control also automatically and accurately provide a reference readjustment for the speed regulator. Thus, the transient speed droop required for stability is retained, but no drift in the regulated steady-state speed occurs when environmental conditions change.

CASC receives fuel from a variable-stroke high-pressure fuel pump. Downstream of the CASC (in the main nozzle fuel line) is a variable orifice. When the low-pressure spool speed is too high, this orifice moves toward the closed position (within the low-pressure spool regulator). The high-pressure pump servo piston senses the oil pressure after the low-pressure spool regulator on one side and the high-pressure pump outlet oil pressure on the other. This pressure difference is used to control the pump stroke.

Returning to the CASC, the regulator includes a device to distribute fuel flow between the engine's main and secondary nozzles. During engine ignition, the full pressure difference controlling the pump (servo piston) acts on the secondary nozzle, sacrificing fuel pressure to the main nozzle to ensure good fuel atomization. At higher engine speeds, the CASC-metered fuel flow is adjusted to the appropriate value by changing the pump stroke until an appropriate pressure difference (related to speed) is established across the controller's main variable metering orifice (VMO).

An important design principle is that the VMO plunger sleeve is rotatable, allowing the VMO plunger and regulator sleeve to move smoothly and accurately under available power. This ensures that the sliding surfaces are always in relative motion, minimizing friction and hysteresis.

Finally, when the throttle lever is set to the maximum position, the requirement for automatic engine control is achieved through several methods, none of which compromise the previously described principles. By reducing the final air pressure acting on the bellows to decrease the size of the main metering orifice (VMO), fuel flow is adjusted to limit the high-pressure compressor outlet pressure ( $P_3$ ). The method for limiting the maximum temperature of the high-pressure turbine or high-pressure compressor involves automatically reducing the "speed selection lever" setting on the CASC beyond the pilot's selected maximum throttle position, then adjusting the fuel flow through the regulator in the normal manner.

## 5. CASC Design Notes

## 5.1 Generation of Acceleration Control Action

During acceleration, the regulator spring pushes the regulator sleeve toward the acceleration stop pin, causing the VMO to operate at a constant gap width. Thus, the metering area depends on the width of the triangular hole exposed by the gap, which in turn depends on the high and low compressor pressures acting on the vacuum bellows (see Appendices 14 and 15). As an example, consider the calibration proposed for the first CASC unit, shown in Appendix 2 (Section 15). This appendix also provides the basic engine operating line and the proposed acceleration and deceleration lines. From a geometric perspective, the appropriate bellows ratio  ${}^{64}a^{99}$  is 0.455, and the appropriate divider ratio "R" is 4.9. The pressure difference is determined by the force generated by the flyweights acting on the differential piston.

$$\text{VMO pressure difference} = K N \square^2 \text{ (See Figure 6 in Section 15),}$$

Equation representing the relationship between VMO pressure difference and the square of the high-pressure spool speed  $N \square$ .

Any imbalance between the pressure difference and the flyweight force is corrected by the pump servo mechanism, which adjusts the pump stroke to change the fuel flow until equilibrium is restored.

$$F, P_2 N \square = f(P_3, P_2) - 0.455$$

Equation for the dimensionless fuel flow function under blocked divider orifice conditions.

At low engine speeds, if the venturi becomes subcritical, the acceleration characteristic curve changes its slope and continues to decrease to zero.

In the Spey MK202, the CASC's VMO is divided into two parts. The first part is a triangular hole located on the side controlled by the regulator gap width. The second part is a rectangular hole moved by the bellows to provide a variable flow area. The rectangular hole is not controlled by the regulator. Slotted holes are preferable to circular holes because they provide a larger area for a given sleeve diameter.

## 5.2 Deceleration Control and Steady-State Operation

Deceleration control is achieved by moving the pilot's throttle lever (which moves the CASC speed selection lever via a cam box) to reduce the required engine speed. The regulator spring force is reduced, and the regulator moves in the direction of closing the VMO gap under the greater flyweight force. To prevent the gap from completely closing and causing flameout, this movement must be limited. The minimum VMO gap width achieved provides a deceleration control (DCU) that is a fixed proportion of the acceleration curve, resulting in a dimensionless deceleration control below the steady-state operating line.

There is a condition where the pilot's speed control lever is in a fixed position (engine idle position) but can provide a variable engine speed. In this case, the engine idle speed is required to increase with altitude to provide sufficient air for aircraft equipment and cabin pressurization and to allow rapid acceleration at any altitude. In the CASC system, this requirement is easily met by setting up a small bypass hole in parallel with the VMO. The flow characteristic number of this hole is approximately 6.5 and can be adjusted via a needle valve, but it cannot be reduced further when set to the minimum flow area. When the throttle lever is pulled back to the minimum (idle) position, the resulting combined flow increases its influence with altitude. During aircraft climb, the engine fuel flow required to maintain a given speed becomes smaller, and as the engine speed gradually increases, the engine fuel demand curve intersects the modified deceleration control characteristic line, achieving an elevated idle speed. Only at low altitudes does the speed regulator control the engine idle speed to a sufficiently low level.

Under International Standard Atmosphere conditions at sea level static state, the throttle lever angle/thrust relationship is approximately linear. This requirement is met by designing an appropriate cam shape. The cam compresses the regulator spring in the CASC, resulting in a predetermined fuel flow at the set speed.

Fuel density compensation is completed as described in Section 14.

The  $P_3$  limiter operates via a bellows sensing  $P_3$  (loaded with a spring).

When the  $P_3$  limit value is reached, the bellows moves to open a throttle hole parallel to the venturi. This throttle hole is designed to be large enough to counteract the effect of the speed regulator increasing the VMO gap width, thereby reducing the fuel flow to the engine.

Maximum temperature control ( $T_e$  and  $T_3$ ) operates through an amplifier. Thermocouple signals (monitoring temperature signals) are sent to the amplifier. When  $T_e$  or  $T_3$  reaches the limit value, the signal from the amplifier is sent to a servo motor, which moves to change the lever ratio and reduce the regulator spring load. This adjusts the fuel flow and overrides the pilot's throttle lever input. The allowable maximum adjusted fuel flow is set to ensure that  $T_e$  or  $T_3$  does not exceed the specified maximum value. If this system fails, the fully adjusted fuel flow is still sufficient to prevent excessive thrust loss.

## 6. Estimation of Flight Idle Speed

Technical Design Report

Technical Design Report	TDR 796
Spey MK202 Estimation of Flight Idle Speed	

### Abstract

This report provides the engine idle speeds across a range of altitudes and Mach numbers under cold, hot, and standard day conditions.

With the current adjustments of the CASC device and standard brochure performance, to prevent overspeed during zoom climbs above a specified altitude, the engine must be shut down as shown in Figures 2 to 6. If such shutdown is not permissible, the CASC device can be recalibrated to operate at higher altitudes. However, this would reduce the low-altitude idle speed and fuel flow, thereby increasing engine oil temperature, which is already at its limit under these conditions. Recent tests, however, indicate that the engine is more sensitive to Reynolds number effects than assumed in the brochure, which also reduces high-altitude idle speed. Thus, the flight envelope limitations are not as stringent as indicated in this report.

### Assumptions

1. Engine performance is based on the latest standards.
2. Performance estimation of the idle regulator characteristics. Air divider characteristics.
3. Inlet pressure recovery coefficient as a function of inlet mass flow and Mach number—predicted performance.
4. Figure 1 shows the adopted atmospheric temperature standards: 1962 U.S. Standard Atmosphere, British Cold and Hot Day Standards, and the most severe weather standards of the UK and U.S.
5. The engine is designed to operate only momentarily when the inlet temperature exceeds 395 K. This is shown in the design (limited) flight envelope in Figures 7 to 9.

### Results

Figures 2 to 6 show engine idle speed curves plotted against altitude and Mach number within the design flight envelope using the atmospheric standards from Figure 1. Idle speeds for temperatures between cold and hot days are determined by interpolation.

The curves in these figures represent the maximum allowable  $N \square$  for the engine with  $T_e$  limitation.

These figures also include curves for the maximum allowable  $N \square$  without  $T_3$  limitation.

The figures indicate the approximate range where the  $N \square / \sqrt{T_1}$  limiter operates.

Figures 7 to 9 show the impact of the above limitations on the design flight envelope under British Standard Cold Day, Hot Day, and 1962 U.S. Standard Day conditions.

## Discussion

To accommodate possible zoom climb conditions, the design flight envelope has been revised to 100,000 feet altitude. These flight envelopes are shown in Figures 7 to 9. With the current fuel system adjustments, some flight conditions at higher altitudes result in idle speeds exceeding the maximum allowable value.

At these high-altitude flight conditions, the engine limiters do not function because the  $T_6$  limiter and  $T_3$  limiter (when present) operate through the  $\Delta N$  regulator, while the  $N$  regulator rests against the deceleration control stop pin. The engine  $P_3$  pressure is below the  $P_3$  limiter setting, and the  $N$  regulator adjustment does not interfere with other flight conditions. Under some extreme conditions, the  $N$  /  $\sqrt{T_1}$  limiter has some effect, but for flight safety, engine speed cannot be significantly reduced.

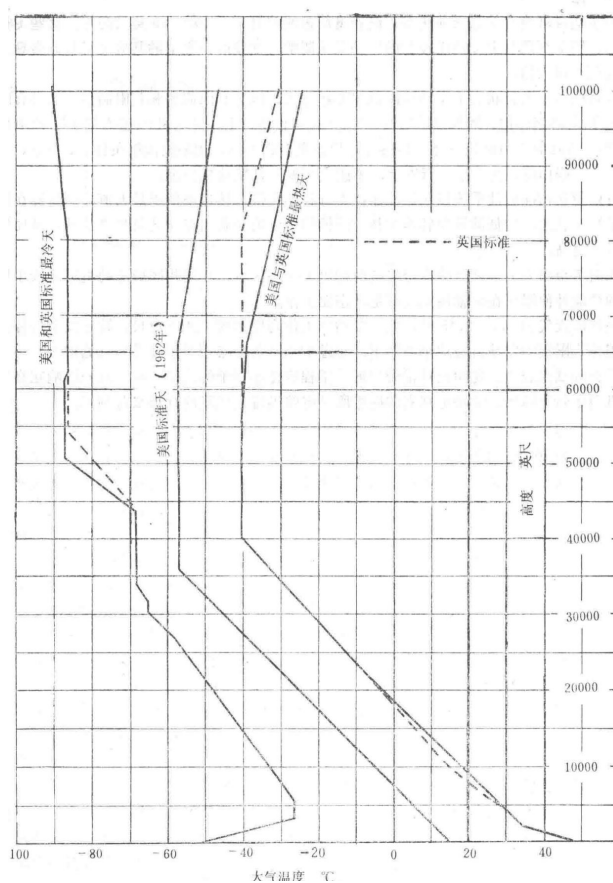
The fuel system can be recalibrated to ensure that idle speed remains below the maximum value at any flight condition. However, this reduces idle speed at low altitudes. The lower idle speed and corresponding reduced fuel flow will cause the engine to heat the oil, leading to higher oil temperatures.

In Figures 7 to 9, some areas within the revised flight envelope are marked where the engine cannot operate according to brochure performance requirements with the current fuel system settings.

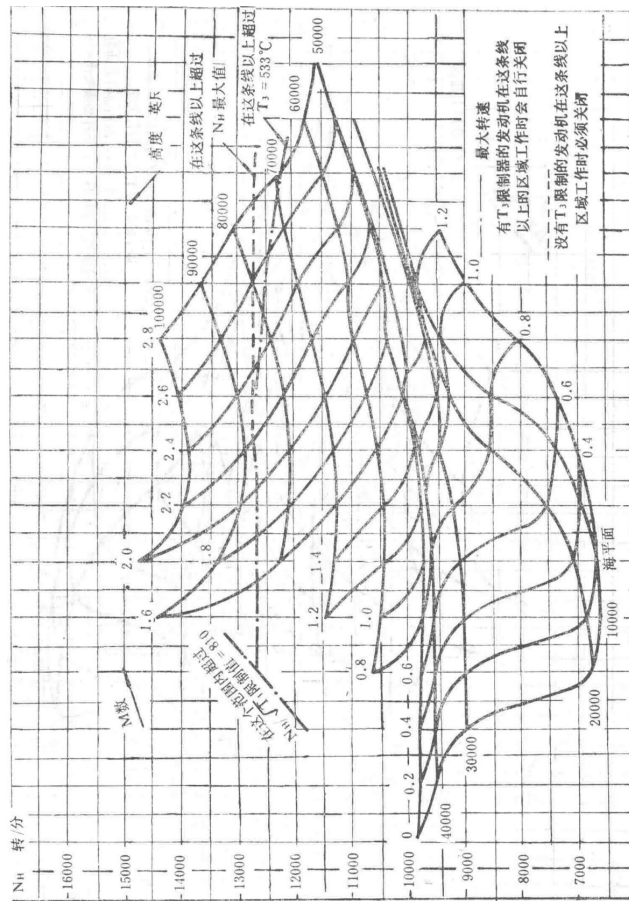
Under standard day conditions and  $M = 2.15$ , the engine is required to operate up to 72,000 feet altitude. This requirement is just met because the  $T_6$ -limited engine must be shut down above 72,000 feet under these conditions (see Figure 8).

Recent tests indicate that the engine is more sensitive to Reynolds number effects than assumed in the brochure. This effect reduces engine idle speed at high altitudes, making the flight envelope limitations less stringent than indicated.

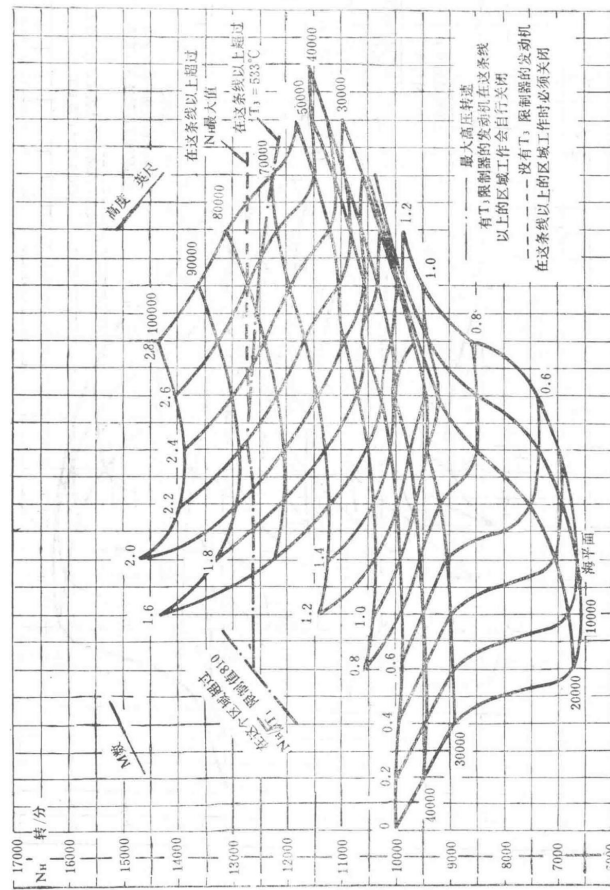
— Section 63 —  
Content from Original Document (Pages 311-315)



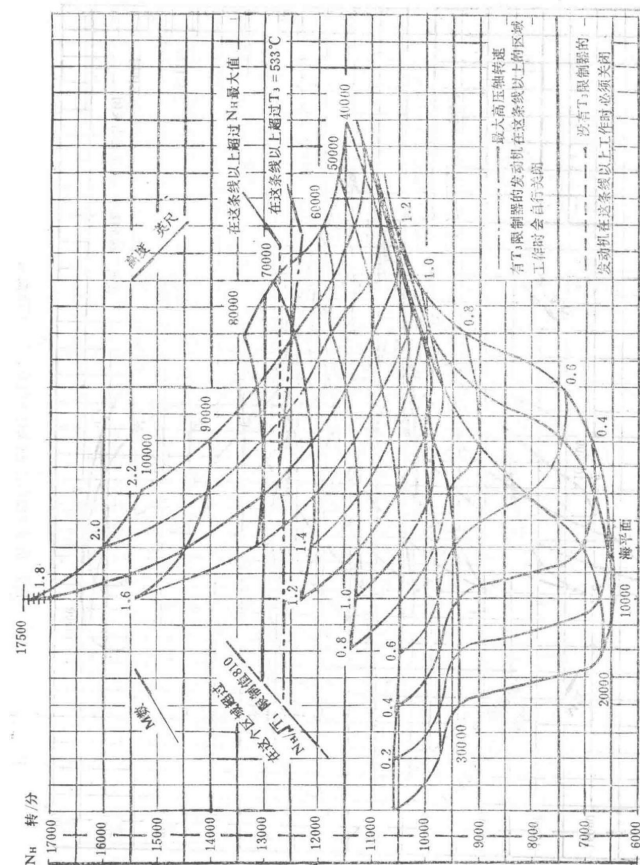
Performance chart of the Spey MK202 engine showing the relationship between high-pressure rotor speed ( $N_{\square}$ ), low-pressure rotor speed ( $N_{\square}$ ), and turbine inlet temperature ( $T_3$ ) under various conditions.



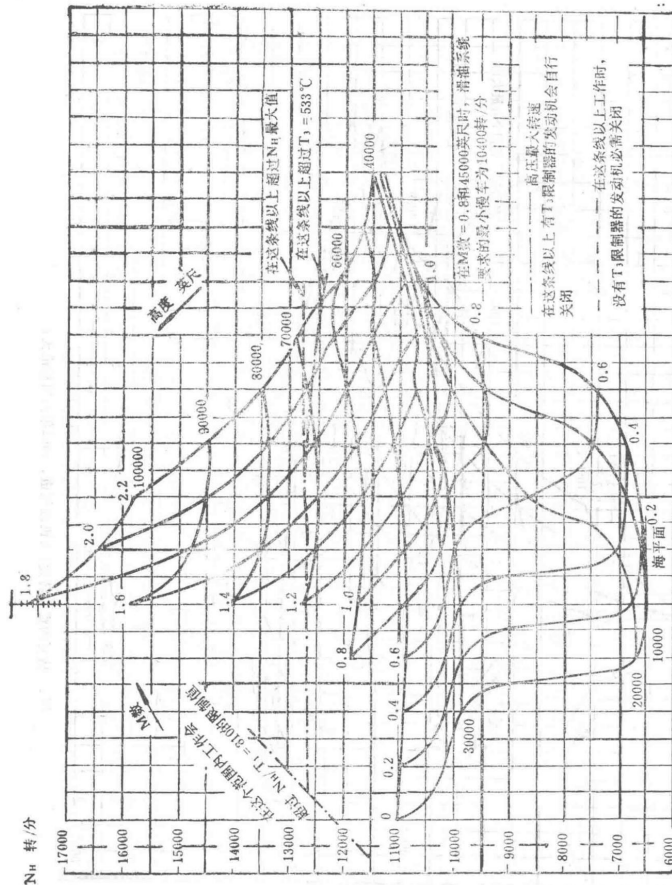
Performance chart of the Spey MK202 engine illustrating the operational limits of high-pressure compressor rotor speed ( $N_1$ ) and turbine inlet temperature ( $T_3 = 533^\circ\text{C}$ ) with annotations for engine behavior.



Graph comparing the altitude and speed performance characteristics of the Spey MK202 engine with British and U.S. standards as of 1962.



Performance chart of the Spey MK202 engine showing the maximum afterburner operational limits with respect to high-pressure rotor speed ( $N_H$ ) and turbine inlet temperature ( $T_3$ ).



Performance chart of the Spey MK202 engine detailing the operational constraints for transient working conditions of the high-pressure rotor above idle speed.

## Spey MK202 Engine Performance Charts

The following performance charts provide detailed operational parameters for the Spey MK202 aircraft engine. These charts are critical for understanding the engine's behavior under various conditions such as rotor speeds ( $N_h$  and  $N_l$ ), turbine inlet temperature ( $T_3$ ), and environmental factors.

Key Parameters in Performance Charts

Parameter	Description	Unit
$N_h$	High-pressure rotor speed	RPM
$N_l$	Low-pressure rotor speed	RPM
$T_3$	Turbine inlet temperature	°C
Altitude	Operational altitude	Meters
Throttle Setting	Engine throttle position	Percentage or qualitative description

The first chart (Figure 1) illustrates the relationship between high-pressure rotor speed ( $N_h$ ), low-pressure rotor speed ( $N_l$ ), and turbine inlet temperature ( $T_3$ ) up to  $533^{\circ}\text{C}$ . It includes annotations for conditions where the engine exceeds operational limits and the corresponding adjustments needed.

- When the condition line is above the maximum  $N_h$  limit, reduce throttle to lower  $N_h$ .
- If  $T_3$  exceeds  $533^{\circ}\text{C}$ , adjust the fuel flow to maintain temperature below this threshold.
- Ensure that the engine operates within the specified rotor speed and temperature constraints to avoid damage.

The second chart compares the altitude and speed performance of the Spey MK202 engine against British and U.S. standards from 1962. This chart is essential for evaluating the engine's performance envelope in different flight conditions.

The third chart focuses on the maximum afterburner operational limits. It highlights the constraints on high-pressure rotor speed ( $N_{\square}$ ) and turbine inlet temperature ( $T_3$ ) during afterburner use, ensuring the engine operates within safe parameters.

The final chart provides guidelines for transient operational conditions of the high-pressure rotor above idle speed. It is crucial for pilots and engineers to understand these constraints to ensure safe and efficient engine operation during rapid throttle changes.

— Section 64 —  
Content from Original Document (Pages 316-320)

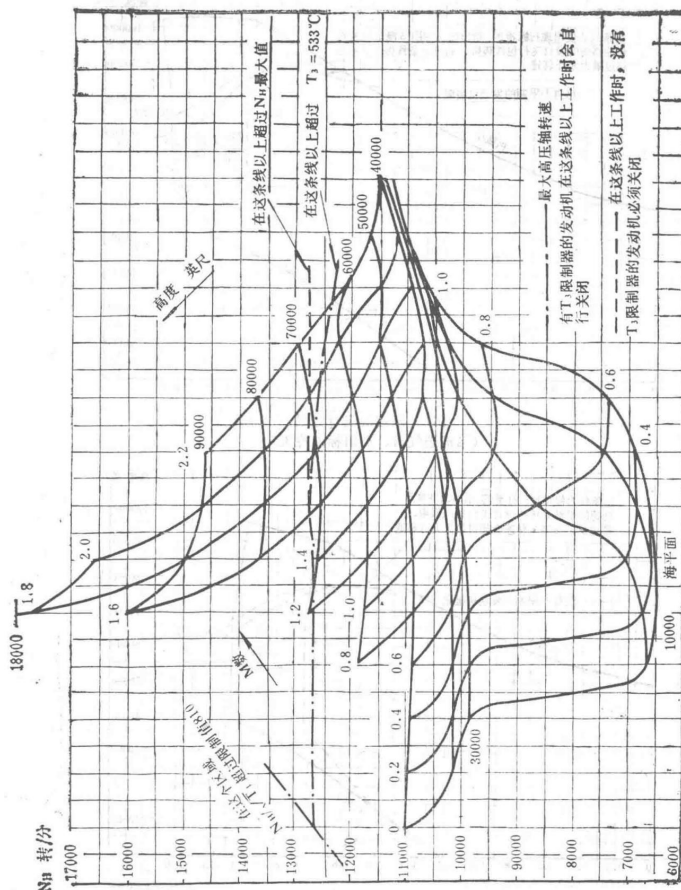


Diagram referenced in the text (no caption provided).

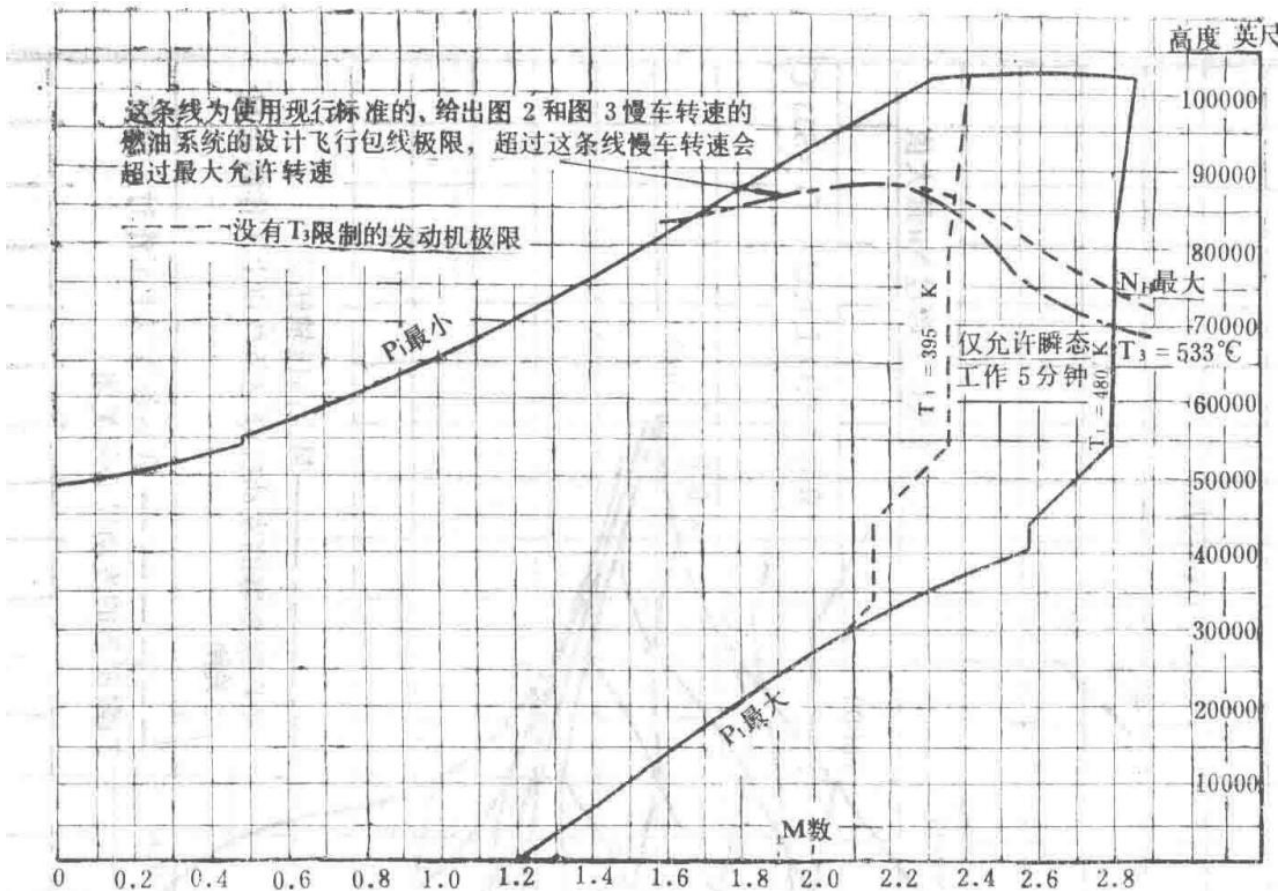


Figure 7: Defined Flight Envelope

Flight envelope for the aircraft intake under British Standard Cold Day conditions.

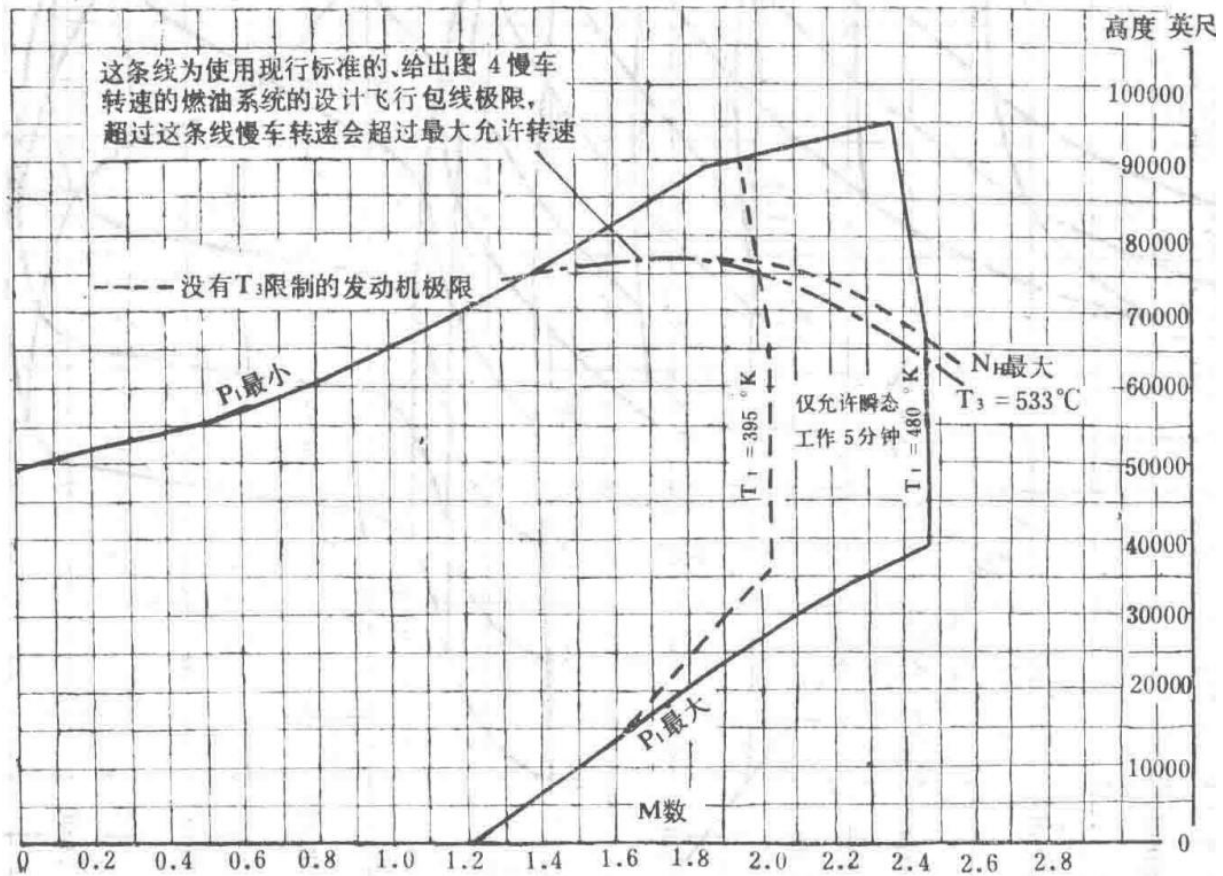


Figure 8: Defined Flight Envelope

Flight envelope diagram (no specific conditions mentioned).

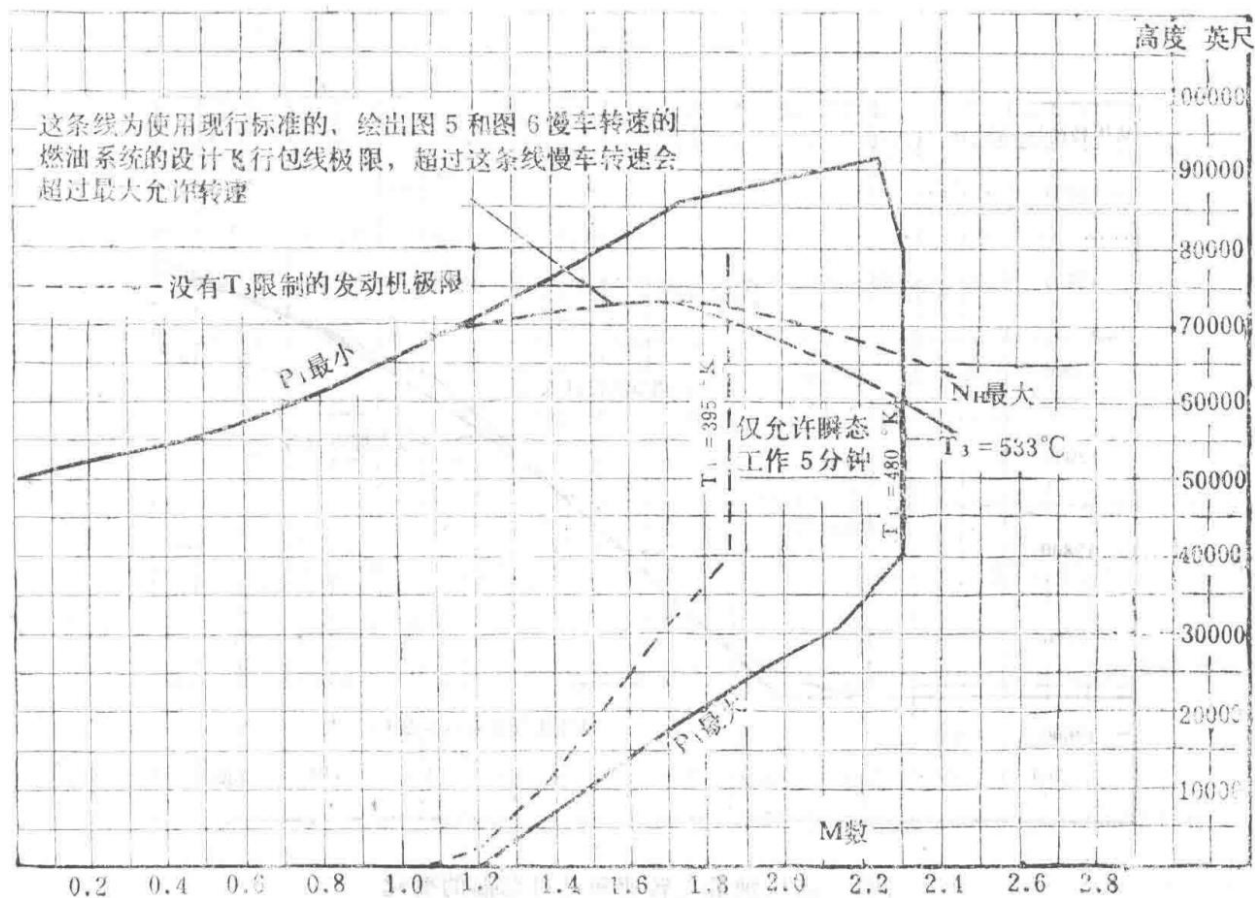
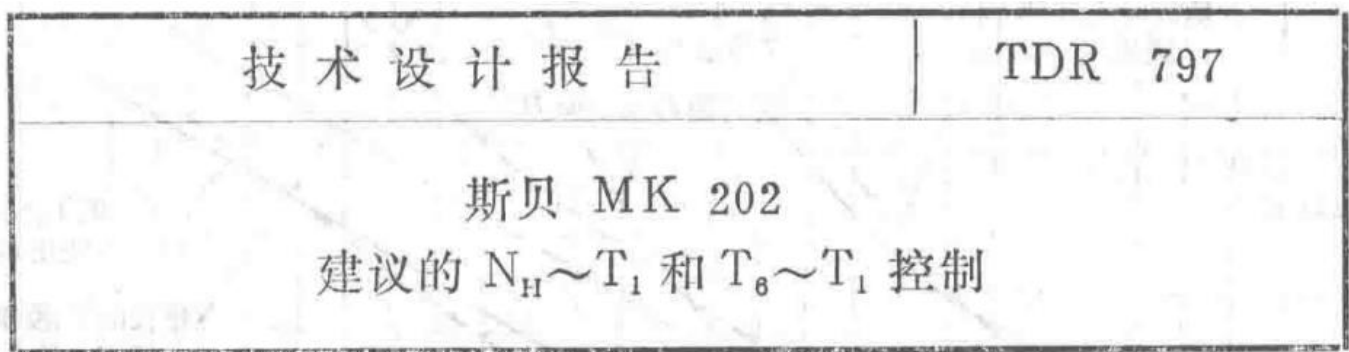


Figure 9: Defined Flight Envelope (Aircraft Intake, British Standard Hot Day)

Flight envelope for the aircraft intake under British Standard Hot Day conditions.

## 7. Recommended $N \square T_1$ and $T_6 \sim T_1$ Control



Version information: 2nd Edition, July 28, 1965.

### Abstract

This report outlines the origins of the recommended  $N \square T_1$  control and nozzle temperature  $T_6$  control, which are included in the engine control system requirements. The  $T_6 \sim T_1$  requirements are directly derived from performance data.

### $N \square T_1$ Requirements

The  $N \square T_1$  control requirements proposed by the Performance Department require modification. Implementing such a curved control characteristic is challenging; therefore, a characteristic line composed of straight segments is proposed (see Figure 1). This linear characteristic is included in the fuel system requirements.

## T<sub>6</sub> T<sub>1</sub> Control Requirements

The currently recommended nozzle temperature (T<sub>6</sub>) limits are shown in Figure 2. It illustrates the baseline values recommended for engine augmentation without using boundary layer control (BLC) and the T<sub>6</sub> signal readjustment values that satisfy engine requirements when using BLC without augmentation.

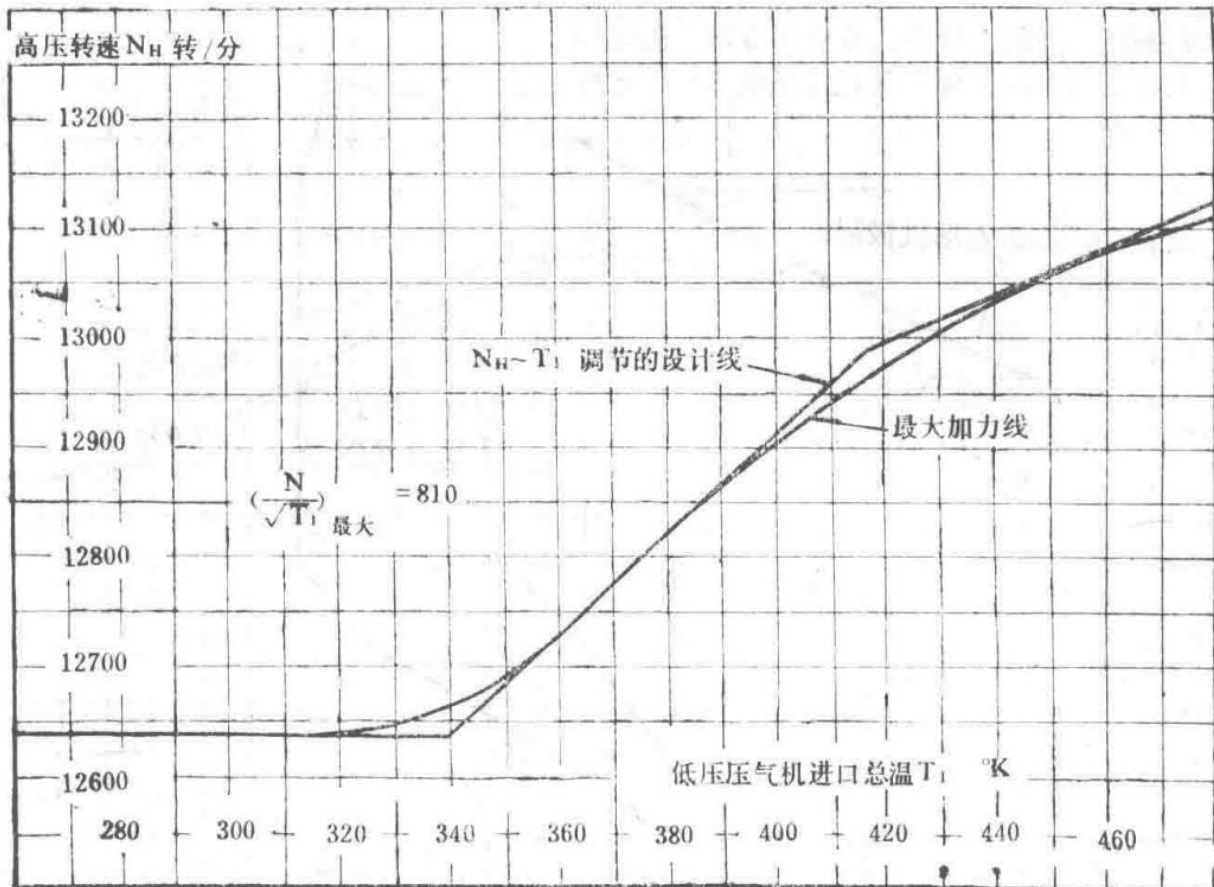


Figure 1: Variation of Maximum High-Pressure Shaft Speed with Inlet Total Temperature

Graph showing the relationship between maximum high-pressure shaft speed ( $N\square$ ) and inlet total temperature ( $T_1$ ).

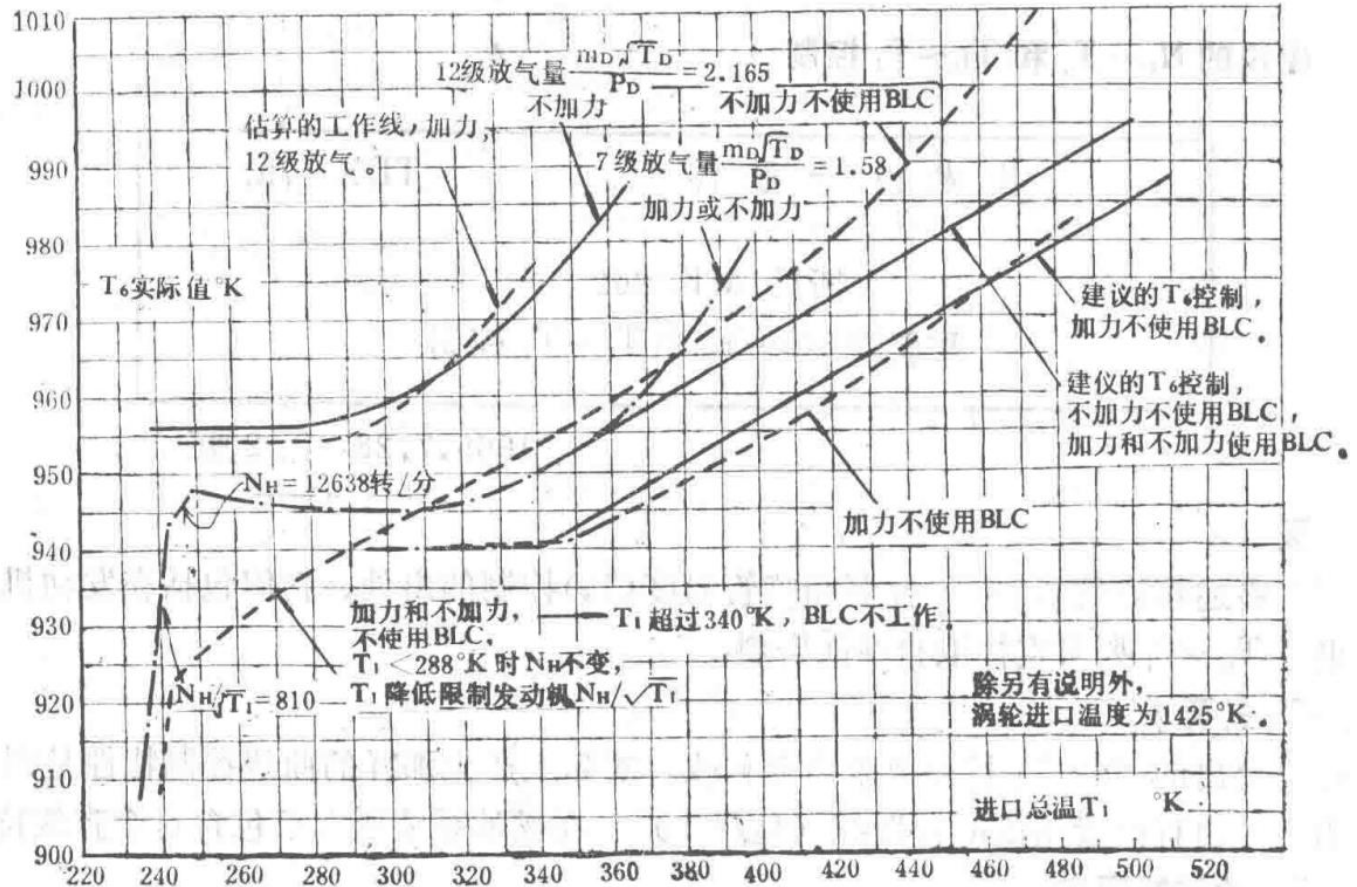


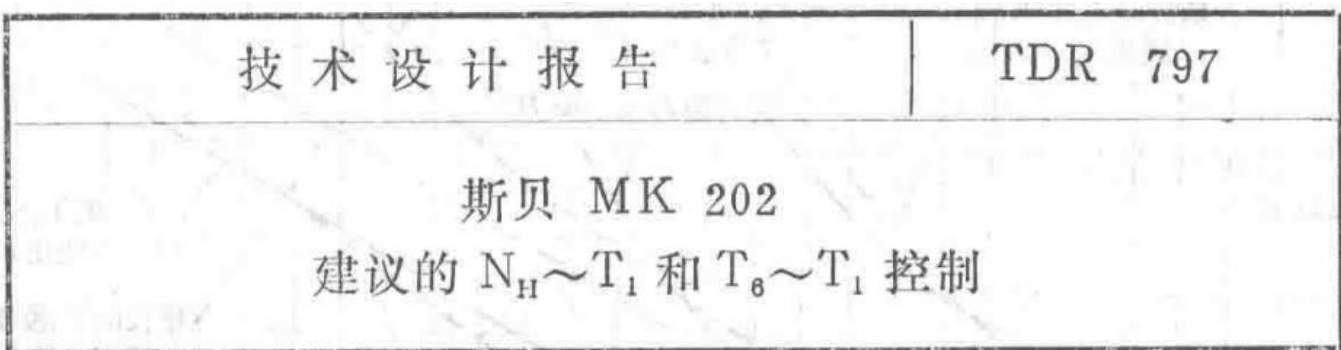
Figure 2: Variation of Actual  $T_e$  ( $^{\circ}$ K) with Inlet Total Temperature

Graph showing the relationship between actual nozzle temperature ( $T_e$ ) and inlet total temperature ( $T_1$ ).

## 8. Relationship Between Net Thrust and Engine Control Input Angle

### Technical Design Report

Spey MK202: Relationship Between Net Thrust and Engine Control Input Angle



Version information: 5th Edition, March 29, 1966.

### Abstract

Figure 1 presents the relationship between thrust, expressed as a percentage of maximum non-afterburning net thrust, and the engine control input angle under International Standard Atmosphere (ISA) sea-level static conditions, without afterburning and without air bleed. The engine control input angle refers to the input angle to

the cam box, connected via linkage to the pilot's control lever.

Figures 3 and 2 show the relationship between the percentage of net thrust and the engine control input angle during normal maximum bleed at the 7th and 12th stages of the high-pressure compressor, respectively.

## Data Used

- In the non-afterburning range, the relationship between high-pressure shaft speed and the angle of the CASC (Combined Acceleration and Speed Control) device is obtained from the latest Lucas CASC cam profile. Considering the variation of  $R_{01}$  with high-pressure shaft speed, this relationship is transformed into the relationship between thrust and CASC device angle.
- The relationship between average engine thrust and the percentage of maximum afterburning fuel flow during afterburning is derived from performance data.
- The relationship between afterburning fuel flow and the afterburning device input lever is assumed to be linear.
- In the non-afterburning range, the maximum and minimum limits of nominal thrust caused by CASC tolerances are provided by Lucas Gas Turbine Equipment Limited.
- The maximum and minimum limits of afterburning fuel flow caused by tolerances in the afterburning fuel control device are provided by Dowty Fuel Systems Limited.
- The limits of afterburning degree caused by tolerances in the afterburning fuel control device are also provided by Dowty Fuel Systems Limited.
- In the non-afterburning range, for a given high-pressure shaft speed, the average engine thrust limit is  $\pm 2\%$ . During afterburning, for a given fuel flow, the average engine thrust limit is -4%.
- The total tolerance in the connection between the fuel control device and the engine input lever is  $\pm 0.5^\circ$  in the engine input lever angle.
- The dimensionless mass flow functions for 7th and 12th stage bleeds are as follows:

Flight Envelope Data for Different Conditions

Condition	Description
Figure 4	This curve uses current standard performance to derive the design flight envelope for the fuel system, aiming for the maximum flight envelope under 4-engine operation with boundary layer control (BLC). The dashed line represents the engine limit with $T_3$ control.
Figure 5 and Figure 6	These curves use current standard performance to derive the design flight envelope for the fuel system, aiming for the maximum flight envelope under twin-engine operation with BLC.

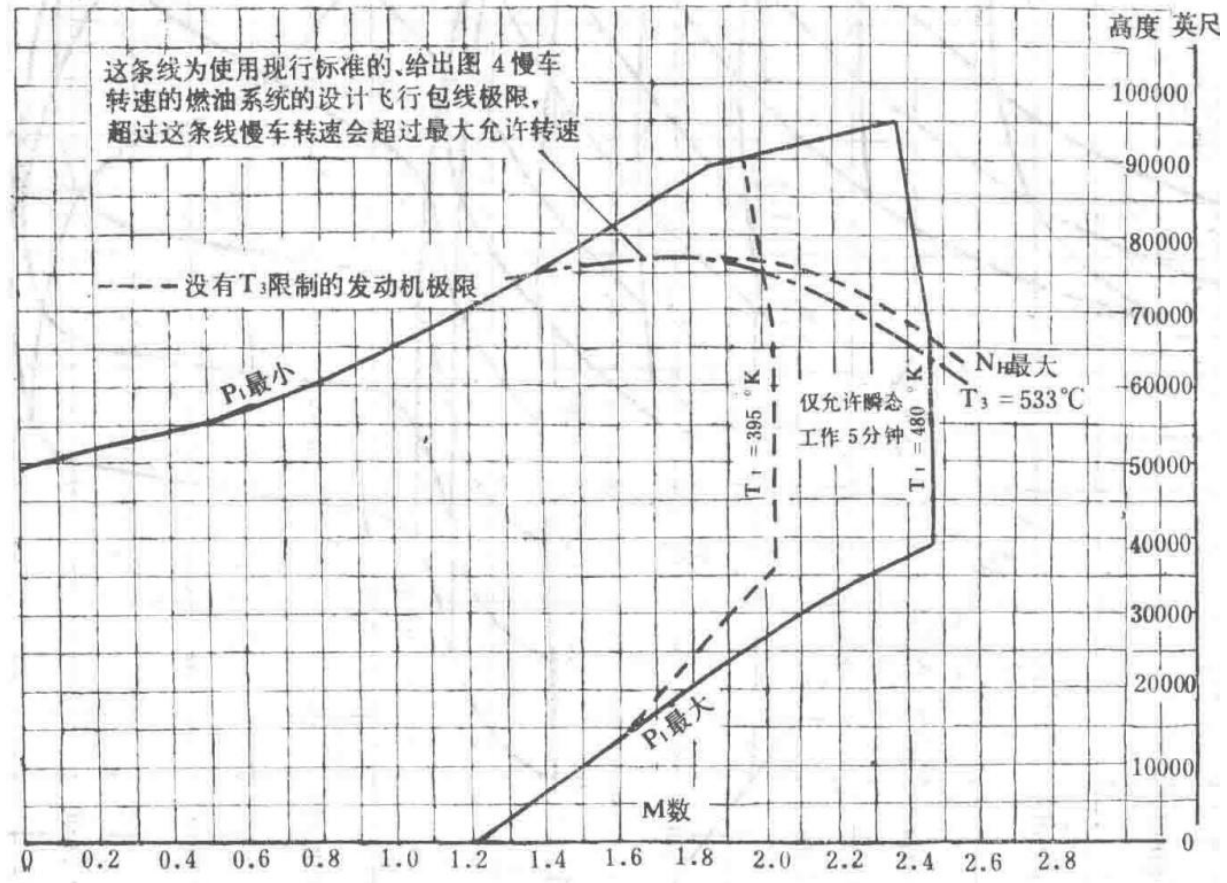


Figure 4: Flight Envelope for 4-Engine Operation with BLC

Flight envelope diagram for 4-engine operation with boundary layer control (BLC), showing parameters such as  $P_1$ ,  $N_h$ ,  $T_1$ , and Mach number.

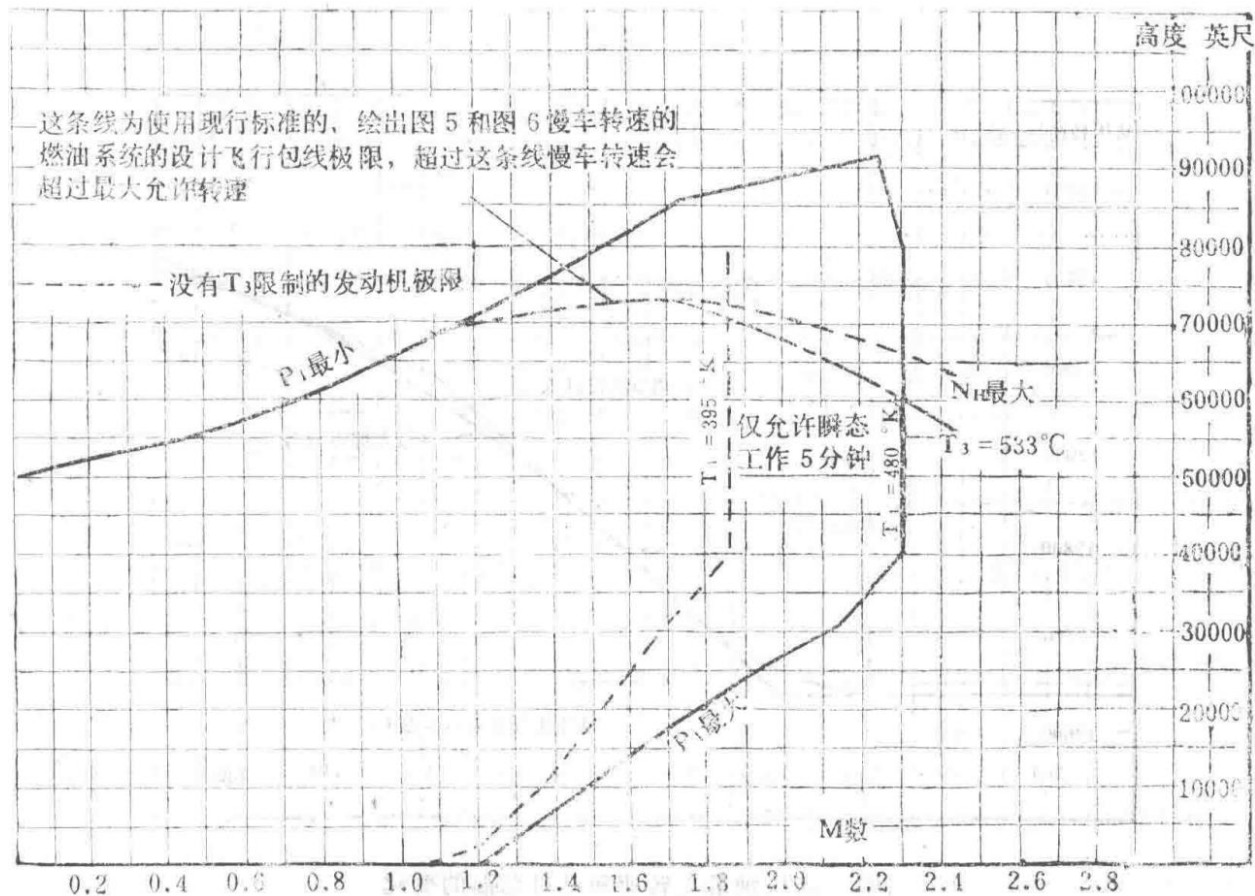


Figure 5: Flight Envelope for Twin-Engine Operation with BLC (Part 1)

Flight envelope diagram for twin-engine operation with boundary layer control (BLC), showing parameters such as  $P_1$ ,  $N_H$ ,  $T_1$ , and Mach number.

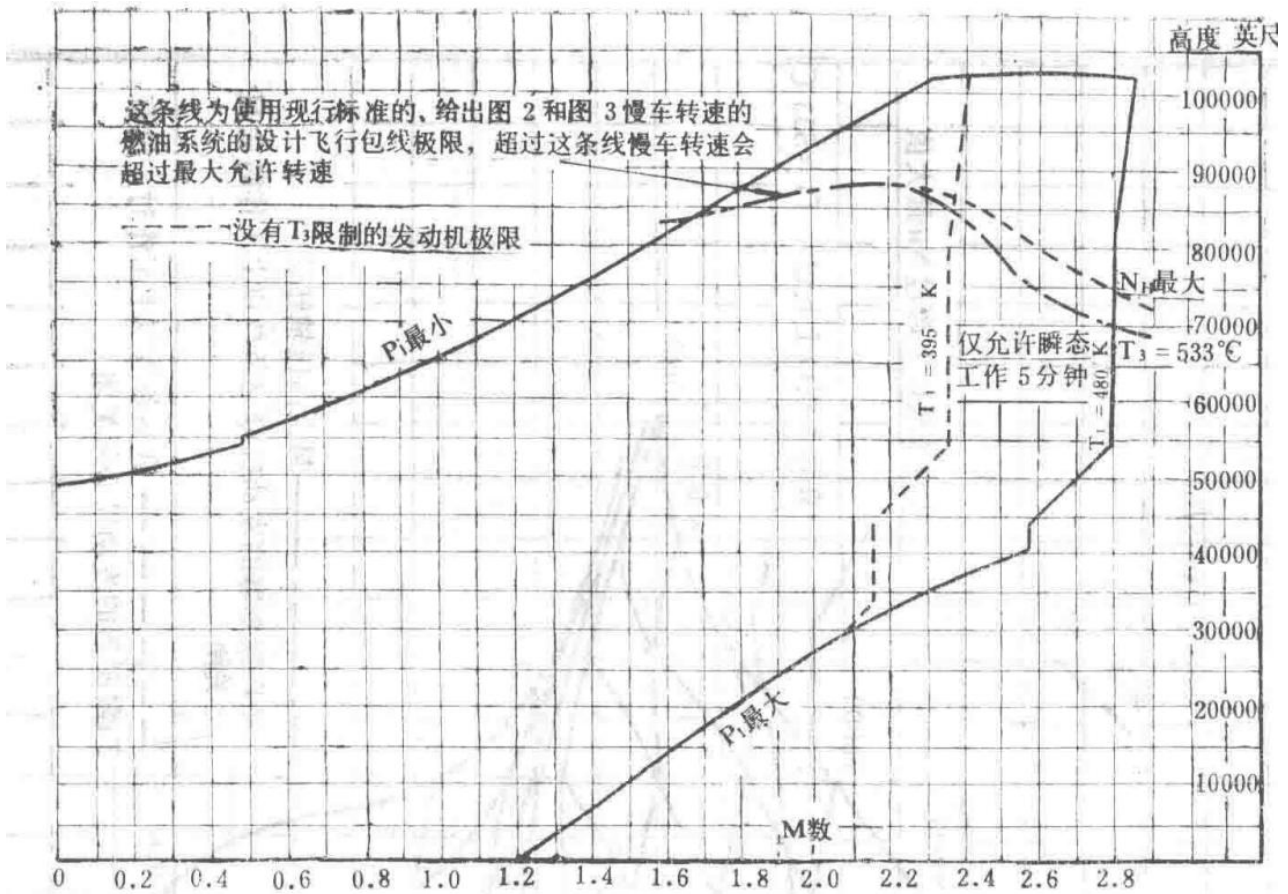
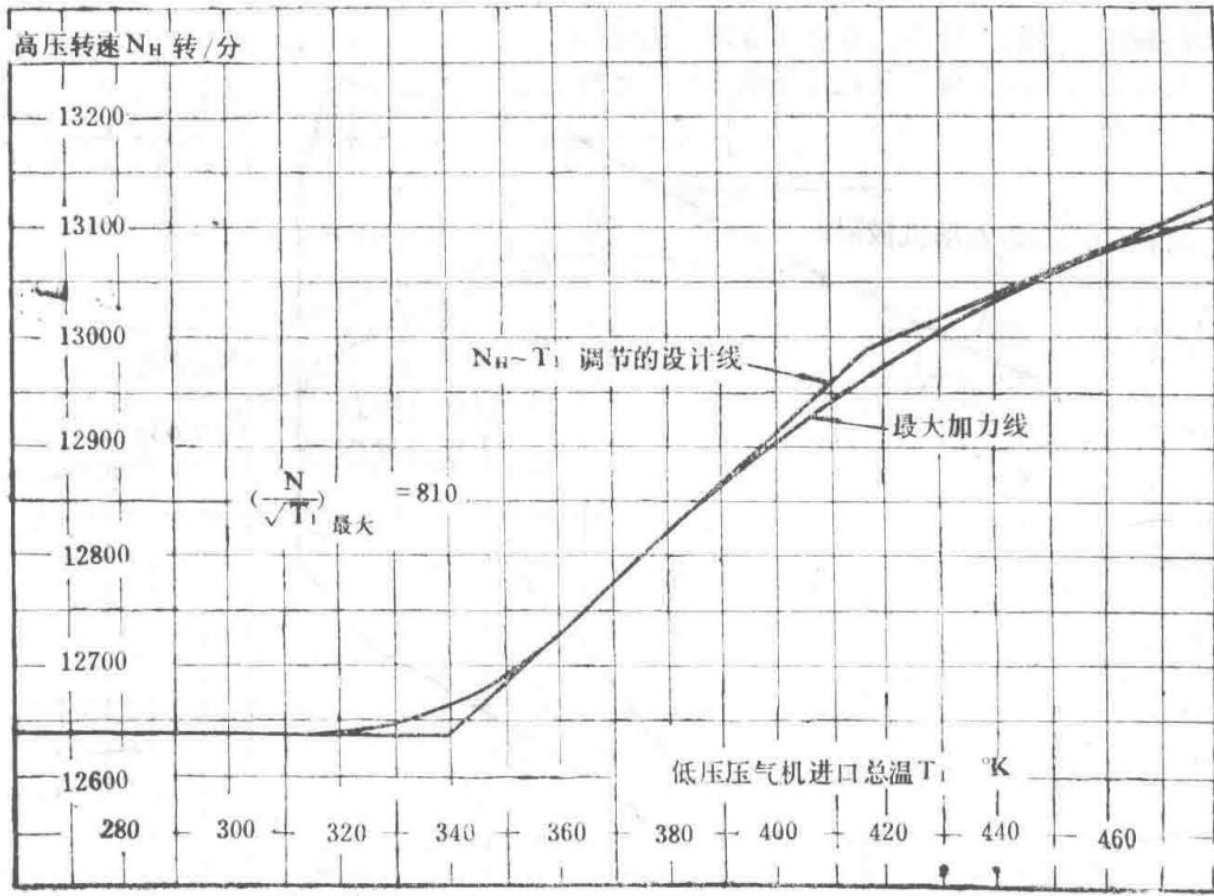


Figure 6: Flight Envelope for Twin-Engine Operation with BLC (Part 2)

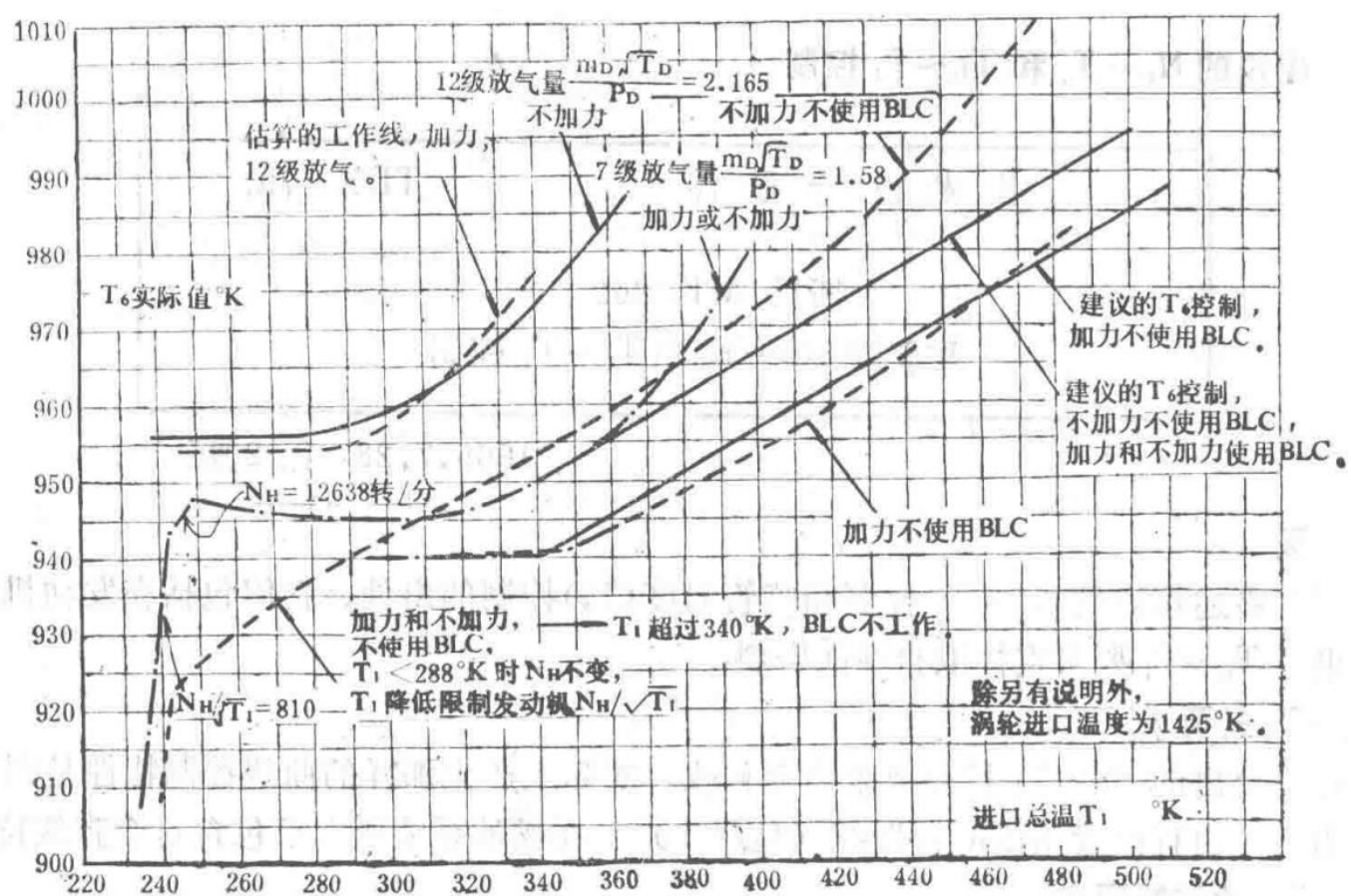
Flight envelope diagram for twin-engine operation with boundary layer control (BLC), showing additional parameters and conditions.

#### Nozzle Temperature ( $T_e$ ) Control Data

Condition	Description
Without BLC, Afterburning	Baseline $T_e$ control value when afterburning without BLC.
With BLC, No Afterburning	Adjusted $T_e$ control value when using BLC without afterburning.
With BLC and Afterburning	Adjusted $T_e$ control value when both BLC and afterburning are used.
$N_{\square} = 12638 \text{ rpm}$	High-pressure shaft speed limit.
$T_1$ Correction	Correction for $T_1$ when $N_{\square} / \sqrt{T_1}$ exceeds limits.
Maximum $T_e$	Maximum allowable $T_e$ under specified $T_1$ conditions.



Graph showing the relationship between  $T_e$  and  $T_1$  under various conditions of BLC and afterburning.



## High-Pressure Shaft Speed ( $N_{\square}$ ) Control Limits

Graph showing the relationship between  $N_{\square}$  and  $T_1$ , including the design line and maximum augmentation line.

Technical Design Report TDR 797 Spey MK 202 Recommended  $\backslash( N_H \sim T_1 \backslash)$  and  $\backslash( T_6 \sim T_1 \backslash)$  Control

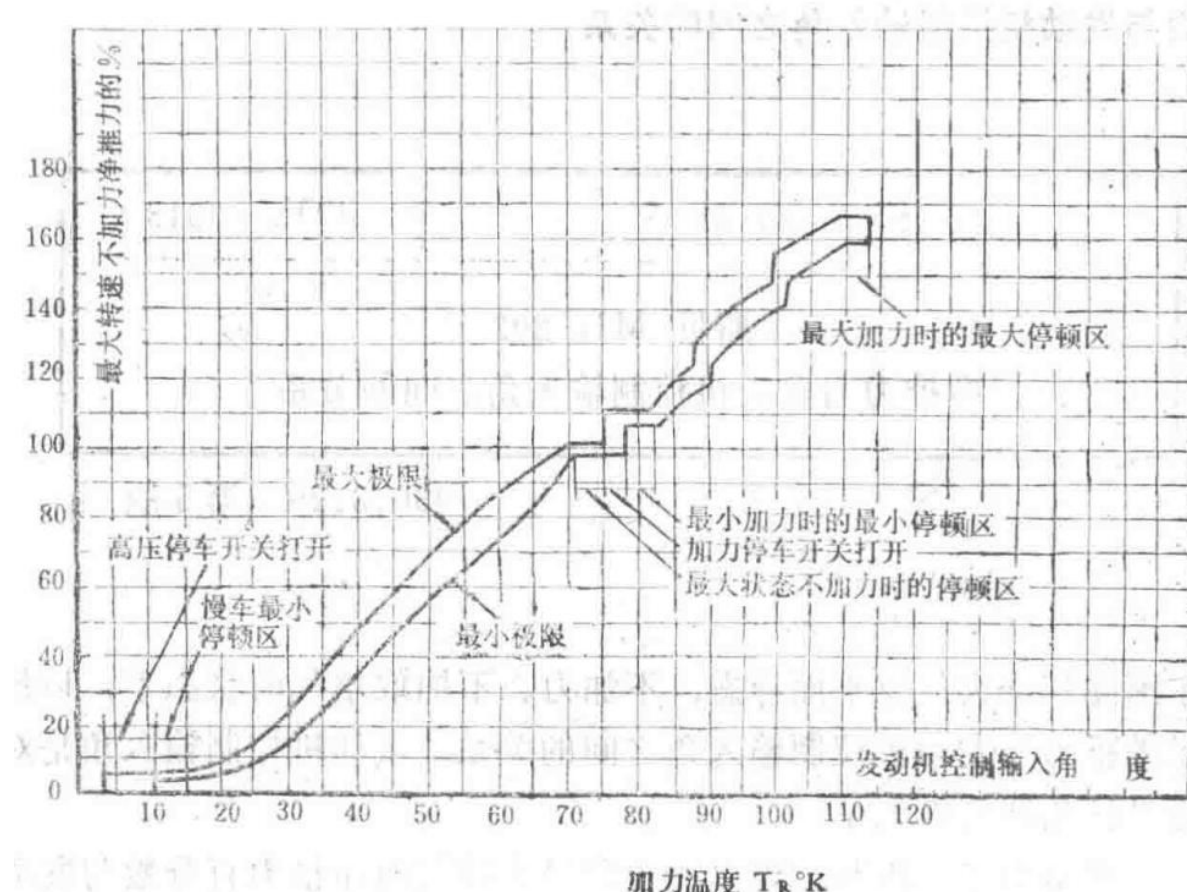


Figure 1: Relationship between thrust and engine controller input angle (International Standard Atmosphere, sea level static, no air extraction)

Graph showing the correlation between engine thrust and the input angle of the engine controller under standard atmospheric conditions at sea level without air extraction.

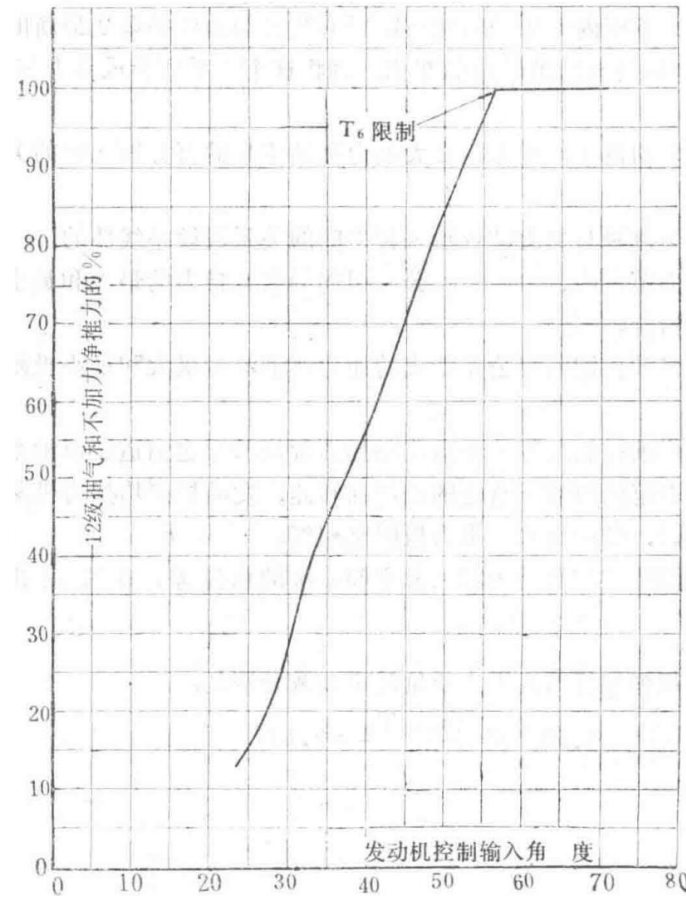


Figure 2: Relationship between thrust and engine controller input angle (International Standard Atmosphere, sea level static, and 12-stage air bleed)

Graph depicting the relationship between engine thrust and the input angle of the engine controller under standard atmospheric conditions at sea level with 12-stage air bleed.

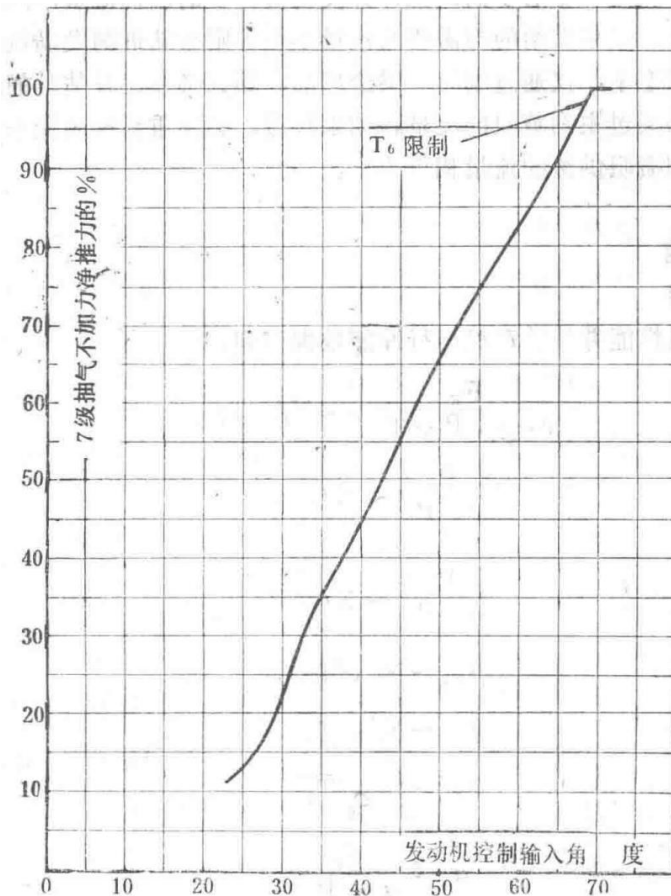


Figure 3: Relationship between thrust and engine control input angle (International Standard Atmosphere, sea level static, and 7-stage air bleed)

Graph illustrating the relationship between engine thrust and the input angle of the engine control under standard atmospheric conditions at sea level with 7-stage air bleed.

First Edition, June 9, 1965

## 9. Method for Estimating Engine Idle Speed

Technical Design Report	TDR4121
Spey MK202 Method for Estimating Engine Idle Speed	

## Abstract

This report provides a method for estimating the idle speed of an engine with current performance standards under any flight condition.

## 1. Introduction

The method for estimating idle speed provided in this report is based on a general approach. The foundation of this method involves hypothesizing an idle speed and calculating the required fuel flow for the engine at this speed from booklet curves. Then, the total fuel flow supplied by the control system to the main and secondary nozzles is estimated. If the supplied and required flows are not equal, the engine speed is re-hypothesized until they match. Under certain flight conditions, if fuel is supplied only through the secondary nozzle, it is necessary to compare whether the estimated fuel flow through the secondary nozzle exceeds the calculated flow through both the main and secondary nozzles. If it does, the idle speed must be re-hypothesized until the required engine

flow matches the flow supplied only through the secondary nozzle.

## 2. Method

### 2.1 Required Performance

#### (a) Engine Performance

The following engine performance parameters are required and obtained from the current engine performance data:

$$F \square, \mu F \square \alpha \square P_1 \sqrt{T_1} N, \sqrt{T_1},$$

Equation for engine required fuel flow as a function of high-pressure shaft speed and inlet temperature.

$$P_2, \mu \square \square P_1 N, \sqrt{T_1},$$

Equation for low-pressure compressor outlet total pressure as a function of high-pressure shaft speed and inlet temperature.

$$P_3, \mu \square \square P_1 N, \sqrt{T_1},$$

Equation for high-pressure compressor outlet total pressure as a function of high-pressure shaft speed and inlet temperature.

$$p \square, p \square \square p \square \square N, \sqrt{T_1},$$

Equation for pressure ratio as a function of high-pressure shaft speed and inlet temperature.

$$\mu \tau B N, \sqrt{T_1},$$

Correction factor for turbine efficiency as a function of high-pressure shaft speed and inlet temperature.

$$\mu \square \square N, \sqrt{T_1},$$

Correction factor for low-pressure compressor outlet pressure as a function of high-pressure shaft speed and inlet temperature.

$$\mu B \cdot / \sqrt{T_1},$$

Correction factor for engine performance parameter as a function of high-pressure shaft speed and inlet temperature.

$$\alpha \square F \square, \alpha \square \sqrt{T_1} \cdot F \cdot F,$$

Equation for engine control input angle as a function of required fuel flow.

#### (b) Fuel System Performance

The following fuel system performance curves are required, which are provided in Figure 1 and Figure 2 of this report:

$$P_3 \square, P_2 P_3, P_2,$$

Equation for the ratio of partial pressure at the high-pressure compressor outlet to the low-pressure compressor outlet total pressure.

$$n \square \square \square (P_3 \square - a \times P_2)$$

Equation for variable metering orifice flow characteristic number as a function of pressure difference.

## 2.2 Symbols Used

- $a$ : Fuel system constant = 0.455
- $F$ : Engine required fuel flow (lb/hr)
- $F$ : Fuel flow supplied by the fuel system (main and secondary nozzles) (lb/hr)
- $F'$ : Fuel flow supplied by the fuel system (secondary nozzle only) (lb/hr)
- $M$ : Flight Mach number
- $N$ : High-pressure shaft speed (RPM)
- $n$ : Variable metering orifice flow characteristic number
- $n_s$ : Secondary nozzle flow characteristic number = 2.5
- $n_t$ : Total flow characteristic number =  $n \times n_s \sqrt{(n^2 + n_s^2)}$
- $p_0$ : Ambient static pressure (psia)
- $P_1$ : Inlet total pressure (psia)
- $P_2$ : Low-pressure compressor outlet total pressure (psia)
- $P_3$ : High-pressure compressor outlet total pressure (psia)
- $p_3$ : High-pressure compressor outlet static pressure (psia)
- $P_{3d}$ : Partial pressure at high-pressure compressor outlet (psia)
- $\Delta P$ : Pressure differential across the variable metering orifice (psi)
- $\Delta P_{CASC}$ : Pressure differential across CASC at low flow = 305 psi
- $R_o$ : Ram recovery ratio
- $KK$ : Correction factor
- $t_0$ : Ambient static temperature (K)
- $T_1$ : Inlet total temperature (K)
- $\Delta V$ : True airspeed (knots)
- $QE$ : Engine fuel flow correction factor
- $HFE$ : Inlet temperature correction factor for engine fuel flow
- $HP2$ : Inlet temperature correction factor for low-pressure compressor outlet total pressure
- $\mu_{3d}$ : Inlet temperature correction factor for high-pressure compressor outlet total pressure
- $\rho$ : Fuel density (7.9 lb/gal)
- $\eta_{01}$ : Inlet total pressure recovery coefficient

The new engine performance calculation package incorporates the effects of these coefficients.

## 2.3 Theory

1. Calculate inlet conditions:
2. 'type': 'equation', 'latex': ' $M = 38.953 \sqrt{t_0}$ ', 'inline': False, 'description': 'Equation for calculating flight Mach number from true airspeed and ambient static temperature.'
3. 'type': 'equation', 'latex': ' $P_1 = p_0 \times R_o$ ', 'inline': False, 'description': 'Equation for calculating inlet total pressure from ambient static pressure and ram recovery ratio.'
4. (2) Hypothesize an idle speed  $N$  to determine  $N / \sqrt{T_1}$ .
5. (3) Calculate the engine required fuel flow:
6. Using specific values of  $N / \sqrt{T_1}$  and  $T_1$ , determine  $\mu_F$ ,  $F$ ,  $\mu_{F_d}$ ,  $\alpha$ ,  $P_1 / \sqrt{T_1}$ ,  $\mu_{P_d}$ ,  $\alpha_P / T$ ,  $HE$ , and  $\alpha$  to find  $F$  (lb/hr).
7. (4) Calculate the fuel flow supplied by the control system:
8. Using specific values of  $N / \sqrt{T_1}$  and  $T_1$ , determine  $P_2$  and  $P_3$ .
9. Since  $p_3 = 0.97 P_3$ , calculate  $P_3 / P_2$ .
10. From the curve in Figure 1, determine  $P_3 / P_2$ , thus finding  $P_3$ , and calculate  $(P_3 - a \times P_2)$ .
11. From the curve in Figure 2, determine  $n$ . Using the specific value of  $N$  and the equation  $\Delta P = (N^2 / 1264)^2$ , determine  $\Delta P$ .

12. (5) Compare the engine required fuel flow and the fuel flow supplied by the control system. If they are not equal, re-hypothesize  $N_c$  until  $F = F_c$ .
13. (6) Check if the flow through the secondary nozzle exceeds the flow through both the main and secondary nozzles. Using the final  $N_c$  and the  $n_c$  value, calculate  $n_o$ :
14. 'type': 'equation', 'latex': ' $n_o = \sqrt{n_c^2 + (n_s^2)^2}$ ', 'inline': False, 'description': 'Equation for total flow characteristic number.'
15. Thus,  $F' = \rho \times \sqrt{(\Delta P_c)} \text{ (lb/hr)}$ .
16. (7) If  $F > F'$ , use the  $N_c$  calculated in step 5. If  $F < F'$ , re-hypothesize  $N_c$  until  $F' = F_c$ . Note that in this case, it is not necessary to calculate  $\Delta P_{c,actual}$  or  $F$ .

## 3. Example Calculation

### 3.1 Flight Conditions

- Altitude: Sea level
- Flight speed: Static
- Atmospheric temperature: International Standard Atmosphere
- No power or air extraction
- $T_1 = t_o = 288 \text{ K}$
- Assumed inlet total pressure recovery coefficient  $\eta_{p1} = 0.995$
- $P_1 = p_o \times 0.995 = 14.62 \text{ psia}$

### 3.2 Hypothesize $N_c = 6500$

$$N_c, \sqrt{T_1} = 383.5$$

Equation for high-pressure shaft speed normalized by the square root of inlet total temperature.

### 3.3 From Performance Data

$$F_c, \mu F_c, \alpha_c P_1 \sqrt{T_1} = 3.54$$

Equation for engine required fuel flow based on performance data.

— Section 66 —  
Content from Original Document (Pages 326-330)

$$\mu_g = 1.0$$

Gas flow coefficient

$$F = \mu_g \times \rho \times A \times C_D \times C_{Laminar} = 3.54 \times 1.0 \times 14.62 \times \sqrt{288} = 877$$

Calculation of fuel flow parameter

$$\dot{F} = \dot{A} \cdot r \cdot \rho \cdot C_D \cdot C_{Laminar} = 877 \cdot \sqrt{14.62} = 229$$

Normalized fuel flow parameter

From performance data, it is known that  $\alpha_z = 1.113$ .

Thus,  $F_B = 978 \text{ lb/hr}$ .

### 3.4 From Performance Data

$$P_2, \mu_w P_1 = 1.05 \quad P_3, \mu_w P_1 = 2.795$$

Pressure ratio relationships

$$\mu_{\rho_2} = 1.0$$

Density coefficient at station 2

$$\mu_{\rho_3} = 1.0$$

Density coefficient at station 3

$$P_3 / P_2 = 2.453$$

Pressure ratio between stations 3 and 2

From Figure 1,  $P_{3p} / P_2 = 1.018$ .

$P_{3p} - a P_2 = 16.46 - 0.455 \times 16.18 = 9.11 \text{ lb/in}^2$ .

From Figure 2,  $n_vMO = 24$ .

$$\Delta P_{VMO} = 6500^2, 1264^2 = 26.45$$

Pressure difference calculation

Thus,  $F = \rho n_vMO \Delta P_{VMO} = 7.9 \times 24 \times \sqrt{26.45} = 978 \text{ lb/hr}$ .

### 3.5 Consistency Check

Since  $F$  and  $F_E$  are consistent, the assumed  $N_H = 6500 \text{ rpm}$  is correct.

### 3.6 Calculation of Corrected Parameter

$$n_c = 24 \times 2.5, \sqrt{24^2 + 2.5^2} = 2.48$$

Corrected parameter calculation

$$F \cdot r \cdot \rho \cdot A = \rho \cdot n_0 \cdot \sqrt{(\Delta P)} = 7.9 \times 2.48 \times \sqrt{305} = 342$$

Corrected fuel flow calculation

### 3.7 Idle Speed Confirmation

Since  $F > F_{\text{idle}}$ , the idle speed  $N_H = 6500$  rpm is confirmed.

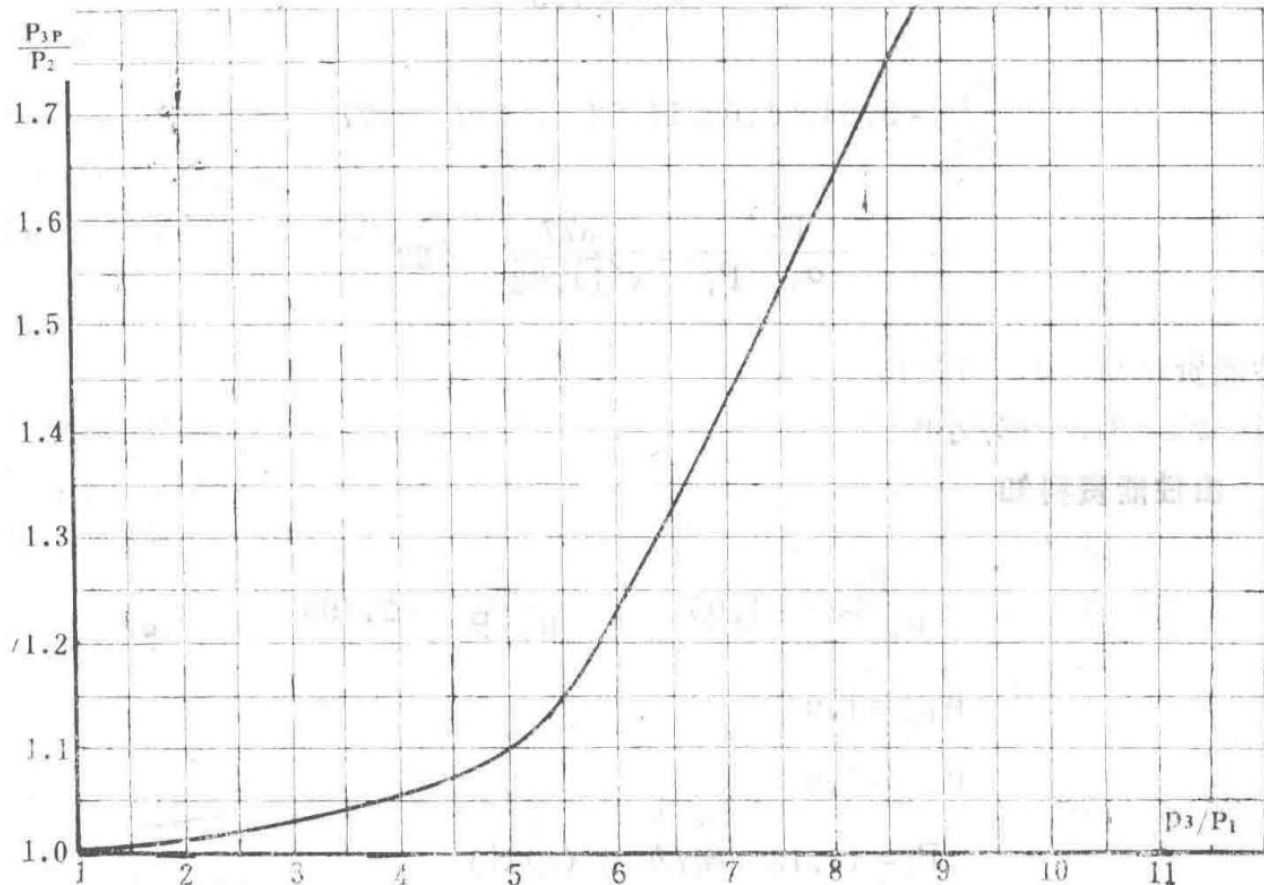


Figure 1: Air Pressure Divider Characteristics (Abscissa should be  $P_3 / P_2$ )

Graph showing the relationship of the air pressure divider characteristics with corrected abscissa.

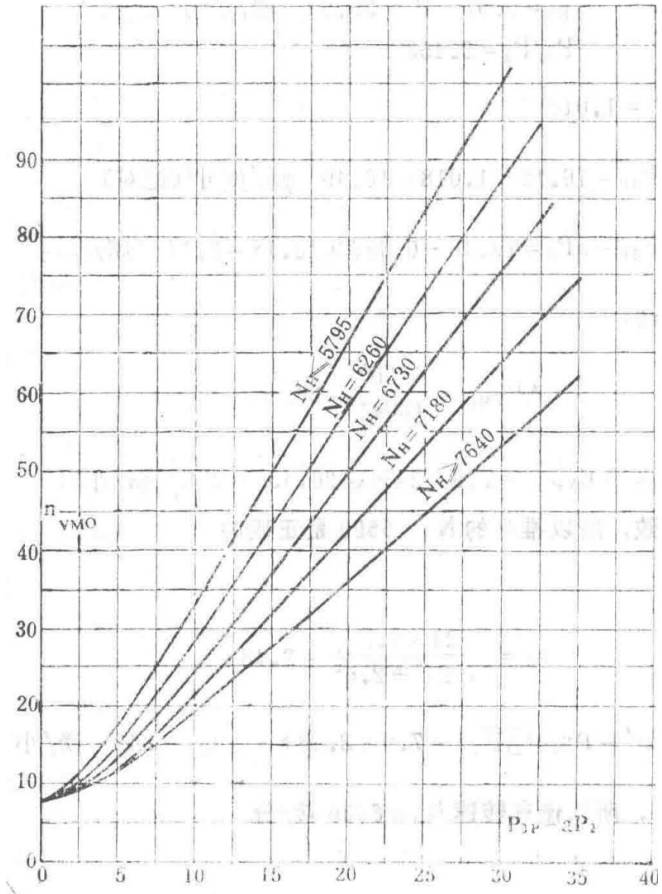


Figure 2: Metering Orifice Characteristics

Graph showing the characteristics of the metering orifice.

## 10. Drift of High-Pressure Rotor Speed Governor

Technical Design Report

Report	Report Number
Technical Design Report	TDR4181
Spey MK202 Drift of High-Pressure Rotor Speed Governor under Various Flight Conditions	

Lucas Gas Turbine Equipment Limited provided the following data on the drift of the high-pressure governor under International Standard Atmosphere (ISA) conditions at 36,089 feet, Mach 1.2 ( $T_1 = 280^{\circ}\text{K}$ ) and Mach 2.2 ( $T_1 = 426^{\circ}\text{K}$ ). This data is based on the operation of Engine No. 37 in the altitude test facility and the CASC calibration of the first seven flight engines with low working lines. It is assumed that the maximum speed regulated at sea level static conditions is 12,640 rpm.

- International Standard Atmosphere, 36,089 feet, Mach 1.2, maximum  $N \square = 12,300$  rpm.
- International Standard Atmosphere, 36,089 feet, Mach 2.2, maximum  $N \square = 13,100$  rpm.

The latter result is based on performance extrapolation and extended fuel system calibration, thus even the most effective estimates can only be considered approximate.

To reduce drift, subsequent CASC units were modified ( $N^2$  term modification).

## 11. Estimation of Idle Conditions for First Flight Engines

Technical Design Report  
Page 390

Report	Report Number
Technical Design Report	TDR4184
Spey MK202 Estimation of Idle Conditions for First Flight Engines	

## Abstract

This report provides the actual high-pressure shaft idle speeds for early flight engines delivered to customers under selected flight conditions.

As seen from the results in Table 1, the high-pressure shaft idle speeds are lower than those predicted in TDR796 and have been proven satisfactory in flight tests because the 4th edition (in TDR796) used generic characteristics.

## Introduction

The requirement for idle speed to increase with altitude in the 'Phantom' aircraft is achieved by bypassing the governor in the control system. This report examines selected flight conditions to check if the idle speeds of early flight engines exceed the maximum allowable engine rated speed.

Data from the altitude test chamber and test bed of flight-standard engines, as well as the latest flight CASC calibration results, were used.

## Data Used

- Average performance data from the test bed of flight engines, sourced from unpublished performance room data.
- Altitude factors for test bed performance.
- $T_1$  correction factors.
- Engine fuel flow correction factors.
- Standard atmospheric temperature.
- CASC idle speed calibration.
- Air pressure divider value of 4.6.

## Results

The following are the idle conditions at selected flight test points.

Table 1: Idle Conditions at Selected Flight Test Points

Flight Condition	F (lb/hr)	T <sub>3</sub> (°K)	N (rpm)	NH (rpm) (Brochure Engine TDR798)
35,000 feet ISA 0.85MN (a) $T_1=249.5\text{K}$ $P_1=5.48\text{ lb/in}^2$ (absolute)	640	454	9510	9750
45,000 feet Hot Day 0.8MN (b) $T_1=262.8\text{K}$ $P_1=3.23\text{ lb/in}^2$ (absolute)	598	507	10090	10440
45,000 feet Hot Day 1.0MN (c) $T_1=279\text{K}$ $P_1=3.96\text{ lb/in}^2$ (absolute)	576	--	10150	10550

72,000 feet ISA 2.15MN (d) $T_1=434K$ $P_1=4.965 \text{ lb/in}^2$ (absolute)	594	745	12170	12550
67,000 feet Cold Day 2.2MN (e) $T_1=368.3K$ $P_1=6.81 \text{ lb/in}^2$ (absolute)	<11000 rpm, insufficient data	--	--	10550
60,000 feet ISA 2.4MN (f) $T_1=466K$ $P_1=11.82 \text{ lb/in}^2$ (absolute)	Accurate value undetermined	--	--	11900
75,000 feet ISA 1.6MN (g) $T_1=329K$ $P_1=2.03 \text{ lb/in}^2$ (absolute)	498	638	11500	12500

## Discussion

Idle speeds are lower than those predicted in earlier reports using brochure performance (compare columns 3 and 4 in Table 1). Within the altitude range of 75,000 feet, idle speeds did not exceed the maximum allowable speed; above 75,000 feet was not studied.

Accurate data is difficult to obtain when flight engines operate at low non-dimensional speeds (i.e., with bleed valves open).

The calculated idle speeds for conditions (e) and (f) are close to ground idle speeds (possibly due to incorrect ram ratio conversion). These results are inconsistent with previous idle speed tests and are therefore disregarded.

For the oil system, the limiting flight condition is at 45,000 feet on a hot day and Mach 1.0.

From the studied conditions, the  $T_3$  limit of 806°K was not exceeded.

## 12. Hysteresis of Cam Box Input Lever

First Edition: 9 November 1966

Technical Design Report

Report	Report Number
Technical Design Report	TDR7005
Spey MK202 Hysteresis of Cam Box Input Lever	

### 1. Purpose of the Report

To summarize the existing hysteresis data of the power control system. The aircraft manufacturer requires a hysteresis band of 1°.

### 2. Conclusions

2.1 The evidence available so far indicates that the current engine system limits the hysteresis of the cam box input angle to 1°, which is a practical requirement for the following usage: power lever movements within the landing approach power range (approximately 80% - 90% N $\square$ , 12-stage boundary layer control) only require small adjustments around the steady-state thrust condition.

2.2 For power lever movements from idle to takeoff and from takeoff to idle, the above requirement is less practical. Tests conducted so far show that one of the two test engines exceeded the requirement for maximum hysteresis.

Further testing is required to empirically establish the requirement in section 2.1 for some engines. Special attention should be given to eliminating instrument backlash and reducing throttle lever friction to enable very small throttle lever movements (less than 0.1%).

Testing should be conducted by making small changes to the throttle lever angle near steady thrust conditions, rather than by pushing from idle to takeoff thrust and pulling back to idle.

### 3. Introduction

3.1 The aircraft manufacturer's requirement specifies a hysteresis limit of 1° for the cam box input lever.

3.2 This report documents and evaluates the data obtained so far from engine and test bed tests regarding this requirement.

### 4. Test Bed Testing of CASC Unit

4.1 Lucas's relevant report documents the hysteresis values of the input levers for three CASC units, with the maximum hysteresis being 30 minutes.

4.2 After setting an appropriate regulator flow and input lever angle set point, the hysteresis is determined by opening and closing the input lever to move away from and return to the set point flow. The hysteresis is the difference between the two input lever angles corresponding to a small deviation from the set point flow and returning to it. The results of these tests are shown in Table 1.

Table 1: Hysteresis Test Results of CASC Units

CASC Unit	Hysteresis (degrees)
Unit 1	0.5
Unit 2	0.3
Unit 3	0.5

— Section 67 —  
Content from Original Document (Pages 331-335)

Table 1

Flow Rate gal/hr	Input Rod Angle Deg Min	P <sub>a</sub> P lb/in <sup>2</sup> (absolute)	CASC Speed rpm	Input Rod Angle After Opening Deg Min	Deg	Input Rod Angle After Closing Min	Hysteresis Min	Control Device No.
900	50 00	229	33	50 00	4000	49 50	10	B950
700	40 00	196	30	40 00	3950	40 10	10	B950
320	30 00	146	25	30 05	3920	30 10	10	B950
300	20 00	96	25	20 05	3370	20 05	5	B950
910	50 00	229	33	49 50	4040	49 40	20	B962
700	40 00	196	30	40 05	3950	40 10	10	B962
450	30 00	146	25	30 05	3350	29 50	15	B962
700	50 00	229	33	50 30	4300	50 25	30	B964
700	40 00	196	30	40 10	4050	40 25		B964
450	30 00	146	25	30 00	3925	30 05	25	B964
350	20 00	96	20	29 19	3380	19 45	20	B964

## 5. Engine Testing

5.1 From the test on Engine No. 503, the relationship between engine speed and cambox input angle was obtained when increasing and decreasing the speed. Figure 1 shows the resulting hysteresis curve.

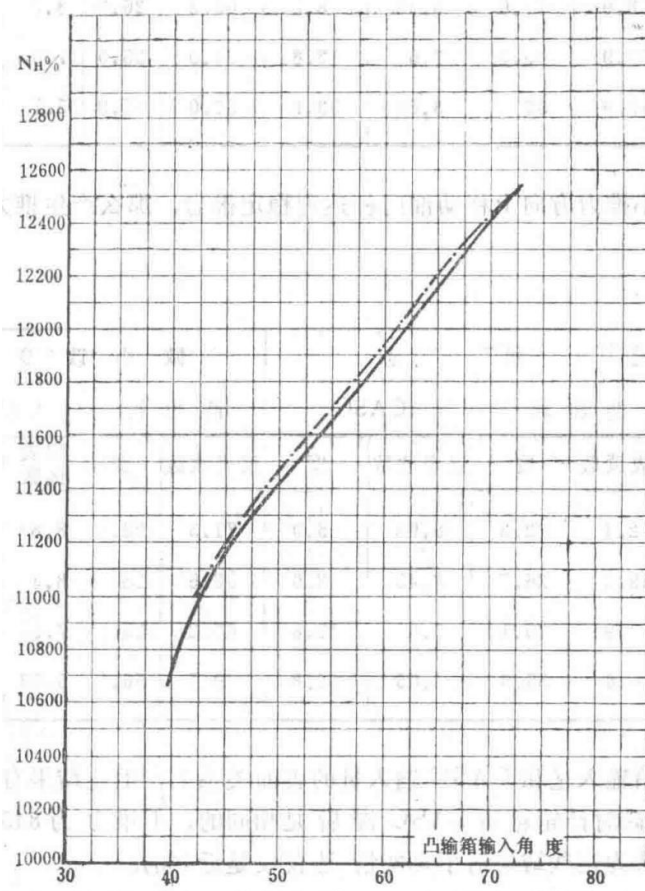


Figure 1 Hysteresis of Engine Speed ( $N_{\text{rpm}}$ ) vs. Cambox Input Angle (Sea Level Static, No Bleed)

Graph showing the hysteresis relationship between engine speed ( $N_{\text{rpm}}$ ) and cambox input angle during engine testing.

5.2 Similar tests were conducted on Engine No. 39 with test instrumentation applied to the cambox input rod and CASC device. The engine was operated at four thrust levels by increasing the input rod setting, then at the same thrust levels by decreasing the input rod setting. The test results are plotted in Figure 2.

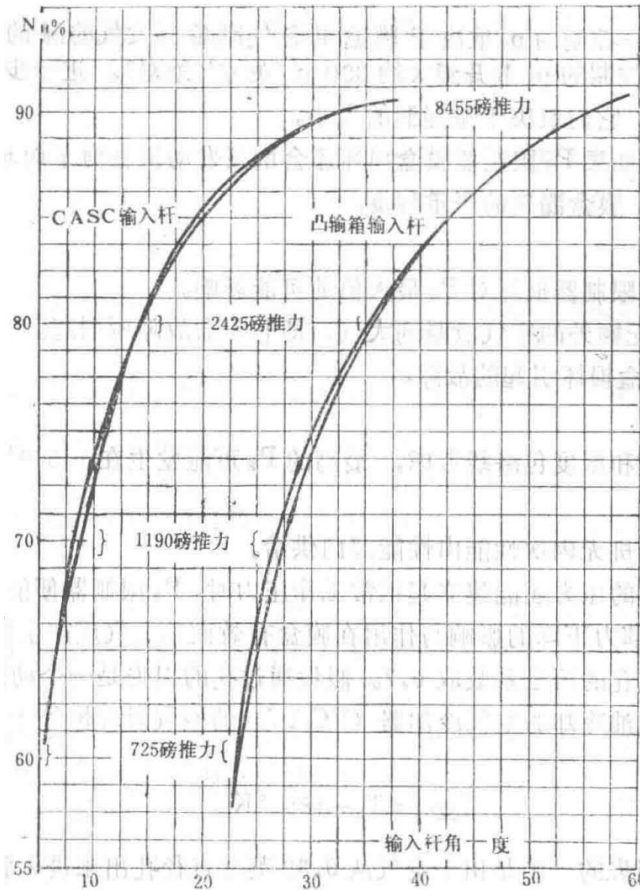


Figure 2 Hysteresis of Cambox and CASC Device Input Angles vs. Engine Speed

Graph showing the hysteresis relationship between cambox and CASC device input angles and engine speed.

5.3 Further tests were conducted on Engine No. 39 to determine hysteresis for small deviations around steady thrust conditions. The test involved several steady thrust conditions, each achieved by moving the throttle lever in a predetermined direction with a small final movement. After engine stabilization, the throttle lever was moved in the opposite direction from the steady setting, and the movement required to detect a change in thrust from the steady state was recorded.

## 6. Results

6.1 Lucas test rig results indicate that the maximum hysteresis of the CASC angle is 30 minutes. The ratio between the cambox input rod and CASC rod is very close to 1, so a 30-minute hysteresis on the CASC approximately results in a 30-minute hysteresis in engine input.

6.2 Figure 1 shows that the maximum hysteresis of the cambox input angle recorded on Engine No. 503 is approximately  $1.2^\wedge$ . Neglecting linkage growth and backlash, the CASC hysteresis is approximately equal to  $1.2^\wedge$ .

$1.2^\wedge \square \square^r \square,$

Maximum hysteresis angle of cambox input.

6.3 The curves for Engine No. 39 (Figure 2) show a maximum cambox input hysteresis of  $1^\wedge$  and a maximum CASC input hysteresis of  $0.75^\wedge$ . However, these results cannot be readily accepted because the CASC device input curve is reversible at high speeds, indicating some backlash in the CASC display system. Therefore, the maximum CASC input hysteresis may be slightly larger than indicated.

$1 \square \square^r \square,$

Maximum cambox input hysteresis.

0.75\□□'□,

Maximum CASC input hysteresis.

6.4 The results of the "small movement" hysteresis test on Engine No. 39 are listed below:

- (a) When a steady thrust is achieved by moving the throttle lever in the increasing thrust direction, the minimum throttle lever displacement that produces a detectable thrust decrease is the hysteresis.
- (b) When a steady thrust is achieved by moving the throttle lever in the decreasing thrust direction, the minimum throttle lever displacement that produces a thrust increase is the hysteresis.

Table 2

N□ %	Thrust lb	Steady State			Small Change			Hysteresis			
60.05	725	71.9	23	8.95	4.9	72.7	22	9.0	4.5	1	0.4
70.08	1190	68.9	27.6	8.43	8.2	69.8	26.3	8.5	7.7	1.3	0.5
80.01	2420	63.9	35.3	7.6	13.8	64.0	35.0	7.65	13.5	0.3	0.3
90.04	8450	49.9	56	5.65	33.8	50.0	55.9	5.7	33.1	0.1	0.7

Table 3

N□ %	Thrust lb	Steady State			Small Change			Hysteresis			
60.1	720	72.4	22.3	8.93	5.0	71.5	23.7	8.8	5.75	1.4	0.75
70.02	1190	69.5	26.7	8.45	8.0	68.6	28	8.4	8.4	1.3	0.4
79.99	2420	63.9	35.1	7.6	13.8	63.2	36	7.53	14.4	0.9	0.6
90.00	8470	50.0	55.9	5.65	33.8	49.7	56.3	5.63	34	0.4	0.2

It should be noted that the above results show some inconsistencies in the apparent relationship between cambox input and CASC input. In section (a), at 2420 lb thrust, the cambox and CASC hysteresis are the same, but at 8450 lb thrust, they differ significantly. The following reasons suggest these results are only approximate for the real situation:

1. The backlash in the test instrumentation mentioned in section 6.3 results in greater control hysteresis under purely mechanical influences. It is known that there is a measurable backlash in the connecting rods and crank system of the CASC input rod test instrumentation.
2. Due to the inherent stiffness of the test rig control rod, it is not always possible to measure the minimum movement required to change thrust. In most cases, the quoted results represent the smallest movement obtainable on the throttle lever. The actual hysteresis may be slightly smaller than indicated by the test.

## 7. Discussion

7.1 It has been noted that the test procedures described in sections 5.1 and 5.2 are not entirely suitable for determining hysteresis limits. The system is more likely to be disturbed by small throttle lever movements at steady thrust, which may have a greater impact than the overall effect of increasing power lever settings from a "cold" state and decreasing from a "hot" state. From the results of the Engine No. 39 test (section 5.2, Figure 2), it is known that engine performance changes when operated in this manner. The speed required to achieve a given thrust by reducing power is lower than that required by increasing power.

7.2 It can be expected that the hysteresis for small movements of the cambox input rod at steady thrust is smaller than measured in the above tests. However, the "small movement" test results (section 6.4) do not clearly demonstrate this. Although there are indications that within the approach power range, the cambox input hysteresis is within the required 1<sup>o</sup> limit, further testing is recommended. Special attention should be given to reducing the stiffness factor of the throttle lever and estimating the backlash in the test instrumentation.

1\□□□□,

Required hysteresis limit for cambox input.

## 13. Estimation of Maximum High-Pressure Compressor Outlet Pressure Due to P<sub>3</sub> Limiter Failure

Technical Design Report

Technical Design Report	TDR 7799
Spey MK202 Estimation of Maximum High-Pressure Compressor Outlet Pressure Due to P <sub>3</sub> Limiter Failure	

First Edition, November 20, 1975

### 1. Purpose

To estimate the maximum high-pressure compressor outlet static pressure (p<sub>3</sub>) caused by P<sub>3</sub> limiter failure.

### 2. Conclusions

2.1 P<sub>3</sub> limiter failure not caused by capsule fault allows P<sub>3</sub> to reach approximately 533 lb/in<sup>2</sup> (absolute). The normal maximum p<sub>3</sub> is 345 lb/in<sup>2</sup> (absolute).

2.2 Additional airflow caused by P<sub>3</sub> limiter capsule failure increases the pressure loss in the p<sub>3</sub> air pipe leading to the CASC, so the controlled p<sub>3</sub> depends on the size of the hole leaking air from the capsule to the atmosphere. For a 3/16-inch diameter hole in the capsule, the controlled p<sub>3</sub> rises to approximately 390 lb/in<sup>2</sup> (absolute). Further increases in hole size will reduce engine power and P<sub>3</sub>, depending on the size of the leak.

2.3 Thus, if the P<sub>3</sub> limiter capsule is damaged, it will also reduce engine power at sea-level takeoff conditions. The degree of power reduction depends on the severity of the capsule air leak.

### 4. Introduction

This report assesses the possible impact of P<sub>3</sub> limiter failure on the maximum P<sub>3</sub> value.

- (a) Failure occurs without additional air leakage to the atmosphere, i.e., not caused by capsule fault.
- (b) Failure caused by P<sub>3</sub> limiter capsule damage.

### 5. Assumptions

5.1 Considering aircraft flight and temperature envelopes, the highest P<sub>3</sub> is likely to occur at 1.209 MN, cold weather (T<sub>1</sub> = 319.5°K).

5.2 The engine's non-dimensional performance with afterburner is provided by the performance department.

5.3 The P<sub>3</sub> limiter operates normally when the pressure in the bellows can still establish normal working pressure. This is because the effect of leaks or cracks reducing the internal force of the capsule is small compared to the force generated by the air pressure acting on the effective area of the capsule.

5.4 The flow coefficient of the leak hole in the capsule is taken as 0.7. The loss through the hole is assumed to be one dynamic head.

5.5 It is assumed that the air temperature drop through the Fuel-Cooled Air Cooler (FCAC) is constant at 180°C. With speed variation, the air temperature is:

$$T_{\text{air}} = T_3 - 180 \text{ K},$$

Air temperature after passing through the FCAC.

5.6 It is assumed that half of the pressure head loss is caused by air exiting from a 0.32-inch diameter hole into the capsule (capsule effective area =  $\pi/4 \times 0.625^2 \approx 0.307 \times 0.625 \approx 0.307 \text{ in}^2$ ). W02A

5.7 The conduit area from FCAC to CASC and the internal hole area of the limiter housing = 0.0804 in<sup>2</sup>.

5.8 Acceleration control is calculated by applying steady P<sub>3</sub> and P<sub>2</sub> pressures to a typical CASC calibration method. Transient effects of P and P<sub>2</sub> are ignored.

5.9 When calculating conduit pressure loss, the leakage flow has been added to the flow through the divider.

5.10 It is assumed that the pressure loss in the hole of the P<sub>3</sub> limiter is small and ignored. Most of the pressure loss due to leakage is caused by the short pipe from FCAC to CASC. When the conduit is 16 inches long, the head loss due to bending is 3.5.

5.11 The additional pressure drop upstream of the FCAC caused by additional flow is ignored. Since the upstream conduit inner diameter is much larger than 5/16 inches and carries afterburner servo airflow, the increase in CASC airflow is unlikely to cause a significant increase in conduit pressure drop.

5.12 The high-pressure compressor outlet total pressure (P<sub>3</sub>) is 1.069 times the CASC pipeline pressure just downstream of the FCAC, and p<sub>3</sub> = 0.97 P<sub>3</sub>.

$$p_3 = 0.97 P_3$$

Relationship between static and total pressure at high-pressure compressor outlet.

The low-pressure compressor outlet pressure (P<sub>2</sub>) = 1.025 P<sub>2</sub> ROD.

5.13 When calculating the maximum speed of the high-pressure regulator, it is assumed that under International Standard Atmosphere sea-level static conditions, the nominal setting of the high-pressure regulator is 98.5% N $\square$ .

5.14 The normal setting range of the F/N $\square$  limiter is between 1.125 and 1.24. When considering the operation of this limiter, the lowest setting of 1.125 is assumed.

## 5.15 Cooling and Servo Flow from High-Pressure Fuel System

The average values of cooling flow and servo flow from the high-pressure fuel system are assumed based on the use of AVTAG fuel. Together, they represent the possible fuel supply capacity of the high-pressure fuel pump that limits fuel flow under extreme failure conditions.

## 6. Results

6.1 At Mach number  $M \square = 1.209$  and under cold-day conditions, the expected maximum  $p_3$  values when the  $P_3$  limiter fails are as follows:

1. When the  $N \square$  regulator takes control,  $p_3 = 531$  psi (absolute), and the low-pressure compressor outlet total pressure ( $P_2$ ) = 86.5 psi (absolute).
2. When the  $F/N \square$  limiter takes control, with  $\text{rac}F, N \square = 1.125$  (minimum setting),  $N \square = 94.7\%$ ,  $p_3 = 489$  psi (absolute).
3. When limited by the fuel pump capacity,  $N \square = 95.5\%$ ,  $p_3 = 509$  psi (absolute). Additionally, when the fuel pump safety valve is open, accurately predicting the maximum  $p_3$  value is difficult.

The above data pertain to  $P_3$  limiter failures not caused by  $P_3$  capsule leakage.

6.2 When the  $P_3$  limiter capsule is damaged with a hole diameter of approximately 3/16 inch, the estimated maximum  $p_3 = 390$  psi (absolute) ( $P_2 = 72.5$  psi (absolute)).

For a 3/16-inch diameter hole, as the capsule leakage increases, the maximum  $p_3$  value rises from 345 psi (absolute) (no leakage) to 390 psi (absolute). If the hole size exceeds this value, the acceleration line will fall below the steady-state operating line, significantly reducing engine power depending on the degree of leakage (see Figure 1).

6.3 Similarly, the acceleration line was plotted for a typical takeoff condition (International Standard Atmosphere sea level,  $M \square = 0.3$ ) with a  $P_3$  limiter capsule hole diameter of 1/4 inch. It shows that the engine speed is controlled at 95%  $N \square$ . Any increase in leakage will further reduce engine power.

## 7. Discussion

7.1  $P_3$  limiter failures not caused by capsule damage are quite rare but can result from one of the following situations: (a) control lever jamming or (b) external adjustment screw causing the hemispherical valve to close completely.

7.2 The results in Section 6.1 indicate that if the bellows reverse stop screw is adjusted to the lowest limit, the engine can be limited by the  $F/N \square$  limiter or the high-pressure shaft speed regulator. The engine may also be limited by the high-pressure fuel pump flow capacity, occurring before the high-pressure speed regulator takes control.

Since the  $P_3$  limit depends on the setting related to the limiter and the high-pressure fuel pump along with its associated leakage, the limit value is difficult to determine precisely. However,  $p_3$  cannot exceed 531 psi (absolute) under any circumstances.

7.3 Discussions with BFA (Stress Department) revealed that the high-pressure compressor casing was tested at 1 times the normal operating pressure, so the casing can withstand additional pressure for short durations. The likelihood of failure occurring first in the coldest weather or during high-speed flight is minimal.

7.4 Since the pressure drop occurs in the pipeline supplying  $P_3$  to CASC, the high-pressure rise caused by  $P_3$  limiter capsule damage can be automatically moderated. The possibility of operating at increased maximum pressure over a period cannot be ruled out. However, leakage can significantly reduce the ACU margin, necessitating further investigation.

7.5 Sufficient leakage causes the acceleration line to fall below the engine operating line, leading to a substantial reduction in engine power. This significantly decreases sea-level takeoff thrust. This conclusion is derived from trend analysis of calculation results.

7.6 If the compressor outlet pressure is still higher than permissible, reducing the F/N□ limiter setting to 0.89–0.91 can lower the outlet pressure. Under sea-level, cold-day,  $M\infty = 1.209$  conditions, this adjustment limits  $P_3$  to approximately 396 psi (absolute). Preliminary checks indicate it is unlikely to significantly interfere with engine acceleration performance.

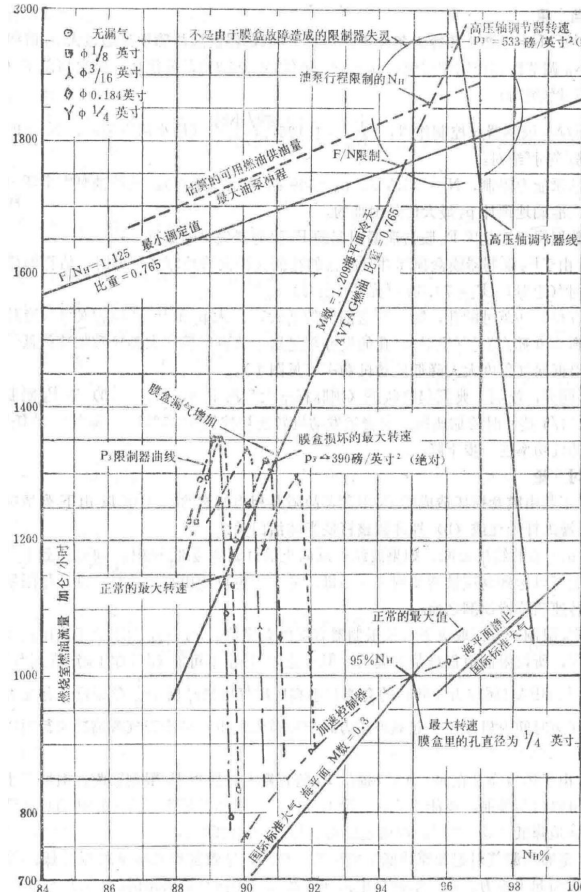


Figure 1: Estimated Effects of  $P_3$  Limiter Failure (During Afterburning)

This figure illustrates the impact of P<sub>3</sub> limiter failure on engine performance, showing acceleration lines and operating limits under various leakage conditions.

7.7 If the potential issue becomes a real problem, adjusting the F/N□ limiter, along with incorporating a suitable small restrictor in the channel leading to the P<sub>3</sub> limiter capsule, can serve as a safety measure to prevent significant engine power loss due to capsule failure.

## 14. Appendix 1: CASC System Theory

By using a generalized dimensionless plot of corrected fuel flow  $\frac{racF}{P_1} \sqrt{T_1}$  against corrected speed  $\frac{racN}{\sqrt{T_1}}$ , the seemingly complex steady-state engine operating characteristics, which vary with inlet conditions, are simplified into a single curve. Similarly, a second unique curve representing the engine stall boundary can be plotted on the same graph. If the acceleration control operates just below the stall boundary, the engine can achieve the maximum allowable excess fuel at any condition, enabling the fastest possible acceleration control.

For the Spey engine, the critical stall condition occurs in the high-pressure compressor. The high-pressure compressor, combustion chamber, and high-pressure turbine can be considered as a complete engine, with its inlet conditions being the low-pressure compressor outlet, i.e., pressure  $P_2$  and temperature  $T_2$ . The appropriate

dimensionless plot representing the Spey stall boundary ( $\frac{F}{P_2} \sqrt{T_2}$ ) is shown in Figure 1 (Section 15).

The difficulty in controlling these parameters lies in the need to measure compressor temperature. However, this additional complexity can be eliminated by rearranging the dimensionless terms. Using pressure ratio instead of  $\frac{N}{\sqrt{T_2}}$  allows the development of a representation that does not explicitly include temperature terms, though it still adequately accounts for temperature effects. The second curve represents the same engine and its control characteristics using these new quantities ( $\frac{F}{P_2} N \frac{P_3}{P_2}$ ). This curve forms the basis of CASC acceleration control. High-quality acceleration control is achieved, and the elimination of explicit temperature terms while retaining implicit temperature compensation is considered a particularly important factor.

## Generation of Acceleration Control Function

The foundation of any fuel system is the control of the variable metering orifice (VMO) area and its pressure differential.

Assuming the fluid passing through the metering orifice loses its dynamic pressure head, a square-law equation for these two parameters can be derived. Thus, the final equation for fuel mass flow rate is  $F = K A \sqrt{\Delta P}$ , where the constant accounts for unit conversion and flow coefficient. The role of CASC is to vary  $A$  and  $\Delta P$  in such a way as to provide the aforementioned acceleration/deceleration schedule and steady-state operation, automatically adjusting for changes in  $P$  caused by fuel type and temperature variations.

The method to achieve the above acceleration schedule based on this principle is as follows:

The metering area  $A$  can be directly altered by selected engine pressures. To minimize the effects of friction, the highest possible engine pressure is used, and the metering valve is rotated to overcome static friction. Since the high-pressure compressor working line is most sensitive to fuel flow changes, the obvious choice is the pressure before and after the high-pressure compressor. Therefore,

$$A = f(P_3) - a P_2,$$

Equation for metering area  $A$  as a function of  $P_3$  and  $P_2$ .

The pressure differential is determined by the force generated by the flyweights acting on the pressure differential piston.

For acceleration conditions, combining these parameters according to the square-law expression for flow through an orifice and rearranging gives:

$$\frac{F}{P_2} N = f(P_3, P_2 - a)$$

Dimensionless equation representing the acceleration control characteristic.

Here, it can be seen that the characteristic is represented by the required dimensionless parameter combination. The precise shape of the characteristic curve depends on the function of compressor pressures delivered to the controller. The overall effect is to modify a basic straight line into a curve in the low engine speed range. The basic straight line arises from directly using  $P_2$  and  $P_3$ , with an intercept of "a" on the  $P_3/P_2$  axis. This allows the adjusted characteristic line to closely approach the engine stall boundary (similar curve shape), especially in the mid-speed range where the allowable excess fuel supply is minimal.

Now, we examine in detail how Equation (1) is actually derived. The schematic of the bellows assembly is shown in Figure 3. The displacement of the bellows assembly is proportional to  $[P_3 R_1 + (P_3 - P_2) R_2]$ , where  $R_1$  and  $R_2$  are the stiffnesses of the vacuum and  $P_2$  bellows assemblies, respectively.  $P_3$  is the partial pressure, whose value lies between  $P_3$  and  $P_2$ .

The displacement of the bellows assembly  $\propto P_3 (R_1 + R_2) - R_2 P_2$ ,

where the bellows stiffness is assumed constant.

The partial pressure ( $P_3$ ) is obtained from the characteristics of the air pressure divider or restrictor orifice system simply represented in Figure 3.

When the venturi is "choked," i.e.,  $\frac{m}{A} \sqrt{T} A_2 P_3 = 0.3964 = Q_2$ , the pressure ratio  $\frac{P_3}{P_3}$  is approximately the required R value.

$$Q_2 = m_1 \sqrt{T} A_1 P_3 = 0.3964$$

Flow parameter for upstream restrictor orifice when choked.

By flow continuity,  $m_1 = m_2$ , and assuming constant temperature,

$$P_3 P_3 = A_2 A_1,$$

Relationship between  $P_3$  and  $P_3$  based on area ratio.

The areas referenced are "effective" areas = flow coefficient (CD) times actual or geometric area. The actual area depends on the relevant flow coefficient.

When the system is "choked,"  $\frac{P_3}{P_3} = R$ , and the partial pressure  $P_3$  is given by the area ratio A (see Figure 4) and depends only on  $P_3$ . Strictly speaking, the pressure supplied to CASC is the high-pressure compressor outlet static pressure (neglecting pipeline losses), denoted as  $p_3$ .

For  $P_3, P_2, P_3 \approx P_2$ .

This yields the  $P_2$  N characteristic line shown in Figure 4.

A well-designed venturi reaches "choke" when the total pressure ratio across it is 1.2. This allows the airflow through the pressure divider system to choke at a much lower total pressure ratio than other venturis, closely approaching the surge characteristic line without entering the surge region while providing high starting flow.

## Deceleration Control

When the pilot moves the control lever to reduce the selected engine speed, the VMO area is scaled relative to the possible acceleration area by a coefficient. Thus, the deceleration control characteristic is a scaled-down version of the acceleration control characteristic below the steady-state operating line, resulting in a dimensionless deceleration control.

## Fuel Density Compensation

The acceleration and deceleration characteristics of the system should be independent of fuel density changes to maintain accurate fuel mass flow. Since the fuel mass flow metered by the VMO at constant pressure differential is proportional to the square root of fuel density, it follows that if the pressure differential changes inversely with fuel density, the metered fuel mass flow remains constant. This is fundamentally achieved in the controller by selecting the material of the pressure differential piston flyweights, which is closely related to fuel density. Thus, changes in fuel density cause an inverse change in the "apparent density" of the flyweights, resulting in a corresponding change in the centrifugal force balancing the VMO pressure differential.

## Full-Range Speed Regulation

The Spey engine employs full-range speed regulation because it provides better thrust response at all altitudes. That is, it gives the engine the same "operational feel" throughout the flight envelope without excessive dead zones in the throttle lever. Since the primary goal of the Spey fuel control system is to keep the system as simple as possible, it is desirable to use the same metering orifice for both acceleration control and speed regulation. The CASC acceleration control principle is well-suited for integration with full-range speed regulation.

Previous regulations indicated that some response and stability issues needed resolution, especially when the engine intended to adopt full-range speed regulation. These issues became more apparent through studies of engine and controller dynamic responses and the impact of operational response requirements within the engine

flight envelope. From this, it became clear that gain compensation was required in the control loop.

The metering orifice sensing used for acceleration control, as described earlier, also provides the basis for direct proportional regulation. The required gain compensation is automatically provided while ensuring stability and near-constant speed control without additional data readjustment devices.

## Achieving Constant Speed Regulation

In the high-pressure ratio portion of the venturi "choke" curve, the acceleration control characteristic is almost linear. Over the same pressure ratio range, the steady-state fuel requirement line is also nearly linear. Since both lines intersect at a single point on the  $P_3/P_2$  axis, simply adjusting the VMO slot width can yield both lines from the same controller. When the steady-state operation requirements are met in this way, the slot width changes only slightly in the high engine speed range. The force generated by the regulator spring is almost entirely dependent on the throttle lever position. Thus, the balancing force provided by the regulator flyweights also corresponds to the throttle lever position. Therefore, regardless of inlet conditions, for each throttle lever position, there is an almost constant high-pressure shaft speed, effectively providing constant speed regulation. Considering the dimensionless parameter  $\frac{racF}{P_2} \propto \frac{racP_3}{P_2}$ , it can be observed that changes in inlet temperature cause slight deviations in constant speed regulation.

To minimize the effect of fuel specific gravity changes on the flyweight force at a given speed, the speed regulator flyweights are made of heavy metal.

## 15. Appendix 2: Initial CASC Calculation Examples

### Acceleration Control Curve

$$F_{P_2} N = f(P_3, P_2 - a)$$

Acceleration control curve equation.

Given that the VMO slot width is constant and assuming the pressure divider system is "choked" ( $P = R$ ), i.e., the engine operates under conditions where the acceleration control curve is derived.

Figure 1 Data Interpretation (Estimated Effects of  $P_3$  Limiter Failure)

Leakage Condition	Description	Impact
No leakage (○)	No leakage from the capsule	Maximum $p_3$ limited to 533 psi (absolute)
1/8 inch diameter (□)	Small leakage from the capsule	Acceleration line constrained by $N$ regulation
3/16 inch diameter (△)	Moderate leakage from the capsule	Reduced maximum $p_3$ (~390 psi absolute)
0.184 inch diameter (◊)	Significant leakage	Acceleration line below steady-state operating line
1/4 inch diameter (Y)	Large leakage	Engine power significantly reduced, hole diameter critical at 1/4 inch

— Section 69 —  
Content from Original Document (Pages 341-345)

At high pressure ratios.

$$F, P_2 N_H = ^* K_A (\partial p_3, \partial P_2 : R - a)$$

Equation relating fuel flow to pressure ratio and system parameters.

The line representing acceleration control (ACU) and the line representing steady-state fuel requirement intersect on the  $P_3 / P_2$  axis, with the intersection coordinates as follows:

Substituting these values into Equation (2):

$$0 = K_A (2.23, R - a),$$

This yields:

$$a = 2.23, R,$$

Point A on the ACU is (6, 0.016).

From Equation (2):

$$0.016 = K_A (6, R - a) = K_A (6, R - 2.23, R)$$

It follows that:

$$K_A = 0.016 R, 3.77,$$

At:

$$p_3, P_2 = 1 H, F, P_2 N_H = 0.0114$$

Note: The original text incorrectly stated 0.0014.

Substituting into Equation (2) gives:

$$0.0114 ^* = 0.016 R, 3.77 (1 - 2.23, R)$$

From this, we derive:

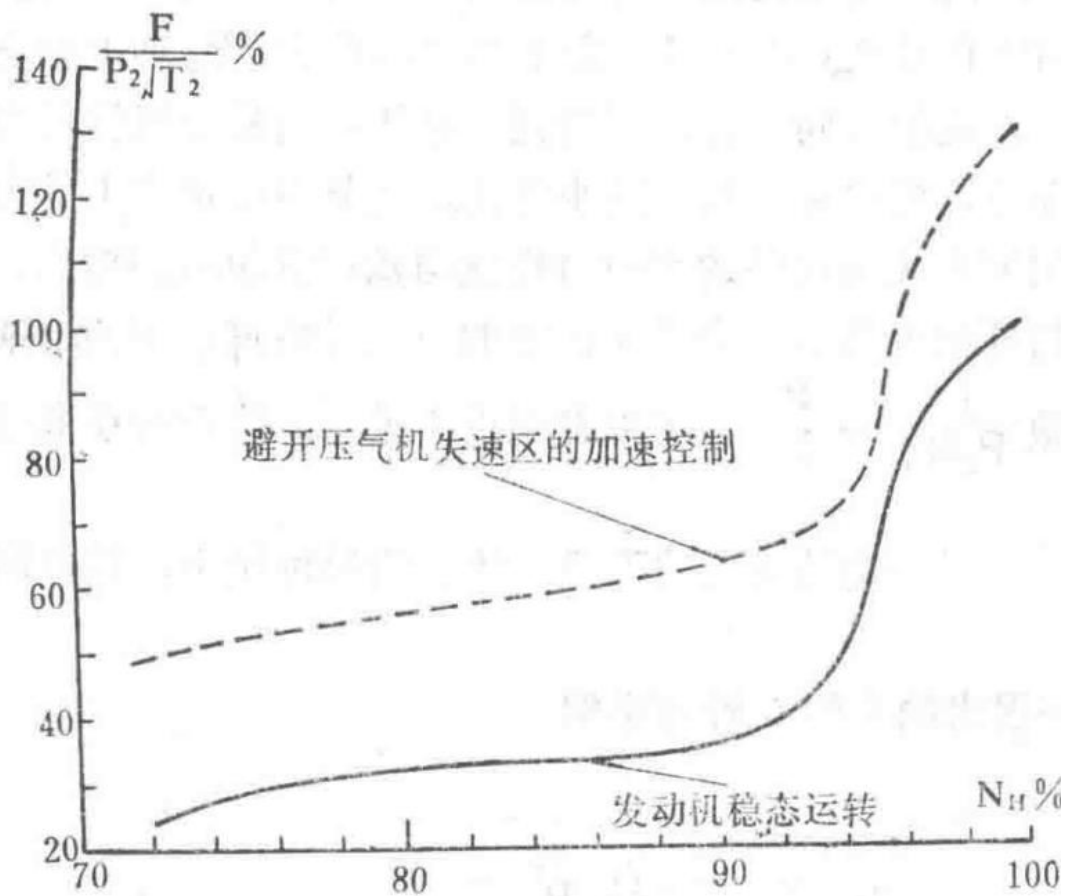


Figure 1 Engine Dimensionless Characteristic Line

Graph showing the dimensionless characteristic line of the Spey MK202 engine.

$$R = 4.91 \quad a = 2.23, \quad R = 0.455$$

Thus, the appropriate area ratio for the air pressure divider system is  $A_2, A_1 = 4.91$ .

Subsequently, considering the appropriate flow coefficients, the sizes of the pressure divider throttle orifice and venturi are selected. To achieve a bellows ratio of  $a = 0.455$ , a total of 11 bellows is suitable, with 5 connected to  $P_2$ .

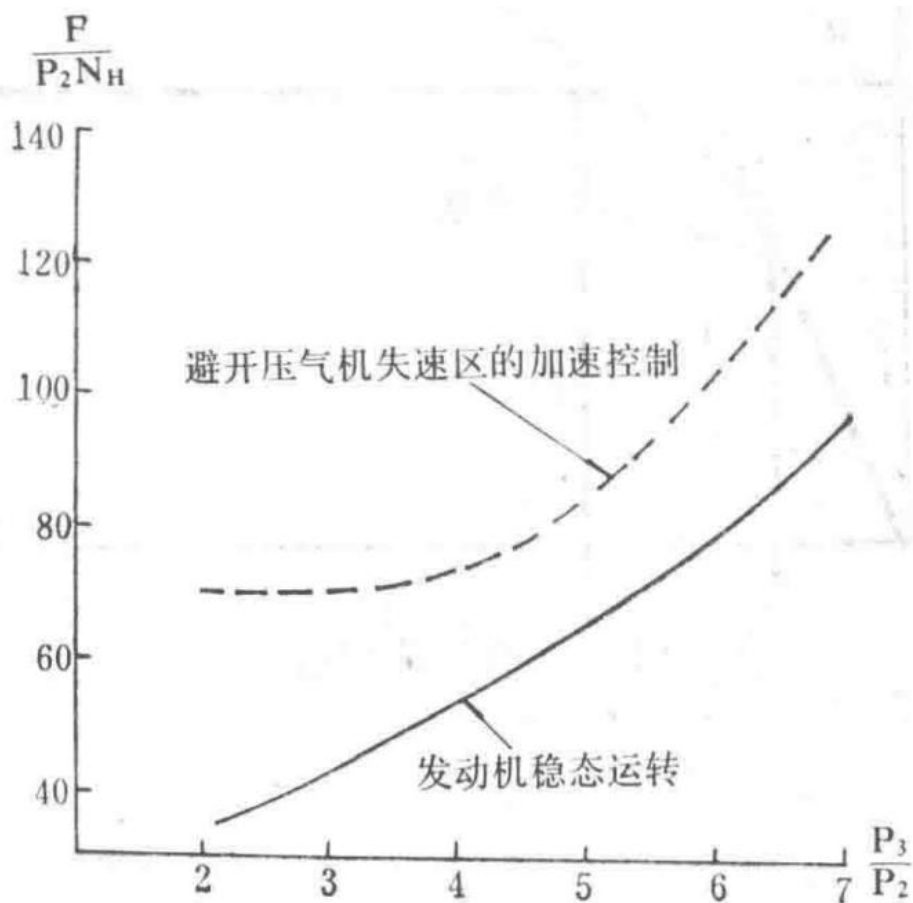


Figure 2 Engine Acceleration Control

Diagram illustrating the acceleration control system of the Spey MK202 engine.

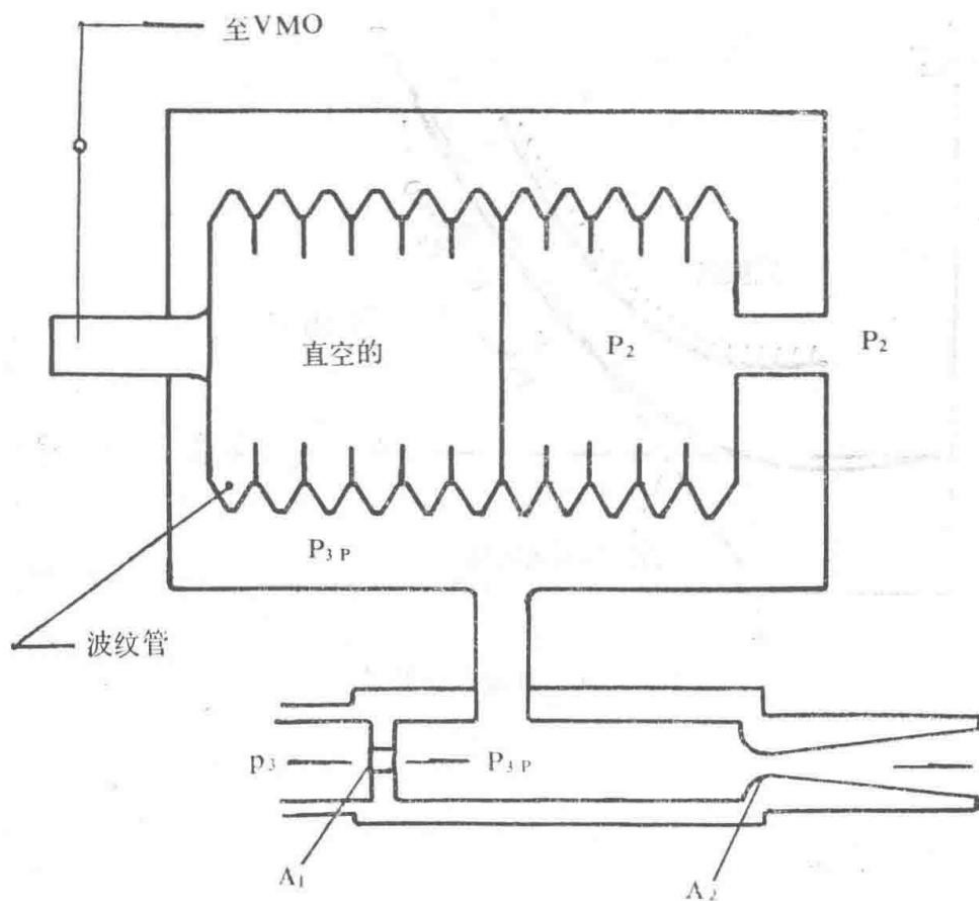


Figure 3 Pressure Divider and Bellows Sketch

Schematic sketch of the pressure divider and bellows assembly.

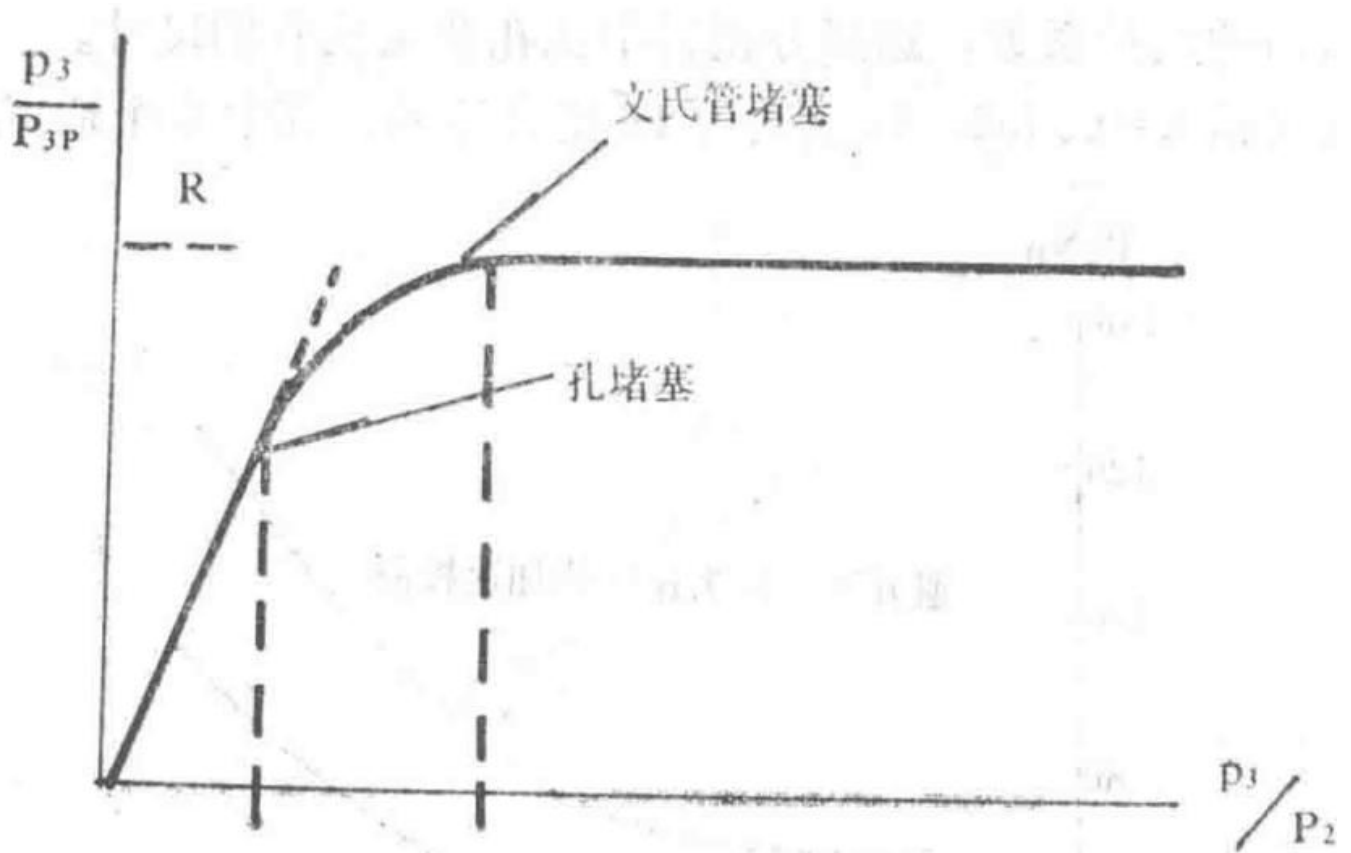


Figure 4 Pressure Divider Characteristics

Graph depicting the characteristics of the pressure divider system.

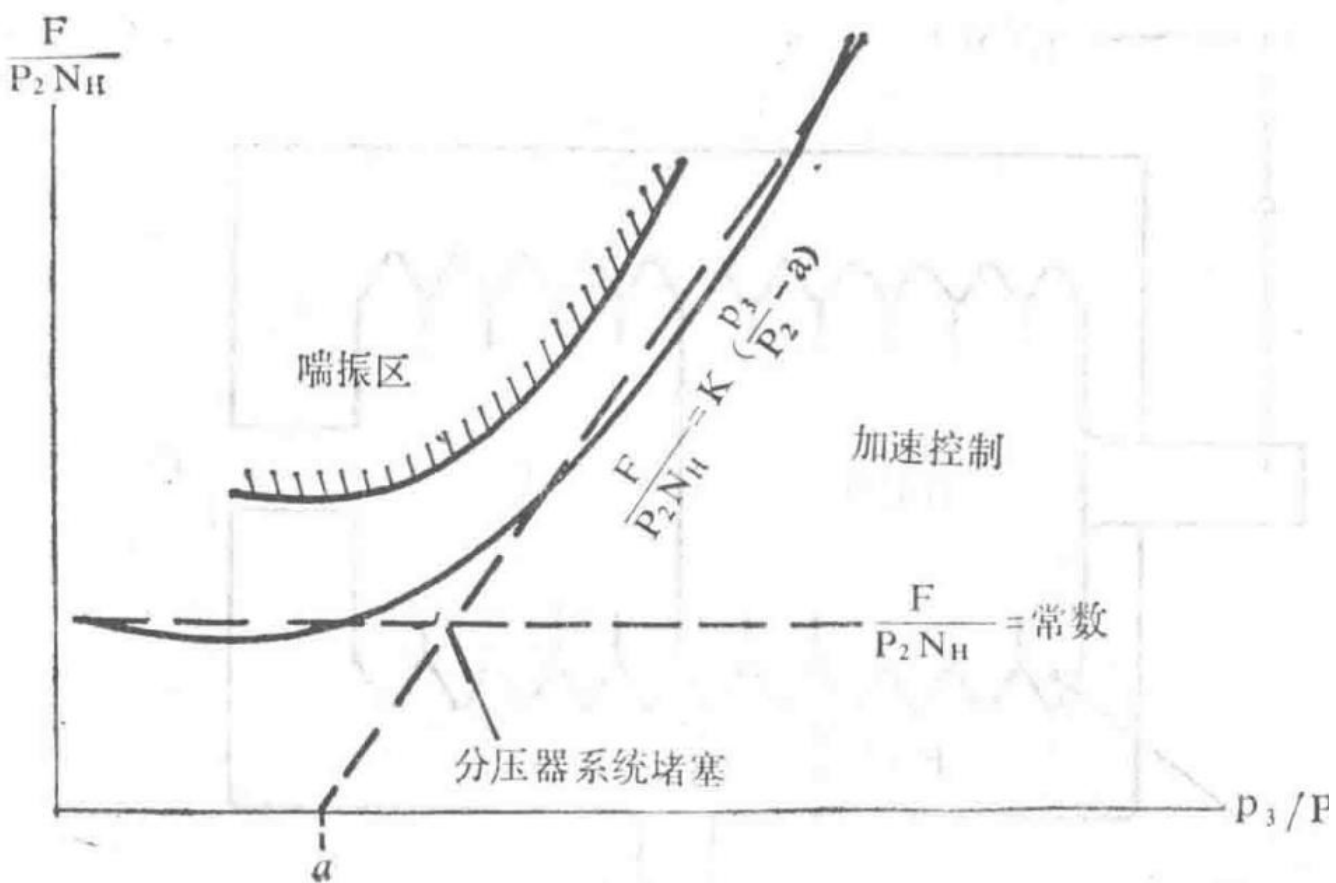


Figure 5 Acceleration Control Characteristics

Graph showing the acceleration control characteristics of the engine.

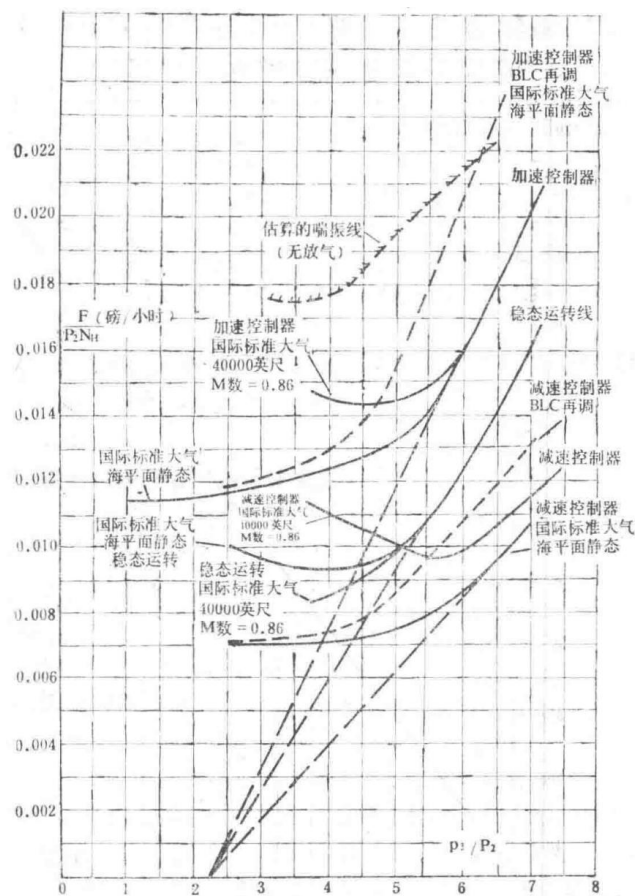


Figure 6 Initial CASC Calibration Curve

Initial calibration curve for the CASC (Combined Acceleration and Speed Control) system.

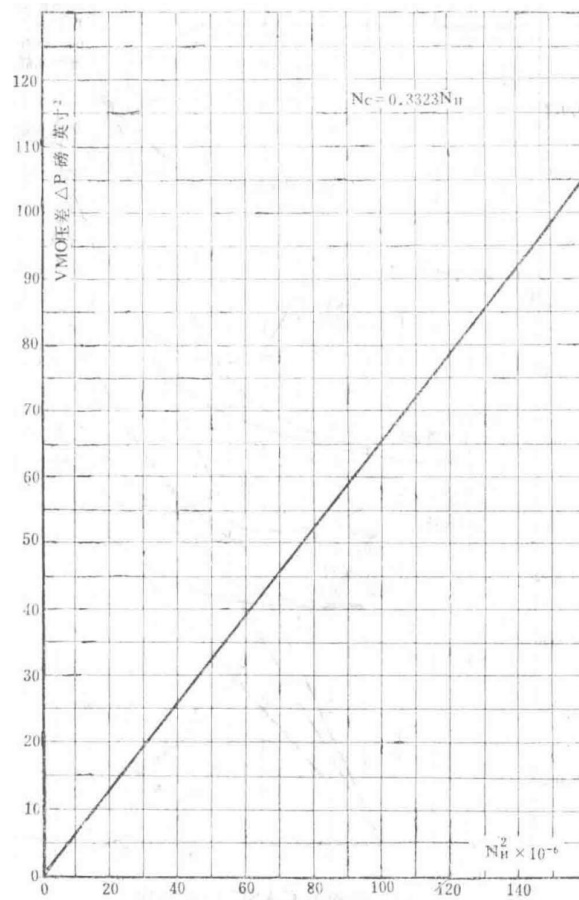


Figure 7 Relationship between VMO Pressure Differential and  $N_H^2$  on CASC

Graph showing the relationship between VMO (Variable Maximum Operating) pressure differential and the square of high-pressure rotor speed  $N_H^2$ .

# Technical Design Report

TDR7787C Section

## Spey MK202 Fuel Control System - Maximum Temperature Limiter, Low-Pressure Shaft Speed Limiter, and Other Items

First Edition, October 29, 1976

### Abstract

This report defines the technical requirements for the amplifier section related to the  $T_3$  and  $T_6$  limiters; the technical requirements for the low-pressure shaft limiter and high-pressure shutdown switch. It also describes the boundary layer control supplementary fuel solenoid valve and the high-pressure fuel flowmeter.

## 1. Introduction

The requirements and main design features of the control system are discussed in TDR7787B. This report supplements the discussion of other components excluding the high-pressure fuel pump and CASC system.

## 2. Maximum Temperature Limiter

### 2.1 Spey MK202 Engine Maximum Temperature Control Amplifier

#### Initial Technical Requirements

2.1.1 Circuit Description: The amplifier includes the following two circuits:

- Compressor outlet temperature adjustment on the full-range speed regulator of the high-pressure shaft.
- Turbine exhaust temperature adjustment on the full-range speed regulator of the high-pressure shaft.

#### 2.1.2 Compressor Outlet Temperature Adjustment on the Full-Range Speed Regulator of the High-Pressure Shaft

##### 2.1.2.1 Technical Requirements Description

- The compressor outlet temperature adjustment circuit shall have the capability to appropriately amplify the compressor outlet temperature  $T_3$  (thermocouple) signal to operate a servo motor for adjusting the high-pressure shaft full-range speed regulator on the fuel flow regulator.
- The set reference value is 533°C; within the range of 500°C to 550°C, the reference value should be easily pre-adjusted via an adjustment screw accessible externally on the amplifier. This temperature range should be achievable (refer to Section 2.1.7).

##### 2.1.2.2 Accuracy

Under steady-state conditions,  $T_3$  should be within  $\pm 3\%$  of the pre-adjusted reference value. For transient conditions, given a 5%/second increment of  $T_3$ , the  $T_3$  overshoot or undershoot should be within  $\pm 10^\circ\text{C}$  of the pre-adjusted reference value.

### 2.1.2.3 Thermocouple Resistance

The resistance of the  $T_3$  thermocouple including wiring should not exceed 1 ohm to ensure no significant impact on the accuracy specified in Section 2.1.2.2. The thermocouple current at the control reference point must not exceed 10 microamperes.

### 2.1.2.4 Effect of a Broken Thermocouple

When one  $T_3$  thermocouple is open-circuited, the accuracy specified in Section 2.1.2.2 should be maintained.

### 2.1.2.5 Effect of Thermocouple Grounding

If any end of the  $T_3$  thermocouple is grounded, the accuracy specified in Section 2.1.2.2 should be maintained. With a leakage resistance of 10 kilo-ohms between the  $T_3$  thermocouple and ground, the accuracy specified in Section 2.1.2.2 should still be maintained.

### 2.1.2.6 Output to Motor

For a 5% error of  $T_3$  above the reference value, the minimum voltage on the motor signal phase should be 10 volts; for a 10°C error of  $T_3$  above the reference value, the minimum voltage should be 18 volts. The maximum motor control voltage should be 26 volts  $\pm 5\%$  (RMS). This maximum voltage should occur when the  $T_3$  error above the reference value is no more than 20°C, at which point the motor should deliver the specified maximum torque.

### 2.1.2.7 Motor Drive Circuit

- The reference winding and drive winding should be orthogonal such that for an increment of  $T_3$  above the reference value, the servo motor rotates clockwise (viewed from the shaft end).
- The maximum average AC interference voltage on the motor signal winding at the balance point should be 0.5 volts.
- When the power supply is at rated voltage and frequency, the motor reference voltage should be 115 volts  $\pm 5\%$ .

## 2.1.3 Turbine Exhaust Temperature Adjustment on the Full-Range Speed Regulator of the High-Pressure Shaft

### 2.1.3.1 Technical Requirements Description

- The turbine exhaust temperature correction circuit shall amplify a signal from the turbine exhaust temperature ( $T_6$ ) thermocouple to drive a servo motor for adjusting the high-pressure shaft full-range speed regulator in the fuel control system.
- The required control characteristic line is shown in Figure 1(c). The three reference values are as follows:
  - (i) Basic Reference Value: This reference value is constant. When  $T_1$  is between 196 K and 244 K,  $T_6 = 925/244 * T_1$  (K); for  $T_1$  above 244 K,  $T_6$  should remain constant. This temperature range should be achievable (refer to Section 2.1.7).
  - (ii) 12-Stage Boundary Layer Control Re-adjustment: The reference value for 12-stage boundary layer control re-adjustment is represented as  $X^\circ C$  relative to the basic reference value across the entire  $T_1$  range. The actual value is expected to be within  $-30^\circ C$  to  $+30^\circ C$ . This temperature range should be achievable (refer to Section 2.1.7).
  - (iii) 7-Stage Boundary Layer Control Re-adjustment: The reference value for 7-stage boundary layer control re-adjustment is represented as  $Y^\circ C$  relative to the basic reference value across the entire  $T_1$  range. The actual value is expected to be within  $-20\%$  to  $+20\%$ . This temperature range should be achievable (refer to Section 2.1.7).

### 2.1.3.2 Reference Value Adjustment

The basic reference value should be adjustable within the range of  $T_e \pm 50^\circ\text{C}$  via an adjustment screw accessible externally on the component. The reference values for 7-stage and 12-stage boundary layer control re-adjustments should follow the basic reference value adjustment. The re-adjustment amount can be set via adjustment screws accessible externally on the amplifier.

The  $T_e$  limit range for 7-stage and 12-stage boundary layer control can be selected through a switching circuit in the amplifier but must be driven by an external power source to the amplifier.

For an increment above the reference value, the motor should rotate clockwise (viewed from the shaft end).

### 2.1.3.3 Accuracy

Under steady-state conditions,  $T_e$  should be within  $\pm 3^\circ\text{C}$  of the pre-adjusted reference value. For transient conditions, given a  $5^\circ\text{C}/\text{second}$  increment of  $T_e$ , the  $T_e$  overshoot or undershoot should not exceed  $\pm 10^\circ\text{C}$  of the pre-adjusted reference value.

### 2.1.3.4 Thermocouple Resistance

The resistance of the  $T_e$  thermocouple including wiring should not exceed 1 ohm and must not significantly affect the accuracy specified in Section 2.1.3.3. The thermocouple current at the control reference point must not exceed 10 microamperes.

### 2.1.3.5 Effect of a Broken Thermocouple

When one  $T_e$  or  $T_1$  thermocouple is open-circuited, the error must remain within the specified range.

### 2.1.3.6 Effect of Thermocouple Grounding

If any end of the  $T_e$  or  $T_1$  thermocouple is grounded, the error must remain within the specified accuracy range. With a leakage resistance of 10 kilo-ohms between either the  $T_1$  or  $T_e$  thermocouple and ground, the accuracy specified in Section 2.1.3.3 must be maintained.

### 2.1.3.7 Output to Motor

For a 5% error of  $T_e$ , the minimum voltage on the motor signal phase should be 10 volts; for a  $10^\circ\text{C}$  error of  $T_e$ , the minimum voltage should be 18 volts. The maximum motor control voltage should be 26 volts  $\pm 5\%$  (RMS), appearing when the  $T_e$  error is no more than  $20^\circ\text{C}$ . At this point, the motor should deliver the specified maximum torque.

### 2.1.3.8 Motor Drive Circuit

- The reference winding and drive winding should be orthogonal. For an increment of  $T_e$  above the reference value, the servo motor should rotate clockwise (viewed from the shaft end).
- The maximum average AC interference voltage on the motor signal winding at the balance point should be 0.5 volts.
- When the power supply is at rated voltage and frequency, the motor reference voltage should be 115 volts  $\pm 5\%$ .

## 2.1.4 Test Terminal Technical Requirements

A test terminal should provide the following conditions:

- Motor reference voltage in the CASC circuit;
- Motor voltage in the CASC circuit;

- Within the accuracy range specified in Sections 2.1.3.3 and 2.1.2.2, the  $T_6$  reference value can be reduced by 50% and the  $T_3$  reference value by 134°C;
- Tachogenerator output voltage in the CASC circuit;
- Tachogenerator  $T_6$  reference value re-adjustment;
- Tachogenerator  $T_3$  reference value re-adjustment.

## 2.1.5 Safety Circuit

If the  $T_6$  or  $T_3$  thermocouple junction is open-circuited, the amplifier should remain stable and switch to a ' $T_6$  non-adjusting' state.

## 2.1.6 Power Supply

The amplifier should be designed to operate on a single-phase 115V, 400 Hz line-to-neutral circuit. Under all conditions where the supply voltage varies within 10% and frequency within 5%, system accuracy should remain unchanged.

## 2.1.7 Control Reference Set Values

The actual temperature adjustment values required within the ranges specified in Sections 2.1.2.1(b) and 2.1.3.1(b) should be provided in relevant engine documentation.

Since the inlet guide vane regulator control and  $T_3$ ,  $T_6$  amplifier sections are assembled in one amplifier assembly, the cooling, heating, and cooling states are the same as specified in TDR7791 Section 14 (refer to 7.1).

## 2.2 Operation of the Engine $T_8$ Limiter

The  $T_8$  limiter prevents the  $T_6$  temperature from exceeding a given maximum value. The signal operating the  $T_8$  limiter comes from the  $T_8$  thermocouple (located in the engine exhaust component, consisting of 8 nickel-chromium/nickel-cobalt single-probe thermocouples connected in parallel).

This signal is compared with a standard voltage inside the amplifier. If the  $T_8$  signal exceeds the standard voltage, the resulting error is amplified to drive the CACS  $T_6$  adjustment control rack towards the maximum adjustment stop (reducing  $N\Box$ ). The drive current remains on the motor control phase, causing the motor to continue rotating until  $T_8$  equals the standard voltage, at which point the error disappears, the control current drops to zero, the motor stops, and the system reaches equilibrium. Any attempt to further increase the engine  $T_6$  will result in additional adjustment. Since the system is a 'zero-balance' type with stepless adjustment, regardless of the adjustment amount, the temperature will eventually stabilize at one value until the maximum adjustment stop is reached. Due to the slow action of the CACS  $T_8$  control, a phase-lead circuit must be introduced. This circuit directly applies the maximum motor rotation voltage when the  $T_6$  increase or decay rate exceeds 70-100°C/second.

Unlike the  $T_3$  control with a single maximum value, the  $T_8/T_1$  control characteristic line has a specific shape to meet engine requirements. Additionally, when the engine uses boundary layer control, the  $T_6/T_4$  relationship changes, and the corresponding  $T_6$  control reference value must be re-adjusted. When air passes through the boundary layer control sensing device to the CASC system to re-adjust the acceleration control unit (ACU), the boundary layer control re-adjustment pressure switch contacts close. The closed switch contacts activate the re-adjustment circuit, and the system re-adjusts to the 7-stage boundary layer control value. If the 12-stage boundary layer control coil is energized, the reference value changes from the 7-stage to the 12-stage value.

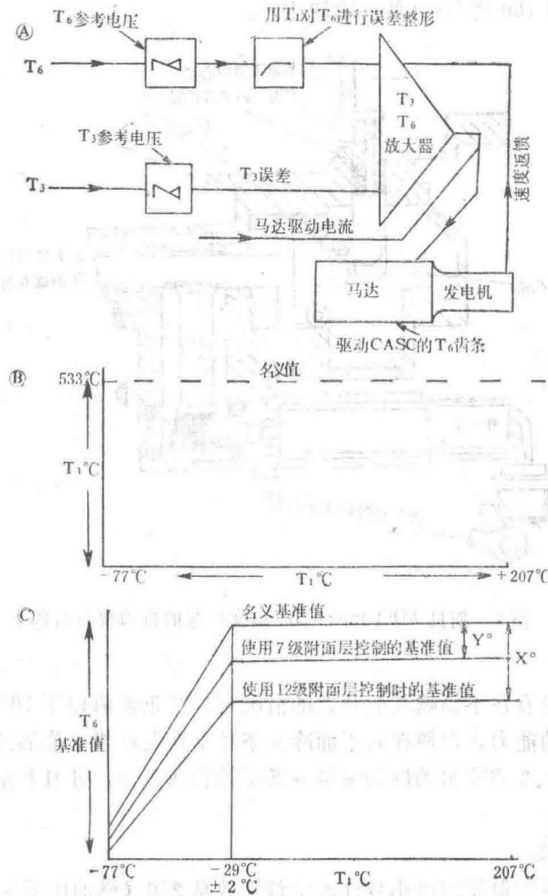


Figure 1 Spey MK202  $T_3$  and  $T_6$  Control

This diagram illustrates the basic system and the relationship between  $T_6/T_1$  in the Spey MK202 engine control system.

## T<sub>3</sub> and T<sub>6</sub> Adjustment Mechanism

Figure 2 shows the actual structure of the  $T_6$  adjustment device in CASC. When the  $T_6$  temperature exceeds the reference value, it causes the regulator spring load to decrease, thereby reducing the regulated speed. As shown in the figure, the adjustment device consists of a lever 'A' acted upon by the regulator spring, a speed selection lever cam, a  $T_6$  temperature-operated roller, and a rack mechanism. The roller moves along a fixed track on a plane perpendicular to the regulator spring axis. When the speed selection lever cam is at a sufficiently high lift, the main lever 'B' will tilt towards the temperature adjustment roller, and the roller's movement will force the main lever to rotate around the speed selection lever cam, thereby increasing or decreasing the regulator spring setting. When the lift of the speed selection lever cam is reduced, the effect of the adjustment roller 'C' is diminished until the speed selection lever cam reaches the minimum lift position, where lever 'B' becomes parallel to the fixed track and no adjustment occurs at any point.

Two stop screws limit the travel of the 'sector gear,' thereby controlling the 'non-adjustment' and 'maximum adjustment' values. The motor driving the  $T_6$  control rack in CASC is an 18-inch two-phase AC motor of international standard size; it is housed together with a 15-inch generator. The generator produces an output proportional to the speed, providing a damping signal to ensure control loop stability. When the maximum  $T_6$  error signal is applied to the amplifier, the CASC  $T_6$  rack moves from 'non-adjustment' to 'maximum adjustment' in 4.5 to 6.0 seconds.

## 3. Low-Pressure Shaft Limiter

### 3.1 Initial Technical Requirements

### 3.1.1 Technical Requirements Description

The low-pressure shaft speed limiter is used to regulate the engine fuel flow to limit the low-pressure shaft speed to a specified value. This limiter should be completely independent of the CASC and is provided for safety reasons, meaning it should not limit the engine under any normal flight conditions.

### 3.1.2 Engine Description

This engine is a dual-shaft turbofan designed as a powerplant for military aircraft. The engine is horizontally mounted and equipped with an afterburner system and a variable geometry nozzle.

### 3.1.3 Low-Pressure Shaft Limiter Characteristics

The characteristics of the low-pressure shaft limiter are determined under the following conditions:

- The adjustment point of the controller is: when the low-pressure shaft speed is 9000 rpm, the fuel flow supplied is 9000 lb/hour.
- The required and maximum flow rate change on any point of the characteristic line is 2.225 gallons/hour/low-pressure shaft speed.
- The characteristic should be smoothly adjustable within  $\pm 1000$  rpm (low-pressure shaft speed) of the given characteristic, maintaining the same controller flow rate change.

### 3.1.4 Control Accuracy

For any fuel specified in Section 3.1.11, when the fuel temperature is between 0°C and 85°C, the control accuracy of the controller for the low-pressure shaft speed is  $\pm 60$  rpm. When the fuel temperature drops to -40°C or rises to +135°C, ...

At this time, the accuracy can be reduced to  $\pm 100$  rpm (low-pressure shaft speed).

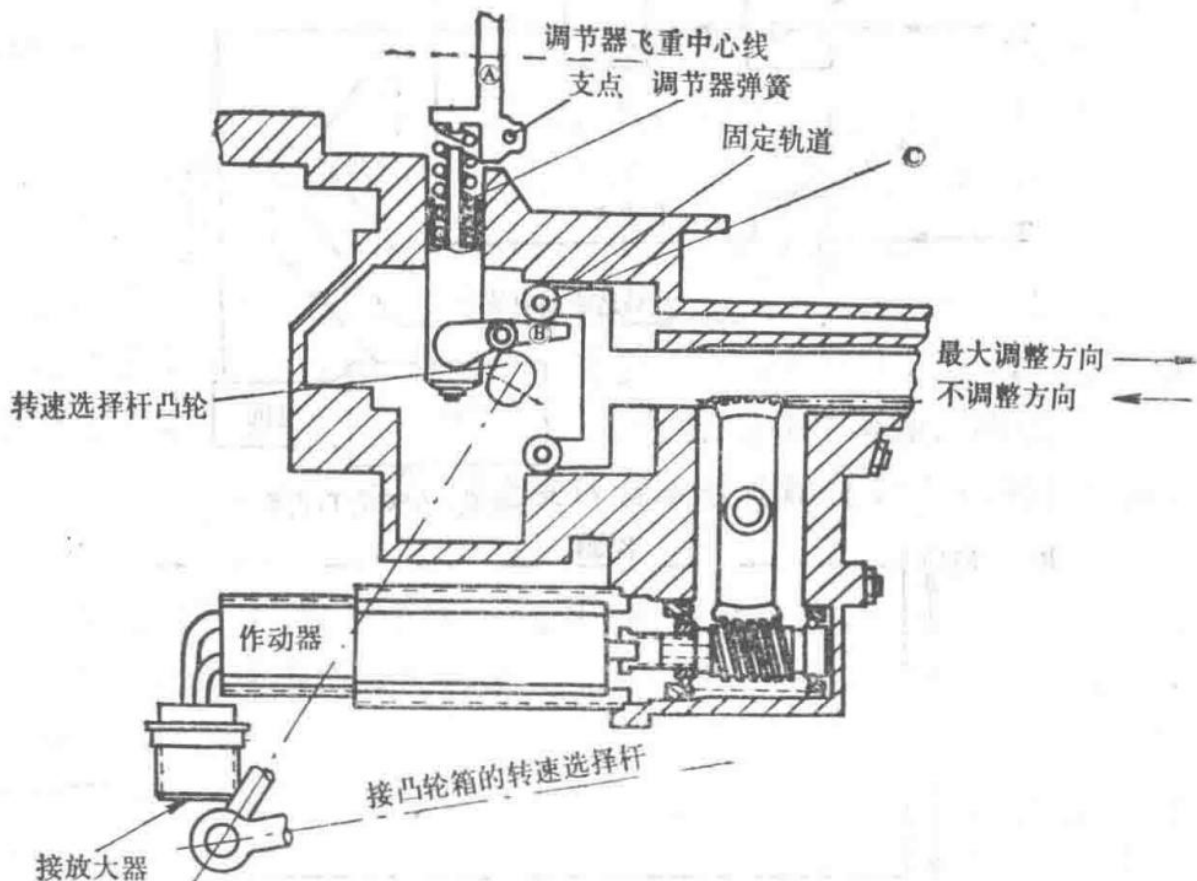


Figure 2 Schematic Diagram of Spey MK202 CASC Temperature Control Mechanism

Diagram illustrating the temperature control mechanism components of the Spey MK202 engine's CASC system.

### 3.1.5 Resetting

This controller must have the capability to be reset within a range of 1000 rpm below the normal value (low-pressure shaft speed) without affecting other devices, to allow adjustment of the limiter on the engine under cold-day sea-level conditions. Canceling this reset should restore the fuel flow vs. low-pressure shaft speed characteristic as given in Section 3.1.3, with accuracy within the range specified in Section 3.1.4.

### 3.1.6 Flow Characteristic Number

The minimum allowable flow characteristic number for the low-pressure shaft limiter when not controlling is 240 (fuel specific gravity of 0.79).

### 3.1.7 Maximum Overshoot

When other engine limiters fail and control is taken over by the low-pressure shaft controller, the maximum overshoot of the high-pressure shaft speed shall not exceed 1.5% of the maximum high-pressure shaft speed.

1.5 \%

Maximum allowable overshoot percentage of high-pressure shaft speed.

### 3.1.8 Drive Ratio

The low-pressure shaft speed controller is driven by the engine's low-pressure rotor, with a speed of 0.4608 times low-pressure shaft speed.

$$0.4608 \times \text{low-pressure shaft speed},$$

Drive ratio of the low-pressure shaft speed controller.

### 3.1.9 Maximum Fuel Pressure

The maximum fuel pressure for this controller is 1930 psi (gauge pressure).

### 3.1.10 Filtration

A low-pressure fuel filter is installed upstream of the low-pressure shaft controller. This filter shall have the following characteristics:

- At least 95% of all 10-micron particles shall be filtered out.
- The maximum particle size passing through the filter shall not exceed 40 microns.

### 3.1.11 Fuel

This device shall be designed to operate with any of the following fuels:

Approved Fuels

Fuel Type	
AVTUR	JP1
AVTAG	JP4
AVCAT	

Fuel may or may not contain 0.1% to 0.15% anti-icing additive (by volume). The fuel temperature at the accessory inlet shall range from -40°C to +135°C.

$$-40^{\circ}\text{C} \text{ to } +135^{\circ}\text{C},$$

Fuel temperature range at the accessory inlet.

### 3.1.12 Fuel Contamination

This device shall be designed to operate without failure when using fuels specified in Section 3.1.11 that are contaminated in accordance with relevant British Ministry specifications. Endurance testing shall comply with standards agreed upon by Rolls-Royce and the customer for specific applications.

The internal components may also be contaminated by saltwater (seawater).

## 3.2 Supplementary Design Requirements

The low-pressure shaft controller is entirely independent of the CASC and can override the fuel flow set by the CASC. In the event of a CASC malfunction causing excessive fuel flow to the fuel nozzles, the low-pressure shaft controller can prevent engine overspeed. In operation, the low-pressure shaft speed is not typically a normal control parameter; the low-pressure shaft controller primarily serves as a safety controller.

Since the low-pressure shaft controller does not control the engine under all normal test-bed conditions, a resetting device is required to enable its control for calibration purposes.

### 3.3 Description of Operation and Design Features

This device primarily consists of a centrifugal governor, metering plunger, balancing spring, and reference reset mechanism.

The centrifugal governor comprises a support driven by a shaft extended from the low-speed gearbox. The support holds flyweights mounted on pins, with each flyweight's arm pressing against the end face of the metering plunger. This assembly is enclosed to prevent disturbance of the fuel around the flyweights.

The metering plunger is driven by a splined shaft extending from the centrifugal governor and rotates within a sleeve containing metering and outlet ports. One end of the plunger presses against a three-shoulder support, which also forms the balancing spring seat. This assembly is designed to allow axial movement of the metering plunger without any lateral loads from the drive or balancing spring.

Between the metering plunger and the three-shoulder support, a buffer piston surrounded by low-pressure oil is used to dampen pulsations of the metering plunger.

The reference reset mechanism consists of a piston with a calibration screw, a spring-loaded locking sleeve, and a locator. This device allows the spring load to be reduced using a specialized reset tool, enabling correct adjustment of the low-pressure shaft controller during engine testing on a sea-level test bed.

The low-pressure shaft controller does not control the secondary fuel circuit flow. As altitude increases, the secondary fuel flow changes relatively little compared to the total fuel flow. The portion of the total fuel flow controlled by the low-pressure shaft controller decreases with increasing altitude. Due to the inherent non-isochronous control nature of this simple flyweight-type controller, the controlled low-pressure shaft speed is allowed to drift upward with increasing altitude.

Another constraint on the low-pressure shaft controller's control characteristics is ensuring system stability when the controller is active. Increasing the gain of the low-pressure shaft controller can reduce drift, but any improvement in drift is always at the expense of reduced stability margin.

The control characteristics of the low-pressure shaft controller are shown in Figure 3.

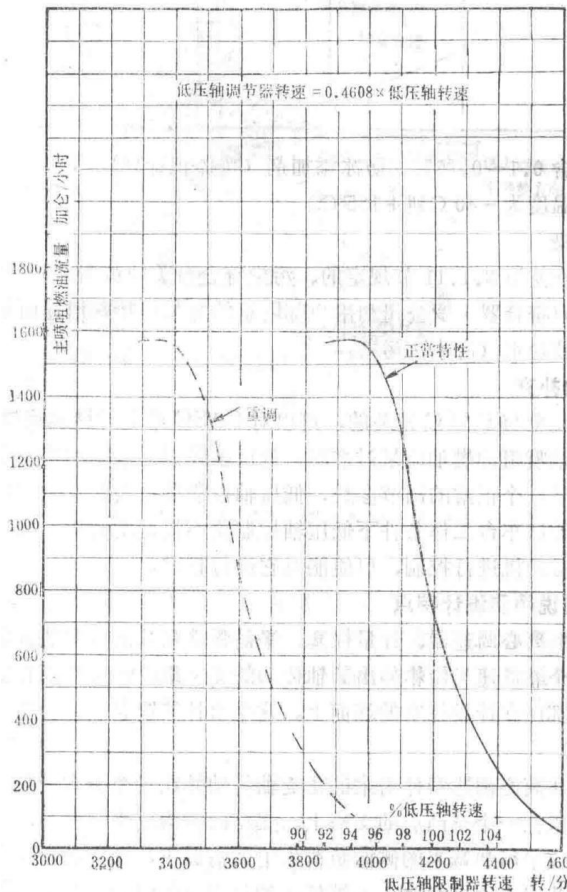


Figure 3 Typical Low-Pressure Shaft Controller Characteristics of Spey MK202

Graph illustrating the control characteristics of the Spey MK202 low-pressure shaft controller.

## 4. High-Pressure Fuel Shutoff Valve

### 4.1 Original Design Requirements

#### 4.1.1 Description of Technical Requirements

When the aircraft is stationary, the low-pressure switch is open, and the shutoff valve is closed, no significant fuel leakage through the closed shutoff valve to the engine is permitted. In the closed position (see Section 4.1.9), the high-pressure fuel shutoff valve shall drain fuel from the main and secondary fuel circuit pipelines. The engine employs a single pilot-operated lever via a cam box to independently actuate both the CASC and the high-pressure fuel shutoff valve; the system shall accommodate this single-lever control.

#### 4.1.2 Fuel Pressure and Temperature

The maximum fuel pressure is 1930 psi (gauge pressure). Under steady-state conditions, the fuel temperature shall range from -40°C to +135°C.

-40°C to +135°C,

Fuel temperature range under steady-state conditions.

#### 4.1.3 Maximum Fuel Flow

The maximum steady-state operating fuel flow through this device is 11,120 gallons per hour. The instantaneous maximum fuel flow is approximately 25% higher than the maximum steady-state flow.

#### 4.1.4 Minimum Flow Characteristic Number

When the high-pressure shutoff valve is fully open, the minimum flow characteristic number is 240 gallons/hour/√(psi) (fuel specific gravity of 0.79).

240 gallons/hour/ √(psi),

Minimum flow characteristic number for the high-pressure shutoff valve.

#### 4.1.5 Filtration

A low-pressure fuel filter is installed upstream of the fuel pump. This filter shall have the following characteristics:

- At least 95% of all 10-micron particles shall be filtered out.
- The maximum particle size passing through the filter shall not exceed 40 microns.

#### 4.1.6 Lever Torque and Travel

Under International Standard Atmosphere (ISA) sea-level conditions, the lever torque required to rapidly close the high-pressure shutoff valve in any operating state shall not exceed 4 lb-in.

The total angular travel of the high-pressure shutoff valve between the open and closed positions shall be as shown in the specific diagram.

#### 4.1.7 Fuel

This device shall be designed to operate normally with any of the following fuels, within the temperature and pressure ranges specified in Section 4.1.2:

Approved Fuels for High-Pressure Shutoff Valve

Fuel Type	
AVTUR	JP1
AVTAG	JP4
AVCAT	JP5

Fuel may or may not contain 0.1% to 0.15% anti-icing additive (by volume).

#### 4.1.8 Fuel Contamination

When using fuels specified in Section 4.1.7 that are contaminated in accordance with relevant British Ministry specifications, this device shall operate satisfactorily. However, endurance testing must comply with standards agreed upon by Rolls-Royce and the customer for specific applications.

The internal components may also be contaminated by saltwater (seawater).

#### 4.1.9 Permissible Leakage of High-Pressure Fuel Shutoff Valve

In the closed state, using fuels specified in Section 4.1.7 and at temperatures specified in Section 4.1.2, when the fuel pressure is 50 psi (gauge pressure), the maximum permissible leakage shall not exceed 50 ml/hour (leaked fuel drained).

### 4.2 Design Features of the High-Pressure Fuel Shutoff Valve

The high-pressure fuel shutoff valve connects the fuel manifold to the high-pressure fuel control system. In addition to draining fuel from the fuel manifold to the fuel drain system when the high-pressure fuel shutoff valve is closed, it is designed to prevent transient overpressure in the high-pressure fuel system during instantaneous shutdown and to maintain cooling flow through the high-pressure fuel system during engine shutdown.

The high-pressure fuel shutoff valve is located downstream of the low-pressure shaft controller and CASC, and outside the high-pressure fuel pump servo loop. It is an axially sliding plunger-type valve operated by a pair of gears and a rack. The operating mechanism is linked to the engine control cam box and connected to the pilot's lever via a linkage mechanism. The shutoff valve can be set to two positions: open or closed. In the open position, both main and secondary fuel flows to the nozzles pass through the shutoff valve. In the closed position, the slide valve or plunger cuts off fuel supply to the main and secondary nozzles; simultaneously, the two high-pressure fuel inlet channels and the high-pressure fuel pump servo oil circuit are connected to the low-pressure fuel outlet. The high-pressure fuel pump servo piston senses low pressure, and the pump immediately moves to the minimum stroke position. This creates a low-pressure fuel circuit through the valve during engine shutdown to prevent transient overpressure (which could otherwise occur) and provides cooling flow through the high-pressure fuel system.

To ensure minimal operating torque, the slide valve is not fitted with seals but relies on a very precise small clearance fit (0.0001 to 0.0002 inches) for sealing.

0.0001 to 0.0002 inches,

Clearance fit for sealing the slide valve.

The slide valve and sleeve materials are high-expansion-ratio stainless steel and aluminum bronze, respectively, with nearly identical thermal expansion coefficients.

# 5. Boundary Layer Control (BLC) Supplementary Fuel Solenoid Valve

When 12th-stage air is extracted for boundary layer control, the engine's steady-state fuel flow must be increased to prevent engine speed drop and the generator from going offline. The increased fuel flow is achieved by controlling a solenoid valve installed in the CASC bypass. When energized, the valve opens, allowing fuel to enter the main nozzle circuit. A flow characteristic number of 2.0 gallons/hour/ $\sqrt{\text{psi}}$  orifice is installed downstream of the solenoid valve. The technical requirements for this valve are detailed in ACS9007 (Reference 7.2).

2.0 gallons/hour/  $\sqrt{\text{psi}}$ ,

Flow characteristic number of the orifice downstream of the solenoid valve.

Technical Design Report

Document	Reference
Technical Design Report	TDR7754
Spey MK202 Secondary Nozzle Fuel Flow Characteristics Relative to Main Nozzle Fuel Flow	

April 25, 1975, First Edition

## Purpose

To provide the latest relationship between secondary nozzle fuel flow and main nozzle fuel flow, enabling calibration of the flowmeter installed in the main fuel circuit to read the total engine fuel flow.

The relationship between main and secondary nozzle fuel flows can be adjusted by changing the servo pressure drop.

## 1.0 Introduction

The total engine fuel flow is measured by a flowmeter installed in the main fuel circuit. This is achieved by calibrating the flowmeter. When the main nozzle fuel flow passes through this flowmeter, it can indicate the sum of the main and secondary fuel flows. Changing the servo characteristics alters the relationship between main and secondary nozzle fuel flows, necessitating recalibration of the flowmeter. This report provides the new relationship between main and secondary nozzle fuel flows for flowmeter recalibration.

## 2.0 Assumptions and Calculations

Main nozzle total flow characteristic number = 55 gallons/hour/ $\sqrt{\text{psi}}$

55 gallons/hour/  $\sqrt{\text{psi}}$ ,

Main nozzle total flow characteristic number.

Secondary nozzle total flow characteristic number = 2.5 gallons/hour/ $\sqrt{\text{psi}}$

2.5 gallons/hour/  $\sqrt{\text{psi}}$ ,

Secondary nozzle total flow characteristic number.

The above flow characteristic numbers are nominal values.

2.2 The pump flow used to determine the servo pressure drop is assumed to be 1.33 times the engine's required fuel quantity. This coefficient accounts for leakage and other factors under cruise conditions. Since the flowmeter is required to measure most accurately during cruise, this coefficient was selected.

## 2.3 Variable Metering Orifice (VMO) Pressure Drop

$$\Delta P_{vwo} = (N_H,1264)^2,$$

Equation for the pressure drop across the variable metering orifice (VMO) as a function of high-pressure shaft speed ( $N\Box$ ).

## 2.4 Servo Pressure Drop ( $\Delta P\Box$ ) Characteristics

The servo pressure drop ( $\Delta P\Box$ ) characteristics are provided in chart DC14733 as a function of pump flow (see Section 2.2) and high-pressure shaft speed  $N\Box$ .

## 2.5 Simplifying Assumptions

Compared to other factors, the influence of the high-pressure fuel shut-off valve is minimal and thus neglected in calculations. For the same reason, pressure drops caused by piping are also ignored. Since both factors appear in the following two equations and largely cancel each other out during calculations, this method minimizes the impact of neglecting these factors.

## 2.6 Pump Pressure Derivation

Pump pressure can be derived via two pathways: one using the main fuel circuit and the other using the secondary fuel circuit. The resulting equations are:

$$P\Delta\Box = P_3 + \Delta P\Box + \Delta P_{MB},$$

Pump pressure derived from the main fuel circuit.

$$P\Box = P_3 + \Delta P_{VMO} + \Delta P_{PB},$$

Pump pressure derived from the secondary fuel circuit.

Where:

$\Delta P_{MB}$ : Pressure drop across the main burner fuel circuit.

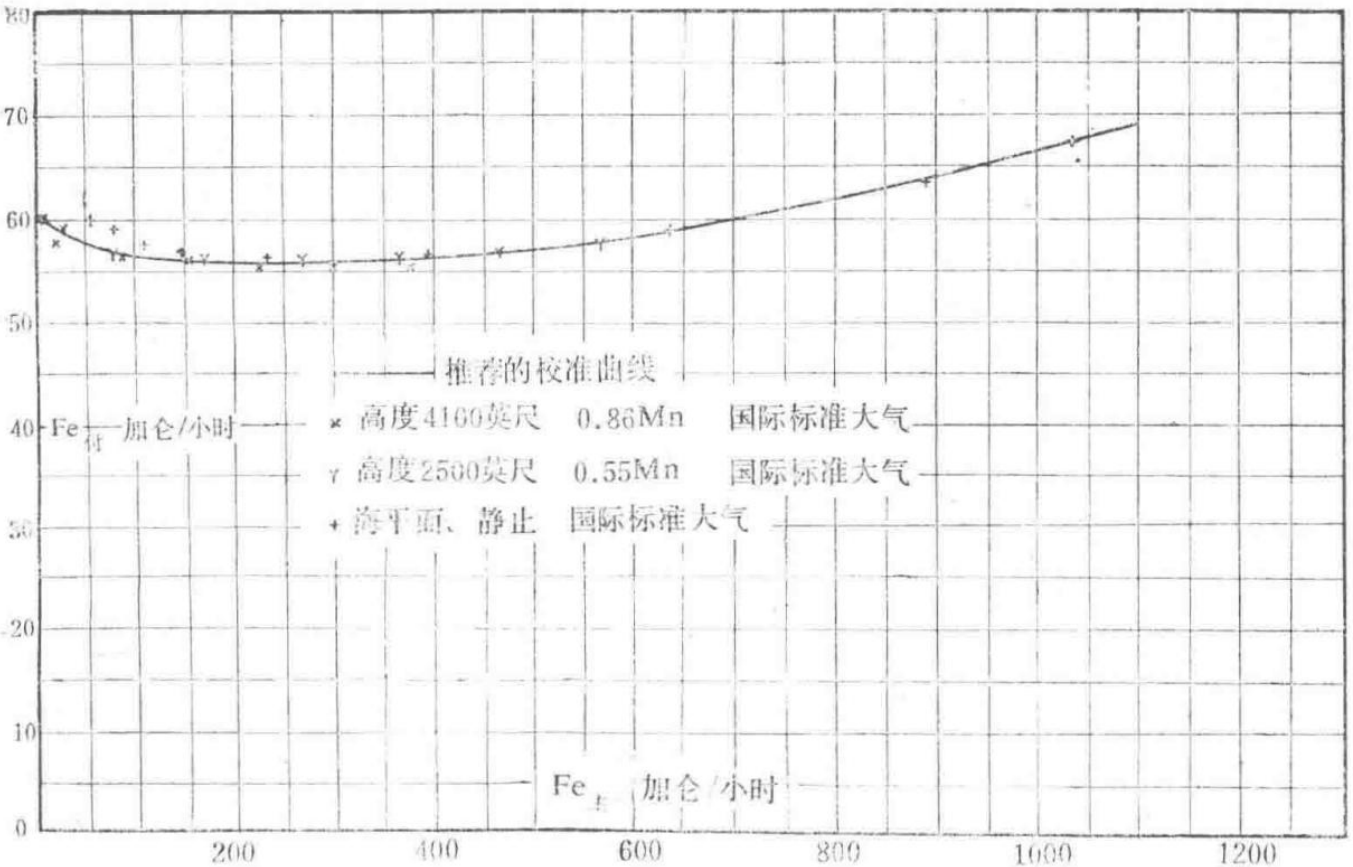


Figure 1: Relationship between main and secondary nozzle fuel flow in the Spey MK202 engine.

Graph depicting the relationship between fuel flow rates in the main and secondary nozzles of the Spey MK202 engine.

Combining equations (1) and (2) yields:

$$\Delta P_{PB} = \Delta P_B - \Delta P_{VMO} + \Delta P_{MB},$$

Combined equation for pressure drop across the secondary burner fuel circuit.

By assuming a main nozzle fuel flow,  $\Delta P_B$  can be calculated, which then allows the calculation of the permissible  $\Delta P_{PB}$  and the secondary nozzle fuel flow. Iterative calculations are required to ensure the sum of the main and secondary nozzle flows equals the total fuel flow demanded by the engine.

## Results

Using three flow relationship curves, a relationship curve between the secondary and main nozzle fuel flows was determined. The given engine conditions are:

### Engine Conditions for Fuel Flow Analysis

Index	Altitude	Flight Mach Number	Atmospheric Conditions
(1)	Sea Level	Static	International Standard Atmosphere
(2)	25,000 feet	0.55	International Standard Atmosphere
(3)	41,000 feet	0.86	International Standard Atmosphere

The results from the three flow relationship curves and the recommended flow calibration curve are shown in Figure 1.

## 7. References

- [1] TDR7791 Inlet Guide Vane and Bleed Valve Control System.
- [2] Accessory Control Specification ACS.No.9007 Boundary Layer Control Supplementary Fuel Solenoid Valve.

Technical Design Report

Report	Identifier
Technical Design Report	TDR7778
	Adoption of the Spey MK202 Acceleration Control Unit Overflow Valve

First Edition, September 24, 1976.

## Abstract

The removal of the distribution valve in the afterburner main fuel manifold and the adoption of high-pressure fuel injection necessitate a device that introduces afterburner fuel only after the injection is complete, followed by a regulated fuel flow rate below the engine surge limit. This report describes how the acceleration control unit overflow valve fulfills these functions.

## Introduction

One function of the distribution valve is to control the rate of fuel flow increase into the fuel manifold to prevent sudden changes. Removing the distribution valve (see TDR777) eliminates this function and raises the issue of fueling the manifold during afterburner activation. Initially, the acceleration control unit overflow valve was used to fulfill both functions. However, as described in TDR7780, the overflow valve produced conflicting results for manifold fueling, necessitating fuel injection into the manifold via a catalytic timer and igniter. This changes the requirements for the acceleration control unit overflow valve to:

1. Introduce afterburner fuel flow only after the manifold fueling process is complete and the fuel in the evaporation trough is ignited.
2. After this process, smoothly introduce afterburner fuel to prevent sudden fuel flow changes.

The following outlines how the acceleration control unit overflow valve system accomplishes this process.

## Operation of the Acceleration Control Unit Overflow Valve

When afterburner activation is initiated, a servo fuel signal from the catalytic ignition timer outlet is transmitted beneath the servo piston. The servo piston then moves upward to the stop point. The movement of the servo piston allows servo fuel beneath the main piston to flow into low pressure. At this time, a high-pressure differential across the control restrictor causes the main piston to move to the maximum overflow position, occurring approximately 0.05 seconds after the start of the afterburner activation sequence. Both the overflow valve servo piston and main piston remain in the maximum overflow position until the catalytic timer inlet closes.

Approximately 3.0 to 3.2 seconds after afterburner activation, the catalytic timer inlet closes, cutting off the servo high-pressure fuel source to the servo piston, reducing the servo piston pressure to low. Subsequently, the servo piston returns to its non-ignition position, once again cutting off the servo fuel leakage to low pressure beneath the main piston. The servo pressure beneath the main piston then begins to rise, causing the main piston to move toward the maximum non-overflow position. During this period, the speed of the main piston movement

depends on the rate of pressure increase beneath it. Typically, with a main piston servo pressure of 860 psi (gauge) and low pressure of 40 psi (gauge), the output flow rate increases linearly from zero to maximum within 1.4 to 1.6 seconds, determined by the size of the control restrictor. After 1.4 to 1.6 seconds from the opening of the overflow valve, the valve is in the non-overflow position. Even if afterburner activation is disengaged, the valve remains in this position until the next afterburner activation.

## Overflow Valve Timing

The fundamental design parameter for the overflow valve is the permissible fuel input rate into the afterburner system that does not cause engine surge after manifold fueling. This fuel flow input rate is limited by the tail nozzle's response rate to commands. As a design rule, the tail nozzle movement time is doubled to provide sufficient margin to accommodate degradation in the nozzle control system performance.

For a well-designed tail nozzle system, the movement time between fully closed and fully open positions is 1.2 seconds. During most of this movement, the tail nozzle hydraulic pump operates at full stroke. Therefore, during afterburner activation, most of the hydraulic pump stroke should also be at full stroke, allowing direct estimation of the nozzle movement time. The estimated time for the tail nozzle to move from the pre-open position to the planned maximum afterburner area position is 0.7 seconds, confirmed by the tail nozzle displacement record curve shown in Figure 1.

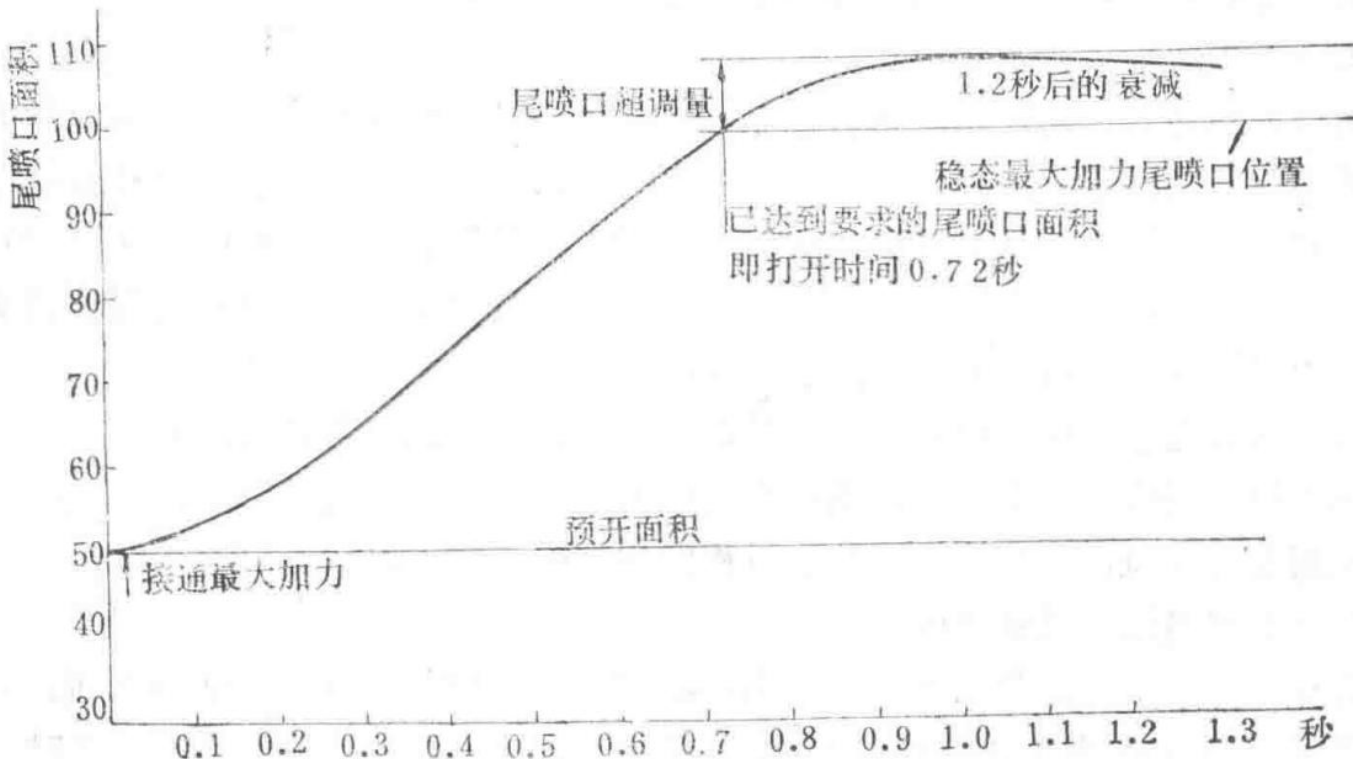


Figure 1: Tail Nozzle Opening Process Record for Engine No. 1969.1220008 at Sea Level with Sudden Maximum Afterburner Engagement

Graph showing the tail nozzle opening process during sudden maximum afterburner engagement at sea level.

Doubling this time results in a movement time of 1.4 seconds, providing a lower operational time limit (i.e., the fastest time fuel can be introduced into the afterburner system). This lower limit is set based on the requirement to achieve the selected afterburner level within 5 seconds of activation. Given that the catalytic timer occupies 3.2 seconds before the overflow valve opens, considering a 0.2-second margin, the upper operational time limit is 1.6 seconds.

## Reference Materials

- [1] TDR7777 - Removal of the Afterburner Manifold Distribution Valve in RB168 MK202
- [2] TDR7780 - Introduction of High-Pressure Fuel Injection in RB168 MK202

# Technical Design Report

TDR 7782 Spey MK202 Pressure Ratio Regulator Two- and Three-Taper Needle Valve First Edition, October 19, 1976

## Abstract

The requirements for the  $P_3/P_6$  orifice needle valve profile in the pressure ratio regulator are somewhat contradictory: fast response requires a small taper, while stability requires a steeper taper. This document traces the evolution from the initial linear high-gain needle valve to the current three-slope nonlinear needle valve that balances these requirements. Additionally, it outlines the conflicting requirements and how the system meets them.

## Introduction

The pressure ratio regulator is a sensing component of the closed-loop nozzle control system, primarily transmitting a signal to the nozzle hydraulic pump. This signal should relate to the error in  $P_6$ , which is the difference between the actual  $P_6$  and the desired  $P_6$  for a given  $P_3/P_2$  (engine condition). This is because the nozzle hydraulic pump acts as an integrator and incorporates the signal from the pressure ratio regulator. In steady-state, a fixed signal value is required to ensure the nozzle hydraulic pump flow exactly compensates for leakage and cooling of the nozzle actuator. This fixed steady-state control position is called the null position.

Following conventional practice, the system uses direct-acting pressure to drive a rotary piston, providing a signal for simplicity and reliability. The rotary piston eliminates hysteresis caused by static friction in stationary pistons. On one side of the  $P_3/P_6$  piston, the actual  $P_6$  acts, while on the other side, the designed  $P_6$  acts, with both sides having equal areas. The designed  $P_6$  is a partial pressure between  $P_3$  and  $P_0$ , and the areas of two orifices in the system are variable. The area of the  $P_3/P_6$  orifice is changed by the movement of a needle valve integrated with the piston. In steady-state, the pressure ratio regulator signal piston remains in a fixed position, so the corresponding orifice area is also fixed. Since the pressure ratios  $P_6/P_0$  and  $P_3/P_6$  both exceed choking values, the airflow is continuous and considered isothermal, making the upstream pressures equal to the ratio of the corresponding orifice areas. When the downstream  $P_3/P_6$  orifice is fixed in steady-state, selecting the upstream orifice's fine-tuning area allows us to obtain the correct  $P_6$  value. Thus, a single-value relationship exists between  $P_3/P_2$  and  $P_3/P_6$ , and the pressure ratio regulator generates a signal linearly related to  $P_3/P_2$  (see TPR7789). This signal can be used to adjust the fine-tuning needle valve in the orifice, achieving the necessary  $P_6$  at a given  $P_3/P_2$  in steady-state. In practice, there are two  $P_3$  fine-tuning needle valves: one for normal engine operation and another for boundary layer control activation. The use of boundary layer control alters the main engine operating line, thus changing the relationship between  $P_3/P_2$  and the required  $P_3/P_6$ . The  $P_3$  signal supplied to the fine-tuning needle valve is regulated by the boundary layer control switching valve. Therefore, in flight conditions, the fine-tuning needle valve adjusts the upstream orifice area, creating the main reference pressure  $P_6$  on one side of the pressure ratio regulator piston. If the actual  $P_6$  differs from the reference  $P_6$ , the piston moves, changing the needle valve position and thus the downstream orifice area. The needle valve's shape allows the system to adjust stably, moving the piston to a position away from the null. The piston displacement depends on the needle valve profile and the pressure difference on both sides of the piston. The displacement of a given needle valve profile becomes a measure of the pressure difference or the difference between actual  $P_6$  and reference  $P_6$ .

The piston's movement adjusts the swashplate angle of the nozzle oil pump, driving the exhaust nozzle to bring the actual  $P_8$  closer to the reference  $P_6$ . During this adjustment process, the pressure on both sides of the piston reverses, moving the piston to balance the pressure, and the downstream orifice area is again used as the controller. This returns the nozzle oil pump stroke to the zero position, slowing the rate of change of the nozzle area. The system then moves toward a steady-state position until it stabilizes at the zero position.

As described above, the profile of the needle valve significantly impacts the system's operation. For example, a needle valve with a very small taper produces an extremely fast system response. A small-taper needle valve requires a large displacement to change the orifice area sufficiently to balance any pressure difference on both sides of the piston. This pushes the oil pump to a large stroke position far from the zero point and rapidly moves the actuator. However, there is a time lag between the change in  $P_8$  and the pressure from the pressure ratio regulator (actual  $P_8$  to the piston). If the response time does not coordinate with the lag, it may cause nozzle instability. On the other hand, a large-taper needle valve can achieve the required change in the oil pump swashplate angle with small displacements, avoiding stability issues. However, these small changes result in minor variations in oil flow, leading to a slow system response, which is unacceptable for systems requiring rapid tracking of fuel flow changes. Therefore, the focus of this document is to find a compromise between these two extremes.

Another factor affecting nozzle instability is the static friction present in the nozzle oil actuator and the piston of the pressure ratio regulator. These forces have been minimized as much as possible. The static friction in the pressure ratio regulator piston arises from the sealing device rotating with the piston. Fixing this sealing device effectively eliminates this source of static friction. Thus, design efforts are required to reduce static friction in the oil actuator. Clearly, addressing side loads should be a priority in the initial design phase, as resolving this effectively reduces static friction.

## Design of the Downstream Needle Valve

The original design of this needle valve is shown in Figure 2 of TDR779 (attached to TDR7789). The needle valve has a very small taper, with a gain of approximately 0.9 inches per turbine pressure ratio (the evolution of the needle valve profile is shown in Figure 1). The needle valve profile design provides a linear relationship between needle valve displacement and orifice area, making  $P_3 / P_8$  and needle valve displacement approximately linear. The small taper profile yields a very fast time response but leads to system instability. Numerous needle valves with different tapers have been tested, each demonstrating a clear linear relationship between  $P_3 / P_8$  and needle valve displacement. The primary limitation for slow nozzle movement is the rate of change in afterburner fuel flow. It has been found that a needle valve with a gain of 0.208 inches per turbine pressure ratio provides the slowest acceptable nozzle response for the fuel system. This needle valve offers a compromise between slow responses that may cause surge and fast responses that lead to instability, though it is not entirely satisfactory.

To eliminate acceleration surge, a needle valve was adopted with a gain of 0.208 inches per turbine pressure ratio in the nozzle closing direction and a limit gain of 0.2 pressure ratio in the nozzle opening direction. When the gain exceeds the limit value, the corresponding profile of the needle valve is a cylindrical segment with a diameter equal to that corresponding to the limit value. For details on improvements and engine test validation of this system, refer to FDR10311.

While this system overcomes some surge issues and is quite stable with no problems in the opening direction, operation in the closing direction remains somewhat sluggish. Since nonlinear elements have been introduced into the system, it was considered that additional nonlinear elements might be necessary to accelerate the response time in the closing direction. To this end, a small-taper profile with a gain of approximately 0.5 inches per pressure ratio replaced the closing taper profile beyond the 0.425 pressure ratio limit. This profile is currently in use, allowing fault-free operation in both the nozzle opening and closing directions.

To simplify needle valve manufacturing, the needle valve profile has been significantly simplified to a conical shape, resulting in minor gain variations along the needle valve profile segment. However, these variations are insignificant in the closing profile segment, as this segment is a high-gain area, and the opening direction profile segment is cylindrical. The actual length of the entire regulating profile segment is only 0.125 inches, so gain variations along this segment can be neglected. It has been confirmed that these small changes are negligible in operation. This type of needle valve profile is acceptable and is currently in use.

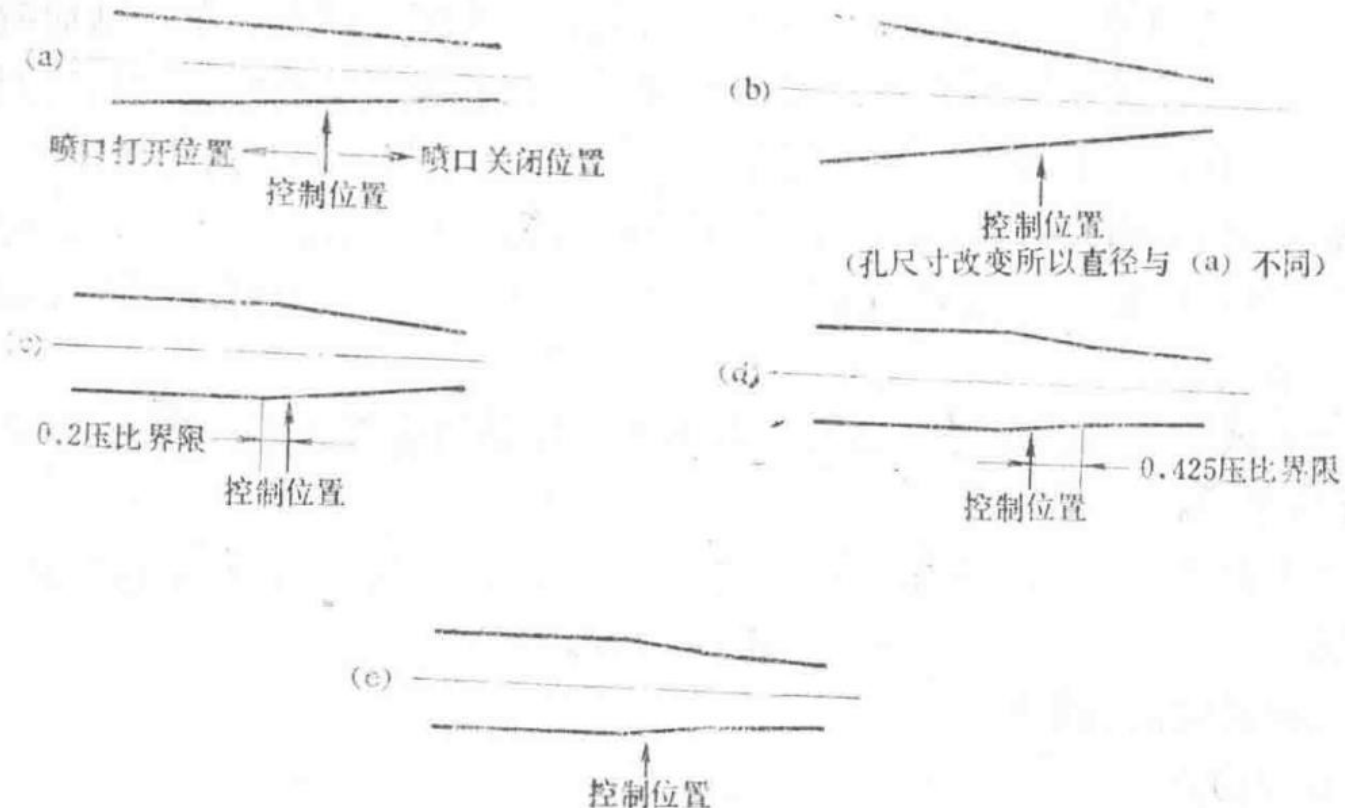


Figure 1 Evolution of the  $P_3 / P_6$  needle valve profile on the Spey MK202 pressure ratio regulator

This figure illustrates the development of the needle valve profile for the  $P_3 / P_6$  pressure ratio regulator from the original design to the current standard.

- Figure 1(a) shows the original small-taper needle valve profile from TDR779 Figure 2, with a gain of approximately 0.9 inches per pressure ratio.
- Figure 1(b) shows a modified large-taper needle valve profile, with a gain of approximately 0.208 inches per pressure ratio.
- Figure 1(c) depicts the first nonlinear needle valve, with infinite gain in the opening direction beyond the 0.2 pressure ratio limit.
- Figure 1(d) shows the second nonlinear needle valve, with the same gain as Figure 1(c) in the opening direction but a gain of approximately 0.5 inches per pressure ratio in the closing direction beyond the 0.425 pressure ratio limit.
- Figure 1(e) is identical to (d) but features a conical profile for ease of manufacturing, representing the current standard needle valve profile.

These diagrams are schematic and not drawn to scale.

## 1.0 Introduction

### 1.1

To achieve surge-free acceleration during afterburning, the rate of nozzle opening must not be less than the rate of increase in afterburner fuel supply. This requirement cannot be met with the existing standard afterburner fuel system and nozzle control system.

## 1.2

- (a) The nozzle system can control the rate of increase in afterburner fuel supply. This principle is the basis of the afterburner acceleration controller.
- (b) The rate of nozzle opening can be increased to be greater than or equal to the maximum rate of increase in afterburner fuel flow.

## 1.3

Method (b) is advantageous because it minimizes acceleration time. However, simply increasing the gain of the nozzle system is not suitable, as it leads to system instability. A pressure ratio regulator with a nonlinear gain characteristic has been tested. To maintain normal operating deviations near the stable value, the current gain error of 0.208 inches per turbine pressure ratio, commonly referred to as the zero-speed point, is retained. If the turbine pressure ratio error exceeds a predetermined value, referred to as the limit value, the gain becomes infinite. This is achieved by designing the relevant profile of the downstream pressure divider needle valve for  $P_3 / P_6$  as a constant cross-section.

# 2.0 Conclusions

## 2.1

Tests to date indicate that a dual-gain  $P_3 / P_6$  needle valve is a satisfactory solution for preventing surge issues during rapid afterburner acceleration.

## 2.2

When the limit value is adjusted to a 0.2 turbine pressure ratio error, the peak error near surge during rapid acceleration from maximum military power to maximum afterburner at sea level static conditions does not exceed 0.43.

# 3.0 System and Test Description

## 3.1 Engine No. 38

The pressure ratio regulator limit value was adjusted to near-surge 0.2 pressure ratio, and rapid acceleration tests were conducted from minimum afterburner and maximum military power to various afterburner ratios.

When fuel is sprayed into the catalytic igniter, the main afterburner fuel returns to the boost pump inlet through the overflow valve. Thus, during rapid acceleration from maximum military power to maximum afterburner, the closing rate of the overflow valve determines the rate of fuel increase. During rapid acceleration from minimum afterburner to maximum afterburner, the control element is the rotary valve.

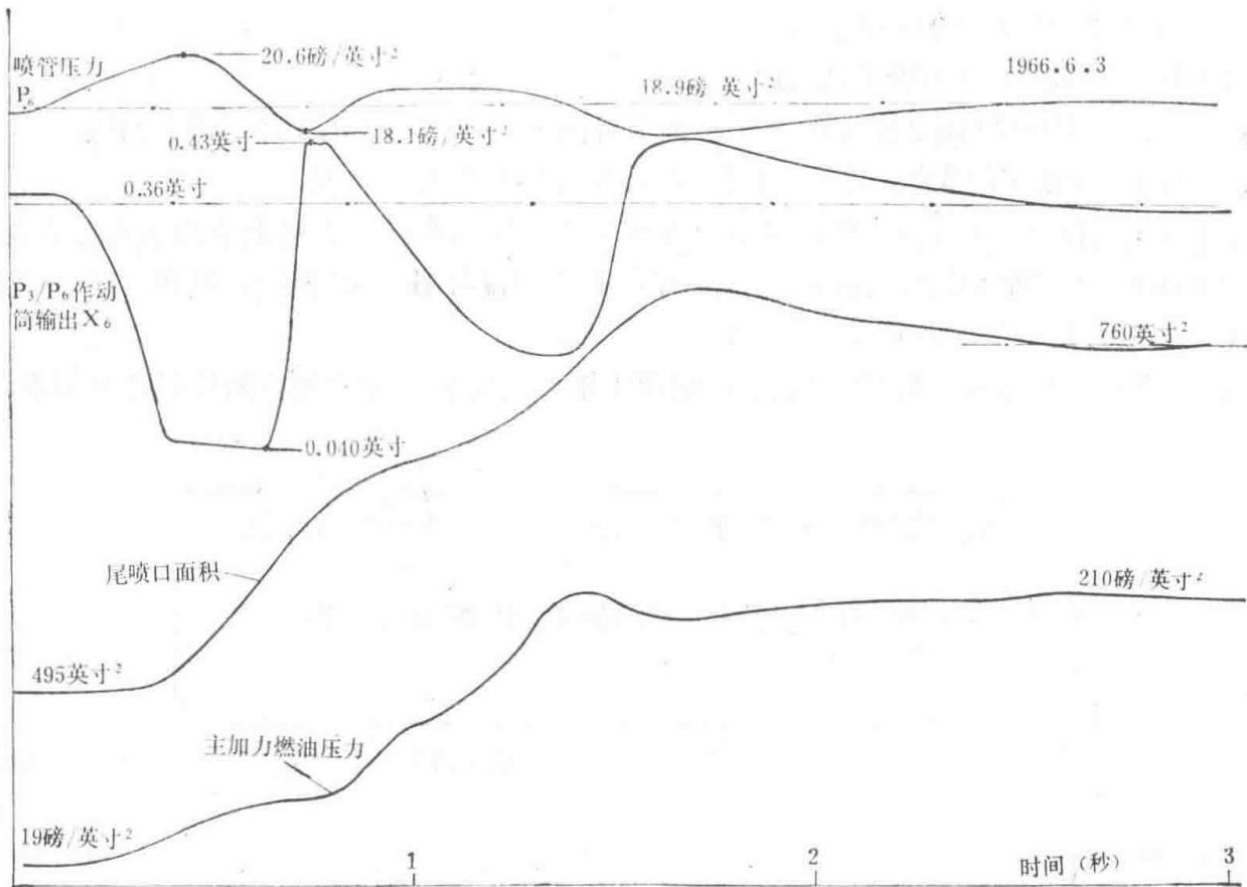


Figure 1 Rapid afterburner acceleration process of Spey Engine No. 8

This figure shows the transient characteristics of rapid acceleration from maximum military power to a main afterburner fuel flow of 4000 gallons per hour. At full stroke, the nozzle opens faster than the maximum rate of fuel increase via the  $P_3 / P_6$  actuator. In such a system, the limited output speed of the actuator causes a lag, resulting in nozzle pressure overshoot. The maximum pressure ratio error near surge is 0.43, while the maximum error near choke flutter is 0.2.

### 3.2 Universal Test Rig

The above tests were completed on a universal test rig by adjusting different limit values. Figures 2 and 3 show the peak pressure ratio errors during rapid throttle acceleration at various speeds. The closest test to the conditions on Engine No. 38 is Test 83, where the limit value was adjusted to approximately 0.18 (the overflow valve was not installed on the universal test rig during testing). At this adjustment, the recorded peak error from rapid acceleration from maximum military power was 0.36. Reducing the limit value also lowers the peak error but makes the system prone to instability.

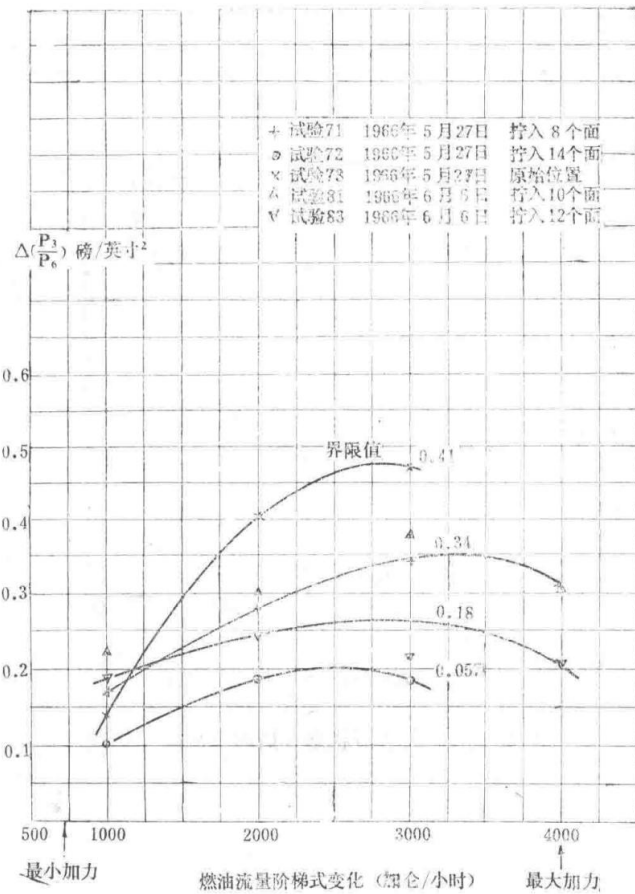


Figure 2 Rapid afterburner acceleration from minimum afterburner

This figure illustrates the pressure ratio error characteristics during rapid acceleration from minimum afterburner.

### 3.3 Nozzle Speed

The maximum nozzle speed recorded during testing on Engine No. 38 was 435 inches per second. The H346 nozzle was equipped with a small-area non-flight-standard nozzle actuator. Based on this, the maximum expected speed on a standard flight nozzle is 356 inches per second. Since this speed slightly exceeds the average nozzle speed (230 inches per second) required to maintain a stable pressure ratio error when fuel flow increases at the maximum rate, it can be concluded that the device's characteristics will be satisfactory when used with a standard flight nozzle.

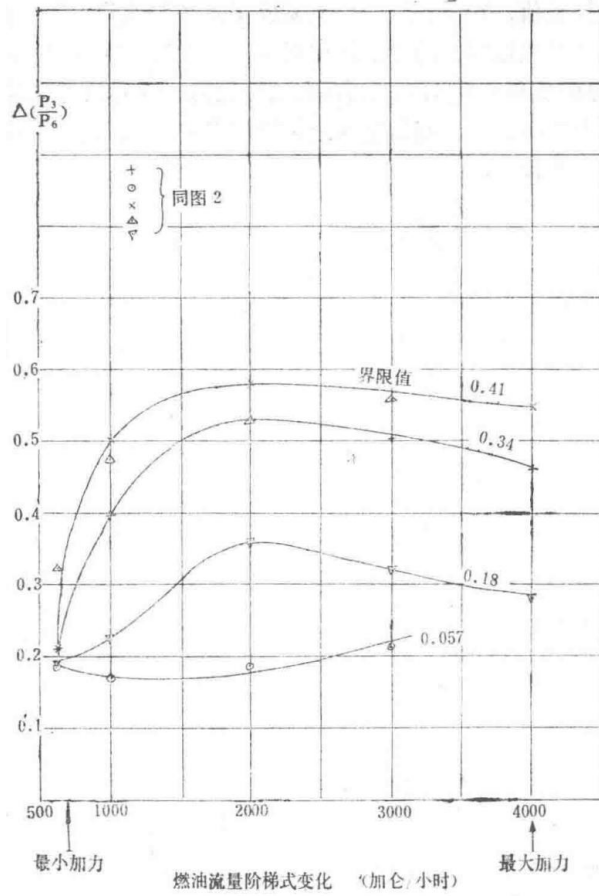


Figure 3 Rapid afterburner acceleration from maximum military power

This figure illustrates the pressure ratio error characteristics during rapid acceleration from maximum military power.

#### Test Data Summary for Needle Valve Performance

Test No.	Date	Description
Test 71	1966.5.27	Incorporated 8 items
Test 72	1966.5.27	Incorporated 14 items
Test 73	1966.5.27	Surge margin
Test 81	1966.6.3	Incorporated 10 items
Test 83	1966.6.6	Incorporated 12 items

# Technical Design Report

TDR7788

## Spey MK202 Afterburner Fuel Control System

First Edition, October 13, 1976

### Abstract

This report provides a general description of the Spey afterburner system, including the selection of basic parameters and the methods by which these parameters are integrated with the system's various components, as well as how these devices plan the afterburner fuel flow.

### Symbols

- $F\Delta$ : Afterburner fuel flow, lb/hr
- $N\Delta$ : High-pressure rotor speed, rpm
- $T_1$ : Inlet temperature, °K
- $P_1$ : Inlet pressure, lb/in<sup>2</sup> (absolute)
- $P_2$ : Low-pressure compressor outlet pressure, lb/in<sup>2</sup> (absolute)
- $P_3$ : High-pressure compressor outlet pressure, lb/in<sup>2</sup> (absolute)
- $P_8$ : Low-pressure turbine outlet pressure, lb/in<sup>2</sup> (absolute)
- $C$ : Proportional constant
- $\beta$ : Afterburner augmentation level
- $f()$ : Function of
- $\alpha\Delta$ : Combustion efficiency
- $K$ : Correction coefficient

### Introduction

Afterburning is a convenient method for obtaining short-term thrust increases in situations such as takeoff, climb, or high-speed aircraft maneuvers. The primary disadvantage of this system is that, compared to other methods of achieving the same thrust increase, the specific fuel consumption rate during afterburning is higher, and the system itself is bulky. To increase thrust, larger engines with greater weight and frontal area are typically required. The advantage of using an afterburner is that it provides a high-speed exhaust jet for supersonic flight. To achieve high-speed airflow, the gas temperature must be raised to levels that the turbine cannot withstand. Afterburning is also affected by the combustion of fuel in the mixed internal and external flows downstream of the turbine. This combustion relies on unburned oxygen in the exhaust to sustain the flame. As detailed in TDR7789, for high-bypass-ratio engines with afterburners, precise fuel scheduling and a closed-loop exhaust nozzle control system are necessary to achieve the required accuracy and performance. In summary, due to pressure changes caused by fuel combustion in the exhaust nozzle, a nozzle area regulator is required. If the nozzle area is not adjustable, back pressure propagates through the bypass duct to the low-pressure compressor, affecting the engine's operating line. Therefore, a nozzle area regulator is needed to maintain the correct back pressure.

The beginning of this report outlines the transformation and selection of basic parameters used to determine and schedule the appropriate afterburner fuel flow to the fuel manifold. The concluding section explains how these functions and parameters are incorporated into the fuel accessories to achieve afterburner fuel regulation.

## Selection of Basic Parameters

The requirement for the afterburner system is to operate satisfactorily under all engine and aircraft flight conditions. Thus, the afterburner fuel supply must be scheduled such that the dimensionless fuel flow varies uniquely with the dimensionless engine speed (i.e., the relationship between  $F \square / P_1 \sqrt{T_1}$  and  $N \square / \sqrt{T_1}$  is single-valued).

Based on this single-valued relationship, it is theoretically possible to design a fuel controller that directly schedules the afterburner fuel flow. However, during high-speed flight, especially during transient maneuvers, the parameters  $P_1$  and  $T_1$  are difficult to measure. By multiplying the fuel flow parameter by the dimensionless combination  $\sqrt{T_1} / N \square$ , the  $T_1$  term can be eliminated, resulting in the dimensionless combination  $F \square / P_1 N \square$ . Since any compressor pressure ratio (or temperature ratio) has a distinct single-valued relationship with  $N \square / \sqrt{T_1}$  (ignoring ram effects, which are minimal in the afterburning range, and specific heat effects),  $N \square / \sqrt{T_1}$  can be replaced by a pressure ratio (e.g.,  $P_3 / P_1$ ). Thus, the fuel flow is regulated based on the single-valued relationship between  $F \square / P_1 N \square$  and  $P_3 / P_1$ .

Absolute pressures are difficult to measure (requiring an absolute vacuum as a reference). However, pressure differences are relatively easy to measure accurately. Mathematical transformations of dimensionless combinations do not affect their dimensionless nature. Therefore, if two ratios, such as  $P_3 / P_6$  and  $P_6 / P_1$ , have a single-valued relationship with  $N \square / \sqrt{T_1}$ , then their difference also has a single-valued relationship with  $N \square / \sqrt{T_1}$ . Thus, this new parameter ( $P_3 / P_1 - P_6 / P_1$ ) also has a single-valued relationship with  $F \square / P \square N \square$ .

As mentioned earlier,  $P_1$  is difficult to measure, so it is convenient to eliminate this parameter from both terms of the above relationship. If the scheduling plan can be made linear and pass through the origin,  $P_1$  can be eliminated from both dimensionless combinations. This linearization can be achieved by introducing another parameter that has a single-valued relationship with  $N \square / \sqrt{T_1}$ . For this purpose, the pressure ratio is adjusted to make the fuel scheduling plan linear and pass through the origin. If  $K$  is the new parameter and  $C$  is the proportional constant between the two dimensionless combinations, the fuel flow relationship becomes:

$$F \square = C N \square (K P_3 - P_6)$$

Afterburner fuel flow equation with correction coefficient  $K$ .

Here,  $K$  and  $N \square / \sqrt{T_1}$  have a single-valued relationship, and thus also with the pressure ratio. Since  $P_3 / P_2$  is the easiest to measure, let  $K = f \square (P_3 / P_2)$ . The relationship then becomes:

$$F \square = C N \square [f \square (P_3 / P_2) P_3 - P_6],$$

Afterburner fuel flow equation incorporating the function of pressure ratio  $P_3 / P_2$ .

For most modern afterburner applications, there is an additional requirement for afterburner augmentation level control, i.e., modulation control, allowing the pilot to select the desired level of afterburner thrust. Since thrust is approximately linearly related to fuel flow, the afterburner thrust modulation control must be proportional to the afterburner fuel flow. Thus, the afterburner fuel flow equation becomes:

$$F \square = C \beta N \square [f \square (P_3 / P_2) P_3 - P_6],$$

Afterburner fuel flow equation incorporating augmentation level  $\beta$ .

This equation remains dimensionless, and the terms on the right-hand side are easily measurable. Thus, in the regulation system, a hydromechanical system is used to achieve the scheduled afterburner fuel flow based on these parameters. The method for obtaining the scheduled fuel flow is explained below.

The equation transformations listed above, aimed at achieving a reasonably simple afterburner fuel control system, use selected practical parameters. The primary reason for preferring these parameters over others is their ease of implementation. In many cases, they also serve other functions and provide a precise and stable control scheme for the system.

## Control Mechanism for Fuel Scheduling

The above transformations of dimensionless combinations were based on the easiest obtainable functional forms. When considering the mechanism of the control device, different approaches can yield the same equation. The considerations made in designing the Spey afterburner system are described below, re-establishing the regulation equation and explaining how each part of the equation is implemented by the regulation devices.

From first principles, the fuel flow must be directly related to a function of the engine's air mass flow. If this is not achieved, there is a risk of the fuel flow exceeding the chemically calculated value, leading to a tendency for rich blowout. Therefore, a method must be found to measure the engine's total air mass flow and schedule the corresponding afterburner fuel flow based on this mass flow.

In engines without a bypass duct, this requirement is relatively easy to meet. Such engines typically use afterburning only beyond the upper limit of the engine's operating range, where the compressor can be considered choked. At this point, there is a simple relationship between the compressor outlet pressure and the air mass flow through it. The fuel schedule can then be built around this parameter. However, in turbofan engines, the selection of basic parameters is more challenging. In this case, no single parameter can determine the air mass flow function. Since the core engine operates between choked states, the air mass flow through the core engine is easily determined. However, the air mass flow at the bypass duct outlet is not as easily determined and is unrelated to the parameters used to determine the core engine's air mass flow. A compromise can be found: under typical engine operating conditions, multiplying the core engine air mass flow by a coefficient approximates the total air mass flow. A correction coefficient is then used to account for variations in the bypass air mass flow. Finally,  $P_3$  is taken as a measure of the core engine air mass flow and thus as the foundation for the entire control system.

The bypass ratio, or the ratio of bypass air mass flow to core engine air mass flow, is determined by  $T_1$  and the low-pressure compressor speed, both of which are related to  $T_1$ . Since a high bypass ratio has the same effect as a high  $T_1$ , a correction for  $T_1$  is needed. However,  $T_1$  itself is difficult to measure, especially during rapid transients, as thermocouples have a longer time constant compared to the engine system, increasing errors. Studying how errors affect the required fuel flow provides a clue to solving the problem. When the actual  $T_1$  is higher (i.e., high bypass ratio), the air mass flow is greater than indicated by the  $P_3$  signal, and the fuel-air ratio is lower. Thus, more fuel flow is needed. Conversely, when  $T_1$  is low, the air mass flow is lower than indicated by  $P_3$ , requiring less fuel flow. We can derive a function of  $N \square / \sqrt{T_1}$ , but the measurement of  $T_1$  remains problematic. Thus,  $P_3 / P_2$  is taken as the correction function. When the high-pressure compressor is choked,  $P_3 / P_2$  varies uniquely with  $N \square / \sqrt{T_1}$ . The function can thus be built around  $P_3 / P_2$ . The shape of the function is shown in Figure 1, which illustrates the correction to  $P_3$ .

$$F_R = CN_H(KP_3 - P_6)$$

Correction function for  $P_3$  based on  $P_3 / P_2$ .

The graph shows the correction applied to  $P_3$  as a function of the pressure ratio  $P_3 / P_2$ .

The  $P_3 / P_2$  signal is derived from a pressure ratio regulator, a specialized device whose operation is detailed in TDR7789. Its primary function is to position a needle valve within an orifice based on the pressure balance between  $P_2$  and the  $P_3$  partial pressure through a throttling orifice to  $P_0$ . The positioning of this needle valve depends on the pressures  $P_3$  and  $P_2$ , as well as the profile shape of the needle valve. The method for deriving the correction term is discussed in the section on needle valve profiles in TDR7789. The needle valve's position within its orifice is transmitted via a mechanical linkage to an air signal generator controlled by  $P_3 / P_2$ . In this device, a rack-and-pinion mechanism positions the needle valve within an orifice from the  $P_3$  air partial pressure to  $P_6$ . This  $P_3$  partial pressure term is used to determine the fuel flow, as it correlates with the required  $P_3 / P_2$ . The needle valve profile of the divider, which meets system requirements and provides the correct  $P_3$  signal shape, is developed by the manufacturer (as shown in Figure 1).

As mentioned in previous sections, measuring absolute pressure requires an absolute vacuum as a reference. In practice, this is not feasible in a simple, cost-effective, and reliable system. Instead, measuring the difference between two pressures and balancing this pressure difference with a spring force is more practical. To provide the most convenient measurement, the secondary pressure should be as small as possible, i.e., providing the maximum possible pressure difference, so that measurement inaccuracies result in minimal errors. The choice of secondary pressure is resolved between  $P_1$  and  $P_6$ . The primary consideration is signal measurability; in this regard,  $P_1$  is more difficult to measure because the  $P_1$  probe requires anti-icing to prevent signal loss at low  $T_1$ . Therefore,  $P_6$  becomes the selected parameter. The term for scheduling fuel flow becomes  $f[(P_3 / P_2) P_3 - P_6]$  (for ease of reference, this term is also called  $P_b$ ).

For simplicity, direct-acting pressures are used as much as possible in the controller. Thus, the pressure function  $P_b$  is formed by balancing the two pressure terms in the above function with a spring on either side of a rotating hollow valve. The position of the spool valve is uniquely related to  $P_b$ . The spool valve is included in the Vaporizing Gutter Flow Metering Valve (VGFMV), which schedules the vaporizing gutter fuel flow. As the spool valve moves from one end of its stroke to the other, the opening of the VGFMV gradually increases. Therefore, since  $P_b$  has a single-valued relationship with the spool valve position, and the valve position determines the valve opening, this establishes a single-valued relationship between  $P_b$  and the valve opening. However, what is needed is the relationship between  $P_b$  and the fuel flow. If the pressure difference across the valve is constant, the fuel flow depends solely on the valve opening. This constraint must be established in the control device.

The Vaporizing Gutter Flow Pressure Difference Regulator (VGFPDR) maintains a constant pressure drop across the valve, approximately 100 lb/in<sup>2</sup>. The total scheduled afterburner fuel flows into the VGFPDR, and most of it is bypassed to the fuel manifold. The spool valve's position allows sufficient fuel to return to maintain a pressure difference of approximately 100 lb/in<sup>2</sup> across the VGFMV. This is achieved by balancing the main manifold fuel injection, spring force, and bypass pressure (fuel manifold pressure and vaporizing gutter outlet pressure).

The vaporizing gutter is required to maintain a stable fuel combustion core, with the remaining afterburner fuel burning around this core. Therefore, under given flight conditions (or  $P_b$  values), the size of the VGFMV is determined to supply approximately 10% of the maximum afterburner total fuel flow. This fuel flow is independent of the afterburner augmentation level. Thus, the valve size introduces a correction coefficient (a combination of constants), and the vaporizing gutter flow is independent of other variables. It should be noted that during engine operation, various spool valves are continuously rotating, which is a design feature of the spool valves to avoid friction hindering the spool valve's response to small changes in control pressure.

However, the vaporizing gutter flow is only related to the maximum afterburner fuel flow required under flight conditions and can be determined solely by  $P_b$ . As mentioned above, the total afterburner fuel flow is related not only to the flight conditions defined by  $P_b$  but also to the afterburner augmentation level selected by the pilot. The Total Flow Metering Valve (TFMV) must account for both parameters. Again, fuel flows through the valve positioned by  $P_b$  and the pilot's throttle lever. The combined input command from  $P_b$  and the pilot's throttle lever is implemented by a spool valve connecting the VGFMV and TFMV, with a variable fulcrum on the pilot's afterburner selection lever. The VGFMV spool valve is positioned only by  $P_b$  (flight conditions), so this small shaft fulcrum acts as a variable fulcrum for the linkage. The fulcrum roller acts as a pivot within the linkage slot. The roller is actually positioned by the linkage from the pilot's afterburner selection lever. The TFMV spool valve is thus positioned by these two parameters. The positioning of the fulcrum roller is achieved by a signal from the pilot's lever, converted through a rack-and-pinion, cam, and follower into the position of a slider on the lever.

Additionally, the combination of  $P_b$  and the pilot's throttle lever is used only to position the spool valve, thus determining the opening size of the TFMV. However, what is required is to determine the needed fuel flow. As previously mentioned, this requires regulating the pressure difference across the valve to provide this relationship. The Main Pressure Difference Regulator (MPDR) serves this function by controlling the pressure difference across the valve. The pressure balance of the total afterburner fuel pressure sets the MPDR regulator to adjust the rotary valve servo signal of the follow-up piston. This adjusts the afterburner fuel pump inlet throttle valve, thus supplying the required fuel flow while maintaining a constant pressure difference across the TFMV.

The system described so far can schedule the appropriate vaporizing gutter fuel flow, while the total afterburner flow is related to the augmentation level and the pressure term  $P_b$ . Thus, the TFMV valve opening size can provide the correct afterburner fuel flow at maximum  $N_d$ . This is suitable for a system where  $N_d$  remains nearly constant within the operating range. However, in the Spey, under certain flight conditions,  $N_d$  can drop by up to 10% due to fine adjustments in the main engine fuel flow. The  $P_b$  term causes  $N_d$  to decrease (i.e., when  $T_d$  is constant,  $N_d / \sqrt{T_d}$  decreases), just as an increased bypass ratio requires more fuel. The shaping of  $P_3 / P_2$  provides the additional fuel required when  $T_d$  changes, which is exactly opposite to the correction needed for  $N_d$  variations. Therefore, an additional  $N_d$  term is needed.

Thus, a linear relationship is needed between  $N_d$  and the fuel flow. Once the fuel flow is determined by the valve opening, the required relationship is between  $N_d$  and  $\sqrt{\Delta P}$ . In the MPDR, the pressure difference causes the required valve opening to change, so a device providing  $N_d^2$  can achieve the needed correction. A pair of centrifugal flyweights in the MPDR provides this relationship. If  $N_d$  decreases, the rotary valve servo piston is adjusted to reduce the fuel flow.

Since the centrifugal flyweights are immersed in fuel, changes in fuel specific gravity affect the flyweights' operation, necessitating an additional term. The fuel schedule is based on mass flow, while the scheduling system provides volumetric flow, leading to changes in fuel mass flow. However, by appropriately selecting the flyweight material, the effect of fuel specific gravity changes on the flyweights can largely offset the changes in fuel mass flow.

The TFMV profile allows for adjustments to the combustion efficiency ( $\alpha_d$ ) margin. The theoretical fuel schedule derived in the previous section is realistic in the engine. The afterburner fuel schedule curve is shown in Figure 2 of TDR7788. It can be seen that the fuel schedule is nonlinear, with the lower nonlinearity caused by the combustion efficiency term. The remaining nonlinear portion results from necessary modifications to the TFMV profile during development.

$$F_R = CN_H [f_n (P_3/P_2) P_3 - P_g]$$

Afterburner fuel schedule curve.

The graph illustrates the nonlinear relationship between the scheduled afterburner fuel flow and engine parameters, including adjustments for combustion efficiency.

## Fuel Supply Nozzles

So far, only the determination and derivation of the correct fuel flow for the afterburner system have been discussed. However, the afterburner system has other considerations that require several additional devices. The scheduled fuel flow must be delivered to the afterburner manifold at the appropriate time. The relationships between these auxiliary devices and the afterburner fuel scheduling system are explained below.

Early experience with afterburner systems showed that if the total afterburner fuel flow is burned through a single manifold system, there is a risk of lean blowout at low fuel flows. To address this issue, the Spey system employs a dual combustion system. One combustion system is the vaporizing gutter, which consumes approximately 10% of the maximum afterburner fuel flow under flight conditions. This fuel flow is effectively independent of the afterburner augmentation level. The vaporizing gutter flow passes through three concentric vaporizing gutters, providing a stable and nearly constant fuel combustion core. The remaining scheduled afterburner fuel flows through another fuel manifold system. Four concentric annular manifolds face the engine's vaporizing gutters, positioned between each vaporizing gutter. Catalytic igniters are located at the center of the vaporizing gutters. The innermost manifold is blocked to prevent fuel from that manifold from dripping onto the catalytic components, which could damage the catalytic igniter. Thus, although four manifolds are present in the current system, only the outermost three have fuel flowing through them. Fuel from the manifolds flows around the vaporizing gutters and is ignited. Since afterburner modulation affects only the fuel flow in the manifolds, the vaporizing gutter provides a stable combustion core, eliminating the risk of lean blowout. The fuel entering the respective combustion systems is scheduled for the vaporizing gutter by the VGFMV and for the entire system

by the TFMV, with the difference being the scheduled fuel flow supplied to the manifolds.

At high altitudes, the minimum afterburner fuel flow required is less than the maximum afterburner fuel flow at sea level. One requirement for the fuel pump is to avoid transferring too much heat to the fuel, preventing damage to the seals of components in contact with high-pressure fuel. Based on thermal balance, a vapor core pump transfers less heat to the fuel than a gear pump or centrifugal pump. For this application, the use of a vapor core pump is a satisfactory choice, as it is much lighter and more economical compared to a piston pump.

## Ignition Sequence

The above discussion only addresses the issue of afterburner ignition. The afterburner system also requires a programmed operation for afterburner selection. As a basic design feature of the Spey afterburner system, afterburning is only required when  $N_{\square}$  is above 80%. A device is incorporated into the system to prevent the pilot from abruptly advancing the throttle lever from idle into the afterburner range when  $N_{\square}$  is below 80%. The 80% synchronizing valve, as the name suggests, consists of a pair of centrifugal flyweights that move spool valves against spring force. Above 80%  $N_{\square}$ , the spool valves have moved sufficiently to open various ports, allowing the afterburner and exhaust nozzle actuators to operate. The 80% synchronizing valve is connected in series with the pilot's selection lever, functioning as an "AND" gate.

Above 80%  $N_{\square}$ , the pilot's lever is the only selection lever. As described above, the signal from the pilot's selection lever is transmitted to the TFMV to determine the selected afterburner augmentation level. The same signal is also sent to the afterburner selection valve. When the system is above 80%  $N_{\square}$  and afterburning is engaged, a port in the afterburner selection valve opens, allowing servo fuel to flow through the 80% synchronizing valve into the rotary valve servo piston of the vapor core pump inlet throttle valve, the exhaust nozzle actuator, and the air purge selection valve.

Thus, the signal to the rotary valve servo piston causes the rotary valve to open, allowing the vapor core pump inlet to enlarge. Fuel then begins to supply the afterburner fuel scheduling system. The signal to the nozzle actuator valve adjusts the nozzle to a pre-opened position, adjusting the nozzle position to match the vapor gutter flow before afterburner ignition. The signal to the air purge selector valve cuts off the airflow through the vapor gutter. The presence of this purge air prevents carbon buildup around the fuel orifices in the pipelines after afterburner shutdown.

The movement of the rotary valve servo piston not only opens the low-pressure shutoff valve (allowing fuel to flow to the scheduling system) but also opens an orifice to deliver engine main fuel to the catalytic ignition system. This fuel also serves as a signal for the PRCU (Pressure Ratio Control Unit), enabling the PRCU to control the nozzle lubrication pump and thus the nozzle position. The fuel to the catalytic igniter passes through the catalytic fuel flow control device, which essentially acts as a 3-second timer. After 3 seconds, the catalytic fuel supply stops. The main fuel passing through the catalytic timer is divided, with part flowing into the catalytic igniter and part into the main fuel manifold. A signal is also sent to the afterburner control spill valve, moving it to its maximum spill position. Up to this point, all described events occur within an extremely short timeframe (on the order of 0.05 seconds), and reviewing the sequence during this specific period is useful.

Movement of the throttle lever causes servo fuel to open the low-pressure shutoff valve, activates the PRCU, cuts off vapor gutter purge air, and adjusts the nozzle to a pre-opened position. Fuel flowing through the vapor core pump is delivered to the scheduling system for the vapor gutter and fuel manifold. The catalytic fuel flow initiates the catalytic timer, the fuel manifold begins to fill, and the main fuel manifold fuel (via the spill valve) is directed to low pressure, while also providing fuel for vapor gutter ignition.

The requirement for the afterburner ignition timer is that the afterburner should activate 5 seconds after engagement. Before introducing main manifold fuel into the system, it is desirable to stabilize the system as much as possible to ensure the vapor gutter establishes the required stable fuel combustion core. However, the system has another limitation: the nozzle system must prevent fuel inflow to eliminate the possibility of surge. It has been demonstrated that the nozzle takes approximately 0.7 seconds to move from the pre-opened position to a stable afterburner position. As a design feature, it is preferable to introduce fuel only after twice the nozzle movement time, i.e., 1.4 seconds. Considering variations in devices, an additional 0.2-second tolerance is added.

This leaves 3.4 seconds of the 5-second period. Assuming a minimum tolerance of 0.2 seconds, the time available for stabilizing vapor gutter fuel is between 3.0 and 3.2 seconds. Within this timeframe, the catalytic timer allows fuel to flow into the igniter, to the acceleration control spill valve, and to fill the afterburner fuel manifold. The size of the manifold filling orifice is determined based on the fuel quantity to be injected into the fuel manifold within the specified time under International Standard Atmosphere sea-level static conditions, normal weather, and takeoff state. Under other flight conditions, this flow rate may vary by approximately 30% above or below the actual filling amount, but such a shortcoming is permissible in the system.

After 3 to 3.2 seconds, the catalytic timer cuts off fuel to the catalytic igniter, leaving only the vapor gutter to maintain ignition. Fuel filling also stops, and the signal fuel to the acceleration control spill valve ceases simultaneously. The pressure in the acceleration control spill valve servo piston drops to low pressure, and the servo piston returns to its non-afterburning position. Servo pressure builds up beneath the main piston, moving it to the maximum non-spill position. The speed at which the main piston moves determines the rate of fuel introduction into the fuel manifold, and the size of the control restrictor is set to meet the requirement based on a movement time of 1.4 to 1.6 seconds. Once the spill valve has fully moved to its non-spill position, the afterburner system begins operation. Thereafter, the acceleration and deceleration of afterburner fuel are controlled by limiting the servo fuel to the rotary valve.

## Afterburner Disengagement

Afterburner disengagement is achieved by moving the throttle lever to the non-afterburning position. This actuates the spool valve in the afterburner selection valve, cutting off servo fuel to the nozzle actuator valve, rotary valve servo piston, and air purge selector valve. The actuator valve then closes, rapidly reducing the nozzle to its non-afterburning position. The signal to the air purge selector valve is removed, allowing the valve to return to its non-afterburning position, and purge air flows through the vapor gutter manifold to clear residual fuel in the system, preventing carbon buildup in the vapor gutter orifices. The removal of servo fuel to the rotary valve servo piston closes the low-pressure shutoff valve, preventing fuel from flowing through the vapor core pump to the scheduling system. Closing the low-pressure shutoff valve also cuts off servo fuel to the PRCU, leaving the nozzle controller uncontrolled by the PRCU. The engine then operates normally as a non-afterburning engine.

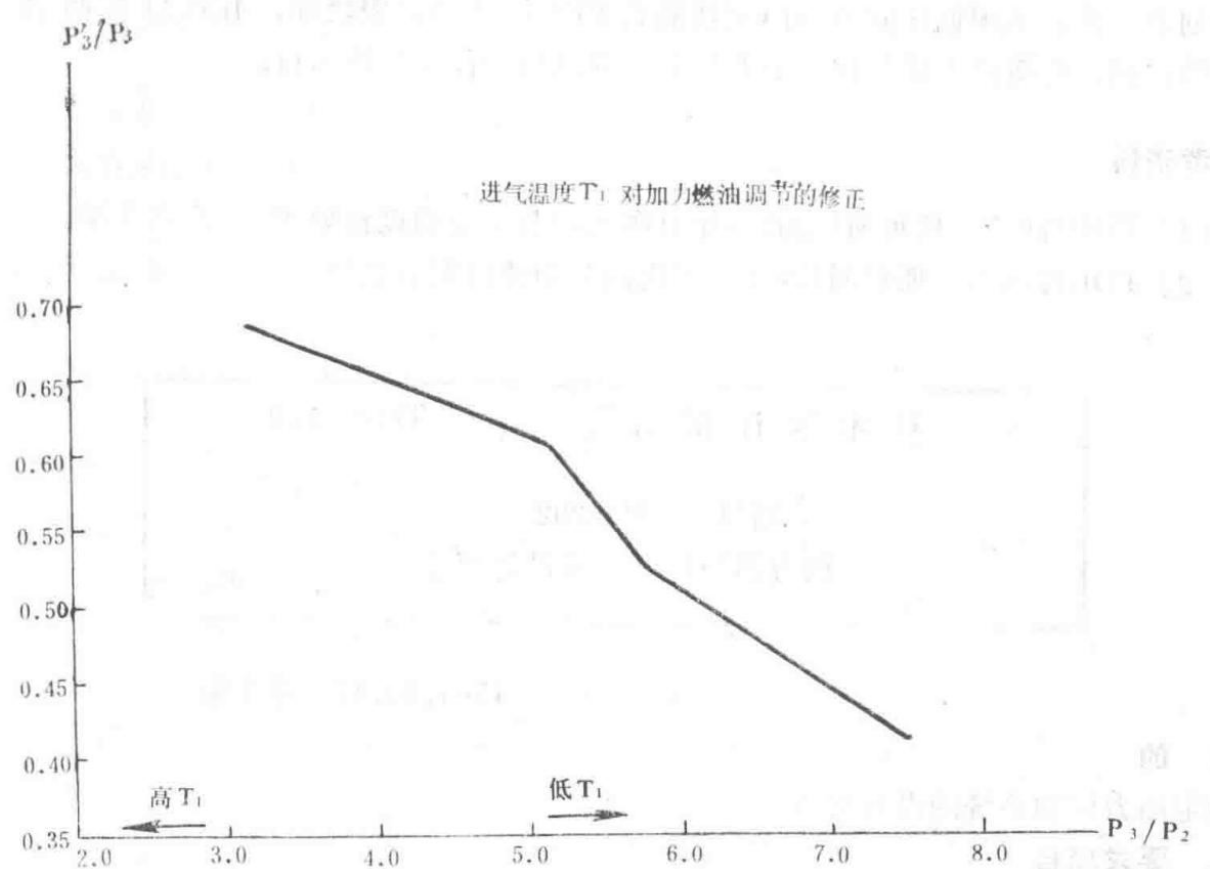


Figure 1: Spey MK202 Afterburner Fuel Scheduling Modification Requirements

Diagram illustrating the modification requirements for the afterburner fuel scheduling system in the Spey MK202 engine.

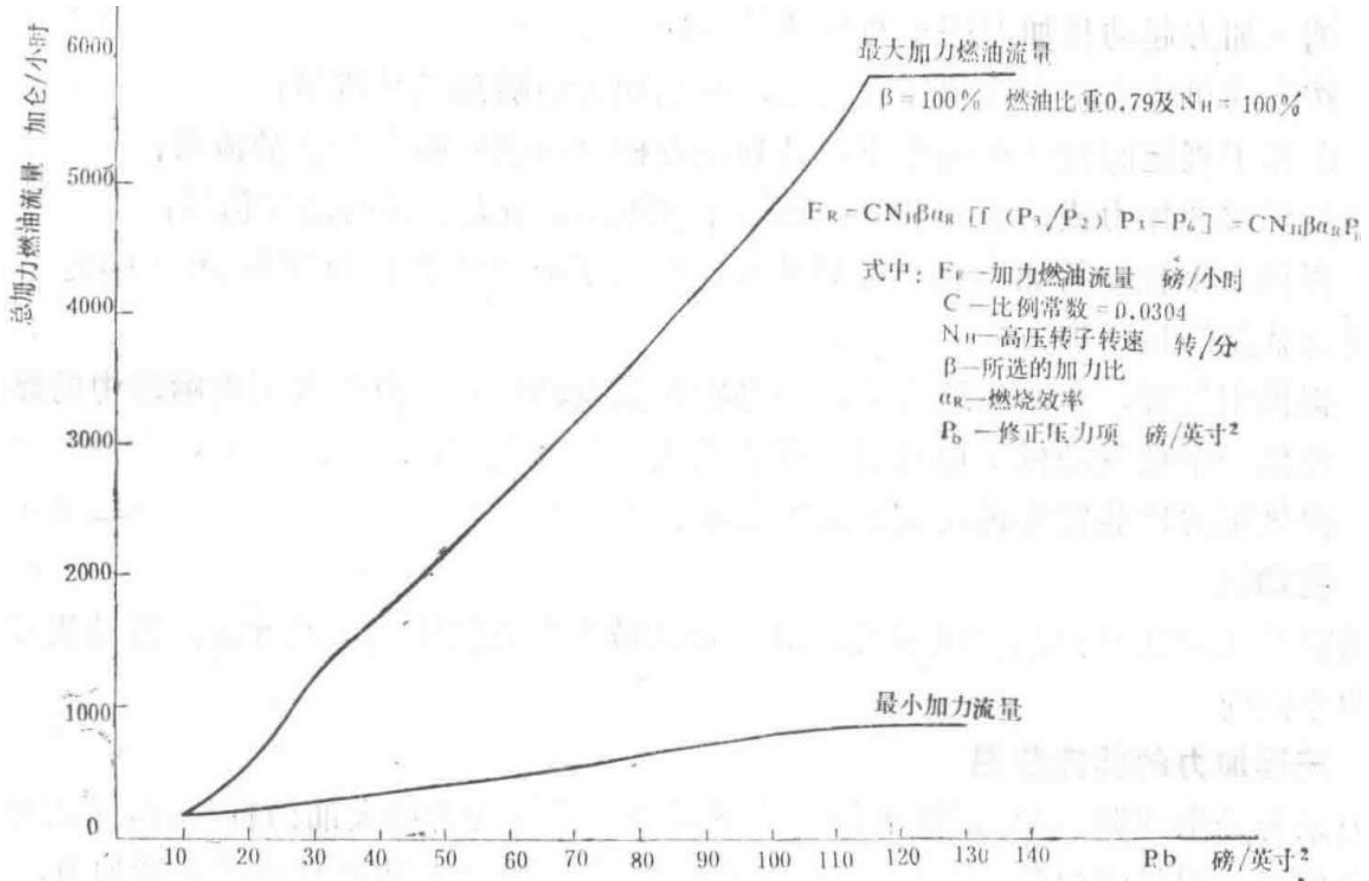


Figure 2: Typical Calibration Curve of Spey MK202 Afterburner Fuel Flow Regulator

Graph showing the typical calibration curve for the afterburner fuel flow regulator in the Spey MK202 engine.

## References

- [1] TDR770 – Spey MK202 Afterburner Fuel Regulation System Design Requirements
- [2] TDR7789 – Spey MK202 Pressure Ratio Regulation and Nozzle Regulation System

Technical Design Report	TDR 770
Spey MK202 Afterburner Fuel Control System Design Requirements	

1st Edition, 17 October 1964

## Objective

To establish the design requirements for the afterburner fuel system.

### 1. Requirements

- Provide a device for modulating afterburner thrust;
- Incorporate mechanical devices for afterburner start and shutdown;
- Schedule the total afterburner nozzle fuel flow based on engine condition and selected afterburner level;
- Schedule the vapor gutter (pilot) nozzle fuel flow below specified engine speeds;
- Provide a hydraulic signal equivalent to approximately 80% of maximum NH speed when engaging or disengaging afterburner;

- Provide an independent afterburner start control device for emergency use, allowing afterburner engagement at 80% of maximum engine NH speed;
- Provide an air source to purge fuel from the vapor gutter manifold, main manifold, and main nozzle ring after afterburner shutdown;
- Provide a device to introduce engine main fuel into the catalytic ignition system;
- Provide a drive and mounting for the pressure ratio device.

## 2. Engine

The engine is an afterburning twin-spool turbofan designed for all-weather fighter aircraft. The engine is installed in a near-horizontal plane.

### 3. Afterburner Engagement Speed Range

The afterburner system is fully modulated. Under normal flight conditions, afterburner is required only when the engine is at the maximum throttle position. For emergency use, a special device is provided to allow afterburner engagement at 80% of maximum N1 engine speed.

## 4. Engine Performance

The dimensionless curves for maximum afterburner fuel flow, low-pressure compressor outlet pressure, high-pressure compressor outlet pressure, and low-pressure turbine outlet pressure as functions of the parameter  $N_1 / \sqrt{T_1}$  are shown in Figures 1 to 4 of this report. The curve for the fuel flow coefficient required to calculate maximum afterburner fuel flow as a function of the corrected parameter  $f(P)$  is shown in Figure 2.

The high-pressure compressor outlet static pressure is limited to 330 psi (gauge), and the ratio of high-pressure compressor outlet static pressure to total pressure is 0.97.

The nozzle is adjustable to maintain engine dimensionless parameters constant at various afterburner ratios.

## 5. Afterburner System Requirements

### 5.1 Afterburner Selection Valve (Normal Operation)

Moving the pilot's throttle lever selects afterburner operation, actuating a valve that supplies fuel to the afterburner fuel system.

A device is provided to ensure that any jamming in the afterburner control mechanism does not hinder the use of the afterburner cut-off switch, main engine throttle lever, or shutdown switch.

For normal operation, afterburner start and shutdown should be achieved using devices other than electrical controls.

### 5.2 Nozzles (Supplied by Rolls-Royce)

The afterburner fuel system should work in conjunction with the following nozzle system.

#### 5.2.1 Pilot Fuel Nozzles

The nozzles on the pilot fuel manifold use a small portion of the total afterburner fuel. Changes in the pilot's throttle position alter the total afterburner fuel flow, but the fuel supplied to the pilot nozzles should not vary beyond the values determined by the agreed test specifications. The nominal required flow rate is 10% of the maximum total afterburner fuel flow.

The fuel flow rate for the pilot system is 29.5 gallons/hour/psi. However, this value may change during development testing.

## 5.2.2 Main Fuel Nozzles

The main fuel nozzles use the remaining portion of the total afterburner fuel flow, but the main fuel system is divided into four parallel flow systems, each with different flow numbers, tentatively set as follows:

System	Flow Number (gallons/hour/psi)
1	16.8
2	65.0
3	116.0
4	87.0

All flow numbers are calculated based on a fuel specific gravity of 0.79.

## 5.3 Afterburner Fuel Regulator

The afterburner fuel regulator schedules the total fuel flow to the afterburner combustor based on engine condition and selected afterburner level. The required fuel flow is determined by the following formula:

$$F = \beta K_1 R [ f(P_3, P_2) P'_3 - P'_6 ] N$$

Formula for calculating total afterburner fuel flow, where  $F$  is the total afterburner fuel flow (lb/hr),  $N$  is the high-pressure rotor speed (rpm),  $\beta$  is the selected afterburner level (i.e., pilot throttle position),  $K_1$  is a constant,  $f(P_3/P_2)$  is a function of  $P_3/P_2$ ,  $P_3$  is the high-pressure compressor outlet total pressure (psia),  $P'_3$  is the high-pressure compressor outlet pressure at the regulator (psia),  $P_2$  is the low-pressure compressor outlet total pressure (psia),  $P_6$  is the turbine outlet total pressure (psia),  $P'_6$  is the turbine outlet pressure at the regulator (psia), and  $R$  is the afterburner fuel flow correction factor.

The pressure ratios at the regulator to the total pressures at the sensing points are given as  $P'_3 / P_3 = 0.955$  and  $P'_6 / P_6 = 0.97$ .

Via the  $P_3 / P_2$  actuator linkage, the movement of the throttle lever is essentially linearly related to changes in the  $P_3 / P_2$  ratio. The total throttle lever travel occurs between pressure ratios of 2.86 and 8.31.

The afterburner level should vary between 15% and 100% of the maximum afterburner flow, and the required minimum afterburner level may change during development testing.

The required minimum total afterburner fuel flow is 15% of the maximum afterburner fuel flow or 2610 lb/hr, whichever is greater. These values may change in the future.

## 5.4 Pilot Nozzle Fuel Scheduling Control

The fuel flow to the pilot nozzles is scheduled similarly to the total afterburner fuel flow but is independent of the pilot's throttle lever movement and engine speed, as follows:

$$F = 0.10 K_1 \times 12640 [ f(P_3, P_2) P'_3 - P'_6 ],$$

Formula for calculating pilot nozzle afterburner fuel flow, where  $F$  is the pilot nozzle afterburner fuel flow (lb/hr), and other symbols are as defined in Section 5.3.

The constant 0.10 may change as development testing progresses.

## 5.5 Afterburner Fuel Pump

The nominal maximum afterburner fuel flow required by the engine is 7000 gallons/hour, regardless of the fuel type specified in Section 10.

A small amount of high-pressure fuel from the engine main system is permitted for servo device use. The engine main fuel pressure is calculated by the following formula:

$$P_m = P_3 + 300 + 3.78 \times 10^{-3} F_m + 5.4 \times 10^{-6} F_m^2$$

Formula for calculating engine main fuel pressure, where  $P_m$  is the engine main fuel pressure (psia),  $P_3$  is the high-pressure compressor outlet total pressure (psia), and  $F_m$  is the engine main fuel flow (lb/hr).

The maximum overload pressure is 1800 psi (gauge).

Mechanical drive is provided from the high-pressure compressor system. At an engine high-pressure rotor speed of 12,640 rpm, the drive speed is 21,045 rpm, rotating counterclockwise (viewed from the engine mounting).

At 21,045 rpm, the maximum power output from the engine drive is 180 horsepower.

## 5.6 Mechanical Drive Device

In addition to the pump drive mentioned in Section 5.5, a low-speed drive is also required from the engine high-pressure rotor. At a high-pressure rotor speed of 12,640 rpm, its speed is 396 rpm, rotating clockwise (viewed from the engine mounting). At 396 rpm, the low-speed engine drive outputs a maximum power of 5 horsepower.

The pressure ratio device is installed on the afterburner fuel regulator and driven by a shaft on the regulator, rotating counterclockwise (viewed from the mounting), at the same speed as the low-speed drive.

At 396 rpm, the maximum power consumption of the pressure ratio device is 1 horsepower.

A device is required to distribute fuel flow to the afterburner main fuel nozzles.

Once the maximum afterburner fuel flow is scheduled, this controller ensures that the fuel supplied to all nozzles is proportional to the flow number of each nozzle.

When sequentially activating each fuel manifold, the total fuel flow discharged from the nozzles should exhibit no significant variation, remain stable, and comply with the range specified in the agreed test specifications.

The staging valve is controlled by the pilot's throttle lever.

## Staging Valve Characteristics

- Circuit 1 is always engaged
- Circuit 2 is always engaged
- Circuit 3 engages at 36% of maximum flow (nominal value)
- Circuit 4 engages at 71.6% of maximum flow (nominal value)

An override function is required to ensure that Circuit 3 and Circuit 4 do not engage until the exhaust nozzle reaches specified areas: 540 square inches for Circuit 3 and 664 square inches for Circuit 4. When the pressure ratio  $P_3 / P_2 \geq 6.93$ , a readjustment device is needed, which reduces these areas by 42 square inches. The oil return port of the readjustment servo piston, which returns to the low-pressure return line, closes when  $P_3 / P_2 \geq 6.93$ .

## 5.8 Speed Override

A device is required to prevent any afterburner fuel from flowing to the nozzles when the engine speed is below a certain threshold, temporarily set at 80% of the engine's maximum speed. This device must be capable of handling the emergency afterburner override engagement described in Section 1.6. At 9% engine speed, an external hydraulic connection is required to provide high-pressure fuel from the engine. This pressure signal must be available throughout the engine's operation to engage or disengage the afterburner. If needed in the future, the pressure signal can be configured to be provided only during afterburner engagement.

## 5.9 Catalytic Ignition Fuel Introduction Valve

During afterburner startup, a valve is required to direct the engine's main fuel supply to the catalytic ignition system. The engine's main fuel pressure can be determined from the equation in Section 5.3, with an overload pressure of 1800 psi (gauge). The maximum fuel flow supplied to the catalytic ignition system is 300 gallons per hour.

## 6. Contamination Sensitivity

The afterburner fuel system is designed to operate with various fuels specified in Section 10, with contamination typically following ACS9008 standards.

## 7. Low-Pressure and Cooling Flow

Normal leakage into the low-pressure system is returned to the boost pump inlet for cooling purposes.

When the afterburner is not engaged, cooling must be provided for the afterburner fuel control unit and staging valve. For this purpose, fuel from the boost pump outlet is used for cooling when the afterburner is not engaged. The pressure increase of the boost pump can be determined from Figure 5.

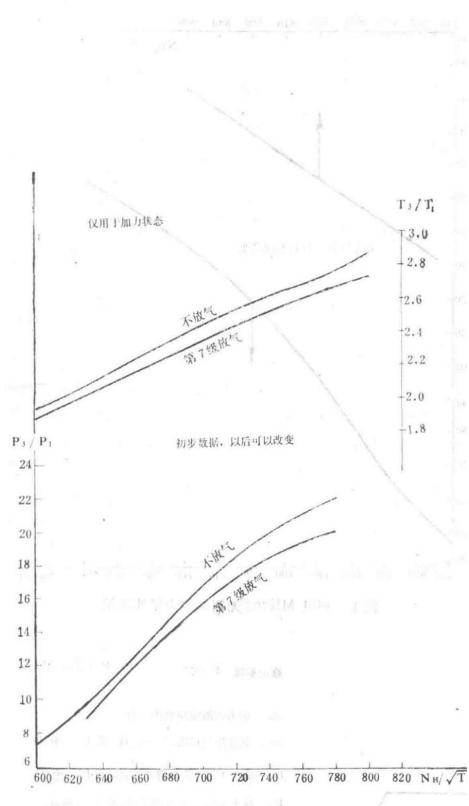


Figure 3 Spey MK202 Dimensionless High-Pressure Compressor Outlet Total Pressure and Total Temperature

Graph showing the dimensionless total pressure and total temperature at the outlet of the high-pressure compressor of the Spey MK202 engine.

## 8. Inlet Pressure Requirements

The system must operate satisfactorily with an inlet pressure of 22 psi above the fuel vapor pressure. The maximum and minimum inlet pressures of the afterburner fuel control unit vary with afterburner fuel flow, as shown in Figure 6.

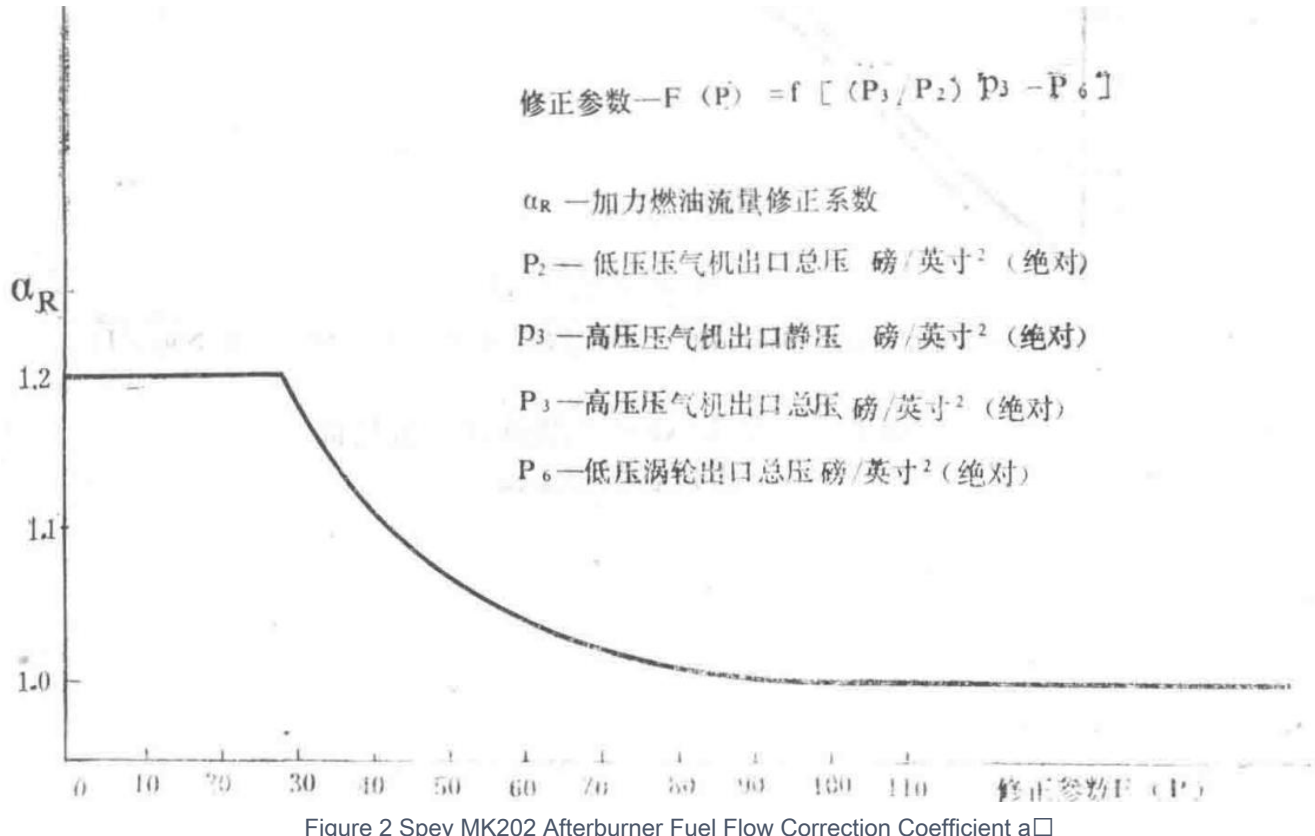


Figure 2 Spey MK202 Afterburner Fuel Flow Correction Coefficient  $\alpha_R$

Graph depicting the afterburner fuel flow correction coefficient  $\alpha_R$  for the Spey MK202 engine.

## 9. Throttle Lever Torque

The maximum torque of the afterburner system throttle lever must not exceed 10 lb-in.

## 10. Operating Fuels

The system must be designed to operate with fuels specified in ACS9008 without adjustment.

The afterburner fuel control unit inlet fuel temperature varies within the following ranges:

- Minimum temperature:
- AVTAG: Temperature corresponding to a fuel viscosity of 12 centistokes
- AVTUR/50, AVCAT/48: Temperature corresponding to a fuel viscosity of 12 centistokes
- Maximum temperature:
- AVTAG: +60°C
- AVTUR/501: +85°C

The maximum temperature corresponds to an afterburner fuel flow of 330 gallons per hour. The fuel for the afterburner servo system is supplied from the engine's main fuel pump, with the following maximum steady-state fuel temperatures:

- +120°C for AVTAG
- +120°C for AVTUR/501
- +120°C for AVCAT/48

At the staging valve, the afterburner fuel temperature is approximately 150°C.

## 11. Operation During Catapult Launch

The afterburner fuel control unit must operate satisfactorily under longitudinal acceleration of up to 5g during catapult launch, without any thrust drop.

During catapult launch, if the throttle lever is rapidly advanced or retarded, the device must enable the engine to accelerate or decelerate normally.

## 12. Air Purging

When the afterburner is disengaged, an air purging device must be provided to purge fuel from the evaporation tank lines, manifolds, and nozzle rings.

## 13. Leakage

The total leakage from all leakage joints must not exceed 50 ml/min (steady state) and 100 ml/min (transient state).

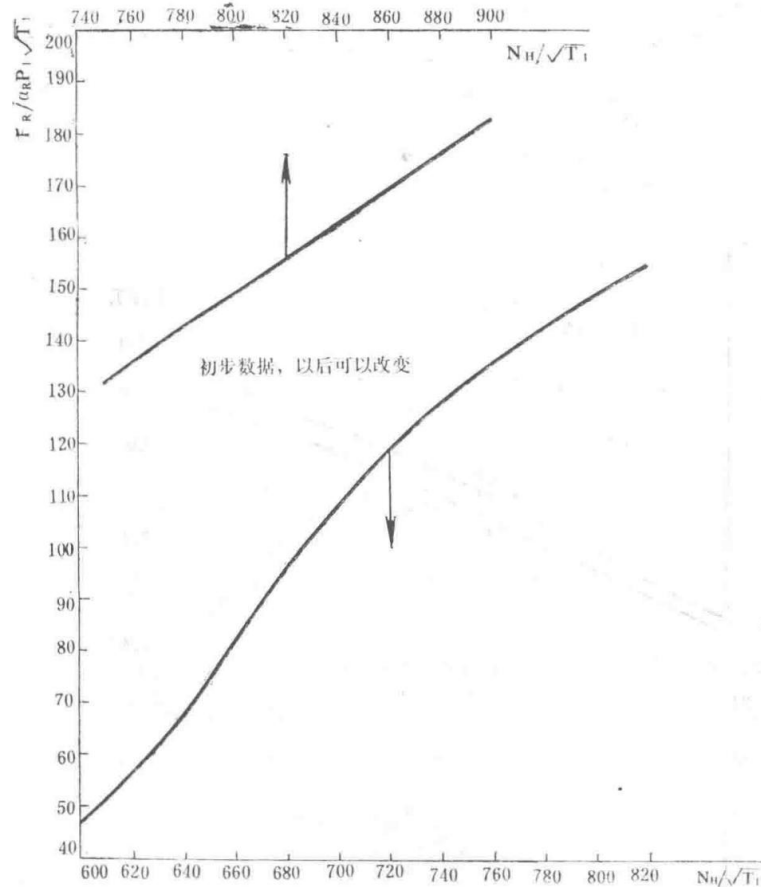


Figure 1 Spey MK202 Dimensionless Afterburner Fuel Flow

Graph showing the dimensionless afterburner fuel flow for the Spey MK202 engine.

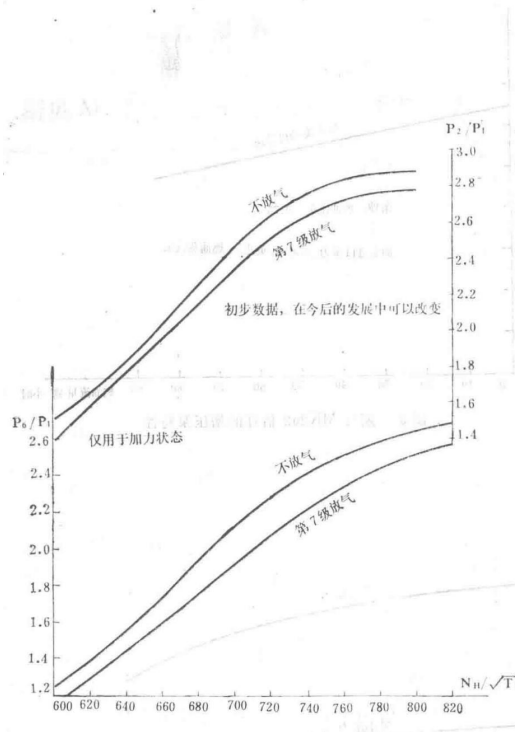


Figure 4 Spey MK202 Dimensionless Low-Pressure Compressor Outlet and Low-Pressure Turbine Outlet Total Pressure

Graph showing the dimensionless total pressure at the outlet of the low-pressure compressor and low-pressure turbine of the Spey MK202 engine.

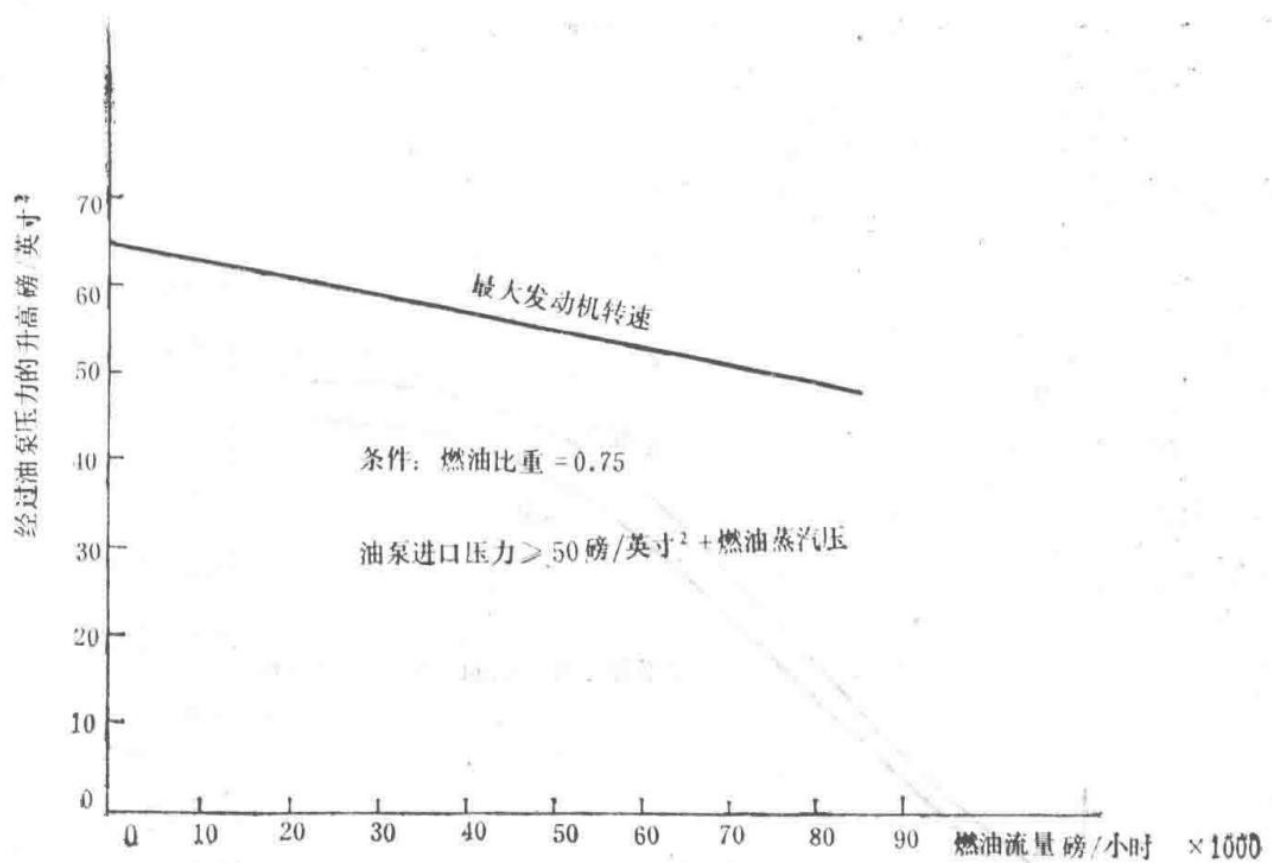


Figure 5 Estimated Boost Pump Characteristics of the Spey MK202

Graph showing the estimated performance characteristics of the boost pump for the Spey MK202 engine.

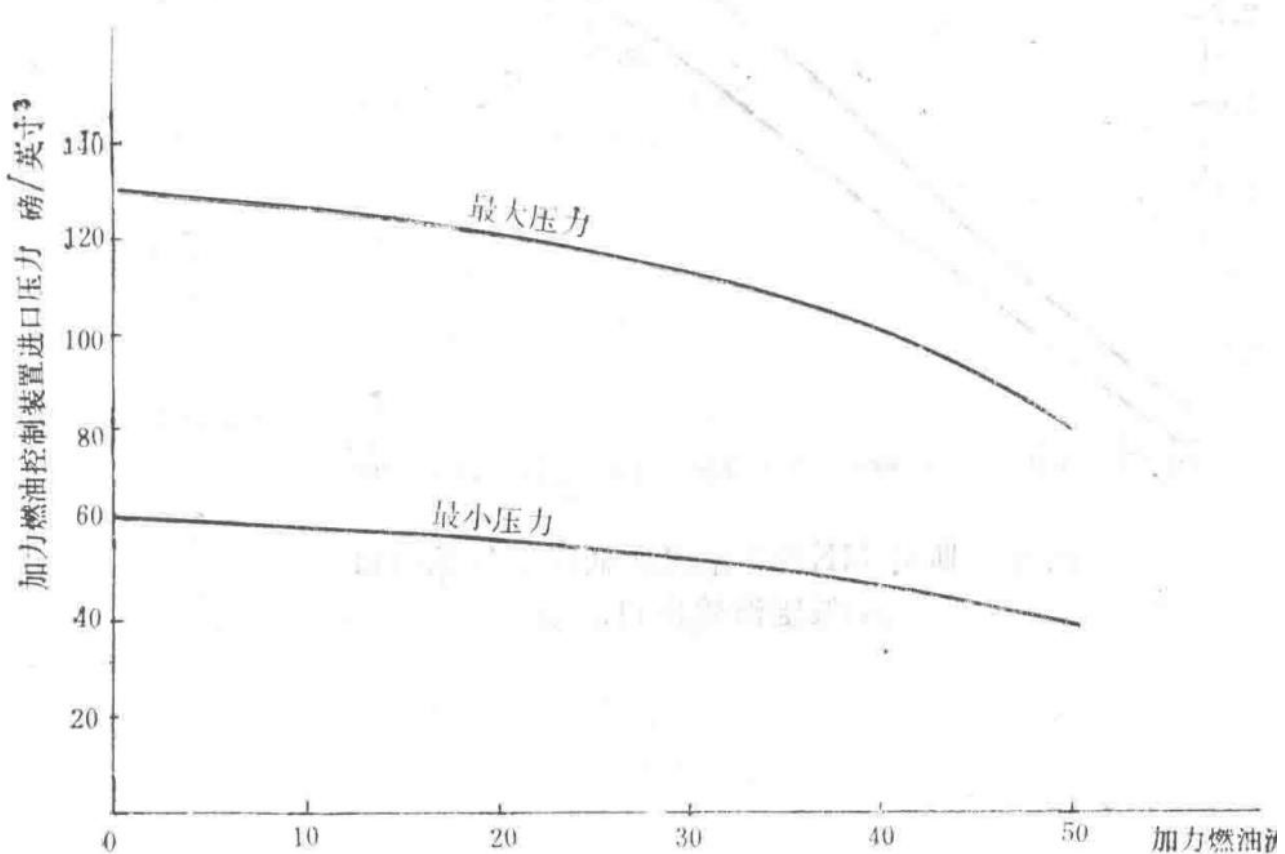


Figure 6 Inlet Pressure and Flow Characteristics of the Spey MK202 Afterburner Fuel Control Unit

Graph depicting the inlet pressure and flow characteristics of the afterburner fuel control unit for the Spey MK202 engine.

Technical Design Report	TDR7789
Spey MK202 Pressure Ratio Control and Nozzle Control System	

1st Edition, October 18, 1976

## Abstract

This report outlines the selection of the nozzle control system and briefly describes the working principles of the chosen system to illustrate the design features of its components. It details the sensing methods and control functions of the pressure ratio regulator and explains the design approaches adopted.

## Symbols

- $N_H$ : High-pressure rotor speed
- $M$ : Air mass flow rate
- $T$ : Absolute temperature
- $A$ : Orifice area
- $P_0$ : Ambient pressure
- $P_1$ : Inlet pressure
- $P_2$ : Low-pressure compressor outlet pressure
- $P_3$ : High-pressure compressor outlet pressure

- P6: Low-pressure turbine outlet pressure

Units: RPM, lb/sec, °K, in<sup>2</sup>, psi

## Introduction

The afterburner fuel combustion increases the back pressure on the low-pressure compressor and turbine, potentially causing abnormal engine operation. To address this, a nozzle control system is incorporated to restore the nozzle pressure to its value without afterburning, ensuring the core engine operates normally. This allows the core engine to remain independent of the afterburner in use, requiring no adjustments during afterburner operation. Given the need to regulate the exhaust area of the nozzle, this report details the current nozzle control system. It introduces the system design criteria, provides fundamental knowledge on system selection, includes design data demonstrating how system requirements are met, and describes the working principles of the entire system.

## Selection of Nozzle Control System

To understand the selection of existing nozzle control systems, it is beneficial to first consider a simpler system for an engine with a lower compression ratio and no bypass (such as an engine without an external bypass system). The afterburning system of such an engine rarely encounters issues even at maximum afterburning conditions due to relatively low combustion temperatures. Since fuel combustion is well below the stoichiometric point under all flight conditions, the relationship between afterburning temperature changes and the percentage change in afterburner fuel flow is essentially linear. Therefore, a choice can be made between a system with scheduled fuel regulation in open-loop and sensed nozzle regulation in closed-loop, or another system with open-loop nozzle regulation and closed-loop fuel system regulation. Theoretically, the latter system is preferred based on response speed. When the fuel system is closed-loop, it is easier to avoid large transient errors between afterburner fuel flow and nozzle area. Typically, the response speed of the afterburner fuel system can be designed to be faster, allowing the fuel system to keep up with nozzle system adjustments.

On the other hand, for systems requiring high afterburning ratios, fuel combustion tends toward the stoichiometric point. Under these conditions, if a closed-loop fuel system is chosen, it can be observed that similar levels of afterburning ratios can be achieved with fuel-air ratios just before or after the stoichiometric point. If the fuel-air ratio is applied after the stoichiometric point, the closed-loop fuel system will attempt to increase fuel flow to correct the nozzle pressure. However, once past the stoichiometric point, additional fuel will only push the combustion point further away from stoichiometry, resulting in a cooling jet that reduces nozzle pressure. The control system will then send more fuel to the nozzles, leading to an unstable system that drifts until a rich blowout occurs.

Thus, the choice between fuel regulation and nozzle sensing control becomes quite deliberative. Since the afterburning region of a straight-flow engine is between two choked nozzles, the afterburner fuel schedule can be established based on a single parameter (such as compressor outlet pressure) to achieve a constant fuel-air ratio. Other secondary factors (such as combustion efficiency) also need to be considered to obtain the final afterburner fuel schedule.

For high afterburning ratio engines, the selection of the afterburner control system leans more toward a scheduled fuel system and a signal-sensing nozzle. In fact, studying the operation of other alternative systems reveals why the aforementioned system must be chosen. For high afterburning ratio bypass engines, fuel combustion needs to be near the stoichiometric point, but the challenge is that no single parameter can determine the air mass flow rate. This is because changes in the bypass ratio or  $T_1$  cause variations in the air mass flow rate in the bypass duct without affecting the core engine's dimensionless mass flow rate. Based on this reasoning, as the bypass ratio deviates from the design state, the scheduled nozzle position requires fuel to flow through a sensing system that could suddenly lose control. If a system is designed to account for the bypass ratio in scheduling the nozzle, the system becomes complex and may produce interactions leading to instability. Therefore, a system must be designed that schedules fuel while considering bypass ratio changes and maintains combustion near the stoichiometric point. Additionally, a signal-sensing nozzle system is used to maintain nozzle

pressure at a level that prevents surge.

In pure jet engines, the primary purpose of nozzle regulation is to prevent changes in turbine back pressure, thereby maintaining the core engine in its design state. In bypass engines, when the bypass flow operates at relatively low-pressure ratios, nozzle regulation becomes more critical because the engine's afterburning region no longer operates between critical nozzles. Small changes in nozzle pressure can affect bypass flow efficiency, and even minor errors can cause the bypass flow to stop or even reverse, leading to surge. The nozzle control system must be designed such that the nozzle response time is sufficiently fast to track the fastest commands from the fuel system and quickly respond to nozzle pressure errors to avoid surge.

Having decided to use a signal-sensing nozzle control system, the method of actuation must be chosen. Factors influencing this choice are briefly discussed below. As mentioned, transient errors in nozzle pressure and nozzle position should be minimized to prevent surge. To achieve this, the actuation speed for opening and closing the nozzle needs to be as fast as possible. To reduce the system's size and weight, the actuation components must be compact.

Considering these factors, four options are available: mechanical screw actuators, and hydraulic actuators using air, fuel, or oil as the medium. Among these, screw actuators and air actuators may not be adopted due to high costs, inconvenience, and slow operation. Between the remaining two, fuel actuators have the advantage of utilizing an existing high-pressure system, while oil actuators require a separate oil tank and boost system. However, fuel actuators also have disadvantages; during large flow, short-duration transients, they can cause a series of interactions with the fuel system due to fuel flow changes. Using a fuel actuation system also increases fire hazards to some extent. Under flight conditions, the system pressure is the fuel pressure, and at high altitudes, the reduction in fuel pressure can severely affect response speed. Considering these factors, the best system is a separate closed system using oil as the working medium. The system components include a nozzle boost oil tank, main oil pump and return pump, nozzle oil heat exchanger, selector valve, and six hydraulic actuators. The sensing signal is provided by the pressure ratio regulator. Among the two pumps, the low-pressure pump is a gear pump, and the high-pressure pump (main nozzle oil pump) is a positive displacement piston pump. The nozzle oil pump size must ensure sufficient oil delivery to the actuators for rapid nozzle movement, while the oil tank should store enough oil for operation and to compensate for any potential leaks. The nozzle oil tank is pressurized to maintain proper inlet pressure for the low-pressure pump, with compressor seventh-stage bleed air used for pressurization. The size of the restrictor for this purpose is detailed in TDR4159.

## Operation of the Nozzle System

For the purposes of this section, the pressure ratio regulator is treated as a device interacting with the nozzle system without detailed explanation. This allows the technical requirements of the nozzle system for the pressure ratio regulator to be defined. The next section will describe how the pressure ratio regulator meets these requirements and its other functions.

During non-afterburning operation, when the engine speed is above 80% N<sub>2</sub>, the nozzle area is required to maintain a reasonably fixed area. To make the engine easier to control at low speeds, a larger readjusted base nozzle area is needed below 80% N<sub>2</sub>. The design characteristics of the nozzle itself (see TDR782) cause the pressure within the nozzle to tend to open it, so the nozzle control system must counteract this movement. To achieve this, the pressure ratio regulator fixes the nozzle oil pump at a 4 rac1,2<sup>nd</sup> stroke position. If left unchecked, the high-pressure oil pressure would increase until it exceeds the relief valve pressure, causing the nozzle to tightly rest against the nozzle actuator stop. Since this results in undesired high nozzle oil pressure, excess heat is generated in the nozzle oil pump, necessitating a selector valve. The mechanical linkage of the selector valve is triggered by the adjustable stop on the nozzle actuator ring housing. When the nozzle closes further, the selector valve's spool moves, diverting high-pressure oil to the low-pressure oil, eliminating high pressure in the actuator. This closes the nozzle to a specified area. A reset valve connected to the mechanical linkage is spring-loaded to maintain its position below 80% N<sub>2</sub>, with pistons on both sides sensing low-pressure fuel. This facilitates the lever that contacts the adjustable stop, causing the selector valve to operate earlier and maintain a larger nozzle area. When passing the 80% N<sub>2</sub> speed limit, the 80% speed switch of the afterburner

system schedules a servo oil flow into one side of the reset valve piston, counteracting the spring force. The opposing movement returns the lever, allowing the nozzle to close beyond the area corresponding to 80% N $\square$  before the selector valve acts again.

The effect of a larger nozzle area below 80% N $\square$  is to lower the low-pressure operating line. At minimum nozzle area, the nozzle flap angle itself is steeper, which is beneficial. Although the flap length is short, it results in a larger area change between the maximum and minimum nozzle areas. Consequently, the flow coefficient at minimum nozzle area and low nozzle pressure ratio is very low. A low flow coefficient tends to increase the back pressure of the low-pressure system, creating a situation similar to that previously described. As nozzle pressure increases, low-pressure surge may occur. This surge is most likely when operating the engine in regions with low flow coefficients. Increasing the nozzle area reduces nozzle pressure, improves the flow coefficient, and moves the low-pressure operating line away from the surge line, making the engine easier to control.

Additionally, lowering the low-pressure operating line is effective when engaging afterburning. During afterburner ignition, a pressure surge occurs within the nozzle, and the operating line must be lowered beforehand. This lowering is achieved by the afterburner reset valve and the nozzle selector valve with mechanical linkage. When afterburning is engaged, a high-pressure fuel servo signal triggered by the pilot's throttle lever is sent to the spring-loaded side of the reset valve chamber. This balances the high-pressure fuel on both sides of the reset valve. Under spring force, the reset piston moves to a pre-open position. This movement is transmitted through the mechanical linkage, and since the selector valve lever is tightly against the nozzle stop position when controlling the nozzle, the reset valve's movement is directly transmitted to the selector valve. The selector valve's movement opens the high-pressure oil return port, allowing the nozzle to open under nozzle load. When the lever quickly contacts the nozzle stop position, it stops moving. During the entire afterburning period, the reset valve and selector valve remain in this position. At this point, the selector valve stops releasing oil, and nozzle regulation is taken over by the pressure ratio regulator. When disengaging afterburning, the servo signal from the pilot's throttle selection lever to the reset valve is canceled, causing the reset valve to return to its position above 80% N $\square$  (afterburning requires the pilot's throttle lever selection valve and the 80% N $\square$  synchronization valve to engage the signal).

When afterburning is ignited, the nozzle control system is required to operate as a closed-loop signal-sensing system. This requires the interlock within the pressure ratio regulator to be canceled, and the pressure ratio regulator to control the swashplate angle of the nozzle oil pump. When afterburning is ignited, a larger nozzle area is required, so the nozzle stop disengages from the selector valve lever, rendering the selector valve inoperative and no longer controlling the nozzle position until afterburning is disengaged.

If leakage is ignored, the actuator system and nozzle oil pump can be considered as an integrator. Therefore, under stable afterburning conditions, the pump's swashplate angle should be at zero degrees, just maintaining the existing pressure in the actuator. When the signal-sensing system requires a change in nozzle position, the swashplate angle becomes positive or negative (closing or opening the nozzle). While the nozzle is moving as required, the pressure within the nozzle also changes, as does the signal from the sensing device. Ideally, the swashplate returns to the zero-degree position, and the nozzle just reaches the required position. Although there is some uncertainty in nozzle position due to leakage flow in the actuator, this is the principle in theory. In practice, a leakage path is designed into each of the six actuators. The idea is that the actuators are located in the high-temperature region of the engine, especially during afterburning, and leakage acts as a cooling flow. As such, the pump should always be operating to maintain pressure balance between the actuators and nozzle load. For this purpose, the swashplate is often at a small positive angle in steady-state conditions. Based on this action, the technical requirement for the pressure ratio regulator is that the input signal to the pump should have a zero position to adjust the oil pump when the system is unbalanced, ensuring system stability (i.e., the swashplate angle is just enough to compensate for leakage).

The technical requirement of the nozzle system for the pressure ratio regulator is that during non-afterburning operation, the pressure ratio regulator should be interlocked in the middle position to achieve a 4 rac1,2 $\wedge$  swashplate angle, keeping the selector valve in the nozzle position. During afterburning operation, the pressure ratio regulator should provide a signal input to the pump to correct nozzle position errors. Since the oil pump acts as an integrator, the signal from the pressure ratio regulator needs to be in the form of an error signal.

## Pressure Ratio Regulator

As mentioned above, the pressure ratio regulator is a signal-sensing device that provides the required signals for the nozzle system. The pressure ratio regulator also sends a signal to the  $P_3 / P_2$  control air signal generator to determine the afterburner fuel flow. As described in TDR7788, the  $P_3 / P_2$  control air signal generator ensures the  $P_3 / P_2$  signal compensates for the effects of the bypass ratio. Since it is an adjustable pressure divider system, its pressure division characteristics can be fully realized by the needle valve shaping within the generator. The pressure ratio regulator is required to provide a linear variation of  $P_3 / P_2$  with position to facilitate needle valve shaping in the generator. To reduce friction in the pressure ratio regulator, the common practice is to use a directly acting, rotating spool valve. A piston with equal areas on both sides balances  $P_2$  on one side with a divided  $P_3$  pressure on the other. The  $P_3$  divided pressure is obtained by releasing  $P_3$  pressure through a fixed orifice and a variable orifice to  $P_0$ . The variable orifice is regulated by a needle valve attached to the piston, which moves until the  $P_3$  divided pressure equals  $P_2$ . Since both  $P_3 / P_2$  and  $P_2 / P_0$  are supercritical, the  $P_3 / P_2$  orifice diameter is constant, and the following equation holds for airflow through the orifice:

$$M \sqrt{T} A P = \text{constant}$$

Equation representing the relationship of airflow through an orifice under supercritical conditions.

— Section 78 —  
Content from Original Document (Pages 386-390)

$$M_1 T_1, A_1 P_3 = M_2 T_2, A_2 P_2,$$

Mass flow rate equation for fixed and variable orifices in the Spey MK202 engine control system.

In this equation, subscript 1 represents the fixed orifice for the pressure ratio  $P_3 / P_2$ , and subscript 2 represents the variable orifice for the pressure ratio  $P_2 / P_0$ .

When there is no cavitation or air source within the system,  $M_1 = M_2$ , and the flow is considered adiabatic, thus  $T_1 \equiv T_2$ . Under these conditions, the equation simplifies to:

$$1, A_1 P_3 = 1, A_2 P_2,$$

Simplified mass flow rate equation under adiabatic conditions with no cavitation.

$$P_3, P_2 = A_2, A_1,$$

Derived relationship between pressure ratio and orifice areas.

$$A_2 = A_1 P_3, P_2,$$

Expression for the variable orifice area in terms of the fixed orifice area and pressure ratio.

In simple terms, the area of the variable orifice equals the area of the fixed orifice multiplied by the high-pressure compressor pressure ratio ( $P_3 / P_2$ ). If the outer orifice area of the variable orifice remains constant and the needle valve moves axially, the annular area of the variable orifice changes linearly with the axial displacement of the needle valve through an appropriately designed needle valve profile. This is implemented in practice.

The nominal stroke of the needle valve is selected, along with the size of the outer orifice used. Thus, the stroke has a linear relationship with the variable orifice area, providing a calibration effect. The area occupied by the needle valve can be calculated using the formula: Needle valve area = Total orifice area - Required orifice area.

From this, the needle valve diameter at a given stroke can be determined, thereby defining the precise needle valve profile.

The piston or needle valve stroke signal is transmitted via a linkage mechanism, which is essentially linear, to an air signal generator controlling  $P_3 / P_2$ . This device receives the signal and provides the required signal for the afterburner system. The precise pressure division characteristics obtained from the needle valve profile are provided by the manufacturer. The  $P_3 / P_2$  signal is also used in the exhaust nozzle control system, explained as follows:

Another function of the pressure ratio regulator mentioned earlier is to adjust the exhaust nozzle area during afterburner operation. As previously stated, since the exhaust nozzle oil pump acts as an integrator in the system, an error signal is required. A reference signal  $P_8$  is generated and compared with the actual nozzle pressure  $P_6$ . Additionally, direct-acting pressure is used to balance the reference pressure  $P_8$  and actual pressure  $P_8$  on both sides of the rotating piston. As mentioned earlier, the rotating piston prevents static friction and hysteresis effects that would occur with a stationary piston. Similar to the  $P_3 / P_2$  piston, this piston positions the needle valve within the orifice connected to  $P_0$ . In steady-state conditions, the upstream pressure of this orifice is  $P_8$ , and the needle valve is required to be in a set position—a null position—otherwise, the nozzle oil pump will move the exhaust nozzle until the null position is reached. To achieve this,  $P_3$  air flows through another variable orifice into this piston. Since the  $P_3 / P_6$  needle valve requires a fixed setting in steady-state, the orifice area remains constant, and thus fixed in steady-state conditions. Using subscripts 3 and 4 to represent the orifices between  $P_8$  and  $P_8'$ , and between  $P_8$  and  $P_0$  respectively, the choked flow mass flow rate equation for the orifice is:

$$\Delta M_3 \sqrt{(T_3)}, \Delta A_3 P_3 = \Delta M_4 \sqrt{(T_4)}, \Delta A_4 P_6,$$

Mass flow rate equation for choked flow conditions in the orifice between  $P_8$  and  $P_8'$ , and  $P_8$  and  $P_0$ .

However, the mass flow rate of air is continuous, and the flow is considered adiabatic, thus:

$$1, A_3 P_3 = 1, A_4 P_6,$$

Simplified mass flow rate equation under adiabatic and continuous flow conditions.

$$1, A_3 = P_3, A_4 P_6,$$

Further simplification of the mass flow rate equation.

Thus, in steady-state conditions, since  $A_4$  is constant, the area  $A_3$  is determined by the above equation. If the  $P_3 / P$  signal relationship is already established, the needle valve system can be designed similarly to the  $P_3 / P_2$  needle valve to provide this relationship. Given the  $P_3 / P_2$  generator, there is a one-to-one relationship between  $P_3 / P_2$  and  $P_3 / P_6$ . Therefore, the  $P_3 / P_2$  output can be used to move the trim needle valve, adjusting the  $P_8$  flow to the piston, incorporating the  $P_3 / P_2$  and  $P_3 / P_8$  relationships into the  $P_3$  trim needle valve profile. In practice, two trim needle valves are used, each for different flight conditions. When boundary layer control is applied, the engine's operating line changes, altering the relationship between  $P_3 / P_2$  and  $P_3 / P_6$ . Thus, one needle valve is used for normal operation, and another is used when boundary layer control is applied. The selection of the needle valve at any given time is achieved by a boundary layer control sensor that signals the boundary layer control switching valve, as described in TDR7790.

During transient operation, such as when afterburner is engaged from steady flight, the pressure ratio regulator functions as follows: The  $P_3 / P_2$  needle valve establishes the afterburner fuel flow signal and sets the position of the  $P_3$  trim needle valve, depending on whether boundary layer control is used. A defined orifice diameter is obtained at this point. When the reference  $P_6$  does not equal the actual  $P_8$ , the piston moves to change the orifice size, aligning the reference  $P_8$  with the actual  $P_6$ . This movement is transmitted to the exhaust nozzle oil pump, altering the pump stroke and causing the actuator to move. When  $P_8$  recovers, the pressure error on the piston decreases, and the piston moves toward its null position. The speed at which the null position is reached can be adjusted by the  $P_3 / P_6$  needle valve profile attached to the piston. A needle valve with a small taper requires a large displacement to balance the forces on the piston, making it easy for the pump to increase its stroke, providing a large flow rate to the actuator and achieving a rapid response. However, in this case, the system is highly sensitive and tends to be unstable. Conversely, a needle valve with a large taper is very stable but responds slowly to exhaust nozzle movement. This necessitates the calibration of multiple needle valves with different profiles to adjust the system's effective gain. The existing needle valve profile is a compromise between these two requirements (see TDR7782). The control section of the needle valve has a large taper, resulting in slow exhaust nozzle movement and stable regulation. The system's null position is also on this large taper section, providing excellent stability. The rest of the needle valve profile consists of two parts: a cylindrical section in the opening direction to achieve virtually infinite gain, and a small taper section in the closing direction to provide very high gain. Thus, the system responds rapidly to large disturbances.

Next, consider the scenario requiring a large change in exhaust nozzle position. Initially, in steady-state, the needle valve regulates the exhaust nozzle using the null position (i.e., the designed taper section). When the piston pressure ratio changes, the piston moves to balance the acting forces. For small pressure differences, the needle valve still regulates the nozzle within the taper section. However, for large changes in nozzle position considered here, the needle valve moves out of the taper section into a high-gain section. At this point, the pressure difference no longer encounters resistance, and depending on the required direction of nozzle movement, the piston moves the exhaust nozzle oil pump to maximum or minimum stroke, providing rapid nozzle movement. As the nozzle moves, the piston pressure begins to recover, and the piston starts moving in the opposite direction to its control position. This slows down the oil pump's supply rate, but the needle valve remains in its high-gain section, quickly returning to the taper section until piston pressure balance is achieved. The end of the return movement is slow back to the null position. Detailed descriptions of early needle valve profile designs can be found in TDR779. The calculation methods therein serve only as a guide, as some profiles have been modified during the adjustment of response speed and stability factors (see TDR7782).

Another factor to consider is performance under 6g load conditions. The afterburner system and exhaust nozzle control system must operate reliably under various flight conditions. The most extreme scenario is catapult takeoff under afterburner conditions. During catapulting, the engine experiences short-term 6g loads. A balanced piston may move under 6g load, altering the control parameters. Further design work has been done to mitigate these load effects. A typical example is described in TDR7107, which considers engine performance compensation for these accelerations.

During non-afterburning operation, the pressure ratio regulator keeps the exhaust nozzle oil pump operating at a fixed stroke. This is achieved by attaching a clutch to the needle valve position. In non-afterburning mode, the clutch engages, holding the pressure ratio regulator needle valve in the required fixed position. When afterburner is engaged, a servo signal from the low-pressure shutdown switch is sent to the pressure ratio regulator. This signal opposes the pressure load holding the clutch engaged. The servo signal disengages the clutch, activating the pressure ratio regulator. The needle valve is positioned to close the exhaust nozzle, which has been pre-opened by the retracting valve schedule. The pump then moves to full positive stroke, maintaining the retracting valve operation until afterburner ignition and  $P_e$  rise. As  $P_e$  increases, the pressure ratio regulator senses  $P_a$ , causing the exhaust nozzle to open beyond the retracting valve lever's range. At this point, the retracting valve ceases operation, and the pressure ratio regulator takes over exhaust nozzle control.

When afterburner is disengaged, the servo signal does not pass through the low-pressure switch, so the pressure on the clutch mechanism piston re-engages the clutch. This fixes the position of the needle valve in the pressure ratio regulator as before, resuming normal non-afterburning operation.

## Reference Reports

- TDR779 Spey MK202 – Afterburner Nozzle Control System – Determination of Servo Needle Valve Profile and Estimation of Afterburner Response Characteristics
- TDR782 (Appendix to TDR794) Spey MK202 – Afterburner Nozzle Loads
- TDR4159 Spey MK202 – Reduction of No. 7 Stage Air for Exhaust Nozzle Control Oil Tank Pressurization
- TDR7107 Spey MK202 – Engine Performance Compensation During Forward Acceleration
- TDR7782 Spey MK202 – Two and Three Taper Pressure Ratio Regulator Needle Valve Profiles
- TDR7788 Spey MK202 – Afterburner Fuel Control System
- TDR7790 Spey MK202 – Boundary Layer Control Reference Re-adjustment System

Technical Design Report

Technical Design Report	Report Number
Determination of Servo Needle Valve Profile for Spey MK202 Afterburner Nozzle Control System and Estimation of Afterburner Response Characteristics	TDR779

## Abstract

This report estimates and provides the needle valve profile for the servo mechanism of the Spey MK202 afterburner exhaust nozzle system. Transfer functions for small changes in afterburner levels have been derived, and responses to step changes in afterburner levels for several flight conditions have been estimated.

Additionally, the report estimates and presents the tolerances of the exhaust nozzle trim needle valve and the impact of exhaust nozzle oil pump swashplate angle errors on the low-pressure compressor operating line.

## Introduction

To control the engine according to the two operating lines shown in Figure 4 for flight conditions with and without boundary layer control bleed, an exhaust nozzle control system is required. A closed-loop control system

maintains the engine's operation according to the appropriate schedule. The closed-loop control system senses the error in the expected turbine pressure ratio  $P_3 / P_9$ , adjusts the exhaust nozzle area to correct this error until the correct  $P_3 / P_6$  value is achieved.

The  $P_3 / P_2$  piston of the pressure ratio regulator generates a displacement proportional to  $P_3 / P_2$ , and thus to the non-dimensional speed  $N / \sqrt{T_1}$ . The reference required for the exhaust nozzle control schedule is ensured by the trim needle valve and the  $P_3 / P_6$  piston needle valve in series. The trim needle valve is connected via a linkage to the  $P_3 / P_2$  piston, so its position is a function of  $N / \sqrt{T_1}$ . The trim needle valve reduces  $P_3$  pressure to  $P_6$ , maintaining the  $P_3 / P_6$  piston in a balanced position. An error in the  $P_3 / P_8$  pressure ratio produces a displacement of the  $P_3 / P_6$  piston, which moves the exhaust nozzle area to return the  $P_3 / P_6$  piston to its balanced position.

The  $P_3 / P_8$  piston needle valve profile is determined by the gain required by the control system, balancing rapid response and system stability.

## Application Data and Performance

### Performance Data

Basic performance data are shown in Figures 1 to 3.

### Partial Derivatives and Time Constants of Engine Parameters

The partial derivatives and time constants of engine parameters used to estimate the stability and response speed of the entire engine system are listed in the coefficient table on page 384.

### Design Requirements and Constants for the Device

The exhaust nozzle is required to move from the fully closed to the fully open position in 1.2 seconds. To meet this requirement, the actuator piston dimensions are set with a high-pressure total area of 13.77 square inches and a low-pressure total area of 15.26 square inches. At a maximum pressure of 3300 psi, the required exhaust nozzle oil pump capacity is 937 gallons per hour free flow.

Constants for the pressure ratio regulator include:

- Piston area  $A_1 = 2.06$  square inches
- Steady-state volume = 2.34 cubic inches
- Total piston displacement = 0.625 inches

Requirements for the two exhaust nozzle control schedules are shown in Figures 4 and 5.

In estimating the response, seven flight conditions were considered, and the constants for the transfer functions are provided in the coefficient table on page 384:

1. Sea level, Mach 0.745, Hot day, Maximum afterburner
2. 61,087 feet, Mach 2.814, Cold day, Maximum afterburner
3. Sea level, Static, ISA, Maximum afterburner
4. 50,000 feet, Mach 0.528, Cold day, Maximum afterburner
5. 2,000 feet, Mach 0.387, Cold day, Maximum afterburner
6. Sea level, Mach 0.745, Hot day, 15% afterburner
7. Sea level, Mach 1.209, Cold day, 15% afterburner

The flow coefficients for the upstream fixed orifice and downstream variable orifice of the  $P_3 / P_2$  servo mechanism are specified as follows:

- Upstream orifice CD = 0.75
- Downstream orifice CD = 0.90

For the  $P_3 / P_6$  servo mechanism, bench test data are available. When the  $P_3 / P_8$  orifice is at minimum area:

When the  $P_3 / P_8$  orifice is at maximum area:

It is assumed that the two CD values vary linearly between the limit positions.

## Assumptions

- The response of the engine main fuel system and afterburner fuel system is faster than that of the exhaust nozzle system.
- Within the afterburner range, the high-pressure rotor speed does not change with throttle lever movement. This assumption has been confirmed by previous experience with other engines. For example, a 7.5% change in net thrust results in only a 0.024% change in high-pressure rotor speed.
- The inertia and friction forces of the pressure ratio regulator actuator piston are neglected.
- For small changes, the transfer function of the pressure ratio device hydraulic amplifier is taken as 1, and the filling lag and acoustic lag of the  $P_2$ ,  $P_3$ , and  $P_6$  pipes of the pressure ratio device are neglected.
- Pipeline losses from the engine connection to the pressure ratio device are taken from TDR3938. For all flight conditions, the following ratios of pressure ratio device pressure to engine total pressure are used:  $P_2' / P_2 = 1.0$ ;  $P_3' / P_3 = 0.946$ ;  $P_6' / P_6 = 1.024$ .

## Results

The required profiles for the  $P_3 / P_2$  servo mechanism,  $P_3 / P_8$  servo piston, and the two  $P_3 / P_2$  trim needle valves are shown in Figures 1 to 3.

Two  $P_3 / P_6$  needle valve profile values have been studied. The first causes a  $P_3 / P_6$  ratio error resulting in a maximum piston stroke error of  $\pm 0.02$ . Under the seven flight conditions mentioned, the effect of a 10% step change in afterburner level on various parameters is shown by the solid lines in Figures 6, 7, and 8. The second  $P_3 / P_6$  needle valve profile is designed to produce the same  $P_3 / P_6$  error as commonly used in similar pressure ratio devices, with a maximum stroke error of  $\pm 0.32$ . Under the same flight conditions and the same afterburner step change, the effect on various engine parameters is shown by the dash-dot lines in Figures 6, 7, and 8. It can be seen that the second needle valve profile (dash-dot lines) provides a slower response than the first (solid lines) but with no overshoot. Moreover, considering the disturbance level measured with the first needle valve profile's  $P_3 / P_6$  pressure ratio piston, which produces a maximum piston position error of  $\pm 0.02$ , the piston is prone to oscillatory movement. Therefore, the second  $P_3 / P_6$  needle valve profile is recommended, as shown in Figure 2 and estimated for this case.

The impact of  $P_3 / P_6$  trim needle valve profile tolerances on the low-pressure compressor operating line has been studied. Due to the fact that two different operating lines are required in the afterburner region without boundary layer control, the  $P_3 / P_6$  trim needle valve itself has two different bend segments (corresponding to  $P_3 / P_2 = 6.40$  and  $7.245$  in Figure 4). This means the pressure ratio device can be precisely adjusted at a certain point on the needle valve profile, while other points on the profile are only accurate within the needle valve diameter tolerance limits. From a manufacturing perspective, the minimum allowable diameter error is 0.0006. Due to inaccuracies in the needle valve profile, it is preferable to lower the operating line rather than raise it. Therefore, the impact of positive (i.e., manufacturing) tolerances has been estimated. This situation is illustrated in Figure 9, showing the effect on the low-pressure compressor operating line. Below an inlet mass flow function of 170, there is no difference between the correct and incorrect operating lines. Even at the worst point, the impact of the tolerance on the operating line, reflected in the pressure ratio, is only 0.06, which is considered acceptable.

Similarly, the impact of exhaust nozzle oil pump swashplate angle errors on the low-pressure compressor operating line has been studied. The required characteristics of the negative ratio orifice should enable the nozzle oil pump to operate normally under the following conditions: in steady-state operation, using oil at temperatures from  $0^\circ\text{C}$  to  $150^\circ\text{C}$ , with a swashplate accuracy of  $\pm 0.5^\circ$ , and an actuator total load between 1500 lbs and 12075 lbs. Using the characteristics of the pump and negative ratio orifice combination, the actual maximum swashplate error within the specified limits is  $-0.16^\circ$ . However, at maximum exhaust nozzle load (30746 lbs, at 31546 feet, Mach number = 2.146, afterburner not ignited—see TDR782), the swashplate error

reaches  $-0.6^\circ$ . This causes a -0.015-inch stroke error in the P<sub>3</sub> / P<sub>6</sub> piston, which raises the operating line by less than one-third of the movement caused by the needle valve profile tolerance, and is considered acceptable.

## Coefficient Tables

Coefficient Table for Different Flight States

Coefficient	Flight State 1	Flight State 2	Flight State 3	Flight State 4	Flight State 5	Flight State 6	Flight State 7
$K_5$	+41.306	+18.863	+31.731	+5.639	+39.926	+41.230	+47.132
$K_6$	+753.6	+892.2	+970.8	+1633.8	+1510.5	+112.8	+70.06
$K_8$	+88.05	+82.56	+50.91	-24.01	-22.57	+13.17	+15.53
$K_9$	-393.9	-456.1	-398.4	-423.4	-392.9	-59.0	-50.9
$K_{10}$	0	-158.4	-129.6	-568.5	-74.47	0	-55.3
$K_{12}$	+26.98	-50.30	-12.33	-92.00	-12.11	-26.98	-11.93
$K_{13}$	+177.2	+479.8	+198.4	+1122.6	+147.5	+177.2	+134.7
$K_{14}$	+0.0904	-0.0859	+0.046	-0.1404	-0.1404	+0.0904	-0.0466
$K_{15}$	-0.2635	-0.6288	-0.3890	-2.4303	-0.3192	-0.2605	-0.1568
$K_{16}$	+0.00866	+0.02091	+0.02678	+0.20684	+0.02717	+0.01360	+0.00613
$K_{17}$	-0.7845	-0.8133	-2.3321	-2.6196	-2.9044	-1.2950	-0.3404
$K_{19}$	+2.9189	+7.3218	-8.4553	+17.3145	+2.2743	-2.9139	+3.3669
$K_{20}$	+0.0958	-0.2485	+0.5822	-1.4737	-0.1936	+0.1504	-0.1318
$K_{21}$	+8.6747	+9.4696	-50.684	+18.663	+20.692	-14.318	+7.3107
$K_{22}$	+0.00824	+0.00304	+0.00270	+0.00040	+0.00279	+0.00824	+0.01275
$K_{24}$	+0.00058	+0.00067	+0.00087	+0.00073	+0.00066	+0.00058	+0.00046
$K_{25}$	+0.00030	+0.00010	+0.00036	+0.00043	+0.00039	+0.00049	+0.00024
$K_{26}$	+0.02641	-0.00332	-0.03025	-0.00551	-0.04197	-0.04209	-0.03990
$K_{27}$	+0.02391	-0.00481	+0.00674	-0.00038	-0.00262	+0.02391	+0.01695
$K_{29}$	+0.00809	+0.00791	+0.00966	+0.01201	+0.01083	+0.00809	+0.00945
$K_{30}$	+0.00113	+0.00023	+0.00192	+0.00230	+0.00207	+0.00186	+0.00111
$K_{31}$	-0.09902	-0.01120	-0.15888	-0.02905	-0.22119	-0.16917	-0.1015
$K_{32}$	+0.00553	+0.00081	+0.00181	+0.00024	+0.00170	+0.00553	+0.00665
$K_{34}$	+0.00105	+0.00067	+0.00124	+0.00126	+0.00114	+0.00105	+0.00099

Additional Coefficients and Time Constants for Different Flight States

Coefficient	Flight State 1	Flight State 2	Flight State 3	Flight State 4	Flight State 5	Flight State 6	Flight State 7
$K_5$	+0.00050	+0.00020	+0.00054	+0.00061	+0.00055	+0.00088	+0.00075
$K_{36}$	-0.04394	-0.00784	-0.04576	-0.00786	-0.05984	-0.07221	-0.07455
$\lambda$	+0.0184	+0.0175	+0.0188	+0.0215	+0.0194	+0.0184	+0.0212
$T\Delta$	+0.1290	+0.2665	+0.2421	+0.7601	+0.1107	+0.1290	+0.0774

# Appendix

## Transfer Functions of Twin-Spool Engine with Afterburner and Variable Area Nozzle

### 1. Transfer Function of the Main Engine

#### 1) High-Pressure Rotor Speed

$$\Delta N_1 = K_{14}, 1 + T \Delta N_1 + K_{15}, 1 + T \Delta F_1 + K_{16}, 1 + T \Delta F_1 + K_{17}, 1 + T \Delta A_1,$$

Equation for high-pressure rotor speed variation

Where

$$K_{14} = (\partial Q, \partial N_1) \times (\partial N_1, \partial Q)$$

Definition of coefficient  $K_{14}$  (assumed constant for small changes)

And  $T = -\Delta I / (\partial Q / \partial N_1)$ . Similarly, the equation for low-pressure rotor speed can be derived as:

$$2) \Delta N_2 = K_{18}, 1 + T \Delta N_2 + K_{19}, 1 + T \Delta F_2 + K_{20}, 1 + T \Delta F_2 + K_{21}, 1 + T \Delta A_2 + K_{22} \Delta A_2$$

Similarly, for dependent variables such as  $P_2$ , the following can be obtained:

$$\Delta P_2 = K_{22} \Delta N_2 + K_{23} \Delta N_2 + K_{24} \Delta F_2 + K_{25} \Delta F_2 + K_{26} \Delta A_2,$$

Equation for pressure variation at station 2

### 2. Transfer Function of the Afterburning Fuel System

$$\Delta F = K_b \Delta \beta + K_f \Delta N + K_g \Delta P_\beta, 1 + 2, \omega D + 1, \omega^2 D^2 + K \Delta P_\beta + K (1 + \lambda_1 D) \Delta P_\beta, (1 + 2, \omega D + 1, \omega^2 D^2)(1 + \lambda_2 D),$$

Transfer function for afterburning fuel system

### 3. Transfer Function of the Nozzle Control System

$$\Delta A = K_{10} \Delta P_2 + K_{12} \Delta P_3 + K_{13} \Delta P_6, D(1 + \lambda_2 D),$$

Transfer function for nozzle area control system

Under the assumptions given in this report, the equation becomes:

$$K_{14} \Delta N_1 + K_{15} \Delta F_1 + K_{16} \Delta F_1 + K_{17} \Delta A_1 = 0$$

$$\Delta N_2 + T \Delta N_2 - K_{19} \Delta F_2 - K_{20} \Delta F_2 - K_{21} \Delta A_2 = 0$$

$$K_{22} \Delta N_2 - K_{24} \Delta F_2 - K_{25} \Delta F_2 - K_{26} \Delta A_2 = 0$$

$$\Delta P_6 - K_{32} \Delta N_2 - K_{34} \Delta F_2 - K_{35} \Delta F_2 - K_{36} \Delta A_2 = 0$$

$$\Delta F - K_6 \Delta P_2 - K_8 \Delta P_3 - K_9 \Delta P_6 = K_5 \Delta \beta$$

$$D \Delta A + \lambda_2 D^2 \Delta A - K_{10} \Delta P_2 - K_{12} \Delta P_3 - K_{13} \Delta P_6 = 0$$

The coefficients for various engine states and flight conditions, as well as the time constants for the engine and nozzle systems, are provided in the coefficient table on page 384. By solving the system of equations, the overall transfer functions for parameters  $\Delta N$ ,  $\Delta A$ ,  $\Delta F$ ,  $\Delta P_2$ ,  $\Delta P_3$ , and  $\Delta P_e$  with respect to throttle lever angle variation  $\Delta \beta$  are obtained.

The effects of a step change in throttle lever angle on various engine parameters have been determined. Examples of these changes are shown in Figure 6, Figure 7, and Figure 8.

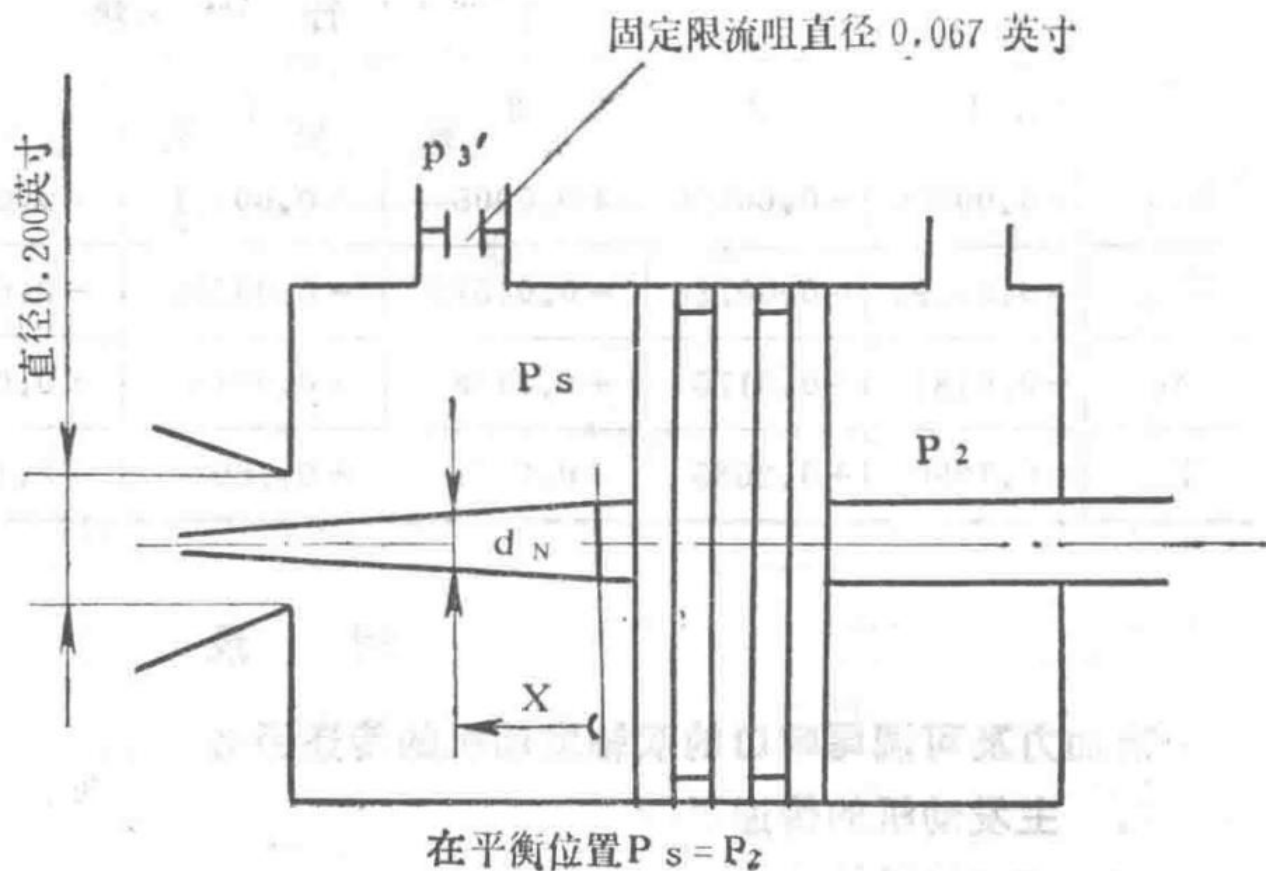


Figure 1 Servo Needle Valve for  $P_3 / P_2$

Diagram of the servo needle valve controlling the pressure ratio  $P_3 / P_2$

Servo Needle Valve Data for  $P_3 / P_2$

$x$ (inches)	$P_3 / P_2$	$P_3' / P_2$	$d$ (inches)
0	3.171	3.000	0.1700
0.05	3.589	3.395	0.1653
0.10	4.006	3.790	0.1609
0.15	4.434	4.195	0.1560
0.20	4.852	4.590	0.1511
0.25	5.280	4.995	0.1460
0.30	5.708	5.400	0.1408
0.35	6.131	5.800	0.1353
0.40	6.559	6.205	0.1298
0.45	6.977	6.600	0.1239
0.50	7.400	7.000	0.1177

0.55	7.822	7.400	0.1111
0.60	8.245	7.800	0.1040
0.625	8.457	8.000	0.1020

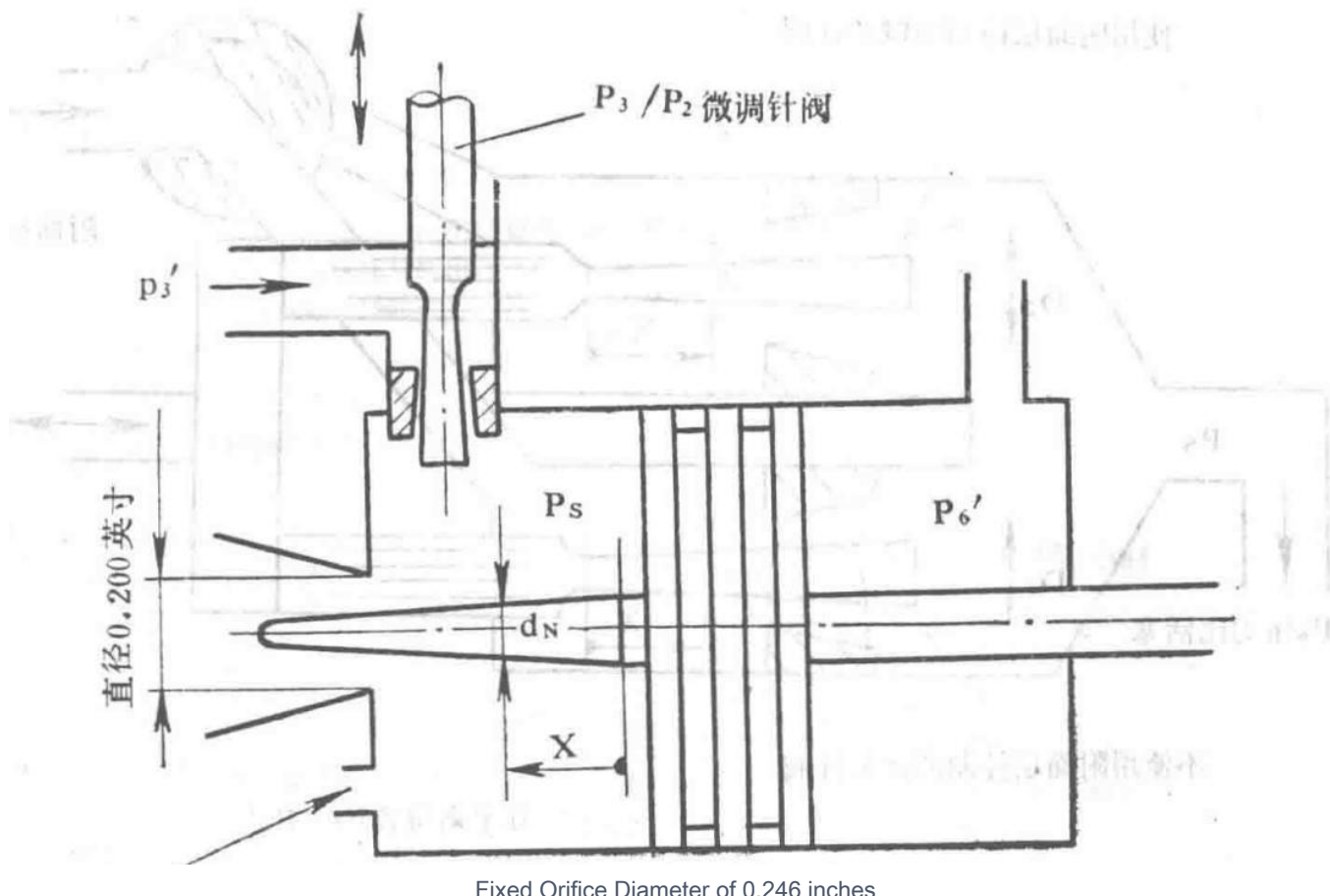


Diagram showing the fixed orifice with a diameter of 0.246 inches at equilibrium position where  $P\square = P$

Figure 2 Servo Needle Valve for  $P_3' / P_6$

Servo Needle Valve Data for  $P_3' / P_6$

x (inches)	$P_3/P_6$	$P_3'/P_6'$	d (inches)
0	6.689	6.188	0.1377
0.05	6.747	6.241	0.1341
0.10	6.805	6.295	0.1304
0.15	6.863	6.349	0.1267
0.20	6.918	6.400	0.1227
0.25	6.976	6.453	0.1183
0.30	7.031	6.504	0.1140
0.35	7.086	6.555	0.1093
0.40	7.141	6.606	0.1046
0.45	7.194	6.655	0.0997
0.50	7.246	6.703	0.0943

0.55	7.301	6.754	0.0885
0.60	7.352	6.801	0.0819
0.625	7.379	6.826	0.0800

\* For the trimming needle valve without boundary layer control, the  $P_3 / P_2$  values given here are valid when  $P_3 / P_2 = 5.750$ .

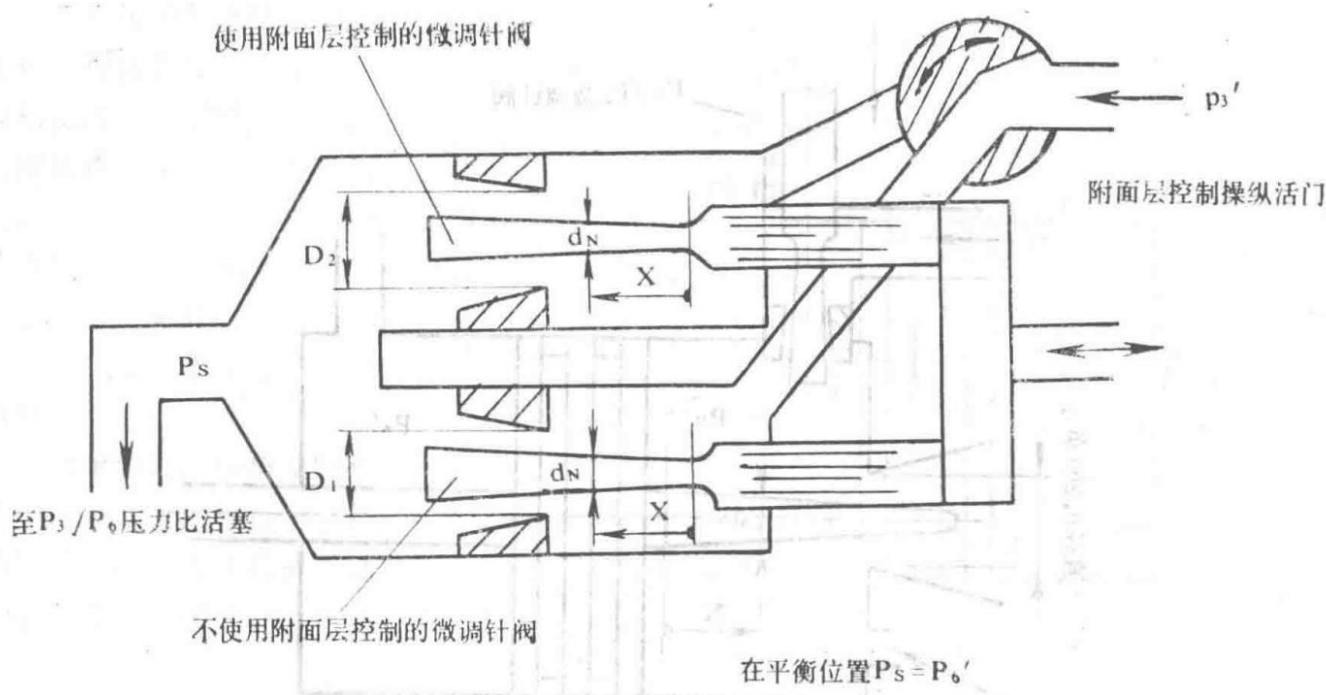


Figure 3 Boundary Layer Control Trimming Needle Valve for  $P_3 / P_2$

Diagram of the trimming needle valve for boundary layer control of  $P_3 / P_2$

#### Trimming Needle Valve without Boundary Layer Control

##### Trimming Needle Valve Data without Boundary Layer Control

x (inches)	$P_3 / P_2$	$P_3'' / P_2$	d (inches)
0	3.171	3.000	0.0800
0.05	3.594	3.400	0.0800
0.10	4.017	3.800	0.0800
0.135	4.329	4.095	0.0800
0.15	4.450	4.210	0.081
0.20	4.873	4.610	0.0841
0.25	5.291	5.005	0.0866
0.30	5.724	5.415	0.0890
0.35	6.163	5.830	0.0910
0.373	6.369	6.025	0.0919
0.425	6.839	6.470	0.0919
0.469	7.241	6.850	0.0919
0.50	7.521	7.115	0.0930

0.528	7.785	7.365	0.0939
0.55	7.997	7.565	0.0945
0.60	8.457	8.000	0.0957

### Trimming Needle Valve with Boundary Layer Control

Trimming Needle Valve Data with Boundary Layer Control

x (inches)	P <sub>3</sub> /P <sub>2</sub>	P <sub>3</sub> "/P <sub>2</sub>	d□ (inches)
0	3.171	3.000	0.0800
0.05	3.594	3.400	0.0905
0.10	4.017	3.800	0.1027
0.15	4.450	4.210	0.1108
0.20	4.873	4.610	0.1168
0.25	5.291	5.005	0.1216
0.30	5.724	5.415	0.1252
0.35	6.163	5.830	0.1279
0.40	6.607	6.250	0.1299
0.45	7.067	6.685	0.1314
0.50	7.521	7.115	0.1325
0.55	7.997	7.565	0.1335
0.60	8.457	8.000	0.1343

Without boundary layer control, orifice diameter D<sub>1</sub> = 0.1380 inches. With boundary layer control, orifice diameter D<sub>2</sub> = 0.1673 inches.

— Section 80 —  
Content from Original Document (Pages 396-400)

$P/P_1$  — Low-pressure compressor outlet total pressure (psia)  $P$  — High-pressure compressor outlet total pressure (psia) 0.30  $P_6'$  — Low-pressure turbine outlet total pressure (psia)

Pressure Ratio Data for Spey MK202 Engine

$P/P_2$
3.6
4.0
4.4
4.8
5.2
5.6
6.0
6.4
6.8
7.2
7.6
8.0
8.4

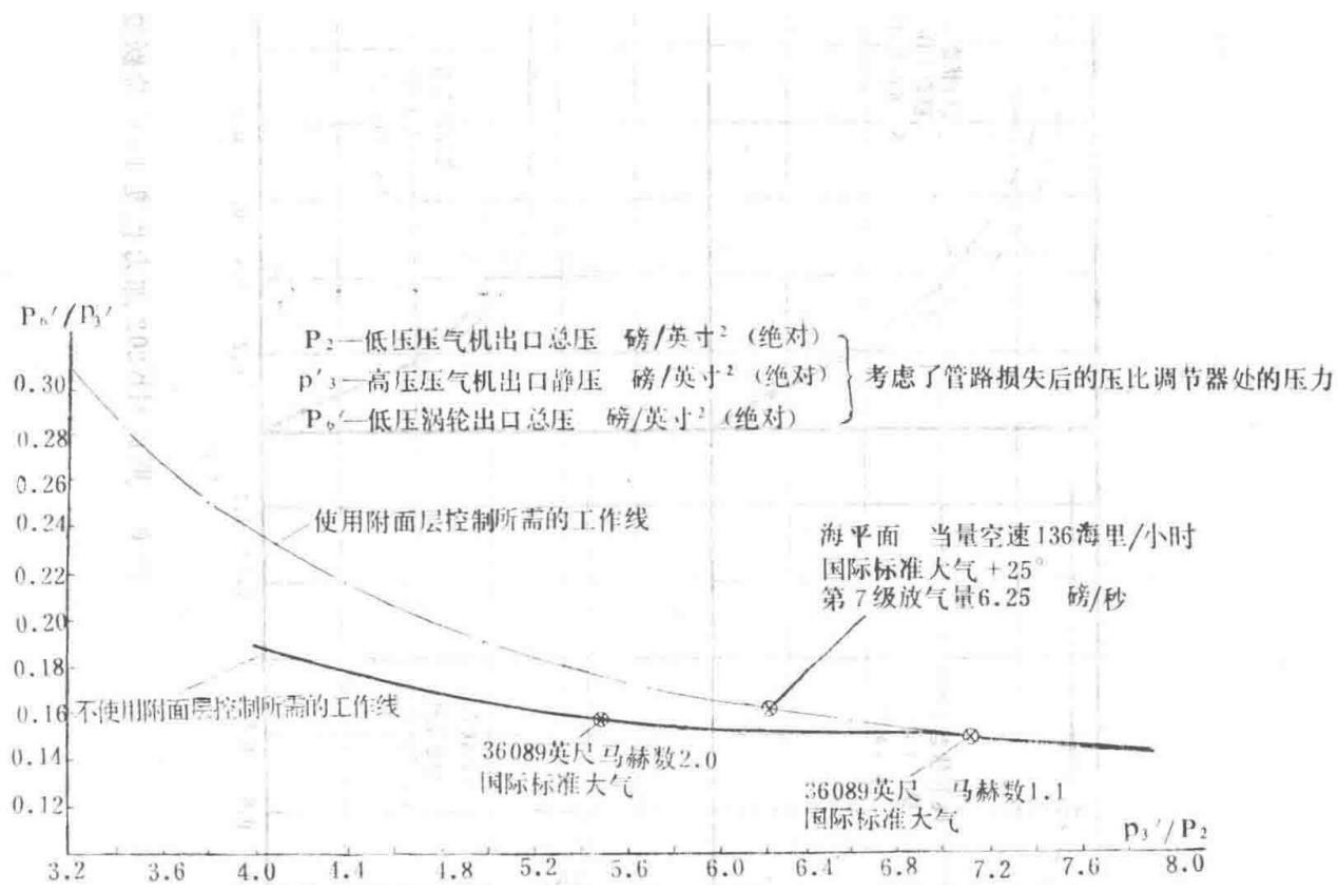


Figure 4: Spey MK202 Operating Lines with and without Boundary Layer Control

Graph showing the required operating lines for the Spey MK202 engine with and without boundary layer control.

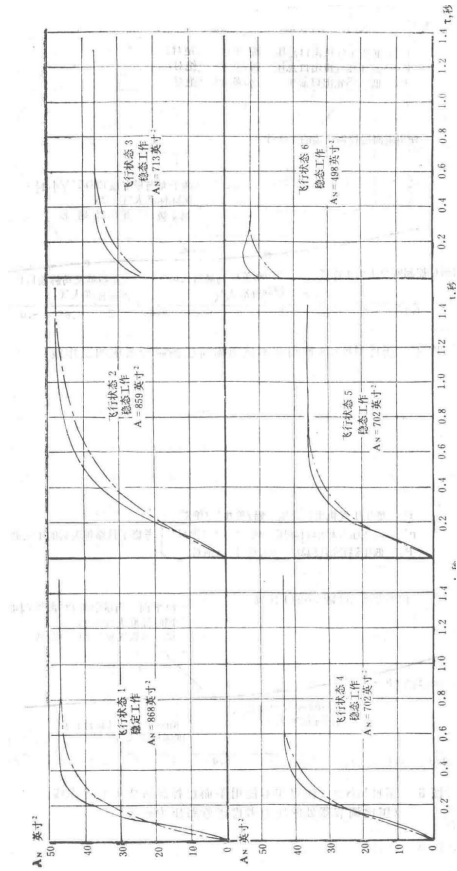


Figure 5: Spey MK202 Operating Lines with and without Boundary Layer Control (Pressure Ratio Regulator Considered Pipe Pressure Loss)

Graph showing the required operating lines for the Spey MK202 engine considering pipe pressure loss at the pressure ratio regulator.

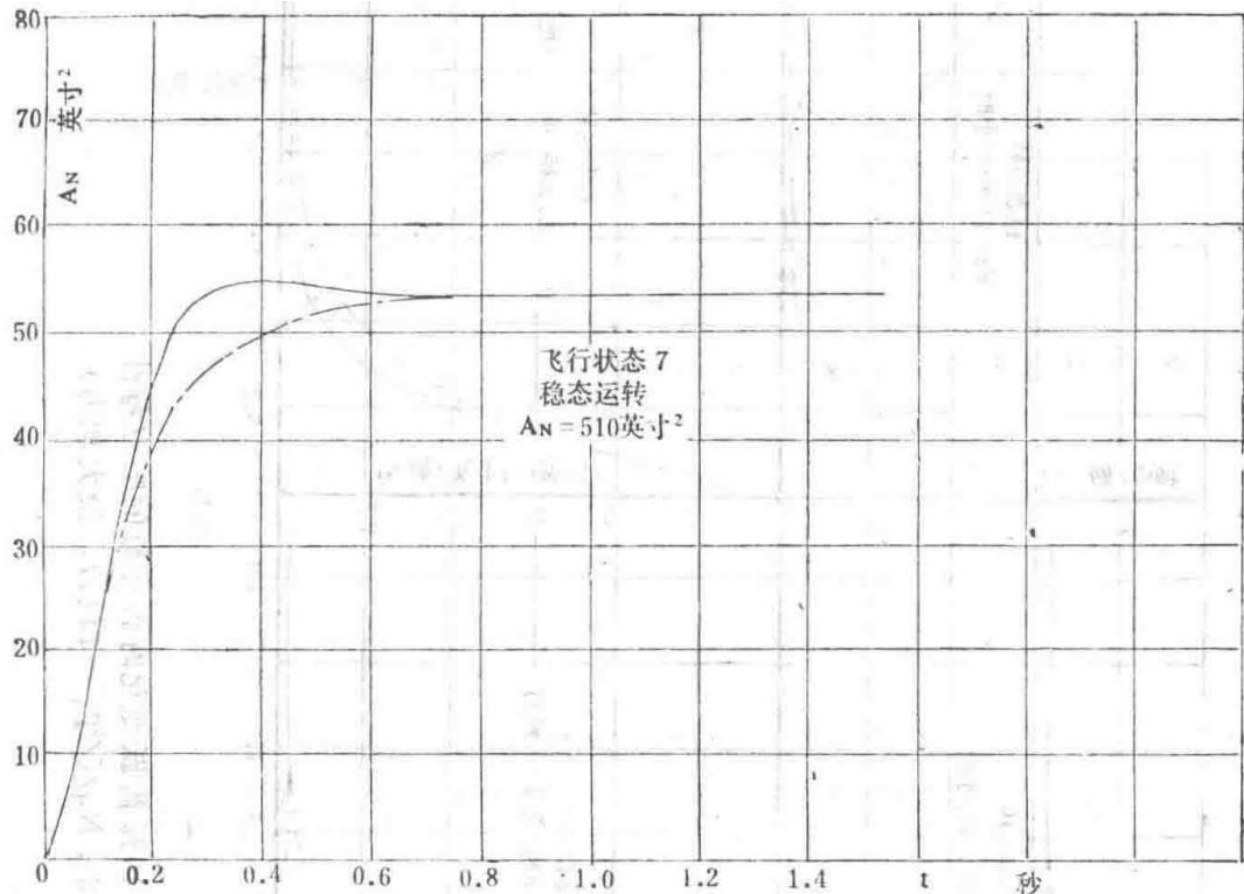
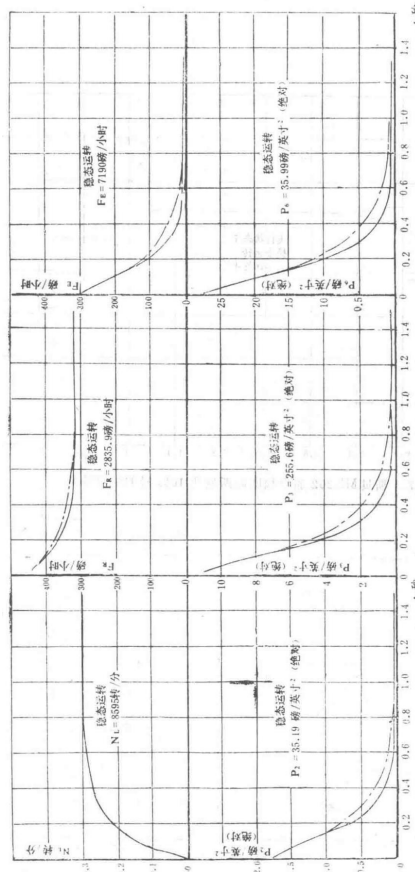


Figure 7: Spey MK202 Response Characteristics for 10% Step Change in Afterburner Level

Graph depicting the response characteristics of the Spey MK202 engine during a 10% step change in afterburner level.



Uncaptioned image, possibly a continuation or related technical diagram.



Uncaptioned image, page number or unrelated diagram.

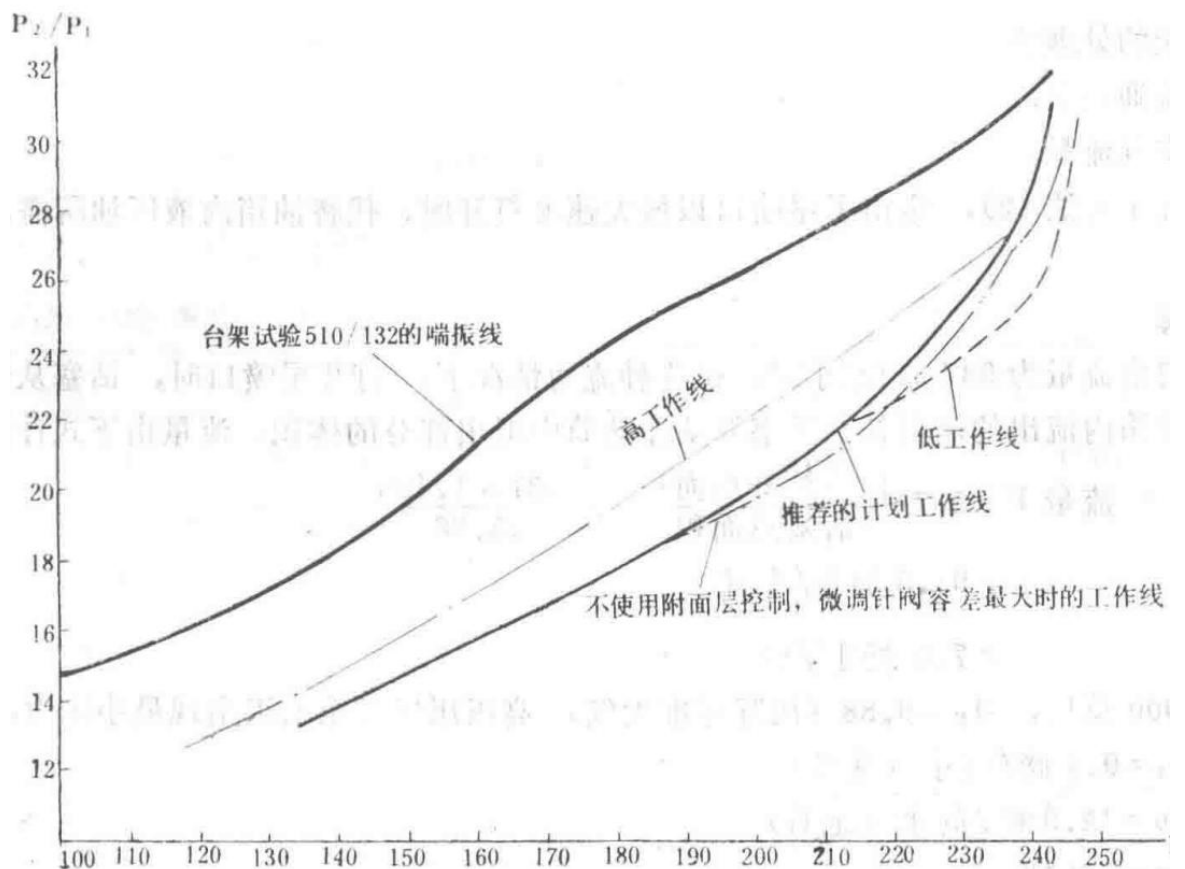


Figure 9: Spey MK202 Low-Pressure Compressor Characteristics (Considering the Influence of Tail Nozzle Adjustment System Micro-Adjustment Valve on Operating Line)

Graph showing the low-pressure compressor characteristics of the Spey MK202 engine, considering the effect of the tail nozzle adjustment system micro-adjustment valve on the operating line.

1965.11.17 First Edition

## Purpose

This report specifies the minimum size of the restrictor orifice installed in the seventh-stage air pipeline for pressurizing the tail nozzle oil tank. The restrictor orifice has a diameter of 0.025 inches and requires filtration.

A restrictor orifice with a diameter of 0.031 inches can provide satisfactory oil tank pressure.

## 1. Introduction

It is appropriate for the pressure inside the tail nozzle hydraulic oil tank to always be approximately 8 psi above ambient pressure. However, the measured oil tank pressure was too high. During high-pressure ratio flight conditions of the engine, the supply pressure after pressure losses through the pressurization valve system and pipeline system was still too high, exceeding the required pressure by 7 psi. Reducing the adjustment of the pressurization valve is not feasible because maintaining only 8 psi at sea level would not meet the required 8 psi at high altitudes.

## Pressure

There are two possible approaches to handling pressure:

1. Increase the flow area;
2. Reduce the airflow rate.

This report investigates method (2), determining the minimum airflow rate required to replace the hydraulic fluid in the oil tank when the tail nozzle is opened at maximum speed.

## 2. Calculation

The maximum free flow rate of the oil pump is 937 gallons per hour. Under this flow condition, when the tail nozzle is opened, the piston retracts from the actuator cylinder, and the flow rate from the oil tank compensates for the volume displaced by the piston rod retracting from the actuator cylinder. The flow rate is calculated using the following equation:

$$P_{7R} P_{hbb} = 1.45$$

Pressure ratio equation for the system.

$$M \sqrt{T} A P_{7X} = 0.373$$

Mass flow rate equation related to temperature and pressure.

At approximately 63,000 feet and Mach number  $M \square = 0.88$  (International Standard Atmosphere), the minimum pressure occurs at the seventh stage of the high-pressure compressor. Under this condition:

- $p_0 = 0.9$  psi (absolute),
- $P_{7R} = 12.9$  psi (absolute),
- $T_{7\text{级}} = 562^\circ\text{K}$ .

The required oil tank pressure should not exceed 8.9 psi (absolute).

Converting the mass flow rate to volumetric flow rate (related to the air density in the tank) yields 7.0 inches per second.

Assuming  $CD = 0.7$ , the diameter of the orifice  $D = 0.025$  inches.

## 3. Estimated Improvements

The current orifice diameter used on the engine is 0.041 inches.

An orifice diameter of 0.031 inches is more suitable than the minimum size of 0.025 inches. The estimated pressure loss margins required for each orifice size are as follows.

Figure 1 in this report shows the pressure loss from the pressurizing valve to the outlet pipe outlet as a function of  $P_7^4, 5$ . This pressure loss is a function of the air mass flow rate because the orifice is in a choked flow condition. For a fixed orifice size, the air mass flow rate is proportional to the pressure  $P_7 / R$ . Conversely, with  $P_7 Z$  constant, the air mass flow rate is proportional to the orifice area. Therefore, for a given  $P_7 = 5\sqrt{2}$  pressure, the effect of calibrating the orifice size can be inferred from Figure 1 by calibrating the  $P_7 = 4\sqrt{2}$  pressure for a fixed orifice size.

The calibrated point on Figure 1 is the maximum  $P_7 = 4\sqrt{2}$ . The maximum  $P_7 * \pi = 182$  psi (absolute), with a corresponding pressure loss of 7.2 psi.

Orifice Size (Diameter, inches)	0.041 (Current)	0.031	0.025 (Minimum)
Air Pressure Loss (psi)	7.2	2.4	1.0
Tank Pressure at Maximum P7 Level with Valve Set per DC9402 and Figure 1 (psi, gauge)	15.0	9.8	7.9

Using two identical orifices in series does not show significant advantages. Two 0.034-inch orifices are equivalent to one 0.031-inch orifice and still require filtering. Two unfiltered 0.041-inch orifices are equivalent to one 0.037-inch orifice, producing an unacceptable tank pressure of 12.6 psi (gauge). To reduce the tank pressure to 2.4 psi (gauge), five 0.041-inch orifices in series are required.

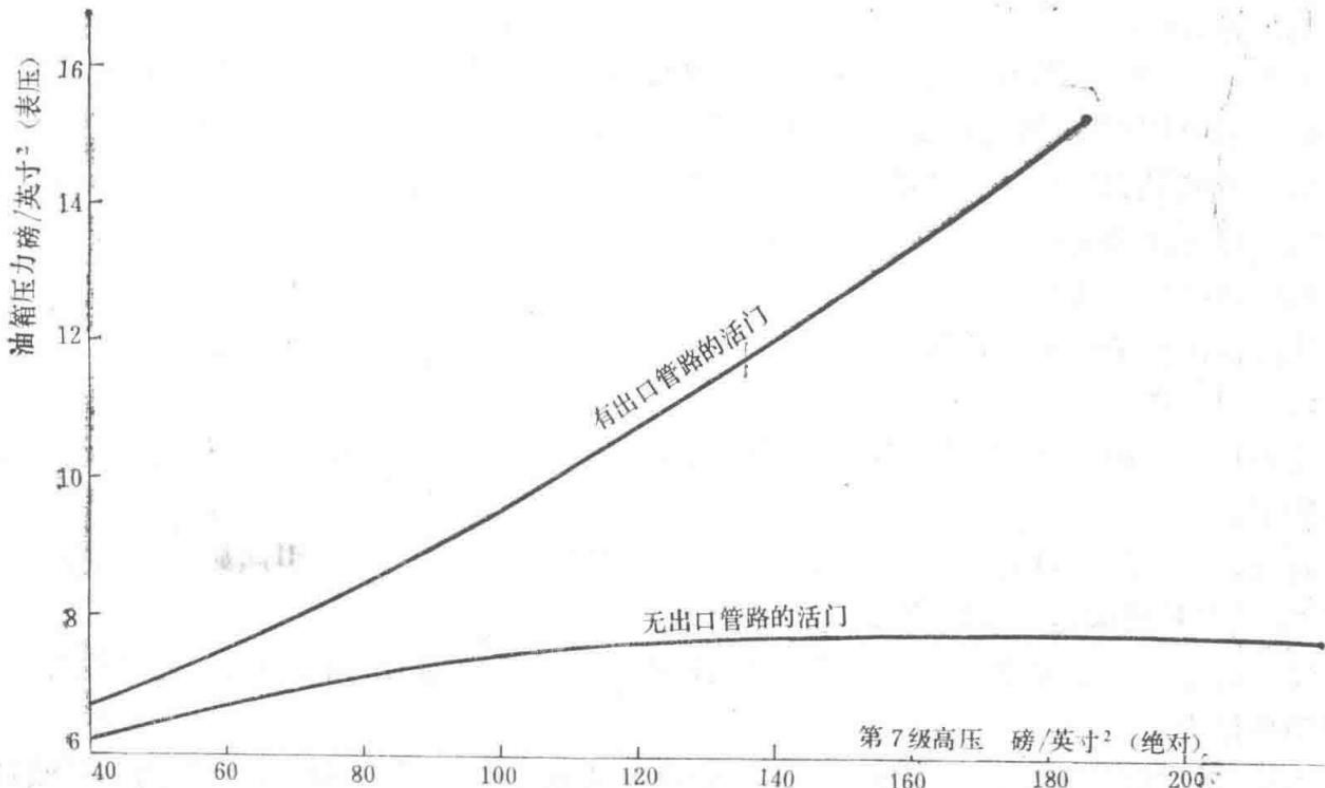


Figure 1: Spey MK202 Tail Nozzle Oil Tank Pressurizing Valve K2 Test Results

Graph showing pressure loss as a function of P7 pressure for the Spey MK202 tail nozzle oil tank pressurizing valve.

#### Technical Design Report Information

Technical Design Report	TDR 7107
Spey MK202 Forward Acceleration Engine Performance Compensation	

## Abstract

This report introduces a method to correct engine thrust loss during catapult takeoff (acceleration of 5g) with the seventh-stage boundary layer control bleed.

The effect of using a prototype  $P_3 / P_2$  air piston with a weight of 0.375 pounds for the  $P_3$  trim needle valve results in a 1.3% thrust loss and a 1.77% increase in tail nozzle effective area. Using a newer model of the  $P_3 / P_2$  piston

with a mass of 0.6 pounds increases thrust by 0.3% and reduces the tail nozzle effective area by 0.58%, raising the engine operating line accordingly.

To achieve the best thrust change, the mass of the  $P_3 / P_2$  air piston should be increased by 48% (i.e., 0.18 pounds), which reduces the tail nozzle area by only 0.132%.

Note: During acceleration outside of 5g, the percentage error in thrust and tail nozzle area can be scaled proportionally.

## 1. Definition of Symbols Used

The definitions of areas  $A_1 \square$ ,  $A_{23}$ ,  $A_3$ ,  $A_4$ , and  $A_5$  are shown in Figure 4. Air pressures  $P \square'$ ,  $P_3'$ ,  $P_5 \Delta$ ,  $P_5'$ , and  $P_6'$  are also defined in the same figure. Pressures  $P_3'$ ,  $P_z'$ , and  $P_6'$  are engine pressures measured on the accessory, corresponding to engine pressures  $P_3$ ,  $P_2$ , and  $P_8$ .

$$P_3' / P_3 = 0.946; P_6' / P_6 = 1.024; P_2' / P_2 = 1.0$$

Pressure ratio conversions between measured and engine pressures.

- $n$  represents aircraft acceleration in g.
- $W$  is the ratio of the new  $P_3 / P_2$  air piston weight to the current piston weight.
- $F \square$  is the afterburner fuel flow rate.
- $A_g$  is the tail nozzle effective area.
- $N \square$  is the high-pressure rotor speed in rpm.

## 2. Introduction

The effect of g loads during catapult takeoff on the engine control system has been practically eliminated through design changes by Lucas.

However, the g load impact on the afterburner fuel control system and tail nozzle pressure ratio piston causes significant thrust errors, specifically a -1.3%  $X \square$  without compensation for 5g.

The engine accessory specification states that during catapult takeoff, acceleration can reach up to 5g, and the afterburner fuel system components should provide accurate engine thrust.

This report calculates the results for an acceleration of 5g. For higher or lower g loads, thrust and tail nozzle area errors can be scaled proportionally.

Previously, the effect of g loads on the afterburner fuel control device's  $P_3 / P_2$  trim needle valve was ignored as a second-order quantity.

In reality, this simplification is inappropriate because, with the original piston weight, a thrust gain of approximately 0.5% is produced under the influence of 5g acceleration.

This issue was studied, and the corrected mass of the  $P_3 / P_2$  air piston assembly was calculated to correct the net thrust loss and operating line.

This raised the question of improving the pressure ratio regulator's trim needle valve profile (with boundary layer control engaged). The reason for modifying the profile is to reduce the possibility of afterburner surge when the 12th-stage boundary layer control bleed is engaged. It was also suggested to use a trim needle valve with a similar profile but moved backward relative to the reference plane, allowing greater axial adjustment. The modified profile necessitates re-evaluating the g load issue described in this report.

## 3. Research

Key calculation results are as follows:

The supplier estimated the effect of g loads on the main pressure differential regulator and fuel control device spool valve, indicating a thrust loss of 0.144% per g.

Based on the needle valve calibration (with boundary layer control engaged) and results from TDR779 Figure 1 ( $P_3 / P_2$  servo needle valve), a graph of  $A_3 / A_2$  versus  $P_3' / P_2'$  was plotted, as shown in Figure 1 of this report.

$A_4 / A_1 = \text{constant}$  (ignoring load drift of the pressure ratio regulator). This constant was calculated using the design operating line pressures for  $A_0 G = 378.5 \text{ inches}^2$ ,  $n = 0$ , and  $W = 1$ . A curve of  $W$  versus  $A_0 G$  was plotted for  $n = 5g$  (Figure 2). Additionally, a curve of  $n = 5g$ ,  $W$  versus  $\% F$  error was plotted (Figure 3). Using appropriate conversion factors, the final graph of total  $\% X$  error versus  $W$  was obtained.

## Results and Conclusions

The final graph indicates that with the current piston mass under g load, although the effects of boundary layer control and  $P_3 / P_2$  trim needle valves increase engine thrust, this increase is insufficient to compensate for the thrust loss due to g load on the  $P_3 / P_2$  piston. Thus, the increased thrust still does not fully compensate for the thrust loss (i.e., at  $W = 1$ , the total  $\% X$  error is negative). Therefore, to enhance the trim needle valve's effect, the mass of the  $P_3 / P_2$  piston must be increased.

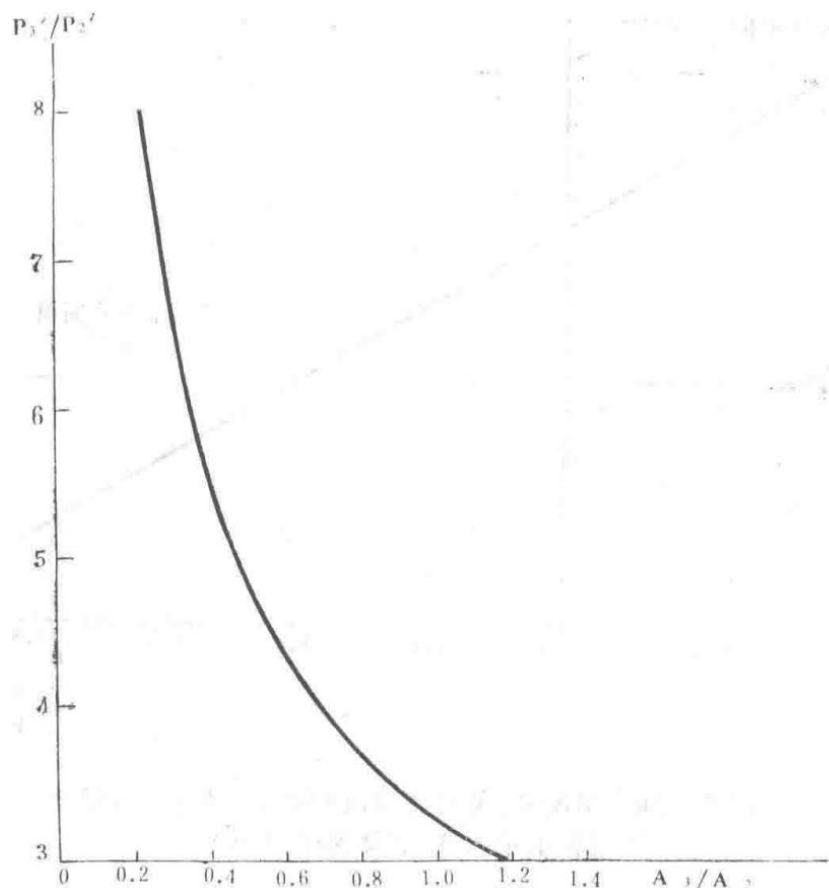


Figure 1: Spey MK202  $P_3' / P_2'$  versus  $A_3 / A_2$  Curve (Orifice Diameter 0.156 inches)

Graph showing the relationship between  $P_3' / P_2'$  and  $A_3 / A_2$  for the Spey MK202 engine.

Using the existing flow metering valve and main pressure differential regulator, the required  $W$  value to precisely restore thrust is 1.48, which reduces the tail nozzle effective area by 1.32%. To maintain the same tail nozzle effective area, the required  $W$  value is 1.45 (this reduces  $X$  by 0.1% but maintains the engine's design operating line).

If a compensated afterburner fuel control device and main pressure differential regulator are used, a lighter weight is needed to achieve zero thrust error, and the operating line is lowered, improving the surge margin (tail nozzle effective area increases by approximately 0.9%).

The advantage of this method is that afterburner acceleration is safer under g loads, and at high altitudes (where g forces are smaller), it is less likely to occur and unlikely to result in operating line errors. Since production devices lack balanced spool valves and main pressure differential controllers, the uncompensated operating line is still considered here.

Therefore, it is recommended that  $W = 1.48$  (maximum value) to correct the  $X\Box$  error, resulting in only a very small reduction in surge margin while increasing the tail nozzle effective area by 0.132%.

This includes increasing the  $P_3 / P_2$  piston mass to 0.555 pounds (total weight), meaning the balance weight mass should be reduced from 0.218 to 0.173 pounds.

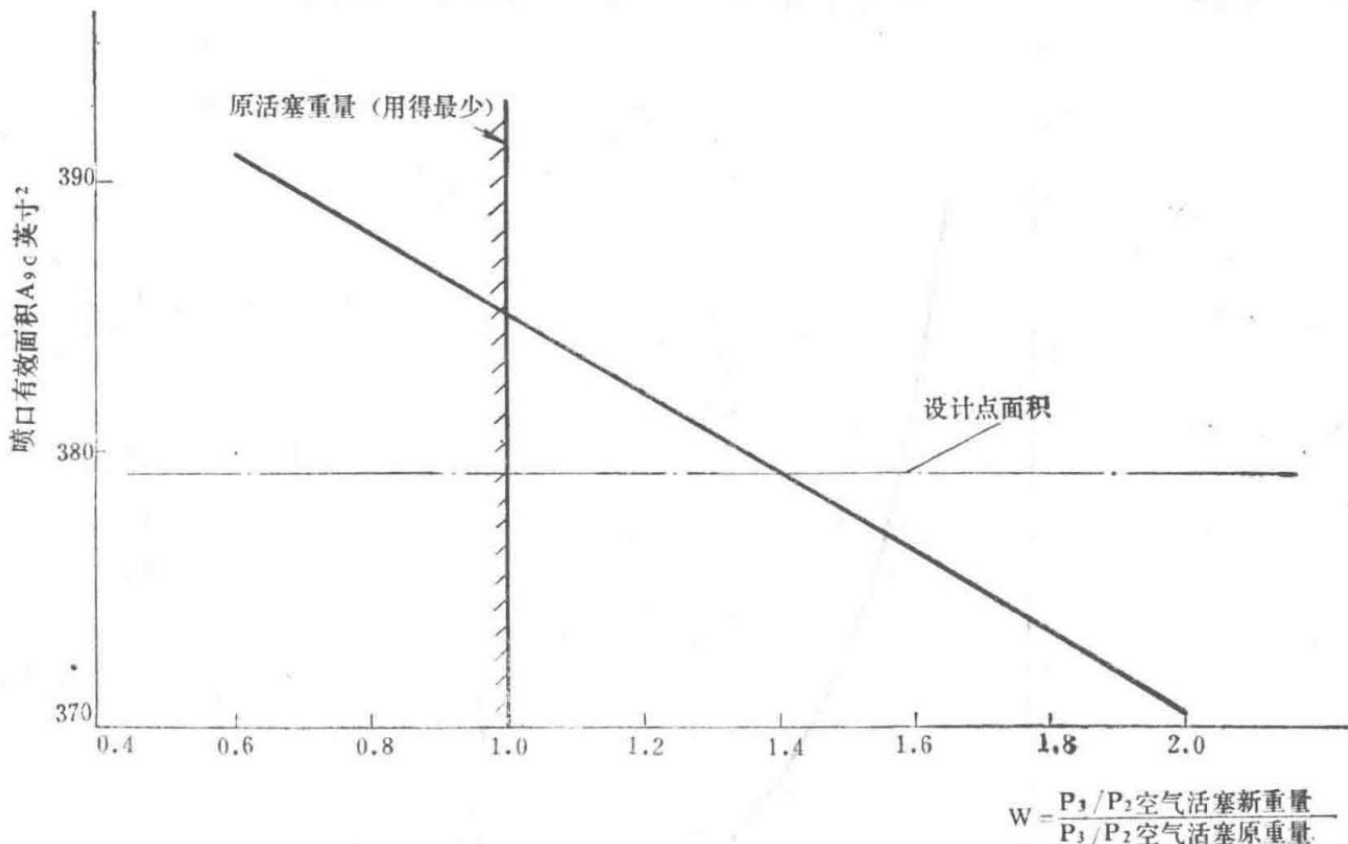


Figure 2: Spey MK202 Nozzle Effective Area versus  $P_3 / P_2$  Air Piston Assembly Weight (Acceleration at 5g)

Graph showing the variation of nozzle effective area with  $P_3 / P_2$  air piston assembly weight under 5g acceleration.

— Section 82 —  
Content from Original Document (Pages 406-410)

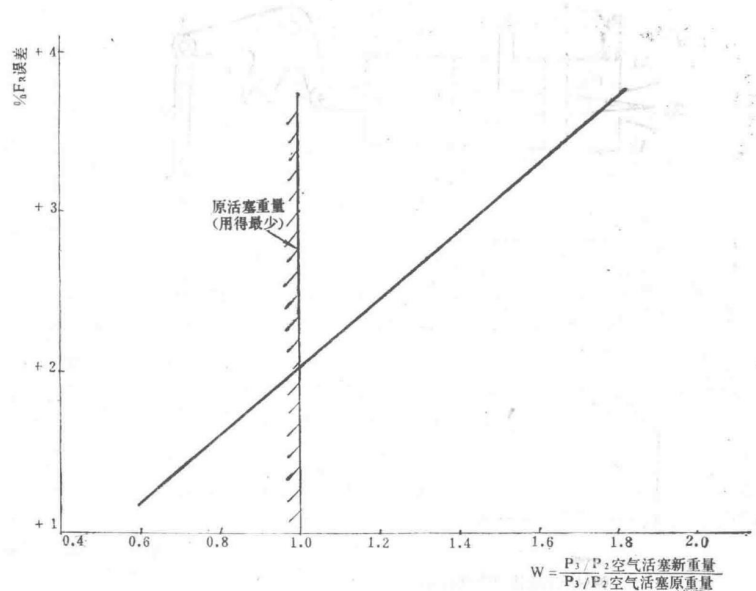


Figure 3 Variation of Spey MK202 Afterburner Fuel Flow Error with P/P2 Air Piston Assembly Weight

Graph showing the relationship between the weight of the P/P2 air piston assembly and the afterburner fuel flow error in the Spey MK202 engine.

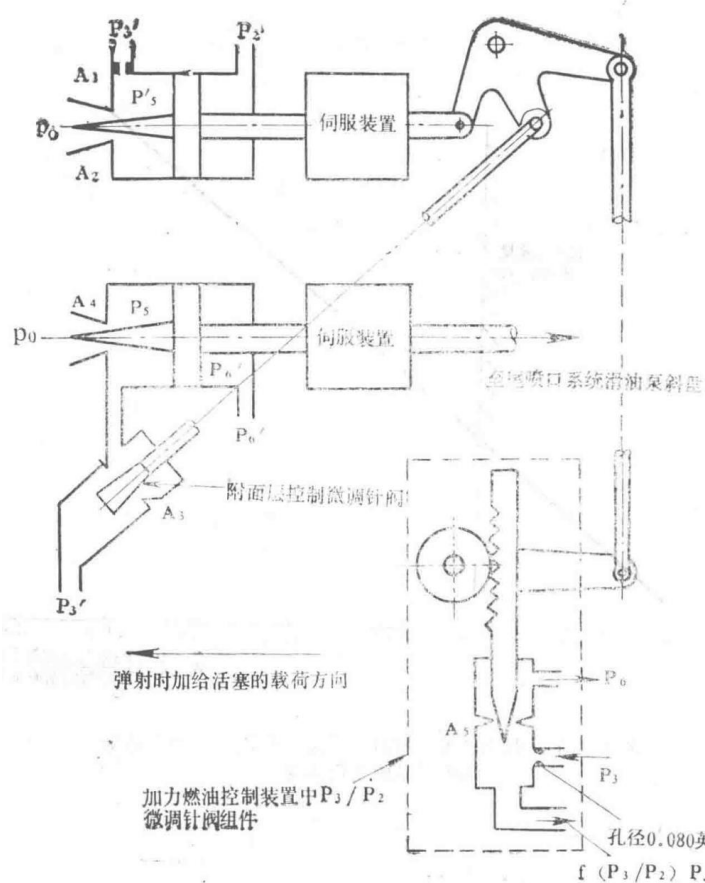


Figure 4 Schematic Diagram of Spey MK202 Pressure Ratio Regulator and Boundary Layer Control Trim Needle Valve

Diagram illustrating the pressure ratio regulator and boundary layer control trim needle valve in the Spey MK202 engine.

Document Type	Report Number
Technical Design Report	TDR7791
Spey MK202 Inlet Guide Vanes and Bleed Valve Control System	

1976.10.12 First Edition

## Abstract

This report specifies the various requirements for the inlet guide vanes and bleed valve control system. It also provides relevant design principles and references related to this design.

## Part One: Introduction

The high-pressure compressor is equipped with variable geometry inlet guide vanes to ensure that air enters the first-stage blades at the correct angle of attack, preventing stall at low speeds while ensuring the optimal predetermined angle of attack at high speeds.

The bleed valve controls the release of some air from the seventh stage into the bypass duct surrounding the compressor casing. At low compressor speeds, the bleed valve opens to prevent blockage in the rear stages of the compressor.

This report outlines the requirements for the inlet guide vanes and bleed valve control system, provides the rationale for the selection of control parameters, and discusses relevant design principles. Some original

technical reports describe the work done during early design phases and include applicable documents, thus gaining widespread use. The design principles of the current control device are based on those initially used in Spey-type turbofan engines. Technical reports related to engines in this scheme, intended to illustrate the original design concepts, are also included here.

## Part Two: System Requirements

1. At low speeds, including engine start-up, the bleed valve is open, and the inlet guide vanes are in an increased angle of attack position.
2. As the high-pressure compressor speed increases, the bleed valve gradually closes and remains closed at high speeds. The angle of the inlet guide vanes gradually decreases with increasing speed and then remains at the optimal angle of attack position.
3. Sudden changes in compressor geometry are not allowed during speed increases or decreases, as this would cause corresponding changes in engine thrust, making aircraft operation difficult.
4. The control schedule is selected based on dimensionless parameters of the high-pressure compressor to minimize deviations arising from a wide range of flight conditions.
5. Finally, the control schedule should prevent the high-pressure compressor from stalling or surging within the normal operating range of the engine.
6. During transient processes, deviations from the steady-state schedule should be minimized to avoid compressor stall or surge. The goal is to keep the angle of attack deviation of the inlet guide vanes within 5 degrees. Considering the characteristics of maneuvering flight, the system should operate well when the inlet total temperature ( $T_1$ ) changes at a rate of  $6^{\circ}\text{C}/\text{second}$ .

## Part Three: Design Principles

For control parameters, the most suitable parameters are those directly related to changes in the high-pressure compressor geometry. The high-pressure compressor pressure ratio  $P_3/P_2$  and  $N\Box/\sqrt{T_2}$  have been considered in detail.

$P_3/P_2$  did not provide satisfactory control characteristics because, during engine operation, the schedule obtained using the  $P_3/P_2$  parameter was higher than the steady-state schedule. The use of  $N\Box/\sqrt{T_2}$  instead of  $P_3/P_2$  is described in Part Five (TDR2638).

Regarding the parameter  $N\Box/\sqrt{T_2}$ ,  $N\Box$  is generally achieved through the action of centrifugal flyweights, which produce a force proportional to  $N\Box^2$ . This force is balanced against a spring force. If this mechanism is driven by an external (high-pressure) gearbox and lubricated, this mechanical method offers high reliability. The resultant motion is used to actuate a valve and schedule the power medium for the actuator.

Here, the choice between fuel or air arises. Since the high-pressure fuel pressure is approximately 3 to 4 times higher than the high-pressure compressor outlet pressure, using high-pressure fuel results in the smallest actuator cross-sectional area, thus minimizing size and weight. Moreover, high-pressure fuel is convenient to use as it can both burn and lubricate, avoiding contact between lubricants and air within the control device. Reference TDR794 provides details on the forces acting on the inlet guide vanes and bleed valve, as well as the actuator load margins.

Feedback for the power actuator is achieved through a linkage mechanism that alters the spring force. The extended mechanical linkage includes a bell crank. If the system's pivot point moves proportionally with temperature, then a function of  $N\Box^2/\text{temperature}$  can be obtained. The resultant motion controls the power actuator via a spool valve.

Although  $N\Box$  is a suitable control coefficient, the high-pressure compressor inlet temperature  $T_2$  is not, because during engine operation, the rate of change of  $T_2$  is too high for existing temperature sensors to track. The parameter  $T_1$  changes only during aircraft maneuvering, up to  $6^{\circ}\text{C}/\text{second}$ . Past experience has shown that  $N\Box/\sqrt{T_1}$  is a suitable control parameter. Therefore,  $T_1$  is chosen instead of  $T_2$ .

To maintain the inlet guide vane angle of attack deviation within 5 degrees in all states (steady and transient), the measurement system delay must be minimized. This requires placing thermocouples axially along the Venturi tube, with the thermocouple hot junctions positioned exactly at the Venturi throat. The airflow reaches a choked flow state over most of the engine speed range and is induced through the Venturi tube by an ejector. The highest available air pressure for the ejector is the high-pressure compressor outlet pressure  $P_3$ , ensuring that the airflow velocity at the Venturi inlet reaches sonic speed.

To increase reliability, three sets of thermocouple elements are connected in parallel within the thermocouple, and the combined signal is fed to an amplifier.

The system includes a position feedback device and an electric actuator. This actuator changes the pivot position through a worm gear drive.

The position feedback mechanism generates an electrical signal whose voltage is a function of angular displacement (pivot position). When fed to the amplifier, it balances the signal generated by the thermocouple, stopping the actuator motor. Thus, the system is designed so that the power actuator position has a single-valued relationship with  $N^2/\sqrt{T_1}$ .

The position feedback device and electric actuator are designed to be compact and reliable, representing first-class patented products.

The original design concept for the inlet guide vane regulator used the approximate relationship  $N^2/(K T_1)$  as the control parameter. Such a regulator produced acceptable errors during subsonic engine operation, but performance was poorer during supersonic operation due to the wide operating range of  $T_1$ . Therefore, a more precise method was adopted to regulate the power actuator position as a function of  $N^2/T_1$ .

All electrical devices are cooled by fuel and, except for the amplifier, are housed within the regulator casing. This avoids additional sealing issues for these devices (except for the electrical connectors). The inlet guide vane control section within the amplifier is part of a larger amplifier used for engine fuel regulation.

## Part Four

Document Type	Report Number
Technical Design Report	TDR2633
Principles of the Inlet Guide Vane and Bleed Valve Control System for a Twin-Spool Engine Using the Spey MK202	

1963.4.4 Fourth Edition

## Purpose

This report describes all the work done on the system to date under the following headings:

1. System Description
2. Design Data
3. Operating Loads and Pressures
4. Dynamic Characteristics

## 1. System Description

Figure 1 shows the general schematic of the system.

The inlet guide vanes and bleed valve are driven by actuators powered by high-pressure engine fuel. The actuator position is made to have a single-valued relationship with  $N/\sqrt{T}$  through the following method: The actuator linkage is connected to the regulator linkage, which rotates a cam to lift one end of the feedback spring. The other end of the spring is acted upon by a component of the force generated by the governor rotating at a

certain transmission ratio from the engine's high-pressure shaft. The magnitude of this force is altered by a movable pivot that changes with  $T_1$ , ensuring that the spring load equals  $K N^2/T_1$ . One end of the spring is connected to the governor valve, which directs high-pressure or low-pressure fuel to either side of the actuator piston based on the valve's movement direction. In steady-state conditions, the valve must be at or near the null position, and the cam lift is linearly related to the spring load. Therefore, the actuator position has a single-valued relationship with  $N^2/T_1$  as determined by the cam profile.

The movable pivot is driven by an electric actuator through a worm gear. A position sensor is connected to the worm gear via a Meyer base reference adjustment mechanism, and the voltage produced by the sensor is proportional to the distance from the spring force line to the pivot. This voltage is compared with the input voltage from the  $T_1$  thermocouple. If there is a voltage error, the actuator moves to eliminate it, ensuring that the distance from the spring force line to the pivot is proportional to  $T_1$ .

The control device assembly is adjusted using the Meyer base reference adjustment mechanism so that when  $T_1 = 0$ , the distance between the spring and the movable pivot is zero.

If this condition is met, adjusting the length of the external lever can eliminate any errors in the ratio of  $N^2$  to  $T_1$  caused by manufacturing precision.

## 2. Design Data (Prototype Engine)

- Regulator speed:  $0.1787 \times N$  rpm
- Regulator centrifugal flyweight mass (3 GEC heavy metal blocks): 0.274 lb
- Governor output force:  $\tau = 0.197 \times 10^{-6} \times N^2$  lb
- Feedback spring stiffness coefficient: 100 lb/inch
- Mass of valve moving parts: 0.726 lb

Valve damping = 0.5 to 1.5 lb·s/in (dependent on tolerances and viscosity)

Actuator piston and linkage assembly mass  $\tau$  = 10 lb

Actuator damping = 100 lb·s/in

Dimensions and linkage movements are shown in relevant drawings.

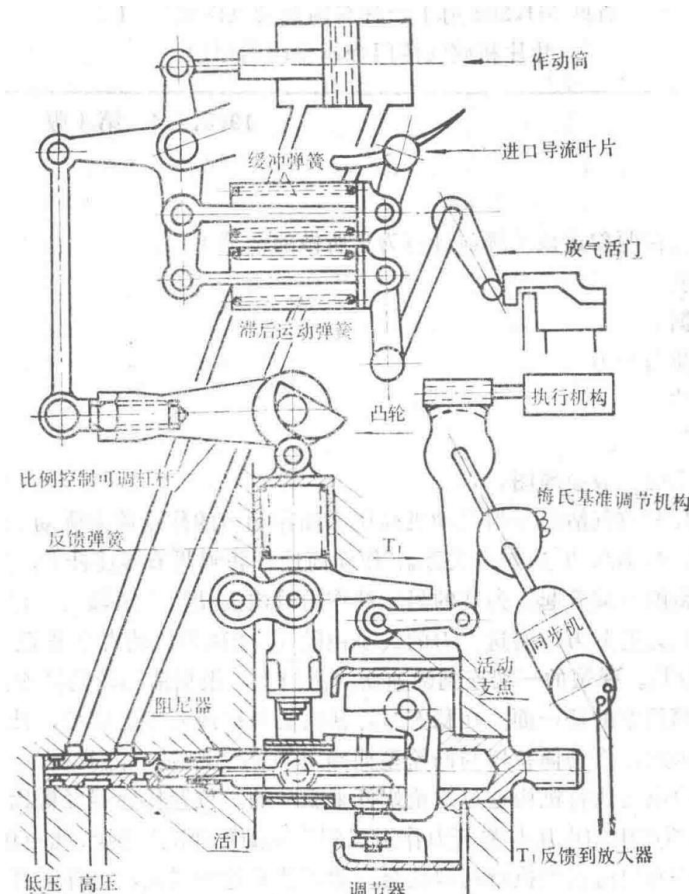


Figure 1 Schematic Diagram of Inlet Guide Vanes and Bleed Valve System

Schematic representation of the inlet guide vanes and bleed valve system in the Spey MK202 engine.

## Estimation of Bernoulli Forces

The theoretical Bernoulli force for a valve with a rectangular area and boss is  $0.43AP$ , where  $P$  is the pressure difference and  $A$  is the area of one port.

This estimation has been adopted in the analysis.

## 3. Operating Loads and Pressures (Prototype Engine)

Operating loads are estimated from test results.

Due to the lack of extensive test sampling data, the load should be multiplied by a dispersion factor of 1.25. To account for friction between the load measurement point and the two joints on the actuator, an additional factor of 1.04 (with  $\mu = 0.2$ ) is applied, resulting in a total load factor of 1.3.

Selecting reasonable values for the maximum bleed valve load and inlet guide vane load, and multiplying by the above factors, the actuator loads are determined as follows:

- Bleed valve:  $8.5 P_2$

- Inlet guide vanes:  $2.0 P_2$
- Total actuator load:  $10.5 P_2$

Here,  $P_2$  is the low-pressure compressor outlet pressure.

During deceleration, as the engine fuel flow decreases, the servo mechanism operating pressure drops, while aerodynamic loads resist actuator movement.

Under International Standard Atmosphere (ISA) conditions at sea level static, with a flight Mach number of 1.15 and a rapid deceleration to a speed where the bleed valve just opens, the system delay caused solely by the hydraulic system (excluding  $T_1$  actuator characteristics) is as follows:

System Delay Characteristics During Deceleration

Parameter	Value 1	Value 2	Unit
Altitude	0	0	feet
Mach Number (MN)	0	1.15	
Pressure ( $P_1$ )	14.7	32.6	psi
High-pressure spool speed ( $N\Delta$ )	13,800	15,500	rpm
$P_2$ (deceleration)	21	43	psi
High-pressure fuel pressure $\times 1.225$ (actuator area)	486	619	lb
Low-pressure fuel pressure $\times 0.737$	51	51	lb
Actuator load	220	450	lb
dN/dt	1500	3000	rpm/s
Control valve displacement	0.0010	0.0022	inches
Inlet guide vane delay	0.6°	0.8°	

Note: The delay was obtained using a simple approximation method. It is assumed that the actuator moves at a constant speed under given conditions, and the system has sufficient time to approach steady-state error. With the control valve opening fixed, an actuator position error is obtained. Under the above flight conditions, the relationship between valve displacement and actuator diameter is shown in Figure 2. From the perspective of actuator load, the high  $P_1$  condition is the most severe. A slight increase in actuator load (e.g., when used in a new installation) would require a larger actuator to avoid excessive inlet guide vane delay. The curve illustrates how an oversized actuator can cause excessive inlet guide vane delay, demonstrating that the current design is optimal.

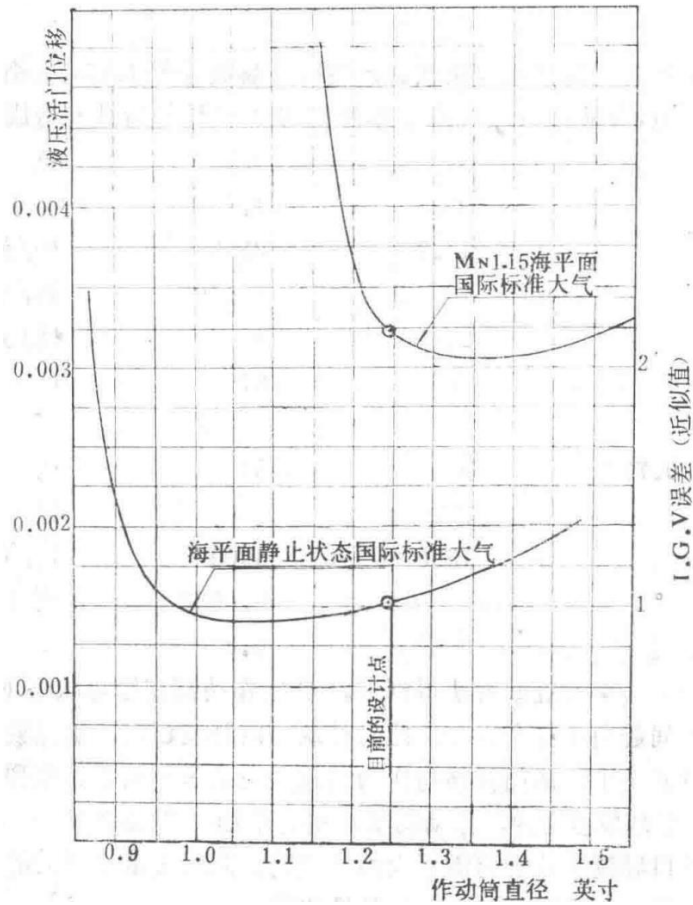


Figure 2 Optimization of Actuator Diameter

Graph showing the relationship between actuator diameter and system delay, illustrating the optimization of actuator size.

## 4. Dynamic Characteristics

It has been found that compressibility, actuator inertia, actuator damping, and the rate of change of actuator load have negligible effects on the system's dynamic characteristics. Ignoring these factors, the equation simplifies to:

$$[ m, G D^3 + K_1, D D^2 + ( R_1, K_3 + R_2 - R_3 ) D + \partial R_1, K_2 K_3 ] h = c^*$$

Simplified dynamic equation of the system, ignoring compressibility, actuator inertia, and other minor factors.

$K_2 = 6.1$  ( $R=0.002$ ) determined by design

$K_3 = 1.7$  ( $T=288K$ )  $m=0.002$

$K_1 = 0.5$  1.5 determined by viscosity and tolerances

$G \sim 70\sqrt{Pv}$  where  $Pv$  is the steady-state valve pressure drop

$R$  – Bernoulli force  $\approx 0.7 P \square$

$R_3$  – Effect of the rate of change of Bernoulli force with  $P \square$ , which is minimal.

A set of typical data is as follows:

Typical System Data

Load Condition	G	R	$R_3$
Medium load	900	140	12
High load	750	70	6

## Stability Criteria

According to the Whiteley criterion, for a system with good quality (10% overshoot), the coefficients should be proportional to:

$$D^3 + 2 aD^2 + 2 aD + a^3$$

Whiteley stability criterion for a third-order system.

Applying the above data (scaling  $D \times 100$ ) and taking the lower damping value ( $K_1 = 0.5$ ):

System Coefficients vs. Whiteley Criterion

Load Condition	System Coefficients	$D^3$	$D^2$	$D^1$	$D^0$
Medium load	Actual value	1	2.5	6.2	3.75
	Whiteley criterion	1	3.1	4.8	3.75
High load	Actual value	1	2.5	9.5	4.5
	Whiteley criterion	1	3.3	5.5	4.5

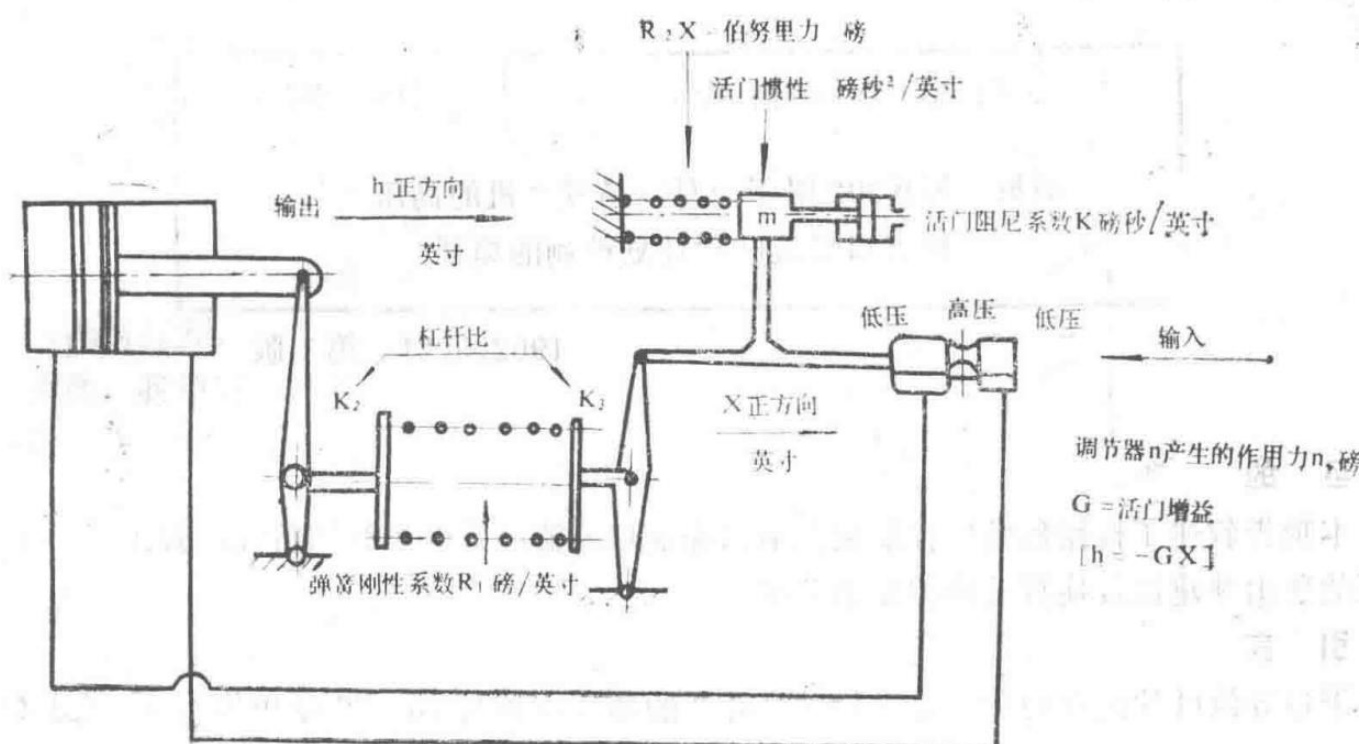


Figure 3 System Schematic (when  $T_1$  is constant)

Schematic diagram of the system under constant  $T_1$  conditions.

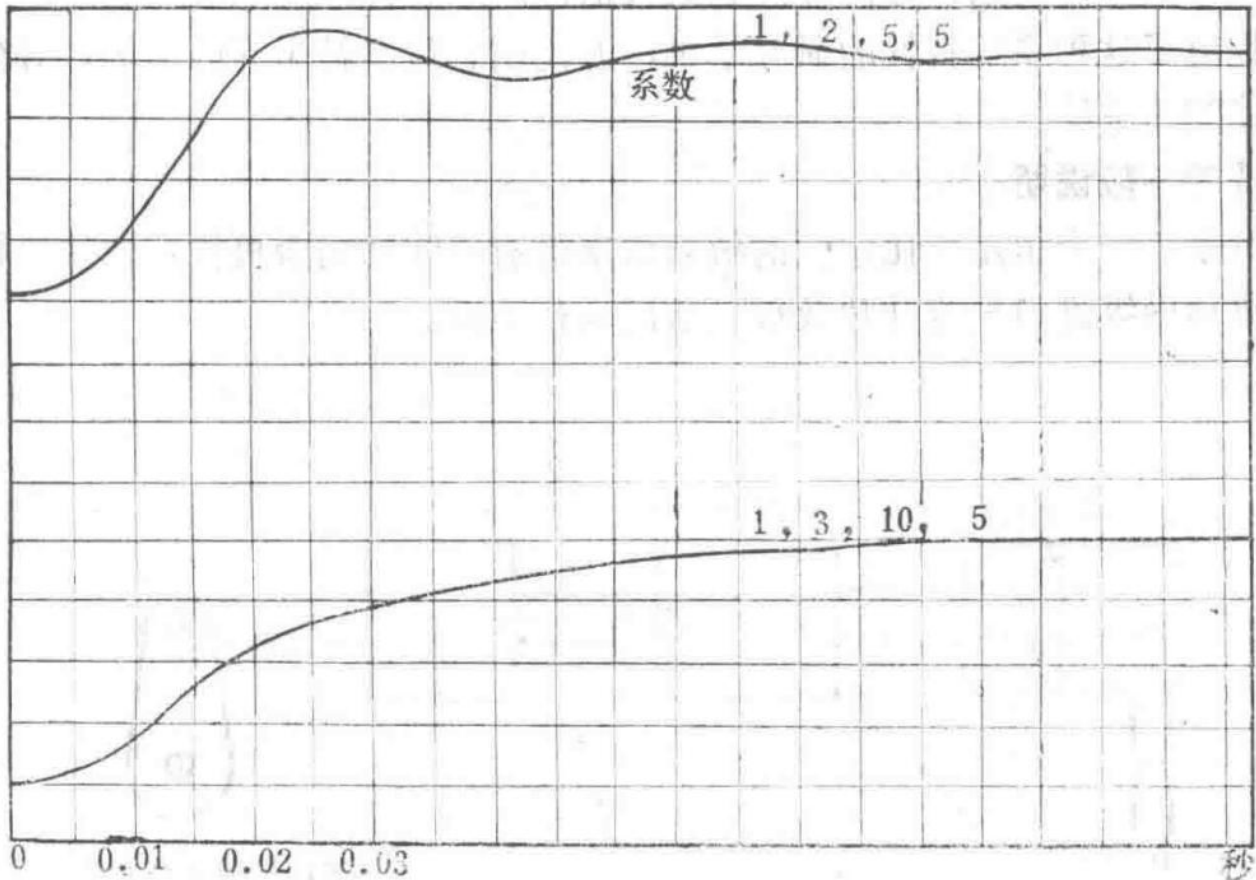


Figure 4 Step Response Characteristics of a Third-Order System

Graph showing the step response characteristics of the system, demonstrating system stability.

It is evident that the system performs well under all conditions (see Figure 4 for typical step response characteristics). However, if necessary, system performance can be improved by adjusting  $R_1$  (keeping  $R_1 / K_2$  constant to maintain the same gain), which changes the third coefficient. This would require a new cam and spring on the regulator.

## Section Five

### Technical Design Report Details

Document	Identifier
Technical Design Report	TDR 2638
Title	Principles of High-Pressure Compressor Inlet Guide Vane Schedule Control for a Twin-Spool Engine Using the Spey MK202

First Edition, May 21, 1962

## Objective

This report describes the characteristics of a system controlling the bleed valve and inlet guide vanes based on compression ratio. It presents the reasons for rejecting this system and recommends a system controlled by corrected speed.

# Introduction

The ideal characteristic for inlet guide vanes is that their angle should have a single-valued relationship with  $N / \sqrt{T}$  (see note on page 413).

The existing controller uses the approximation  $N^2 - K T_1$ , but current methods for measuring  $T_1$  have slow response times. However, using dimensionless parameters avoids these drawbacks. The compressor pressure ratio is commonly used for adjusting afterburner fuel and exhaust nozzle control. Therefore, it is proposed to use this signal for scheduling the inlet guide vanes and bleed valve.

This report presents the results of the study on this system, explains why it was ultimately abandoned, and recommends a system controlled by corrected speed.

## 1. General System Description

As shown in Figure 1, a sensing piston positioned by the pressure ratio drives a servo mechanism, which in turn drives a linkage assembly that operates the actuator for the inlet guide vanes and bleed valve.

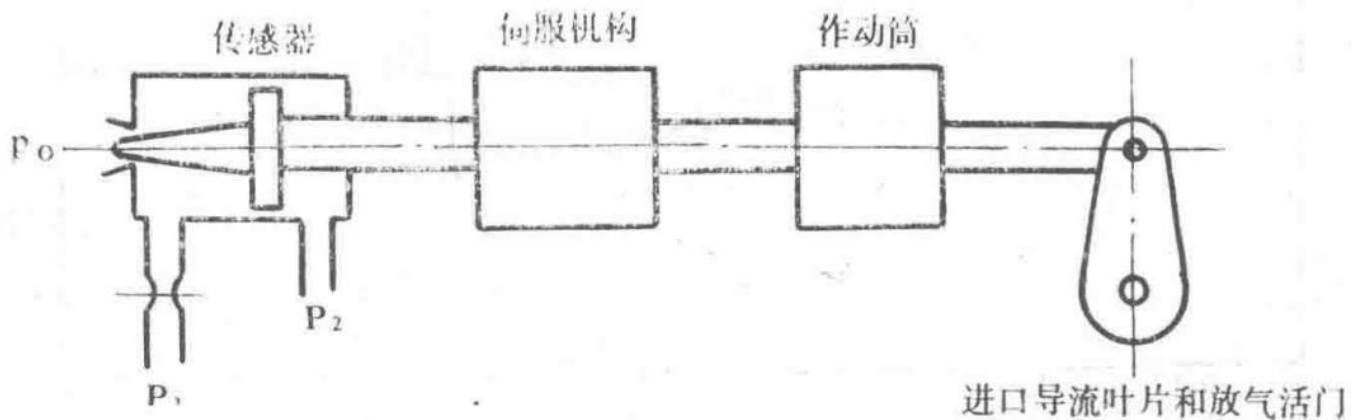


Figure 1

Diagram illustrating the general system for controlling inlet guide vanes and bleed valve based on pressure ratio.

Figure 2 shows the compressor characteristics with steady-state, acceleration, and deceleration operating lines.

This diagram shows that if the inlet guide vane (IGV) angle is scheduled according to the pressure ratio, then regardless of whether the engine is accelerating or decelerating, the resulting angle will be higher than the angle required by the  $N/\sqrt{T}$  schedule.

This reasoning also applies to the bleed valve—during acceleration, it closes prematurely, and during deceleration, it opens prematurely.

Thus, we observe that if the servo mechanism and actuator have no time delay, and if the steady-state operation schedule is correct, during acceleration, there will be insufficient bleed and a positive inlet swirl angle, leading to compressor surge. During deceleration, there will be excessive bleed and a positive inlet swirl angle, but this is desirable.

What must be followed is that for steady-state operation, at least in the high-speed range of variable geometry, this schedule should be corrected because the engine operates in this range during high-speed cruise.

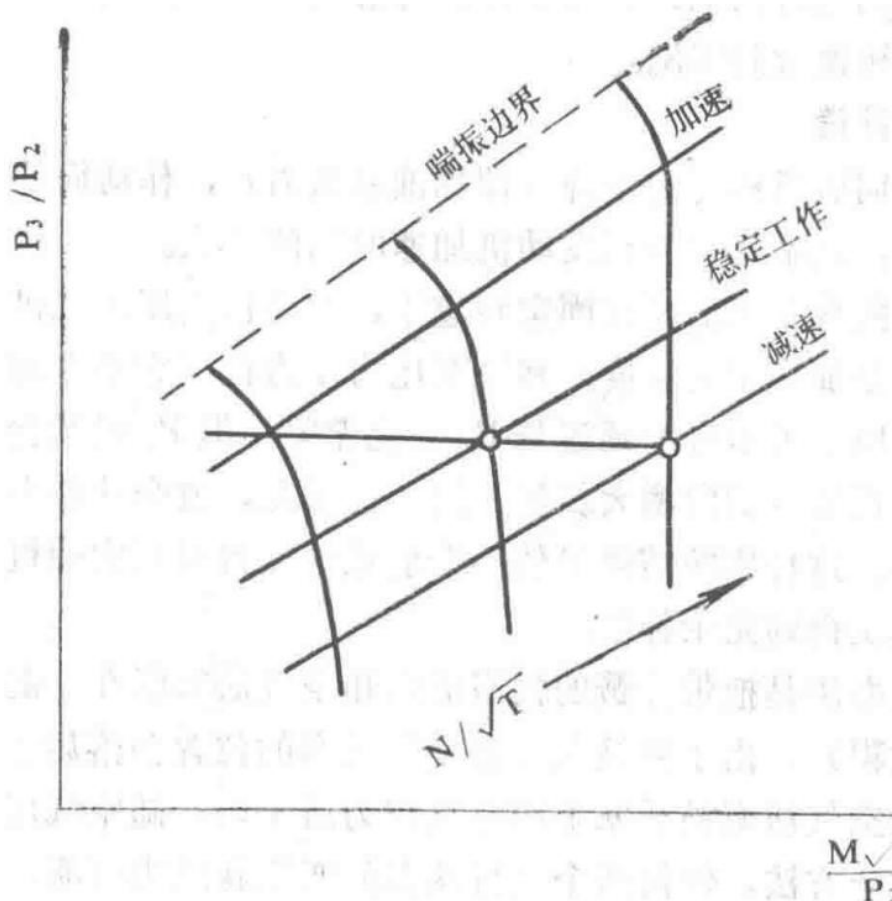


Figure 2

Diagram illustrating the relationship between pressure ratio scheduling and inlet guide vane angle during acceleration and deceleration.

## Reducing Lead

This error can be reduced through a follow-up servo mechanism with an appropriate time delay.

Figure 3 shows the curves of rotational speed and inlet guide vane angle varying with time during rapid acceleration and deceleration.

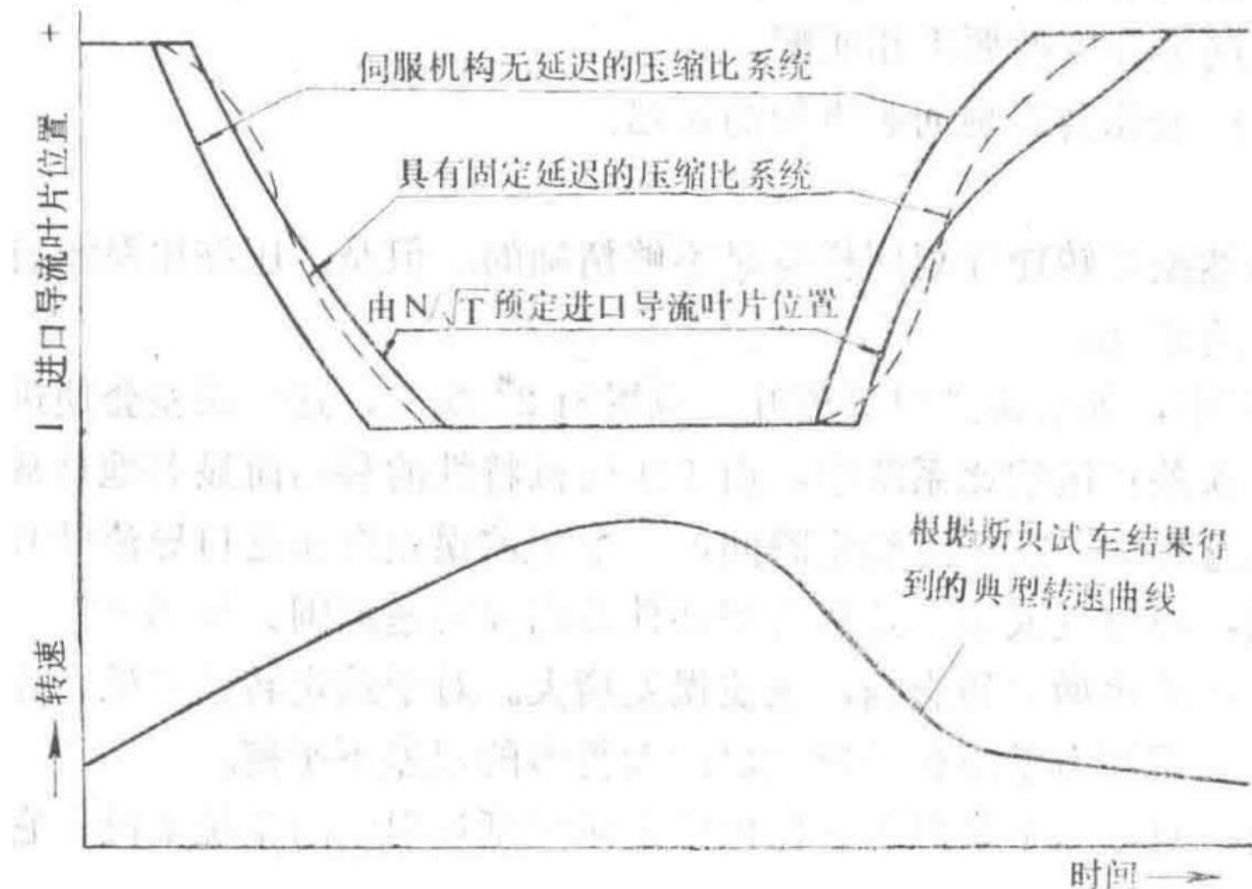


Figure 3

Time-based curves of rotational speed and inlet guide vane angle during rapid acceleration and deceleration.

During acceleration at a certain speed, the delay of the servo mechanism can be selected to match the lead. It can be seen that, in general, it is impossible to achieve a match between delay and lead for both acceleration and deceleration. During deceleration, matching can only be achieved at a certain speed.

## Altitude Compensation

Due to the drop in servo mechanism pressure (i.e., fuel pump pressure), the delay of the actuator slightly increases as  $P_1$  decreases.

However, this is insufficient to compensate for the increase in engine acceleration time.

The curves in Figure 6 show a comparison at a fixed rotational speed between the high-pressure compressor mass flow rate of the engine (which is a measure of acceleration rate for a given excess fuel ratio) and the square root of the pump pressure (which is a measure of actuator delay). It must be noted that the delay of the pressure ratio device itself is independent of  $P_1$  changes, but  $P_1$  will further reduce the sensitivity of the entire system.

Increasing the constant pressure differential across the valve using a spring-loaded valve makes the response time of the entire system more sensitive to changes in pump pressure. While this does not make the system overly sensitive to other random influences, the maximum pressure differential is still insufficient to fully compensate the system.

The solution is to link the spring-loaded servo piston with an air piston. If the pressure ratio changes smoothly (as during engine acceleration), the position of the air piston, due to spring loading, will lag behind its position without the spring. Since the air piston without a spring is balanced by the air pressure on the piston, the delay will increase as air pressure decreases.

Using this method, matching between any two flight conditions becomes possible.

## 2. System Drawbacks

### Sources of Error

Although we have demonstrated above that, theoretically, the system can be accurately compensated at certain points, errors are still generally present.

Errors are related to the following factors:

1. Manufacturing tolerances of the servo mechanism, actuator, and sensors will cause variations in total delay.
2. Engine characteristic tolerances affect parameter relationships and acceleration rates.
3. Under any given flight condition, matching of delay can only be achieved at one specific rotational speed.
4. Only the requirements for two altitudes can be matched.
5. Changes in fuel temperature affect the delay of the servo mechanism.

### Error Amplification

It can be demonstrated that although the corrected speed schedule is also imprecise, the pressure ratio system has a significant drawback that the corrected speed system does not.

In the  $N / \sqrt{T}$  schedule, if there is a  $2^{\wedge}$  error in the inlet guide vane position, this error will cause a  $2^{\wedge}$  deviation in the inlet guide vane. The same error in the pressure ratio system is significantly amplified due to the shift in compressor characteristics.

For example, during acceleration, at any given moment, a lead error will cause the inlet guide vane to produce an excessive negative incidence angle, resulting in insufficient bleed. Both factors shift the characteristics toward the high-speed range. See Figure 4.

Due to the effect of increased compressor pressure ratio, the error is also amplified. For a given rotational speed within the variable geometry range, the system will balance at a much larger error than that suggested by a simplified mechanical analysis of the system.

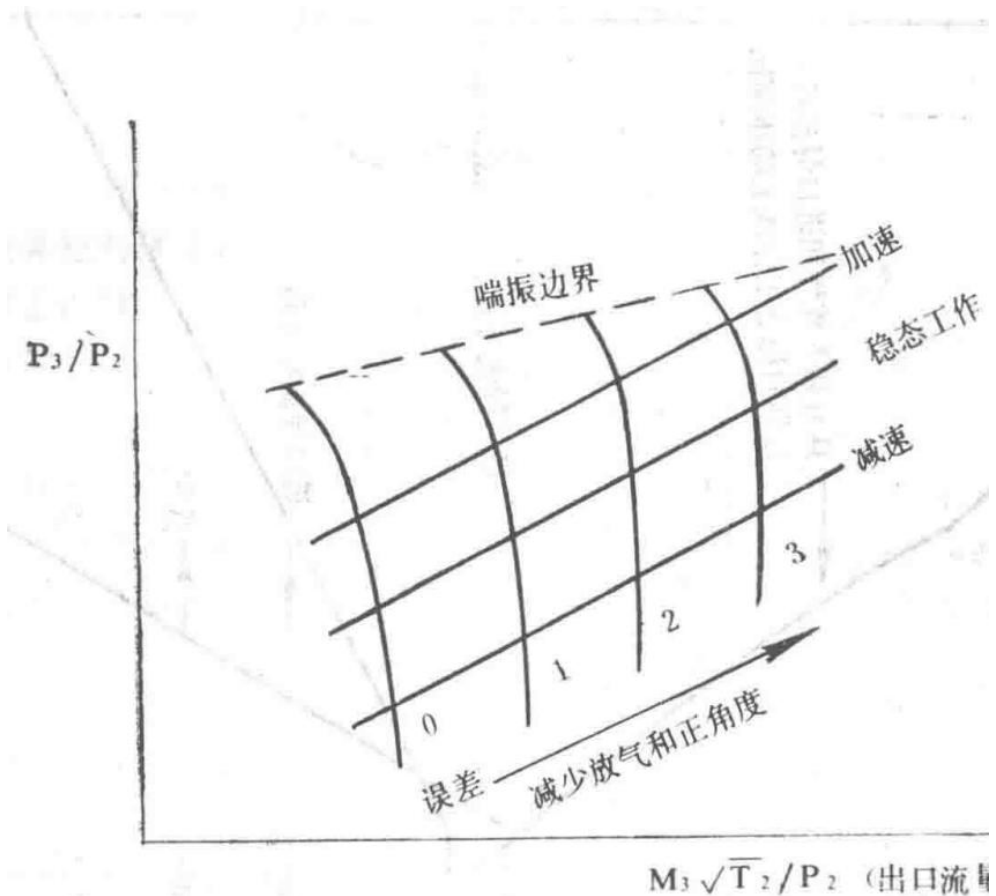


Figure 4

Compressor characteristic shift due to inlet guide vane error during acceleration.

The curves in Figure 5 indicate how a system with a delay equal to any given matching delay degree reaches equilibrium error.

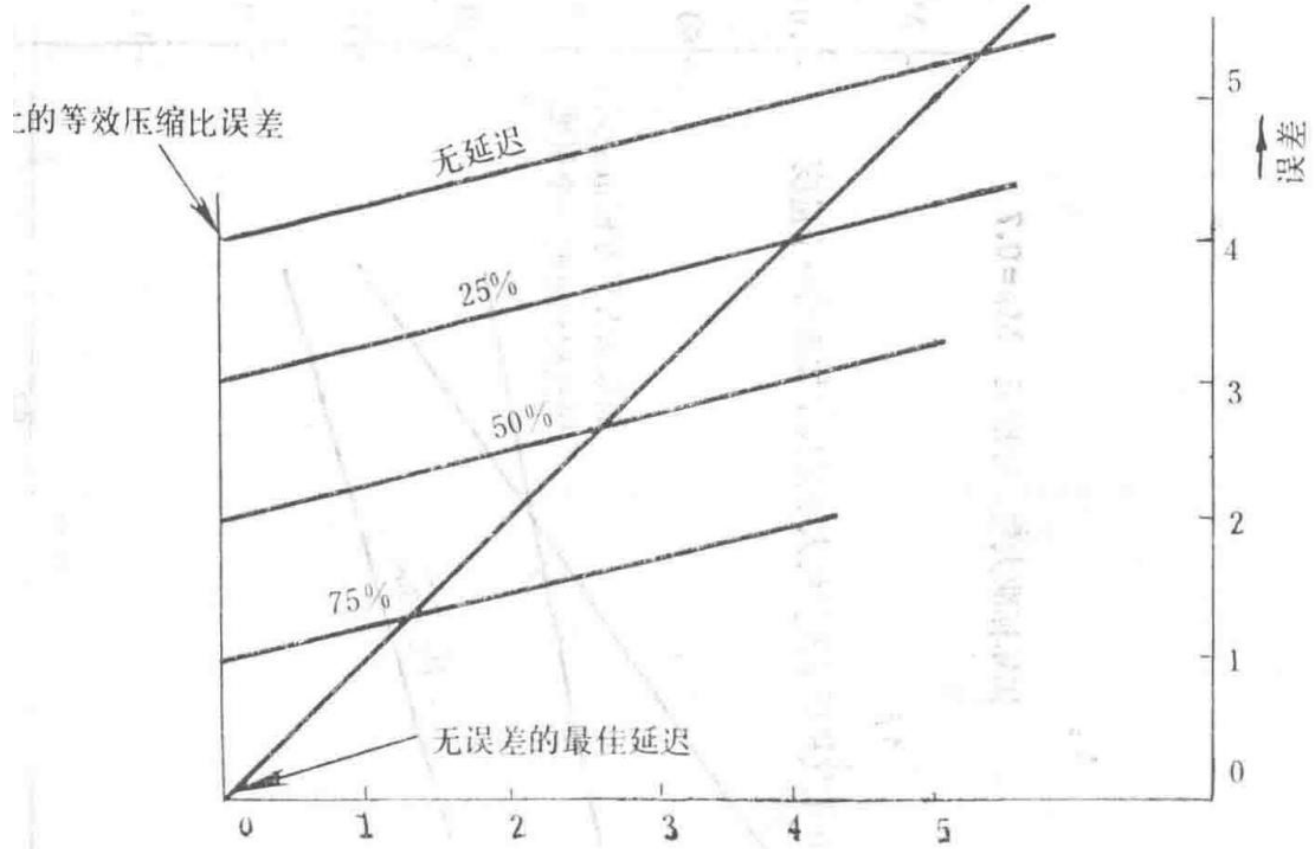
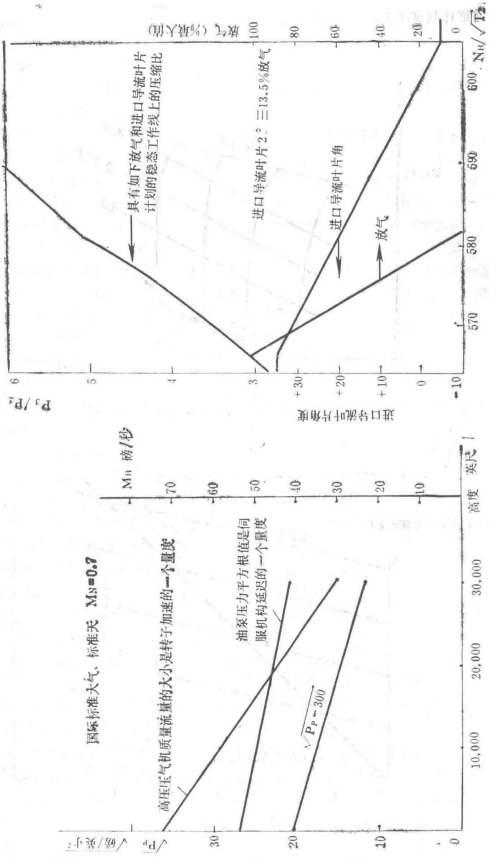


Figure 5: Error Characteristics

Equilibrium error characteristics for a system with a given delay.

## Example

To establish the magnitude of relevant quantities, a typical Spey compressor with bleed and inlet guide vane adjustment schedules is taken as an example. The detailed schedule is shown in Figure 7.



Detailed bleed and inlet guide vane adjustment schedule for the Spey compressor.

At constant rotational speed, the compressor characteristics and convergence lines with variable schedule errors are shown in Figure 8. For this specific case, it can be seen that an infinitely fast system cannot converge within the limits set by the schedule. Moreover, the graph indicates that if the actual delay deviates from the optimal value by 30%, the inlet guide vane error is 4°, and the bleed error is 27%.

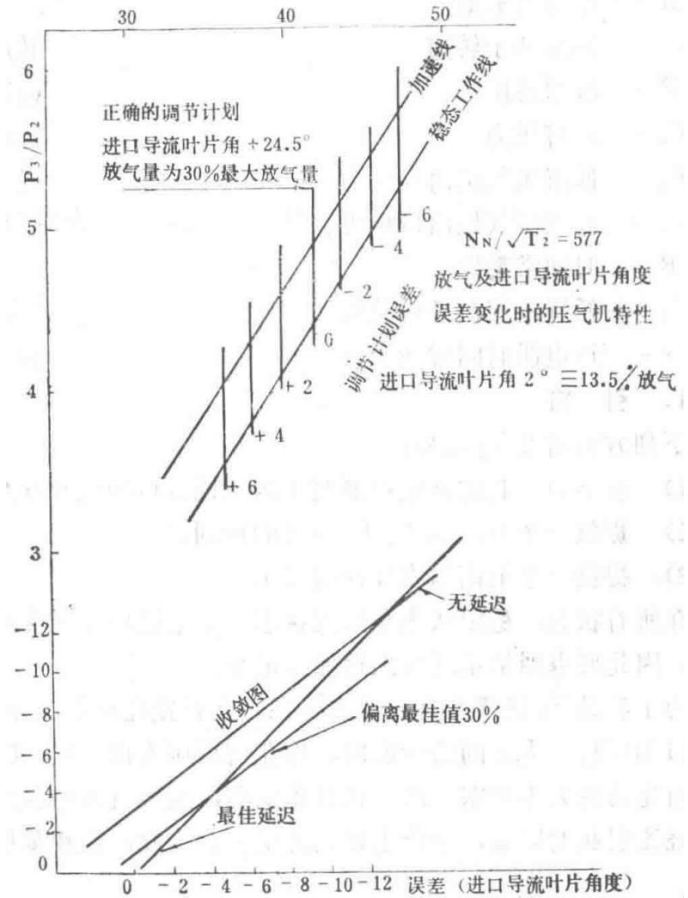


Figure 8: Spey High-Pressure Compressor Outlet Mass Flow  $M_3 \sqrt{T_2} / P_2$  at  $N \sqrt{T_2} = 577$

Compressor characteristics and convergence lines with variable schedule errors at constant rotational speed.

## Summary

Although the pressure ratio system has the advantage of rapid and accurate measurement of dimensionless parameters, when the engine deviates from the operating line, it may cause unacceptable errors in the  $N / \sqrt{T}$  schedule.

Because it is theoretically impossible to precisely define the magnitude of the error or set exact limits for allowable errors under any given condition.

However, as indicated above, the characteristics may be such that a 30% deviation of system delay from the optimal value can cause a 4<sup>th</sup> order error in inlet guide vane position and a corresponding bleed error.

After comprehensive consideration, the pressure ratio system was abandoned in favor of a system regulated by corrected speed.

Note: At constant rotational speed, when moving from the steady-state operating line to the acceleration control device operating line, the change in  $T_2 / T_1$  is not significant. Therefore, it is better to use  $N / \sqrt{T_1}$  to schedule the high-pressure compressor geometry.

## Part Six

Technical Design Report	TDR 2664
Spey MK202: Thermocouple Requirements and Ejector Design Principles for a Twin-Spool Engine	

## Abstract

### 1. Proposal of thermocouple requirements

## 2) Estimation of Thermocouple Response Characteristics

## 3) Preliminary Design of the Ejector

### Nomenclature

- D – Thermocouple wire diameter
- M – Throat Mach number
- Ny – High-pressure rotor speed
- P – Throat total pressure
- $P_0$  – Ambient pressure
- $P_2$  – Low-pressure compressor outlet pressure
- $P_3$  – High-pressure compressor outlet pressure
- R – Time constant ratio
- $T_1$  – Low-pressure compressor inlet total temperature
- T – Thermocouple time constant

## 1 Introduction

The following aspects require the  $T_1$  signal:

1. Control the high-pressure compressor inlet guide vane angle as a function of  $N^{\square} / \sqrt{T}$ .
2. Provide a schedule for NF max varying with  $T_1$ .
3. Provide a correction for maximum temperature control.

In all conditions, both steady-state and transient, it is desirable for the inlet guide vane angle to be accurate within 5° of its correct value. Therefore, the delay in the measurement system must be minimized.

To meet the requirements of transient states with continuously varying  $T_1$ , a thermocouple must be placed at the sonic throat. This throat should be located in the duct between the compressor inlet and ambient pressure, i.e., the pressure ratio across the throat  $\tau = P_0/1$  (losses neglected). Thus, at low pressure ratios, the flow in the throat becomes unchoked. At static conditions, the compressor inlet pressure is lower than atmospheric pressure, causing backflow. The backflow induced by airflow circulation can result in significant errors. To address this, an ejector system that generates sonic flow at the throat is proposed.

## 2. Requirements for the Thermocouple (for an Engine Configuration)

The thermocouple at the sonic throat must meet the following requirements, where  $T_1$  is the throat total temperature.

### Temperature and Pressure Range

Thermocouple Operating Range

Temperature ( $T_1$ )	Pressure (Throat Total Pressure)
-70°C to +155°C	2.3 to 33 psi (absolute)

### Steady-State Accuracy

Within the specified pressure and temperature range, the steady-state accuracy is  $\pm 1^{\circ}\text{C}$ .

## Transient Accuracy

Assuming  $T_1$  changes at a constant rate of 5% per second, the measurement error shall not exceed 5.7%.

## Materials

Thermocouple materials with a linear voltage-temperature characteristic are preferred.

## 3. Study of Thermocouple Time Constant

### Introduction

The inlet guide vane schedule must be within  $5^{\circ}$  of the required position, equivalent to 11.5 units of the  $N\Box / \sqrt{T_1}$  value.

Assuming a  $T_1$  variation rate of 5% per second, to ensure this accuracy, the maximum allowable time constant is 1.14 seconds.

### Analysis

Time constants for both choked and unchoked throat conditions were estimated. For a 0.02-inch diameter nickel-chromium vs. nickel-aluminum thermocouple, the time constant is given by:

$$\tau = 3.7 P^{-1.2} T_1^{-0.185} M^{-1.2} (0.742 + 0.126 M^2)^{1.4},$$

Time constant for unchoked throat condition

When the throat is choked, the time constant is:

$$\tau = 3.94 P^{-1.2} T_1^{-0.185},$$

Time constant for choked throat condition

Using these formulas, the time constants across the flight temperature and pressure range can be determined, as shown in Figure 1.

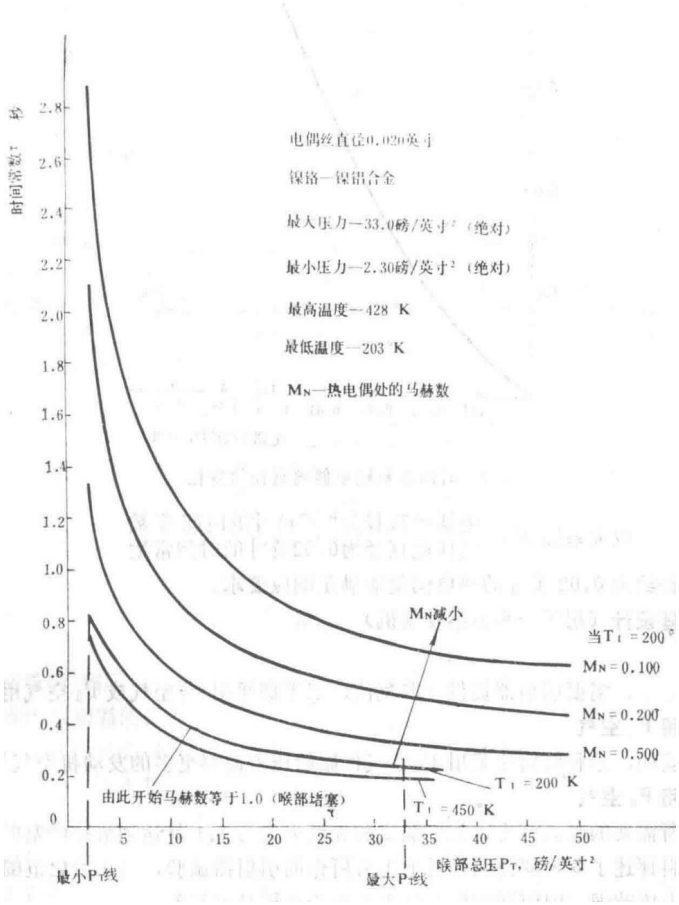


Figure 1 Variation of  $T_t$  thermocouple time constant with venturi total pressure, total temperature, and throat Mach number

Graph showing the relationship between thermocouple time constant and parameters such as total pressure, total temperature, and throat Mach number.

It can be demonstrated that the time constant is proportional to:

- $3$  (thermocouple wire diameter)

Thus, the effect of any thermocouple wire diameter can be determined. The magnification factor for estimating the time constant of various wire diameters is shown in Figure 2.

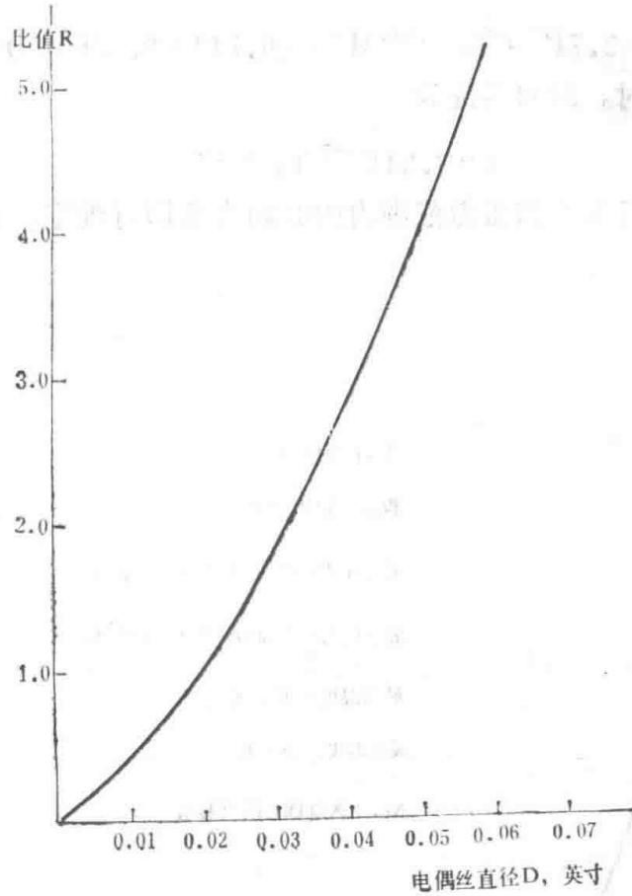


Figure 2 Variation of time constant with thermocouple wire diameter

Graph showing how the time constant varies with different thermocouple wire diameters.

The time constant magnification factor for a thermocouple wire diameter of 'D' inches is  $R = \text{Time constant for } 0.02\text{-inch diameter wire}$ . Thus, a thermocouple with a diameter of approximately 0.02 inches meets the response requirements.

## 4. Ejector Design (for an Engine Configuration)

### Introduction

At static conditions, an ejector is required to provide airflow. Consideration has been given to using  $P_2$  or  $P_3$  air for the ejector.

#### Ejector Using $P_2$ Air

Preliminary studies indicate that this configuration requires more engine airflow than using  $P_3$  air as the primary pressure source.

#### Ejector Using $P_3$ Air

To reduce the required suction pressure, the thermocouple is placed in the throat of a venturi where flow choking occurs at a pressure ratio of 1.1. A review of ejector tests conducted by Rolls-Royce and other organizations, covering the required pressure ratio range for this application, confirms the feasibility of using measured results for theoretical analysis.

For the required primary ejector pressure ratio  $P_3 / P_0$ , the ejector dimensions are determined based on a pressure ratio of  $P_3 / P_0 = 16:1$  to achieve flow choking in the venturi. This pressure ratio approximately

corresponds to the sea-level static maximum speed condition.

Across the entire operating range of the inlet guide vanes for  $N/\sqrt{T}$  values, although the venturi does not choke at aircraft static conditions, the throat Mach number remains high. Under these conditions, since  $T_1$  variations are minimal, the thermocouple does not require a fast response even at  $M = 1.0$ .

## Ejector Details (Figure 3)

- Primary nozzle diameter: 0.091 inches
- Mixing section diameter: 0.55 inches
- Mixing section length: 2.75 inches
- Diffuser angle: 6°
- Diffuser length: 2.1 inches
- Discharge pipe diameter: 0.77 inches
- Maximum primary ejector airflow: 0.042 lb/s (at 340°C)

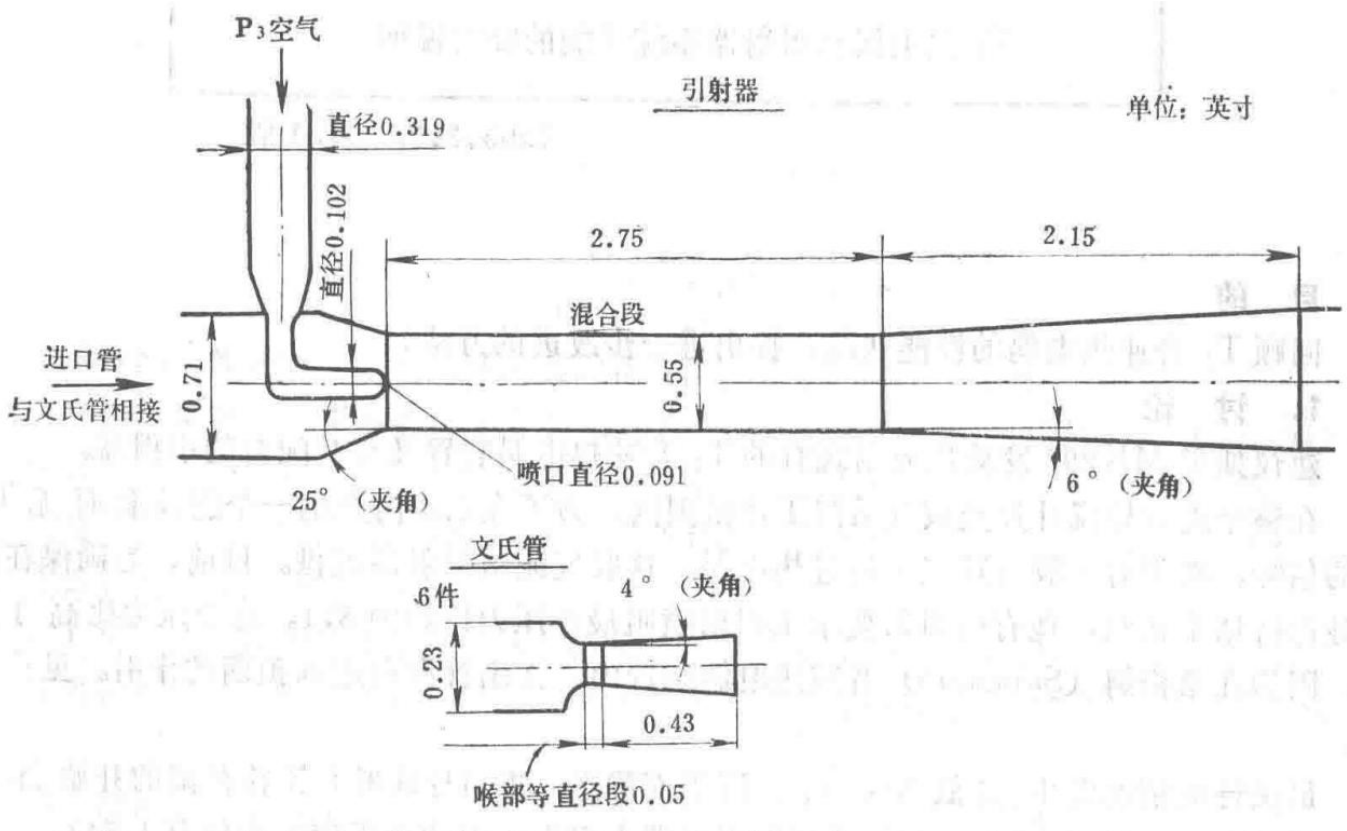


Figure 3 Ejector

Technical drawing of the ejector system showing dimensions and components.

Six venturis are connected to a manifold leading from the compressor inlet, with each venturi outlet connected to a manifold communicating with the ejector airflow outlets.

- Bleed air manifold diameter from compressor inlet: 0.569 inches
- Individual venturi inlet pipe diameter: 0.23 inches
- Venturi throat diameter: 0.10 inches
- Venturi outlet diameter: 0.13 inches
- Venturi diffuser section length: 0.43 inches
- Outlet pipe diameter: 0.29 inches
- Ejector manifold diameter: 0.71 inches

For the above ejector, at sea-level static maximum speed conditions, the effect of bleed air (0.04% of high-pressure compressor airflow) reduces engine thrust by 0.025%.

## Future Work

1. Characteristics of the device under various states of the flight plan.
2. Influence of secondary time constants of the thermocouple.

## Part Seven

### Technical Design Report

Technical Design Report	TDR 3990
Spey MK202	Lü Shang
Interim Statement on T <sub>1</sub> Thermocouple and Ejector System Performance	

1965, March 25, First Edition

## Objective

Review the performance status of the T<sub>1</sub> sonic thermocouple and propose methods for further improvement.

### 1. Discussion

It is recommended that the existing T<sub>1</sub> sonic thermocouple device and its associated ejector be applied to the Spey MK202 engine.

Across the entire operating range of the inlet guide vanes and bleed valves, a sonic airflow must pass through the thermocouple to generate a signal that can be calibrated without T<sub>1</sub> error. This airflow is provided by the ejector. Currently, to ensure choked flow at the thermocouple, the existing ejector requires a minimum primary ejector nozzle pressure ratio of approximately 8:1. This pressure ratio is higher than anticipated because the venturi in the Sangamo sonic thermocouple device did not perform as expected. See Part Two.

The most critical condition occurs at low N / √T<sub>1</sub>, sea-level static, at the beginning of the inlet guide vane operating range. Under this condition, using P<sub>3</sub> air, the available primary ejector pressure ratio for the existing device is approximately only 4.5:1.

For the Spey MK202, the pressure ratio at the start of the inlet guide vane rotation range depends on whether P<sub>3</sub> or seventh-stage high-pressure air is used. Early studies recommended using seventh-stage air, but in this case, even the maximum P<sub>3</sub> pressure is insufficient. Therefore, P<sub>3</sub> air is used on the Spey MK202 to minimize T<sub>1</sub> errors caused by the venturi not reaching choking. This issue is further exacerbated by the fact that most P<sub>3</sub> air is drawn from the anti-icing manifold. When anti-icing air flows at full capacity, the pressure loss in the anti-icing manifold reduces the available ejector pressure ratio from 4.7:1 to less than 4:1.

Thus, it is desirable to improve the device so that the sonic thermocouple maintains choked flow across the entire range, even when the maximum primary ejector pressure ratio drops to 4:1.

### 2. Reasons for Requiring High Pressure

Due to the thermocouple venturi not performing as expected, the required primary ejector pressure ratio is higher than anticipated. The thermocouple venturi reaches choked flow at a pressure ratio of approximately 1.25:1. However, after the thermocouple is installed in the venturi and the device is mounted with two 90° joints, the

venturi choking pressure ratio increases to 2:1, and the choked mass flow rate...

— Section 86 —  
Content from Original Document (Pages 426-430)

The pressure recovery is reduced by approximately 20%, as shown in Figure 1.

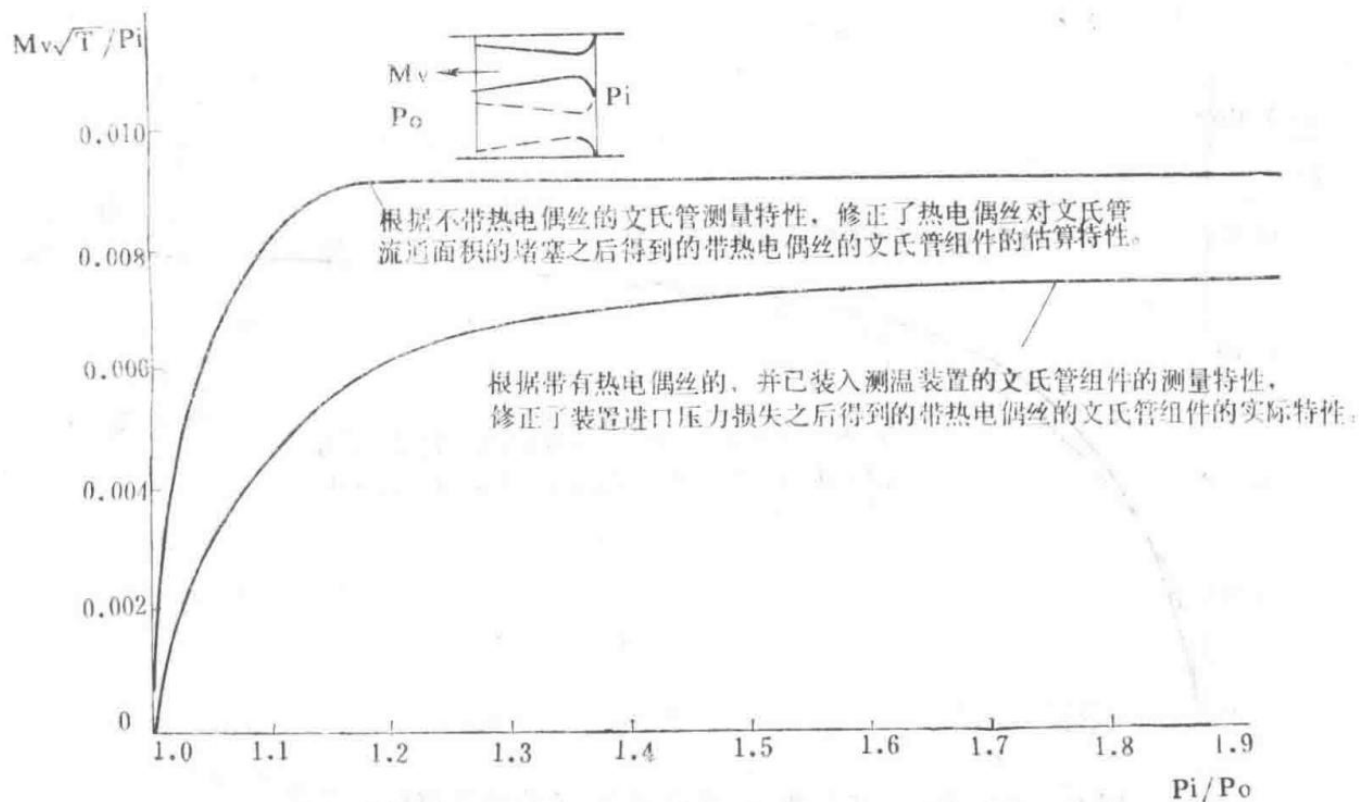


Figure 1: Characteristics of the three-element Venturi tube thermocouple

Characteristic curves of the three-element Venturi tube thermocouple assembly.

When comparing the actual characteristics of the Venturi tube assembly with thermocouple wires to those of a simple orifice (Q-curve corresponding to  $M \sqrt{T} / P = 0.0074$ , see Figure 2), a high degree of consistency is observed. This allows us to conclude that the difference in characteristics between Venturi tubes with or without thermocouple wires is primarily due to flow separation caused by the presence of the thermocouple in the Venturi throat. Some results may be influenced by disturbances and vortices at the Venturi inlet, but this effect is likely minor and difficult to estimate.

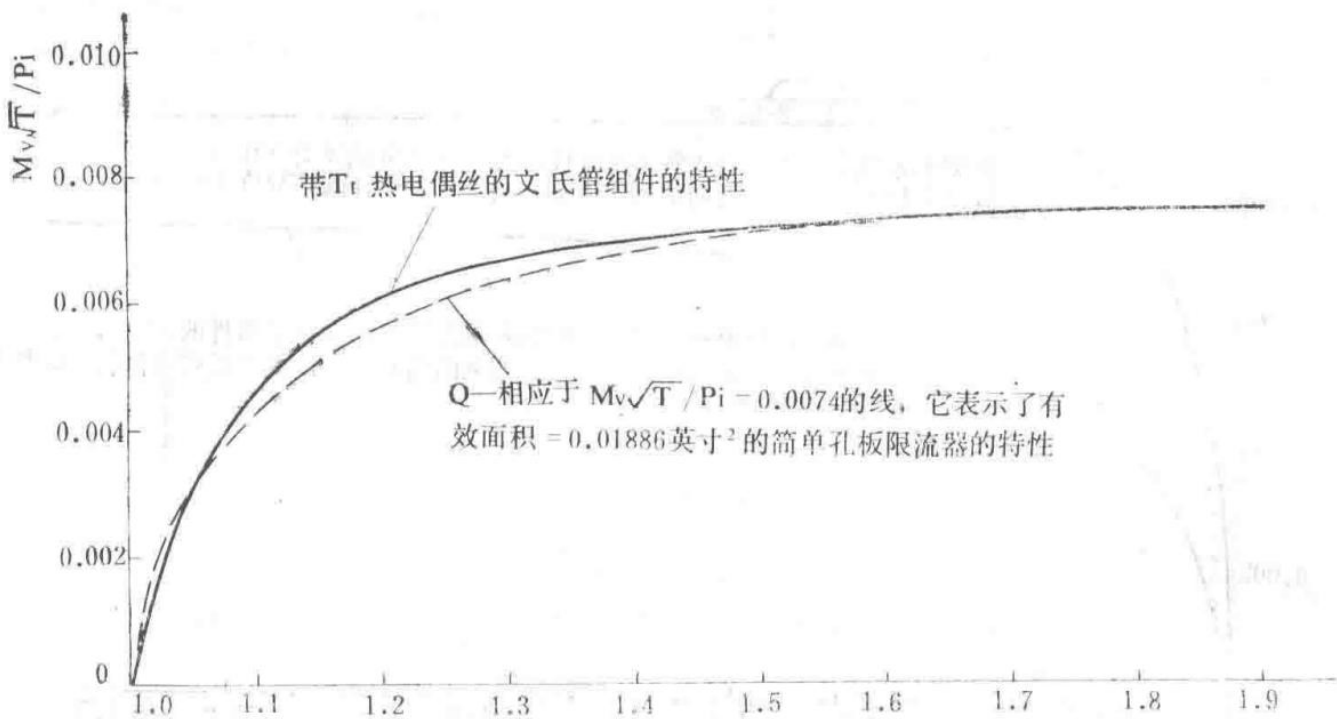


Figure 2: Comparison of characteristics between a three-element Venturi tube assembly (with thermocouple wires) and a simple orifice-type restrictor

Comparison of flow characteristics for a Venturi tube with thermocouple wires and a simple orifice restrictor.

Flow separation in the Venturi throat has two effects:

1. It reduces pressure recovery in the Venturi diffuser, thereby increasing the choking pressure ratio to a value close to that of a plain orifice. The ejector's pumping effect is significantly impacted, and the secondary flow pressure ratio required to pump the same secondary mass flow increases from 1.25 to 1.9.
2. It reduces the flow coefficient, an effect that is inherently minor but clearly related to the above (1).

If the Venturi tube functions satisfactorily, then at a primary ejector pressure ratio of 4:1, a Venturi pressure ratio of 1.25:1 would cause choking.

### 3. Possible Improvement Methods

Optimizing the size and position of the primary ejector nozzle may improve ejector performance. This would inevitably lead to some improvements in the Sangamo thermocouple assembly.

By reviewing the current ejector performance and comparing it with past experience, it is evident that reducing the secondary airflow can significantly improve the performance of this sonic thermocouple. Reducing the number of thermocouples (and thus the number of Venturi tubes) from 3 to 2 is an easy way to achieve this. While the effect may not be as significant as perfecting the Venturi tube itself, it is still valuable.

To verify performance, tests were conducted using an orifice plate with an effective area of 0.0187 in<sup>2</sup> instead of the Sangamo tube. Ejector characteristic tests were performed for each of the 2,3 orifice restrictors.

Assuming Cd = 0.74 as a first estimate, the diameters of the two orifices were 0.18 inches and 0.147 inches, respectively.

It must be noted that if reducing the number of thermocouples from 3 to 2 results in significant improvement, the size and position of the primary ejector nozzle must be re-examined to achieve a new optimal configuration. For example, if a smaller secondary flow is required, a larger primary ejector nozzle can be installed.

During this test, a Sangamo tube equipped with Venturi components but without thermocouple wires was also tested to verify whether the primary influence is the small airflow passage at the Venturi inlet or, as suspected,

the presence of the thermocouple wires.

## Part Eight

Technical Design Report	TDR4115
Spey MK202 T Thermocouple and Inlet Guide Vane System Error	

## Abstract

Based on the "Initial Technical Requirements," the technical specifications for each device in the inlet guide vane system were provided, specifying the maximum allowable error for each device. From these allowable errors, the overall maximum possible error for the entire inlet guide vane system was estimated.

The maximum error expressed in  $N / \sqrt{T_1}$  is as follows:

- At  $T_1 = 203\text{ K}$ :  $\pm 13 \text{ } N / \sqrt{T_1}$
- At  $T_1 = 288\text{ K}$ :  $\pm 9 \text{ } N / \sqrt{T_1}$  (steady state)
- At  $T_1 = 480\text{ K}$ :  $\pm 5 \text{ } N / \sqrt{T_1}$
- At  $T_1 = 347\text{ K}$ :  $-16 \text{ } N / \sqrt{T_1}$  (transient state)

## Introduction

The errors in the  $T_1$  signal used in the  $N / \sqrt{T_1}$  device have been estimated based on the individual errors of each component.

Steady-state errors:

- Thermocouple:  $\pm 3.5\text{ C}$
- Position feedback device:  $\pm 2.25\text{ C}$
- Amplifier:  $\pm 1\%$
- Linkage device:  $\pm 0.5\text{ C}$
- Total maximum possible error:  $\pm 7.25\text{ C}$

The corresponding error expressed in  $N / \sqrt{T_1}$  is as follows:

T Thermocouple (K)	203	288	480
Maximum $N / \sqrt{T_1}$ Error	13	9	5

Transient-state error:

At  $T_1 = 347\text{ K}$ , the thermocouple response is  $9.9\text{ C}$ . After a transient change in  $T_1$ , the maximum possible error is:

$$\text{Total maximum error} = (9.9 + 7.25) \text{ C}$$

Summation of transient and steady-state errors.

The corresponding  $N / \sqrt{T_1}$  error is 16.

## Part Nine

Technical Design Report	TDR4147
Spey MK202 Estimation of Allowable Inlet Temperature Variation Rate	

## Abstract

To ensure satisfactory performance of the inlet guide vane and bleed valve control systems, this report estimates the allowable variation rate of  $T_1$ .

During certain maneuvers,  $T_1$  variation rates as high as  $5^\circ\text{C}/\text{second}$  (increase or decrease) may be encountered (see Section 3 of this report).

Under flight conditions where high  $T_1$  decay rates may occur, the analysis indicates that the control system can tolerate variation rates up to 12% per second without encountering choking, stall, or flutter issues.

In the absence of test data, to determine the allowable deviation of the inlet guide vanes from the nominal schedule without causing compressor surge, the range of  $N / \sqrt{T_1}$  deviation from the nominal value is estimated to be -10 to -50  $N / \sqrt{T_1}$  for states where  $T_1$  may vary significantly (see Table on Page 424). The allowable  $T_1$  increase rate can only be evaluated after determining the allowable deviation from the nominal regulation schedule. Phase-lead circuits must be incorporated into the  $T_1$  sensing system to ensure the system can respond to  $T_1$  variation rates of  $5^\circ\text{C}/\text{second}$ , thereby keeping the maximum allowable deviation of  $N / \sqrt{T_1}$  below 20. With a circuit time constant of 1 second, a  $T_1$  increase rate of  $5^\circ\text{C}/\text{second}$  and an inlet guide vane schedule limit of -15  $N / \sqrt{T_1}$  are permissible.

It must be noted that at  $T_1 = 200 \text{ K}$ , if the tolerances of all components in the  $T_1$  system are assumed to be at their maximum specified values, the cumulative error may exceed the allowable deviation of -10  $N / \sqrt{T_1}$  from the nominal regulation schedule, potentially causing surge under normal steady-state  $T_1$  conditions. However, if no surge occurs, a deviation of -13  $N / \sqrt{T_1}$  is still considered acceptable.

## 1. Introduction

The customer has indicated that  $T_1$  variation rates may exceed 1.1% per second. During certain maneuvers,  $T_1$  variation rates of up to  $5^\circ\text{C}/\text{second}$  may be experienced. Examples include:

1.  $T_1$  increase: From 50,000 feet at  $M_\infty = 1.8$  diving to 43,000 feet at  $M_\infty = 2.0$ .
2.  $T_1$  decrease: During a rapid throttle reduction at  $M_\infty = 2.0$ .

During  $T_1$  changes, the time constant of the thermocouple causes the  $T_1$  signal fed into the inlet guide vane scheduling device to lag behind the actual  $T_1$ , resulting in an incorrect inlet guide vane and bleed valve schedule. This error is compounded by steady-state errors arising from manufacturing tolerances in the thermocouple and amplifier, as well as adjustment limitations in the  $N / \sqrt{T_1}$  device on the test rig.

This report estimates the allowable  $T_1$  variation rate for the inlet guide vane scheduling device that does not cause compressor surge or choking-induced stall flutter.

## 2. Data

### 2.1 High-Pressure Compressor Inlet Guide Vane Schedule

The nominal inlet guide vane schedule is set to a  $40^\circ$  angle at  $N / \sqrt{T_1} = 595$  and a  $0^\circ$  angle at  $N / \sqrt{T_1} = 695$ .

Note: The original schedule corresponded to 592 and 655. This change was made because the original schedule data could not meet requirements when using  $T_2 / T_1$  measurements and expressing the regulation schedule in terms of  $N / \sqrt{T_2}$ .

### 2.2 Deviation from Nominal Schedule

Earlier research expressed the allowable deviation from the nominal schedule in terms of  $T_1$  signal error, as follows:

$T_1$  at 200 K: Corresponding  $T_1$  limit values are -18 C and +6.2 C.

Allowable  $T_1$  signal error limits.

In states where  $T_1$  decreases, the  $T_1$  signal delay should not exceed 18%, while during  $T_1$  increases, the delay should not exceed 6.2%.

At  $T_1 = 335$  K ( $M_\infty = 2.0$ , 50,000 feet, cold day), the corresponding values become -30°C and +10.4°C.

These figures are based on current allowable deviations provided by the compressor and development departments to prevent compressor choking and surge. Specifically, 1.031 is derived from the allowable deviation of  $-10 N / \sqrt{T_1}$ . To determine the actual deviation from the nominal schedule and subsequently assess the dispersion of this deviation, test data is required. The extreme values considered in this report reach up to  $-50 N / \sqrt{T_1}$ .

## 2.3 $T_1$ Measurement System Tolerances

- \*\*Allowable Manufacturing Tolerances:\*\*
- Thermocouple and connecting wires:  $\pm 3$  C
- Amplifier:  $\pm 1$  C
- Position feedback device:  $\pm 2.25$  C
- Linkage device:  $\pm 0.5$  C
- \*\*Test Rig Adjustment Range:\*\*
- For an inlet guide vane angle of 40°, the maximum adjustment tolerance of the  $N / \sqrt{T_1}$  device on the test rig, corresponding to  $T_1$  variation, is approximately 4°C across most  $T_1$  operating regions.

These adjustment limits include errors from the position feedback and linkage devices. Therefore, considering the amplifier and thermocouple errors, the maximum possible error is  $\pm 8$  C.

This exceeds the +6.2 C error specified in Section 2.2 for  $T_1 = 200$  K. This implies that even if the maximum allowable deviation of the inlet guide vane schedule from the nominal schedule does not exceed  $-10 N / \sqrt{T_1}$ , surge may still occur under steady-state  $T_1$  conditions.

## 2.4 Sonic Thermocouple Time Constant

The transfer function of the sonic thermocouple can be expressed as:

$$1 + a D, (1 + R_1 D)(1 + R_2 D),$$

Transfer function of the sonic thermocouple, where  $a$ ,  $R_1$ , and  $R_2$  depend on the inlet total pressure  $P_1$ .

## 3. Analysis

### 3.1 $T_1$ Decrease

As noted by the customer (see Introduction), high  $T_1$  decay rates can occur during high Mach number rapid throttle reductions and abrupt aircraft deceleration. For studying the inlet guide vane control system, the throttle is only reduced to the idle position, and the engine is not shut down. Above 50,000 feet, the difference between maximum and idle states is minimal, so it is not considered when analyzing high  $T_1$  decay rates.

The maximum thermocouple time constant occurs at low  $P_1$  values. Therefore, the state at 50,000 feet and  $M_\infty = 2.0$  is studied, where the thermocouple time constants are  $R_1 = 0.66$  seconds,  $R_2 = 17.9$  seconds,  $a = 16.75$  seconds, and  $T_1 = 335$  K.

From Section 2.2, the maximum allowable deviation for  $T_1$  decrease is  $30.0^{\circ}\text{C}$ . From Section 2.3, the maximum steady-state error is  $8.0^{\circ}\text{C}$ . Therefore, the maximum allowable delay during a transient state is  $\square\square\square = 22.0\text{ C}$ . For a constant  $T_1$  variation rate of  $x\text{ C/second}$ , the delay is given by:

$$= (R_1 + R_2 - a) x$$

Equation for delay in  $T_1$  signal during transient state.

Thus, for this condition, the maximum permissible rate of change (  $X\Box\Box\Box$  ) is 12.1  $\Box$  per second.

## 3.2 $T_1$ Increase

Under the same condition, high  $T_1$  rates of change occur during high Mach number flight. During a dive, altitude decreases and ambient temperature rises.

Therefore, for  $M\Box = 2.0$ , when diving from 70,000 feet to 43,000 feet (below 43,000 feet, due to high  $R_1$ , the thermocouple response characteristics tend to remain unchanged), the permissible  $T_1$  rate of change is estimated using a method similar to that in Section 3.1.

As described in Section 2.2, assuming the tolerance range for deviation from the nominal inlet guide vane scheduling is from  $-10 N / \sqrt{T_1}$  to  $-50 N / \sqrt{T_1}$ , the  $T_1$  rate of change was estimated. The results are shown in the table below.

### Estimation Results of Permissible $T_1$ Increase Rate

For  $T_1 = 355 \Box$ ,  $M\Box = 2.0$  (amplifier without phase-lead circuit):

Permissible  $T_1$  Increase Rate Estimation Results

Maximum Permissible Deviation from Nominal (Assumed)		Permissible Delay Considering Steady-State Error	Permissible $T_1$ Rate of Change ( $^{\circ}\text{C}/\text{s}$ )			
$N / \sqrt{T_1}$	Expressed as $\Delta T$	$\Delta T - 8\Box$	70,000 ft	60,000 ft	50,000 ft	<43,000 ft
-10	10.4	2.4	0.8	1.1	1.3	1.4
-20	23.4	15.4	5.4	7.4	8.5	8.9
-30	36.9	28.9	10.2	13.9	16.0	16.7
-40	48.5	40.5	14.3	19.4	22.4	23.4
-50	64.3	56.3	19.8	27.0	31.1	32.6

## 4. Discussion

The estimation in Section 3.1 indicates that under conditions with a high  $T_1$  decrease rate, the  $T_1$  measurement system's response permits a decrease rate on the order of 5  $\Box$  per second.

As noted in Section 2.3, when the inlet guide vanes deviate from the nominal scheduling by the permissible limit of  $-10 N / \sqrt{T_1}$  and all components of the  $T_1$  measurement system operate at their specified maximum errors, the total error at  $T_1 = 200 \Box$  will exceed the permissible value, which is unacceptable for  $T_1$  transient processes.

Furthermore, from the table above, under conditions of high  $T_1$  rate of change, a deviation of  $-20 N / \sqrt{T_1}$  from the nominal inlet guide vane scheduling is required to achieve a  $T_1$  rate of change of 5  $\Box$  per second, which is twice the current tolerance.

By introducing certain phase-lead circuits in the amplifier, if further testing shows that the safe deviation from the nominal scheduling is less than  $20 N / \sqrt{T_1}$ , the control system can be improved. This would allow an increased permissible  $T_1$  rate of change in all conditions, including  $T_1$  decrease states. For example, with a phase-lead circuit having a time constant of 1 second for a constant-slope input, the permissible  $T_1$  increase rate can reach 5  $\Box$  per second, while the permissible deviation from the nominal inlet guide vane scheduling is  $-15 N / \sqrt{T_1}$ .

Note: When considering the maximum total tolerance, this report uses the arithmetic sum of individual tolerances. For approval at guarantee points, the normal practice is to use the root mean square of individual errors to determine the maximum total error (when considering instrument errors, etc.).

In this application, the total steady-state error is  $\pm 5.1 \text{ } \square$ , rather than the  $\pm 8\%$  obtained by arithmetic summation. The result of this change is that a  $T_1$  increase rate of  $5 \text{ } \square \text{ per second}$  is permissible, and for such a  $T_1$  increase rate, the maximum permissible deviation from the nominal scheduling for the inlet guide vanes is  $-16.5 \text{ N} \square / \sqrt{T_1}$  (without phase-lead circuit) and  $-12 \text{ N}_{11} / \sqrt{T_1}$  (with phase-lead circuit).

#### Technical Design Report

Technical Design Report	TDR 4164
Spey MK202 Estimation of Inlet Temperature Rate of Change Limits to Prevent High-Pressure Compressor Surge	

First Edition, December 22, 1965

## Abstract

An estimation was made of the maximum rate of change of inlet temperature  $T_1$  suitable for continuous operation and the time limits for higher rates of change. The curves in Figure 1 provide:

- The estimated maximum permissible continuous rate of change and time limits for higher rates of change to prevent compressor surge. The maximum permissible deviation from the nominal scheduling of the inlet guide vanes and bleed valves is  $-20 \text{ N} \square / \sqrt{T_1}$ . This value is derived from high-pressure compressor test data and the most severe inlet distortion.
- For comparison, assuming the currently cited data of  $1.1 \text{ } \square \text{ per second}$  as the specified higher rate of change, the corresponding time limit just permits continuous operation.

This report supplements the TDR4147 report, which provides extensive data on this research topic. As noted in TDR4147, the  $T \square$  rates of change cited in this report are also applicable to preventing compressor choke, stall, and flutter.

## 1. Data

### 1.1 Maximum Tolerance for Deviation from Nominal Scheduling of Inlet Guide Vanes and Bleed Valves to Prevent High-Pressure Compressor Surge

Based on bench tests of the worst-case inlet pressure variations, the compressor development department estimated that the deviation from the nominal scheduling should not exceed  $-20 \text{ N} \square / \sqrt{T_{10}}$ . Under given conditions, considering the variation in  $T_2 / T_1$ , this report uses a maximum deviation of  $-20 \text{ N} \square / \sqrt{T \square}$ .

### 1.2 Permissible Error of $T_1$ Signal in $N \square / \sqrt{T_1}$ Scheduling Device

In TDR4147, after considering the maximum instrument error and the adjustment limits of the  $N \square / \sqrt{T_1}$  device, a deviation of  $-20 \text{ N} \square / \sqrt{T \square}$  from the nominal scheduling was found to correspond to a  $T_1$  signal error of  $15.4 \text{ } \square$  in the  $N \square / \sqrt{T_1}$  device.

### 1.3 Device Time Constants

The thermocouple time constant is the same as that used in TDR4147.

In addition, the following time constants were used in the analysis:

- $T_1$  bogie in  $N / \sqrt{T_1}$  device: 1.15 seconds
- Amplifier: 0.02 seconds

## 2. Analysis

For various constant-slope inputs to the  $T_1$  thermocouple, the signal delay in the  $N / \sqrt{T_1}$  device was estimated as it increased over time to the final steady-state error.

From these estimations, the following data were obtained:

- The steady-state error produced by the maximum constant-slope input is less than 15.4  $\square$ .
- For constant-slope inputs, the time required to reach a 15.4  $\square$  delay is greater than the above value.

Additionally, the following data were obtained:

Assuming a continuous rate of change of 1.1  $\square$  per second as the current requirement, the time limits for higher rates of change can be determined.

The results are shown in Figure 1.

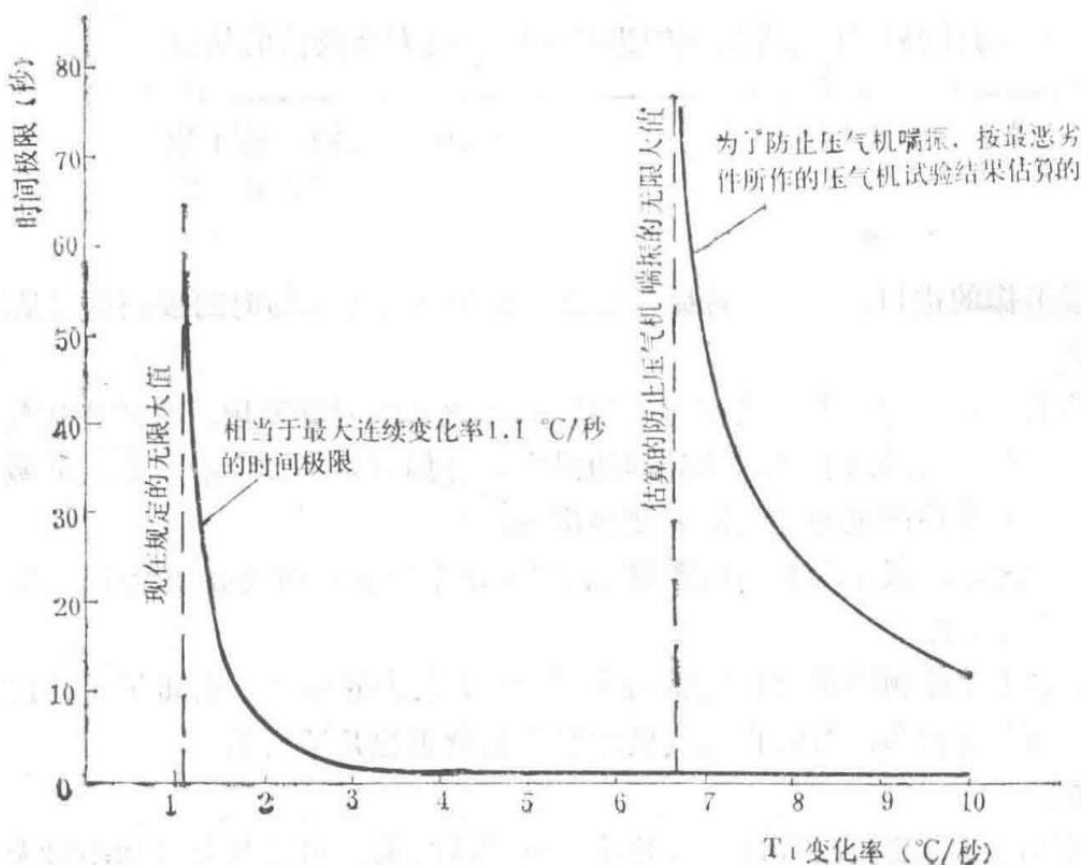


Figure 1 Estimation of Spey MK202 Inlet Temperature Rate of Change Limits

Graph showing the estimated permissible continuous and transient inlet temperature ( $T_1$ ) rate of change limits for the Spey MK202 engine to prevent compressor surge.

## Spey MK202 Engine Inlet Sensing Component Initial Technical Requirements – March 10, 1965

### 1.1 Description of Technical Requirements

An electrical signal representing the inlet temperature rate  $T$  must be provided to the engine control amplifier. For this purpose, a device consisting of three thermocouple junctions connected in parallel is required. When  $T$  changes, the measurement system delay must be minimized to meet transient state requirements. Each thermocouple junction must be placed at the throat of a sonic orifice. The entire assembly is installed inside a duct, with engine inlet air induced through the duct by an ejector. In static conditions, due to the low pressure at the compressor inlet, an ejector is necessary to prevent backflow.

## 1.2 Temperature and Pressure

The ranges of inlet temperature and total pressure during engine operation are as follows:

1. Temperature: -77 °F to +207 °F
2. Sonic orifice throat pressure: 1.5 to 35 psi (absolute)

## 1.3 Accuracy

The entire thermocouple assembly and connecting wires, within the temperature range of -77 °F to +207 °F, shall not deviate from the table values by more than  $\pm 0.12$  millivolts. This is related to the selection and stock of the thermocouple materials (Nickel-Chromium/Nickel-Aluminum alloy).

Thermocouple Electromotive Force vs. Temperature

Temperature (°C)	Electromotive Force (mV)	Temperature (°C)	Electromotive Force (mV)
-80	-2.87	-81	-2.90
-40	-1.50	-41	-1.54
0	-0.00	-1	-0.04
40	1.61	41	1.65
80	3.26	81	3.30
120	4.92	121	4.96
160	6.53	161	6.57
200	8.13	201	8.17
210	8.54	211	8.58

## 1.4 Transient State Accuracy

For a constant  $T_1$  rate of change of 1.2 °F per second, the measurement error (excluding the error specified in Section 1.3) over 2 minutes shall not exceed:

- At -70 °F:  $\pm 5.7$  °F
- At +15 °F:  $\pm 8.2$  °F
- At +155 °F:  $\pm 12.2$  °F

## 1.5 Sonic Orifice Dimensions

- Venturi throat diameter: 0.1 inches
- Venturi outlet diameter: 0.16 inches
- Venturi inlet diameter: 0.23 inches
- Venturi diffuser length: 0.43 inches

# Spey MK202 Servo Motor and Tachogenerator Initial Technical Requirements – July 5, 1966

## 1.1 System Description

The amplifier receives a signal from the engine inlet thermocouple, which is appropriately amplified to drive the servo motor. The motor output shaft rotates to provide inlet guide vane and bleed valve control system movement according to the inlet temperature schedule.

The motor output shaft also actuates a position feedback device, which outputs a signal back to the amplifier. When this signal equals the thermocouple signal, the amplifier has no output, and the servo motor output shaft stops rotating, maintaining the inlet temperature schedule requirement. The speed feedback signal for the amplifier is provided by a tachogenerator mounted on the servo motor to prevent overshoot of the motor output shaft position.

## 1.2 Device Description

The servo motor and tachogenerator form a complete unit. The relative position of the servo motor output shaft shall be directly proportional to the engine inlet total temperature. When voltage is applied to the motor from the amplifier, the motor shall rotate. The direction of rotation is determined by the phase angle.

The tachogenerator is a 400 Hz induction type.

- At 20 °C and 1000 rpm, the output is  $3 \pm 0.5$  V (RMS).
- At 20 °C, the maximum residual voltage is 25 mV.
- At 20 °C and 3000 rpm, the phase shift from the reference phase is  $10^\circ$ .
- Over the entire range of environmental conditions, the maximum permissible output variation is 0.31% °C.
- Residual voltage variation over the entire range of environmental conditions is insignificant.
- At 20 °C and a torque load of 50 g·cm, the starting voltage is 30% lower than the control voltage.

## 1.3 Power Supply Voltage

1. Tachogenerator: Excitation voltage of 115 V, 400 Hz, single-phase AC.
2. Servo Motor: Reference power supply voltage of 115 V, 400 Hz, single-phase AC. Control winding voltage of 13–0–13 V AC, with a  $90^\circ$  phase difference from the reference winding. Maximum locked-rotor current: Reference winding: 200 mA, Control winding: 840 mA.

## 1.4 Maximum Starting Torque

In the locked-rotor condition, the servo motor requires a maximum starting torque of 172 g·cm.

## 1.5 Rotor Travel

From start to lock, the rotor shaft has a full travel of 16 turns, and the motor can maintain its full power state during prolonged lock conditions.

## 1.6 Environment

The device is installed on the engine and is fully immersed in engine fuel (thus, internal oil immersion is possible). The fuel temperature range is:

- Operating:  $-40$  °C to  $+100$  °C

- Non-operating: -70 °F to -40 °F and +100 °F to +150 °F

Maximum fuel pressure: 260 psi (gauge) (relief valve pressure). The device is suitable for operation in the following fuels:

- AVTUR (Eastwood IP-1)
- AVTAG (JP-4)
- AVCAT (JP-5)

The above fuels may or may not contain 0.10 to 0.15% (by volume) antifreeze agent.

## 1.7 Fuel Contamination

The device shall operate well with the generally contaminated fuel specified in Section 1.6, and durability tests shall be revised as necessary to comply with the test standards agreed upon by Rolls-Royce and the user based on specific usage conditions.

# Spey MK202 Position Feedback Device Initial Technical Requirements – June 14, 1966

## 1.1 Function of the Device

The position feedback device is part of the engine inlet guide vane and bleed valve control system based on the engine inlet temperature  $T_1$ . Its function is to generate an electrical signal whose voltage is a function of angular displacement. When this signal is fed back to the amplifier and balances the signal generated by the thermocouple, the actuator motor stops rotating.

## 1.2 Displacement

- The device has an angular displacement.
- The maximum travel on each side of the nominal zero point is 14° ± 5' (i.e., total travel is 29° ± 10').

## 1.3 Output

Figure 1 illustrates the required 'effective' characteristics of the device. The entire travel is linear. When the specified reference voltage is  $3 \pm 5\%$  volts (RMS), the impedance of the feedback and output windings is 12 kΩ, and the ambient temperature is  $22^\circ \text{C} \pm 0^\circ \text{C}$ , the design center of the output characteristic slope is 0.112 volts/volt (reference)/degree (mechanical)  $\pm 5\%$ .

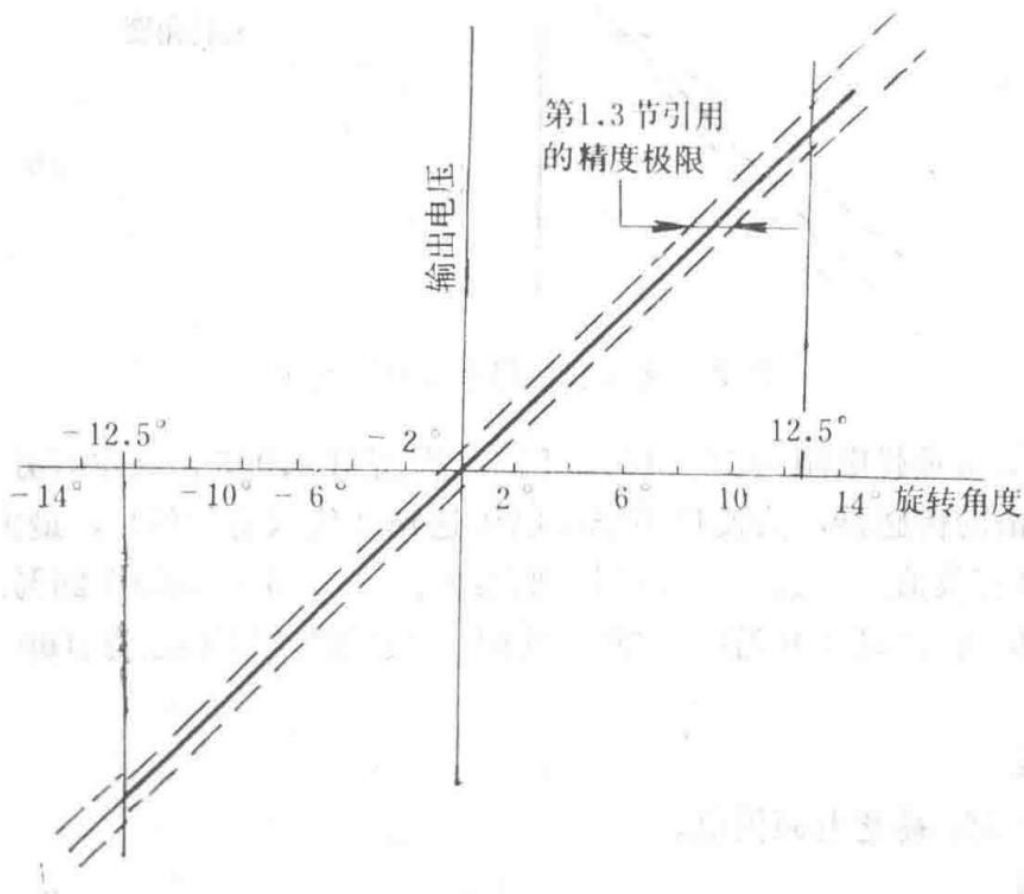


Figure 1 Nominal Effective Characteristics with Accuracy Limits for Control System Requirements

Graph showing the nominal output characteristics of the device with accuracy limits under specified conditions.

Under all permissible conditions in this document, the excitation voltage required for the excitation winding does not exceed 20 volts (RMS).

The accuracy range, shown by dashed lines, indicates that for deviations from the nominal value curve within  $\pm 12.5^\circ$ , the allowable variation is  $\pm 15'$ , and within  $\pm (12.5^\circ \text{ to } 14^\circ)$ , the allowable variation is  $\pm 18'$ . This applies to any combination of ambient temperatures from  $+100^\circ \text{C}$  to  $-26^\circ \text{C}$  and permissible power supply or impedance conditions specified in this document. Between  $-26^\circ \text{C}$  and  $-54^\circ \text{C}$ , the allowable tolerance increases proportionally, reaching  $\pm 30'$  at  $-54^\circ \text{C}$ .

Throughout the operational lifespan, all devices must remain within the accuracy limits relative to the nominal slope.

For linkage devices within the control system, a slope variation of  $\pm 5\%$  between devices can be accommodated by adjustments to meet the performance shown in Figure 1.

The slope variation is illustrated in Figure 2. The performance of any specific device may fall on or within any pair of accuracy limit lines of a nominal characteristic line in Figure 2. The pair of accuracy limit lines associated with any device should be specified such that the system can conform to the nominal characteristic limits shown in Figure 1 through internal adjustments. When linkage devices are adjusted based on their characteristic slope variations, their accuracy limits should still remain within the range shown in Figure 1.

## 1.4 System Impedance

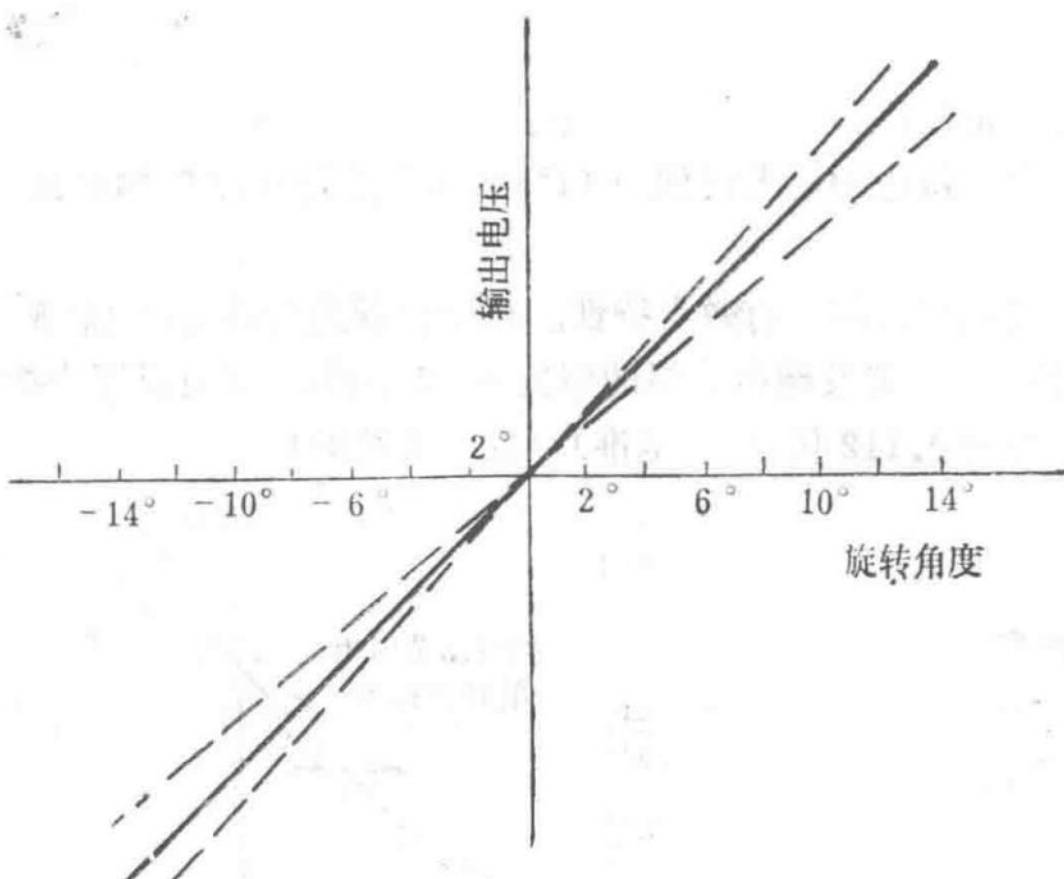


Figure 2 Permissible Variation of Nominal Characteristic Slope

Graph showing the permissible slope variations of the nominal characteristics.

The load resistance of the output and feedback windings is  $12 \pm 10\% \text{ k}\Omega$ , and it can be shunted with a  $0.005 \mu\text{F}$  capacitor.

For an adjusted sensor, to achieve a feedback winding voltage of 3 volts (RMS), the maximum excitation voltage must be less than or equal to 20 volts (RMS), applied to an impedance approximately equal to  $(330 + 740j) \pm 20\% \text{ ohms}$ .

The output winding impedance is  $(280 + 900j) \pm 20\% \text{ ohms}$ , and the feedback winding impedance is  $(60 + 30j) \pm 20\% \text{ ohms}$ .

## 1.5 Power Supply

The device is powered by a  $400 \pm 5\% \text{ Hz}$  power supply.

## 1.6 Environment

The device is installed on the engine and is fully immersed in engine fuel (thus, internal components may be oil-immersed). The fuel temperature range and maximum fuel pressure are as follows:

- Maximum fuel pressure: 260 psi (gauge) (thermal relief valve pressure)
- The device is suitable for operation in the following fuels:
  - AVTUR JP.1
  - AVTAG JP.4
  - AVCAT JP.5

The fuel may or may not contain 0.1 to 0.15% (by volume) of anti-icing additive.

## 1.7 System Compensation

The feedback device includes a temperature-compensated feedback winding. The excitation voltage is derived from a feedback amplifier that maintains a constant output from the feedback winding.

# Section Fourteen

## Initial Technical Requirements for Spey MK202 Inlet Guide Vane and Bleed Valve Control Amplifier – 13 October 1966

### 1.1 Circuit Description

The device includes a circuit that adjusts the inlet guide vanes and bleed valve via an actuator motor based on the engine inlet temperature.

### 1.2 Inlet Guide Vane and Bleed Valve Operation

#### 1.2.1 Requirements

- The inlet guide vane and bleed valve circuit amplifies the  $T_1$  thermocouple signal from the inlet and provides power to the servo motor, causing the output shaft to rotate to a position proportional to the engine inlet total temperature. The output shaft is directly connected to an angular displacement sensor and meets the requirements of the inlet guide vane and bleed valve system scheduled by inlet temperature.
- If  $T_1$  increases, the motor rotates clockwise (viewed from the output shaft), causing the angular position sensor to rotate counterclockwise (viewed from the shaft). The gear ratio between the motor and sensor is approximately 730:1.

#### 1.2.2 Inlet Temperature Range

The inlet temperature range for the operation of the inlet guide vane and bleed valve circuit is  $-77^{\circ}\text{F}$  to  $+207^{\circ}\text{F}$ . This range causes the sensor to rotate  $\pm 14^{\circ}$  around the electrical zero point.

#### 1.2.3 Thermocouple Characteristics

Refer to the technical requirements for the engine inlet sensing assembly.

#### 1.2.4 Accuracy Requirements

- The sensor position accuracy, represented by the AC synchronous output voltage, equals  $\pm 2\%$  of the sensed temperature  $T_1$ .
- Time delay is no more than 25 milliseconds.

## 1.2.5 Thermocouple Resistance

- The resistance of the thermocouple and wiring does not exceed 10 ohms.
- At the control reference temperature, the thermocouple current does not exceed 2.5 microamperes.

## 1.2.6 Effect of an Open Thermocouple

If one thermocouple is open-circuited, the circuit maintains its accuracy without being affected.

## 1.2.7 Effect of Grounding on Thermocouple

- If either side of the  $T_1$  thermocouple is grounded, the accuracy specified in section 1.2.4 is maintained.
- If one side of the thermocouple has a leakage resistance to ground of  $10\text{ k}\Omega$  and the other side is grounded, the accuracy requirements specified in section 1.2.4 are still met.

## 1.2.8 Motor Output

For a  $1\text{ VDC}$  error, the motor signal phase voltage is at least 10 volts (RMS), and for a  $2\text{ VDC}$  error, the signal phase voltage is at least 18 volts (RMS). The maximum control voltage of the motor is  $26 \pm 5\%$  volts (RMS). At an error not exceeding  $4\text{ VDC}$ , the motor can deliver the specified full torque.

## 1.2.9 Motor Excitation Circuit

- The reference winding and excitation winding have a phase difference of  $90^\circ$ . When  $T_1$  increases, the motor rotates clockwise (viewed from the drive shaft).
- The average AC interference voltage on the motor balance signal winding is 0.5 volts (maximum).
- At rated voltage and frequency of the power supply, the motor reference voltage is  $115 \pm 5\%$  volts.

## 1.2.10 Sensor Circuit

- The amplifier device provides AC power for sensor excitation. The sensor output is phase-rectified within the amplifier. The system maintains an output accuracy within  $\pm 0.25\%$  across the ambient temperature range.
- For counterclockwise rotation of the sensor shaft, the phase-rectified signal has a positive slope.

The output and feedback winding load resistance is  $12 \pm 10\% \text{ k}\Omega$ , shunted by a  $0.005 \mu\text{F}$  capacitor.

## 1.2.11 Tachogenerator Circuit

- The tachogenerator load resistance is greater than  $2\text{ k}\Omega$ .
- The tachogenerator excitation voltage at the power supply frequency is  $115 \pm 10\%$  volts.
- The generator output is phase-adjusted and fed back to the amplifier as negative feedback to stabilize the control loop.

These circuits, along with other amplifier circuits (such as the  $T_8$  controller), are installed in a common fuel-cooled housing.

## 1.3 Requirements for Test Connector

There is a test connector for extracting the  $N/\sqrt{T}$  sensor position signal. At room temperature, with the rated sensor connected to a  $40\text{ k}\Omega$  resistor circuit, the connector outputs 0.5 volts/degree (mechanical), with an error of  $\pm 25\%$  of the sensor position.

## 1.4 Safety Circuit

A safety circuit is included in the N/(T) channel. In the event of a fault causing an open circuit in the motor, sensor, or thermocouple connections, an alarm device activates, and the motor stops at the position it was in before the fault occurred.

## 1.5 Power Supply

The amplifier operates on a single-phase power supply with a phase-to-ground voltage of 115 volts at 400 Hz. System accuracy is maintained with power supply voltage variations of  $\pm 10\%$  and frequency variations of  $\pm 5\%$ .

## 1.6 Cooling

Flowing fuel around the amplifier provides cooling. It should be noted that the fuel-containing housing is part of the entire device.

The following fuels are used:

- AVTUR JP.1
- AVTAG JP.4
- AVCAT JP.5

The fuel may or may not contain 0.10 to 0.15% (by volume) of anti-icing additive. The fuel temperature range is -40°C to +100°C. The maximum fuel flow rate is 55 gallons/hour. The maximum fuel pressure is 260 psi (thermal relief valve pressure).

## 1.7 Warm-Up

Under International Standard Atmosphere conditions, 20 seconds after engine start, or under cold conditions at -40°C, 45 seconds after start, the device tolerance increases by 50% compared to section 1.2.4. Normal accuracy is achieved within 2 minutes.

## 1.8 Cooling Conditions

The device must operate satisfactorily under the following fuel cooling and ambient temperature conditions as shown in Figure 1:

- At Mach 2.3, 60,000 feet, hot day:
  - Fuel inlet temperature: 62°C
  - Fuel inlet-to-outlet pressure difference: 55 psi
  - Air mass flow rate: 0.85 lb/s·ft<sup>2</sup>
  - Air temperature: 215°C
  - Installation base temperature: 280°C
  -
- At idle descent (Mach 1.0, 45,000 feet, hot day):
  - Fuel inlet temperature: 100°C
  - Fuel inlet-to-outlet pressure difference: 35 psi
  - Air mass flow rate: 0.119 lb/s·ft<sup>2</sup>
  - Air temperature: 5°C
  - Installation base temperature: 100°C

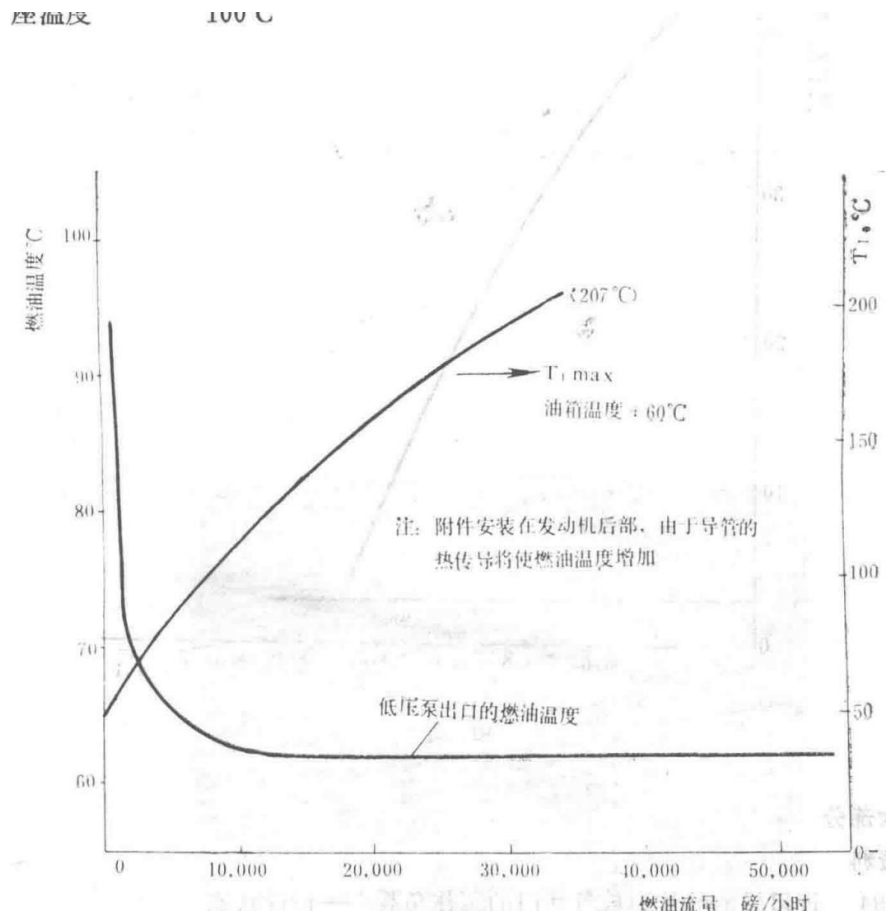


Figure 1

Graph depicting the relationship between fuel temperature, rotational speed, and time under various operating conditions.

## Section Fifteen

Typical Regulation Schedule for Spey MK202 Inlet Guide Vanes and Air Bleed Valve

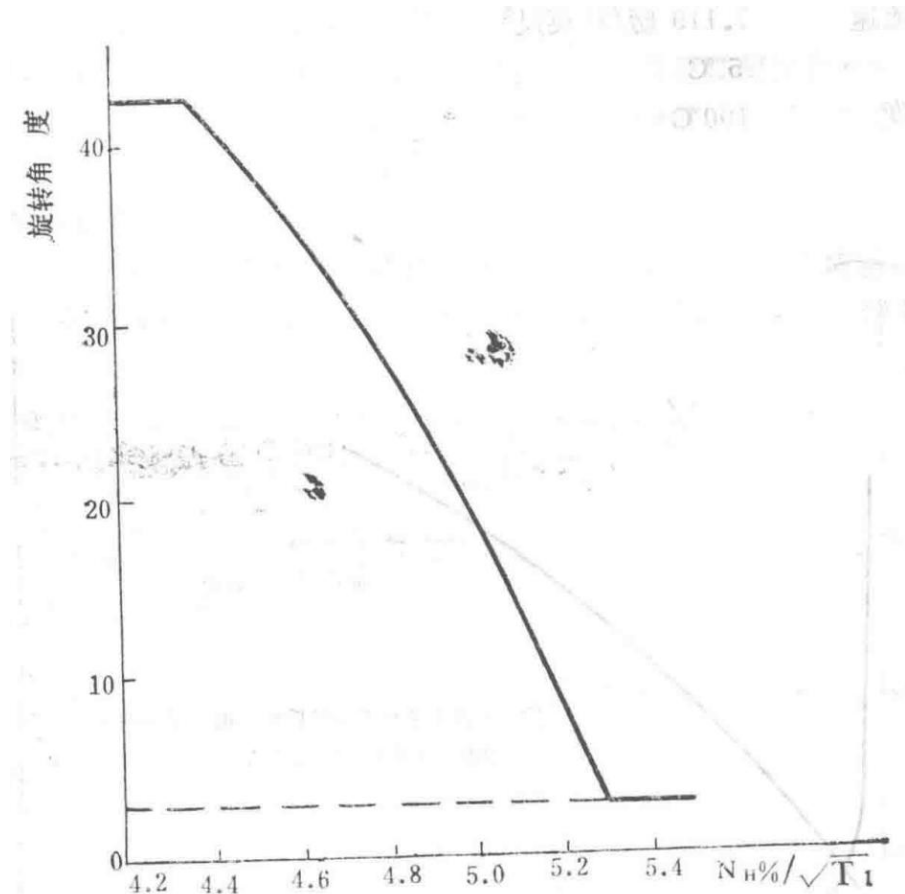


Figure 1

Graph depicting the relationship between rotational speed (expressed as  $N_H\% / \sqrt{T_1}$ ) and vibration amplitude for the Spey MK202 inlet guide vanes and air bleed valve.

## Section Sixteen

### References

- TDR794 Workload of Inlet Guide Vanes and Air Bleed Valve – Design Condition